

# PLASMA PHYSICS AND CONTROLLED NUCLEAR FUSION RESEARCH 1982

VOL. II



INTERNATIONAL ATOMIC ENERGY AGENCY, VIENNA, 1983



**PLASMA PHYSICS  
AND CONTROLLED  
NUCLEAR FUSION RESEARCH  
1982**

**VOL. II**

The following States are Members of the International Atomic Energy Agency:

AFGHANISTAN	HUNGARY	PHILIPPINES
ALBANIA	ICELAND	POLAND
ALGERIA	INDIA	PORTUGAL
ARGENTINA	INDONESIA	QATAR
AUSTRALIA	IRAN, ISLAMIC REPUBLIC OF	ROMANIA
AUSTRIA	IRAQ	SAUDI ARABIA
BANGLADESH	IRELAND	SENEGAL
BELGIUM	ISRAEL	SIERRA LEONE
BOLIVIA	ITALY	SINGAPORE
BRAZIL	IVORY COAST	SOUTH AFRICA
BULGARIA	JAMAICA	SPAIN
BURMA	JAPAN	SRI LANKA
BYELORUSSIAN SOVIET SOCIALIST REPUBLIC	JORDAN	SUDAN
CANADA	KENYA	SWEDEN
CHILE	KOREA, REPUBLIC OF	SWITZERLAND
COLOMBIA	KUWAIT	SYRIAN ARAB REPUBLIC
COSTA RICA	LEBANON	THAILAND
CUBA	LIBERIA	TUNISIA
CYPRUS	LIBYAN ARAB JAMAHIRIYA	TURKEY
CZECHOSLOVAKIA	LIECHTENSTEIN	UGANDA
DEMOCRATIC KAMPUCHEA	LUXEMBOURG	UKRAINIAN SOVIET SOCIALIST REPUBLIC
DEMOCRATIC PEOPLE'S REPUBLIC OF KOREA	MADAGASCAR	UNION OF SOVIET SOCIALIST REPUBLICS
DENMARK	MALAYSIA	UNITED ARAB EMIRATES
DOMINICAN REPUBLIC	MALI	UNITED KINGDOM OF GREAT BRITAIN AND NORTHERN IRELAND
ECUADOR	MAURITIUS	UNITED REPUBLIC OF CAMEROON
EGYPT	MEXICO	UNITED REPUBLIC OF TANZANIA
EL SALVADOR	MONACO	UNITED STATES OF AMERICA
ETHIOPIA	MONGOLIA	URUGUAY
FINLAND	MOROCCO	VENEZUELA
FRANCE	NAMIBIA	VIET NAM
GABON	NETHERLANDS	YUGOSLAVIA
GERMAN DEMOCRATIC REPUBLIC	NEW ZEALAND	ZAIRE
GERMANY, FEDERAL REPUBLIC OF	NICARAGUA	ZAMBIA
GHANA	NIGER	
GREECE	NIGERIA	
GUATEMALA	NORWAY	
HAITI	PAKISTAN	
HOLY SEE	PANAMA	
	PARAGUAY	
	PERU	

The Agency's Statute was approved on 23 October 1956 by the Conference on the Statute of the IAEA held at United Nations Headquarters, New York; it entered into force on 29 July 1957. The Headquarters of the Agency are situated in Vienna. Its principal objective is "to accelerate and enlarge the contribution of atomic energy to peace, health and prosperity throughout the world".

© IAEA, 1983

Permission to reproduce or translate the information contained in this publication may be obtained by writing to the International Atomic Energy Agency, Wagramerstrasse 5, P.O. Box 100, A-1400 Vienna, Austria.

Printed by the IAEA in Austria  
June 1983

NUCLEAR FUSION SUPPLEMENT 1983

PLASMA PHYSICS  
AND CONTROLLED  
NUCLEAR FUSION RESEARCH  
1982

PROCEEDINGS OF THE  
NINTH INTERNATIONAL CONFERENCE ON PLASMA PHYSICS  
AND CONTROLLED NUCLEAR FUSION RESEARCH  
HELD BY THE  
INTERNATIONAL ATOMIC ENERGY AGENCY  
IN BALTIMORE, 1-8 SEPTEMBER 1982

*In three volumes*

VOL. II

INTERNATIONAL ATOMIC ENERGY AGENCY  
VIENNA, 1983

PLASMA PHYSICS AND CONTROLLED NUCLEAR FUSION RESEARCH 1982

IAEA, VIENNA, 1983

STI/PUB/626

ISBN 92-0-130183-9

## FOREWORD

Considerable progress towards demonstrating the feasibility of controlled fusion as well as economically favourable fusion reactor characteristics was reported at the Ninth IAEA Conference on Plasma Physics and Controlled Nuclear Fusion Research. This progress extends to all approaches to controlled fusion and fusion technology.

The Conference was organized by the Agency in co-operation with the United States Department of Energy, with the assistance of the Princeton Plasma Physics Laboratory. It took place on 1–8 September, 1982, in Baltimore, Maryland, USA, and was attended by 488 participants and 145 observers from 31 countries and five international organizations. One hundred and forty-seven papers were presented at the technical sessions, including two poster sessions. They included contributions on theory, open and closed magnetic confinement systems, inertial confinement systems, and related technology. The traditional Artsimovich Memorial Lecture was given at the beginning of the Conference.

These Proceedings, which include all the technical papers and four conference summaries, are published in English as a supplement to the IAEA journal, *Nuclear Fusion*.

The Agency promotes close international co-operation among plasma and fusion physicists and engineers of all countries by organizing these periodic conferences on controlled nuclear fusion and by holding seminars, workshops and specialists' meetings on appropriate topics. It is hoped that the present publication, as part of these activities, will contribute to the rapid demonstration of fusion power as one of the world's future energy resources.

### **EDITORIAL NOTE**

*The papers and discussions have been edited by the editorial staff of the International Atomic Energy Agency to the extent considered necessary for the reader's assistance. The views expressed and the general style adopted remain, however, the responsibility of the named authors or participants. In addition, the views are not necessarily those of the governments of the nominating Member States or of the nominating organizations.*

*Where papers have been incorporated into these Proceedings without resetting by the Agency, this has been done with the knowledge of the authors and their government authorities, and their cooperation is gratefully acknowledged. The Proceedings have been printed by composition typing and photo-offset lithography. Within the limitations imposed by this method, every effort has been made to maintain a high editorial standard, in particular to achieve, wherever practicable, consistency of units and symbols and conformity to the standards recommended by competent international bodies.*

*The use in these Proceedings of particular designations of countries or territories does not imply any judgement by the publisher, the IAEA, as to the legal status of such countries or territories, of their authorities and institutions or of the delimitation of their boundaries.*

*The mention of specific companies or of their products or brand names does not imply any endorsement or recommendation on the part of the IAEA.*

*Authors are themselves responsible for obtaining the necessary permission to reproduce copyright material from other sources.*

## CONTENTS OF VOL. II

### TOKAMAK EXPERIMENTS II (Session I)

High-power ICRF and ICRF plus neutral-beam heating on PLT (IAEA-CN-41/I-1) .....	3
<i>D. Hwang, M. Bitter, R. Budny, A. Cavallo, R. Chrien, S. Cohen, P. Colestock, C. Daughney, S. Davis, D. Dimock, P. Efthimion, H. Eubank, D. Gambier, R. Goldston, D. Herndon, E. Hinnov, J. Hosea, J. Hovey, R. Kaita, D. Manos, E. Mazzucato, D. McNeill, D. Mikkelsen, D. Mueller, A.L. Pecquet, D. Post, G. Schilling, C. Singer, J. Strachan, S. Suckewer, H. Thompson, S. von Goeler, J. Wilson</i>	
Discussion .....	15
Dominant role of wave conversion mechanism in TFR ion cyclotron heating experiments (IAEA-CN-41/I-2) .....	17
<i>Equipe TFR</i>	
Discussion .....	25
Energy and impurity transport in the Alcator C tokamak (IAEA-CN-41/I-3) .....	27
<i>B. Blackwell, C.L. Fiore, R. Gandy, A. Gondhalekar, R.S. Granetz, M. Greenwald, D. Gwinn, E. Källne, J. Källne, S.E. Kissel, B. Lipschultz, N.G. Loter, E.S. Marmor, S. McCool, D. Overskei, D.S. Pappas, R.R. Parker, R. Petrasso, M. Pickrell, P.A. Politzer, M. Porkolab, P. Pribyl, J.E. Rice, F. Seguin, J.J. Schuss, J.L. Terry, R. Watterson, S.M. Wolfe</i>	
Discussion .....	39
Lower-hybrid heating experiments in the Frascati tokamak (FT) (IAEA-CN-41/I-4) .....	41
<i>F. Alladio, M.L. Apicella, E. Barbato, G. Bardotti, R. Bartiromo, F. Bombarda, G. Bracco, G. Buceti, P. Buratti, R. de Angelis, F. de Marco, M. de Pretis, D. Frigione, M. Gasparotto, R. Giannella, M. Grolli, M. Haegi, A. Mancuso, V. Merlo, V. Pericoli, L. Pieroni, S. Podda, E. Purchi, J.P. Rager, G.B. Righetti, F. Romanelli, F. Santini, S.E. Segre, T. Tanga, A. Tuccillo, O. Tudisco, J. Wells, V. Zanza</i>	
Discussion .....	49

High-beta poloidal plasmas and current drive by ECRH on Tosca (IAEA-CN-41/I-5) .....	51
<i>M.W. Alcock, B. Lloyd, A.W. Morris, D.C. Robinson, D.F.H. Start</i>	
Discussion .....	60
Measurements of transport coefficients in the T-10 device (IAEA-CN-41/I-6) .....	63
<i>A.B. Berlizov, G.A. Bobrovskij, N.L. Vasin, A.N. Vertiporokh, N.D. Vinogradova, V.A. Vershkov, N.M. Gegechkori, E.P. Gorbunov, Yu.V. Esipchuk, S.L. Efremov, V.A. Zhuravlev, V.S. Zaveryaev, A.Ya. Kislov, S.Yu. Luk'yanov, Yu.S. Maksimov, G.E. Notkin, A.A. Medvedev, A.B. Pimenov, K.A. Razumova, V.A. Rantsev-Kartinov, M.M. Stepanenko, V.S. Strelkov, V.V. Timonin, V.M. Chicherov, D.A. Shcheglov, A.N. Fyakhretdinov</i>	
Discussion .....	77

#### PLASMA HEATING II (Session J)

Alfvén wave experiments in TCA (IAEA-CN-41/J-1-1) .....	81
<i>A. de Chambrier, A.D. Cheetham, A. Heym, F. Hofmann, B. Joye, R. Keller, A. Lietti, J.B. Lister, A. Pochelon, W. Simm, J.L. Toninato, A. Tuszel</i>	
Plasma heating and current drive by Alfvén waves (IAEA-CN-41/J-1-2) .....	91
<i>R.A. Demirkhanov, A.G. Kirov, G.I. Astapenko, S.E. Il'inskij, Eh.M. Lomakin, V.V. Onishchenko, L.F. Ruchko, A.V. Sukhachev, V.D. Medun, N.I. Malykh</i>	
Discussion on papers IAEA-CN-41/J-1-1 and J-1-2 .....	101
Comprehensive analysis of antenna-plasma coupling in ICR heating of tokamaks and study of energy deposition (IAEA-CN-41/J-2) .....	103
<i>V.P. Bhatnagar, M.P. Evrard, D.W. Faulconer, P. Geilfus, R. Koch, M. Luwel, A.M. Messiaen, D.I.C. Pearson, P.E. Vandenplas, R.R. Weynants</i>	
ICRF heating experiment in JFT-2 (IAEA-CN-41/J-3) .....	113
<i>H. Kimura, H. Matsumoto, K. Odajima, S. Konoshima, T. Yamamoto, N. Suzuki, K. Hoshino, Y. Miura, T. Matsuda, H. Takeuchi, T. Sugie, S. Kasai, T. Yamauchi, H. Kawashima, T. Ogawa, T. Kawakami, T. Shoji, M. Mori, H. Ogawa, Y. Uesugi, K. Ohasa, S. Yamamoto, M. Maeno, S. Sengoku, H. Nakamura, H. Ohtsuka, T. Matoba, A. Funahashi, Y. Tanaka</i>	
Discussion .....	122

Investigation of electron cyclotron heating in the FT-1 tokamak over a wide range of plasma densities (IAEA-CN-41/J-4)	125
<i>Yu.F. Baranov, N.E. Bogdanova, D.G. Bulyginskij, V.K. Gusev, M.M. Larionov, L.S. Levin, G.T. Razdobarin, V.I. Fedorov</i>	
Discussion	133
Equilibrium, stability and heating of plasmas in linear and toroidal Extrap pinches (IAEA-CN-41/J-5)	135
<i>B. Bonnevier, H.E. Dalhed, J.R. Drake, T. Hellsten, P. Karlsson, R. Landberg, B. Lehnert, J. Scheffel, M. Tendler, E. Tennfors, B. Wilner</i>	
High-beta neoclassical current and stability experiments (IAEA-CN-41/J-6)	143
<i>J.D. Callen, R.N. Dexter, C.M. Fortgang, H.R. Garner, A.G. Kellman, D.W. Kerst, M.W. Phillips, S.C. Prager, J.C. Sprott, E.J. Strait, J.C. Twichell, M.C. Zarnstorff</i>	
Discussion	150

#### POST-DEADLINE PAPERS (Session K)

Lower-hybrid current-drive experiments in T-7 tokamak (IAEA-CN-41/K-1)	153
<i>V.V. Alikaev, V.L. Vdovin, D.P. Ivanov, N.V. Ivanov, V.I. Il'in, A.M. Kakurin, A.Ya. Kislov, P.E. Kovrov, V.A. Kochin, P.P. Khvostenko, I.N. Khromkov, V.V. Chistyakov, J. Āatlov, F. Jaček, P. Klíma, V. Kopecký, J. Preinhaelter, K. Jakubka</i>	
Discussion	161
Fusion reactor plasmas with polarized nuclei (IAEA-CN-41/K-2)	163
<i>R.M. Kulsrud, H.P. Furth, E.J. Valeo, R.V. Budny, D.L. Jassby, B.J. Micklich, D.E. Post, M. Goldhaber, W. Happer</i>	
Discussion	173
Curvature-driven trapped-particle modes in tandem mirrors (IAEA-CN-41/K-3)	175
<i>H.L. Berk, M.N. Rosenbluth, H.V. Wong, T.M. Antonsen, D.E. Baldwin, B. Lane</i>	

## STELLARATORS, BUMPY TORI, MULTIPOLES I (Session L)

Plasma properties and ion heating in EBT-S and hot electron rings at TRW (IAEA-CN-41/L-1) .....	185
<i>F.W. Baity, L.A. Berry, L. Bighel, J.A. Cobble, R.J. Colchin, W.A. Davis, H.O. Eason, J.C. Glowienka, G.R. Haste, D.L. Hillis, S. Hiroe, R.K. Richards, T. Uckan, T.L. White, J.B. Wilgen, J.D. Barter, W.F. DiVergilio, L.L. Lao, N.H. Lazar, B.H. Quon, T.K. Samec, W. Wuerker, F.M. Bieniosek, J.H. Mullen, T.L. Owens, R.A. Dandl, G.E. Guest, G.A. Hallock, L. Solensten</i>	
Discussion .....	196
Experimental and numerical studies on plasma confinement in Nagoya Bumpy Torus (NBT) (IAEA-CN-41/L-2) .....	197
<i>M. Fujiwara, T. Kamimura, M. Hosokawa, T. Shoji, H. Iguchi, H. Sanuki, M. Tanaka, M. Aizawa, K. Takasugi, F. Tsuboi, H. Tsuchidate, K. Matsunaga, K. Kadota, A. Tsushima, K.W. Whang, H. Ikegami</i>	
Discussion .....	207
Heliotron studies (IAEA-CN-41/L-3) .....	209
<i>K. Uo, A. Iiyoshi, T. Obiki, O. Motojima, S. Morimoto, A. Sasaki, K. Kondo, M. Sato, T. Mutoh, H. Zushi, H. Kaneko, S. Besshou, F. Sano, T. Mizuuchi, S. Sudo, K. Hanatani, M. Nakasuga, I. Ohtake, M. Iima, Y. Nakashima, N. Nishino</i>	
Discussion .....	225
Plasma heating and confinement in the Khar'kov stellarators (IAEA-CN-41/L-4) .....	227
<i>A.V. Arsen'ev, V.E. Bykov, V.K. Bocharov, M.P. Vasil'ev, Ya.F. Volkov, A.V. Georgievskij, Yu.V. Gutarev, A.G. Dikij, V.G. Dyatlov, G.V. Zelenin, A.N. Letuchij, A.S. Loginov, S.S. Kalinichenko, V.G. Konovalov, V.D. Kotsubanov, P.G. Krishtal', A.E. Kulaga, A.I. Lysojvan, N.I. Mitina, N.I. Nazarov, O.A. Opalev, O.S. Pavlichenko, V.K. Pashnev, N.F. Perepelkin, D.P. Pogozhev, G.N. Polyakova, Yu.F. Sergeev, A.S. Slavnyj, K.N. Stepanov, V.A. Suprunenko, V.F. Tarasenko, F.A. Tkhoryak, V.T. Tolok, V.M. Tonkopryad, O.M. Shvets</i>	
Discussion .....	240

Neutral-injection heating in the Wendelstein VII-A Stellarator (IAEA-CN-41/L-5) .....	241
<i>G. Cattanei, D. Dorst, A. Elsner, G. Grieger, H. Hacker, J. Hartfuss, H. Jäckel, R. Jaenicke, J. Junker, M. Kick, H. Kroiss, C. Mahn, S. Marlier, G. Müller, W. Ohlendorf, F. Rau, H. Renner, H. Ringler, F. Sardei, M. Tutter, A. Weller, H. Wobig, E. Würsching, M. Zippe, K. Freudenberger, G.G. Lister, W. Ott, F.-P. Penningsfeld, E. Speth</i>	
Discussion .....	260

## HIGH-BETA SYSTEMS II (Session M)

Experimental investigation of the spheromak configuration (IAEA-CN-41/M-1) .....	265
<i>M. Yamada, R. Ellis, Jr., H.P. Furth, R. Hulse, A. Janos, S.C. Jardin, D. McNeill, C. Munson, M. Okabayashi, S. Paul, D. Post, J. Sennis, C. Skinner, Y.C. Sun, F. Wysocki, C. Chin-Fatt, A.W. DeSilva, G.C. Goldenbaum, G.W. Hart, R. Hess, R.S. Shaw, C.W. Barnes, I. Hennins, H.W. Hoida, T.R. Jarboe, S.O. Knox, R.K. Linford, J. Lipson, J. Marshall, D.A. Platts, A.R. Sherwood, B.L. Wright</i>	
Discussion .....	280
Experimental studies of field-reversed configuration confinement in FRX-C (IAEA-CN-41/M-2-1) .....	283
<i>R.E. Siemon, W.T. Armstrong, R.R. Bartsch, R.E. Chrien, J.C. Cochrane, R.W. Kewish, P.L. Klingner, R.K. Linford, J. Lipson, K.F. McKenna, D.J. Rej, E.G. Sherwood, M. Tuszewski</i>	
Compact toroidal plasmas: simulations and theory (IAEA-CN-41/M-2-2) .....	293
<i>D.S. Harned, D.W. Hewett, C.G. Lilliequist, R.W. Moses, D.D. Schnack, J.L. Schwarzmeier, A.G. Sgro, R.L. Spencer, D.V. Anderson, J. Killeen, A.A. Mirin, N.J. O'Neill, A.I. Shestakov, D.E. Shumaker, S.P. Auerbach, J.K. Boyd, T.A. Brengle, B.I. Cohen, J.H. Hammer, C.W. Hartman, W.C. Turner, A. Aydemir, D.C. Barnes, C. Bernhard, W.M. Tang, C. Seyler, J. Tataronis</i>	
Discussion on papers IAEA-CN-41/M-2-1 and M-2-2 .....	301
Experimental studies on confinement of field-reversed-configuration plasma (IAEA-CN-41/M-3) .....	303
<i>T. Minato, M. Tanjyo, S. Okada, Y. Ito, M. Kako, S. Ohi, S. Goto, T. Ishimura, H. Ito, Y. Nogi, S. Shimamura, Y. Osanai, K. Saito, K. Yokoyama, S. Shiina, S. Hamada, H. Yoshimura, Y. Aso, C.H. Wu, S. Himeno, M. Okamoto, K. Hirano</i>	
Discussion .....	309

Merging experiment and simulation of compact toroids (IAEA-CN-41/M-4) .....	311
<i>K. Watanabe, K. Ikegami, M. Nagata, M. Nishikawa, A. Ozaki, N. Satomi, T. Uyama, T. Sato, S. Otsuka, T. Hayashi, K. Nishikawa</i>	
High-beta tokamak plasma physics studies (IAEA-CN-41/M-5-1) .....	321
<i>C.K. Chu, A.V. Deniz, D.J. Elkin, G. Erlebacher, R.A. Gross, R. Izzo, S. Johnston, C. Kostek, F. Levinton, M. Machida, T.C. Marshall, R.L. Merlino, G.A. Navratil, D. Oepts</i>	
Beta increase in a belt-pinch plasma by fast magnetosonic wave heating (IAEA-CN-41/M-5-2) .....	331
<i>V. Erckmann, A. Mayer, G. Müller, K. Schwörer, M. Thumm, R. Wilhelm</i>	
Discussion on papers IAEA-CN-41/M-5-1 and M-5-2 .....	341
Suppression of losses in a compact torus with programmed shaping of the magnetic structure (IAEA-CN-41/M-6) .....	343
<i>V.V. Belikov, V.M. Goloviznin, V.K. Korshunov, A.P. Kreshchuk, R.Kh. Kurtmullaev, Ya.N. Laukhin, A.I. Malyutin, A.P. Proshletsov, O.L. Rostovtsev, V.N. Semenov, V.F. Strizhov</i>	
Discussion .....	349

### INERTIAL CONFINEMENT III (Session N)

Inertial fusion research based on pulsed power (IAEA-CN-41/N-1) .....	353
<i>G. Yonas</i>	
Light-ion inertial confinement fusion research at Naval Research Laboratory (IAEA-CN-41/N-2) .....	361
<i>G. Cooperstein, R.J. Barker, D.G. Colombant, A. Drobot, Shyke A. Goldstein, R.A. Meger, D. Mosher, P.F. Ottinger, F.L. Sandel, S.J. Stephanakis, F.C. Young</i>	
Discussion .....	370
Research progress in intense ion beam production for inertial confinement fusion at Cornell University (IAEA-CN-41/N-3) .....	371
<i>H. Bluhm, J.B. Greenly, D.A. Hammer, B.R. Kusse, J. Maenchen, A. Mankofsky, J. Neri, R. Pal, T.J. Renk, G.D. Rondeau, R.N. Sudan</i>	
Discussion .....	381
Light ion beam fusion research in Japan (IAEA-CN-41/N-4) .....	383
<i>K. Imasaki, S. Miyamoto, S. Higaki, T. Ozaki, K. Nishihara, S. Ido, S. Nakai, C. Yamanaka, K. Yatsui, K. Masugata, M. Matsui</i>	
Discussion .....	392

Status of relativistic-electron-beam-generator-driven inertial-confinement fusion (IAEA-CN-41/N-5) .....	393
<i>L.E. Aranchuk, M.V. Babykin, K.A. Bajgarin, N.U. Barinov, A.V. Bartov, S.L. Bogolyubskij, V.V. Bulan, V.D. Vikharev, V.S. Volkov, Yu.M. Gorbulin, E.M. Gordeev, V.V. Gorev, E.V. Grabovskij, A.V. Gubarev, S.A. Dan'ko, S.K. Dolotov, V.I. Zajtsev, D.M. Zlotnikov, Yu.G. Kalinin, V.N. Kiselev, Yu.V. Koba, V.D. Korolev, P.V. Kuksov, V.I. Liksonov, V.I. Mizhiritskij, S.L. Nedoseev, G.M. Olejnik, L.I. Rudakov, V.A. Skoryupin, V.P. Smirnov, E.A. Smirnova, E.Z. Tarumov, M.V. Tulupov, S.D. Fanchenko, V.Ya. Tsarfin, A.S. Chernenko, R.V. Chikin, A.Yu. Shashkov, Yu.I. Shestakov, I.R. Yampol'skij, V.V. Yan'kov</i>	
Discussion .....	403
Investigation of the neutron production phases of a large plasma focus device (IAEA-CN-41/N-6-1) .....	405
<i>H. Herold, L. Bertalot, R. Deutsch, W. Grauf, U. Jäger, H.J. Kaeppler, F. Lepper, T. Oppenländer, H. Schmidt, R. Schmidt, J. Schwarz, K. Schwörer, M. Shakhatre, A. Hayd, M. Maurer, P. Meinke</i>	
Experimental progress in plasma dynamics and generation of energetic particles in dense plasma focus (IAEA-CN-41/N-6-2) .....	415
<i>M. Yokoyama, Y. Kitagawa, Y. Yamada, M. Okada, Y. Yamamoto, C. Yamanaka, K. Hirano, Y. Kondoh, K. Shimoda, T. Yamamoto, M. Hattori, M. Sato</i>	
Discussion on papers IAEA-CN-41/N-6-1 and N-6-2 .....	423

## TECHNOLOGY AND REACTOR CONCEPTS II (Session O)

TASKA – a tandem mirror fusion engineering test facility (IAEA-CN-41/O-1) .....	427
<i>TASKA Team (P. Komarek – Compiler)</i>	
KARIN-I: Conceptual design of a moving-ring reactor (IAEA-CN-41/O-2-1) .....	439
<i>KARIN-I Working Group</i>	
Conceptual design of a moving-ring reactor (IAEA-CN-41/O-2-2) .....	447
<i>A.C. Smith Jr., C.P. Ashworth, K.E. Abreu, G.A. Carlson, W.S. Neef Jr., H.H. Fleischmann, K.R. Schultz, C.P.C. Wong, D.K. Bhadra, R.L. Creedon, E.T. Cheng, G.R. Hopkins, W. Grossman Jr., D.M. Woodall, T. Kammash</i>	
Discussion on papers IAEA-CN-41/O-2-1 and O-2-2 .....	459

Development of hydrogen pellet injectors and pellet fuelling experiments at Oak Ridge National Laboratory (IAEA-CN-41/O-3) .....	461
<i>S.L. Milora, S.K. Combs, C.A. Foster, W.A. Houlberg, J.T. Hogan, D.D. Schuresko, S.E. Attenberger, G.L. Schmidt, M.J. Greenwald, S. Wolfe, J. Parker</i>	
Blanket and shield experiments in Fusion Neutronics Source (FNS) (IAEA-CN-41/O-4) .....	471
<i>T. Nakamura, H. Maekawa</i>	
Discussion .....	484
Feedback control of thermal instability by compression and decompression (IAEA-CN-41/O-5) .....	485
<i>M. Okamoto, M. Ohnishi, K. Hirano, T. Amano</i>	
<b>POSTER SESSION (Session V)</b>	
Low-m magnetic-mode activity, disruptions in tokamak discharges and their control (IAEA-CN-41/V-1) .....	495
<i>M. Cotsaftis</i>	
RF current drive in tokamaks and compact tori (IAEA-CN-41/V-2) .....	507
<i>E. Canobbio, R. Croci</i>	
Resistive ballooning modes in three-dimensional configurations (IAEA-CN-41/V-3) .....	519
<i>D. Correa-Restrepo</i>	
Filamentary structures in tokamaks and their importance to anomalous electron energy loss (IAEA-CN-41/V-4) .....	531
<i>M.G. Haines, F. Marsh</i>	
Computation of plasma equilibrium and stability in stellarators on the basis of a generalized two-dimensional equilibrium equation (IAEA-CN-41/V-5) .....	541
<i>V.D. Pustovitov, V.D. Shafranov, L.E. Zakharov, L.M. Degtyarev, V.V. Drozdov, S.Yu. Medvedev, Yu.Yu. Poshekhonov, M.I. Mikhajlov</i>	
Current generation by interaction of alpha particles with ICRF waves (IAEA-CN-41/V-6) .....	557
<i>K. Okano, N. Inoue, T. Uchida, R. Sugihara, Y. Ogawa</i>	
Ballooning MHD modes in toroidal systems with complicated magnetic-field geometry (IAEA-CN-41/V-7) .....	567
<i>A.B. Mikhajlovskij, V.V. Demchenko, A. Ya. Omel'chenko</i>	
Plasma heating by anomalous absorption of large-amplitude Alfvén (ion cyclotron) waves (IAEA-CN-41/V-8) .....	581
<i>A.G. Dikij, S.S. Kalinichenko, A.I. Lysojvan, V.S. Mikhajlenko, N.I. Nazarov, A.I. Pyatak, V.L. Sizonenko, A.S. Slavnyj, K.N. Stepanov, V.F. Tarasenko, O.M. Shvets</i>	

Theory and simulation of RF heating and current drive (IAEA-CN-41/V-9) .....	595
<i>J.M. Dawson, B.D. Fried, G.J. Morales, A.T. Lin, V.K. Decyk, M. Caplan</i>	
Stellarator, hybrid stellarator, torsatron and low-shear stellarator studies (IAEA-CN-41/V-10) .....	603
<i>G. Anania, R.C. Grimm, D. Ho, J.L. Johnson, R.M. Kulsrud, J. Manickam, K.E. Weimer, G. Berge, W.H. Choe, J.P. Freidberg, J.M. Noterdaeme, Y.P. Pao, P.A. Politzer, P. Rosenau, D. Sherwell, O. Betancourt, M. Mond, H. Weitzner</i>	
Theory of transport and heating in EBT (IAEA-CN-41/V-11) .....	613
<i>C.L. Hedrick, D.B. Batchelor, G.L. Chen, L.E. Deleanu, R.C. Goldfinger, D.E. Hastings, E.F. Jaeger, D.K. Lee, C.W. Nester, L.W. Owen, D.A. Spong, J.S. Tolliver, N.A. Uckan, N.T. Gladd, S. Hamasaki, N.A. Krall, J.L. Sperling, H. Weitzner, R.J. Kashuba, M.R. Gordinier, T.L. Owens, D.G. Swanson, S. Tamor</i>	
Chairmen of Sessions .....	623
Secretariat of the Conference .....	624



**Session I**

**TOKAMAK EXPERIMENTS II**

Chairman

D. PALUMBO

CEC

## HIGH-POWER ICRF AND ICRF PLUS NEUTRAL-BEAM HEATING ON PLT

D. HWANG, M. BITTER, R. BUDNY, A. CAVALLO\*,  
 R. CHRIEN, S. COHEN, P. COLESTOCK, C. DAUGHNEY,  
 S. DAVIS, D. DIMOCK, P. EFTHIMION, H. EUBANK,  
 D. GAMBIER<sup>+</sup>, R. GOLDSTON, D. HERNDON, E. HINNOV,  
 J. HOSEA, J. HOVEY, R. KAITA, D. MANOS,  
 E. MAZZUCATO, D. McNEILL, D. MIKKELSEN,  
 D. MUELLER, A.L. PECQUET<sup>+</sup>, D. POST, G. SCHILLING,  
 C. SINGER, J. STRACHAN, S. SUCKEWER,  
 H. THOMPSON, S. VON GOELER, J. WILSON  
 Plasma Physics Laboratory,  
 Princeton University,  
 Princeton, New Jersey,  
 United States of America

### Abstract

#### HIGH-POWER ICRF AND ICRF PLUS NEUTRAL-BEAM HEATING ON PLT.

PLT ICRF experiments with RF powers up to  $\approx 3$  MW have demonstrated efficient plasma heating in both the minority fundamental and the second harmonic ion-cyclotron regimes. In the minority  $^3\text{He}$  regime, ion temperatures of  $\approx 3$  keV have been produced along with  $\approx 1$  kW of  $\text{D-}^3\text{He}$  fusion power and substantial electron heating. In the second harmonic H regime, an equivalent averaged ion energy of  $\approx 4$  keV has been achieved. Combined ICRF plus neutral-beam heating experiments with auxiliary powers totalling up to 4.5 MW have provided insight into auxiliary heating performance at stored plasma energy levels up to  $\approx 100$  kJ. Values of  $\beta_\phi$  in the range of 1.5–2% have been attained for  $B_\phi \approx 17$  kG. Energetic discharges with  $\bar{n}_e$  up to  $\approx 6 \times 10^{13} \text{ cm}^{-3}$  at  $B_\phi \approx 28$  kG have also been investigated. Preliminary confinement studies suggest that energetic ion losses may contribute to a direct loss of the input RF power in the H minority heating regime but are insignificant in the  $^3\text{He}$  minority case. The energy confinement time for the H minority regime is reduced somewhat from the Ohmic value.

#### 1. INTRODUCTION

Since the previous IAEA meeting[1], the power levels of the ICRF experiments have been increased substantially while maintaining the ion heating efficiencies observed at lower power and providing substantial electron heating. These

\* University of Maryland, College Park, Maryland, USA.

<sup>+</sup> Permanent address: CEN de Fontenay-aux-Roses, France.

results permit extrapolation to future devices (TFTR, FED, etc.) with higher stored energy and  $\beta$  [2-4]. Investigations of the stability and transport properties at these higher power levels have now begun.

In this paper, the present status of the high-power ICRF and ICRF plus NB experiments is presented. The combination of up to 6 half-turn loop antennae located at the outside of the torus with improved feedthroughs[5] now provides up to  $\sim 1.6$  MW at 25 MHz and up to  $\sim 3$  MW at 42 MHz. The lower frequency is used for the  $^3\text{He}$  and H minority heating regimes at  $\sim 25$  kG and 17 kG, respectively, while the higher frequency provides heating in the H minority and H second harmonic regimes at  $B_\phi \sim 28$  kG and 14 kG. Up to 2.5 MW of NB power is currently available.

Emphasis is placed on heating efficiencies obtained in the various regimes and the energy confinement for the minority regime with and without the addition of neutral beams. The influence of  $m = 2$  MHD instability and possibly energetic particle losses on the heating performance is discussed.

## 2. ION HEATING

### 2.1. Minority Ion Heating

The central deuterium temperature increments obtained for the  $^3\text{He}$  minority, H beam, and H minority plus  $\text{D}^0$  neutral beam injection regimes are summarized in Fig. 1a for a range of densities and powers up to  $\bar{n}_e \sim 6 \times 10^{13} \text{ cm}^{-3}$  and  $P_{\text{aux}} \sim 4.5$  MW. Both the highest value of  $T_d(0)$  and the best ion heating efficiencies have been achieved in the  $^3\text{He}$  minority case[3].  $T_d(0)$  has been increased from  $\sim 0.7$  keV to  $\sim 2.8$  keV at  $\bar{n}_e \approx 3.2 \times 10^{13} \text{ cm}^{-3}$  with 1.3 MW of 25 MHz rf power. The ion heating efficiency in this case is  $\sim 5 \times 10^{13} \text{ eV cm}^{-3}/\text{kW}$  as compared with  $\sim 3 \times 10^{13} \text{ eV cm}^{-3}/\text{kW}$  for the H minority case. Both the negligible charge-exchange loss

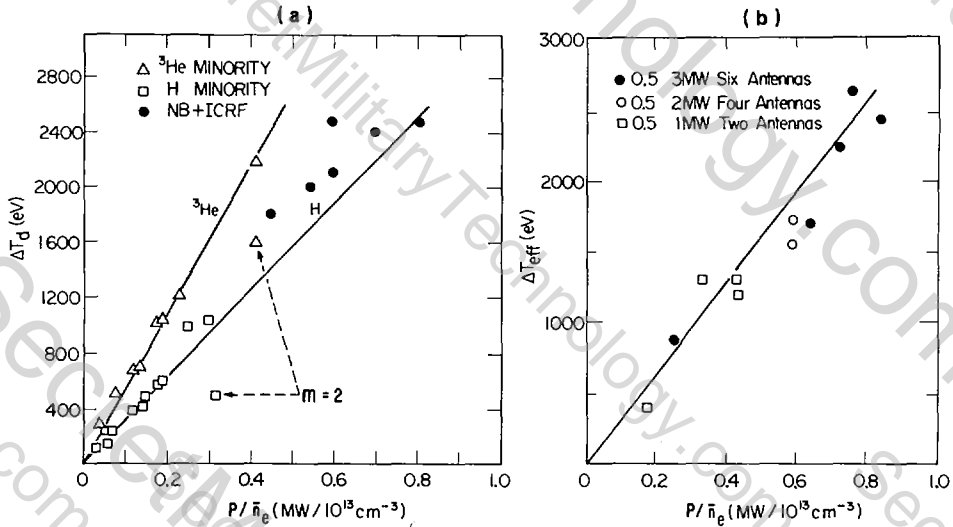


FIG.1. Plasma ion heating rates with (a) minority ICRF and H minority –  $D^0$  beam heating and (b) H second harmonic heating.

and the stronger coupling to the deuterium ions of the energetic <sup>3</sup>He ions contribute to the better ion heating performance in the <sup>3</sup>He minority regime.

The deleterious effect on ion heating by  $m = 2$  MHD activity is demonstrated in Fig. 1a. Similar degradation of the electron heating in the minority regimes also occurs. Thus, as in the studies of ohmic and NB heating, the  $m = 2$  instability must be avoided to optimize heating performance.

## 2.2. Second Harmonic Heating

The highest rf power coupled into PLT to date, 3.2 MW, has been reached in the hydrogen second harmonic regime with the 42 MHz rf system. The central hydrogen energy distribution measured with a passive charge-exchange system (confirmed with a diagnostic neutral beam) is non-Maxwellian (Fig. 2a) in general agreement with the theory of quasi-linear velocity space diffusion [6]. The energy contained in such a distribution can be described in terms of the average ion energy  $\langle E_n \rangle$  or,

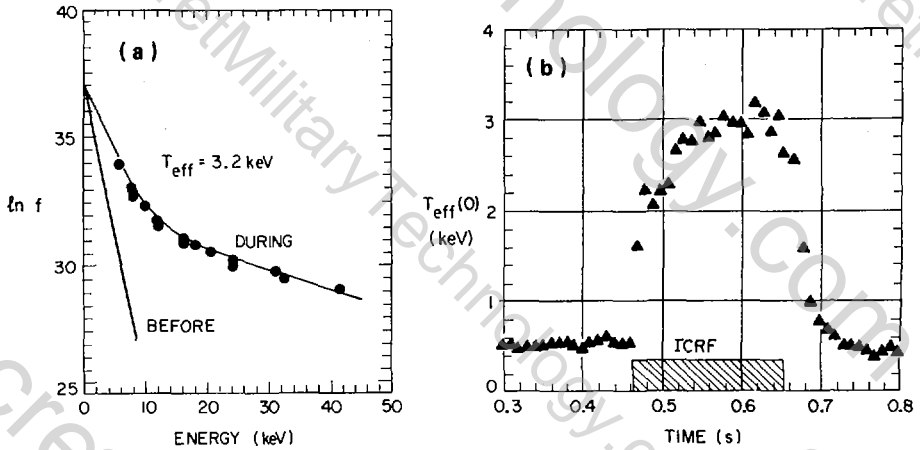


FIG.2. Second harmonic heating characteristics in H with  $B_\phi \approx 14 \text{ kG}$ ,  $\bar{n}_e \approx 3.8 \times 10^{13} \text{ cm}^{-3}$ , and  $P_{\text{RF}} \approx 2.8 \text{ MW}$ . (a) Charge-exchange distribution; (b)  $T_{\text{eff}}$  versus time.

for comparison to the minority ion heating case, by an effective temperature [3]  $T_{\text{eff}} = 2/3 \langle E_h \rangle$ .  $T_{\text{eff}}$  versus time for  $P_{\text{rf}} \sim 3 \text{ MW}$  is given in Fig. 2b, where a maximum value of  $T_{\text{eff}} \sim 3 \text{ keV}$  is attained. Fig. 1b illustrates the scaling of  $\Delta T_{\text{eff}}$  with  $P_{\text{rf}}/\bar{n}_e$  for several combinations of antennae. An ion heating efficiency comparable to that of the minority H regime is obtained. Note that if a similar distribution is produced in a deuterium plasma by second harmonic heating at  $T_{\text{eff}} = 3.2 \text{ keV}$  the fusion output would be  $\sim 4$  times that for the thermal case assuming adequate confinement of the energetic tail of the non-Maxwellian distribution.

### 2.3. ICRF Plus Neutral Beam Heating

Earlier investigations have revealed that in the  $^3\text{He}$  minority regime with  $\text{H}^0$  beam injection, for which there is no direct rf-beam ion interaction, the ICRF and NB ion heating increments are essentially additive [7]. However, rf beam ion interaction is expected in the hydrogen minority regime with  $\text{H}^0$  ( $\omega_{\text{CH}}$ ) and  $\text{D}^0$  ( $2\omega_{\text{cd}}$ ) beam injection. The beam energy dis-

tribution measured by charge-exchange for H<sup>0</sup> injection has been observed to fall off at a substantially slower rate above the beam injection energy during ICRF heating[8].

The high-power results reported here are for the H minority - D<sup>0</sup> beam regime for which the interaction is expected to be less than in the H<sup>0</sup> beam case. However, ion temperature must be measured from Doppler broadening of impurity lines since energetic components are added to both the H and D ion energy distributions. This regime has been employed to achieve toroidal  $\beta$  values on PLT in the range of ~ 1.6 - 2.2% with ~ 3 MW of ICRF plus NB power [3,4]. In addition, the heating properties of the H minority - D<sup>0</sup> beam regime have been studied at higher toroidal field  $B_{\phi}$  ~ 28 kG, for ICRF plus NB power levels up to 4.5 MW and  $\bar{n}_e$  ranging up to ~  $6 \times 10^{13} \text{ cm}^{-3}$ . The values of  $T_d(0)$  deduced for the bulk deuterium component from Doppler broadening measurements of hydrogen-like titanium line radiation are plotted in Fig. 1a. The NB + ICRF data points lie somewhat above the minority hydrogen curve, indicating an ion heating efficiency of ~  $3.5 \text{ eV} \times 10^{13} \text{ cm}^{-3}/\text{kW}$  for the conditions studied.

### 3. ENERGETIC PARTICLE MEASUREMENTS DURING ICRF HEATING

#### 3.1. Energetic <sup>3</sup>He Ion Effects

In the <sup>3</sup>He minority case not only have D-D fusion neutron fluxes exceeded  $10^{12}$  n/sec, but also the D-<sup>3</sup>He fusion proton fluxes measured with surface barrier detectors at the plasma edge have reached levels up to  $\geq 3 \times 10^{14}$  p/sec which approaches ~1 kW of fusion power[9]. The presence of an energetic <sup>3</sup>He ion tail has been further demonstrated by the width measured for the escaping proton energy spectrum centered about 14.7 MeV corresponding to a reacting <sup>3</sup>He energy of greater than ~ 200 keV (Fig. 3a). Finally, the D-<sup>3</sup>He reaction rate has been found to be proportional to  $n_e^{-3} P_{rf}^{\alpha}$  ( $2 < \alpha < 3.5$ ) with no evidence

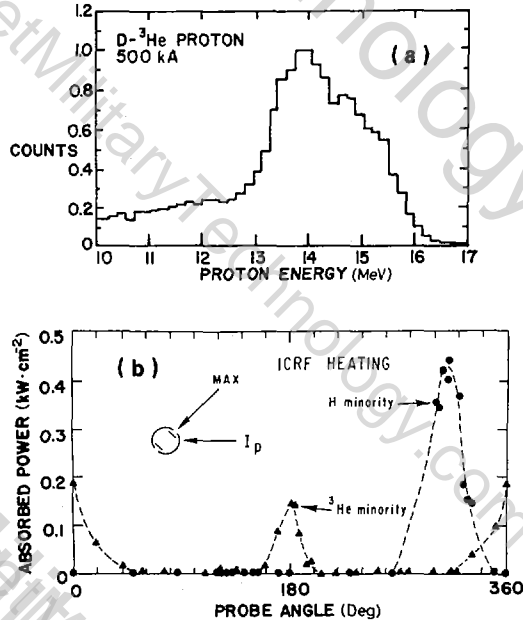


FIG.3. Energetic particle measurements. (a) Proton spectrum from  $D-^3\text{He}$  reactions and (b) bolometer probe measurements for  $P_{\text{RF}} \approx 1 \text{ MW}$  (for H minority case, the OH level has been subtracted).

for saturation up to the highest powers [10]. A one-dimensional model based on the minority distribution predicted from quasi-linear diffusion theory [2] has been used to calculate the  $D-^3\text{He}$  reaction rate. The experimental power scaling can be described by assuming a Gaussian rf deposition profile with a width of  $\sim 12 \text{ cm}$  in the core plasma containing  $\sim 10\%$   $^3\text{He}$  minority.

### 3.2. Energetic Particle Losses in the Minority Regime

Good confinement of the energetic ions created by ICRF heating continues to be a major consideration for optimizing the heating performance. Charge-exchange losses of the energetic ions have been suggested as a contributing cause of the reduced ion heating efficiency in the hydrogen regimes. In addition, direct energetic ion losses at the plasma periphery may potentially be significant.

Measurements of the energetic ions at the periphery are made with a particle bolometer located at the limiter radius[11]. Measurements of the energetic neutrals produced in the plasma are made with a fast ion charge-exchange system[12]. The bolometer is covered by a stainless-steel cylinder with acceptance slits along its axis which is oriented along the major radius (insert in Fig. 3b). Rotation about this axis provides discrimination between particles having different gyroradii and different ratios of  $V_{\perp}/V_{\parallel}$ , with respect to the magnetic field. The charge-exchange system allows discrimination of  $V_{\perp}/V_{\parallel}$  by scanning in the horizontal midplane of the plasma.

The particle bolometer measurements of energetic ions during ICRF heating of a deuterium plasma with hydrogen (42 MHz) and  $^3\text{He}$  (25 MHz) minorities are given in Fig. 3b. The flux in the  $^3\text{He}$  minority regime is indistinguishable from the ohmic level. The observed flux in the H minority regime peaks at  $\sim 50^\circ$  relative to the plasma current direction and represents particles with large gyroradii having  $V_{\perp}/V_{\parallel} \sim 1.2 - 1.3$ . (Energetic ion fluxes during co- and counter-injection are centered about  $0^\circ$  and  $180^\circ$ , respectively.) From geometric considerations, these particles have  $V_{\parallel} > 10$  keV and could give a direct power loss of up to  $\sim 15\%$  of the input power if the flux is uniform both toroidally and poloidally. The absence of energetic ion flux in the case of  $^3\text{He}$  minority heating might partially explain the better heating efficiency observed for that regime.

Charge-exchange analyzer measurements made during H minority heating at 42 MHz indicate the presence of energetic trapped ions (91 keV) that just fit inside the PLT plasma with their banana tips located near the top and bottom of the tokamak. These ions intersect the ion cyclotron layer near the high voltage points of the rf antennae. It is possible that these ions could be those measured directly by the bolometer probe.

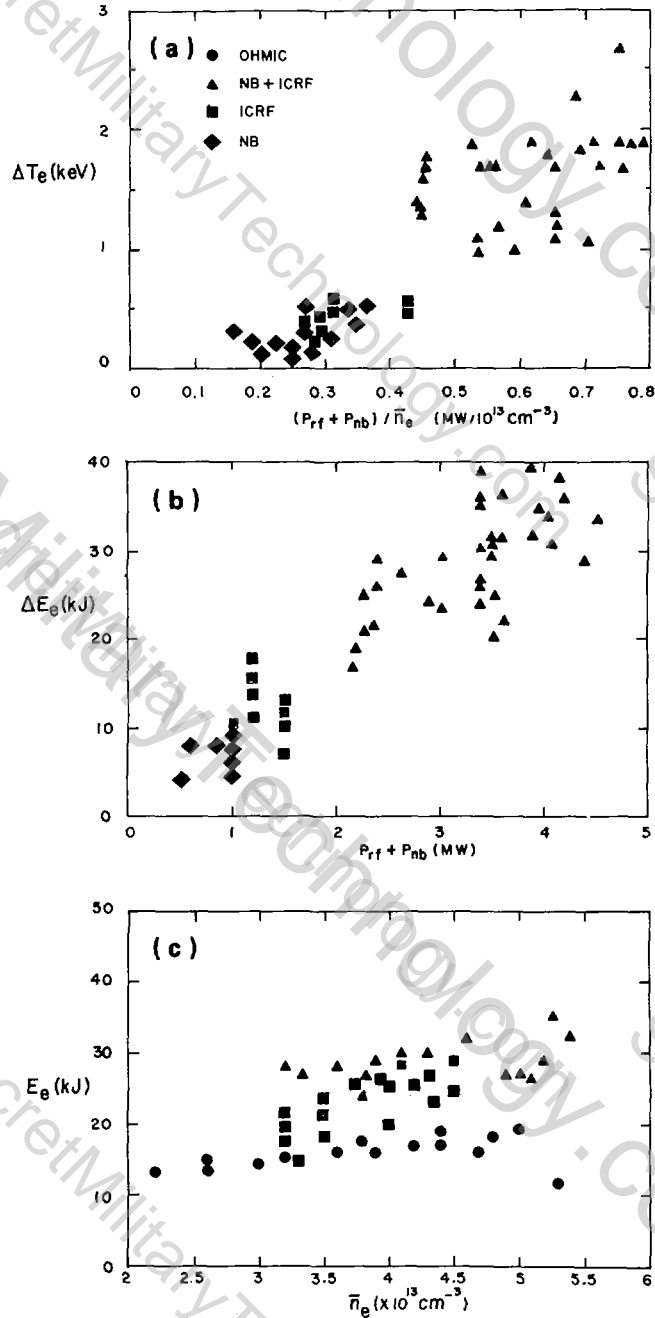


FIG. 4. Electron heating characteristics for the minority H,  $H^0$  beam, and minority H plus  $D^0$  beam regimes. In (c) the power levels for the three cases are Ohmic  $\approx 0.5$  MW, ICRF  $\approx 1$  MW, ICRF + NB  $\approx 2$  MW.

Evaluation of the energetic ion losses due to surface wave acceleration is important to the power balance and can potentially be controlled with appropriate antenna design.

#### 4. ELECTRON HEATING

In the minority regimes substantial electron heating has been obtained at the higher power levels [3,4]. For the  $^3\text{He}$  minority case  $T_d(o) > T_e(o)$  has been observed in contrast to  $T_d(o) < T_e(o)$  for the H minority case. Transport studies reveal that the electron heating can be accounted for by coupling to the energetic minority ions in the  $^3\text{He}$  minority case, but that direct wave electron heating could also be occurring, especially in the minority H case.

Systematic studies of the electron heating have begun in the H minority regime, with and without D $^{\circ}$  beam injection. Initial results of electron heating in the H minority, H $^{\circ}$  beam, and H minority plus D $^{\circ}$  beam regimes obtained for similar target plasma conditions are given in Fig. 4 for  $\bar{n}_e$  up to  $\sim 6 \times 10^{13} \text{ cm}^{-3}$  and auxiliary power,  $P_{\text{aux}}$ , up to  $\sim 4.5 \text{ MW}$ .

The rate of central incremental electron heating (Fig. 4a), measured by Thomson scattering,  $\omega_{ce}$  and  $2\omega_{ce}$  emission and x-ray pulse height analysis, is generally higher for the H minority plus D $^{\circ}$  beam case and is comparable to the incremental ion heating rate ( $\sim 3 \text{ eV} \times 10^{13} \text{ cm}^{-3}/\text{kW}$ ). However, the change in electron energy for all three cases (Fig. 4b) is roughly linear in power, in keeping with the  $T_e$  profile being more peaked for the combined ICRF + NB heating regime. The incremental volume heating efficiency,  $(2/3)\Delta E/P_{\text{AUX}}$  of  $\sim 1.0 \text{ eV} \times 10^{13} \text{ cm}^{-3}/\text{kW}$  best fits the set of data in Fig. 4b.

The scaling of electron stored energy with  $\bar{n}_e$  is shown in Fig. 4c for constant power levels. Small increases in  $E_e$  with  $\bar{n}_e$  are indicated for the ohmic and ICRF cases whereas  $E_e$  is relatively constant in the ICRF + NB case. The ohmic data for this study does not represent the best  $\bar{n}_e$  scaling observed on

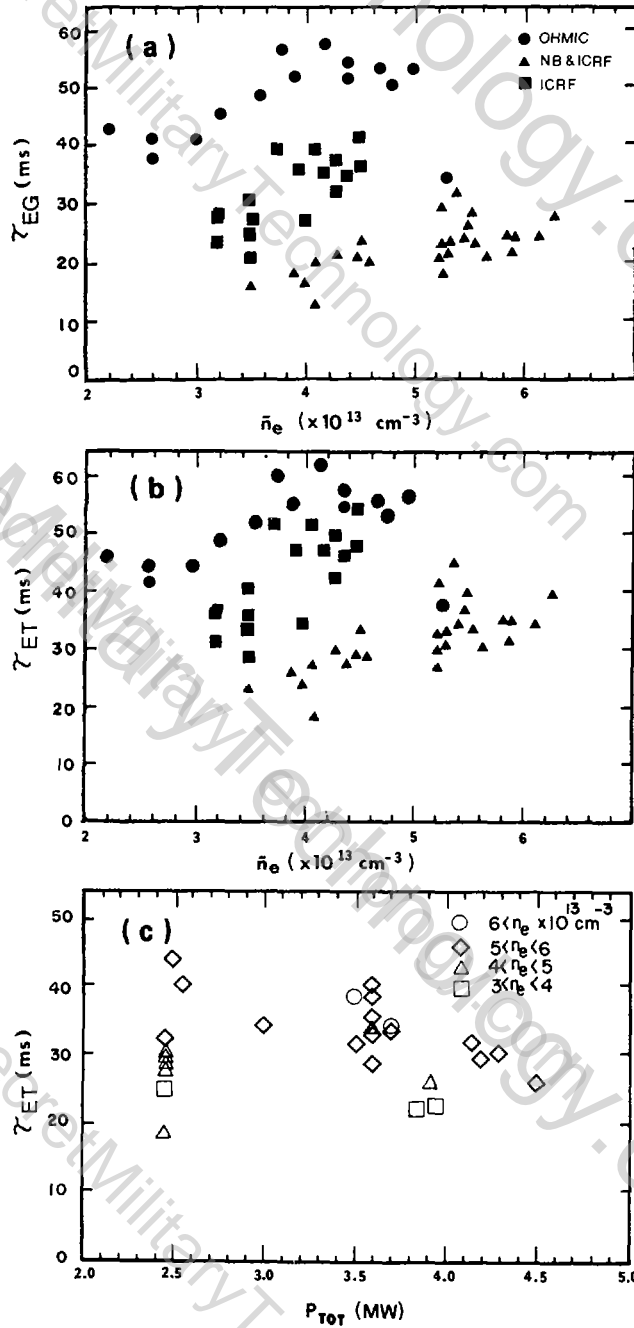


FIG. 5. Confinement time characteristics for the minority H and minority H plus  $D^0$  beam regimes ( $Z_{\text{eff}} \approx 1.5$ ).

PLT and suggests that the confinement properties of the target plasma have not been optimized, especially at higher  $\bar{n}_e$ .

## 5. ENERGY CONFINEMENT

Combining the electron and ion heating results for the case studied in the previous section yields the energy confinement times plotted in Fig. 5. The global confinement time, defined as  $\tau_{EG} = (E_e + E_d)/(P_{rf} + P_{nb} + P_{oh})$ , incorporates all of the energy loss processes whereas the "transport" confinement time, defined as  $\tau_{ET} = (E_e + E_d)/(P_{rf} + P_{nb} + P_{oh} - P_{cx} - P_{rad})$ , represents primarily conduction and convection losses inside the radius where the charge-exchange and radiation losses are subtracted. Other possible losses such as direct energetic ion loss are under investigation but have not been separated out in the calculation of  $\tau_{ET}$ . Also, the energy stored in the energetic ions has not been included here.

$\tau_{EG}$  generally increases somewhat with  $\bar{n}_e$  (Fig. 5a) for the ohmic, ICRF and ICRF + NB regimes. (The ohmic case is affected by  $m = 2$  MHD activity at the higher densities.)  $\tau_{EG}$  progressively decreases upon adding ICRF and then ICRF + NB power.

The  $\tau_{ET}$  values shown in Fig. 5b are obtained at a minor radius of 30 cm within which most of the energetic ion charge-exchange losses occur and ~ 15% of the input power is radiated. At the higher densities the "transport" confinement in the ICRF case is approaching that of the ohmic case and  $\tau_{ET}$  of up to ~40 msec is obtained in the ICRF + NB case. Thus it is possible that by incorporating the energetic ion contributions to the stored energy and the direct rf power loss, the reduction in  $\tau_{ET}$  in the ICRF case could be removed altogether. Extensive investigation over a greater power range will be required to determine the actual functional dependence of  $\tau_{ET}$  on  $P_{rf}$ . In the ICRF + NB case,  $\tau_{ET}$  is substantially below the ohmic value over the density range shown (Fig. 5b), and at

least at the higher densities appear to be a function of the total power (Fig. 5c). This result suggests that an energy confinement time lower than the ohmic value characterizes the auxiliary heated discharge at large auxiliary power.

## 6. CONCLUSION

The ICRF heating and ICRF plus NB heating experiments on PLT have demonstrated efficient ion and electron heating at multimewatt power levels and densities up to the mid- $10^{13}$   $\text{cm}^{-3}$  range. Taken together, the heating results for the minority and second harmonic regimes strongly support the use of minority - second harmonic regimes to achieve the desired high- $\beta$  operation for fusion devices.

The observed energy confinement time in the ICRF + NB regime is less than that for the ICRF regime which is less than the ohmic value for the conditions studied. Energetic ion losses appear to be important in both auxiliary heating cases. Moreover, the plasma energy confinement time may depend on the auxiliary power level.

## ACKNOWLEDGEMENTS

The continuing support of the PPPL staff and of Drs H. Furth, P. Rutherford and D. Meade is gratefully acknowledged. This work supported by the U.S. Department of Energy Contract No. DE-AC02-76-CJ03073.

## REFERENCES

- [1] HOSEA, J.C., et al., in *Plasma Physics and Controlled Nuclear Fusion Research (Proc. 8th Int. Conf. Brussels, 1980) Vol. 2, IAEA, Vienna (1981) 95.*
- [2] COLESTOCK, P.L., et al., in *Proc. 2nd Joint Grenoble-Varenna Int. Symp. on Heating in Toroidal Plasma, Como, 1980, Vol. 1.*
- [3] HOSEA, J.C., et al., in *Proc. 3rd Joint Varenna-Grenoble Int. Symp. on Heating in Toroidal Plasma, Grenoble, 1982, Vol. 1.*

- [4] DAVIS, S.L., et al., to be published in Plasma Phys.  
[5] HWANG, D.Q., WILSON, J.R., Proc. IEEE No. 8 (1981).  
[6] HWANG, D.Q., et al., to be published.  
[7] DAVIS, S.L., et al., Bull. Am. Phys. Soc. (Sep. 1981) Paper 4Q23.  
[8] MEDLEY, S., et al., Proc. 9th Europ. Conf. on Controlled Fusion and Plasma Physics, Oxford, 1979, paper B2-6.  
[9] CHRIEN, R.E., et al., Phys. Rev. Lett. **46** (1981) 535.  
[10] CHRIEN, R.E., STRACHAN, J.D., to be published.  
[11] MANOS, D., et al., to be published in J. Nucl. Mater.  
[12] KAITA, R., GOLDSTON, R.J., BUSSAC, J.-P., Nucl. Fusion **21** (1981) 953.

## DISCUSSION

P.E. VANDENPLAS: Could you comment on the relationship between energy confinement time and impurities in the case of OH, ICRH, NI and ICRNH+NI?

D. HWANG: In the PLT discharges, the total radiated power integrated to the limiter is 20% of the input power for Ohmic heating, 30–35% for ICRF, 20–30% for co-injection, 30–35% for counter-injection and about 35% for ICRF+NI. The profile of the radiation is hollow because of the carbon limiter. Within three-quarters of the minor radius less than 50% of the total radiated power is produced, so radiation is not a dominating factor in the energy balance.

F. SÖLDNER: In the case of hydrogen second harmonic heating you calculate an effective temperature from the distorted ion energy distribution. What is the increase in the bulk ion temperature in that case?

D. HWANG: The stored energy is divided, with 70% in the bulk and 30% in the tail.

F. SÖLDNER: What are the decay times of the high-energy tail and of the bulk ion temperature increase?

D. HWANG: The decay time  $\tau_{\text{tail}} \approx 0.5 \tau_{\text{bulk}}$ .

F. SÖLDNER: Does that mean that the energy in the tail is not thermalized?

D. HWANG: Although the tail distribution can be represented by a Maxwellian, the scanning charge-exchange measurement shows the distribution to be anisotropic in velocity space with a higher perpendicular velocity.



## DOMINANT ROLE OF WAVE CONVERSION MECHANISM IN TFR ION CYCLOTRON HEATING EXPERIMENTS

EQUIPE TFR

Association Euratom-CEA sur la fusion,  
Département de recherches sur la fusion contrôlée,  
Centre d'études nucléaires,  
Fontenay-aux-Roses, France

### Abstract

#### DOMINANT ROLE OF WAVE CONVERSION MECHANISM IN TFR ION CYCLOTRON HEATING EXPERIMENTS.

Experimental evidence demonstrating the essential role played by the wave conversion layer in TFR ICRF experiments is reviewed: the mode structure of the wave in the torus, the conditions for efficient heating of both ions and electrons, local generation of the slow wave as evidenced from the scattering of a laser beam, and ejection of a third ion species in the prescribed conditions lead to a general agreement with theoretical schemes.

In a tokamak plasma containing two ion species, wave propagation in the ion cyclotron range of frequency (ICRF) is characterized by the existence of a wave conversion layer (WCL) and a cut-off layer, located, respectively, at the two major radii  $R_1$  and  $R_2$ , such that

$$(S - n_{\parallel}^2)_{R_1} = (L - n_{\parallel}^2)_{R_2} = 0$$

Here,  $n_{\parallel}$  is the wave refractive index component parallel to the tokamak confining field,

$$S = 1 - \sum_i \frac{\omega_{pi}^2}{(\omega^2 - \omega_{ci}^2)}$$

$$L = 1 - \sum_i \frac{\omega_{pi}^2}{(\omega \omega_{ci} - \omega_{ci}^2)}$$

As we know from Budden's cold-plasma model [1], the presence of these two layers, located between the cyclotron layers of the two ion species, will introduce a significant asymmetry into the propagation and damping characteristics of the fast wave, depending on whether the wave is generated from the high- or low-field side of the torus:

a) When the wave is emitted from the low-field side (LFS) and the densities of the two ion species are comparable, the wave will undergo reflection at the cut-off layer; its energy will be mainly confined between this layer and the outer wall, and its damping will be determined by the transparency of the critical region.

b) When the wave is generated from the high-field side (HFS), it will be converted into a slow electrostatic mode transporting the RF-energy backward, in the vicinity of the equatorial plane, towards the cyclotron layer of the high-Z/M species in the upper and lower regions of the torus. The slow wave will then be absorbed effectively by electron Landau and ion cyclotron damping [2].

This picture should be modified for a hot plasma containing a sufficiently small amount of minority species; in this case the WCL will be smoothed out by thermal effects and the wave will now be able to cross the critical region without reflection or strong damping [11].

The experiments summarized here confirm the validity of this theoretical scheme, by describing the predicted asymmetry in the wave structure, the heating effects actually observed in the expected conditions, a direct observation of the slow wave, and the effect of the local resonance on a third ion species when its cyclotron resonance coincides with the WCL.

## 1. INFLUENCE OF WCL ON WAVE STRUCTURE

A series of data on the wave structure, derived from signals of the magnetic probes located near the torus wall and from the evolution of the antenna radiation resistance during the RF pulse, leads to a general – although qualitative – confirmation of the model.

In experimental conditions such that the WCL is absent from the plasma ( $\omega > \omega_{ci}$ ), or located on its very edge (single-ion plasma), the evolution of  $n_e$  during the RF pulse leads to a sequence of sharp toroidal eigenmodes with Q-values reaching 500. This fact was observed during the first ICRF experiments in earlier tokamaks [3].

When the WCL is inside the plasma, however, the wave pattern strongly depends on the location of the emitting antenna:

a) Most experiments in TFR were done by using antennas short-circuited on the HFS of the plasma and characterized by an electrical length close to  $\lambda/4$  (at 60 MHz); the wave power is mainly radiated near the equatorial plane and propagates towards the LFS. In a high-density D-plasma ( $\bar{n}_e \approx 10^{14} \text{ cm}^{-3}$ ) containing a large fraction of H (20%) and for  $\omega/\omega_{CH_0}$  conditions such that the WCL is near the plasma axis, no evidence of resonant cavity modes is noticed and the wave is clearly damped in the immediate vicinity of the antenna. This is in agreement with Budden's model which predicts, in these conditions, that the wave power should be completely absorbed in a single transit through the WCL.

However, in a lower-density D-plasma ( $\bar{n}_e \approx 3 \times 10^{13} \text{ cm}^{-3}$ ) and provided  $n_H/n_D$  is lower than 5%, an occurrence of low-Q toroidal modes is observed; thermal effects, which lead, in this case, to partial transparency of the critical region (for  $n_H/n_D \approx k_{\parallel} v_H / \omega$ ), determine, in these conditions, toroidal damping lengths that are comparable to the torus circumference.

b) A series of experiments using an antenna located on the LFS of the torus underlines the striking contrast with the previous situation: for  $\bar{n}_e = 10^{14} \text{ cm}^{-3}$  and  $n_H/n_D = 20\%$  (1% of the predicted power absorption during a transit across the WCL), sharp peaks occur in the probe signals, with a corresponding 50% time modulation of the antenna loading resistance R. This is in strong contrast with the perfectly flat R(t) signal observed in the same plasma conditions but with the antenna radiating from the HFS (Fig. 1).

## 2. PLASMA HEATING

RF energy coupled from the HFS should be transferred effectively, in the vicinity of the WCL, to the three components of the plasma: to the electrons by Landau damping of the slow wave, to the protons by cyclotron damping of the cyclotron wave generated outside the tokamak equatorial plane, and to the deuterons by equipartition with the protons and, to a lesser extent, by harmonic cyclotron damping. Measurements of the temperature evolution during the RF pulse confirm that this picture remains valid over a wide range of RF power. The most important heating effects have been obtained in a high-density ( $\bar{n}_e = 10^{14} \text{ cm}^{-3}$ ) D-plasma containing 20% of H, by locating the WCL in the centre of the plasma ( $f = 60 \text{ MHz}$ ,  $B_T = 45 \text{ kG}$ ). In conditions where the  $\omega = \omega_{CH}$  layer is located 14 cm away from the plasma axis, the RF power generated from the HFS by two sets of antennas has been coupled to the plasma up to a level of 2.2 MW [4]. As is shown in Fig. 2, the increase in the D-temperature on the axis remains a linear function of the RF power up to the highest level. Most measurements were done at an RF power level of 1.3 to 1.5 MW. In these conditions,  $T_{i0}$  increases from 0.8 to 1.6 keV, the corresponding ion thermal energy growing from 9 to 15 kJ.

While the energy distribution function of D remains Maxwellian up to 15 keV, a substantial distortion of this function is observed at high power for the H population, as was expected from theory [5]. However, the average thermal energy per proton does not exceed the corresponding value for deuterons by more than 15 to 20%.

The various diagnostics measuring  $T_e(r)$  lead to the results shown in Fig. 2, where some saturation of the heating effect at high RF power should be attributed to an increasing contamination by metallic impurities [4]. For 1.3 MW delivered by the generator,  $T_{e0}$  grows from 1 to 1.5 keV with an increase in the total

## EQUIPE TFR

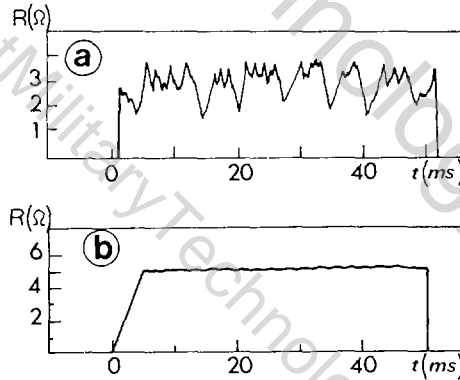


FIG. 1. Loading resistance of two antennas coupling RF power from (a) low- or (b) high-field side of plasma. Plasma conditions:  $n_{e0} = 1.5 \times 10^{14} \text{ cm}^{-3}$ ;  $n_H/n_D = 0.2$ ;  $B_\phi = 45 \text{ kG}$ ;  $f = 60 \text{ MHz}$ .

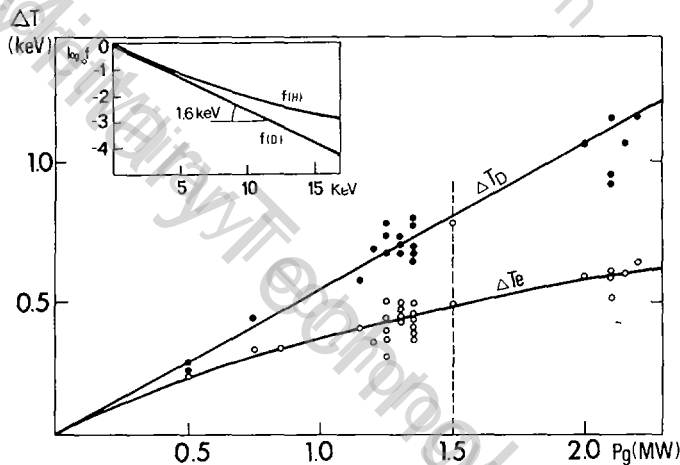


FIG. 2. Increase in D and e temperature for RF-power delivered by generator between 0.5 and 2.2 MW,  $n_{e0} = 1.5 \times 10^{14} \text{ cm}^{-3}$ ;  $B_\phi = 45 \text{ kG}$ ;  $f = 60 \text{ MHz}$ . Comparison of D and H energy distribution functions for  $P_g = 1.3 \text{ MW}$ .

electron thermal energy from 9 to 13.5 kJ. That electron heating results from direct interaction with the wave is suggested by two observations:

- At a power level of 1 MW,  $dT_{e0}/dt$ , when the RF pulse is applied is  $40 \text{ keV} \cdot \text{s}^{-1}$ , compared to  $25 \text{ keV} \cdot \text{s}^{-1}$  for the ions. This indicates that a large fraction of the electron heating power is not due to collisional transfer.
- Direct information on the electron velocity distribution function is obtained from an analysis of the electron cyclotron emission [6]: the radiation

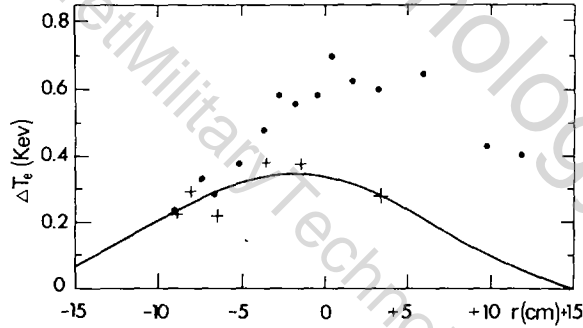


FIG.3.  $\Delta T_e$  radial profile derived from  $\omega_{ce}$  radiation detected from the low-field side (+) and the high-field side (●). Solid line is average  $\Delta T_e$  measured by Thomson scattering in same conditions as in Fig. 2,  $P_g = 1$  MW.

detected by two horns located on the inner and outer sides of the torus at a given frequency  $\omega$  originates from the high-field part of the plasma, where  $\omega_{ce}(R) \geq \omega$ . While radiation towards the LFS of the torus is necessarily re-emitted as blackbody thermal radiation, the light radiated in the opposite direction, towards the HFS, contains a contribution from the supra-thermal part of the electron distribution function. The occurrence of such an asymmetry is actually observed during the RF pulse, indicating that, at least, a part of the electron heating is due to direct interaction between the wave and the electron population (Fig. 3).

### 3. HEATING WITH $\omega < \omega_{CH}$

A series of experiments was carried out at 60 MHz at a toroidal field of 49 kG in a D-plasma containing 30 to 40% of H ( $\bar{n}_e = 10^{14} \text{ cm}^{-3}$ ). In these conditions, the  $\omega = \omega_{CH}$  layer is outside the plasma (24 cm from the axis) while the WCL, as is shown in Fig. 4, is now a closed surface encircling the plasma axis. Strong electron heating is observed,  $T_{e0}$  rising from 1 to 1.7 keV for an RF-power level of 1 MW, while the loop voltage drops from 2 to 1 V. Ion heating, evidenced from the neutron rate and charge-exchange measurements, in this case leads to a  $\Delta T_{i0}$  of 0.4 keV (Fig. 4). Fast increase in  $T_e$  is another evidence for direct interaction of the electrons with the slow wave generated by wave conversion and damped by Landau damping. The ion heating mechanism is, however, less obvious: cyclotron damping of the slow wave in the central area where  $\omega = 0.8 \omega_{CH}$  would require  $k_{\parallel}$  values larger than  $2 \text{ cm}^{-1}$ , which is incompatible with the values computed near the WCL. On the other hand, collisional power transfer from the electrons does not explain the fast rise of  $T_i$  when RF is applied.

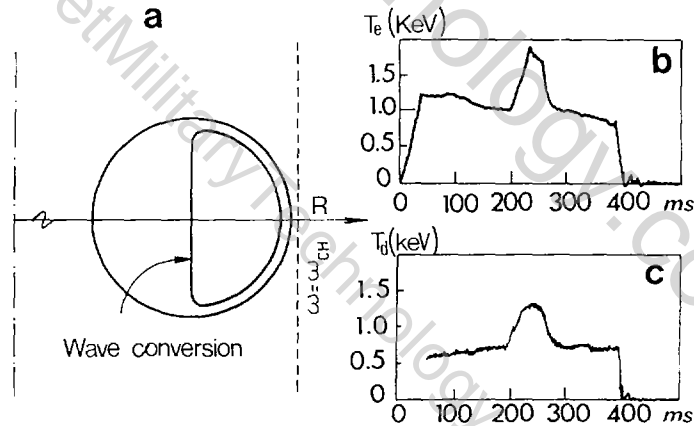


FIG. 4. Position of wave conversion layer and measured  $T_{e0}(t)$  and  $T_{i0}(t)$  for  $n_{e0} = 1.5 \times 10^{14} \text{ cm}^{-3}$ ;  $n_H/n_D = 0.35$ ;  $f = 60 \text{ MHz}$ ;  $B_\phi = 49 \text{ kG}$ .

Several explanations may be considered: collisional damping of the motions induced in opposite phase by the wave in the two ion species, cyclotron acceleration of an impurity in the vicinity of the WCL with subsequent fast collisional transfer to the other ion species, or damping by a non-linear mechanism. More detailed experimental data and an evaluation of the wave electric field in the WCL would be required for a better understanding of this effect.

#### 4. EVIDENCE OF MODE CONVERSION FROM COHERENT SCATTERING OF A $\text{CO}_2$ LASER BEAM [7]

Direct observation of the wave conversion process was made possible through the analysis of the coherent scattered light of a vertical  $\text{CO}_2$  laser beam ( $10.6 \mu\text{m}$ ) crossing the plasma axis in one port of TFR, between the two sections of an HFS antenna. The scattered light as analysed by homodyne techniques allows detecting perturbations induced by the RF corresponding to  $k_x$  values (along the major radius) of 8, 11 and  $14 \text{ cm}^{-1}$ . Although the location of the laser beam is fixed, an analysis of the wave structure on both sides of the WCL remains possible by scanning the  $n_H/n_D$  ratio in a series of experiments and, hence, moving the critical region with respect to the laser beam.

Frequency analysis of the scattered signal gives a spectrum centred around the RF frequency (60 MHz) and similar to the one shown in Fig. 5. The general shape of such a signal can be interpreted as follows: the electron density fluctuations and, hence, the scattered light observed during the RF pulse have two origins:

a) the slow mode (Bernstein or ion cyclotron wave), characterized by an electric field polarized along  $x$ , leading to electron density fluctuations and, hence, to light scattered at the frequency  $\omega_0$  of the RF generator and at an angle from the laser beam defined by the  $k_x$ -value of the slow wave. This corresponds to the central peak of the detected frequency spectrum.

b) non-linear coupling between the fast wave and the drift modes naturally present in the plasma and characterized by a frequency spectrum of about 500 kHz bandwidth. This will lead to the broad-band part of the scattered light whose spectral densities  $S_2$  can be related to the one of the drift wave  $S_1$  by

$$S_2/S_1 = 1/(2\omega_0 B_\varphi)^2 [k_{XD}^2 E_{yF}^2 + (\frac{d}{dx} E_{yF})^2]$$

where  $k_{XD}$  is the drift mode wave number and  $E_{yF}$  the average value of the fast wave electric field along the line of observation.

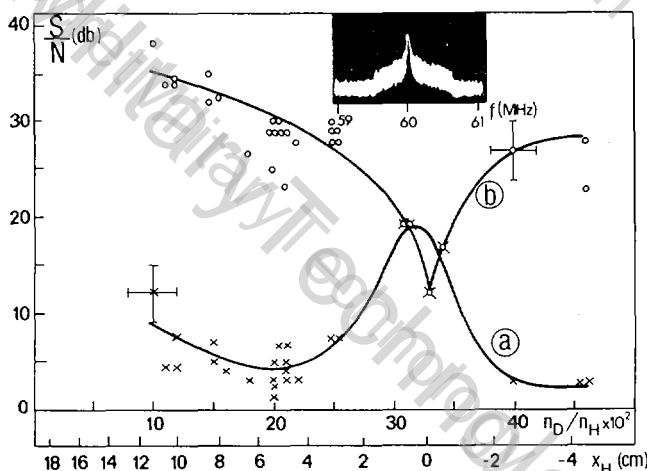


FIG.5. Example of scattered signal detected at  $1.35 \text{ mrad}$  from the laser beam ( $k_x = 8 \text{ cm}^{-1}$ ). Comparison of signal radiances corresponding to the (a) fast and (b) slow modes as function of WCL position.

Figure 5 shows, for example, the amplitudes of the two components of the scattered signal corresponding to  $k_x = 8 \text{ cm}^{-1}$ , as measured in a series of experiments at 60 MHz, 47 kG, 100 kW RF power, by varying  $n_H/n_D$  between 10 and 45%; this variation moves the WCL between  $R = 93 \text{ cm}$  and  $R = 110 \text{ cm}$ .

Several conclusions can be derived from the shape of these signals:

a) Curve a which related to the amplitude of the fast wave, shows a maximum for  $n_H/n_D = 0.33$ , a value which corresponds to the exact coincidence

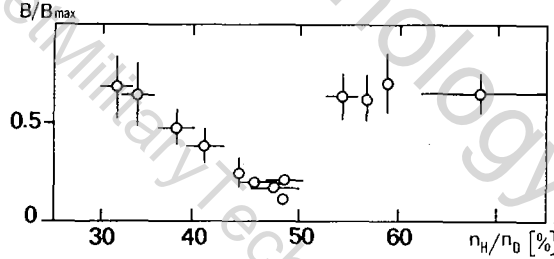


FIG. 6. Ratio of radiances at end of and before RF pulse of one Ar XVI line ( $\lambda = 354 \text{ \AA}$ ) versus  $n_H/n_D$ . Locations of WCL and Ar<sup>16+</sup> harmonic resonance coincide for  $n_H/n_D = 0.47$ .

of the WCL and the laser beam. This indicates a large amplification of  $E_y$  or its derivative at the WCL.

b) The V-shape of curve b, corresponding to the slow mode, confirms the model-predicted propagation of the Bernstein wave on the HFS and of the ion cyclotron wave on the LFS of the WCL. For  $n_H/n_D = 0.33$ , the scattered light is emitted from a region near the WCL where the slow modes are characterized by relatively small  $k_x$  ( $\approx 2 \text{ cm}^{-1}$ ) and, hence, do not appreciably contribute to the signal corresponding to  $k_x = 8 \text{ cm}^{-1}$ . This is not the case on both sides of the WCL, where the  $k_x$ -values computed for the slow waves do reach values near  $8 \text{ cm}^{-1}$  and, hence, should lead to large scattered signals, as is actually observed.

## 5. EJECTION OF RESONANT IMPURITIES [8]

If the  $n_H/n_D$  plasma contains a low-density third ion species and the experimental conditions are such that one of the harmonic cyclotron resonances of this species coincides with the location of the WCL, one expects strong perpendicular acceleration of these ions, leading to a large banana structure of their trajectories and – for a sufficiently high RF-field – to their ejection from the plasma. This mechanism, suggested earlier for plasma purification [9], has been confirmed experimentally by adding a small amount (0.1%) of Ar to a D-plasma containing variable proportions of H (30 to 70%) and coupling 600 kW RF power at 60 MHz and for  $B_\phi = 51 \text{ kG}$ .

An appreciable reduction in the radiance of every line of the Ar ions observed, independently of the  $n_H/n_D$  ratio; the origin of this effect remains obscure. However, for  $n_H/n_D$  between 0.4 and 0.5, a much faster and deeper decay of the radiances occurs, reducing the intensity of Ar XVI lines to 15% of their initial value for  $n_H/n_D = 0.47$  (Fig. 6). This corresponds exactly to the coincidence of the WCL with the second-harmonic cyclotron layer of the Ar<sup>16+</sup> ion. Numerical simulation, discussed in more detail in another paper at this Conference shows that the decay of Ar<sup>16+</sup> should be followed by a corresponding

decrease in the densities of the other states of ionization, in good agreement with the observations.

### REFERENCES

- [1] BUDDEN, K.G., Rep. Phys. Soc. Conf. Cavendish Lab., Phys. Soc. London (1954).
- [2] PERKINS, F., Nucl. Fusion **17** (1977) 1197; JACQUINOT, J., RF Plasma Heating, (Proc. 3rd Top. Conf. Pasadena, 1978).
- [3] IVANOV, N., KOVAN, J., LOS, E., Sov. Phys. – JETP **14** (1971) 212; ADAM, J., in Plasma Physics and Controlled Nuclear Fusion Research (Proc. 5th Int. Conf. Tokyo, 1974) Vol.1, IAEA, Vienna (1975) 65.
- [4] EQUIPE TFR, Rapport EUR-CEA-FC-1108 (1981) to be published in Plasma physics (1982).
- [5] STIX, T.H., Nucl. Fusion **15** (1975) 737.
- [6] EQUIPE TFR (Proc. 3rd Joint Varenna-Grenoble Symp. Grenoble, 1982) C26; EUR 7979 EN, I (1982) 423.
- [7] TFR GROUP, TRUC, A., GRESILLON, D., Nucl. Fusion **22** (1982) 1577.
- [8] TFR GROUP, Nucl. Fusion **22** (1982) 1173.
- [9] DEI CAS, R., REQUIN, G., SAMAIN, A., J. Nucl. Mater. **76 & 77** (1978) 1577.
- [10] EQUIPE TFR, these Proceedings, Vol. 3 (paper IAEA-CN-41/R-5).
- [11] TAKAHASHI, H., J. Phys. (Paris) **38**, suppl. C6 (1977) 171.

### DISCUSSION

J.C. HOSEA: In your discussion of RF pump-out of Ar<sup>16+</sup>, you state that the pump-out effect should be a function of the electric field strength at the two-ion hybrid resonance layer and hence a function of the RF power level. In your brief experiment, was it possible to determine the power dependence of the pump-out rate?

J. ADAM: The experiments on RF pump-out were performed during the last weeks of operation of TFR in August 1981. The data collected are unfortunately insufficient for me to answer your question, but this is certainly an important point which will be further investigated as soon as TFR is back in operation.

F.W. PERKINS: With regard to the unexplained ion heating under ion-ion hybrid resonance conditions, what fraction of the ion heating can be explained by electron temperature increases and the resultant collisional energy transfer, and what part remains to be explained?

J. ADAM: Simulation of the temperature evolution during RF-heating at high magnetic field, assuming no direct heating of ions by the wave, was done using a 1-D code. Taking into account the observed level of impurity, equipartition cannot explain more than half the measured heating of the ions. Moreover, the initial rate of heating of D ions, when the RF is applied, is clearly inconsistent with the hypothesis of ion heating by collisions.



## ENERGY AND IMPURITY TRANSPORT IN THE ALCATOR C TOKAMAK\*

B. BLACKWELL, C.L. FIORE, R. GANDY,  
 A. GONDHALEKAR<sup>†</sup>, R.S. GRANETZ, M. GREENWALD,  
 D. GWINN, E. KÄLLNE<sup>††</sup>, J. KÄLLNE<sup>††</sup>, S.E. KISSEL<sup>§</sup>,  
 B. LIPSCHULTZ, N.G. LOTER<sup>§§</sup>, E.S. MARMAR, S. McCOOL,  
 D. OVERSKEI<sup>§§§</sup>, D.S. PAPPAS, R.R. PARKER,  
 R. PETRASSO<sup>§§</sup>, M. PICKRELL, P.A. POLITZER,  
 M. PORKOLAB, P. PRIBYL, J.E. RICE, F. SEGUIN<sup>§§</sup>,  
 J.J. SCHUSS, J.L. TERRY, R. WATTERSON, S.M. WOLFE  
 Plasma Fusion Center,  
 Massachusetts Institute of Technology,  
 Cambridge, Massachusetts,  
 United States of America

### Abstract

#### ENERGY AND IMPURITY TRANSPORT IN THE ALCATOR C TOKAMAK.

Energy and impurity confinement times,  $\tau_E$  and  $\tau_I$ , have been investigated in Ohmically heated Alcator C discharges in the following parameter range: density  $\bar{n} \leq 8 \times 10^{20} \text{ m}^{-3}$ , current  $I_p \leq 0.75 \text{ MA}$  and toroidal field  $B_T \leq 13 \text{ T}$ . Geometrical dependences have been studied by operation with full circular apertures of various major and minor radii,  $R$ ,  $a_q$ . In all cases the dependence of energy confinement time on  $\bar{n}$  is characterized by a low-density regime, in which electron conduction dominates and  $\tau_E$  increases linearly with  $\bar{n}$ , and a high-density regime, in which ion conduction dominates and  $\tau_E$  increases only slowly or not at all with  $\bar{n}$ . At all densities, the dependence of  $\tau_E$  on  $a_q$  is weak. At  $\bar{n} = 2 \times 10^{20} \text{ m}^{-3}$ , the results of size-scaling experiments are summarized by the relation  $\tau_E \propto a^{0.8} R^{2.3}$ . At high density, the inferred ion thermal conductivity  $\chi_i$  apparently exceeds the neoclassical value of Hinton and Hazeltine by a factor which varies from 2 to about 4 depending on geometry and plasma parameters. Other interpretations of the data are, however, possible. Impurity confinement has also been studied in these discharges using the laser blow-off technique. The principal new results concerning  $\tau_I$  are (1) independence of the charge and mass of the injected impurity ion; (2) a linear dependence on  $a_q$ ; (3) a rapid deterioration as a function of the amplitude of the  $m = 2, 3$  tearing modes; and (4) an approximately linear dependence on the effective charge.

\* Research sponsored by US Department of Energy Contract DE-AC02-78ET51013.

<sup>†</sup> Present address: JET Joint European Undertaking, Abingdon, Oxon., UK.

<sup>††</sup> Permanent address: Center for Astrophysics, Harvard University, Cambridge, MA, USA.

<sup>§</sup> Present address: Max-Planck Institut für Plasmaphysik, Garching bei München, Fed. Rep. Germany.

<sup>§§</sup> Permanent address: American Science & Engineering, Cambridge, MA, USA.

<sup>§§§</sup> Present address: General Atomic Company, San Diego, CA, USA.

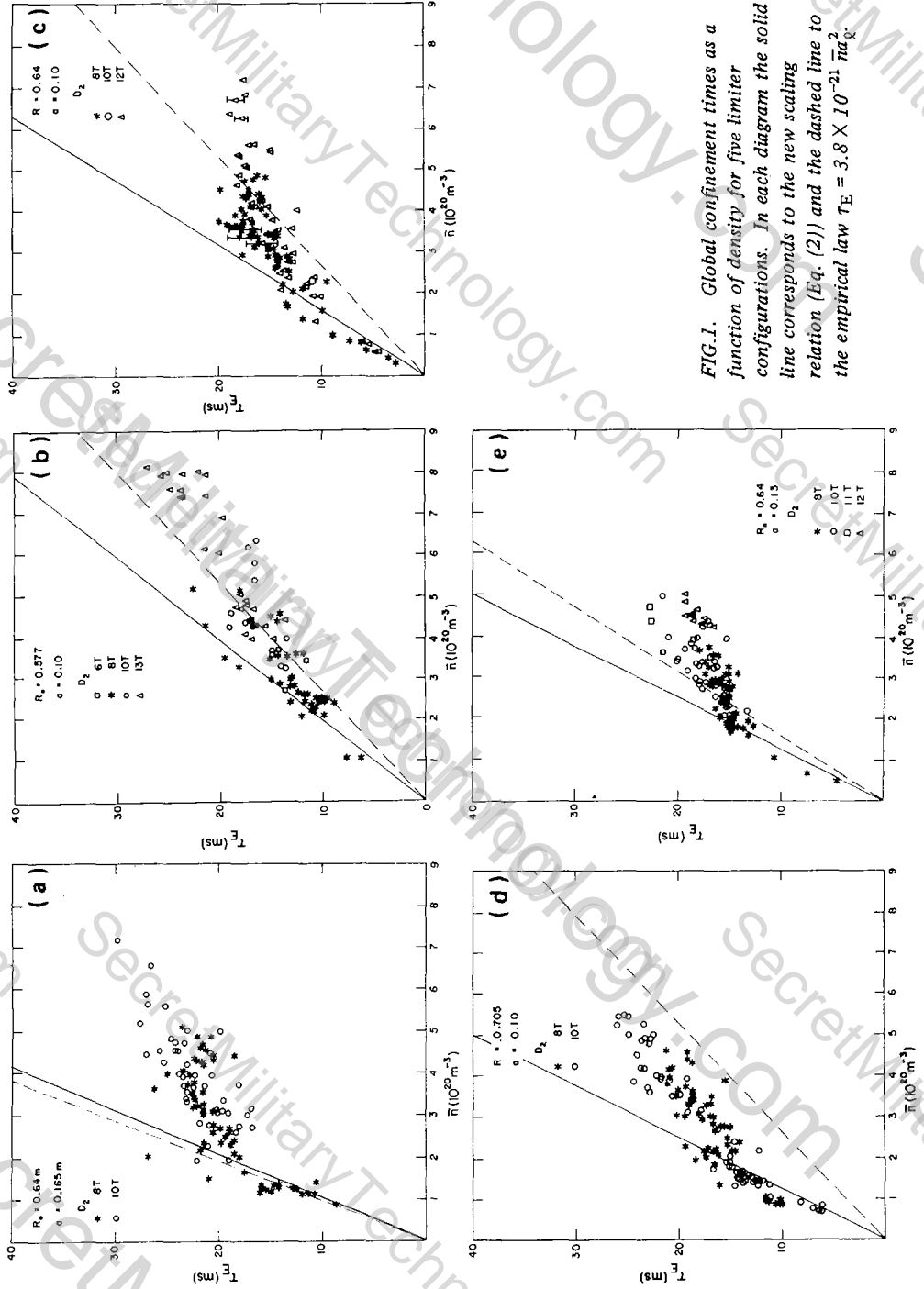


FIG. 1. Global confinement times as a function of density for five limiter configurations. In each diagram the solid line corresponds to the new scaling relation [Eq. (2)] and the dashed line to the empirical law  $T_E = 3.8 \times 10^{-21} \bar{n} a^2$ .

## 1. INTRODUCTION

Energy and impurity confinement in ohmically heated discharges in ALCATOR C have been investigated over the following wide range of plasma and machine parameters: line-averaged density  $0.5 \times 10^{20} < \bar{n} < 8 \times 10^{20} \text{m}^{-3}$ , plasma currents  $0.10 < I_p < 0.75 \text{ MA}$  and toroidal magnetic field  $B_T < 13 \text{ T}$ . In addition, we have operated with a variety of limiter configurations in order to study the dependence of energy and impurity confinement time on plasma size and geometry. Full circular molybdenum limiters have been used with minor radii  $a_g$  of 0.165 m, 0.13 m and 0.1 m, the latter having been moved to major radii of 0.577 and 0.705 m in addition to the nominal value of 0.64 m used in all other cases. These limiter configurations have permitted operation with a range of aspect ratios,  $3.9 < A < 7.05$ . The energy confinement studies reported below include only deuterium discharges which exhibit sawtooth activity, i.e.  $q(0) < 1$ .

Impurity confinement studies have also been made on non-sawtooth discharges and in hydrogen and helium working gases in addition to deuterium.

## 2. ENERGY CONFINEMENT

A commonly used model of tokamak energy confinement is one in which electron confinement time  $\tau_{Ee}$  is given by an empirically justified formula of the form  $\tau_{Ee} \propto \bar{n} a_g^2$ , together with an ion confinement time based on neoclassical theory. In this paper we deal with some important deviations from this formulation and present an improved model which is more consistent with the experimental observations. The modifications to the previous model include enhanced ion transport which reduces global energy confinement at high density and the introduction of a strong dependence of confinement on major radius in the low-density, electron-dominated regime.

Confinement times observed for various limiter configurations are shown as a function of density in Figure 1(a-e). Each exhibits a linear region at lower density and a slower rise or saturation as the density increases above  $n > 2.5 \times 10^{20} \text{m}^{-3}$ . Comparison of the absolute values of the confinement times reveals a significant departure from the empirical scaling. We would expect that the confinement times with  $a=0.10\text{m}$  (Figure 1b,c,d) should be smaller than those with  $a=0.165\text{m}$  (Figure 1a) by a factor of nearly three; the data, however, indicate a much weaker dependence on minor radius. In addition, comparison of Figures 1b,c,d indicates a significant dependence of confinement on major radius, which is not considered in the empirical formulation.

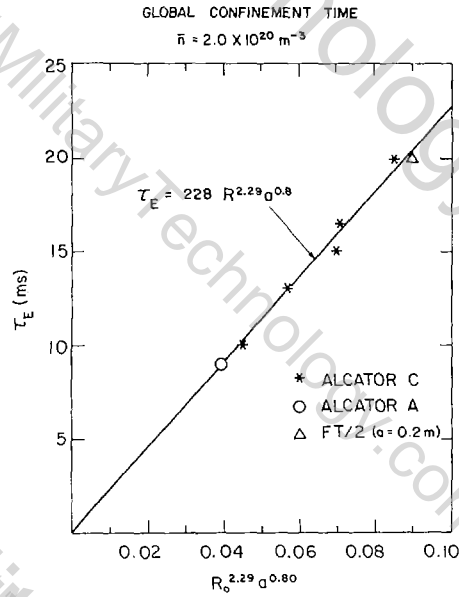


FIG. 2. Global energy confinement time at  $\bar{n} = 2 \times 10^{20} \text{ m}^{-3}$  versus the regression parameter obtained for a power law fit to data from Alcator A and five configurations of Alcator C. The FT point, shown with both scales divided by two, was not used in performing the regression.

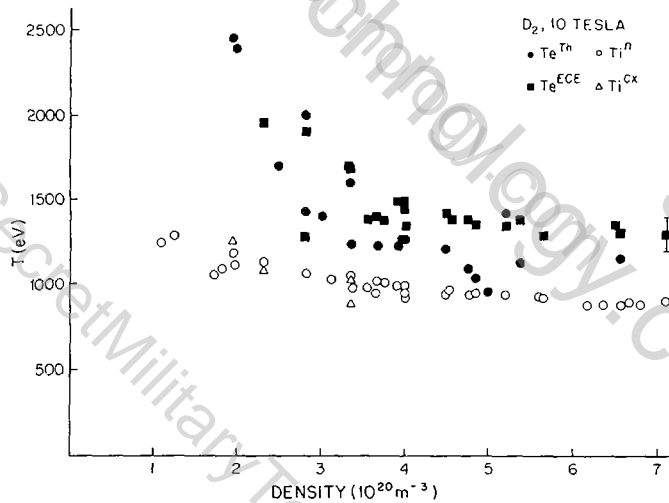


FIG. 3. Central electron and ion temperatures for  $B_t = 10 \text{ T}$ ,  $R = 0.64 \text{ m}$ ,  $a_q = 0.165 \text{ m}$ . All points are for deuterium discharges.

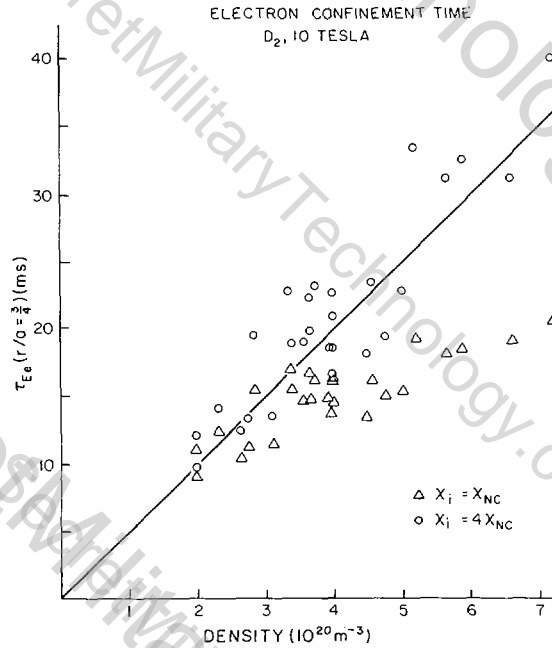


FIG. 4. Electron energy confinement times, evaluated at 0.75 of the limiter radius. The two sets of points result from assuming ion thermal diffusivity of one and four times the neo-classical value.

Regression analysis of the data for fixed density  $n = 2 \times 10^{20} \text{ m}^{-3}$  under the assumption that the geometrical dependence of confinement is of the form  $\tau_E \propto R^H a^V$  leads to the fit shown in Figure 2. Here a data point from ALCATOR A ( $R = 0.54 \text{ m}$ ,  $a = 0.10 \text{ m}$ ) has been included in the analysis along with data from ALCATOR C. The resulting expression

$$\tau_E (n = 2 \times 10^{20} \text{ m}^{-3}) = 228 R^{2.29} a_l^{0.8} \text{ msec} \quad (1)$$

is also found to be in good agreement with the point from the FT tokamak ( $R = 0.83$ ,  $a = 0.20 \text{ m}$ ) [1], which was not included in the regression.

Introducing this geometrical factor, we find that the confinement times in the lower density range,  $n < 2.5 \times 10^{20} \text{ m}^{-3}$ , can be well represented by a modified scaling law of the form

$$\tau_E = 1.15 \times 10^{-21} \bar{n}_e R^{2.3} a_l^{0.8} \text{ sec} \quad (2)$$

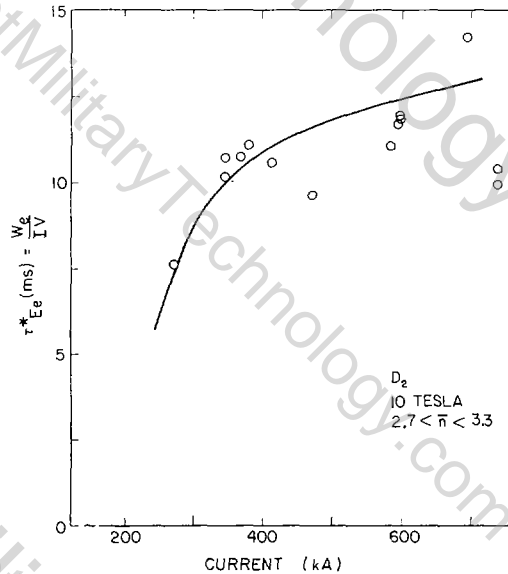


FIG.5. Gross electron energy confinement times plotted against plasma current for  $\bar{n} = 3 \times 10^{20} \text{ m}^{-3}$ ,  $R = 0.64 \text{ m}$ ,  $a = 0.165 \text{ m}$ . The solid curve represents the expected result for  $\tau_{Ee} = 15 \text{ ms}$ , ion thermal conduction four times the neoclassical value.

which is shown as the solid line in Figure 1a-e. For comparison, the expression  $\tau_{Ee} = 3.8 \times 10^{-21} n a^2$ , which was inferred from ALCATOR A data<sup>[2]</sup>, is shown as a dashed line in each figure. It is apparent that while the two forms are indistinguishable for the  $R=0.64$ ,  $a=0.165\text{m}$  case, the new form (2) gives much better agreement with the small limiter data at the lower densities.

At higher densities each of the data sets shows a significant departure from the anticipated linear behavior. To examine this effect in more detail we consider a set of shots at a toroidal field of 10 Tesla with  $a=0.165\text{m}$ . The behavior of central electron and ion temperatures as a function of density is illustrated in Figure 3. The difference between  $T_e(0)$  and  $T_i(0)$  at the higher densities is too large to be accounted for by neoclassical ion thermal conduction, assuming that the electron-ion power transfer is not less than classical.

We may evaluate the electron energy confinement time, given by  $\tau_{Ee} = W_e/P_e$  where  $W_e$  is the electron energy content and  $P_e$  is the net power to the electrons, i.e. the ohmic power diminished by the ion heat loss  $Q_i$ . In order to evaluate  $\tau_{Ee}$  it

is necessary to introduce a model for the ion heat flux. Figure 4 shows the result of determining  $\tau_{Ee}$  for the data shown in Figure 3, using two models for calculating  $Q_i$ .

In the first case the ion thermal diffusivity,  $\chi_i$ , is taken to be that given by the neoclassical formulation [3]. In the second case the value of  $\chi_i$  is enhanced by a factor of four, which is found to be compatible, within experimental error, with the measured difference between central electron and ion temperatures. In each case the electron temperature and density profiles are taken as given and a self-consistent ion temperature profile is inferred from the ion power balance equation using the assumed model of  $\chi_i$ .

It may be seen that neoclassical ion thermal conduction as given in [3] is not sufficient to explain the observed difference between central electron and ion temperatures or to account for the non-linear dependence of global confinement on density. If the ion thermal diffusivity is taken to be neoclassical then we conclude that the electron confinement time does not increase significantly with density for  $\bar{n}_e > 3 \times 10^{20}$ . However, ion conduction of four times the neoclassical value is consistent with the temperature data and implies a linear dependence of  $\tau_{Ee}$  on  $\bar{n}$ .

To further investigate the problem of energy transport at middle to high density,  $\bar{n} > 2 \times 10^{20} \text{m}^{-3}$ , and to test the scaling of the apparent anomalous ion conduction, we have conducted a series of experiments to determine the scaling of confinement with plasma current at fixed density, toroidal field, and machine geometry. In Figure 5 we present the results of a scan at  $\bar{n}_e = 3 \times 10^{20} \text{m}^{-3}$ ,  $B_t = 10$  Tesla,  $R = .64$  and  $a = .165 \text{m}$ . The gross electron confinement time,  $\tau_{Ee}^*$ , defined as the electron energy content divided by the total ohmic power input, is seen to increase with plasma current up to  $I_p = 700$  kA. The solid curve gives the predicted dependence under the assumptions that the true electron confinement time, at  $r/a = 0.75$ , remains constant at  $\tau_{Ee} = 15$  msec, the ion conduction scales as the neoclassical value with an enhancement factor of four, the electron temperature profile is Gaussian in shape, and the resistivity is given by the Spitzer formula with  $Z_{eff} = 1.2$ . The apparent degradation of confinement at the highest current can be understood as being due to increased radiative power loss; the central radiated power, which amounts to only 10-15% of the central ohmic power for  $I_p < 600$  kA, rises rapidly to over 30% for  $I_p > 700$  kA, due to increased Mo levels.

We therefore conclude that the dependence of global confinement on density and current in the mid-to-high density

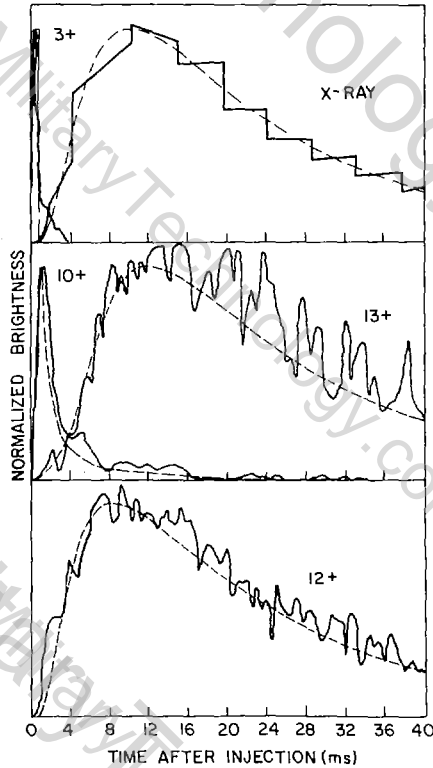


FIG. 6. Normalized chordal brightnesses from different ionization states of injected silicon. The dashed curves are predictions from the computer model.

regime is consistent with enhanced ion thermal transport; for this data set, the required anomaly factor on  $\chi_i$  relative to the Hinton and Hazeltine value is approximately four, and the factor seems to be independent of current over the range  $250 < I_p < 720$  kA. However, due to experimental uncertainties and particularly to the lack of a measurement of the ion temperature profile it is not possible to discriminate unambiguously between electron and ion transport. An alternative model, consistent with the data, would require enhanced ion losses only in the central region, to account for the observed difference between Te(0) and Ti(0). The anomalous electron transport would then have a less favorable dependence on density than that implied by the empirical scaling law, together with a favorable dependence on plasma current.

In the case of the reduced-aperture limiters, the departure of the confinement from the linear dependence at higher density may also be ascribed to the role of ion transport. However, the anomaly factor appears to depend on geometry, with an enhancement of two being sufficient to account for some of the behavior, particularly for the  $R=0.705\text{m}$  data. Whether this apparent improvement in ion transport is in fact due to geometry or is an indirect result arising from changes in profiles or boundary conditions is not yet clear.

### 3. IMPURITY CONFINEMENT

In order to study the particle transport of impurities, the laser blow-off technique<sup>[4]</sup> has been utilized to inject trace amounts of various impurities into ALCATOR C plasmas. Aluminum, silicon, titanium and molybdenum have been injected, and subsequent emissions from the various charge states have been monitored with a variety of UV and X-ray instruments.

A detailed look at specific Si emission lines (with the backgrounds subtracted off) during a sequence of similar deuterium discharges ( $B_T=6.0\text{ T}$ ,  $I=385\text{ kA}$ ,  $\bar{n}_e=3.6\times 10^{20}\text{ m}^{-3}$ ,  $T_{e0}=1100\text{ eV}$ , and  $q_L=3.13$ ) is provided in Figure 6. The normalized chordal brightnesses of sodium-, beryllium-, helium-, and hydrogen-like silicon, as well as the central chord soft X-ray

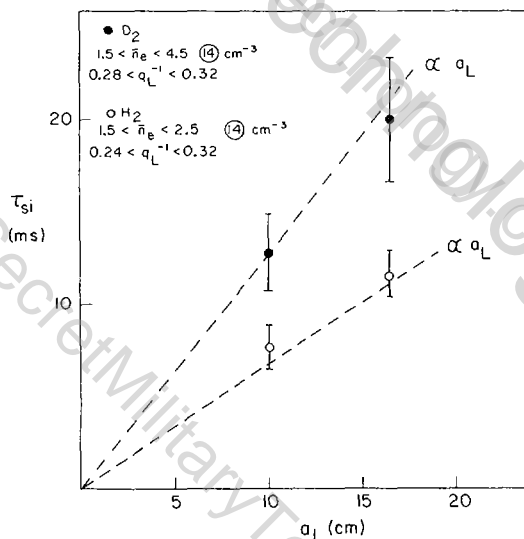


FIG. 7. Silicon confinement time as a function of minor radius for hydrogen and deuterium discharges.

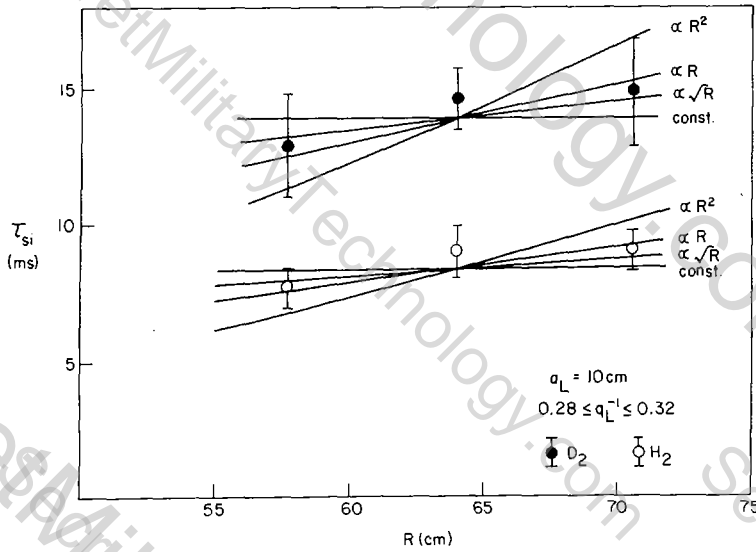


FIG. 8. Silicon confinement time as a function of major radius for hydrogen and deuterium discharges at constant  $q_0$ ,  $a_0 = 0.1$  m.

( $h\nu > 1$  keV) brightness are shown as functions of time after the injection. For comparison, the results of a computer calculation modeling the process assuming diffusion only, with a spatially uniform diffusion coefficient  $D = 0.26 \text{ m}^2/\text{sec}$ , are shown as the dashed curves. The agreement is excellent. A similar calculation, assuming the transport is due to neoclassical processes<sup>[5]</sup> alone, yields results which are clearly inconsistent with the experimental observations, as the calculated influx is too slow, and the impurities are predicted to remain at the center of the plasma for a much longer time than is observed.

The falling signals of  $Si^{12+}$  and  $Si^{13+}$  in Fig. 6 are well described by an exponential decay. This characteristic decay time is interpreted as the global particle confinement time ( $\tau_I$ ) for non-recycling injected trace impurities<sup>[6]</sup>. In previous studies, on the ALCATOR A device<sup>[6]</sup>, it was found that  $\tau_I$  was proportional to the mass of the background majority ion species ( $m_{bg}$ ) times  $q_0^{-1}$ , and that  $\tau_I$  was independent of  $n_e$ . These results have been confirmed by the results on ALCATOR C. Fig. 7 shows the silicon confinement time as a function of limiter radius for hydrogen and deuterium discharges on ALCATOR C at fixed  $q_0$ . The data are consistent with a linear dependence on minor radius. The dependence of  $\tau_I$  on major radius is shown in Fig. 8. In this case, the results are not so clear-cut,

the dependence being best described as  $\tau_I \propto R^\gamma$ ,  $1/2 < \gamma < 1$ ; however, within experimental errors,  $\gamma=0$  would also be consistent with the data. At low densities ( $n_e < 2 \times 10^{20}$ ), the impurity confinement times increase, apparently in tandem with an accompanying increase in the  $Z_{\text{eff}}$  of the plasma due to intrinsic impurities. Over the range  $1 < Z_{\text{eff}} < 3$ , the results can be described by  $\tau_I \propto Z_{\text{eff}}/Z_{\text{bg}}$ . All of these results for the scaling of impurity confinement time may be summarized by an empirical scaling law:

$$\tau_I(\text{ms}) = \frac{2.4 \times 10^2 a_\ell m_{\text{bg}}}{q_\ell} R^{.75} \frac{Z_{\text{eff}}}{Z_{\text{bg}}} \quad (3)$$

with  $R$  and  $a_\ell$  in m,  $m_{\text{bg}}$  in amu, and where  $Z_{\text{bg}}$  is the charge of the background majority ion species. Note that the dependences on major radius and  $Z_{\text{eff}}/Z_{\text{bg}}$  should not be interpreted too literally, since other scalings would be in equally good agreement with the data. It is, however, well established empirically from these results that  $\tau_I$  is approximately proportional to  $a_\ell m_{\text{bg}} q_\ell^{-1}$ .

At the highest densities obtainable at a particular magnetic field, the impurity confinement times are somewhat shorter than at lower densities. This decrease of impurity confinement

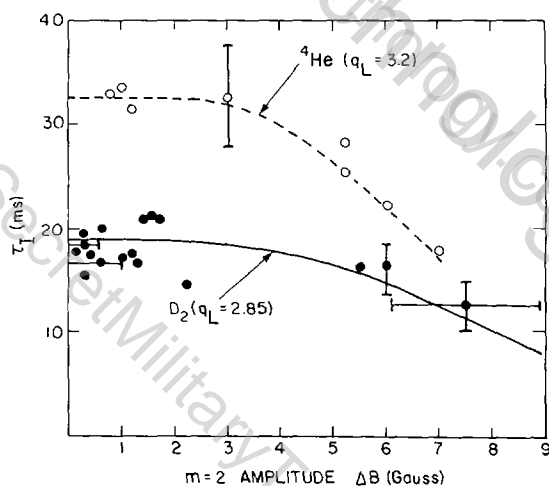


FIG. 9. The impurity confinement time as a function of  $m = 2$  amplitude for injections into helium and deuterium discharges.

time is not believed to be due to a direct density dependence, per se, but rather to the increase in  $m=2$  and  $m=3$  MHD activity which is observed at these high densities on ALCATOR C [7]. This is borne out by the observation that the thresholds for both MHD activity and impurity confinement deterioration occur at a higher density when the field is increased from 6 to 8 T. The degradation of impurity confinement with an increasing level of MHD activity is shown by the upper points in Fig. 9. These data are from injections of aluminum into  $^4\text{He}$  plasmas. If it is assumed that the MHD activity introduces a new transport mechanism whose diffusion coefficient depends only upon the MHD fluctuation level, and that this adds linearly to the diffusion present without significant MHD activity (as given by Eq. (3)), then

$$\tau_{\text{total}} = [\tau_{\text{MHD}}^{-1} + \tau_{\text{I-eq.(3)}}^{-1}]^{-1} \quad (4)$$

A fit to the  $^4\text{He}$  data yields  $\tau_{\text{MHD}} \propto (\Delta B)^{-4}$ , and is shown as the dashed line in Fig. 8. The behavior for injections into deuterium plasmas may then be determined by using Eq. (4) with the same  $\tau_{\text{MHD}}(\Delta B)$ , and is shown as the solid line in Fig. 8, consistent with the data.

#### REFERENCES

- [1] FT GROUP, High Field Tokamak Workshop, Boston, June 1981, unpublished.
- [2] GONDHALEKAR, A., et al., in Plasma Physics and Controlled Nuclear Fusion Research 1978 (Proc. 7th Int. Conf. Innsbruck, 1978) Vol. 1, IAEA, Vienna (1979) 199.
- [3] HINTON, F.L., HAZELTINE, R.D., Reviews of Modern Physics 48 (1976) 239.
- [4] MARMAR, E.S., CECCHI, J.L., COHEN, S.A., Rev. Sci. Instrum. 46 (1975) 1149.
- [5] RUTHERFORD, P.H., Phys. Fluids 17 (1974) 1782.
- [6] MARMAR, E.S., RICE, J.E., ALLEN, S.L., Phys. Rev. Lett. 45 (1980) 2025.
- [7] GRANETZ, R.S., A Density Threshold for MHD Activity in ALCATOR C, M.I.T. Plasma Fusion Center Report PFC/JA-81-28, submitted to Phys. Rev. Lett. (1982).

## DISCUSSION

F. SANTINI: How can you tell that the  $\tau_E$  scaling deterioration is due to ions rather than to electrons, since  $\hat{T}_e$  and  $\hat{T}_i$  are very close?

S.M. WOLFE: The difference between  $\hat{T}_e$  and  $\hat{T}_i$  is in fact larger than expected for neoclassical ion heat loss. In particular, the power flow from electrons to ions implied by the observed difference suggests an enhancement of the central ion heat flux by the factors indicated in the paper. Assuming the same enhancement in the transport coefficient over the profile gives results consistent with the observed  $\tau_E$  scaling.

F. SANTINI: In the FT tokamak the electron thermal conductivity is found to increase with current if other plasma parameters are kept fixed. You have shown an opposite tendency in your experiment; could you comment on this?

S.M. WOLFE: In fact, our interpretation of the current scaling experiments is that the ion thermal conductivity decreases with current, as expected for neoclassical-like transport. The electron confinement time is modelled as being current-independent, leading to a favourable scaling of global confinement with  $I_p$ .

G. von GIERKE: I do not want to defend any scaling law, but I do have doubts whether the stated minor-radius dependence is conclusive. Changing the limiter radius alters the distance to the wall, and hence the limiter shadow. This can have a strong influence on the boundary layer and, therefore, on the confinement time.

S.M. WOLFE: In the case where  $a = 0.10$  m and  $R = 0.577$  and  $0.705$  m, the minimum distance to the wall is the same as for the  $a = 0.165$  m case ( $\Delta \approx 2.5$  cm); the average plasma-to-wall distance is of course increased by the same amount for each of the former configurations. The major radius dependence of confinement cannot therefore be explained in these terms. Furthermore, in Alcator A ( $a = 0.10$  m,  $R = 0.54$  m) the wall-to-limiter separation was the same as for the  $a = 0.165$  m case in Alcator C. Therefore it seems to me that the limiter shadow thickness does not correlate well with energy confinement in these experiments and does not account for the observed scaling.

K. MOLVIG: I want to make some comments on the interpretation of your results, since I know you are reluctant to do so. First, the observation that confinement increases with size cubed,  $\tau_E \propto L^3$ : this type of behaviour is a generic property of saturated drift-wave microturbulence, irrespective of specific models, and your observations lend support to that interpretation of the underlying source of the anomaly. Secondly, the observation of improvement with major radius gives some clues to the details of this turbulence. Specifically, major radius dependence would arise from either shear or toroidicity (and trapped particles). Since these effects lead to opposite dependences, and since shear

would go the other way from your observations ( $\tau_E \propto R^{-\alpha}$ ), the implication is that toroidicity and trapped particles are causing the anomaly. This interpretation is general and needs qualification, of course, but it should serve as stimulus and a direction indicator for theoretical efforts.

S.M. WOLFE: I agree in general with your comment. The fact that confinement scales with the third power of a linear dimension is certainly suggestive of a diffusivity which depends on a scale length, while toroidal effects are a likely source of a favourable R-dependence. I would like to point out that these results were obtained in Ohmically heated discharges, and the fact that the power is not independent of the transport in this case, owing to the  $T_e^{-3/2}$  dependence of the resistivity, complicates the analysis. There can exist quite different forms of thermal conductivity, arising from different driving terms, saturation mechanisms, etc., which lead to the observed geometrical scaling for an Ohmic plasma.

R.J. TAYLOR: You are arguing that you can properly extract the a-dependence from your experiments. Since you are programming the minor radius by means of a limiter, the relative importance of the plasma interaction can change in ways not yet understood. No absolute relationship can at present be established, therefore, although you imply that it can.

S.M. WOLFE: Although it is impossible to eliminate all "hidden variables" from any experiment of this kind, I feel that we have considered the most likely effects, such as differences in impurity levels and the change in limiter-to-wall spacing referred to by Dr. von Gierke. In addition, the successful extrapolation of our results to other machines constitutes supporting evidence. I think the direct interpretation, that a<sup>2</sup> scaling does not hold and that the major radius has a strong influence on confinement, is the most likely explanation of our data.

H.L. BERK: Since the ion classical transport coefficient depends on the difference between electron and ion temperature, the absolute ion transport formula must depend sensitively on the ion temperature measurement. What is the uncertainty in the final ion transport coefficient?

S.M. WOLFE: The uncertainties in the electron and ion temperatures are each typically about 10%. For the cases discussed, the range of the anomaly factor in the ion conductivity is about 3 to 5 with respect to the Hinton and Hazeltine values. An anomaly factor of 1 is well outside the error bars for these cases.

## LOWER-HYBRID HEATING EXPERIMENTS IN THE FRASCATI TOKAMAK (FT)

F. ALLADIO, M.L. APICELLA\*, E. BARBATO,  
G. BARDOTTI, R. BARTIROMO, F. BOMBARDA\*\*,  
G. BRACCO, G. BUCETI, P. BURATTI, R. DE ANGELIS,  
F. DE MARCO, M. DE PRETIS, D. FRIGIONE,  
M. GASPAROTTO, R. GIANNELLA, M. GROLI, M. HAEGI,  
A. MANCUSO, V. MERLO\*\*, V. PERICOLI, L. PIERONI,  
S. PODDA, E. PURCHI\*\*, J.P. RAGER, G.B. RIGHETTI,  
F. ROMANELLI\*, F. SANTINI, S.E. SEGRE, A. TANGA,  
A. TUCCILLO, O. TUDISCO, J. WELLS\*, V. ZANZA

Associazione Euratom-ENEA sulla Fusione,  
Centro Ricerche Energia Frascati,  
Frascati, Rome,  
Italy

### Abstract

#### LOWER-HYBRID HEATING EXPERIMENTS IN THE FRASCATI TOKAMAK (FT).

RF power at the LH frequency (2.45 GHz) has been launched in FT. The maximum injected power was 250 kW corresponding to  $6 \text{ kW} \cdot \text{cm}^{-2}$ . In low-density D operation ( $\bar{n} = 4 \times 10^{13} \text{ cm}^{-3}$ ) a strong interaction with electrons causes current-drive effects and electron and ion bulk heating. At  $\bar{n} = 10^{14} \text{ cm}^{-3}$ , fast neutral tail in H and neutron enhancement in D have been observed. At higher densities, this ion-wave interaction tends to disappear with the onset of parametric decay instabilities.

### INTRODUCTION

RF power in the LH range of frequencies (2.45 GHz) was injected in FT [1] ( $R = 83 \text{ cm}$ ,  $a = 20 \text{ cm}$ ,  $B_0 = 60 - 80 \text{ kG}$ ,  $I_p = 300 - 400 \text{ kA}$ ). The grill is a  $2 \times 2$  waveguide structure, each waveguide being  $7.1 \text{ cm}$  high and  $1.5 \text{ cm}$  wide. The grill characteristics related to the plasma conditions are given in Ref. [2]. A power up to 250 kW corresponding to  $6 \text{ kW/cm}^2$  was coupled to the plasma. The experiment was performed with plasmas having peak ion and electron temperatures of about 1 keV and peak density up to  $4 \times 10^{14} \text{ cm}^{-3}$  in D and  $2 \times 10^{14} \text{ cm}^{-3}$  in H. In most conditions electrons and ions are strongly coupled [1] so that the electron

\* ENEA Fellow.

\*\* Guest.

energy confinement time is the principal relaxation time. Ohmic power is in the range 400-700 kW, i.e. 2-3 times the maximum RF power used. The main results are: a) coupling characteristics are in satisfactory agreement with theoretical predictions; b) in D plasmas for  $3 \times 10^{13} < \bar{n} < 5 \times 10^{13} \text{ cm}^{-3}$  strong interaction with electrons has been observed, an electron peak temperature increase of about 400 eV and an ion temperature increase of about 200 eV with a net power of 110 kW was measured; c) in D at  $\bar{n} \cong 10^{14} \text{ cm}^{-3}$  a twofold neutron enhancement occurs; d) in H plasma energetic ion tails were observed for  $\bar{n} < 1.5 \times 10^{14} \text{ cm}^{-3}$ . At higher densities parametric decay occurs, probably playing a role in wave penetration and absorption. Except for the study of coupling, all the results here reported were obtained with a phase of  $180^\circ$ .

### COUPLING

The RF power system, described in Ref. [3], is fed by two klystrons of 500 kW x 1 s each. At present this system delivers power to a 2 x 2 waveguide grill which has ceramic breaks 15 cm away from its mouth, to insulate the pressurized parts of the waveguides. The structure can move radially 3 cm. Except in operations at very low density ( $\bar{n} \cong 2 \times 10^{13} \text{ cm}^{-3}$ ), the grill mouth was at 2.5 cm from the plasma edge since here the reflection coefficient exhibited an appreciable minimum. Measurements by Langmuir probes in the limiter shadow [4] show that edge densities (at the grill mouth) higher than  $10 n_c$  ( $n_c =$  cutoff density) favour higher reflected power and discharges<sup>c</sup> in the grill. Parametric decay instabilities with peaks at the harmonics of the ion cyclotron frequency are generated at the plasma border. The relative signal tends to disappear when the edge density  $n_w$  is reduced ( $\cong n_c$ ) and the edge electron temperature is above about 10 eV. This tendency agrees with the predictions for the threshold of resonant decay instabilities [5].

Tests of power transmission of the plasma have been performed by exciting only left (right) waveguides and measuring the backward power in the other right (left) waveguides. Figure 1 shows the latter power as a function of the power transmitted through the adjacent waveguides. A linear relationship is apparent. The full line is the result of a coupling code [6] which takes into account also a density step at the grill mouth and uses experimental values of  $n_w/n_c$  and grad  $n$ . For standard excitation of both left and right waveguides of the grill with the same amplitude but different phase, the reflected power as a function of the phase is shown in Fig. 2. The coupling code with  $n_w = 10^{11} \text{ cm}^{-3} = 2n_c$  gives the full line for grad  $n = 2 \times 10^{11} \text{ cm}^{-4}$  and the dashed line for grad  $n = 1 \times 10^{12} \text{ cm}^{-4}$ . The measured values are  $n_w \cong 10^{11} \text{ cm}^{-3}$ , grad  $n \cong 10^{12} \text{ cm}^{-4}$ . The low values of  $n_w/n_c$  fitting the experimental results are connected [6] with the low values of  $n_{H1} (< 2.5)$  excited by our grill [2].

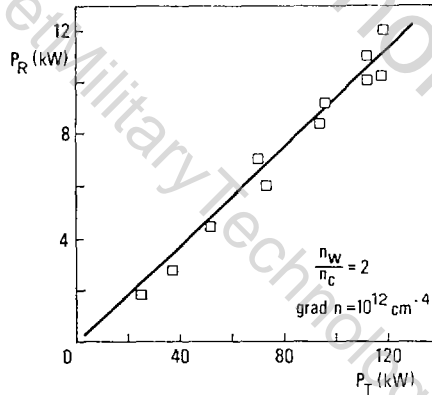


FIG.1. Backward power in the right (or left) waveguides versus power transmitted in the left (or right) waveguides. The line represents the result of a coupling code assuming the experimental values for  $n_w/n_c$  and  $\text{grad } n$ .

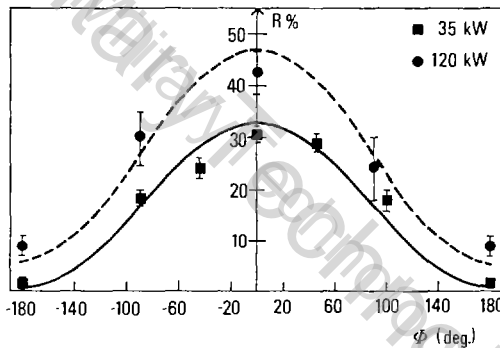


FIG.2. Reflectivity versus phase between adjacent waveguides at RF power 35 kW and 120 kW.

#### INTERACTION WITH ELECTRONS

As expected by the low  $n_{ll}$ -spectrum excited by our grill, a direct interaction with electrons takes place only at relatively low density when energetic electron tails develop.

Operating in D at  $B_0 = 60$  kG,  $\bar{n} = 3 - 5 \times 10^{13} \text{ cm}^{-3}$  and  $P_{RF} = 100 - 200$  kW a strong interaction of waves with electrons has been observed. In Figure 3 a case with  $\bar{n} = 3 \times 10^{13} \text{ cm}^{-3}$  and  $P_{RF} = 120$  kW is shown. The main features are: a decrease of the loop voltage and of the hard X-ray emission, an outward shift of

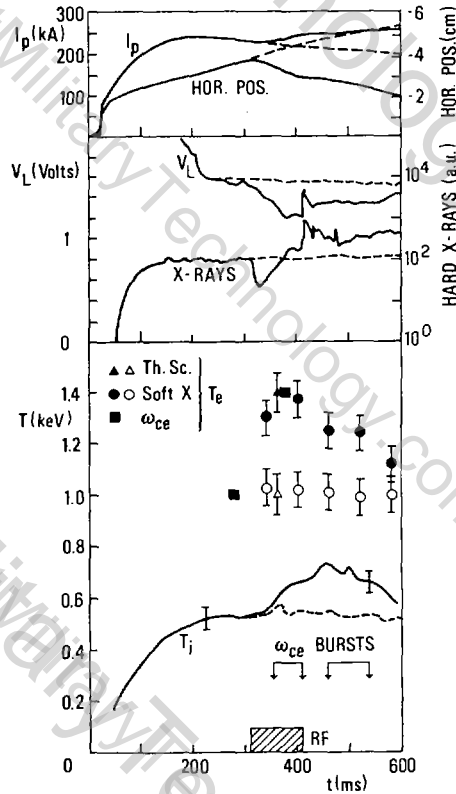


FIG. 3. From the top:  $I_p$ , horizontal position;  $V_{loop}$ , hard X-rays monitor signal;  $T_e$  and  $T_i$  versus time (continuous line or solid symbols and broken line or open symbols for discharges with and without RF respectively). Temporal location of the bursts in the  $\omega_{ce}$  emission is also indicated. (Th.Sc. = Thomson scattering.)

the plasma column, a slow increase of current, an increase of  $T$  (Thomson scattering,  $2\omega_{ce}$  and soft X-ray emission) and  $T_i$  (CX)<sup>e</sup>. The emission in the  $\omega_{ce}$  frequency range contains a strong enhancement during the RF pulse and trains of bursts, whose timing is indicated in Fig. 3. Radial  $T_e$  profiles with and without RF are shown in Fig. 4. An electron energy tail accelerated by LH waves close to the plasma center seems responsible for the current drive effects and for the bulk electron heating. The latter is due to tail energy thermalization via non-collisional phenomena (e.g. anomalous Doppler instability [7]) as indicated by the bursts in  $\omega_{ce}$  emission. A typical spectrum in the  $\omega_{ce}$  range is shown in Fig. 5. Strong enhancement over the thermal level appears around  $\omega_{pe}$ ,  $1.5\omega_{ce}$  and  $\omega \geq 3\omega_{ce}$  as an effect of the high

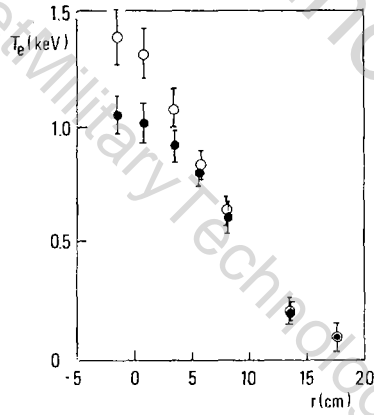


FIG.4. Radial profile of the electron temperature measured by Thomson scattering in two consecutive discharges with (open circles) and without (closed circles) RF.

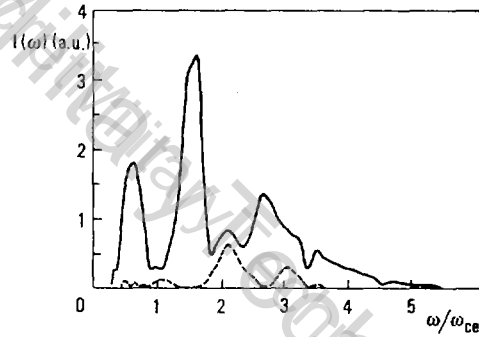


FIG.5. Spectrum of the emission in the  $\omega_{ce}$  range of frequency with (solid line) and without (broken line) RF.

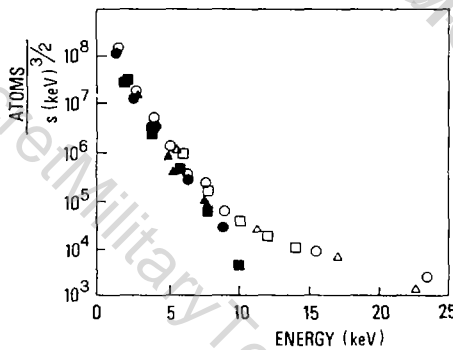


FIG.6. Energy spectrum of neutrals before (solid symbols) and during (open symbols) LH heating. H plasma at 60 kG with  $\bar{n} = 9 \times 10^{13} \text{ cm}^{-3}$ .

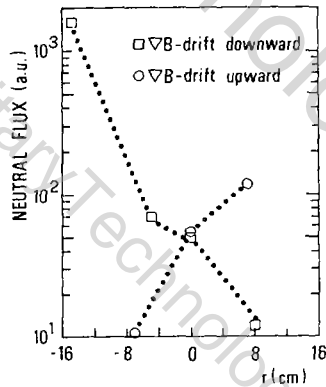


FIG. 7. 7 keV fast neutral hydrogen flux versus radius of viewed chord during RF.  $\bar{n} = 9 \times 10^{13} \text{ cm}^{-3}$ ;  $P = 120 \text{ kW}$ .

energy electrons. The optically thick  $2\omega_{ce}$  emission is only sensitive to the bulk temperature and the relative enhancement agrees with other  $T_e$  measurements. Bulk ion heating (no tails are observed) takes place via classical collisional transfer from the electrons in agreement with the observed rise and decay time of  $T_i$  ( $\approx 50 \text{ ms}$ ). Since energy transfer from the e-fast tail to e-bulk lasts also after the RF shut-off (see Fig. 3),  $T_e$  does not drop immediately and  $T_i$  keeps growing for another 50 ms (the CX acquisition time is 10 ms).

As the density is increased at the same current, the above effects become weaker, and above  $\bar{n} \approx 7 \times 10^{13} \text{ cm}^{-3}$  electron-wave interaction is negligible. This density dependence seems to be connected with a decrease of the fast electron component as the streaming parameter ( $\propto I_p/n_e$ ) decreases.

#### INTERACTION WITH IONS

In H-plasma, linear turning points (LTP) are expected for  $n_{H^+} = 2$  at density  $1.3 \times 10^{14} \text{ cm}^{-3}$  at 80 kG and  $1.6 \times 10^{14} \text{ cm}^{-3}$  at 60 kG. Energetic ion tails have been observed perpendicularly by neutral analyzer at  $B = 60 \text{ kG}$  and in the range of peak density  $0.8 - 1.5 \times 10^{14} \text{ cm}^{-3}$ . Figure 6 shows a typical energy spectrum of neutrals before and during the RF pulse at a power of 140 kW. Since the CX neutral analyzer looks at the plasma with an extremely small angle ( $\approx 10^{-3} \text{ rad}$ ) around the direction perpendicular to  $B_z$ , the observed neutrals came from ions with high perpendicular velocity which are trapped in the  $B_z$  ripples (0.4% to 3% from center to edge). In time the signal decays in less than an acquisition interval. A vertical tilting of the analyzer shows a

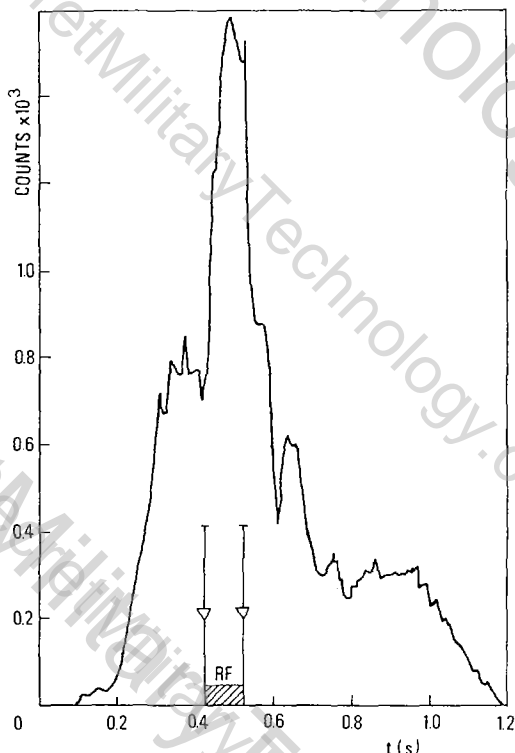


FIG.8. Neutron emission versus time in a D plasma at 60 kG with  $\bar{n}_e = 1 \times 10^{14} \text{ cm}^{-3}$ .

strong up-down asymmetry. The result of a vertical scan during the RF pulse at energy of 7 keV is shown in Fig. 7. Very few counts are recorded when one looks through a chord crossing more than 7 cm from the center on the side opposite the ion toroidal drift. This is taken as evidence that the fast neutrals are coming from the plasma center and the increase in signal as the chord approaches the border is due to fast ions drifting into regions of higher neutral density, as has been verified by inverting the direction of the toroidal  $B_0$  field. For peak density roughly above  $1.5 \times 10^{14} \text{ cm}^{-3}$ , decay instability signal increases significantly and the fast neutrals disappear. The spectral analysis of a RF probe shows sideband peaks separated from the pump frequency by harmonics of  $\omega_{ci}$ . Up to 10 satellites are present, depending on the density and temperature profiles of the discharge. Resonant decay instability justifies this feature and an evaluation of the threshold [5] for its onset is in rough agreement with the observed density and temperature at the border.

In D plasma turning points for  $n_{||} = 2$  are expected at  $\tilde{n}_e = 3.5 \times 10^{14} \text{ cm}^{-3}$  for 80 kG. A less extensive campaign has been done in D at LTP regimes. The onset of decay signal is observed at  $\tilde{n}_e \geq 2 \times 10^{14} \text{ cm}^{-3}$ . Even at lower densities fast neutrals were not observed in the measured range 1 - 10 keV. Only for  $\tilde{n}_e \cong 10^{14} \text{ cm}^{-3}$  neutron emission has shown an appreciable relative enhancement (100%), probably due to a weak tail of very high energy (Fig. 8).

This discrepancy between H and D behaviour at densities below their respective thresholds for parametric decay onset could be due to the different perpendicular energy of the ions resonating with the waves [8]. For the actual plasma conditions of the experiments, ray-tracing calculations in toroidal geometry indicate an internal decrease of  $n_{||}$  and part of the RF spectrum can meet the LTP only in H-discharges. In these conditions, no direct effect on the bulk is expected but an ion tail should develop above a minimum resonant energy  $\varepsilon_c$ . Indeed, for the main part of the ray trajectories,  $\varepsilon_c$  is around 10 keV for H, while in D-plasma it is above 80 keV.

Finally, during the RF pulse no significant increase of impurities (C, O, Fe) was observed.

#### REFERENCES

- [1] ALLADIO, F., BARDOTTI, G., BARTIROMO, R., BUCETI, G., BURATTI, P., CRISANTI, F., DE ANGELIS, A., DE MARCO, F., DE PRETIS, M., GASPAROTTO, M., GIANNELLA, R., GROLLI, M., MADDALUNO, G., MAZZITELLI, G., PIERONI, L., RIGHETTI, G.B., SANTINI, F., SEGRE, S.E., TANGA, A., TUCCILLO, A., TUDISCO, O., ZANZA, V., Nucl. Fusion 22 (1982) 479.
- [2] DE MARCO, F., SANTINI, F., "Proposal of Lower Hybrid Heating Experiment on the Frascati Tokamak", 3rd Topical Conf. on RF Plasma Heating, Pasadena, 1978, paper B.11 (1978).
- [3] ANDREANI, R., PAPITTO, P., SASSI, M., "The RF additional system for the FT Tokamak", 10th Symp. on Fusion Technology (SOFT), Padova, 1978, Proc. EUR-6215 1 (1979) 269.
- [4] MANDOLEI, C., TANGA, A., to be published in J. Nucl. Materials.
- [5] PORKOLAB, M., Phys. Fluids 20 (1977) 2058.
- [6] STEVENS, J., ONO, M., HORTON, R., WILSON, J.R., Nucl. Fusion 21 (1981) 1259.
- [7] PARAIL, V.V., POGUTSE, O.P., Soviet J. Plasma Phys. 2 (1976) 126.
- [8] BARBATO, E., SANTINI, F., TARONI, A., "Lower Hybrid Wave Trajectories and Heating Simulation in Tokamak Discharges", 2nd Joint Grenoble-Varenna, Int. Symposium on Heating in Toroidal Plasmas, Como, 1980, 1 (1981) 417.

## DISCUSSION

V.S. STRELKOV: How do you explain the small decay in  $T_e(t)$  and  $T_i(t)$  after heating?

F. De MARCO: Bulk heating takes place via energy transfer from a fast electron beam accelerated by RF. As indicated by the activity in the  $\omega_{ce}$  emission, this transfer is non-collisional and lasts for about 100 ms after RF shut-off.

J.J. SCHUSS: Is the increase in plasma conductivity during your low-density RF experiments consistent with that expected from the electron temperature increase?

F. De MARCO: An evaluation of the plasma resistance decrease through the temperature profiles can justify the voltage drop. Nevertheless, owing to the uncertainties in the measurements, an appreciable contribution of current drive cannot be excluded.

R. HAWRYLUK: In the electron heating regime, did  $Z_{eff}$ , the power radiated by impurities, or the MHD activity change during the RF pulse?

F. De MARCO: A significant variation of  $Z_{eff}$  can be excluded. In some discharges a weak increase in the iron line radiation as well as some change in MHD activity have been observed. Their influence on the power balance and discharge behaviour remains to be investigated.

C.S. LIU: In your observation of parametric decay of the lower hybrid wave, does the ion-cyclotron sideband correspond to the local ion-cyclotron frequency at the centre or at the edge of the plasma?

F. De MARCO: The RF probe is located  $180^\circ$  in the toroidal direction away from the grill and at a poloidal angle corresponding to  $R = 95$  cm. The frequency shift of the sidebands corresponds to locations  $75 \leq R \leq 100$  cm. This indicates that detected decay instabilities do not take place in front of the grille only. Of course, a minor radius determination can be deduced only by making an assumption about the poloidal location.



## HIGH-BETA POLOIDAL PLASMAS AND CURRENT DRIVE BY ECRH ON TOSCA

M.W. ALCOCK, B. LLOYD\*, A.W. MORRIS\*,  
D.C. ROBINSON, D.F.H. START  
Culham Laboratory,  
(Euratom/UKAEA Fusion Association),  
Abingdon, Oxon.,  
United Kingdom

### Abstract

#### HIGH-BETA POLOIDAL PLASMAS AND CURRENT DRIVE BY ECRH ON TOSCA.

High-power ECRH has been used on the TOSCA device to produce high values of beta poloidal and to investigate current drive. Plasmas with values of poloidal beta up to 2.5 have been produced by gas puffing and Ohmic heating alone. The value of poloidal beta decreases as the current increases. Experiments and theory on wave-driven currents are in reasonable agreement but give low efficiency. This current decreases as the resonance is moved to the outside of the tokamak, providing possible evidence for the reduction of the current due to trapped electrons.

### 1. INTRODUCTION

The small tokamak, TOSCA ( $R=0.3\text{m}$ ,  $a=0.08\text{m}$ ) has been used to investigate the production and behaviour of high poloidal beta plasmas using both ECRH and ohmic heating alone. The ECRH plasmas [1] have low density and high temperature whereas the ohmically heated plasmas have high density but relatively low temperature. In the electron cyclotron resonance heating experiments, microwave power has been injected at a frequency of 28 GHz for pulse lengths of up to 3 ms and power levels of up to 200 kW from the low field side of the torus using the  $TE_{02}$  mode in an oversized circular waveguide. Investigations have been at the second harmonic ( $B_{\phi}=0.5\text{T}$ ) as accessibility conditions for the radio frequency power give a maximum beta twice that of the fundamental for a given temperature. Preionisation at the fundamental with an 18 GHz radio frequency source (800 W) makes it possible to obtain a large range of line-averaged electron densities, efficient plasma start-up with a substantial saving in volt-seconds, and the removal of the initial non-thermal cyclotron emission from the plasma. The plasma position is feedback-controlled to  $\pm 2\text{ mm}$ .

\* University of Oxford, UK.

## 2. HIGH POLOIDAL BETA PLASMAS WITH ECRH

Using high-power electron cyclotron resonance heating, it is possible to heat plasmas in small tokamaks to high values of toroidal and poloidal beta to test beta limits. Strong absorption and local heating can occur [2]. It is easy to reach regimes of operation where the absorbed radio frequency power dominates the ohmic heating power, which is typically 10 kW in these experiments. The initial target plasmas for ECRH have to have central densities less than  $5 \times 10^{18} \text{m}^{-3}$  for the extraordinary mode at the second harmonic to be strongly absorbed. The absorption per single pass initially is  $\approx 30\%$  theoretically but this quickly rises due to the electron temperature increase during the heating. To avoid runaway in the initial target plasmas, preionisation at the fundamental, 18 GHz, has been used and this permits an initial loop voltage of as little as 6V. In addition the initial plasma carries only a small current, typically less than 6 kA, though after the heating pulse is applied the current can be raised without producing a runaway discharge.

Under these conditions very strong absorption of the RF power occurs. Careful control of the vertical field is required to maintain the plasma position as the plasma energy content can increase by more than an order of magnitude. The vertical field increase can be up to  $\approx 75\%$ , and the soft X-ray emission may increase by up to 100 times over a width of some 2 cm about the resonance. Strong heating is observed provided the resonance is in the central hot core of the plasma ( $\pm 3$  cm). Figure 1 shows the variation in poloidal beta,  $\beta_I$ , obtained from a diamagnetic loop as a function of plasma current for a number of discharges in which this current is varied slowly during the heating pulse. The injected power in these cases was 100 kW. It is worthy of note that although  $\beta_I$  reaches a value comparable to the aspect ratio ( $R/a_p \approx 5$ ) for these plasmas, the separatrix would not be expected to invade the plasma during the heating pulse, which is applied for less than a field diffusion time.

The variation of  $\beta_I$  with  $I$  is close to that expected if the energy confinement time remained constant with the current variation. The global energy confinement time can be estimated from the rise and fall times of the plasma energy content, typically 300-400  $\mu\text{s}$ . The heating efficiency is then 50-75%. This energy confinement time is comparable to that before the application of the RF. Also shown on Fig. 1 are spot points at power inputs of 50 and 150 kW for a current of  $\approx 5$  kA. The maximum plasma energy and  $\beta_I$  do not increase linearly with the incident power. It is not clear whether the saturation is due to nonlinear effects associated with the radio frequency heating or that some other beta-induced phenomena are present in the plasma.

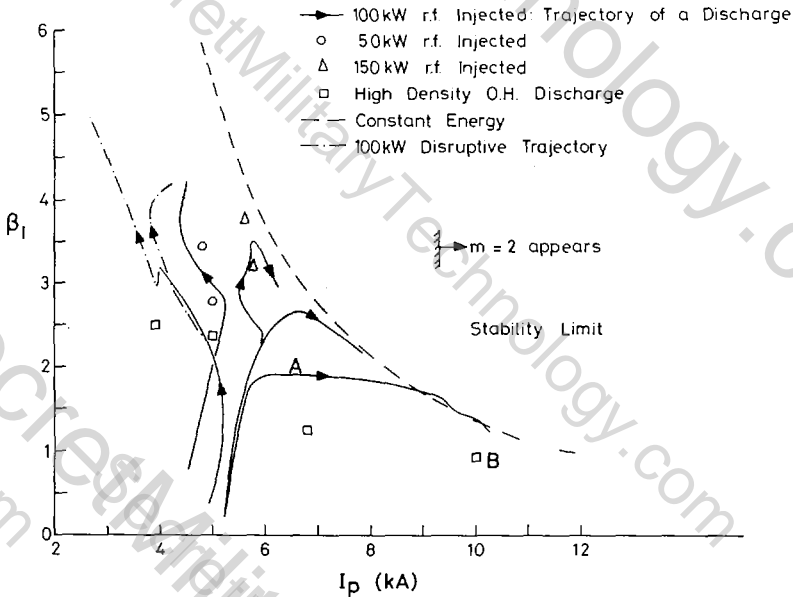


FIG.1.  $\beta_I$  as a function of  $I_p$  for a number of discharges. The dashed line is the behaviour expected for fixed energy confinement time. The square boxes are for high-density Ohmic discharges. The circles are for 50 kW and triangles for 150 kW. The left-hand curve shows a discharge which is characterized by a minor disruption. The shaded curve is an ideal MHD stability limit.

Many calculations have been made on both ballooning mode and kink mode limits for tokamak plasmas [3]. These all indicate that the critical  $\beta_I$  should vary approximately inversely with the plasma current. The absolute value to compare with these experiments is model-dependent. In these hot electron plasmas, finite-ion Larmor radius effects are unlikely to enhance the stability significantly and, as the plasma is relatively small in the high- $q$  discharges, wall stabilisation will be very weak. Shown in Fig. 1 is a particular stability limit [4] which intercepts the experimental observations when  $\beta_I \approx 3$ . For higher values, nonlinear MHD effects might influence the confinement time though there is little evidence to support this. These plasmas, as is usual for tokamak plasmas at large  $q$ , do not exhibit sawtooth activity and no significant ( $\delta b_\theta / B_\theta < 0.1\%$ ) mode activity is observed on external coils. The current distribution is probably frozen in by the high-temperature plasma and the situation is thus akin to the flux-conserving tokamak. When the current is slowly increased to  $\approx 9$  kA an  $m=2$  mode appears late in the heating pulse and then disappears only to reappear again as the current decays after the RF has been turned off. This is shown in Fig. 2

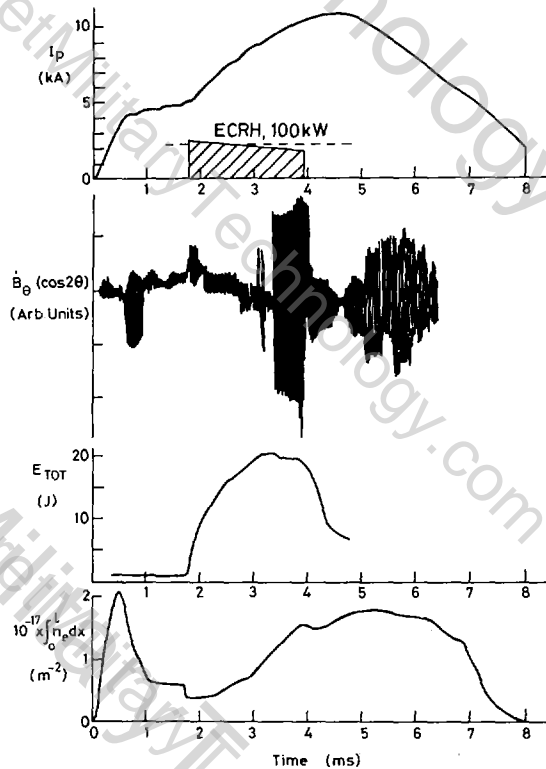


FIG.2.  $m=2$  mode activity induced by ECRH when the current and density are increased. This discharge is curve A in Fig.1. (Here the length  $l \lesssim a$ .)

together with the evolution of plasma energy which appears weakly correlated with the mode activity, unlike most ohmic discharges where the activity does not affect the plasma energy except close to the time of disruption. At these lower  $q$  values ( $\approx 3$  for  $a_p \approx 6$  cm) some  $\beta$ -induced MHD mode activity may be present. The average value of beta is  $\leq 1\%$ . Figure 3 shows the plasma energy variation during the heating pulse for a number of discharges as the position of the resonance is varied. Discharges with the resonance on the outside are often characterised by a small disruption accompanied by a negative voltage spike and a drop in plasma energy though only a small transient drop in  $\beta_I$  (Fig 1, left-hand curve), whereas with the resonance on the inside no such phenomenon is observed. This is possibly a beta-related phenomenon as it is not observed at lower power inputs. It should be noted that, as on many other ECRH experiments [5], the line-of-sight density drops initially on application of the heating pulse and then returns to its original level when the ECRH is

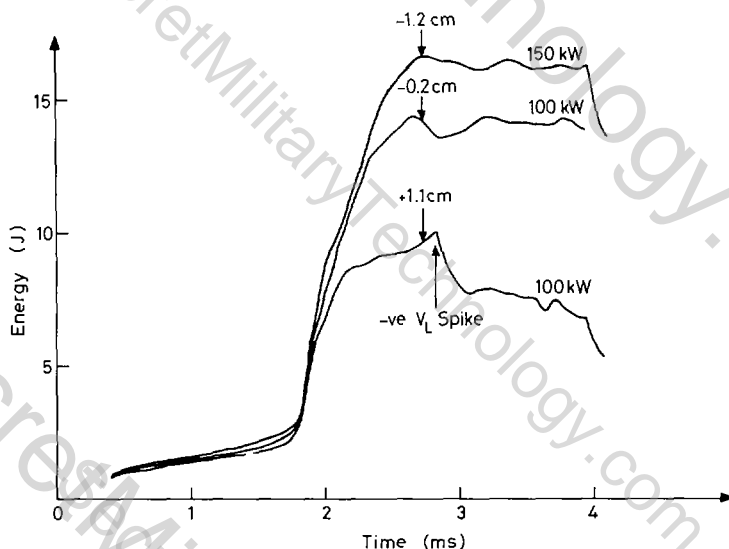


FIG. 3. Evolution of the plasma energy during ECRH at power levels of 100 and 150 kW at different resonant positions. The influence of a disruption when the resonance is moved outwards is shown.

turned off. The drop appears to be associated with a redistribution of density in the plasma column. If the density is increased during the heating pulse (Fig 2) then efficient heating is maintained until the extraordinary mode (X-mode) cut-off appears in the plasma. The value of  $\beta_I$  does decrease at higher densities[1].

### 3. HIGH POLOIDAL BETA PLASMAS WITH OHMIC HEATING

Plasmas with poloidal beta values of up to 2.5 have been created by gas puffing to high densities ( $\lesssim 2.5 \times 10^{19} \text{m}^{-3}$ ) at low magnetic fields and relatively low electron temperatures as shown in Fig 1. The  $\beta_I$  values are substantially below the ECRH results but the power input in the ohmic discharges is typically only  $\approx 30$  kW. Ion heat conduction losses will dominate in these low magnetic field plasmas ( $B_0 \approx 0.5$  T). Figure 4 shows a set of waveforms for a gas-puffed discharge where the final  $\beta_I$  reaches unity. This is accompanied by strong sawteeth and also  $m=2$  activity shortly before disruption. The density limit here is in accord with that obtained on many other tokamaks (and pinches) namely:  $I/N \approx 10^{-14} \text{A.m}$ [6] where  $N$  is the line density. Note that the ECRH-heated plasmas at higher values of  $\beta_I$  for the same current are not accompanied by such mode activity, indicating a current and pressure profile more favourable for stability.

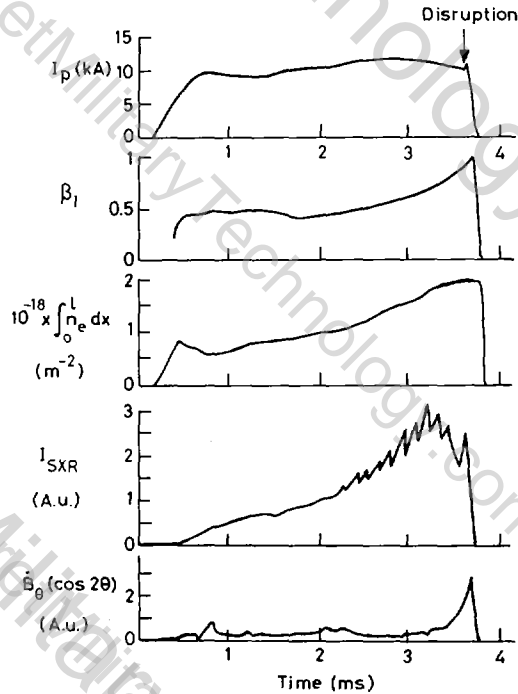


FIG. 4. Waveforms for a high-density Ohmic discharge in which  $\beta_1 \rightarrow 1$  accompanied by sawtooth activity which terminates in a disruption. This is point B on Fig. 1.

#### 4. PLASMA CURRENTS DRIVEN BY LOCALISED ECRH POWER ABSORPTION

The method of driving the plasma current in a tokamak by asymmetric ECRH is expected to be particularly sensitive to the presence of trapped electrons [7]. This sensitivity is due to the diffusion in the electron's perpendicular velocity generated by the wave which drives these electrons from the passing to the trapped region of velocity space. The current is diminished both by the reduction in the number of current carriers and by the depletion of the passing resonant electrons. The latter effect causes an asymmetry in the electron distribution function which appears as a current flowing in the opposite direction to the Fisch-Boozer current [8]. This depletion-driven current component is the basis of Ohkawa's [9] current-drive scheme and can become dominant at small aspect ratios and can reverse the net current.

When the wave power is absorbed locally, the reduction in current due to trapping on a given flux surface depends on the poloidal angle  $\theta_a$  of the power absorption. The present calculation determines the current flowing on the flux surface as a

function of  $\theta_a$  for the local values of power density  $P_d$  and parallel wave vector  $k_{\parallel}$ , as obtained from a ray-tracing code for example. For a given flux surface, and neglecting electron-electron collisions, the electron Fokker-Planck equation can be used together with poloidal and toroidal magnetic fields of the form

$$(B_{\theta}, B_{\phi}) = [b(r)/h, B_o/h]$$

(where  $h = 1 + \epsilon \cos \theta$ ) to obtain an equation for the distribution function of the passing particles. Conventional 'banana' regime analysis<sup>[10]</sup> gives

$$v_{ei} \frac{\partial}{\partial \mu} \left( \langle v_{\parallel}/B \rangle \mu \frac{\partial f_p^0}{\partial \mu} \right) + \left[ \sqrt{2D\sigma} (\xi - \mu B)^{-\frac{1}{2}} \left( \frac{2B}{v_e^2} \right)^{\ell-1} \left( \frac{\partial}{\partial \mu} + B \frac{\partial}{\partial \xi} \right) \left( \mu^{\ell} \delta(v_{\parallel} - v_o) \frac{\partial F_m}{\partial \xi} \right) \right] \theta_a = 0 \quad (1)$$

where the subscript p denotes passing particles, the second term is the quasi-linear diffusion operator rewritten in terms of  $\mu (=v_{\parallel}^2/2B)$  and  $\xi (=v^2/2)$ ,  $\ell$  is the cyclotron harmonic number,  $\omega$  and  $\Omega$  are the wave frequency and electron gyrofrequency respectively,  $D$  is a constant in velocity space proportional to the wave intensity,  $v_o = (\omega - \ell\Omega)k_{\parallel}$  and  $F_m$  is a Maxwellian distribution. In eq(1),  $B = (B_{\theta}^2 + B_{\phi}^2)^{\frac{1}{2}}$ ,  $\sigma = v_{\parallel} / |v_{\parallel}|$ ,  $v_{ei} = Z v_o (v/v_e)^{-3}$ ,

$$v_e = (2T/m)^{\frac{1}{2}}, v_o = \frac{\sqrt{2\pi e^4 n \ell n \lambda}}{m^{\frac{1}{2}} T^{\frac{3}{2}}}, T, m \text{ and } n \text{ are the electron}$$

temperature, mass and density respectively,  $Z$  is the effective plasma charge and  $\ell n \lambda$  is the Coulomb logarithm. The triangular brackets denote a flux surface average.

Integrating eq(1) with respect to  $\mu$  gives

$$\mu \frac{\partial f_p^0}{\partial \mu} = \frac{2D_a}{B_a v_{ei} \langle v_{\parallel}/B \rangle} \left( \frac{2\mu_o B_a}{v_e^2} \right)^{\ell-1} \left[ \ell \frac{\partial F_m}{\partial \xi} + B_a \mu_o \frac{\partial^2 F_m}{\partial \xi^2} \right] H(\mu - \mu_o) \quad (2)$$

where  $H$  is the Heaviside function,  $\mu_o = (2\xi - v_o^2)/2B_a$  and the subscript a denotes evaluation at  $\theta = \theta_a$ . Using eq. 2, the current density is found to be

$$\frac{\langle J \rangle}{P_d} = -\frac{e x_o}{Z \ell!} (1 + \epsilon \cos \theta_a) \int_{x_o}^{x_m} x^2 (x - x_o)^{\ell-1} (x - x_o - \ell) e^{-x} dx \int_{\lambda_o}^{1/B_{\max}} \frac{d\lambda}{\langle (1 - \lambda B)^{\frac{1}{2}} / B \rangle} \quad (3)$$

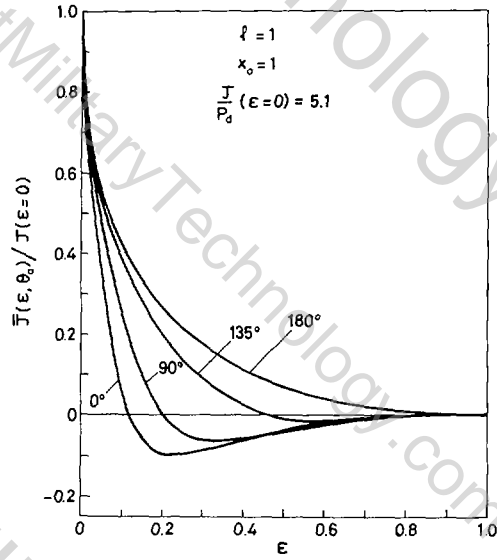


FIG. 5. Normalized  $J/P_d$  versus  $\epsilon$  for fundamental ECRH,  $x_0 = 1$  and several poloidal angles of absorption.

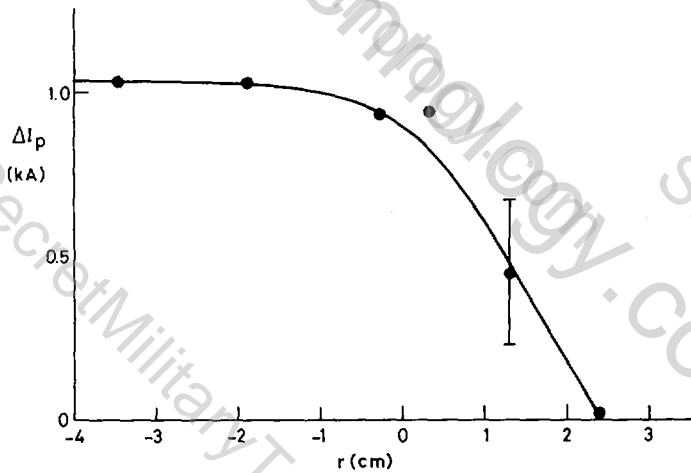


FIG. 6. Plasma current in TOSCA driven by ECRH as a function of ECR position. The current drive efficiency is about 0.01 A per watt of injected power in this case.

where  $x = m\xi/T$ ,  $\lambda = \mu/\xi$ ,  $x_o = v_o^2/v_e^2$ ,  $x_m = x_o B_{max}/(B_{max} - B_a)$ ,  $\lambda_o = \mu_o/\xi$ .  
The current density is expressed in units of  $nev_e$  and  $P_d$  in units of  $nmv_e^2v_o$ .

Values of  $\langle J \rangle / P_d$  from eq (3), normalised to  $J/P_d$  for a uniform field, are shown in Fig. 5 as a function of  $\epsilon_d$  for fundamental ECRH ( $\ell=1$ ), for  $x_o=1$  and poloidal angles  $\theta_a=0, 90^\circ, 135^\circ$  and  $180^\circ$ .

The current is strongly dependent on  $\epsilon$  and reverses direction as the Ohkawa component, driven by the depletion of the passing electrons, exceeds the forward component driven by the reduced collisionality. The curves for different values of  $\theta_a$  show that the current is most sensitive to trapping at small poloidal angles as expected since the smaller the value of  $\theta_a$  the greater the fraction of trapped electrons in the resonance zone.

Some preliminary experimental evidence for the effect of electron trapping on ECRH-driven currents has been found on the TOSCA tokamak. In this experiment an angled antenna was used and an injected power level of 85 kW. The target plasma was formed by an ohmic discharge with a plasma current of 8.4 kA. The line-average plasma density was  $\approx 5 \times 10^{18} m^{-3}$ . The ECR resonance position was scanned across the major radius by varying the toroidal field from 0.44 T to 0.54 T. The observed ECRH-driven current is shown in Fig. 6 as a function of the distance between the resonance on the equatorial plane and the minor axis ( $R=0.3$  m). The dramatic reduction in current observed as the resonance is moved outwards is qualitatively in agreement with the above calculation since  $\epsilon$  increases and  $\theta_a$  decreases with this movement.

#### CONCLUSIONS

Very high values of poloidal beta have been obtained by both ECRH and ohmic heating alone. These values have equalled the aspect ratio and challenged optimised beta limits. The high values do not necessarily lead to disruptions or enhanced MHD activity and the confinement does not appear to be impaired. The poloidal beta decreases with increasing plasma current but this may be due to a power input limitation in the present experiments. Experiments on ECRH current drive give relatively low efficiency and this efficiency falls when the resonance is in the region where trapped electrons may exist, which is in accord with theoretical predictions.

#### ACKNOWLEDGEMENTS

We would like to thank the TOSCA and microwave heating teams for their valuable assistance in these experiments.

REFERENCES

- [1] ROBINSON D C et al, Proc. of 3rd Joint Varenna-Grenoble Int. Symp. on Heating in Toroidal Plasmas, Grenoble 1982 (CEA Brussels 1982) Vol II 647.
- [2] FIELDING P J, Culham Report CLM-P615 (1980).
- [3] TODD A M et al, Nuclear Fusion 19 No 6 (1979) 743.
- [4] BERNARD L C et al, Bulletin of the American Physical Soc., 24th Meeting of the Plasma Physics Div. New Orleans, Nov. 1982.
- [5] LAHAYE R J et al, Nuclear Fusion 21 (1981) 1425.
- [6] ROBINSON D C and TODD T N, Culham Laboratory Report CLM-R222(198
- [7] CORDEY J G et al, Plasma Physics 24 (1982) 73.
- [8] FISCH N J et al, Phys. Rev. Letters 45 (1980) 720.
- [9] OHKAWA T, General Atomic Report GA-A13847 (1976).
- [10] RUTHERFORD P H et al, Phys. Rev. Letters 25 (1970) 1090.

DISCUSSION

D. HWANG: Do you have any scaling of the decrease in sawtooth activity with increasing  $P_{RF}$  or toroidal magnetic field?

D.C. ROBINSON: In the low-density high-q discharges in which strong absorption occurs, sawtooth activity is not observed. If the density is raised so that sawtooth activity is seen, then poor absorption of the RF power is obtained and no influence on the sawtooth activity is observed.

A. KITSUNEZAKI: What is the confinement time as  $\beta_I$  increases, particularly when  $\beta_I \approx R/\alpha$ ?

D.C. ROBINSON: When  $\beta_I$  exceeds about 3 for a power input of 100 kW, the confinement time starts to decrease, and when  $\beta_I \approx 5$  at low plasma currents the confinement time has decreased by a factor of 2 (see Fig 1). It should be noted that the reduction in confinement is unlikely to be due to the invasion of the separatrix into the plasma, as the heating pulse duration is less than the field diffusion time.

H.W. PIEKAAR: The purpose of ECRH is to obtain efficient heating by deposition of energy as  $f(R)$ . Can you comment on this? And do you absorb your power in a single pass, and if so, by what mechanism?

D.C. ROBINSON: The temperature profile obtained from soft X-ray observations varies as the resonance position is moved through the plasma by varying the magnetic field in low-density plasmas. Strongly peaked profiles are obtained with the resonance on the magnetic axis, whereas flat to hollow profiles

are obtained with the resonance on the inside edge of the plasma. At the high temperatures obtained in these plasmas the extraordinary mode is almost completely absorbed in a single pass at the second harmonic.

P. EFTHIMION: During the ECRH experiment the line-average density drops to half its value with the application of power. Is it possible that the observed increase in the soft X-ray signal is due not to electron heating but to an impurity influx?

D.C. ROBINSON: There is no evidence for any impurity influx from spectroscopic observations in the edge regions of the plasma provided the walls have been conditioned.

P. EFTHIMION: What do you attribute the change in the density profile to?

D.C. ROBINSON: It is possible that the change in density profile is due to an inverse wave pinch effect associated with the large increase in  $\beta_1$  and decrease in voltage.



## MEASUREMENTS OF TRANSPORT COEFFICIENTS IN THE T-10 DEVICE

A.B. BERLIZOV, G.A. BOBROVSKIJ, N.L. VASIN,  
A.N. VERTIPOROKH, N.D. VINOGRADOVA,  
V.A. VERSHKOV, N.M. GEGECHKORI,  
E.P. GORBUNOV, Yu.V. ESIPCHUK, S.L. EFREMOV,  
V.A. ZHURAVLEV, V.S. ZAVERYAEV, A.Ya. KISLOV,  
S.Yu. LUK'YANOV, Yu.S. MAKSIMOV, G.E. NOTKIN,  
A.A. MEDVEDEV, A.B. PIMENOV, K.A. RAZUMOVA,  
V.A. RANTSEV-KARTINOV, M.M. STEPANENKO,  
V.S. STRELKOV, V.V. TIMONIN, V.M. CHICHEROV,  
D.A. SHCHEGLOV, A.N. FYAKHRETDINOV  
I.V. Kurchatov Atomic Energy Institute,  
Moscow,  
Union of Soviet Socialist Republics

### Abstract

#### MEASUREMENT OF TRANSPORT COEFFICIENTS IN THE T-10 DEVICE.

A description is given of experiments for determining the transport coefficients from measurements of the radial profiles of the plasma parameters in the T-10 in regimes with different magnetic fields  $B_z$ , different  $q(a_L)$  and different densities. It is shown that heat conductivity is determined by different mechanisms in three distinctive zones of the discharge.

### 1. INTRODUCTION

Estimates of the electron heat conductivity,  $\kappa_e = n_e \chi_e$ , made in the T-10 in regimes with a longitudinal magnetic field,  $B_z = 15$  kG, a discharge current  $I_p = 240$  kA [ $q(a_L) = 2$ ] and an average density  $\bar{n}_e = (2-3) \times 10^{13} \text{ cm}^{-3}$  [1, 2] have shown that in the region of the column with maximum electron temperature ( $T_e$ ) gradient (the gradient region given by  $r = 0.5a_L$ ), we have  $\kappa_e = (2-3) \times 10^{17} \text{ cm}^{-1} \cdot \text{s}^{-1}$ . This value is considerably smaller than that given by the Alcator scaling [3] but is in good agreement with the T-11 scaling [4]. In experiments involving plasma heating at the second electron cyclotron resonance harmonic [2] it has been shown (though not to any high degree of accuracy) that the dependence of  $\kappa_e$  on  $T_e$  under such discharge conditions is weak, being not stronger than  $\kappa_e \sim T_e^\alpha$ , where  $|\alpha| \lesssim 0.5$ .

When, however,  $B_z$  is increased to 30 kG and  $I_p$  is kept constant ( $q(a_L) = 4-4.5$ ), values of  $\kappa_e \approx 0.6 \times 10^{17}$  were obtained in the plasma core

( $r \lesssim (1/3) a_L$ ) [5]; these are much smaller than all the usual scalings and less than ten times greater than the neoclassical values.

To determine the reasons for such a low heat conductivity (in the plasma core) and to find the dependence of the anomalous behaviour of  $\kappa_e$  on the plasma parameters, studies have been carried out over a wide range of discharge parameters. The results are given below.

## 2. DIAGNOSTICS AND EXPERIMENTAL CONDITIONS

For measuring the parameters required in the calculation of the electron and ion heat conductivities  $\kappa_e$  and  $\kappa_i$ , we used the following diagnostic techniques:

1. The electron temperature in the steady-state stage of the discharge was measured (averaged over a time interval  $\Delta t = 200$  ms) from the X-ray spectra by means of two Si(Li) detectors which scanned the plasma column in mutually perpendicular directions. No deviations from a Maxwellian shape were observed over the energy range  $E = 1.5 - 10$  keV. The results of the X-ray measurements were also used to determine the effective plasma charge  $Z_{\text{eff}}$ . Measurements of the  $T_e(r)$  profile by the Thomson scattering technique have also been carried out in regime V (Fig.1). This figure shows that  $T_e(r)$  profiles measured by the two techniques mentioned differ substantially. Therefore, the calculations of the electron heat conductivity,  $\kappa_e$ , are carried out independently by using both profiles. The two techniques have yielded good agreement in previous experiments [5, 7] for regimes similar to those designated as III and IV.
2. The ion temperature  $T_i$  was determined from the spectra of the charge-exchange neutrals. The values of  $T_i$  in the peripheral region of the column were determined for all regimes from the Doppler broadening of the C V and O V ion lines. In the plasma core,  $T_i$  was also monitored from the intensity of the neutron emission.
3. In all the regimes studied, the sawtooth oscillations were observed by means of a pin-hole camera with simultaneous recording of the signals from ten surface-barrier Si-detectors.
4. The radial distribution of the radiative losses from the plasma column was determined by means of a nine-channel system of pyroelectric detectors.
5. The total energy confinement time was found from diamagnetic measurements.

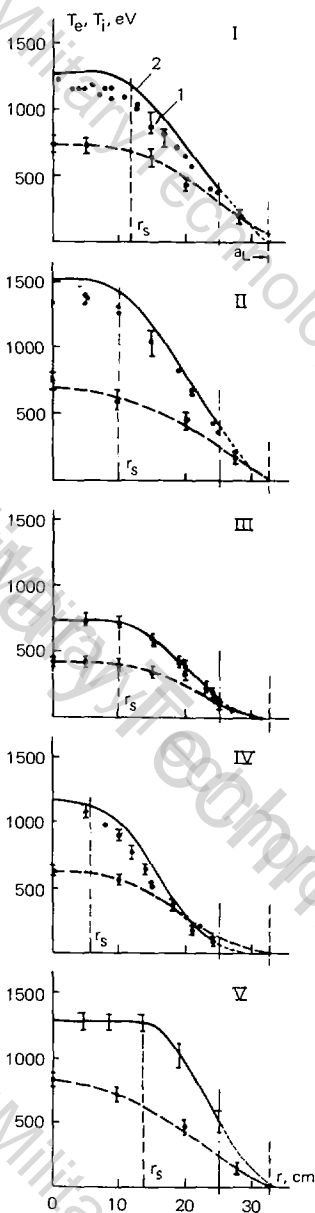


FIG.1. Electron ( $T_e$ ) and ion ( $T_i$ ) radial temperature profiles for regimes I-V (see Table I). 1 - experimental points as results of measurements along chords; 2 -  $T_e(r)$  after Abel inversion;  $T_{e1}$  (regime V)-laser profile of  $T_e$ ;  $r_s$ -radius of phase reversal in sawtooth oscillations.

TABLE I. PRINCIPAL PARAMETERS OF FIVE DISCHARGE REGIMES

Regimes	I	II	III	IV	V
$B_z$ (kG)	30	30	16	30	30
$I_p$ (kA)	430	430	240	240	580
$q(a_L)$	2.4	2.4	2.3	4.4	1.8
$\bar{n}_e (\times 10^{13})$ ( $\text{cm}^{-3}$ )	4.5	2.7	3.4	3.9	5.3
$\tau_E^d$ (ms)	70-87	45-57	—	40-53	79-90 100 at $\bar{n}_e = 6.0$
$\tau_E^p$ (ms)	76-77	48-49	23-24	44-46	65-67

Five different discharge regimes in the tokamak were studied. The principal parameters are given in Table I. In this table,  $q(a_L)$  is the safety factor at the limiter ( $a_L = 32.5$  cm);  $\tau_E^d$  is the total energy life-time determined from the diamagnetic measurements; and  $\tau_E^p$  is the life-time calculated from the measured  $T_e$  and  $T_i$  profiles. Regimes III and IV were similar to those described in Refs [1, 5].

### 3. DETERMINATION OF THE HEAT CONDUCTIVITIES

The electron and ion heat conductivities were determined from the steady-state energy balance equations in the corresponding components:

$$\langle Q_{OH} \rangle - \langle Q_{ei} \rangle - \langle Q_{rad} \rangle + \alpha_r r \kappa_e \frac{d T_e}{dr} = 0 \quad (1)$$

$$\langle Q_{ei} \rangle + \alpha_r r \kappa_i \frac{d T_i}{dr} = 0 \quad (2)$$

Here,

$$\langle Q \rangle = 2\pi R_0 \cdot 2\pi \int_0^r Q(r) r dr$$

$$\alpha_r = 2\pi R_0 \cdot 2\pi$$

It follows from Eqs (1) and (2) that the 'heat conduction' fluxes  $Q_{\kappa_e}$  and  $Q_{\kappa_i}$  determined in this way include also the diffusion fluxes and, in the case of the ions, the charge-exchange losses as well. Thus, Eqs (1) and (2) yield somewhat over-estimated values for  $\kappa_e$  and  $\kappa_i$ .

The current density  $j(r)$  was calculated on the assumption that the electrical field  $E_z$  was constant across the radius and that the conductivity was of the Spitzer form with toroidal corrections; the experimentally determined  $Z_{\text{eff}}$  profiles were used.

The calculations have shown that the total current,

$$I_p = 2\pi \int_0^a j(r) r dr$$

differs from the measured value by no more than 10–12%. The quantities  $\tau_E^a$  and  $\tau_E^p$  are in good agreement with each other, with an accuracy not worse than 10–15%, as follows from Table I.

For comparing the calculated thermal conductivities with the neoclassical values, we used the approximation equation

$$\kappa_j^{\text{neo}} = \kappa_{\text{PS}} + \frac{\kappa_{\text{pl}} \kappa_{\text{ban}}}{\kappa_{\text{pl}} + \kappa_{\text{ban}}} \quad (3)$$

where  $\kappa_{\text{PS}}$ ,  $\kappa_{\text{pl}}$  and  $\kappa_{\text{ban}}$  are the values of  $\kappa_i$  for the Pfirsch-Schlüter, plateau and banana regions, respectively [6].

In the calculation of the deuteron density, allowance was made for the presence of impurities, the amount of which was determined from the measured value of  $Z_{\text{eff}}(r)$ .

The greatest uncertainty in the measured parameters occurred with the ion temperature  $T_i$  and was due to the fact that it was necessary to introduce corrections for the opacity of the plasma and to allow for the neutral-spectrum distortions caused by trapped particles.

The analysis of these processes has shown that the experimental value,  $T_i^{\text{exp}}$  (Fig.1), should be increased by no more than 20%. In this connection, a value of  $T_i = 1.2 T_i^{\text{exp}}$  has been used in the calculations. Some profiles of measured and calculated parameters are given in Figs 1 to 3. The electron and ion heat conductivity coefficients have been found from those profiles. The value of  $q(0)$  is found to be appreciably less than one in regimes with low  $q(a_L)$  and T-10, i.e. in the regimes where strong sawtooth oscillations occur. If we assume that the current density in the region  $r \leq r_s$  for some reason

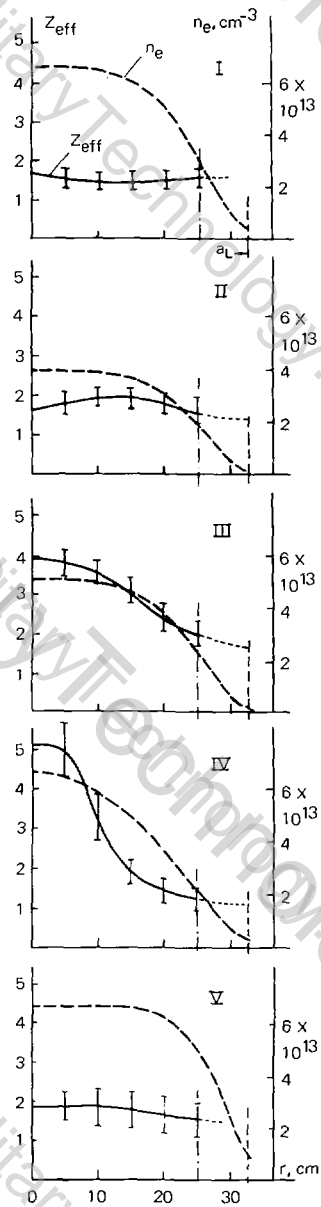


FIG. 2. Electron density,  $n_e(r)$ , and effective plasma charge,  $Z_{eff}(r)$ .

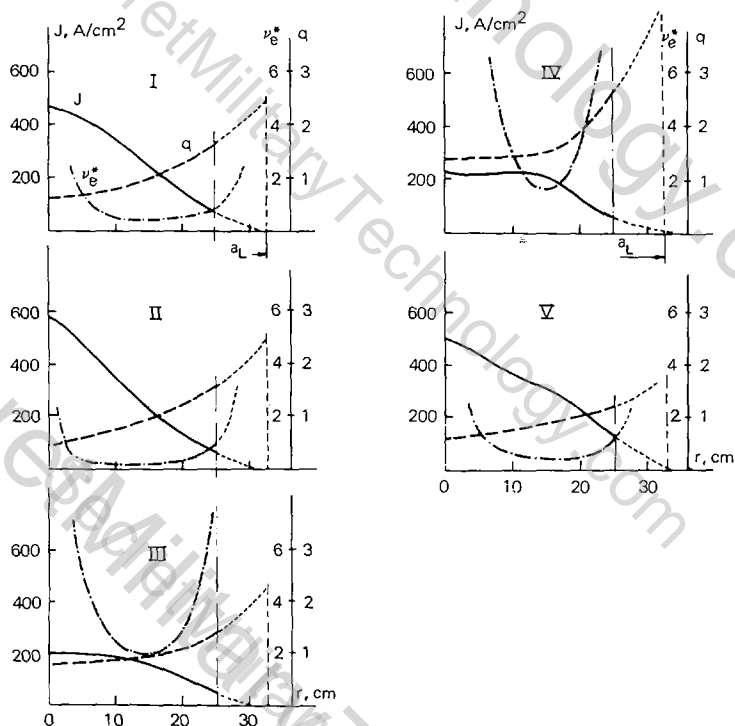


FIG. 3. Current density,  $j(r)$ , safety factor,  $q(r)$ , and collisionality parameter,  $\nu_e^*$ , profiles (calculated).

(e.g. an anomalously high resistance at  $r \leq r_s$ ) corresponds to  $q = 1$ , serious contradictions in the energy balance will emerge. In this case, the Joule energy deposition  $\langle Q_{OH} \rangle$  inside  $r_s$  is found to be less than or equal to the heat transfer from electrons to ions,  $\langle Q_{ei} \rangle$ .

#### 4. ELECTRON HEAT CONDUCTIVITY

The electron heat conductivity coefficients,  $\kappa_e(r) = n_e \chi_e$ , for the various regimes calculated from the measurement results are given in Fig.4. From the point of view of heat transport by electrons, we can distinguish three regions of the plasma column:

Region I – the sawtooth oscillation region ( $r \lesssim r_s$ ). The enhanced value of  $\kappa_e$  in this region for regimes with small  $q(a_L)$  most probably reflects the fact that the temperature gradient  $d T_e / dr$  is determined not by a thermal conduction mechanism but by convective flux in the sawtooth oscillation process. If there

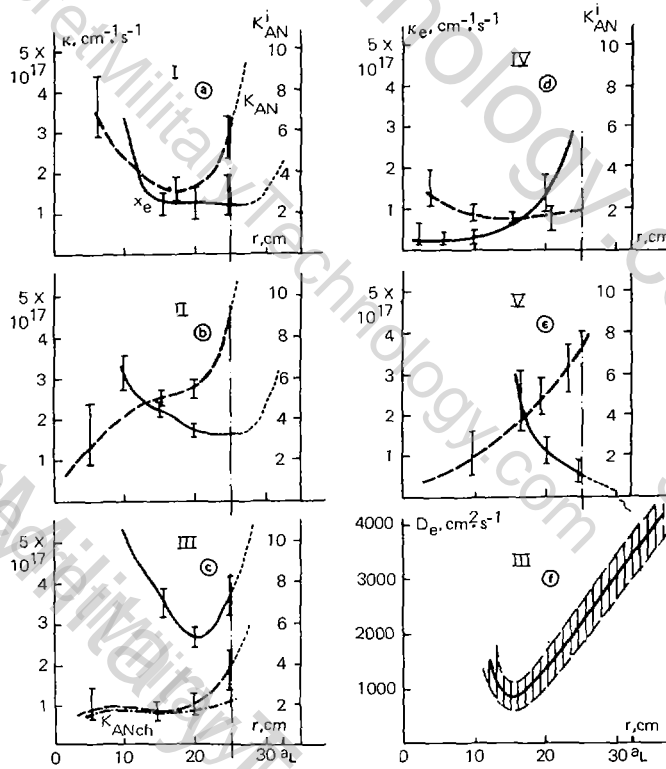


FIG.4. a) b) c) d) e) Electron heat conductivity coefficients,  $\kappa_e$ . [e] – electron heat conductivity as a result of laser measurements; f) Electron diffusion coefficient,  $D_e$  (regime III).

are no sawtooth oscillations (the regime of Ref.[5]) or if their region of existence is small (regime IV,  $r_s \approx 5$  cm), the values of  $\kappa_e$  in the plasma core,  $r \leq (1/3) a_L$ , are small:  $\kappa_e \leq 0.6 \times 10^{17}$  for the regime of Ref.[5] and  $\kappa_e \approx 0.4 \times 10^{17}$  for regime IV.

In this connection, the question arises whether the low  $\kappa_e$  values in the plasma core are simply a characteristic of regimes with large  $q(a_L)$  or whether they represent a general phenomenon which is difficult to detect in regimes with  $q(a_L) \approx 2$ , because of the presence of the sawtooth oscillations. To analyse this problem, let us turn to Fig.6a, which shows oscillograms of the sawtooth oscillations in the given region of the column, obtained by means of the surface-barrier detectors.

From the energy balance for instants of time before ( $t_2$ ) and after ( $t_1$ ) the internal disruption, we derive the following connection between the electron energy life-times associated with heat conduction  $\tau_{Ee}^k$  and the convective flux  $\tau_{Ee}^{con}$ :

$$\tau_{Ee}^k = \frac{\tau_{Ee}^{con}}{1 - \frac{(dI/dt)_1}{(dI/dt)_2}} \quad (4)$$

where  $\tau_{Ee}^{con} = 2 T_{st}/(\delta I/I)$ ;  $T_{st}$  is the period of the sawtooth oscillations,  $I$  the intensity of the X-ray signal and  $\delta I$  is its amplitude in the sawtooth oscillations. In the above equation, we have allowed for the fact that the intensity of the experimentally observed X-ray radiation,  $I(t)$ , is related to  $n_e T_e$  by the following expression:

$$\frac{d}{dt}(n_e T_e) \cong \frac{\overline{n_e T_e}}{2} \frac{1}{I} \frac{dI}{dt} \quad (5)$$

where  $\overline{n_e T_e}$  is the time average of the energy, and have neglected the change in the Joule heating in the oscillation process (which leads to a lower bound for  $\tau_{Ee}^k$ ).

The steady-state calculations give good agreement between

$$\tau_{Ee}(r_s) = (3/2) \langle n_e T_e \rangle V / \{ \langle Q_{OH} \rangle - \langle Q_{ei} \rangle - \langle Q_{rad} \rangle \}$$

and  $\tau_{Ee}^{con}$ . A characteristic feature of the sawtooth oscillations (Fig.6) is the almost linear increase of  $I(t)$  in the relaxation phase, i.e. the small difference between  $(\partial I/\partial t)_2$  and  $(\partial I/\partial t)_1$ . Thus, for regimes with  $q(a_L) = 2$ ,  $\tau_{Ee}^k > \tau_{Ee}^{con}$ . For example, for regime I with  $T_{st} = 10-12$  ms and  $\delta I/I \approx 0.2-0.3$ , we have  $\tau_{Ee}^k(r_s) > 150-200$  ms, i.e. it is greater than  $\tau_{Ee}^k$ , characteristic of the 'gradient region'. Thus, the low values of the electron heat conductivity in the plasma core are not only characteristic of regimes with large  $q(a_L)$ .

Region III – periphery of the plasma column. In regime IV with its large  $q(a_L)$ , the heat conductivity  $\kappa_e$  increases with  $r$ ; this rise begins in the region of the resonance surface  $q(r) = 2$  (Fig.4d). As  $q(a_L)$  increases on the column boundary the enhanced-conductivity region is shifted and when  $q(a_L) \cong 2$  it is appreciable only for low value of longitudinal field  $B_z = 16$  kG (Fig.4c). We may, therefore, assume that if the resonance surface  $q = 2$  is either outside or actually on the boundary of the plasma column, there is no enhancement of the heat conductivity at the periphery. This may indicate that the increase in conductivity is related to an MHD activity, i.e. convective transport near the resonance surface. The existence of such processes can be inferred from Fig.6b, which shows, for purposes of comparison, oscillograms of the X-ray signal from the surface-barrier detectors (regime IV) during observation of the core ( $h = 0$ ) and the peripheral ( $h > r_s$ ) regions ( $h$  is the observation chord). The last part also exhibits characteristic sawtooth oscillations but the period is quite different from that in the core.

TABLE II. VARIOUS QUANTITIES IN FIVE DISCHARGE REGIMES

Regime	I	II	III	IV	V
$r$	19	19	19	10	21
$\kappa_e (\times 10^{-17}) (\text{cm}^{-1} \cdot \text{s}^{-1})$	1.2	1.8	2.7	0.4	1.0 (2.0-laser)
$T_e (\text{eV})$	800	900	460	970	910
$\bar{n}_e (10^{-13}) (\text{cm}^{-3})$	5.4	3.2	4.1	5.8	6.2
$Z_{\text{eff}}$	1.6	1.8	2.6	3.1	1.5
$q$	1.2	1.2	1.0	1.4	1.0

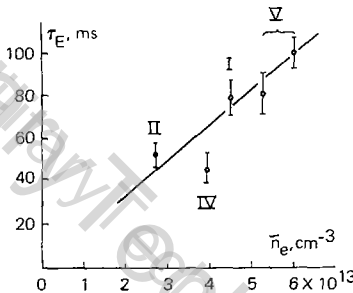


FIG. 5. Total energy confinement time,  $\tau_E$ , versus average density,  $\bar{n}_e$ , from diamagnetic measurements.

Region II – main gradient region. In this intermediate region, where the radial gradient of the electron temperature  $dT_e/dr$  is maximum, the heat conductivity has its lowest value. In regime II, where there is a low value of the magnetic field, the width of this region is small and it may be assumed that the values of  $\kappa_e$  in such cases may show the influence of the two other regions, i.e. the convective transport in the core and the enhanced heat conductivity of the peripheral zone. For small  $q(a_L) = 2$ , the gradient region shifts outwards with increasing density and can thus be seen even from the initial  $T_e(r)$  and  $n_e(r)$  profiles, which become wider while the zone between the wall and the good-confinement region gets narrower. It is, therefore, important that there should be no resonance surface  $q = 2$  in this zone since otherwise a region of enhanced transport occurs which might overlap (for large  $n_e$ ) with the gradient

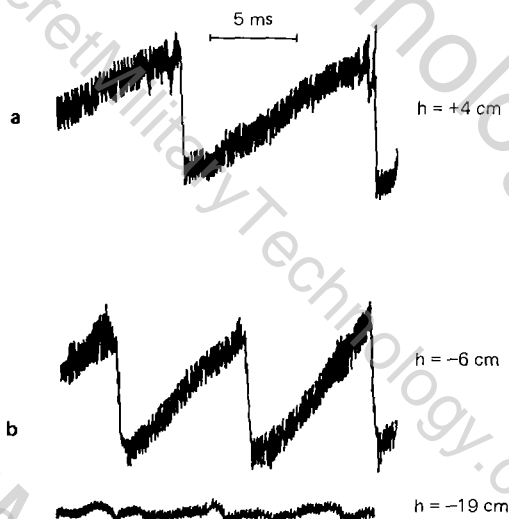


FIG.6. Soft-X-ray sawtooth oscillations: a) regime V; observation along chord,  $h = +4$  cm. (+) sign corresponds to measurements in external region along major radius,  $R = R_0 + h$ . b) regime II; sawtooth oscillations in zone with  $r < r_s$  ( $h = -6$  cm) and  $r > r_s$  ( $h = -19$  cm).

zone and this should lead to impairment of the energy confinement in the plasma. We believe, in fact, that an important feature of the results obtained on the T-10 is that it is possible to achieve regimes with a high density in the absence of a resonance surface  $q = 2$  inside the plasma.

Since the main gradient region determines the energy confinement in the electron component, it is of interest to consider how the thermal conductivity  $\kappa_e$  varies with the discharge parameters in this particular region. The values of  $\kappa_e$  in this zone determined for the different regimes are summarized in Table II.

In all regimes, except that with a low field,  $B_z = 1.6$  T,  $\kappa_e$  is substantially lower (two to four times lower than  $\kappa_e$  corresponding to the T-II scaling law). Note that, for low  $q$ ,  $\kappa_e$  tends to decrease with rising  $n_e$  and  $B_z$ . This is not inconsistent with diamagnetic-measurement results shown in Fig. 5. The dependence of the total energy confinement time,  $\tau_E$ , on the line-average density is close to linear in the range of  $\bar{n}_e = (2-6) \times 10^{13} \text{ cm}^{-3}$ .

## 5. MEASUREMENT OF THE ELECTRON DIFFUSION COEFFICIENT

Measurements of the electron diffusion coefficient were made in regime III by the gas-puffing method. The puffing valve was opened for 10–12 ms, which led to a density change of  $\Delta n_e/n_e \cong 0.02$ . The electron influx profile was determined from the neutral-atom ionization.

From a model solution of the diffusion equation

$$\frac{\partial n_e(r,t)}{\partial t} = S(r,t) + \frac{1}{r} \frac{\partial}{\partial r} \left[ r D_e(r) \frac{\partial n_e(r,t)}{\partial r} \right] + \frac{1}{r} \frac{\partial}{\partial r} [r n_e(r,t) v_p] \quad (6)$$

we were able to determine  $D_e(r,t)$  from the condition for best agreement between the time change in the profile  $n_e(r,t)$  and the experimental results. In Eq.(6),  $S(r,t) = f(r)P(t)$  is the electron influx produced by the ionization of the neutrals. The radial profile of the influx  $f(r)$  was determined from the profile for the increment  $\delta n_e(r,t)$ , 8 ms after the start of the puffing. The best agreement between the experimental  $n_e(r,t)$  profile and the model was obtained for a value of the steady-state neutral flux into the plasma  $P_{ss} = 8 \times 10^{15} \text{ cm}^{-2} \cdot \text{s}^{-1}$ .

The pinching rate  $v_p$  was found to have a neoclassical value ( $20 \text{ cm} \cdot \text{s}^{-1}$ ). The experimental results are given in Fig.4e. The estimates are upper bounds, since with anomalous pinching by an increase in  $v_p$  at the periphery with simultaneous decreases in  $D_e$  and  $P_{ss}$  it is possible to satisfy both the steady-state equation and the equation describing the time change in the density increment.

As can be seen from Fig.4f the three regions discussed above are also found in the radial dependence  $D_e(r)$ . In the main gradient region ( $r \lesssim 0.5a_L$ ), the diffusion coefficient is a minimum –  $D_e \cong 800 \pm 300 \text{ cm}^2 \cdot \text{s}^{-1}$ . An increase in  $D_e$  by a factor of about four is observed at the periphery. Since  $\nabla_r n_e$  vanishes inside the zone  $r \lesssim r_s$ , it is impossible to reach any conclusion about the behaviour of  $D_e$  in this zone.

In the minimum region, the value of  $D_e$  is  $\sim 10\%$  of the heat conductivity coefficient  $\chi_e = \kappa_e/n_e$  and a factor of 4–5 greater than the neoclassical value  $D_e^{\text{neo}}$ .

By comparison with earlier experiments carried out in a similar regime with a smaller density ( $\bar{n}_e = 1.4 \times 10^{13} \text{ cm}^{-3}$ ) [1], the diffusion coefficient in our experiments was a factor of 2–2.5 smaller (it is inversely proportional to the density).

## 6. ION HEAT CONDUCTIVITY

The values determined for the anomaly factor  $K_{\text{an}}^i = \kappa_i/\kappa_i^{\text{neo}}$  are shown in Fig.4. It follows from Eq (4) that the ion heat flux determined in this way also includes the losses connected with diffusion and charge exchange. Estimates for a density  $\bar{n}_e \approx 4.5 \times 10^{13} \text{ cm}^{-3}$  and a neutral-atom concentration  $n_0(a_L) \approx 10^{10} \text{ cm}^{-3}$  show that allowance for charge exchange becomes important when  $r \gtrsim (2/3)a_L$ .

The normally observed increase in  $K_{\text{an}}^i$  at the periphery of the plasma column may therefore be caused by an increase in the fraction of the losses involving charge exchange and in the relative importance of the diffusion fluxes. The

TABLE III. RESULTS OF CALCULATIONS IN REGION  $r \approx (1/2)-(2/3)a_L$ 

Regimes	I	II	III	IV	V
$\kappa_i (\times 10^{-17}) (\text{cm}^{-1} \cdot \text{s}^{-1})$	4-3	2.4-2	4-3.5	3.5-2	3.5-4.5
$K_{\text{an}}^i$	3	5	2	1.5	3.5

uncertainty in the determination of  $\kappa_i$  is much greater than that for  $\kappa_e$ . We shall therefore discuss only the main gradient region [ $r \approx (1/2)-(2/3)a_L$ ]. The results of the calculations are given in Table III.

It can be seen from these data that for large  $q(a_L)$  (regime IV), when the electron thermal conductivity  $\kappa_e$  in the central regions of the column is low,  $K_{\text{an}} = 1.5$ , i.e. the ions can be considered as neoclassical. The extent of the ion anomaly increases with decreasing  $q$ . For constant conditions relating to  $q$ , the ion anomaly is greater for lower densities (regime II,  $K_{\text{an}}^i \gtrsim 4$ ): finally, for identical  $q(a_L)$ ,  $K_{\text{an}}^i$  decreases as the toroidal field gets smaller (regime III). We also carried out calculations of the ion temperature in the plasma core assuming a neoclassical ion thermal conductivity and using the experimental values of  $T_e(r)$ ,  $n_e(r)$  and  $Z_{\text{eff}}(r)$ . To ensure that the calculated  $T_i$  did not contradict the experimental results for  $T_i^{\text{exp}}(r)$  and the neutron radiation yield, it was necessary in the calculations to introduce an anomaly factor  $K_{\text{an}}^i$  which was close to those in Table III for the main gradient region.

In the  $\kappa_i$  calculations we did not allow for the fact that part of the flux  $\langle Q_{ei} \rangle$  is transferred to the impurity ions. For  $Z_{\text{eff}} \approx 2$ , this fraction amounts to  $\sim 15\%$  of  $\langle Q_{ei} \rangle$ . For all regimes except III and IV the corrections are within the limits of accuracy. Moreover, comparative estimates of the thermal conduction fluxes carried by deuterons and impurity ions shows that the contribution of impurities to the thermal conduction losses is small. These estimates do not contradict the results obtained in the regimes with the greatest values of  $Z_{\text{eff}}$  (III and IV), where the ion anomaly factor  $K_{\text{an}}^i$  is least, although no allowance was made for the transfer from electrons to impurity ions.

We can thus say that under the conditions of the T-10 experiment it is impossible to describe the ion thermal transport in terms of neoclassical theory [6] in regimes with large  $H_z$  and small  $q(a_L)$ . The decision of whether the ion heat transfer is neoclassical requires the losses due to diffusion or locally trapped particles to be taken into account accurately.

## DISCUSSION

Over the last decade there has been lively discussion amongst tokamak physicists with regard to scaling laws which could be used to describe the whole

range of available results and to predict the parameters of next-generation devices. The scaling laws are usually written down in the form of a product of the plasma parameters

$$\tau_E = q^\alpha n^\beta T^\gamma$$

From a consideration of the above results on the measurement of the local heat conductivities we can say that this approach is invalid, in principle. Different laws govern the particle and energy confinement in different zones of the discharge.

If we want to find a scaling law for this situation, the expression for the energy confinement time must be taken not as a simple product but as a more complicated function for which the freedom of choice of the functions then becomes very great. A better approach, therefore, is to gain an understanding of the processes which occur in each zone. The fact that zone III is shifted radially together with  $q = 2$  as the transport coefficients increase shows that MHD-instabilities play an important and possibly a decisive role in the processes leading to high values of  $\kappa_e$  and  $D_e$ . A study of these processes would probably enable us to find conditions under which the transport coefficients here would not be so large. A simpler approach, though, is to explore the possibility of working with a plasma in which  $q(a_L) = 2$  and zone III does not exist at all (regime V). However, in this case, there is a very wide zone I inside  $r \lesssim r_s$ , where rapid scattering of heat and particles occurs because of the development of sawtooth oscillations. If the current density could be re-distributed so as to reduce the activity of the  $m = 1$  mode, it ought to be possible to achieve better confinement conditions than currently exist.

The question of the magnitude of the heat transport coefficients in zone II is a complicated one which requires detailed study since, as we pointed out above, zones I and III may have a considerable effect on the value of the thermal conductivity in zone II.

#### ACKNOWLEDGEMENTS

In conclusion, the authors would like to express their gratitude to B.B. Kadomtsev, V.S. Mukhovatov, P.N. Yushmanov, and V.G. Merezhkin for useful discussions and to the staff of T-10 for assistance in the experiments.

#### REFERENCES

- [1] BERLIZOV, A.B., et al., *Fiz. Plazmy* 7 (1981) 11.
- [2] ALIKAEV, V.V., et al., in *Controlled Fusion and Plasma Physics (Proc. 10th Europ Conf. Moscow, 1981)* Vol.1 (Moscow, 1981) paper H-3.

- [3] POST, D.E., in Plasma Physics and Controlled Nuclear Fusion Research (Proc. 7th Int. Conf. Innsbruck, 1978) Vol.1, IAEA, Vienna (1979) 471.
- [4] MEREZHKIN, V.G., MUKHOVATOV, V.S., Pis'ma Zh. Ehksp. Teor. Fiz. 33 (1981) 463.
- [5] ALIKAEV, V.V., et al., Pis'ma Zh. Ehksp. Teor. Fiz. 35 (1982) 136.
- [6] GALEEV, A.A., SAGDEEV, R.Z., in Voprosy teorii plazmy (Problems of Plasma Theory) Atomizdat 7, Moscow (1973) 205.

## DISCUSSION

M. NAGAMI: Your comparison of typical discharges shows that  $\tau_E$  decreases with  $B_T$  while the other parameters are fixed. How do you explain this in terms of  $\chi_e$  or  $q = 1$  or 2 location in minor radius?

V.S. STRELKOV: It may be concluded from a comparison of regimes III and IV that  $\tau_E$  decreases as B decreases. Examination of the local values of  $\chi_e(r)$  shows a difference between the regimes due to the wider zone  $q \leq 1$  in the lower-field case and to the influence of convective transfer in this zone on the value of  $\chi_e$  outside the zone  $q \leq 1$ .

B. COPPI: Is the thermal conductivity you measured in the region outside the  $q = 1$  surface lower than in other experiments?

V.S. STRELKOV: Yes, the minimum local value of the thermal conductivity we obtained is several times smaller than in the Alcator scaling.

R.R. PARKER: Dr. Strelkov, you stated that the ion thermal conductivity did not differ substantially from neoclassical calculations (except in one regime). By what factor was this an 'anomaly', and according to what theory? Is the dependence of  $\chi_i$  on radius also consistent with the neoclassical theory?

V.S. STRELKOV: The comparison of the experimental values for the ion thermal conductivity coefficient was performed using the usual neoclassical theory. Sufficient experimental data on the ion thermal conductivity coefficient have not yet been obtained, so it is difficult to compare the data with the theoretical dependence of  $\chi_i$  on the radius.

D. OVERSKEI: For the past several years you have been performing ECRH experiments on T-10. Would you please comment on the results, or more directly, on the variance in  $\chi_e$  or  $D_e$  with the application of ECRH?

V.S. STRELKOV: The influence of ECRH on the total energy confinement time  $\tau_E$  is discussed in the paper presented by the T-10 group last year at the Tenth European Conference on Controlled Fusion and Plasma Physics, Moscow, USSR (14-19 September 1981). Detailed investigation of the dependence of the local values of  $\chi_e$  and  $D_e$  in ECRH has not yet been completed.

F.B. MARCUS: In previous results from T-10, you reported asymmetries in plasma profiles. Were these observed in these studies, and did they have any effect?

V.S. STRELKOV: Asymmetries in the electron temperature profile have been seen in low-density regimes. In the high-density regimes discussed in our paper, there was no asymmetry in the distribution of  $T_e(r)$ .



**Session J**

**PLASMA HEATING II**

Chairman

W.M. HOOKE

USA

Papers J-1-1 and J-1-2 were presented  
by J.B. Lister as Rapporteur

## ALFVÉN WAVE EXPERIMENTS IN TCA

A. de CHAMBRIER, A.D. CHEETHAM\*,  
 A. HEYM, F. HOFMANN, B. JOYE,  
 R. KELLER, A. LIETTI, J.B. LISTER,  
 A. POCHELON, W. SIMM, J.L. TONINATO,  
 A. TUSZEL

Centre de Recherches en Physique des Plasmas,  
 Association Euratom – Confédération Suisse,  
 Ecole Polytechnique Fédérale de Lausanne,  
 Lausanne,  
 Switzerland

### Abstract

#### ALFVÉN WAVE EXPERIMENTS IN TCA.

The low-power experiments carried out on the TCA tokamak have shown that the antenna system excites the shear Alfvén wave as predicted by numerical codes. The existence of sets of discrete spectra corresponding to global eigenmodes of the Alfvén wave has been experimentally shown. Preliminary higher power experiments have produced increases in electron and ion temperatures accompanied by a substantial increase in the radiated power loss. Indications are that metal impurities are playing a dominant role, but their source has not yet been determined. It appears that energy is transferred directly both to the electrons and to the ions. The antenna structure was completely unshielded for these experiments.

### 1. INTRODUCTION

TCA is a tokamak built with the express aim of studying the launching and absorption of Alfvén Waves. It has been working since mid-1980, was described in detail in Ref. [1], and has the following operating characteristics :

$$\begin{aligned}
 R, a &= 0.605, 0.14-0.18 \text{ m} \\
 B_{\phi} &= 0.78 - 1.51 \text{ T} \\
 I_p &\leq 135 \text{ kA during } \approx 100 \text{ ms} \\
 q &= 2.2 - 22 \\
 n_{e0} &= 0.8 - 9 \times 10^{19} \text{ m}^{-3}, \text{ D}_2 \text{ and H}_2 \\
 T_{e0}, T_{i0} &\leq 900, 250 \text{ eV}
 \end{aligned}$$

\* Present address: Australian National University, Canberra, Australia.

In this experiment we aim to excite the Shear Alfvén Wave resonance at the radial position at which the toroidal transit time of the Shear Alfvén Wave is an integral number of periods of an applied generator frequency. This leads to the requirement that

$$\frac{2\pi R}{V_A} = \frac{2\pi n}{\omega} ; \quad \omega^2(r) = \frac{(n + m/q(r))^2 B_\phi^2}{\mu_0 \rho(r) R^2} \quad (1)$$

where  $n$  and  $m$  are the toroidal and poloidal modenumbers. Since both the  $q$  and density profiles are functions of minor radius in a tokamak discharge, we obtain a set of continua for the various combinations  $n, m$ . At a particular applied frequency there may be several resonant surfaces at different minor radii for different modes. Energy can be transferred from an external antenna system, via a surface wave, to this resonant layer where it can be absorbed, or alternatively converted to other waves which may dissipate elsewhere. The basic theory of the excitation of Shear Alfvén Waves has already been treated in detail by many authors [2,3] and is currently being studied at Lausanne using an ideal MHD approach and at Austin using a kinetic model. The resonant frequency given by Eq. (1) is of the order of several megahertz in present tokamaks, for the low- $n$  modes, and is generally much less than the ion-cyclotron frequency; the ratio  $\omega/\omega_{ci}$  is given by

$$\omega/\omega_{ci} = 0.073 \times (A/n_{19})^{1/2} \times (n + m/q)/R$$

in which  $n_{19}$  and  $q$  are the ion density and safety factor at the Shear Alfvén Wave resonant layer and  $A$  is the atomic mass.

In our experiment the waves are excited by an antenna structure inside the vacuum vessel [4]. The complete structure comprises eight groups of three wide stainless steel antenna plates sited above and below the plasma at four equally spaced

toroidal locations. The phase of the current in each group can be inverted, creating several possible excitation structures which can couple preferentially to different  $n,m$  modes. The rf system [5] was commissioned in Spring 1981 and the first year was spent mostly on low power experiments to understand the mechanism of antenna loading. Since the Grenoble conference, work has been started on higher power experiments. The tokamak is equipped with fairly standard diagnostics not all of which are fully commissioned. In this present paper we shall briefly describe the low power studies, followed by the high power experiments presently underway.

## 2. LOW POWER EXPERIMENTS

Some low power experiments at 2.6 and 5.0 MHz have already been reported [6,7] and the results will be summarized here. The first result is that the value of the antenna loading resistance has been shown to scale correctly as a function of applied frequency and magnetic field, and is independent of the antenna current. Fine structure in the antenna loading as a function of the plasma density was observed near the thresholds of the Shear Alfvén Wave continua, but for only one sign of helicity of the waves. These resonance peaks have been attributed to global eigenmodes of the Alfvén Wave (Discrete Alfvén Waves) which occur just below the continua and are described in ideal MHD theory [8]; the existence of this discrete spectrum had already been indicated theoretically by Goedbloed. Since the antenna loading is roughly doubled at these resonances, they may also offer an interest for plasma heating. The identification of the wave mode structure at the loading peaks, first made by its corresponding threshold, has been confirmed by magnetic pick-up coil measurements made inside the vacuum vessel.

During these studies the solid screens placed either side of the antennae were removed and the loading was thereby doubled due

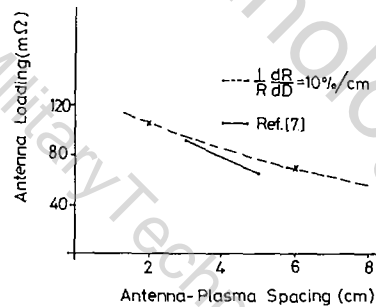


FIG.1. Variation in loading resistance as the antenna-plasma spacing is varied.

to an improved magnetic field distribution at the plasma surface. The loading is typically  $\approx 120 \text{ m}\Omega$  per group outside the peaks for a full aperture plasma corresponding to  $\approx 1\Omega$  for the full antenna system. This figure agrees well with ideal MHD calculations. The variation of the loading as a function of the plasma density agrees better with theoretical estimates if the  $\omega/\omega_{ci}$  corrections are added to the MHD calculations [9].

The antenna loading as a function of antenna-plasma separation has been studied by changing the plasma position [7] and recently by varying the limiter radii from 14 to 18 cm. The latter measurements have confirmed the previous value of a decrease of  $\approx 10\%$  per centimetre of additional space as shown in Fig. 1. The evanescence of the wave in the tenuous plasma between the antenna and the limiter radius is negligible at this low frequency and the reduction in loading resistance is a purely geometrical effect.

### 3. HIGHER POWER STUDIES

Experiments have been performed at 2.6 MHz using rf power of up to 150 kW for 30 ms, which is a power similar to the Ohmic heating power. The antennae were phased so as to excite predominantly the  $n = 2, m = 1$  mode. We find that the antenna loading resistance remains constant up to the maximum power

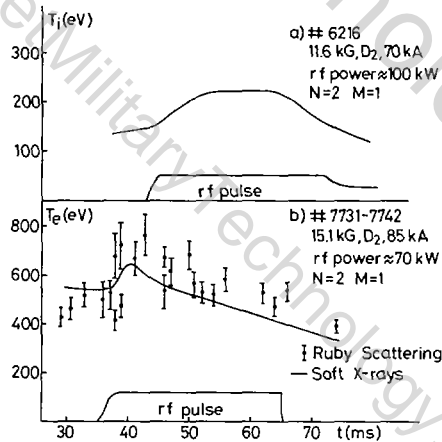


FIG.2. Evolution of (a) ion temperature and (b) electron temperature during the rf pulse.

delivered and that the increased loading of the antennae which resulted from the removal of the side-screens did not lead to a change in the character of the loading. The experiments discussed here were all carried out without any antenna screening. Rf currents up to 700 A were used, corresponding roughly to  $\pm 300$  V across the antenna plates and  $\pm 600$  V across the feedthroughs, with no evidence of any arcing or glow problems. When the rf power is applied during a tokamak discharge we observe an increase in  $T_i$  for most of the pulse and an increase in  $T_e$  which lasts up to 15 ms, after which it can drop below its normal value (Fig. 2). The electron density also rises at the start of the rf pulse and then levels off; the increase depends on the plasma parameters and also, it appears, on the condition of the antennae. The plasma resistance increases during the pulse, recovering subsequently, and the plasma current falls below its normal curve. There is a large increase in the bolometer signal and in the Fe II impurity line emission. The value of  $\beta + I_i/2$  measured from the equilibrium field increases during the rf pulse and the plasma current position moves out. The increases in temperature are found to be linear with the rf

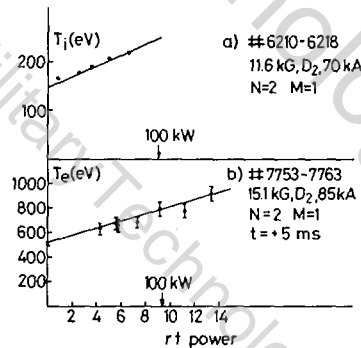


FIG.3. Increase in (a) ion temperature and (b) electron temperature as a function of rf power.

power delivered (Fig. 3) and the maximum power used has been limited by the increase in plasma resistance, which causes a rapid decrease in plasma current. We found that operation with a limiter radius of 18 cm was superior to operation at 17 or 14 cm, and that higher power could be delivered at 15 kG than at 11.6 kG. In what follows we shall separately discuss the electron and ion behaviour during the rf pulse, and the power balance.

Under good conditions we observe an increase in the central electron temperature of up to 60 % with  $\approx 130$  kW rf power. This increase is followed by a slower decrease which lasts until the end of the rf pulse, at which time the electron temperature falls faster. The radial profile of radiated power during the rf pulse shows an intense peaking which takes some 5-10 ms to reach its maximum (Fig. 4). This intense power loss can well explain the subsequent decrease in electron temperature. There is an increase in the internal inductance of the plasma, due to evident current peaking during the rf pulse, which can simply explain only 30 % of the observed increase in electron temperature. Similarly, the current peaking cannot fully explain the observed change in  $\beta + I_1/2$ . An increase in sawtooth activity or MHD activity also often accompanies the start of the rf pulse. The source of the

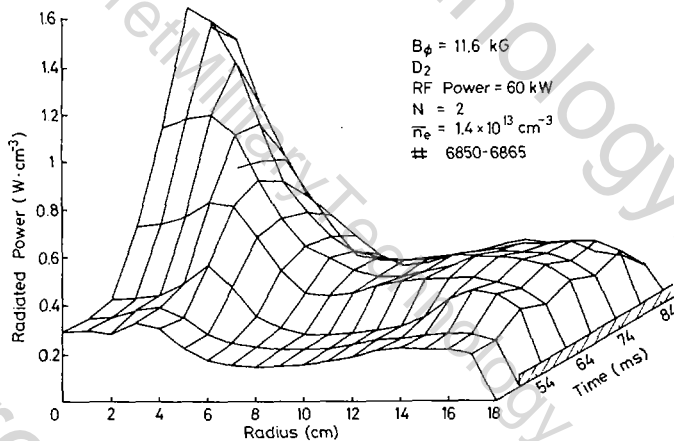


FIG.4. Evolution of the radial profile of the radiated power loss during the rf pulse.

impurities is as yet unknown. An outer carbon limiter has been added with no immediate improvements, and all four steel limiters will soon be replaced by carbon limiters. A spectroscopic study has just been started to identify the impurities responsible for the radiated power loss. Surface deposition-probe measurements have shown an increase in iron deposited during discharges with rf power [10].

Increases in the ion temperature of up to 50% for  $\approx 80$  kW rf power have been observed to be proportional to the delivered rf power. Most measurements were made at 11.6 kG,  $n_{e0} = 2 \times 10^{19} \text{ m}^{-3}$ , in deuterium, since at 15 kG the increase in electron-ion collisional power transfer ( $P_{ei}$ ) obscures any direct ion-heating. We are obliged to increase the density at higher toroidal field to retain the same Alfvén Wave resonances, as seen from equation (1). The increase in electron density alone cannot explain the increase in ion-temperature if the dependence  $T_i \sim (n_e I_p B_\phi)^{1/3}$  is maintained. When we estimate the effect on  $P_{ei}$  of the drop in the electron temperature at the end of the rf pulse, we find that  $P_{ei}$  almost certainly decreases for

a wide range of estimated radial profiles of density and electron and ion temperatures. The results indicate that there must be a direct input of power to the ions if the collision frequency remains classical.

We have attempted to calculate the energy flow, before and at the end of the rf pulse, in a discharge at 11.6 kG with 70 kW rf power. During the rf pulse the radiated power increases from 70 kW (50% x  $P_{OH}$ ) to 130 kW (90% x  $P_{OH}$ ). The losses plus  $P_{ei}$  are estimated to change from 70 kW to 50 kW, resulting in a net input of approximately 40 kW to the electrons. The ions require about 30 kW to produce the observed increase in temperature with appropriately scaled losses and reduced  $P_{ei}$ . The sum of input powers is in credible agreement with the rf power absorbed from the antenna system. The present lack of profile information denies us the possibility of a more detailed analysis.

#### 4. DISCUSSION

The preliminary interpretation of the results obtained during the rf pulse suggests that a large fraction of the absorbed rf power is being deposited in the bulk of the tokamak plasma. Power appears to be transferred directly to both the electrons and the ions. Previous work [3] had foreseen that absorption would be dominantly due to Electron Landau Damping and that ion heating would require a much more collisional plasma.

The present power levels are limited by the problem of the radiated power loss which dominates the power balance of the electrons towards the end of the rf pulse. Work is underway to study and reduce this problem.

Low power measurements have shown the existence of the Discrete Alfvén Waves in tokamak plasma, and have confirmed the nature of the Shear Alfvén Wave excitation process as described in MHD codes.

The fall-off of antenna loading resistance with increasing antenna-plasma spacing is relatively slow, which presents a possible eventual advantage of plasma heating using Shear Alfvén Waves.

#### ACKNOWLEDGEMENTS

This work is partly supported by the Swiss National Science Foundation. We thank Professor H. Schneider of Fribourg University for his collaboration with the bolometric measurements.

#### REFERENCES

- [1] CHEETHAM, A.D., et al., Proc. 11th Symp. on Fusion Technology, Oxford, 1980.
- [2] CHEN, L., and HASEGAWA, A., Phys. Fluids 17 1399 (1974); TATARONIS, J.A., and GROSSMAN, W., Z. Physics 261 203, 207 (1973).
- [3] HASEGAWA, A., and CHEN, L., Phys. Rev. Lett. 35 370 (1975).
- [4] DE CHAMBRIER, A., et al., 3rd Symp. on Heating in Toroidal Plasmas, Grenoble, 1982 (presented by R. Keller).
- [5] LIETTI, A., et al., Proc. 9th Symp. on Eng. Problems of Fusion Research, Chicago, 1981.
- [6] DE CHAMBRIER, A., et al., 10th EPS Conf., Moscow, 1982.
- [7] DE CHAMBRIER, A., et al., 3rd Symp. on Heating in Toroidal Plasmas, Grenoble 1982 (presented by A. Pochelon).
- [8] APPERT, K., et al., Plasma Physics 24 (1982).
- [9] APPERT, K., and VACLAVIK, J., Lausanne Report LRP 207/82 (1982).
- [10] VEPRECK, S., private communication.



## PLASMA HEATING AND CURRENT DRIVE BY ALFVÉN WAVES

R.A. DEMIRKHANOV, A.G. KIROV, G.I. ASTAPENKO,  
S.E. IL'INSKIJ, Eh.M. LOMAKIN, V.V. ONISHCHENKO,  
L.F. RUCHKO, A.V. SUKHACHEV, V.D. MEDUN,  
N.I. MALYKH

Sukhumi Institute of Physics and Technology,  
Sukhumi, Union of Soviet Socialist Republics

### Abstract

#### PLASMA HEATING AND CURRENT DRIVE BY ALFVÉN WAVES.

The results of experimental studies on plasma heating, stationary current drive and impurity transport phenomena with Alfvén waves excited in the R-O5 tokamak and the R-O stellarator are given. In contrast to previous results, the experiments at R-O have been conducted at higher RF-field frequencies and lower electron-ion collision frequencies. The RF-driven current is studied as a function of the plasma parameters. It has been shown experimentally that it is possible to remove the impurity ions when their cyclotron frequency is close to the Alfvén wave frequency:  $\omega_{BI} \approx \omega_A \ll \omega_{BH}$ . The effect of the RF-field on the pre-ionization and current rise stages has been studied in the R-O5 tokamak. The RF-field allows a tokamak discharge at high densities and relatively small magnetic fields to be achieved. In the stationary stage, Alfvén heating leads to an increase in the plasma temperature, a rise in  $\beta_j$  ( $\beta_j \approx 2-3$ ) and in the confinement time, together with an improvement in MHD stability.

### 1. INTRODUCTION

Alfvén waves can be used to introduce RF-energy into a plasma and to bring about an efficient transfer of the electromagnetic wave momentum to the plasma particles [2-4]. The reason for this latter effect is that the phase velocity of these waves for a typical thermonuclear plasma is not high:  $v_A/v_{Te} < 1$ . So far, experimental studies on Alfvén heating (demonstrating its fairly high efficiency) have been made on stellarators only: R-O, R-O2, Uragan-2, and Heliotron-D [5-7]. At present, experiments on RF-heating over the Alfvén frequency range are being started on the R-O5 [8], TCA [9], and PRETEXT [10] tokamaks. The results of the R-O5 tokamak experiments are given in the first part of this paper.

The generation of quasi-stationary longitudinal RF-driven currents and the possibility of effects being produced on the entire plasma radial transport through the absorption of Alfvén waves by electrons have already been demonstrated on the R-O stellarator [1]. It is quite clear that the relative merits of various RF-current drive methods (lower-hybrid, ion cyclotron and Alfvén) will ultimately

depend on their energetic efficiencies at high plasma densities,  $n_e \approx 10^{14} \text{ cm}^{-3}$ . As a measure of the efficiency, we may introduce the quantity  $\eta = P_{\text{OH}}/\tilde{P}$ , where  $P_{\text{OH}}$  is the Ohmic power necessary for exciting a current of the same magnitude as that generated by the RF-power,  $\tilde{P}$ . Using the drive-current density formula from Ref. [11]:

$$j \propto \tilde{P} T^{3/2} / (n_e \omega / k_{\parallel}) \quad (1)$$

we obtain an expression for  $\eta$ , which does not depend on the temperature and is quite convenient for analysing the experimental data, while permitting extrapolation over a wide parameter range for the Alfvén frequency region ( $v_{\text{ph}} < v_{T_e}$ ):  $\eta = v_d / v_{\text{ph}}$ , where  $v_d = j / en_e$  is the drift current velocity in an Ohmic discharge and  $v_{\text{ph}} = \omega / k_{\parallel}$  is the RF-wave phase velocity ( $v_{\text{ph}} \approx v_A$  for Alfvén waves). For tokamaks,  $\eta \propto (n^{1/2} q R)^{-1}$ .

The first part of the R-O stellarator experiments was devoted to a verification of expression (1).

The use of Alfvén waves with  $\omega \ll \omega_{\text{BiD}}$  ( $\omega \approx \omega_{\text{BiD}}/\alpha$ ,  $\alpha \gg 1$ ), introduces the possibility of their absorption (and hence, their heating and momentum transfer) by weakly stripped impurity ions with  $Z^+/Z \approx \alpha^{-1} \ll 1$ , where  $Z^+$  is the ion charge and  $Z$  is the charge on the nucleus. In a high-temperature plasma, these ions are created at the boundary region where they must be and can conveniently be removed to prevent them from penetrating into the plasma column interior. Of particular interest is the possibility of removing helium ions (thermonuclear ash). Recently, experiments on TFR [12] showed the effect produced by ion-cyclotron heating,  $\omega = \omega_{\text{BiD}}$ , on the content of highly stripped ions ( $\text{Ar}^{+16}$ ) at the centre of the plasma column. Theory suggests several mechanisms of impurity control in toroidal systems. These mechanisms are related both with the heating proper (increase in transverse energy of the impurity ions) and the momentum transfer from the RF-wave [13, 14]. If the cyclotron zone of the corresponding impurity ions coincides with the local Alfvén resonance region where short-wavelength ( $k_{\perp} a \gg 1$ ) Alfvén waves with large  $\vec{E} \perp \vec{B}$  values are generated, it should be possible, in particular, to achieve azimuthally asymmetric conditions for effective action on the impurity transport considered in Ref. [14]. The second part of the R-O stellarator experiments was devoted to the effect on impurity transport.

## 2. R-O5 TOKAMAK EXPERIMENTS

### 2.1. Experimental conditions

The R-O5 tokamak has a quartz vacuum discharge chamber; the major radius  $R = 65 \text{ cm}$ , the minor radius of the chamber is  $8.5 \text{ cm}$ , and there is no

limiter. The experiments were carried out with a toroidal field  $B_0 = 7-10$  kG and a plasma current  $I_p = 5-10$  kA. The plasma column is held in equilibrium by an automatic system providing vertical and horizontal position control. Outside the discharge chamber, there are eight helical conductors making three revolutions around the minor cross-section of the chamber over its whole length. These turns provide a stellarator field ( $\ell = 2$ ,  $\iota = 16^\circ$  at  $B_0 = 4$  kG,  $\tau_{st} \approx 5$  ms) and an RF-field ( $m = 0$ ,  $n = 0$ ,  $f = 0.2$  MHz,  $\tau_{RF} \approx 2.5$  ms,  $I_p \leq 0.5$  kA) in order to produce a plasma with  $\langle n_e \rangle \leq 2 \times 10^{12}$  cm $^{-3}$ , using no current; an RF travelling or standing field ( $m = 2$ ,  $n = 6$ ,  $f = 3$  MHz,  $\tau_{RF} \approx 2.5$  ms + 2.5 ms,  $\tilde{B}_0 \leq 50$  G) to ensure final ionization, Alfvén heating and an RF-driven current.

## 2.2. Discharge formation stage

The  $m = 0$ ,  $n = 0$  RF-field is switched on 2.5 ms before the onset of the plasma current. The stellarator is switched on at the same time and remains so during the first millisecond of the discharge current. The main RF-field (RF-1, 2,  $m = 2$ ,  $n = 6$ ) is switched on 0.5–1 ms before the start of the plasma current in order to provide the final ionization. The plasma density before the onset of the current  $\langle n_e \rangle \approx 1 \times 10^{13}$  cm $^{-3}$ , while 1 ms after the current onset  $\langle n_e \rangle \approx 4 \times 10^{13}$  cm $^{-3}$ . With  $n_{res} = 5 \times 10^{13}$  cm $^{-3}$ , a local Alfvén resonance condition,  $\omega = k_{||}(r) v_A(r) = (m-nq) B_0/qR \sqrt{4\pi m_i n_{res}}$ , is fulfilled at some magnetic surface inside the plasma column and plasma heating takes place.

An ordinary Ohmic discharge is produced for pressures up to  $4 \times 10^{-4}$  torr, without additional RF-heating, i.e. without switching the RF-field on. The average density measured by an interferometer,  $\langle n_e \rangle_{max} \approx 1 \times 10^{13}$  cm $^{-3}$ . The plasma temperature,  $T_{e\sigma max} \approx 100$  eV,  $\tau_E \leq 62$  ms,  $\beta_J \approx 0.2$ ,  $q(a) = 5$ ,  $I_p \leq 10$  kA,  $B_0 = 10$  kG,  $U_\ell \approx 6$  V.

Increasing the initial pressure further and pre-ionizing by an  $m = 0$ ,  $n = 0$  RF-field only leads to accelerating discharge regimes. Sometimes, after training by powerful discharges, we succeeded in producing a discharge at a large initial pressure,  $p > 4 \times 10^{-4}$  torr D $_2$ . The reproducibility of the discharge is very poor. Figure 1 shows the current and the loop voltage of this discharge. Apparently, for these discharge conditions, the density limit [15] is  $n_e \approx (1-2) \times 10^{13}$  cm $^{-3}$ .

The application of a high-power  $m = 2$ ,  $n = 6$  quadrupole RF-field (RF-1 pulse in Fig. 1) 0.5 ms before the discharge and during its initial stage, in order to finally ionize the plasma, increases the plasma current and its duration, while the initial loop voltage decreases (Fig. 1a). After the end of the RF-1 pulse, the plasma current ceases to grow, the loop voltage rises rapidly and oscillations of a significant magnitude begin to appear.

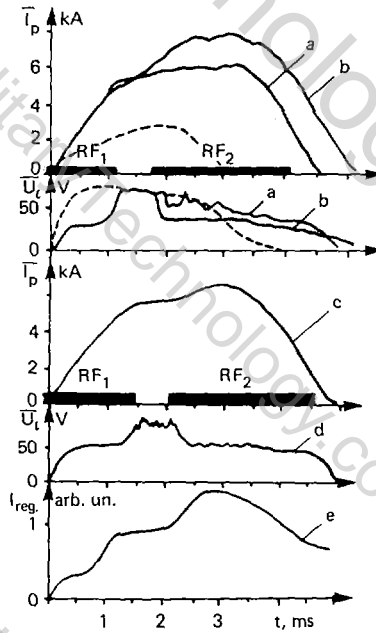


FIG.1. (a)  $I_p$ , plasma current, and  $U_l$ , discharge loop voltage, with RF-1 switched on; (b) the same, with RF-1 and RF-2 switched on; (c)  $I_p$ , plasma current, with RF-1 and RF-2 switched on; (d)  $U_l$ , discharge loop voltage; (e)  $I_{reg}$ , current of equilibrium control system.  $D_2$  is the operating gas, traces for  $I_p$  and  $U_l$  without RF-1 are dashed.  $B_0 = 9$  kG.

### 2.3. Heating in the stationary stage

After some time, the second pulse of the  $m = 2$ ,  $n = 6$  RF-field is switched on (pulse RF-2 in Fig. 1), which again leads to a slow rise ( $\tau_{I_p} \approx 1$  ms) of the plasma current and a rapid drop ( $\tau_{U_l} \approx 200$  ms) of the loop voltage; the oscillations are suppressed (Fig. 1 b to d). At the same time, the current in the system for automatically controlling equilibrium along the major radius ( $J_{reg}$ ) increases (Fig. 1e). This indicates that  $\beta_J = 8\pi nT/B_J^2$  rises to a value of  $\beta_J \approx 3$ . After application of RF-2, the energy confinement time increases by a factor of 1.2–1.5. The peak value of  $\langle n_e \rangle \approx 1 \times 10^{14}$  cm $^{-3}$ , the plasma temperature on the column axis, on the assumption of a parabolic profile, is  $T_{e0} \approx 50$  eV,  $\tau_E \approx 0.1$  ms. On increasing the RF-1, 2 power, the plasma current grows and the loop voltage decreases. It is quite possible that the rapid drop in  $U_l$  and the relatively slow rise in plasma current when the RF-2 pulse is switched on is due not only to plasma heating but also to the generation of current drive by the travelling Alfvén wave. The direction of this propagation coincides with that of the electron current drift in the plasma.

## 2.4. Summary

Thus, the RF quadrupole field which satisfies the Alfvén resonance condition provides the possibility of

- a) producing a high-density tokamak discharge in a relatively low magnetic field by switching on the RF-pulse in the plasma ionization and current formation stages;
- b) increasing the plasma temperature  $\Delta T/T \approx 1$  in the stationary stage; and
- c) improving the MHD stability of the discharge.

## 3. R-O STELLARATOR EXPERIMENTS

### 3.1. Parameters of the experiment

The R-O stellarator parameters are as follows: the major and minor radii of the quartz discharge chamber,  $R = 50$  cm and  $b = 5$  cm, respectively;  $B_0 \leq 8$  kG;  $\tau_0 < 0.8$ ;  $\varrho = 3$ . The RF-circuit, consisting of eight helical conductors, generated an RF-field with  $m = 2$ ,  $n = 2$  at  $f = 1.5$  MHz ( $m$  and  $n$  are the poloidal and toroidal wave numbers, respectively). Varying the phases of the RF-oscillators, it was possible to excite a wave propagating in the direction of the toroidal magnetic field and, simultaneously, opposite to the poloidal magnetic field, i.e. '(+) wave'; a wave in the opposite direction was designated by '(-) wave', and a standing wave '(±) wave'.

The experiments were carried out in hydrogen and deuterium plasmas with  $n_e = (2-10) \times 10^{13}$  cm<sup>-3</sup> and  $T_e = 10-40$  eV. Plasma density and energy content were measured by an interferometer with  $\lambda = 2.3$  mm and a diamagnetic probe, respectively. The electron temperature,  $\langle T_e \rangle$ , was measured from the conductivity ( $Z_{\text{eff}} = 2$ ) with a moderate Ohmic current ( $P_{\text{OH}} \ll \tilde{P}$ ), which did not affect the discharge parameters.

### 3.2. RF-driven current

The RF-driven current was studied in deuterium plasmas for two values of the rotational transform angle,  $\iota_0 = 0.2$  and  $\iota_0 = 0.4$ , with the Ohmic-heating transformer switched off and full ionization and plasma heating produced by the RF-field alone. Because of the two-fold increase in the RF-field frequency, compared to Ref.[1], and the corresponding decrease in the resonant Alfvén density value, the experiments could be carried out at  $(n_e) = (2-8) \times 10^{13}$  cm<sup>-3</sup>, higher temperatures  $\langle T_1 \rangle \lesssim 40$  eV (where  $\langle T_1 \rangle$  is the plasma temperature measured from the diamagnetism) and lower collision frequencies corresponding to the 'plateau' regime ( $\nu^* \lesssim (R/a)^{3/2}$ ).

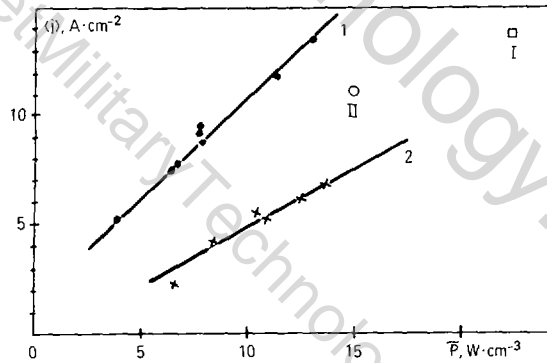


FIG.2. Average current density versus specific RF-power absorbed (RF '(–) wave'):  
 1)  $t_0 = 0.2$ ,  $\langle n_e \rangle = (2-3) \times 10^{13} \text{ cm}^{-3}$ ,  $\langle T_{e0} \rangle = 14-18 \text{ eV}$ ,  $\langle T_1 \rangle = 14-22 \text{ eV}$ ,  $D_2$ ; 2)  $t_0 = 0.4$ ,  
 $\langle n_e \rangle = (6-8) \times 10^{13} \text{ cm}^{-3}$ ,  $\langle T_{e0} \rangle = 7-12 \text{ eV}$ ,  $\langle T_1 \rangle = 13-17 \text{ eV}$ ,  $D_2$ ; I)  $t_0 = 0.2$ ,  
 $\langle n_e \rangle \approx 1 \times 10^{14} \text{ cm}^{-3}$ ,  $\langle T_{e0} \rangle \approx 15 \text{ eV}$ ,  $H_2$ , ( $f = 0.8 \text{ MHz}$ ); II)  $t_0 = 0.4$ ,  $\langle n_e \rangle = 3 \times 10^{13} \text{ cm}^{-3}$ ,  
 $T_1 = 40 \text{ eV}$ ,  $D_2$ .

Figure 2 shows the current density, averaged over the plasma column cross-section, versus the average specific RF-power absorbed in two regimes. In regime 1, the density is lower and the temperature higher than in regime 2. Point I is taken from earlier experiments [1] and corresponds to regime 1 ( $t_0 = 0.2$ ), but was obtained for a lower phase velocity and a higher density. Point II corresponds to regime 2 ( $t_0 = 0.4$ ), but with lower density and higher temperature.

It follows from these experimental data that, according to expression (1), at nearly constant average plasma density and temperature (no local measurements were made of density and temperature in the region of RF-field absorption and current generation), the RF-driven current density grows in proportion to  $\tilde{P}$ , while  $j/\tilde{P}$ , the so-called energy efficiency of the current drive, increases for  $\tilde{P} = \text{const}$  with decreasing plasma density and rising temperature. The absolute value,  $\langle j \rangle$ , agrees with that of Eq. (1) to within a factor of 2 or 3. The value of  $\eta$  (Fig. 2, regime 1) is about 4%.

### 3.3. Removal of impurities

In the experiments on impurity removal, the impurity was simulated by adding helium or nitrogen to deuterium or hydrogen plasmas. To avoid a change in the plasma dispersion properties or a serious deterioration of the discharge parameters, the impurity density in the main regimes did not exceed 5–10% of that of the main gas.

Variations in the luminosity intensities of the He II, N III, N II, O II, Si III, and Si II lines at the plasma column centre and the boundaries demonstrated

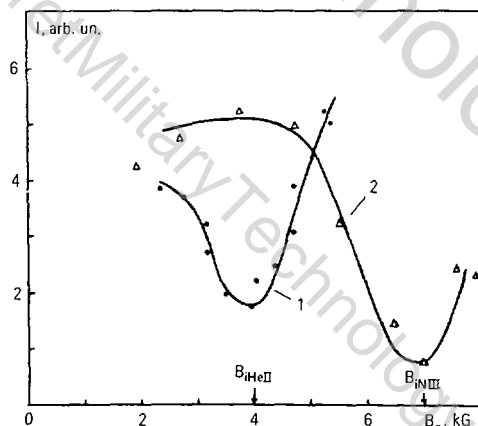


FIG.3. He II 4686 Å (1) and N III 4515 Å (2) luminosity intensities (lines emitted from plasma column centre) versus toroidal magnetic field (RF (-) wave): 1)  $t_0 = 0.2$ ,  $H_2 + 10\% He$ ; 2)  $t_0 = 0.2$ ,  $D_2 + 5\% N_2$ .

the behaviour of the impurities. A corona model was used to relate the luminosity intensities of the impurity lines to their densities. For a qualitative analysis of the experimental data, the particle balance has been considered where the equilibrium is established as a result of shock ionization and removal of particles from the plasma through radial transport. The analysis showed that for  $T_e = 10-30$  eV,  $n_e = (2-10) \times 10^{13}$  cm $^{-3}$ , the luminosity intensities of the He II and N III lines depend only weakly on the temperature, but fairly strongly on the life-times. This parameter region is, therefore, the most suitable for studying the effect of the RF-field on the impurity ion transport. Moreover, the electron temperature in discharges with various values of the toroidal magnetic field was kept at a relatively constant level.

The experiments show that, as the magnetic field changes, the intensity of the He II ( $H_2 + 10\%$ ) and N III ( $D_2 + 5\% N_2$ ) lines decrease when the cyclotron resonance condition,  $\omega \approx \omega_{BI}$ , is fulfilled for these species (Fig. 3). The intensity of the O II, Si II, and Si III lines, which are out of resonance with the RF-field, either does not change or grows (Si III) with increasing magnetic field.

Figure 4 shows the He-II line intensity (Fig. 4a, curve 1), the RF-power absorbed (curve 2), the density (Fig. 4b, curve 1) and the electron temperature (curve 2) as functions of the magnetic field. The He-II ion luminosities decrease, both at the centre and at the boundaries of the plasma column. The increase in RF-power absorbed by the plasma in resonance magnetic-field conditions (Fig. 4a, curve 2) suggests a cyclotron-type of RF-field energy absorption by impurity ions.

The experiments with the RF-power absorption kept constant showed a small decrease in  $\langle nT_1 \rangle$  in the resonance magnetic-field region and a corresponding

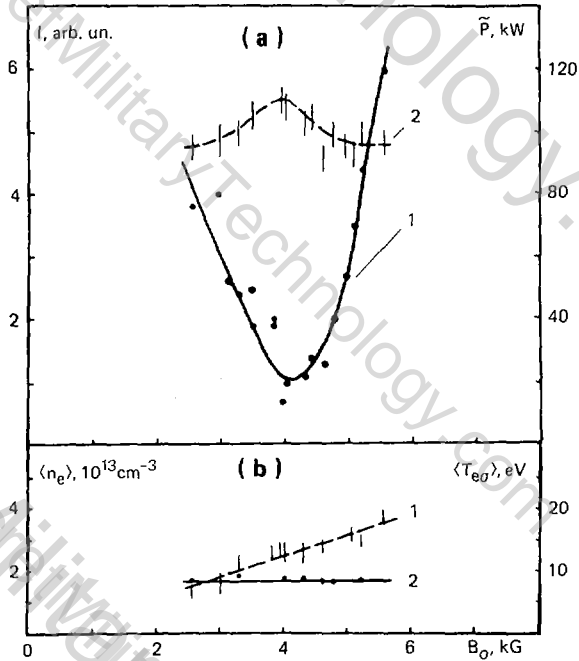


FIG.4. (a) Luminosity intensity for He II 4686 Å emitted from plasma column centre (1), RF-power absorbed by plasma (2); (b) plasma density (1) and electron temperature (2) versus magnetic field. RF (+) wave,  $\tau_0 = 0.4$ ,  $H_2 + 7\% \text{ He}$ .

reduction in the energy confinement time. This fact can easily be explained by an enhanced removal of added impurity ions, implying, at the same time, that the process of enhanced impurity removal does not seriously affect the confinement of the main plasma component, which is heated as a result of Alfvén wave absorption by the electrons.

The experiments showed that the impurity removal at cyclotron resonance is only slightly dependent on the direction of RF-wave propagation (Figs 3 and 4).

It seems, at present, rather difficult to come to any final conclusion on the mechanism by which the RF-field causes enhanced removal of impurities; but estimates suggest that the removal is probably due to, first, the increase in transverse energy of the impurity ions and, secondly, to the direct transfer to these ions of RF-field momentum and the production of directed drift fluxes [14].

### 3.4. Final remarks

Hence, the experiments show that, in the case of Alfvén heating,

(1) travelling Alfvén waves absorbed by electrons rather efficiently generate a longitudinal current, whose value depends on the plasma parameters, over a wide range of values, in a way which is in fair agreement with the predictions of an approximate theory;

(2) the cyclotron absorption of Alfvén waves by weakly stripped impurity ions results in a reduction of their density in the discharge.

#### REFERENCES

- [1] DEMIRKhanov, R.A., KIROV, A.G., RUCHKO, L.F., SUKHACHEV, A.V., *Pis'ma Zh. Eksp. Teor. Fiz.* **33** 1 (1981) 31; SFTI-12 preprint, Sukhumi (1980).
- [2] HASEGAWA, A., *Nucl. Fusion* **20** (1980) 1158.
- [3] BOORDO, O.S., GORIN, V.V., DMITRENKO, A.G., ELFIMOV, A.G., in *Controlled Fusion and Plasma Physics (Proc. 10th Europ. Conf. Moscow, 1981)* Vol. 1, paper H10.
- [4] ELFIMOV, A.G., KOMOSHVILLI, K.G., MINENKO, V.P., SIDOROV, V.P., *ibid.*, Vol. 2, paper H10a.
- [5] DEMIRKhanov, R.A., et al., in *Plasma Physics and Controlled Nuclear Fusion Research (Proc. 6th Int. Conf. Berchtesgaden, 1976)* Vol. 3, IAEA, Vienna (1977) 31.
- [6] DIKIJ, A.G., et al., *ibid.*, Vol. 2, 129.
- [7] OBIKI, T., et al., *Phys. Rev. Lett.* **39** (1977) 812.
- [8] *Novosti Termoyadernykh Issledovaniy v SSSR*, **3** (9) (1978) 5; *ibid.*, **2** (16) (1980) 6.
- [9] BUGMANN, G., et al., in *Controlled Fusion and Plasma Physics (Proc. 10th Europ. Conf. Moscow, 1981)* Vol. 1, paper H4.
- [10] LIN, S.H., et al., *Bull. Am. Phys. Soc.* **26** 7 (1981) 1019.
- [11] KLIMA, R., *Plasma Phys.* **15** (1973) 1031.
- [12] TFR GROUP, Preprint EUR-CEA-FC-1131 (1981).
- [13] CONSOLI, T., LE GARDEUR, R., TONON, G.F., in *Plasma Physics and Controlled Nuclear Fusion Research (Proc. 5th Int. Conf. Tokyo, 1974)* Vol. 1, IAEA, Vienna (1975) 571.
- [14] PARKS, P.B., BURRELL, K.H., WONG, S.K., *Nucl. Fusion* **20** (1980) 27.
- [15] EQUIPE TFR, *Nucl. Fusion* **20** (1980) 1227.



## DISCUSSION

ON PAPERS IAEA-CN-41/J-1-1 AND J-1-2

F.B. MARCUS: Could you quote a heating efficiency in terms of  $\text{eV} \cdot \text{kW}^{-1}$  and density?

J.B. LISTER: For the ions, we obtain, on TCA,  $2.5 \times 10^{13} \text{ eV} \cdot \text{cm}^{-3} \cdot \text{kW}^{-1}$ . The electron temperature profile peaks during heating and the measured figure of  $6 \times 10^{13} \text{ eV} \cdot \text{cm}^{-3} \cdot \text{kW}^{-1}$  for electrons is subject to verification.



## COMPREHENSIVE ANALYSIS OF ANTENNA-PLASMA COUPLING IN ICR HEATING OF TOKAMAKS AND STUDY OF ENERGY DEPOSITION\*

V.P. BHATNAGAR, M.P. EVRARD, D.W. FAULCONER,  
P. GEILFUS\*\*, R. KOCH, M. LUWEL, A.M. MESSIAEN†,  
D.I.C. PEARSON, P.E. VANDENPLAS, R.R. WEYNANTS‡

Laboratoire de Physique des Plasmas – Laboratorium voor Plasmafysica,  
Association Euratom-Etat belge – Associatie Euratom-Belgische Staat,  
Ecole royale militaire – Koninklijke Militaire School,  
Brussels, Belgium

### Abstract

#### COMPREHENSIVE ANALYSIS OF ANTENNA-PLASMA COUPLING IN ICR HEATING OF TOKAMAKS AND STUDY OF ENERGY DEPOSITION.

A unified account of the modelling of launching structures for heating tokamaks in the ion-cyclotron range of frequencies is given. The problem is examined from the points of view of coupling and of energy deposition profile. Three mechanisms of coupling energy to the plasma are identified: (a) direct coupling, (b) coaxial modes propagating in the vacuum layer between plasma and wall, and (c) surface waves in the outer plasma gradient. The relative importance of these different mechanisms in typical situations is outlined. It is briefly shown that slot and waveguide coupling rest on the same underlying physics as antenna coupling. Power deposition profiles are computed using a ray-tracing code which takes full account of the toroidal geometry. The solution of these coupling problems gives the initial conditions for ray-tracing. All the usual hot plasma wave-damping mechanisms are included.

### 1. MODEL OF THE ICRH ANTENNA

Figure 1(a) shows the geometrical model used for analysing the ICRH coupling structure at present most widely used [1–4], known as the all-metal shielded strip line antenna. The following features of the coupling model are essential:

\* This work is partially supported by JET Joint Undertaking under contract No. JB1/9019.

\*\* At present with SIE, Brussels.

† Maître de Recherches au FNRS.

‡ Onderzoeksleider bij het NFWO.

(a) *A finite-length strip line* taking due account of the end effects introduced by the antenna feeders (called the "3-D treatment"). This antenna is represented by its exciting surface current distribution  $\bar{J} = (J_x \gamma(x), J_y \delta(x), 0)$  with  $J_y(y, z) = [\gamma(y) - \gamma(y - 2w_y)] \cos \beta_y J(z)$  and  $J_x(y, z) = [\delta(y - 2w_y) \cos 2\beta_w - \delta(y)] J(z)$ . The toroidal direction is denoted by  $z$  and the poloidal by  $y$ ;  $\gamma(x)$  and  $\delta(x)$  are, respectively, the step and delta functions. The current propagation constant  $\beta$  is estimated from transmission line theory [5].

(b) *An electrostatic (ES) shield* consisting of an array of metal strips suppressing unwanted polarizations and preventing particles from impinging on the antenna. It is modelled by a plane of anisotropic conductivity ( $\sigma_{zz} = \infty$ ;  $\sigma_{yy} = 0$ ) placed at  $x = -s$ . Only the TE part of the field (with respect to the direction  $z$ ) excited by the antenna will pass through the screen.

(c) *The TE field* excites the magnetosonic wave inside the plasma of density  $N(x)$ . Single-pass absorption in the bulk of the plasma is modelled by the presence of a plateau in the density profile where only outgoing waves exist. Numerical integration of the magnetosonic wave equation through the density profile yields the quantity  $\xi_1 = (E_y / \omega B_z)_{x=-a}$ .

(d) *The induced e.m.f. method* [6] is used to compute the complex power radiated by the antenna [7, 8]:

$$P_A = - \frac{\omega \mu_0}{8\pi^2} \iint_{-\infty}^{\infty} \psi_A(k_y, k_{\parallel}) dk_y dk_{\parallel} \quad (1)$$

where the integrand is

$$\psi_A = \frac{-ip \sinh pd}{H^2 p^2} \frac{U_A}{p^2 \Delta} |p^2 \mathcal{J}|^2 + \frac{id |J_x|^2}{p^2}$$

We have defined  $\mathcal{J} = J_y - ik_y J_x / p^2$ ;  $H^2 = k_0^2 - k_{\parallel}^2$ ;  $k_0 = \omega/c$ ;  $p^2 = k_y^2 - H^2$ ;  $U_A = i \xi_1 H^2 \cosh pa + p \sinh pa$ ; and  $\Delta = i \xi_1 H^2 \cosh p(a+d) + p \sinh p(a+d)$ . This expression has been obtained by analysing the problem in Fourier harmonics  $\exp(ik_y y + ik_{\parallel} z - i\omega t)$  and does not contain the power  $P_{TM}$  associated with the TM field confined inside the screen [8]; it is related to the antenna input impedance  $Z_A$  by the formula:

$$\frac{1}{2} Z_A |I_A|^2 = P_A + P_{TM} \quad \text{with } I_A = I(2w_y), \quad I(y) = \int_{-\infty}^{\infty} J_y(y, z) dz$$

It should be noted that  $P_A$  depends on the plasma properties uniquely through  $\xi_1$ .

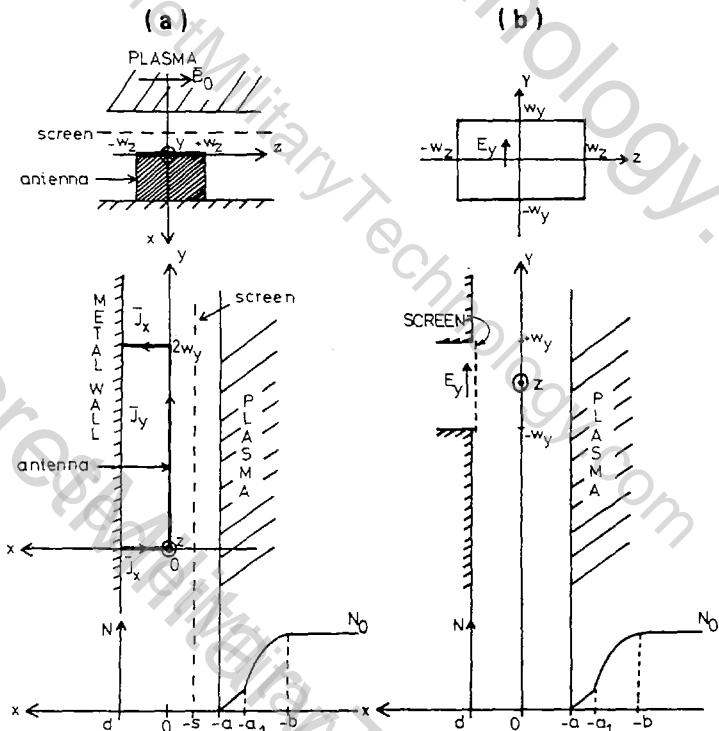


FIG.1(a) Model of the strip line antenna with plasma density profile. The shaded area represents the ends at  $y = 0$  and  $y = 2w_y$ .  
 (b) Model for the slot antenna.

2. SLOT OR WAVEGUIDE EXCITATION

The computation of energy coupling and deposition for a slot [9] or waveguide excitation is fundamentally similar to the antenna coupling problem. Keeping the same notations and assuming the electric field  $E_y(y, z)$  applied at the slot ( $x = d$  in Fig.1(b)) to be known, the following expression is obtained for the complex power radiated by the slot [10]:

$$P_s = \frac{1}{8\pi^2 \omega \mu_0} \iint_{-\infty}^{\infty} \left[ \frac{iH^2}{p} \frac{U_s}{\Delta} \right]^* |E_y|^2 dk_{||} dk_y \quad (2)$$

with  $U_s = i\xi_1 H^2 \sinh p(a+d) + p \cosh p(a+d)$ . This quantity can be related to the aperture admittance  $\bar{Y}$  by the formula:

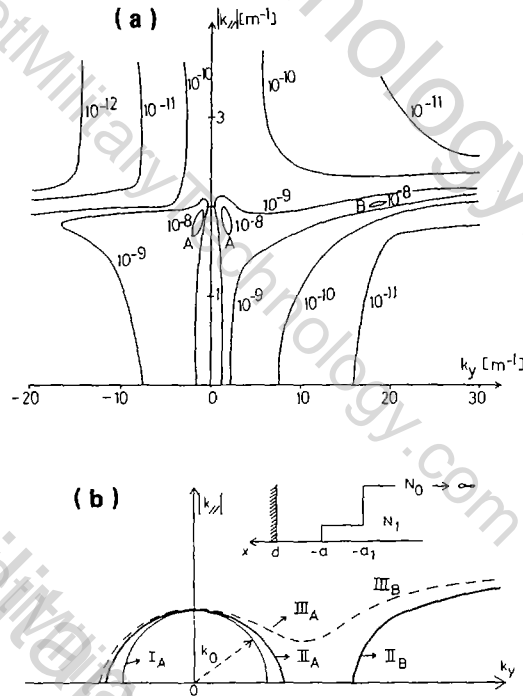


FIG.2(a) Contour of the function  $3 \times 10^{-6} \text{Re}(\psi_A)$  (labelled in MKSA units) for the conditions of Fig.3, profile 3 and  $k_0 = 2$ .

(b) Dispersion relation for edge vacuum propagation (A) and surface wave (B): curve I for  $N_1 = 0$  and curve II or III for  $N_1 \neq 0$ .

$$\frac{1}{2} Y^* \int_{-\infty}^{\infty} \int_{-\infty}^{\infty} |E_y|^2 dy dz = P_s$$

In the mathematical similarity of Eq.(2) to Eq.(1) the identical nature of the coupling physics for the two excitations is manifest. However, consideration of specific cases is necessary to determine the relative importance of the several coupling mechanisms for each excitation. In the following, we shall discuss only the antenna case.

### 3. PHYSICS OF THE POWER COUPLING

The active power radiated by the antenna is given by the real part of  $P_A$  in Eq.(1). It is made up of: (a) residues of poles of the imaginary part of the integrand,  $\text{Im}(\psi_A)$ , and (b) a non-zero real part,  $\text{Re}(\psi_A)$ .

The contributions (a) represent the power radiated in directions orthogonal to  $x$  which never reaches the plasma bulk. There are two such sets of poles in  $\text{Im}(\psi_A)$ . The first sets occur for  $H^2 = 0$  and correspond to power guided by the infinite electrostatic screen. They should be neglected, as in reality the screen is closed. The second sets correspond to roots of  $\Delta = 0$  for real  $k_{\parallel}$  and  $k_y$ , occurring when  $k_x^2 = k_{\perp}^2 - k_y^2 < 0$  everywhere in the plasma (the magnetosonic wave is evanescent). These are associated with surface waves. For high density plasmas their contribution is generally negligible and will therefore henceforth not be considered.

The contribution (b) is proportional to the real part of  $\xi_1$  and accounts for the power loss at  $x = -\infty$ , i.e. inside the plasma. It can be analysed in terms of the topology of  $\text{Re}(\psi_A)$ , which can exhibit pronounced maxima corresponding to particular coupling mechanisms. In general, they are related to the existence of complex roots of  $\Delta = 0$  (e.g. complex  $k_{\parallel}$ , real  $k_y$ ) whose meaning only becomes clear when appropriate limits which move the location of these roots to the real ( $k_y, k_{\parallel}$ ) plane are taken. Figure 2(a) shows a contour plot of  $\text{Re}(\psi_A)$ ; two regions of pronounced maxima, labelled A and B, can be identified.

Region A lies close to the locus  $k_{\parallel}^2 + k_y^2 - k_0^2 = 0$ . Taking the limit of an infinitely large density step, this locus becomes a root of  $\Delta = 0$ . This corresponds to the existence of TEM waves characterized by  $E_x, B_z$  and  $B_y$  components and excited by the feeder currents  $J_x$ . These waves carry energy away to infinity in the vacuum region between wall and plasma. In realistic cases, the power carried by these waves, instead of being lost at infinity, progressively penetrates into the plasma. The lower the density adjacent to the vacuum, the more easily these waves penetrate into the plasma and the less pronounced will be the maxima A of  $\text{Re}(\psi_A)$ .

Region B in Fig.2(a) corresponds to a surface wave type mode, as becomes clear in the limit of a step density profile. This is illustrated in Fig.2(b), which shows the locus of the roots of  $\Delta = 0$  for the case of an infinitely high bulk plasma density (see density profile in the inset). Branch  $\text{II}_B$  or  $\text{III}_B$  of this locus corresponds to the surface mode described here. In the present case of a smooth density profile, this surface mode gradually leaks its energy into the plasma.

The bulk of the  $\text{Re}(\psi_A)$  surface away from these maxima corresponds to direct magnetosonic coupling. This coupling mechanism was the only one accounted for in earlier 2-D theories [10, 11].

The result is that there will always be a part of the energy entering the plasma in the form of waves grazing the plasma edge. Depending on the actual density profile, they will penetrate more or less readily into the bulk plasma. Their excitation can be minimized by appropriate shaping of the excitation currents [12].

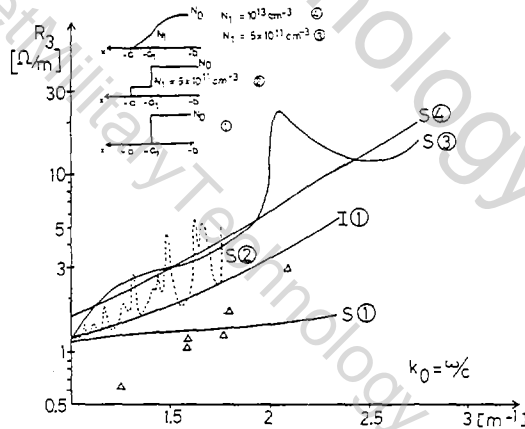


FIG.3. Specific resistance versus  $k_0$  for different plasma density profiles in the case of the wide TFR antenna ( $N_0 = 10^{14} \text{ cm}^{-3}$ ,  $a = 0.6 \text{ cm}$ ,  $a_1 = 3.5 \text{ cm}$ ,  $d = 2.8 \text{ cm}$ ,  $w_z = 15.75 \text{ cm}$ ,  $w_y = 11 \text{ cm}$ ,  $R_0 = 98 \text{ cm}$ ,  $r = 21.5 \text{ cm}$ ,  $\omega = 2\omega_{cD}$  for  $B_0 = 4T$  in  $D$  plasma,  $\beta = 1.88 k_0$ ). Fourier integral and series evaluations are indicated respectively by I and S. TFR experimental points [13] are shown ( $\Delta$ ).

#### 4. ANTENNA SPECIFIC RESISTANCE

The dependence of the antenna specific resistance:

$$R_3 = 2\text{Re}(P_A) / \int_0^{2w_y} |I(y)|^2 dy$$

on the frequency is shown in Fig.3 for the case of the TFR wide antenna [13]. Curves I1 and S1 were computed [8] for the step-density profile shown in the inset. Curve I1 is the result of a Fourier-integral analysis as described by Eq.(1). All the other curves in Fig.3 (labelled S) have been computed using Fourier series [8], thus correctly taking into account the toroidal and poloidal periodicity of the inner space of the torus. Curves I take into account the bulk plasma absorption and the TEM vacuum modes. Adding a low-density step to the model (curve S2), surface waves are introduced as an additional coupling mechanism leading to sharp resonances when the surface mode locus (curve  $\Pi_B$  or  $\text{III}_B$  of Fig.2(b)) crosses a sampling point of the  $k_y = n/r$ ,  $k_{||} = m/R_0$  lattice ( $n, m = 0, \pm 1, \pm 2, \dots$ ;  $r$  is the radius of the antenna and  $R_0$  is the tokamak major radius).

Curves S3 and S4 are computed for more realistic density profiles. The relative agreement between these curves and the Fourier integral result I1 shows

that, owing to the edge density gradient, all the energy is quickly fed into the plasma regardless of the particular coupling mechanism involved at the plasma edge. In marked contrast to S1, these three curves follow the overall behaviour of the experimental results even though precise numerical agreement is not achieved. With respect to this last point, it should be noted that, for accurate numerical comparison, the edge density should be better known. Also note that  $J(z) = \text{const.}$  has been assumed in the calculations. Recent studies [14] have shown that the shield blade discreteness and finite cross-section: (i) reduce coupling in a way that diminishes the disagreement with experiment; and (ii) cause a marked increase in Ohmic loss on shield blades. The lateral protection elements in Ref. [13] should produce an effect hybrid between (i) and (ii) and that of bump limiters [15]. The mismatch between the direction of the screen blades and that of the total magnetic field at the plasma edge can also play a role [16].

## 5. POWER DEPOSITION

When solving this power-coupling problem, one determines the amplitude of the magnetosonic wave excited in the plasma or, more simply, the antenna radiation pattern at the plasma edge. To compute the energy deposition profile inside the plasma, the real toroidal geometry and profiles must be taken into account; this is most easily done by computing geometric optics solutions of the wave equations by "ray-tracing" techniques. The conditions of validity of geometric optics expansions are easily satisfied in JET and reactor-size devices owing to the large size of the plasma and their high density and magnetic field. It has been shown [17] that appropriate initial conditions for starting the rays inside the plasma can be derived using the antenna radiation pattern computed from coupling models. The ray-tracing code takes fully into account the geometry, plasma species density and temperature profiles, the toroidal and poloidal magnetic fields, and the various damping mechanisms [17]. The energy-deposition profile is computed by summing over rays the power deposited in each annular region bounded by two flux surfaces. The transport of power flux along each ray is computed starting from its initial value derived from the antenna radiation pattern. When computing for a sufficiently large number of rays, a deposition profile is generated for each particle species.

Figures 4(a) and (b) show, for a JET-type case, the bunch of rays launched from a constant-phase surface drawn inside the plasma from the antenna radiation pattern. Twenty-one rays are launched from the low magnetic field side, seven each at the three poloidal angles  $\phi = 0, \pm 30^\circ$ . The toroidal spread of the bundle and the focussing in a poloidal cross-section should be noted. The present constant-phase surface was computed from a 2-D coupling model

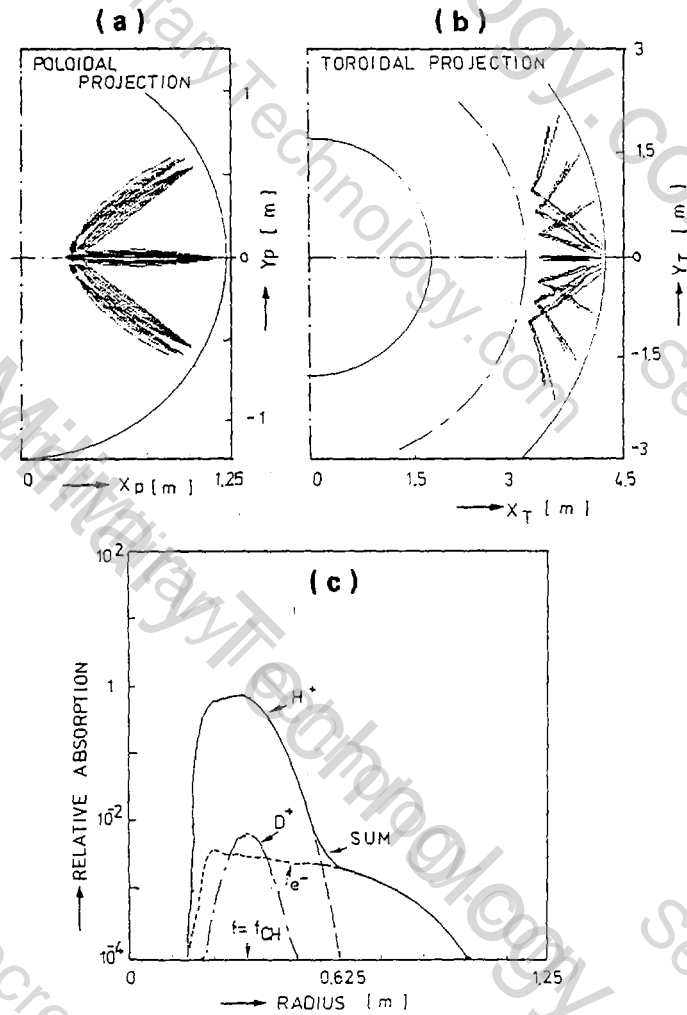


FIG.4. Ray-tracing results obtained for the following parameters:  $w_z = 0.15$  m,  $w_y = 0.73$  m,  $d = 0.1$  m,  $a = 0.05$  m, H-D plasma,  $N_H/N_D = 0.1$ ,  $B_0 = 34.5$  kG; practically flat density  $N_0 = 2.67 \times 10^{13}$  cm $^{-3}$ ,  $f = 47$  MHz,  $R_0 = 2.96$  m,  $r_0 = 1.25$  m, parabolic  $T_e = T_H = T_D = 1.7$  keV, parabolic current density profile with  $q = 3$  at the edge. (a) Poloidal projection of the rays. (b) Toroidal projection. (c) Relative power absorbed by different species as a function of radius.

assuming poloidal symmetry along the antenna. The rays primarily deposit energy in the minority species; this takes place at its cyclotron layer. The minority species subsequently transfers its energy to the electrons and majority ions. These electrons and ions receive a small fraction of the wave energy directly. The hollowness of the deposition profile shown results from the cyclotron layer falling off-centre in the minor cross-section for the parameters chosen.

#### REFERENCES

- [1] EQUIPE TFR, Plasma Physics and Controlled Nuclear Fusion Research 1980 (Proc. 8th Int. Conf. Brussels, 1980) Vol.2, IAEA, Vienna (1981) 75.
- [2] BHATNAGAR, V.P., et al., *ibid.*, p.85.
- [3] HOSEA, J., et al., *ibid.*, p.95.
- [4] KIMURA, H., et al., *ibid.*, p.105.
- [5] WEYNANTS, R.R., et al., Heating in Toroidal Plasmas (Proc. 2nd Joint Varenna-Grenoble Int. Symp. Como, 1980) Vol.1, CEC, Brussels (1980) 487.
- [6] RAMO, S., WHINNERY, J., VAN DUZER, T., Fields and Waves in Communication Electronics, Wiley, New York (1965).
- [7] BHATNAGAR, V.P., et al., Nucl. Fusion **22** (1982) 280.
- [8] MESSIAEN, A.M., et al., Heating in Toroidal Plasmas (Proc. 3rd Joint Varenna-Grenoble Int. Symp. Grenoble, 1982) Vol.1, CEC, Brussels (1982) 243.
- [9] SHVETS, O.M., et al., Sov. J. Plasma Phys. **7** (1981) 261.
- [10] ADAM, J., Assoc. Euratom-CEA, CEN de Fontenay-aux-Roses Rep. EUR-CEA-FC-1004 (1979).
- [11] MESSIAEN, A.M., MEYNAERT, R., WEYNANTS, R.R., Ecole royale militaire, Brussels Rep. LPP-ERM/KMS-76 (1981).
- [12] MESSIAEN, A.M., WEYNANTS, R.R., Heating in Toroidal Plasmas (Proc. 3rd Joint Varenna-Grenoble Int. Symp. Grenoble, 1982) Vol.3, CEC, Brussels (1982).
- [13] EQUIPE TFR, Assoc. Euratom-CEA, CEN de Fontenay-aux-Roses Rep. EUR-CEA-FC-1115 (1981).
- [14] FAULCONER, D.W., Heating in Toroidal Plasmas (Proc. 3rd Joint Varenna-Grenoble Int. Symp. Grenoble, 1982) Vol.1, CEC, Brussels (1982) 347.
- [15] BHATNAGAR, V.P., et al., *ibid.*, p.325.
- [16] EVRARD, M.P., WEYNANTS, R.R., *ibid.*, p.339.
- [17] BHATNAGAR, V.P., et al., *ibid.*, p.561.



## ICRF HEATING EXPERIMENT IN JFT-2

H. KIMURA, H. MATSUMOTO, K. ODAJIMA,  
 S. KONOSHIMA, T. YAMAMOTO, N. SUZUKI,  
 K. HOSHINO, Y. MIURA, T. MATSUDA,  
 H. TAKEUCHI, T. SUGIE, S. KASAI,  
 T. YAMAUCHI, H. KAWASHIMA, T. OGAWA,  
 T. KAWAKAMI, T. SHOJI, M. MORI, H. OGAWA,  
 Y. UESUGI, K. OHASA, S. YAMAMOTO,  
 M. MAENO, S. SENGOKU, H. NAKAMURA,  
 H. OHTSUKA, T. MATOBA, A. FUNAHASHI,  
 Y. TANAKA

Japan Atomic Energy Research Institute,  
 Tokai-mura, Naka-gun, Ibaraki-ken, Japan

### Abstract

#### ICRF HEATING EXPERIMENT IN JFT-2.

High-field-side excitation is investigated in detail in the JFT-2 ICRF heating experiment. For  $n_H/n_D \leq 10\%$ , the RF-power preferentially couples with the ions in the plasma core. Specifically, D-majority heating is dominant in the very dilute minority region ( $n_H/n_D = 2-4\%$ ). The non-Maxwellian high-energy tail of D, which indicates direct power absorption, is confirmed by the mass-discriminating charge exchange spectra. The power deposition profile is reasonably centrally peaked, which is confirmed by the  $B_T$  scan and also by an analysis of the temperature profiles. With  $P_{net} \approx 500$  kW, the central ion temperature increase from 0.4 keV to 0.7 keV, and the central electron temperature from 0.5 keV to 0.75 keV at  $\bar{n}_e \approx 5 \times 10^{13} \text{ cm}^{-3}$  and  $n_H/n_D = 2-4\%$ . — For the mode conversion regime ( $n_H/n_D \gtrsim 30\%$ ), the RF-power couples dominantly with electrons.  $B_T$  and  $n_H/n_D$  scans indicate that maximum  $\Delta T_e(0)$  is obtained when the two-ion hybrid resonance layer is shifted by about 7 cm off the vessel axis. This observation can be explained by the propagation characteristics of an ion Bernstein wave. Some ion heating mechanism exists even in this regime. It is found that the ion heating is sensitive to the amount of impurity ions such as Fe and Ti, suggesting that the ion heating may be due to harmonic cyclotron damping by impurities. — The origin of metal impurities during heating is investigated in the mode conversion regime. A strong correlation is confirmed between influx and fast ions localized in the scrape-off layer.

#### 1. INTRODUCTION

JFT-2 is a tokamak with major radius  $R_0 = 0.9$  m and minor radius  $a = 0.25$  m. The toroidal magnetic field is up to 15.5 kG and the plasma current is 160 kA at maximum. The RF generator is mainly operated at 18 MHz, which is the second-harmonic cyclotron frequency of deuterons with a toroidal field of 11.8 kG. We use a pair of one-quarter-turn all-metal antennas located on the high-field

side of the torus. A detailed description of the RF equipment is given in Refs [1–3]. The maximum RF-power including the circuit loss is 820 kW, and the net power to the plasma is 600 kW. The power densities on the antenna surface and in the power feedthrough reach 1.4 and 8.9 kW·cm<sup>2</sup>, respectively.

To obtain good heating results in the high-power experiment, control of the power deposition profile and the impurity influx during the heating is of paramount importance. It should be emphasized that an understanding of wave propagation and damping, including the antenna-plasma coupling, makes this control possible.

First, our principal efforts were concentrated on clarifying the heating mechanism of the pure high-field-side excitation in the two-ion plasma.

In a deuteron plasma with a minority proton component, from the high-field side, a two-ion hybrid resonance layer (HBR layer), a two-ion hybrid cut-off layer and a second-harmonic cyclotron resonance layer (CR layer) are formed, in this order. The fast wave excited from the higher-field side propagates to the HBR layer and is partly converted to an ion Bernstein wave and partly absorbed at the region of confluence with the ion Bernstein wave, which results in plasma heating. It is theoretically predicted that the extent of coupling with the ion Bernstein wave and the power partitioning among the species change mainly with the proton-to-deuteron density ratio,  $n_H/n_D$  [5, 6].

The heating experiments were performed over a wide range of plasma parameters, i.e.  $1 \times 10^{13} \lesssim \bar{n}_e \lesssim 6 \times 10^{13} \text{ cm}^{-3}$ ,  $2 \lesssim n_H/n_D \lesssim 70\%$ , and  $8 \lesssim B_T \lesssim 15.5 \text{ kG}$ . In Sections 2 and 3, the heating results are described, with special emphasis placed on the power deposition profile for the ion heating regime ( $n_H/n_D \lesssim 10\%$ ) and the mode conversion regime ( $n_H/n_D \gtrsim 30\%$ ), respectively.

Secondly, we have investigated the impurity problem associated with ICRF heating. Recently, we have changed the materials of the limiter (from stainless steel to carbon) and Faraday shield (from molybdenum to TiC) [7]. As a result, metal impurities such as Fe, Ti, Mo are substantially reduced in both the Joule and the RF-heating phases. The reduction is most remarkable for iron, which is reduced to 20–30% of the previous level. Although carbon increases by a factor of two, the total radiation loss remains at 50–100% of the previous value. Thus, the effectiveness of low-Z materials for limiter and Faraday shield has been confirmed for impurity influx control in ICRF heating [4].

In Section 4, the origin of the impurity influx is discussed in the mode conversion regime.

## 2. ION HEATING REGIME ( $n_H/n_D \lesssim 10\%$ )

The most prominent feature in this regime is the change of power partitioning among deuterium and hydrogen as a function of  $n_H/n_D$ .

From the relatively low electron density and the low power used in the experiment ( $\bar{n}_e \lesssim 3 \times 10^{13} \text{ cm}^{-3}$ ,  $P_{\text{net}} \approx 100 \text{ kW}$ ), we have obtained the following results [8]:

- (i) In the very-dilute minority region ( $n_{\text{H}}/n_{\text{D}} = 2\text{--}4\%$ ), second-harmonic deuteron heating is dominant. A prominent proton high-energy tail also appears, but the RF-power coupled to the protons is much lower than that coupled to the deuterons, according to a power balance analysis and a Fokker-Planck calculation [9].
- (ii) The RF-power transferred to the protons increases with increasing  $n_{\text{H}}/n_{\text{D}}$  and has a maximum at  $n_{\text{H}}/n_{\text{D}} \sim 10\%$ . At least half of the RF-power goes to the proton component at  $n_{\text{H}}/n_{\text{D}} \sim 10\%$ .

In fact, for  $n_{\text{H}}/n_{\text{D}} = 2\text{--}4\%$ , the deuterium high-energy tail became detectable with decreasing electron density and increasing power, indicating that deuteron second-harmonic heating actually occurs in this case. Understanding of these experimental results needs full wave treatment [5].

The RF-power is absorbed by the ions between the HBR layer and the CR layer in this regime. A scan of the toroidal field indicates that the increase in ion temperature is sharply peaked when the HBR and CR layers are near the axis. This observation is an indirect evidence for the fact that the RF-power is deposited in the ions in the narrow region between the two layers.

Figure 1 shows temperature profiles of ions and electrons for  $n_{\text{H}}/n_{\text{D}} = 2\text{--}4\%$ . The line average electron density and the RF net power are  $\bar{n}_e \approx 5 \times 10^{13} \text{ cm}^{-3}$  and  $P_{\text{net}} \approx 500 \text{ kW}$ , respectively. A significant increase in the ion and electron temperatures was observed in the entire plasma region. The ion and electron temperatures in the centre are almost identical. These data were obtained before the limiter and antenna materials were changed. The radiation loss in this case is five times as large as that of the Joule heating phase although, at least in the plasma core, the radiation loss does not fatally affect the energy balance.

A 1-D tokamak code was employed to analyse the experimental electron and ion temperature profiles by assuming the ion and electron heat conduction coefficients, to be once the neoclassical value and  $2 \times 10^{19} (1/n_e) (\text{m}^{-1}\cdot\text{s}^{-1})$ , respectively. From this analysis, it was made clear that 60% of the power goes into ions with an 8-cm-wide power deposition profile, with an almost negligible power deposition to the electrons in the plasma core.

Thus, the existence of a centrally peaked deposition profile is again confirmed by the temperature profile.

### 3. MODE CONVERSION REGIME ( $n_{\text{H}}/n_{\text{D}} \gtrsim 30\%$ )

In this region, mode conversion is a dominant heating process. To obtain information on the power deposition profile, we investigated the  $B_{\text{T}}$ -dependence

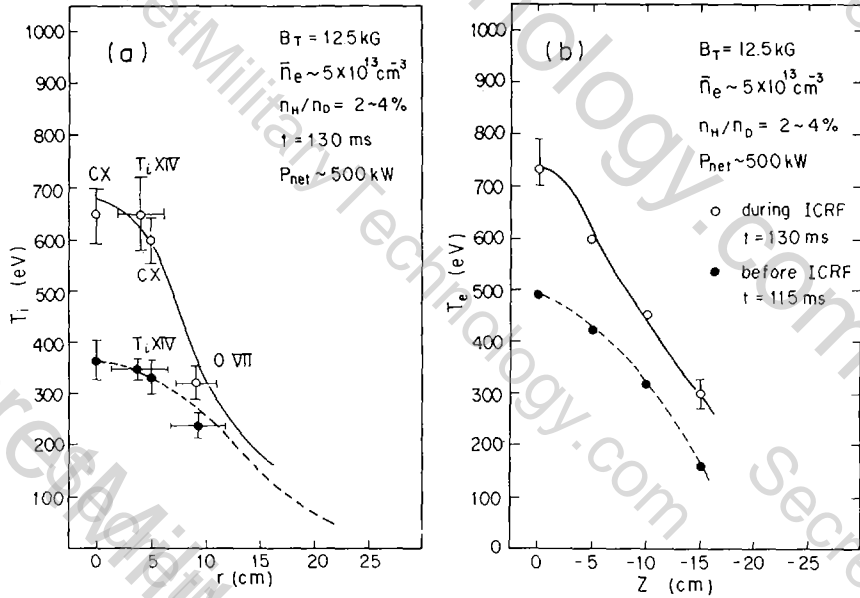


FIG.1. Temperature profiles of (a) ions and (b) electrons during and before ICRF heating for the ion heating regime;  $P_{\text{net}} \approx 500 \text{ kW}$ ,  $\bar{n}_e \approx 5 \times 10^{13} \text{ cm}^{-3}$ ,  $n_H/n_D = 2-4\%$ .  $B_T = 12.5 \text{ kG}$ ,  $I_p = 140 \text{ kA}$ . The ion temperature profile was measured by mass-discriminating charge-exchange analyser and impurity Doppler broadening. The electron temperature profile was measured by laser scattering.

of the heating, keeping  $n_H/n_D \approx 30\%$ .  $B_T$  was scanned from 12 kG to 15.5 kG, which corresponds to  $0 \leq (R_{\text{CR}} - R_0)/a \leq 1.13$ , where  $R_{\text{CR}}$  is the major-radius position of the CR layer.

Figure 2 shows the increase in the central electron and ion temperatures, normalized by the net power, as a function of  $B_T$ . It is found that both electron and ion temperatures have their maxima at  $B_T = 15 \text{ kG}$ . The major-radius position of the HBR layer,  $R_{\text{HB}}$  is 97 cm at 15 kG. In contrast to the ion heating regime, the maximum increase in the temperature is obtained when the HBR layer is shifted by a certain length off the vessel axis.

The reason for this shift can be explained by the propagation characteristics of the converted ion Bernstein wave. Figure 3 shows the ray trajectory [10] in the poloidal cross-section for  $B_T = 15 \text{ kG}$  and  $n_H/n_D = 30\%$  together with the HBR layer (A), the two-ion cut-off layer (B), the fast-wave cut-off layer (C), and the CR layer (D). The fast wave propagating from the high-field side is converted to the ion Bernstein wave near the HBR layer and is then heavily damped through electron Landau damping in the plasma core away from the HBR layer. The power deposition profile is calculated by summing up the absorbed power of many rays emanating from the antenna. Figure 3b shows

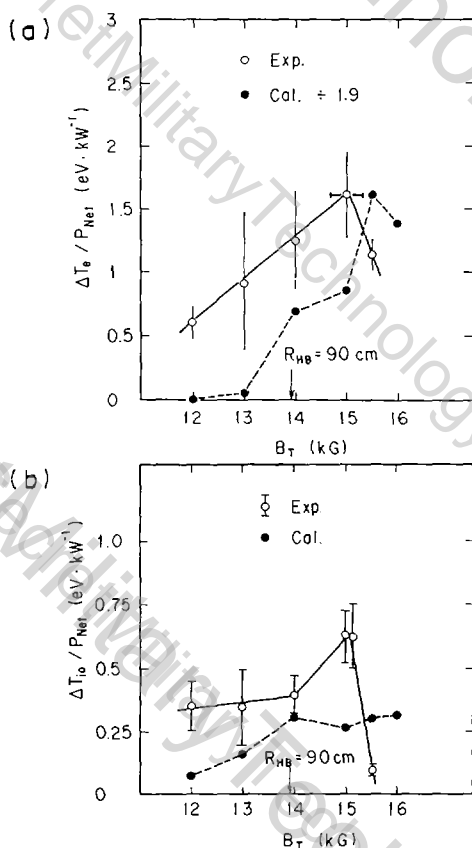


FIG.2. Increase in (a) central electron and (b) central ion temperatures, normalized by net RF-power as a function of toroidal field for mode conversion regime;  $\circ$  denotes experimental data;  $P_{net} \approx 200$  kW,  $\bar{n}_e \approx 3 \times 10^{13}$  cm<sup>-3</sup>,  $n_H/n_D \approx 30\%$ ,  $I_p = 130$  kA. Calculation results from 1-D tokamak code and ray-tracing analysis are shown by  $\bullet$ . The toroidal field placing the two-ion hybrid resonance layer on axis is about 14 kG.

the power deposition profile obtained in this way. Almost all power goes into the electrons in the plasma core. The closed circles in Fig.2a, b are results calculated by the 1-D tokamak code, using the power deposition profile based on the ray-tracing analysis. The shift of the  $\Delta T_e$  peak is qualitatively explained by this analysis although the calculated  $B_T$ -dependence of  $\Delta T_e$  is much more sensitive than the experimental results.

Similar experimental results were obtained in changing  $n_H/n_D$  from 30 to 70% at  $B_T = 15$  kG, which corresponds to scanning the HBR layer from 97 to 86 cm. The electron temperature shows a maximum at  $n_H/n_D = 30\%$  and decreases monotonically with increasing  $n_H/n_D$ . This behaviour is also consistent with the calculation.

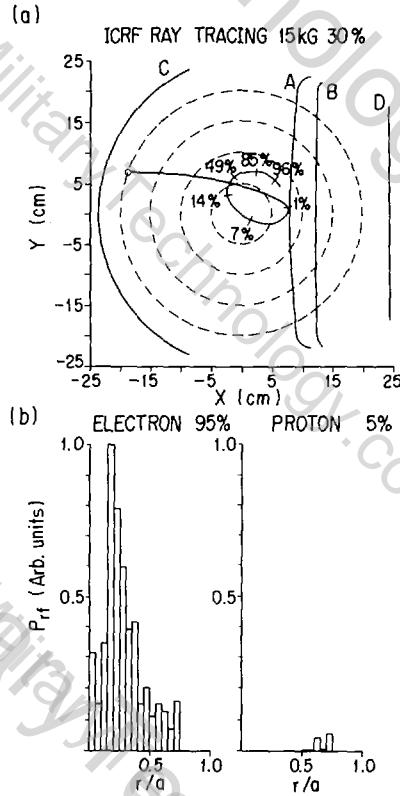


FIG.3. (a) Ray trajectory from the high-field side. A, B, C, and D indicate two-ion hybrid resonance layer, two-ion cut-off layer, fast-wave cut-off layer, and second-harmonic cyclotron resonance layer, respectively. Calculation parameters are  $T_e = 600$  eV,  $T_i = 350$  eV,  $\bar{n}_e = 3 \times 10^{13} \text{ cm}^{-3}$ ,  $n_H/n_D = 30\%$ ,  $q_a = 4$ ,  $B_T = 15$  kG,  $k_z = 5 \text{ m}^{-1}$ . Fraction of absorbed power is indicated along the ray path; (b) calculated radial power deposition profile for electrons (left) and protons (right).

As is shown in Fig.2b, the significant increase in the ion temperature at  $B_T = 15$  kG cannot be explained by power transfer from electrons to ions. Some ion heating mechanism must exist.

Spatial profiles of the electron and ion temperatures are given in Fig.4. The solid and broken curves in this figure are calculations by the 1-D tokamak code and the ray-tracing analysis. The thermal-conduction coefficients are the same as those described in Section 2. Fairly good agreement between experiment and calculation is obtained.

To match the ion temperatures in experiment and calculation, it is sufficient that 20% of the power directly goes to the ions.

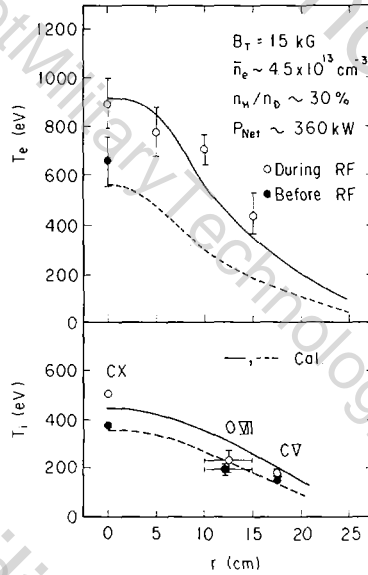


FIG.4. Temperature profiles of electrons (upper) and ions (lower) during and before ICRF heating for mode conversion regime;  $P_{\text{net}} \approx 360 \text{ kW}$ ,  $\bar{n}_e \approx 4.5 \times 10^{13} \text{ cm}^{-3}$ ,  $n_{\text{H}}/n_{\text{D}} \approx 30\%$ ,  $B_{\text{T}} = 15 \text{ kG}$ ,  $I_{\text{p}} = 140 \text{ kA}$ . Solid and broken curves are results of numerical simulation by 1-D tokamak code and ray-tracing analysis.

This result is very different from the previous result [1, 2], where much more significant ion heating was observed, in spite of identical heating conditions. The power partitioning among the ions and electrons was about 1:1, in the former case.

The main difference in the plasma conditions of the two cases is the amount of impurities due to the change in limiter and Faraday shield materials (see Section 1). In the present experiment, metal impurities such as Fe and Ti have been reduced to 30 and 50%, respectively, with respect to the previous case. It is likely that harmonic cyclotron resonance of impurities plays a role in ion heating [9]. It should be noted that if we consider the  $2\omega_{\text{ci}}$  resonance of Fe and Ti, a substantial amount of  $\text{Fe}^{22+}$  and  $\text{Ti}^{19+}$  (say, 0.1% of the electron density) must exist. This is not realistic for JFT-2 plasma parameters. One of the remaining possibilities is the  $3\omega_{\text{ci}}$  resonance of impurities. The corresponding charge states are  $\text{Fe}^{15+}$ – $\text{Fe}^{16+}$  and  $\text{Ti}^{13+}$ – $\text{Ti}^{14+}$ . A quantitative investigation is underway.

#### 4. ORIGIN OF IMPURITIES DURING HEATING

The origin of impurity production was examined in the mode conversion regime ( $n_{\text{H}}/n_{\text{D}} = 30\%$ ), where no energetic minority species tail is observed in

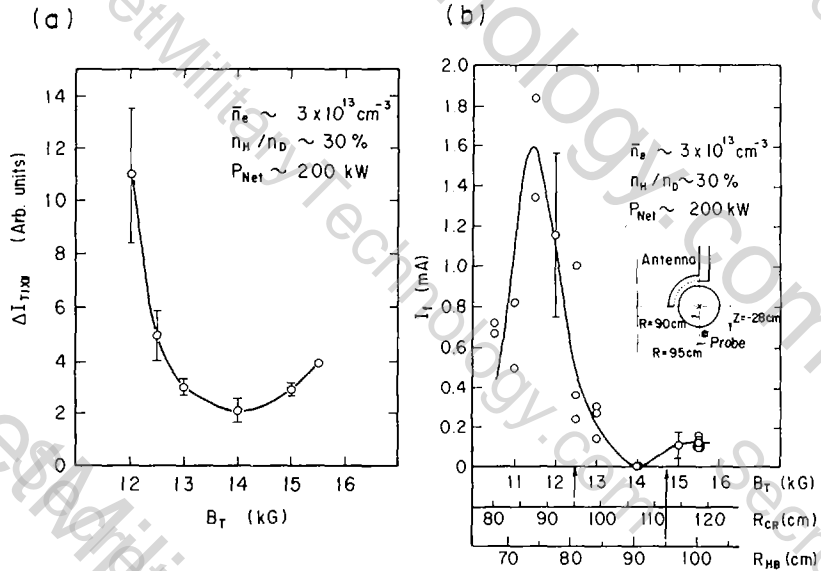


FIG. 5. (a) Increase of spectral line intensity of Ti XII as a function of toroidal field in the mode conversion regime. Experimental parameters are the same as those of Fig. 2. (b) Corresponding data of fast ions measured by ion-sensitive probe located in scrape-off layer. The probe position, which is set on the ion toroidal-drift side, is  $R = 95$  cm and  $Z = -28$  cm. Horizontal axis indicates corresponding positions of cyclotron resonance layer  $R_{CR}$  and two-ion hybrid resonance layer  $R_{HB}$ .

the plasma core. Figure 5a shows the  $B_T$ -dependence of the spectral-line intensity increase of Ti XII. The discharge conditions are the same as those of Fig. 2a, b. Titanium increases remarkably with decreasing  $B_T$ . Other impurity lines such as O VI, C IV, Fe XV, and Mo XIII as well as the total radiation loss measured bolometrically show similar behaviour. From measurements of the mass-discriminating charge-exchange analyser viewing the horizontal chord in the equatorial plane, the energy spectra of the majority and minority species were found to be almost in accord; no high-energy tail was observed. As was described in Section 3, the central ion temperature has a maximum at  $B_T = 15$  kG. Therefore, the impurity production is not correlated with the energetic ions in the plasma core.

At the same time, we observed the fast-ion flux ( $I_f$ ) in the scrape-off layer by using an ion-sensitive probe, which can extract ions with energy higher than about 1 keV. The probe was located at  $R = 95$  cm and could be scanned vertically. Figure 5b shows the  $B_T$ -dependence of  $I_f$ . The probe was set on the

ion toroidal-drift side. It is worth while noting that there is a strong correlation between  $I_f$  and the Ti XII line intensity.

The maximum of  $I_f$  was obtained at  $B_T = 11.5$  kG. However, at this toroidal field, the R-position of the probe agrees neither with that of the CR layer nor that of the HBR layer. It may rather be assumed that the probe signal increases rapidly when the toroidal field becomes lower than the value where the CR layer begins to cross the antenna ( $B_T \leq 12$  kG).

When the direction of  $B_T$  was reversed at  $B_T = 12$  kG,  $I_f$  was still detected although the signal level was reduced to 20%. From this, we should suppose that the fast ions are localized in the scrape-off layer. In fact, it was confirmed that the probe signal had a peak value at  $|Z| = 27-29$  cm, by scanning the probe in the Z-direction.

On the other hand,  $I_f$  at  $B_T = 15$  kG disappeared completely when  $B_T$  was reversed. In this region,  $I_f$  may be interpreted as being due to the orbit loss ions from the plasma core. The maximum Ti(0) was obtained at  $B_T = 15$  kG.

It may be concluded that the significant increase in impurities when  $B_T$  is lowered is strongly correlated with fast ions localized in the plasma periphery. Considering the  $B_T$ -dependence and the electron density in the production region of the fast ions ( $n_e = 5 \times 10^{10} - 2 \times 10^{11} \text{ cm}^{-3}$ ), coupling to the slow wave may be a possible explanation of these observations.

## 5. CONCLUSIONS

In the JFT-2 ICRF heating experiment, pure high-field-side excitation was investigated with D-H plasma. It was demonstrated that power partitioning among the species changes with  $n_H/n_D$ , i.e. D-majority heating ( $n_H/n_D = 2-4\%$ )  $\rightarrow$  H-minority heating ( $n_H/n_D \approx 10\%$ )  $\rightarrow$  electron heating ( $n_H/n_D \gtrsim 30\%$ ). For each heating regime, the power deposition profiles are reasonably centrally peaked, and a similar heating rate  $(\Delta T_{e0} + \Delta T_{i0}) \times \bar{n}_e / P_{\text{net}} = (5-7) \times 10^{13} \text{ eV} \cdot \text{cm}^{-3} \cdot \text{kW}^{-1}$  has been obtained for  $3 \times 10^{13} \leq \bar{n}_e \leq 5 \times 10^{13} \text{ cm}^{-3}$  and  $P_{\text{net}}$  up to 500 kW.

Specifically, in the mode conversion regime, the highest  $\Delta T_e(0)$  is obtained by placing the two-ion hybrid resonance layer about 7 cm off the axis. The result is consistent with the propagation of the converted ion Bernstein wave. Some ion heating mechanism still exists in this regime. It becomes evident that the ion heating is sensitive to the amount of impurity ions such as Fe and Ti.

A strong correlation is confirmed between impurity influx and the fast ions localized in the scrape-off layer. Coupling to the slow wave may be a possible explanation for the production of such fast ions. On the basis of this result, it should be emphasized that further investigation of the physics of antenna-plasma coupling is required in order to minimize the impurity influx and to maximize the heating power going into the plasma core.

## ACKNOWLEDGEMENTS

The authors are grateful to the members of the JFT-2 and NBI operation groups for their excellent work and efficient support. They are also indebted to Drs S. Mori, Y. Iso, Y. Obata, and M. Tanaka for continuous encouragement.

## REFERENCES

- [1] KIMURA, H., MATSUMOTO, H., ODAJIMA, K., KONOSHIMA, S., SUZUKI, N., et al., Experimental Results on ICRF Heating in JFT-2, Japan Atomic Energy Research Institute Rep. JAERI-M 82-046 (1982).
- [2] JFT-2 GROUP, ICRF Heating Experiment in JFT-2, in Heating in Toroidal Plasmas (Proc. 3rd Joint Varenna-Grenoble Int. Symp. Grenoble, 1982).
- [3] JFT-2 GROUP, Technical and Design Aspect of JFT-2 ICRF Heating, *ibid.*
- [4] JFT-2 GROUP, Impurities During ICRF Heating Experiment in JFT-2, *ibid.*
- [5] COLESTOCK, P., DAVIS, S., et al., in Heating in Toroidal Plasmas (Proc. 2nd Joint Varenna-Grenoble Int. Sym. Como, 1980) Vol.1 (1981).
- [6] SWANSON, D., Nucl. Fusion **20** (1980) 949.
- [7] NAKAMURA, H., SENGOKU, S., et al., TiC/Mo Faraday Shield and Carbon Limiter for Reduction of Metal Impurities in JFT-2 ICRF Plasmas, to be published in Japan Atomic Energy Research Institute Rep. JAERI-M.
- [8] JFT-2-GROUP, in Controlled Fusion and Plasma Physics (Proc. 10th Europ. Conf. Moscow, 1981) Vol.2 (1981).
- [9] STIX, T., Nucl. Fusion **15** (1975) 737.
- [10] McVEY, B., Nucl. Fusion **19** (1979) 461.
- [11] TFR GROUP, in Heating in Toroidal Plasmas (Proc. 3rd Joint Varenna-Grenoble Int. Symp. Grenoble, 1982).

## DISCUSSION

R. GOLDSTON: You compared recent with older data and showed that the latter reflected both higher metallic impurity radiation and more efficient ion heating. What fraction of the central input power was radiated by impurities in the two cases?

H. KIMURA: We believe that the efficient ion heating in the older case was due to the harmonic resonance of impurity ions (Fe). Quantitative estimation of radiation losses by Fe is difficult to perform experimentally. From the point of view of power balance in the plasma core, the radiation loss does not play a dominant role in either case.

D. HWANG: How is the transport study done with second-harmonic D-heating when the charge-exchange spectrum is non-Maxwellian, and how is the power deposition profile obtained in this case?

H. KIMURA: In the high-density case, the energy spectrum of D was found to be almost Maxwellian, even in the dilute minority case. We deduced the power deposition profile from the experimental temperature profiles, assuming  $\chi_i = 1 \times \chi_{\text{neoclassical}}$  and  $\chi_e = 2 \times 10^{19} (1/n_e) (\text{m}^{-2}\cdot\text{s}^{-1})$ . In the low-density case, the energy spectrum of D is non-Maxwellian, and we use an effective temperature derived from the average energy.

R.R. WEYNANTS: Have you checked whether such deuterium heating results as you report in your low-density experiment can also be predicted theoretically?

H. KIMURA: No, we have not done the full wave calculation yet.



## INVESTIGATION OF ELECTRON CYCLOTRON HEATING IN THE FT-1 TOKAMAK OVER A WIDE RANGE OF PLASMA DENSITIES

Yu.F. BARANOV, N.E. BOGDANOVA, D.G. BULYGINSKIJ,  
 V.K. GUSEV, M.M. LARIONOV, L.S. LEVIN,  
 G.T. RAZDOBARIN, V.I. FEDOROV  
 A.F. Ioffe Physicotechnical Institute of the USSR  
 Academy of Sciences,  
 Leningrad, Union of Soviet Socialist Republics

*Presented by V.S. Strelkov*

### Abstract

#### INVESTIGATION OF ELECTRON CYCLOTRON HEATING IN THE FT-1 TOKAMAK OVER A WIDE RANGE OF PLASMA DENSITIES.

By using an extraordinary wave fed into a tokamak from the high-magnetic-field side, electron cyclotron heating (ECH) can be performed at increased plasma densities. This is important in applying ECH to controlled thermonuclear fusion. This method of injecting power is studied on the FT-1 tokamak, and a numerical simulation of the experiment is carried out. The distributions of the absorbed ECH power over the discharge cross-section are found for different plasma densities, and the corresponding variations in electron temperature and other discharge parameter profiles, under the action of ECH, are calculated with a transport code. In the experiment, a study of ECH is made with a 60-kW, 30-GHz gyrotron, in the presence of Ohmic-heating power of the same value. The electron temperature profiles are measured by laser scattering at central discharge densities exceeding the critical density for the ECH frequency by factors of 1 to 2.4. In all cases, the electron energy is increased by 30–35%, and the loop voltage is reduced. On increasing the density, the heating zone is displaced towards the plasma edge. Comparison of experiment with numerical simulation shows that an observed decrease in the energy confinement time with ECH, relative to that for Ohmic heating, could be explained by the displacement of the heating zone towards the plasma edge. However, it is not possible to exclude the possibility of there also being an increase in the electron thermal conductivity during the application of ECH.

Electron cyclotron heating (ECH) by a wave with ordinary polarization, fed into a plasma from the outer side of the torus, is considered to be a promising method of auxiliary heating for thermonuclear reactors based on the tokamak principle. Its use is, however, limited by the propagation conditions for a wave of this type. For the cyclotron resonance zone to be accessible to the radiation, the following conditions must be satisfied:  $\omega = \omega_{ce}$ ;  $\omega_p/\omega_{ce} < 1$ . Here,  $\omega$  is the frequency at which heating takes place and  $\omega_p$  and  $\omega_{ce}$  are,

respectively, the plasma and cyclotron frequencies. As the ratio  $\omega_p/\omega_{ce}$  approaches unity, the wave becomes more strongly refracted, it then being difficult to localize the heating near the discharge axis. Tokamak reactor design involves operation at high plasma densities. The average density for the INTOR project is  $\bar{n} = 1.4 \times 10^{14} \text{ cm}^{-3}$ , with  $\bar{\beta} = 5.6\%$  at  $B_0 = 5.5 \text{ T}$ . In this case,  $\omega_p/\omega_{ce} \geq 0.8$  is required near the discharge axis. It is difficult to utilize the ordinary wave for ECH under these conditions. Introducing power in the extraordinary wave from the inner side of the torus enables this limiting density to be increased by a factor of two, since for  $\omega = \omega_{ce}$  this mode propagates in a plasma with  $(\omega_p/\omega_{ce})^2 < 2$ . This fact, and also the possibility of heating by using linear conversion into a plasma wave, at the upper hybrid resonance, makes the use of the extraordinary wave very attractive [1–3]. The application of this type of heating to large tokamaks was considered in Ref. [4].

Electron cyclotron heating has been carried out on the FT-1 tokamak, the power being fed in from the inside and the main attention being given to heating a dense plasma with  $\omega_p/\omega_{ce} > 1$ . The tokamak ( $R = 62 \text{ cm}$ ,  $a = 15 \text{ cm}$ ,  $B_0 \leq 1.2 \text{ T}$ ) was equipped with a 30-GHz gyrotron microwave oscillator, operating at an output power of 60 kW with a pulse duration of 2 ms. The Ohmic-heating power was 55–75 kW. The design of the microwave input coupling and the details of the experiment were described in Refs [5,6]. A wave, polarized in a direction perpendicular to the magnetic field, was excited with a waveguide antenna on the inner side of the toroidal discharge vessel and entered the plasma at an angle of  $42^\circ$  to the direction of the magnetic field. The polar diagram of the antenna was broad in a direction perpendicular to the discharge axis and did not focus the energy into the central plasma region. The wave was partially absorbed in passing through the electron cyclotron resonance zone, and was then converted into a plasma wave at the upper hybrid resonance surface.

A numerical simulation of the experiment was carried out. The distribution of the auxiliary heating power over the discharge cross-section was calculated by using the ray trajectory method, taking the directional properties of the antenna into account. The code included reflection from the walls of the discharge vessel, depolarization on reflection, cyclotron absorption, and conversion into a plasma wave with subsequent absorption. The temperature and density profiles corresponded to those observed with Ohmic heating. The calculations showed linear conversion to be the principal absorption mechanism under the conditions of our experiment. The contribution from direct cyclotron absorption was small, since the majority of the ray trajectories intersected the electron cyclotron resonance zone in cold plasma near the edge. On raising the density, it became important to take multiple reflections into account. Figure 1 shows the radial distributions of the absorbed ECH power, averaged over the magnetic surfaces. The dimensionless plasma density,  $n(0)/n_c$ , was

used as a parameter, where  $n_c$  is the critical density for which  $\omega_p = \omega$ . When  $n(0)/n_c = 1$ , the power is absorbed relatively uniformly in a broad central region. As the density is increased, the absorption becomes concentrated in a layer near  $r/a = 0.7$ .

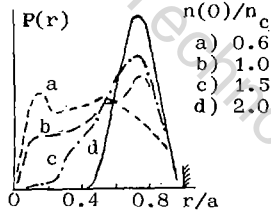


FIG. 1. Radial distribution of absorbed ECH power, averaged over magnetic surfaces.

The electron temperature profiles,  $T_e(r)$ , with auxiliary electron heating, were also simulated. The transport code took into account Ohmic and auxiliary heating, the electron thermal conductivity and the radiation losses. It was assumed that the density profile  $n(r)$  remained constant during the heating process. The magnitude and radial dependences of the thermal conductivity  $\kappa(r)$  and radiation losses  $P_{\text{rad}}$  were chosen such that the calculated temperature profile coincided with the experimental one in the case of pure Ohmic heating. Two models were taken:

- (1)  $\kappa(r) = \kappa_0 (1 + 4r^2/a^2)$ ,  $\kappa_0 = 3.3 \times 10^{17} \text{ cm}^{-1} \cdot \text{s}^{-1}$ ,  $P_{\text{rad}} = 0$ ;
- (2)  $\kappa(r) = \text{const} = 4.0 \times 10^{17} \text{ cm}^{-1} \cdot \text{s}^{-1}$ ,  $P_{\text{rad}} = 0.9 P_j^*$ ;

where  $P_j^*$  is the Ohmic power in the absence of auxiliary heating.

The temperature profiles for various auxiliary heating distributions over the discharge cross-section,  $P(r)$ , were calculated on the assumption that  $\kappa(r)$  and  $P_{\text{rad}}$  did not change in the presence of auxiliary heating.

Figure 2 shows the steady-state temperature profiles for an auxiliary heating power  $P_h = P_j^*$ , absorbed near the discharge axis in zones of different radius:  $r_h/a = 0.2, 0.4, 0.6$  and  $0.8$ . The dashed curve indicates the temperature profile with Ohmic heating alone. The calculation was performed by using model (1). In Figs 3 and 4 are shown the steady-state temperature profiles with the same heating power being absorbed in concentric annular zones of width  $\Delta/a = 0.2$ , having their midpoints located at distances  $r_h/a = 0, 0.2, 0.4, 0.6$  and  $0.8$  from the discharge axis. An absorbed radial power distribution of this form can be expected with ECH in a high-density plasma,  $n(0) > n_c$ , and also in experiments on heating with lower hybrid waves. The profiles in Fig.3

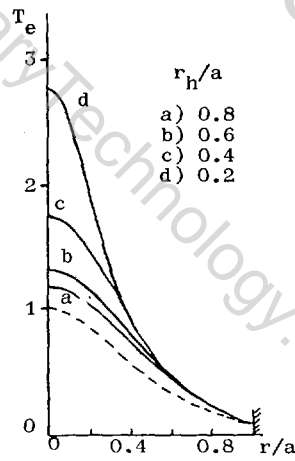


FIG.2. Steady-state temperature profiles for  $P_h = P_j^*$ .

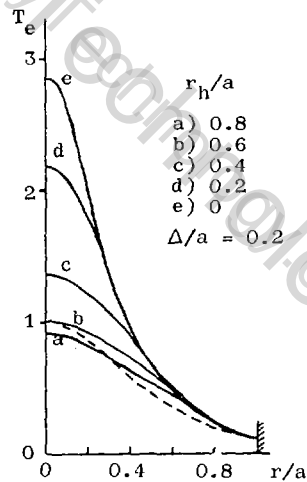


FIG.3. Steady-state temperature profiles with the same heating power absorbed in concentric annular zones of width  $\Delta/a = 0.2$  (model (1)).

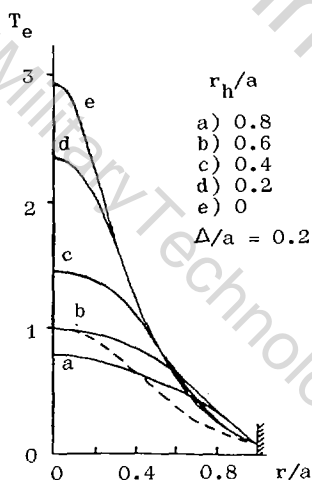


FIG.4. Same as Fig.3, but using model (2).

were calculated using model (1), while those in Fig.4 used model (2). The difference between them is slight.

Figure 5 shows the dependences of the integrated discharge characteristics on the radius of the heating zone: the energy  $W$  of the electron component, the loop voltage  $U_L$  and the electron energy confinement time  $\tau_e = W/(P_h + P_j)$  (normalized to their values with Ohmic heating), as calculated from the temperature profiles in Fig.2. The density profile coincided with the experimental one. Figure 6 gives the same dependences, calculated from the temperature profiles in Fig.3 (full curves) and in Fig.4 (dashed curves). The following conclusions can be drawn from an analysis of the numerical simulation results:

- (1) The temperature on the axis of the discharge is a strong function of the radius of the heating zone. Decreasing the latter increases  $T_e(0)$  but leads to a narrowing of the temperature and current profiles, and this can influence the MHD stability of the discharge.
- (2) Edge heating,  $r_h/a = 0.6-0.8$ , can lead to a lowering of  $T_e(0)$  relative to that for Ohmic heating, because of a redistribution of the current density over the cross-section. Edge heating can be useful for forming the optimum current profile.
- (3) Auxiliary heating with  $r_h/a = 0.4$  creates a temperature profile similar to that from Ohmic heating.
- (4) Variations in the electron energy and in the loop voltage are coupled by an expression which is only weakly dependent on the changes in the shape of the  $T_e(r)$  profile with auxiliary heating [6]:  $W/W_j \approx (U_L/U_{Lj})^{-2/3}$ . This expression is valid if  $n(r)$  and the effective ionic charge number remain constant during the heating.

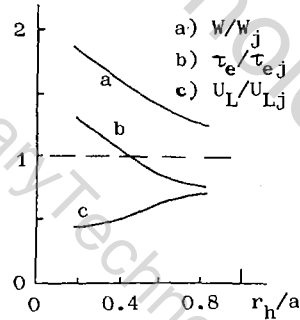


FIG. 5.  $W/W_j$ ,  $\tau_e/\tau_{ej}$  and  $U_L/U_{Lj}$  versus heating zone radius.

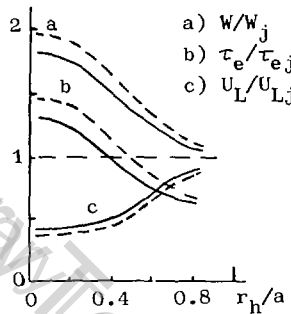


FIG. 6. Same as Fig. 5, calculated from temperature profiles in Fig. 3 (full curves) and in Fig. 4 (dashed curves).

(5) The energy confinement time with auxiliary heating can increase or decrease relative to that with Ohmic heating, depending on the position of the energy absorption zone. The influence on  $\tau_e$  of localizing the heating, along with a possible change in the electron thermal conductivity during heating, must be included in an analysis of the experimental results.

The study of ECH in the FT-1 tokamak was carried out in discharge regimes with a current of 28 kA and magnetic fields of 1.06 T (electron cyclotron resonance zone at the centre) and 0.97 T (electron cyclotron resonance zone displaced inwards by 5 cm). A 2-ms heating pulse was applied during the steady-state part of the discharge. At the end of this pulse, the profiles  $T_e(r)$  and  $n(r)$  were determined by laser scattering. At the same moment, measurements were made with pure Ohmic heating. The average plasma density varied over a wide range, from  $0.4 \times 10^{13}$  to  $1.6 \times 10^{13} \text{ cm}^{-3}$ . From the laser scattering data,

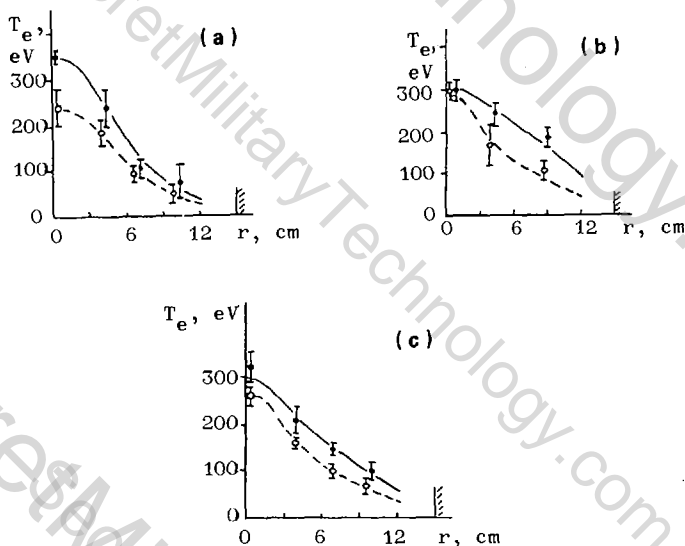


FIG. 7.  $T_e(r)$  profiles:

- (a)  $\bar{n}_e = 0.53 \times 10^{13} \text{ cm}^{-3}$ ,  $W_j = 33.5 \text{ J}$ ,  $W = 45 \text{ J}$ ; (b)  $\bar{n}_e = 1.05 \times 10^{13} \text{ cm}^{-3}$ ,  $W_j = 52 \text{ J}$ ,  $W = 70 \text{ J}$ ; (c)  $\bar{n}_e = 1.40 \times 10^{13} \text{ cm}^{-3}$ ,  $W_j = 67 \text{ J}$ ,  $W = 87 \text{ J}$ .

the average density was 0.55–0.6 of the maximum value. Thus, the central discharge density  $n(0)$  varied from  $0.7n_c$  to  $2.5n_c$ , where  $n_c$  is the critical density for the gyrotron frequency. A reduction in the loop voltage and a diamagnetic effect were observed during ECH in all operating regimes. The diamagnetic measurements, and also the behaviour of the soft-X-ray and microwave emission during ECH, were described in Refs [5, 6]. The average density during the heating pulse, as determined with a microwave interferometer, decreased only very slightly ( $\delta\bar{n} \leq 0.5 \times 10^{12} \text{ cm}^{-3}$  over 2 ms). The loop voltage decreased from 1.8–2.4 V with Ohmic heating to 1.2–1.8 V with ECH. The value of  $U_L/U_{Lj} = 0.7$ –0.75 was almost constant over the whole density range studied. The characteristic time scale for variations in  $U_L$  was of the order of 1 ms, which corresponds to the electron energy confinement time with Ohmic heating. Laser scattering measurements of  $T_e(r)$  and  $n(r)$  were made for  $n(0)/n_c = 1, 1.8$  and  $2.4$ . The results yielded the electron energies with Ohmic heating,  $W_j$ , and with ECH,  $W$ . The  $T_e(r)$  profiles and the values of  $W_j$  and  $W$  are given in Figs 7a to c. At low density,  $n(0) = n_c$ , the central temperature increased by a factor of 1.4 during ECH. The profile shape showed little change, the electron energy rising by a factor of 1.35 (Fig. 7a). For  $n(0)/n_c = 1.8$  and  $2.4$ , there was little change in the temperature on the discharge axis, although it showed a marked increase at the remaining points in the profile, which was consequently broadened. The electron energy increased

TABLE I. VARIOUS PLASMA PARAMETERS

$\bar{n}$ ( $\text{cm}^{-3}$ )	$0.55 \times 10^{13}$	$1.05 \times 10^{13}$	$1.4 \times 10^{13}$
$n(0)/n_c$	1	1.8	2.4
$\tau_{ej}$ (ms)	0.67	0.90	1.05
$\tau_e(\text{ECH})$ (ms)	0.48	0.70	0.83

by factors of 1.35 (Fig. 7b) and 1.30 (Fig. 7c). The increase in energy was confirmed in all cases by a corresponding decrease in the loop voltage. We recall that in comparing the results of the experiment and of the numerical simulation, the powers of the microwave generator and of the Ohmic heating were taken as being approximately equal. For  $n(0) = n_c$ , the ECH energy should be absorbed, according to Fig. 1 (curve b) in a broad central zone. Indeed, the measured temperature profile was close to that calculated for central absorption with  $r_h/a = 0.6$  (Fig. 2, curve b). For a higher density,  $n(0) = 2n_c$ , the ECH energy absorption zone should be displaced towards the plasma edge (Fig. 1, curve d). Comparing the temperature profiles shown in Figs 7b and c with the calculated ones, we find agreement with the cases of heating in a layer located at  $r_h/a = 0.6$  (curves b in Figs 3 and 4). The increase in energy of 30–35% and the decrease by the same amount in the loop voltage  $U_L$  which were obtained experimentally are in good agreement with the transport code calculations (Figs 5 and 6).

It should be mentioned that ECH was accompanied by an appreciable decrease in the energy confinement time. Estimates of  $\tau_e$  with Ohmic heating and with ECH are given in Table I. The reduction in  $\tau_e$  is explained by the displacement of the heating zone towards the plasma edge compared with the Ohmic-heating case. However, one cannot exclude some increase in the electron thermal conductivity in the presence of ECH, especially in the case with  $n(0) = n_c$ . A slight reduction in the density during ECH indicated a possible increase in the diffusion coefficient.

The large width of the heating zone which lowers the efficiency of ECH is a consequence of the broad polar diagram of the antenna which was used. It can be assumed that the use of an antenna with optimum directional properties would enable the heating to be localized in a narrower region near the discharge axis. According to the transport code calculations, doing this would considerably increase the central temperature and the energy confinement time.

## REFERENCES

- [1] BULYGINSKIJ, D.G., GOLANT, V.E., LARIONOV, M.M., LEVIN, L.S., SHUSTOVA, N.V., in Controlled Fusion and Plasma Physics (Proc. 9th Europ. Conf. Oxford, 1979) Vol.2 (1979) 547.
- [2] SUZUKI, M., in Controlled Fusion and Plasma Physics (Proc. 10th Europ. Conf. Moscow, 1981) Vol.2 (1981).
- [3] GILGENBACH, R.M., et al., Phys. Rev. Lett. **44** (1980) 647.
- [4] BARANOV, Yu.F., FEDOROV, V.I., in Controlled Fusion and Plasma Physics (Proc. 10th Europ. Conf. Moscow, 1981) Vol.1 (1981) paper H-13.
- [5] BARANOV, Yu.F., et al., ibid., paper H-8.
- [6] BARANOV, Yu.F., et al., Fiz. Plazmy **8** (1982) 473.

## DISCUSSION

M. THUMM: What was the reason for launching the X-mode into the plasma at an angle of  $42^\circ$  with respect to the  $B_0$ -field? Is this an optimum angle for direct X-mode absorption in FT-1?

V.S. STRELKOV: This value of  $42^\circ$  is the result of optimization. Further details may be found in Refs [5, 6] of the paper.

R. GOLDSTON: You state that in the case of  $n_e(0) > n_{crit}$  the power density profile due to ECH was broader than the initial  $P_{OH}$  profile. Therefore  $\tau_E$  fell by about 20% with ECH heating. In the case of  $n_e(0) < n_{crit}$  the heating profile was well peaked on axis. What happened to  $\tau_E$  in this case?

V.S. STRELKOV: The paper gives, for a mathematical model of the heating process, a calculation of the total energy release  $P_{OH} + P_{ECH}$ , and confirms that in both cases –  $n_e(0) > n_{crit}$  and  $n_e(0) < n_{crit}$  – the total energy release profile in the presence of SHF heating is wider than with purely Ohmic heating. This may be the reason for the reduction in  $\tau_E$  in the case of SHF heating.

P. BURATTI: It seems to me that for your kind of wave launching the correct definition of critical density (such that cut-off is at  $r = 0$ ) is not  $\omega_{pe} = \omega_{ce}$ , and that the  $m_c$  result is underestimated, possibly by a factor of two.



## EQUILIBRIUM, STABILITY AND HEATING OF PLASMAS IN LINEAR AND TOROIDAL EXTRAP PINCHES

B. BONNEVIER, H.E. DALHED\*, J.R. DRAKE, T. HELLSTEN,  
P. KARLSSON, R. LANDBERG, B. LEHNERT, J. SCHEFFEL,  
M. TENDLER, E. TENNFORS, B. WILNER  
Royal Institute of Technology, Stockholm,  
Sweden

### Abstract

#### EQUILIBRIUM, STABILITY AND HEATING OF PLASMAS IN LINEAR AND TOROIDAL EXTRAP PINCHES.

The Extrap scheme consists of a Z-pinch immersed in an octupole field. The total magnetic field has no component along the pinch axis. Globally stable Z-pinch equilibria with a distributed plasma current density and a duration of about 100 Alfvén transit times have been observed in linear and toroidal sector experiments. Theoretical studies indicate that this stability can be the result of constraints introduced by the octupole field and the resulting separatrix of the total field, in combination with finite-Larmor-radius effects. A scheme for ICRF heating of the plasma in configurations with a magnetic neutral line, being applicable to Extrap and FRC, is analysed. Wave propagation arises owing to the Hall effect. Particle resonances are responsible for the absorption, owing to a high parallel wavenumber and a weak magnetic field.

### 1. INTRODUCTION

In the Extrap scheme, shown in Fig. 1, a Z-pinch plasma is immersed in an octupole field produced by currents in external conductors [1, 2]. Four magnetic x-type zero points are generated when the Z-pinch and octupole fields are combined. The resulting separatrix forms a magnetic limiter which is important for stabilizing the Z-pinch. There is no magnetic field along the pinch axis in this configuration, which can be either linear or toroidal.

### 2. STABILITY OF TOROIDAL EQUILIBRIA

The Extrap plasma is built up by drawing a current along the weak field region of the octupole field. The plasma expands radially outwards owing to its loop force. By programming the external field, various equilibria can be obtained.

---

\* Lawrence Livermore National Laboratory, Livermore, California, USA.

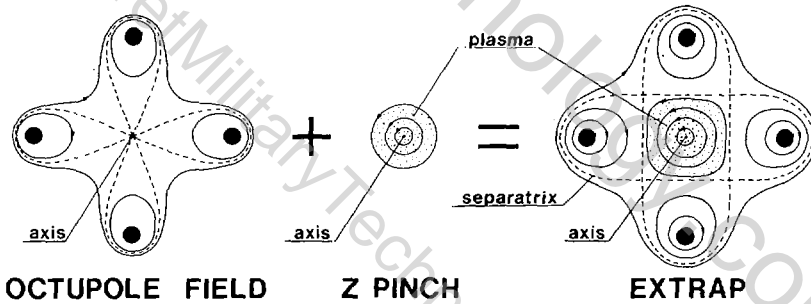


FIG.1. An Extrap pinch is obtained by creating a Z-pinch immersed in an octupole field.

Stability investigations using the GATO code have shown that all except square-shaped equilibria are MHD-unstable against a vertical displacement. The unstable MHD spectrum can be separated into internal and free-boundary modes (a typical spectrum is shown in Fig. 2). For small toroidal wavenumbers, the free-boundary modes have the largest growth rates, denoted by VK and RK. For a square-shaped cross-section these are stabilized if the current density vanishes smoothly at the boundary. This can be achieved if a magnetic separatrix is made to approach the plasma boundary by increasing the external field. The transport coefficients at the boundary are then increased, resulting in a reduced pressure gradient favouring stability.

The internal modes ( $S_j$ ,  $j = 0, 1, 2$ , in Fig. 2) have a lower growth rate for small toroidal wavenumbers than the free-boundary modes. The internal modes can be stabilized by a number of finite-Larmor-radius phenomena, including charge separation arising from the electric field inhomogeneity and from effects of inertia.

The engineering beta can be increased and the inductance of the external coil system reduced when using eight conductors with alternating current directions.

### 3. LINEAR EXPERIMENTS

The equilibrium and global stability of Extrap Z-pinch discharges have been studied in linear experiments. The following observations were made:

- (1) Breakdown occurs along the null in the octupole field, and the discharge then builds up radially outwards without contact with a limiter or the walls [3].
- (2) A Z-pinch region is formed, with closed magnetic flux inside the separatrix [4].

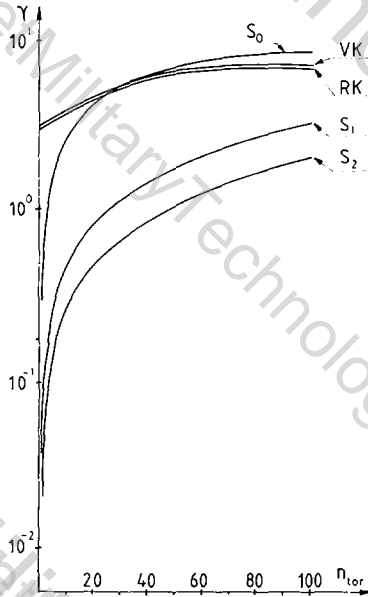


FIG.2. Unstable MHD spectrum. Growth rate  $\gamma$  versus toroidal mode number  $n_{\text{tor}}$  for a pressure distribution  $p \propto (\psi - \psi_b)^{1.2}$  where  $\psi_b$  denotes the magnetic flux  $\psi$  at the plasma boundary.

(3) The scaling of the integrated radial pressure balance with pinch current is consistent with Bennett scaling, as discussed further below.

(4) Interferometer measurements of the line-of-sight integrated density perpendicular to the axis of the pinch indicate that the pinch radius,  $a$ , for stable discharges follows approximately the separatrix radius  $a_s$ . Thus we have  $a \approx a_s = (a_v/\sqrt{2})(J_p/J_v)^{1/4}$ , where  $a_v$  is the radius to the external conductors and  $J_p$  and  $J_v$  are the pinch and conductor currents. This is consistent with theory, where the true parameter determining the stability limit would be the magnitude of the self-consistent Z-pinch radius relative to the radial distance to the separatrix. If the pinch radius is too small, the stabilizing effect due to the separatrix is lost.

(5) Experiments have been performed with  $a_v = 28$  mm and 42 mm. Macroscopically stable equilibria are observed when the ratio  $f = J_p/J_v$  is below a certain limit,  $f_c$ . This limit is a function of a variety of parameters, including pinch length, filling pressure and vacuum vessel material (glass or stainless steel). In general, if  $f_c \lesssim 0.25$ , the pinch discharges are stable for the 65  $\mu\text{s}$  duration of the flat-topped discharge pulse. This corresponds approximately to 100 Alfvén transit times.

The integrated radial pressure balance for the case with constant temperature profile has the form  $NkT = g\mu_0 J_p^2 / 16\pi$  where  $N = 2\pi \int_0^a nr dr$  and where  $g \approx 1$

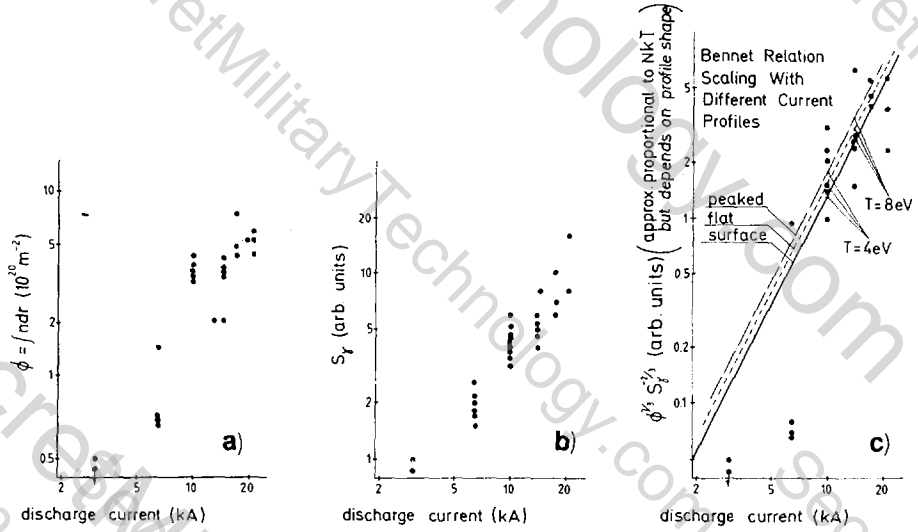


FIG. 3. Scaling of: (a) line-of-sight integrated density  $\phi = \int ndr$  versus  $J_p$ ; (b) line-of-sight integrated emitted Balmer  $\gamma$ -line intensity  $S_\gamma = \int n^2 T^{-3/2} dr$  versus  $J_p$ ; (c)  $\phi^{7/3} S_\gamma^{-2/3}$  (which is approximately proportional to  $NkT$ ) versus  $J_p$ . In (c) the units for the data points are arbitrary. Lines corresponding to calculated values of the Bennett relation for various profile shapes are also shown, and for these the arbitrary units become  $\text{J} \cdot \text{m}^{-1}$ .

is a factor that depends on the shape of the current profile. To study the scaling of  $NkT$  we used interferometry for density information (phase shift  $\phi \propto \int ndr$ ) and the Balmer  $\gamma$  spectral line for temperature information (line-of-sight integrated emitted  $\gamma$ -line intensity  $S_\gamma \propto \int n^2 T^{-3/2} dr$ ). The use of this scaling for the  $\gamma$ -line intensity is valid since the energy levels involved are above the thermal limit at the plasma parameters of the pinch, and the pinch is optically thin.

The Bennett relation can then be expressed in terms of the observed quantities  $\phi$  and  $S_\gamma$  to give  $\phi^{7/3} S_\gamma^{-2/3} a^{1/3} \propto J_p^2$ . We neglect the  $a^{1/3}$  factor since it is a weak function of  $J_p$ . In Fig. 3 we plot: (a)  $\phi$ , (b)  $S_\gamma$ , and (c)  $\phi^{7/3} S_\gamma^{-2/3}$ , versus  $J_p$ . The data shown are for  $10 \mu\text{s}$  after irradiation of discharge. In Fig. 3(c) we see that  $\phi^{7/3} S_\gamma^{-2/3}$  is proportional to  $J_p^2$ , which is consistent with the Bennett relation. It is assumed that the shape factor  $g$  is constant as  $J_p$  is varied. Changes in  $g$  do not, however, introduce significant changes in the scaling relation, so this assumption is not a restriction here. The calculated range in  $\phi^{7/3} S_\gamma^{-2/3}$  that would occur owing to different current profiles is shown in Fig. 3(c), and this range is less than the spread in the data points.

From the pressure balance, an average temperature can be estimated using interferometry scans to estimate  $N$ . Several calculated temperatures are shown in Fig. 3(c). In this experiment, the pinch length is 22 cm and the filling density is  $n_H = 7 \times 10^{21} \text{ m}^{-3}$ . The temperatures are limited by large end losses due to

the electrodes and large radiation losses due to the high filling density. The parameters of this experiment were selected in order to allow access to a large range of  $J_p$  to check scaling.

In other experiments, stable discharges have been obtained, to date, for pinch lengths up to 60 cm and filling densities as low as  $n_H = 1.6 \times 10^{21} \text{ m}^{-3}$ . For this case the temperatures are higher.

#### 4. TOROIDAL SECTOR EXPERIMENT

A  $60^\circ$  sector experiment of 0.4 m average major radius has been used in a first study of toroidal effects on equilibrium and stability. The main external field was generated by four ring-shaped coils. There were also two trim coils for adjustments of the vertical field. Discharges were run at pinch currents up to 11 kA. Breakdown occurred along the weak field region of the octupole field. After breakdown, the current channel expanded radially outwards to an equilibrium position. The pinch could be stably positioned, provided the external field was properly programmed. A quasi-steady state of  $30 \mu\text{s}$  could thus be sustained when the Alfvén transit time was about  $0.5 \mu\text{s}$ . Under other unfavourable external field conditions the pinch became unstable against vertical displacements, in agreement with the numerical computations.

#### 5. ICRF HEATING

The stability of the Extrap plasma is favoured if the pinch radius reaches out to the vicinity of the separatrix. To sustain a pinch with relatively large cross-section, it may be necessary to supply heating power in addition to the Ohmic heating. The use of frequencies in the ion-cyclotron resonance regime was proposed earlier [5] and is further analysed here.

The physics describing wave propagation and absorption in Extrap and FRC is quite different from that in systems with a strong toroidal magnetic field. Owing to the high  $k_{\parallel}$  and the low  $\omega_{ci}$  in Extrap, ion-cyclotron damping already becomes important at moderate temperatures,  $T$ . Close to the magnetic axis, where the field vanishes, the particles move in meandering and figure-of-eight orbits rather than in cycloids [5, 6]. Furthermore, for these systems the orbit dimensions are of the same order as the scale length of the magnetic field.

A schematic picture of the wave propagation in Extrap can be obtained from the cold-plasma model using the WKB method, which yields

$$k_r^2 [(m/r)^2 - (\omega/c)^2 \epsilon_{rr}] = (\omega/c)^4 |\epsilon_{rz}|^2 - [(m/r)^2 - (\omega/c)^2 \epsilon_{zz}] [k_z^2 + (m/r)^2 - (\omega/c)^2 \epsilon_{rr}] \quad (1)$$

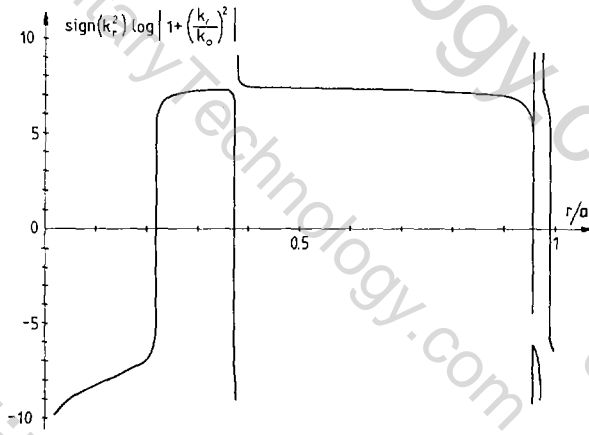


FIG. 4. Radial wavenumber  $k_r$  for Extrap with a parabolic density distribution with maximum density  $3 \times 10^{15} \text{ cm}^{-3}$  and  $n_H/n_D = 0.25$ ; plasma current  $10^4 \text{ A}$ ; wavenumbers  $m = 1$ ;  $k_z = 0$ ;  $\omega = 1.5 \text{ MHz}$ ; and  $a = 2 \text{ cm}$ .

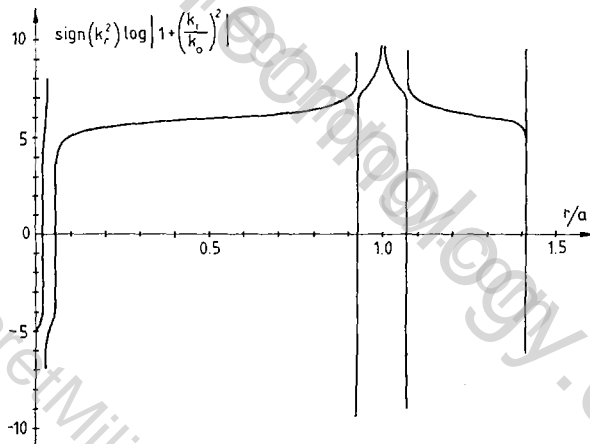


FIG. 5. Radial wavenumber  $k_r$  for reserved  $\theta$ -pinch with a parabolic density distribution for  $0 < r < a$  with maximum density  $10^{15} \text{ cm}^{-3}$ ;  $B_{\text{max}} = 0.5 \text{ T}$ ; wavenumbers  $m = 0$ ;  $(k_z/k_0)^2 = 10^5$ ;  $a = 4 \text{ cm}$ ; and  $\omega = 1.9 \text{ MHz}$ .

where  $\vec{\epsilon}$  is the dielectric tensor and  $m/r = k_{\parallel}$ . The variation of the radial wavenumber in a model of an Extrap equilibrium is outlined in Fig.4. In the frequency range bounded by the fundamental ion-cyclotron resonances of a two-ion plasma, the magneto-acoustic wave also propagates for  $\epsilon_{rr} < 0$ , owing to the Hall effect. Propagation is thus possible in almost the entire plasma. The radial wavelength depends on the particle density and on the concentration of the species. Thus, for given concentration, the condition for a global resonance defines a line density, i.e. ion density integrated over the plasma cross-section, of the order of  $5 \times 10^{15}$  ions  $\cdot$  cm $^{-1}$  ( $m = 1$ ), which falls within the typical experimental line-density range. Consequently, global magneto-acoustic resonances can be used to increase the coupling to the antenna system by adjusting the composition of species.

When warm plasma effects are included,  $\vec{\epsilon}$  becomes complex-valued. The fast wave is still decoupled from the slow wave and is not strongly changed by the thermal effects since it is mainly determined by the component  $\epsilon_{rz}$ . Particle resonances are important for absorption since  $r(\omega - \omega_{ci})/v_{thi} \lesssim 1$  for moderate temperatures also. Local absorption near the surface  $(\omega/c)^2 \epsilon_{rr} = (m/r)^2$  can only occur at low temperatures.

The propagation of the fast wave in a model of an FRC equilibrium is outlined in Fig.5. The situation is similar to that of Extrap, but the parallel wavenumber can be lower, allowing for mode conversion to the slow wave becoming important.

#### ACKNOWLEDGEMENT

This work was supported by the Euratom Communities under an association contract between Euratom and Sweden.

#### REFERENCES

- [1] LEHNERT, B., Phys. Scr. **10** (1974) 139; **16** (1977) 147.
- [2] DRAKE, J.R., HELLSTEN, T., LANDBERG, R., LEHNERT, B., WILNER, B., in Plasma Physics and Controlled Nuclear Fusion Research 1980 (Proc. 8th Int. Conf. Brussels, 1980) Vol. 2, IAEA, Vienna (1981)717.
- [3] DRAKE, J.R., Royal Inst. Technology, Stockholm, Rep. TRITA-PFU-82-04 (1982).
- [4] DRAKE, J.R., in Proc. 3rd Symp. Physics and Technology of Compact Toroids in the Magnetic Fusion Energy Program, Los Alamos, Los Alamos Scientific Labs Rep. LA-8700-C (1980) 196.
- [5] HELLSTEN, T., TENNFORS, E., in Proc. 3rd Joint Varenna-Grenoble Int. Symp. Heating in Toroidal Plasma, Grenoble, 1982, CEC, Grenoble (1982) paper C17.
- [6] ÅSTRÖM, E., Tellus **8** (1956) 260.



## HIGH-BETA NEOCLASSICAL CURRENT AND STABILITY EXPERIMENTS

J.D. CALLEN, R.N. DEXTER, C.M. FORTGANG,  
H.R. GARNER, A.G. KELLMAN, D.W. KERST,  
M.W. PHILLIPS, S.C. PRAGER, J.C. SPROTT,  
E.J. STRAIT, J.C. TWICHELL, M.C. ZARNSTORFF  
Department of Physics,  
University of Wisconsin,  
Madison, Wisconsin,  
United States of America

### Abstract

#### HIGH-BETA NEOCLASSICAL CURRENT AND STABILITY EXPERIMENTS.

Equilibrium neoclassical plasma currents and plasma stability at high values of beta have been studied in the Levitated Toroidal Octupole. In a collisionality regime at the border between the banana and plateau regimes, the bootstrap and Pfirsch-Schlüter currents have for the first time been experimentally observed in agreement with neoclassical theory. Also, stable plasmas have been produced with extremely high beta values (2.5 times the MHD ballooning instability beta limit) and compared with the results of a kinetic stability calculation, implicating finite-ion-gyroradius effects as a possible cause for the observed stability. To augment both the bootstrap current and stability studies, four megawatts of ion cyclotron resonance heating power are being optimized.

### 1. Introduction

The Levitated Toroidal Octupole device has been operated as a facility for the investigation of high beta plasma phenomena relevant to fusion. We report here on (1) the first experimental observation of the neoclassical equilibrium currents (both 'bootstrap' and 'Pfirsch-Schlüter') that have long been predicted to flow in toroidal plasmas and (2) comparison of extremely high beta stable plasmas with results of a rigorous kinetic calculation of ballooning instability in the actual machine geometry. In addition, four megawatts of ion cyclotron resonance heating will be applied to the plasma (1.3 MW coupled to date) to enlarge the high beta parameter space available for the above equilibrium current and stability studies.

## 2. Machine description

The poloidal octupole magnetic field (figure 1) is created by four internal, current-carrying, 17 cm diameter, aluminum rings which are levitated for 30 msec, excited by a 0.7 volt-sec iron core transformer, and situated within the 1.4 meter major radius torus. For the neoclassical current studies, a toroidal magnetic field is also applied to produce helical field lines. High beta plasmas are created by simultaneous injection from up to three coaxial Marshall guns.<sup>1</sup> The background pressure within the toroid is  $7 \times 10^{-9}$  torr, achieved through turbomolecular titanium getter, and liquid-helium-cooled cryo pumping.

The ICRH system consists of two 2-MW sources, each connected to a faraday-shielded antenna that extends one-third the way around the machine in the toroidal direction. One source has been in routine operation for two years, and the other is presently being installed. The sources are self-excited, push-pull triode oscillators, and produce a 10 msec pulse of rf at typically 1.3 MHz. The power is absorbed at the fundamental proton cyclotron frequency in the near field of the antenna. Wave propagation is negligible, and the rf field near the resonance is the same as the vacuum field.

In addition to spectroscopic, charge exchange, and interferometric diagnostics, probes may be successfully inserted within the large, ohmic-current-free, octupole plasma for local density and temperature measurements. Moreover, the full three-dimensional spatial structure of the plasma current is measurable by two different probe techniques. Firstly, one can evaluate the magnetic field gradients, and thereby the plasma current, from the difference between appropriately placed coils, 1 cm apart. Secondly, the ion current is determined with a two-sided Langmuir probe that consists of two plane faces, insulated from each other and oriented with the planes perpendicular to the current to be measured. The difference between the ion saturation current to each plane yields the ion current.

## 3. Bootstrap and Pfirsch-Schlüter Current Studies

Although the importance of the bootstrap current has long been recognized,<sup>2</sup> its existence has hitherto only been demonstrated theoretically. The current, which flows parallel to the magnetic field, is of great importance for many reasons--it provides the possibility of driving a steady-state tokamak, it creates the danger of a current-driven instability, it provides a minimum current in a stellarator, and it plays an integral part in the

theory of neoclassical transport. The Octupole device is especially well-suited to a thorough investigation of the neoclassical currents for several reasons-- there is no ohmic current to mask the neoclassical current, high beta plasmas have been attained to optimize the current, probe diagnostics have been developed for local current measurements, and the field transform and plasma collisionality may be varied over a wide range. It should be noted that the theory of neoclassical currents,<sup>3</sup> when cast in magnetic flux coordinates, is virtually identical in a multipole (with toroidal field) and a tokamak. Thus the Octupole results are directly applicable to other axisymmetric toroids with helical field lines with little qualification, and to stellarators with some care.

Initial measurements in the Octupole, performed in a range of collisionality from the collisional Pfirsch-Schlüter regime to the collisionless border between the plateau and banana regimes, demonstrate the existence of the neoclassical current (including both bootstrap and Pfirsch-Schlüter components) in rough agreement with theory. At the plateau-banana border, where the electron-ion mean free path ( $\lambda_{ei}$ ) is about equal to the connection length between mirroring points, the ion current has been measured at two points along a field line and on two different magnetic surfaces. For this plasma,  $\beta=2\%$ ,  $\lambda_{ei}=1m$ ,  $B_p=0.86kG$ ,  $B_T=0.3kG$ ,  $n=10^{13}cm^{-3}$  and  $T_e=T_i=20eV$ . All local quantities, such as beta, are in this report evaluated on the separatrix between the outer ring and wall, as shown in figure 1. Figure 2 shows the result for a surface outside the separatrix. The perpendicular diamagnetic current agrees well with theory in both magnitude and shape of its parallel and radial structure (not shown), thus lending credence to the diagnostic technique. The agreement of the parallel ion current with the kinetic theory of neoclassical currents, solved for the Levitated Octupole device, is also quite good. Roughly, the offset of the curve represents the unidirectional bootstrap current, and the variation of the current along a field line represents the Pfirsch-Schlüter component that flows to ensure current continuity. Similar results are obtained on a magnetic surface further inside.

To display the collisionality dependence of the results it is useful to recall that, in all collisionality regimes, the plasma diamagnetism ( $j=\nabla P \times B/B^2$ ) and current continuity ( $\nabla \cdot j=0$ ) require that the parallel current has the form

$$J_{\parallel} = - \frac{B_T}{B_p} \frac{\nabla P}{B} + BK(\psi)$$

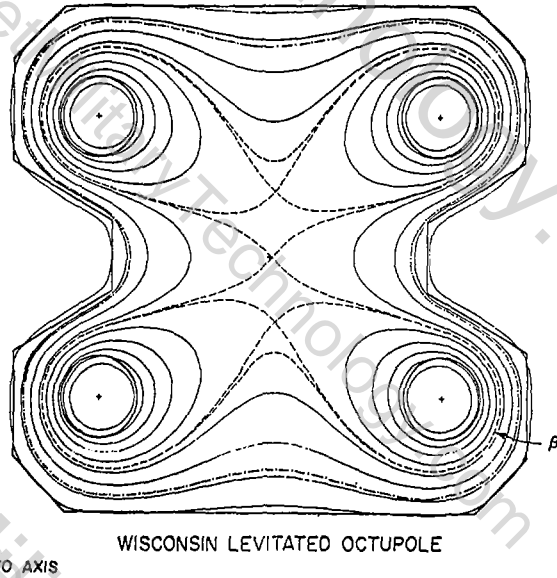


FIG.1. Poloidal magnetic flux plot of the Wisconsin Levitated Toroidal Octupole indicating the region where  $\beta$  is evaluated, Major radius is 1.4 m.

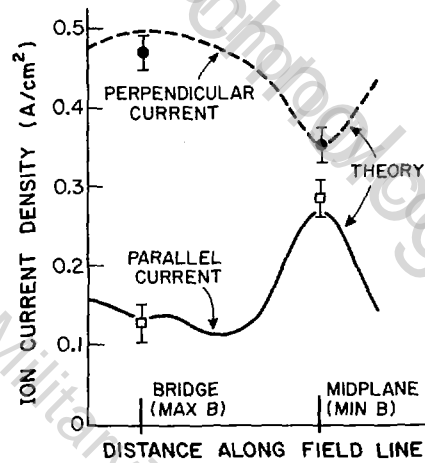


FIG.2. Ion perpendicular and parallel (neoclassical) currents measured at two points along a magnetic field line on a surface outside the separatrix. Shown also are initial results of a theoretical calculation for the currents in the Levitated Octupole.

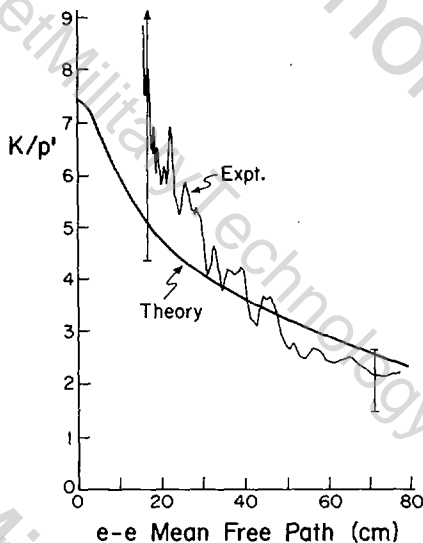


FIG.3. Collisionality dependence of constants of integration  $K$  (normalized by  $p' = \partial P / \partial \psi$ ) as measured experimentally and predicted theoretically.

where  $K(\psi)$  is a flux surface quantity and constant of integration. In the collisional limit,  $K$  is determined by a simple Ohm's law to yield the so-called Pfirsch-Schlüter current, whereas in the collisionless limit a kinetic calculation for  $K$  results in the unidirectional bootstrap current. Experimental measurement of these currents is thereby equivalent to an experimental determination of  $K$ . As the plasma becomes more collisionless the poloidal field inhomogeneity generates viscosity which resists poloidal current flow.<sup>3</sup> Since  $K(\psi)$  is proportional to the poloidal current,  $K$  is reduced.

As the temperature of the gun-injected plasmas decays in time during a shot, the plasma collisionality varies from the above-mentioned plateau-banana regime to the collisional regime. The total plasma current has been measured for this case (see section 2), enabling one to plot in figure 3 the dependence of the experimentally determined  $K$  value on collisionality. Agreement with theory is quite good although the error bars are large (due to electronic noise presently being eliminated).

#### 4. High Beta Stability Studies

Plasmas have been studied with beta values between 11% and 44%. In all cases the plasma is stable to an MHD-like

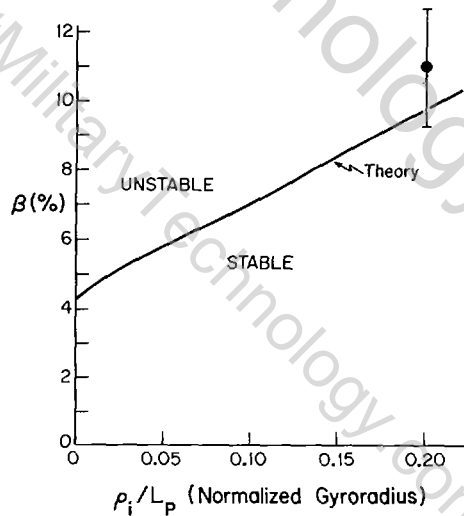


FIG.4. Dependence of theoretical ballooning-instability beta limit on thermal ion gyroradius,  $\rho_i$ , according to a detailed collisionless kinetic theory solved for the Levitated Octupole device.  $\rho_i$  is normalized for the pressure gradient scale-length,  $L_p = |P/\nabla P|$ . Shown is the  $\beta = 11\%$  experimental case.

ballooning mode in that (1) the plasma decays slowly compared to an MHD growth time (decay time  $\sim 1000$  Alfvén transit times) with no apparent degradation in confinement and (2) no  $\beta$ -related fluctuations occur to within an accuracy of  $\tilde{B}/B < 0.1\%$ ,  $\tilde{n}/n < 5\%$  and  $\tilde{T}/T < 5\%$ . Whereas the plasma equilibrium (i.e. the diamagnetic current) at  $\beta = 11\%$  is well-described by MHD, at  $\beta = 44\%$  the diamagnetism deviates from the MHD prediction, probably due to ion gyroviscosity. Thus, for the sake of this report we will consider this case as pathological and only discuss the  $\beta = 11\%$  case, obtained with  $n = 5.7 \times 10^{13}$ ,  $T_e = T_i = 18$  eV,  $B_p = 0.86$  kG,  $B_t = 0$ , five ion gyroradii within a pressure gradient scale length (ion gyroradius  $\rho_i = 0.5$  cm.),  $\lambda_{ei} \approx 20$  cm, magnetic connection length  $\approx 50$  cm and an energy decay time of 350  $\mu$ sec.

The MHD stability equations have been solved explicitly for the Levitated Octupole device including all realistic geometric factors. The MHD ballooning beta limit for the Octupole is 4.3%, a factor of 2.5 less than the experimental value. Thus the MHD approximation is not satisfied experimentally.

To attempt to explain the observed stability, a detailed kinetic theory has been formulated and solved explicitly for the Octupole device. The linearized Vlasov

equation is employed to treat electromagnetic modes and solved through an expansion in powers of the ion gyroradius. Solution is obtained for the beta limit and the 3-dimensional structure of the mode. Calculation to zero order in gyroradius includes particle trapping and free streaming effects which negligibly influence the beta limit. The powerful finite ion gyroradius ('FLR') effects, primarily the manifestation of the ballooning mode as an oscillatory ion drift wave, are obtained from the first-order equations and displayed in figure 4.

The experimental  $\beta = 11\%$  Octupole case, with  $5 \rho_i = L_p =$  pressure gradient scale length, is seen to be marginally stable within experimental accuracy. Thus, there are two possible causes for the observed stability -- FLR stabilization or collisional effects. For example, although the equilibrium of these plasmas is observed to agree with MHD with negligible viscous influence, it is possible that gyroviscosity may play a role in the stability equations.

#### 5. Summary and Plans

The bootstrap and Pfirsch-Schlüter currents have been observed in the Levitated Octupole by measuring the parallel ion current at two points along a magnetic field line (and on two different magnetic surfaces) and total parallel current at one location. Work is in progress to directly measure the full three-dimensional structure of the currents and examine their sensitive dependence on collisionality and field transform. The relationship between the existence of the bootstrap current and the plasma fluctuations and particle transport will also be explored in detail.

The attainment of extremely high beta plasmas without onset of the ballooning instability is likely due to finite ion gyroradius stabilization (as indicated by a thorough collisionless kinetic stability calculation) or collisional effects (not included in the theory). To unravel the two effects, four megawatts of ion cyclotron resonance heating power is available<sup>4</sup> and being optimized to create collisionless, small gyroradius, high beta plasmas.

This work was supported by the U.S. Department of Energy.

#### REFERENCES

- [1] Halle, J.H., Kellman, A.G., Post, R.S., Prager, S.C., Strait, E.J., and Zarnstorff, M.C., Phys. Rev. Lett. 46 (1981) 1394.

[2] Bickerton, R.J., Connor, J.W., and Taylor, J.B., Phys. Sci. 229 (1971) 110.

[3] Hirshman, S.P. and Sigmar, D.J., Nuclear Fusion 21 (1981) 1079.

[4] Dexter, R.N., Fortgang, C.M., Prager, S.C., Sprott, J.C., Strait, E.J., and Twichell, J.C., Proceedings of the Third Varenna-Grenoble International Conference on Heating in Toroidal Plasmas (1982).

### DISCUSSION

W.B. KUNKEL: Could you describe in a little more detail how you measure the ion current in your device, as distinct from the total current?

S.C. PRAGER: The ion component of the current is measured with a double-sided Langmuir probe containing two plane faces which are parallel and insulated from each other. The difference between the ion saturation current to the two planes yields the net drift in the ions, or the ion current. The total current is measured by determining the difference in the signal to two magnetic pick-up coils, spaced 1 cm apart, in order directly to evaluate  $\nabla \times \vec{B}$  (employing various machine symmetries, etc.) and thereby the total current.

It is well-established that small probes do not perturb the current they are measuring, since the plasma is large, relatively cold ( $\sim 20$  eV), Ohmic-current-free and flowing. For example, measurement of the simple perpendicular diamagnetic current is in excellent agreement with theory ( $\nabla P \times \vec{B}/B^2$ ).

T. TAMANO: I am surprised that you observed neoclassical currents in spite of anomalous diffusion.

S.C. PRAGER: The preliminary observation that the particle diffusion is measured to be greater than ten times the neoclassical value, in the presence of neoclassical currents, was mentioned as a topic for future study. We do not yet know the cause of the enhanced diffusion, and it is not yet well established theoretically, to my knowledge, that the existence of enhanced diffusion necessarily implies the destruction of the currents. We will study this question experimentally.

D.R. SWEETMAN: The bootstrap current should be very sensitive to the presence of fluctuations. Do you have measurements of these in the region near where the current is believed to exist?

S.C. PRAGER: Although a detailed study of the fluctuations has not yet been undertaken, the relative density fluctuation ( $\tilde{n}/n$ ) appears to be less than 10% and the magnetic fluctuation ( $\tilde{B}/B$ ) less than 1%.

**Session K**

**POST-DEADLINE PAPERS**

Chairman  
M. BRENNAN  
Australia

## LOWER-HYBRID CURRENT-DRIVE EXPERIMENTS IN T-7 TOKAMAK

V.V. ALIKAEV, V.L. VDOVIN, D.P. IVANOV,  
N.V. IVANOV, V.I. IL'IN, A.M. KAKURIN,  
A. Ya. KISLOV, P.E. KOVROV, V.A. KOCHIN,  
P.P. KHVOSTENKO, I.N. KHROMKOV,  
V.V. CHISTYAKOV  
I.V. Kurchatov Institute of Atomic Energy, Moscow,  
Union of Soviet Socialist Republics

J. ĎATLOV, F. JAČEK, P. KLIMA, V. KOPECKÝ,  
J. PREINHAELTER, K. JAKUBKA  
Institute of Plasma Physics,  
Czechoslovak Academy of Sciences,  
Czechoslovakia

*Presented by V.S. Strelkov*

### Abstract

#### LOWER-HYBRID CURRENT-DRIVE EXPERIMENTS IN T-7 TOKAMAK.

Experiments on current drive by lower-hybrid waves have been carried out in the T-7 tokamak. The RF-system includes a magnetron operating at a frequency of  $\sim 900$  MHz, with a maximum power, in this case, of 250 kW, a pulse duration of 50 ms, a waveguide transmission line and a radiator of three phased waveguides (three-waveguide grill). The necessary phase shift between waves in adjacent waveguides of the grill can be set with a phase shifter. — By interacting with the plasma electrons, the wave transfers its momentum to them; thus, the directed motion of the electrons is sustained and the current is driven. The current drive by a lower-hybrid wave manifests itself by a drop in the loop voltage and a rise in the total plasma current. The current drive is accompanied by suppression of X-ray ripple intensity emitted from the plasma, which depends on the fan-like instability. The experimental dependence of the current drive on RF-power, plasma density and phase shift among the waveguides is in qualitative agreement with the theoretical predictions. — From the experimental results, there seems to be some hope that a stationary plasma with a constant superconducting toroidal magnetic field can be achieved in T-7.

### 1. INTRODUCTION

The possibility of current drive in a plasma by lower-hybrid waves to be used in a steady-state tokamak reactor is attracting a good deal of attention, at present [1–5]. The experiments in T-7 are especially interesting because a

constant toroidal field is sustained by a superconducting solenoid; in principle, a steady-state plasma can be obtained. Results of first experiments on current drive in T-7 are presented in this paper.

## 2. ARRANGEMENT OF THE EXPERIMENT

The T-7 tokamak [6] has a discharge chamber with a major radius of  $R = 122$  cm and a minor radius of  $r = 35$  cm. Graphite limiters are placed inside the chamber: a circular limiter with an aperture radius of 31.5 cm and a movable limiter rail. In the experiments described, the movable limiter was located at a distance of 28 cm from the chamber axis. The experiments were carried out at a toroidal magnetic field of  $B_T = 19$  kG. The discharge was formed by consecutive conversions of a 'breakdown' condenser bank and of an LC-shaper into a vorticity field winding of the tokamak. The RF-system is switched on at the steady-state stage of the discharge. The RF-system is on for 50 ms, the maximum power amounts to 250 kW.

The RF-energy source in T-7 is a magnetron operating at a frequency of  $f \approx 900$  MHz. The RF-energy is transferred to the tokamak by waveguides arranged in three parallel channels. Each channel includes an attenuator, a phase shifter, a ferrite valve, and a ceramic vacuum window. The vacuum window is at a distance of 3 m from the tokamak. The RF-energy reaches the chamber by a system of three phased waveguides – a three-waveguide grill – which are located within a horizontal branch conduit of the device. The face of the grill protrudes into the tokamak chamber for a distance of one centimeter from the wall. The cross-section of each waveguide at the grill face is  $2 \times 22$  cm<sup>2</sup>, the distance between the waveguide axes is 2.4 cm.

The inner surface of the waveguide, made of stainless steel, was sputtered by titanium and treated by RF-pulses, of 50 ms duration with a power of up to 600 kW, in order to increase the electric field strength of the waveguides. In this case, the relative phase shift of waves in adjacent waveguides is  $\Delta\Phi = 180^\circ$ . Measurements without tokamak discharge have shown that, after such a treatment of the grill, the phase at the waveguide opening does not depend on the RF-power introduced.

Our initial intention was to use the RF-system for lower-hybrid plasma heating. It was this goal which determined its parameters (generator frequency and grill design). One of the purposes was to reduce the Landau damping effect on the electrons. As the Landau damping mechanism is used for current drive in the plasma and the RF-power absorption at the lower-hybrid resonance is a parasitic one, in our case, the parameters of the RF-system have restricted the discharge regime to one of rather low plasma density. Indeed, for a phase shift between adjacent waveguides of  $\Delta\Phi = 90^\circ$ , which is necessary for providing a travelling wave, the longitudinal phase velocity spectrum has a maximum at  $v_p = 10^{10}$  cm·s<sup>-1</sup>

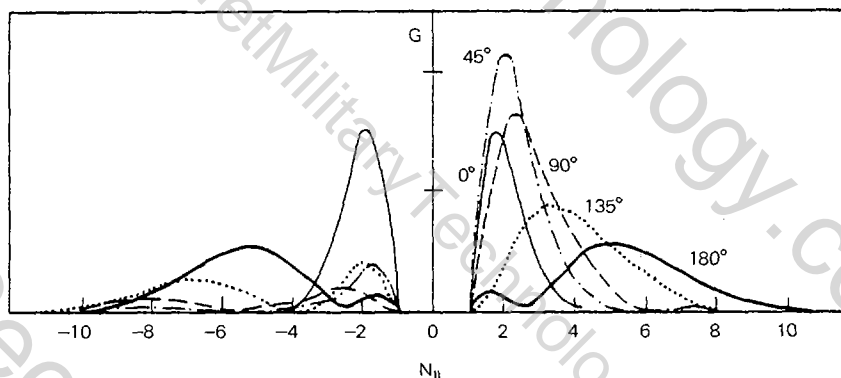


FIG. 1. Spectral density of radiated power for different grill phasings,  $\Delta\Phi$ , calculated for plasma density gradient near grill face of  $\text{grad } n_e = 3 \times 10^{11} \text{ cm}^{-4}$ .

(Fig. 1). For a Maxwellian distribution at a realizable plasma temperature, the number of electrons with appropriate velocity is not sufficient for an appreciable current drive, which induces us to go over to regimes with a sufficient number of 'runaway' electrons. These regimes are achieved at low plasma density. The same density limitation is necessary to avoid RF-power losses at the lower-hybrid resonance, the parametric effects [7, 8] including the domain of  $\omega > 2\omega_{\text{LH}}$  ( $\omega$  is the angular frequency of the generator).

The deuterium plasma parameters satisfying this condition are shown in Fig. 2 as the shaded region. In the case of hydrogen, the density restriction becomes more severe.

### 3. EXPERIMENTAL RESULTS

Measurements have shown that switching on the RF-generator affects the main discharge parameters in the tokamak. This effect depends on the discharge regime, the wave phasing in the waveguides,  $\Delta\Phi$ , and the generator power. Oscillograms of loop voltage,  $U_p$ , and of current,  $I_p$ , in regimes with different initial values of  $I_p$  are shown in Fig. 3. For the regime with  $I_p = 45 \text{ kA}$  (a), the phase difference is  $\Delta\Phi = 120^\circ$ , for  $I_p = 230 \text{ kA}$  (b), it is  $\Delta\Phi = 90^\circ$ . These phase difference values correspond to an excitation of waves that are close in their structure to a wave travelling in the direction of the electron current. As we see in the figure, by switching on the RF-generator the voltage drops and the current rises in the discharge. These changes increase if the plasma column is displaced outwards. The displacement is prescribed in time by the software of the vertical control magnetic field.

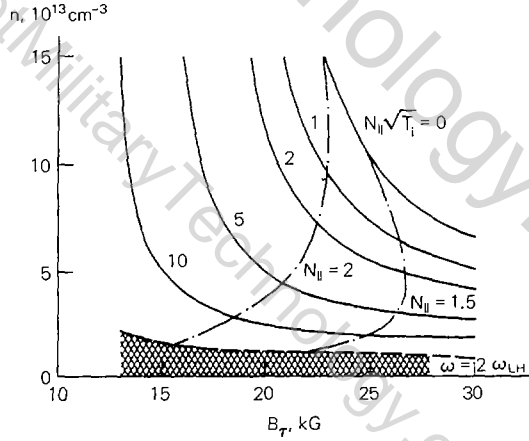


FIG.2. Plasma density versus magnetic field at conversion point for different values of parameter  $N_{\parallel} \sqrt{T_i}$ , where  $T_i$  is measured in keV. Dashed line corresponds to condition  $\omega = 2\omega_{LH}$ . Dot-dashed lines are borders of propagation regions for different  $N_{\parallel}$ . Current drive region is shaded.

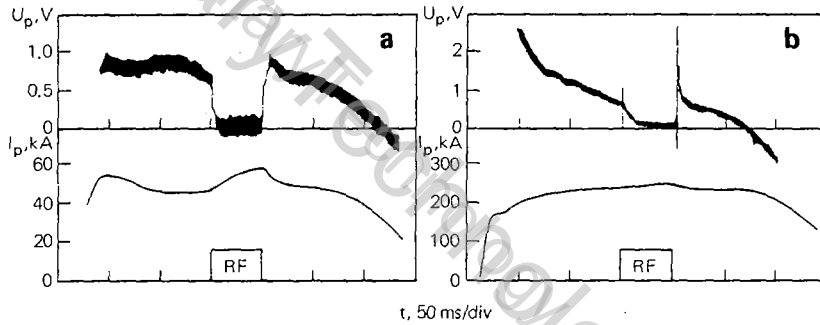


FIG.3. Voltage and current oscillograms for two discharge regimes in T-7. RF-power  $P = 200$  kW, (a)  $\bar{n}_e = 10^{12} \text{ cm}^{-3}$ ; (b)  $\bar{n}_e = 2 \times 10^{12} \text{ cm}^{-3}$ .

Figures 4 to 6 show the dependence of the loop voltage on the phase shift,  $\Delta\Phi$ , the RF-power and the plasma density. The generator power is plotted on the abscissa of Fig. 5. This power is nearly equal to the RF-power introduced into the tokamak chamber because, in the presence of plasma, the fraction of reflected power is negligible, as has been shown by the measurements.

The value of  $\bar{n}_e$  in Fig. 6 is the plasma density average over the tokamak liner diameter. Note that the plasma density rises by 10–30% during the RF-pulse.

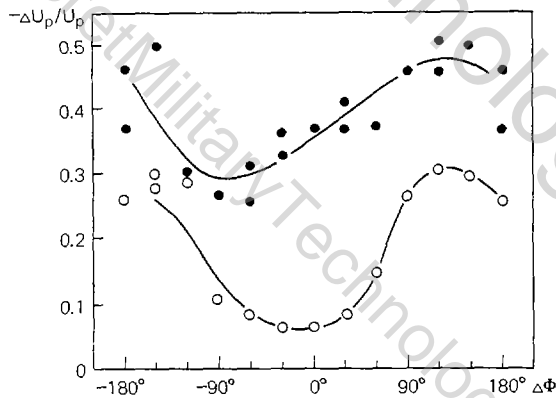


FIG. 4. Relative discharge voltage drop,  $-\Delta U_p/U_p$ , versus phase shift in adjacent grill waveguides for two values of plasma density:  $\bar{n}_e = (2-3) \times 10^{12} \text{ cm}^{-3}$  (●),  $n = (5-6) \times 10^{12} \text{ cm}^{-3}$  (○),  $P = 200 \text{ kW}$ ,  $I_p = 230 \text{ kA}$ .

Signals from the surface-barrier detectors of X-rays are given in Fig. 7.  $X_1$  is a signal from the probe located in the lower vertical diagnostic port with a 0.4-mm-thick Al-foil filter,  $X_2$  is a signal from the probe located in a horizontal diagnostic port with a 0.018-mm-thick Al-foil. In the regimes under study, the signal X consists of a periodic ripple with a period of the order of a few milliseconds. The RF-effect on the signal depends on the phase,  $\Delta\Phi$ . The ripple disappears in the  $\Delta\Phi$  range from  $90^\circ$  to  $180^\circ$ , when the RF-generator is switched on. At other values of  $\Delta\Phi$ , the ripple is sustained, but its period becomes longer. The least effect on the ripple period is observed in the  $\Delta\Phi$  range from  $-90^\circ$  to  $0^\circ$ . The X-ray signal ripple is not accompanied by a change in the discharge voltage.

The results presented are related to macroscopically stable discharge regimes in the tokamak, where helical perturbations of the plasma column recorded by magnetic probes are absent. A number of shots with MHD-activity and peaks on the oscillograms of the discharge voltage (Fig. 8) are also observed.

#### 4. DISCUSSION

The experimental results in T-7 are in agreement with the results of similar experiments made in other devices; they confirm the accepted mechanism of current drive by lower-hybrid waves. The main external indications of the current drive are a rise in the total current and a drop in the voltage of the discharge. In T-7 these changes occur simultaneously, because the primary circuit of the tokamak with respect to the plasma is a source of electromotive force with an internal impedance comparable to the impedance of the plasma column. If we

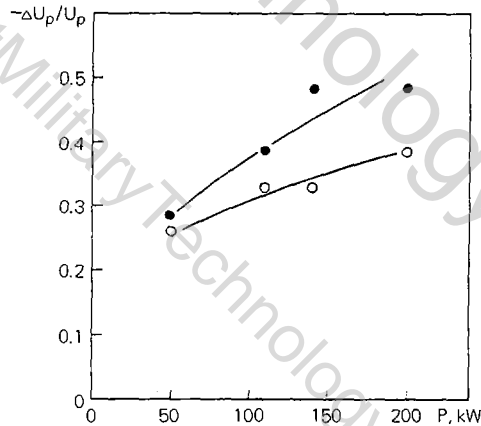


FIG. 5.  $-\Delta U_p/U_p$  versus RF-power,  $P$ , at  $\Delta\Phi = 90^\circ$  for two values of plasma density:  $\bar{n}_e = 1.5 \times 10^{12} \text{ cm}^{-3}$  (●),  $\bar{n}_e = 3.5 \times 10^{12} \text{ cm}^{-3}$  (○),  $I_p = 230 \text{ kA}$ .

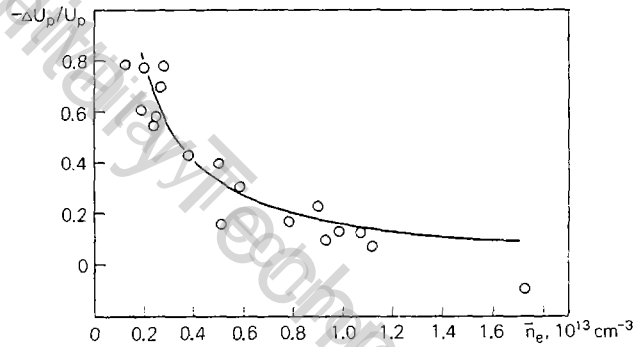


FIG. 6.  $-\Delta U_p/U_p$  versus  $\bar{n}_e$  at  $P = 200 \text{ kW}$ ,  $I_p = 230 \text{ kA}$ .

assume a possible change in the internal inductance of the plasma column when the RF-power is introduced,  $\Delta l_i < l_i$ , we may state that, for the case of Fig. 3a, the current drive produced will exceed the initial discharge current; for the case of Fig. 3b, the two currents will be comparable.

A specific feature of the dependence of  $-\Delta U_p/U_p$  on  $\Delta\Phi$  is a displacement of the maximum from  $\Delta\Phi = 90^\circ$  towards larger angles. An increase in  $\Delta\Phi$  from  $90^\circ$  to  $180^\circ$  corresponds to an increasing wave modulation and to a transition from a travelling to a standing wave. The displacement of the maximum mentioned can be explained by allowing for an asymmetry in the distribution function of the longitudinal electron velocities produced by the electric field before switching on the RF-generator. A calculation shows that the asymmetry in the initial distribu-

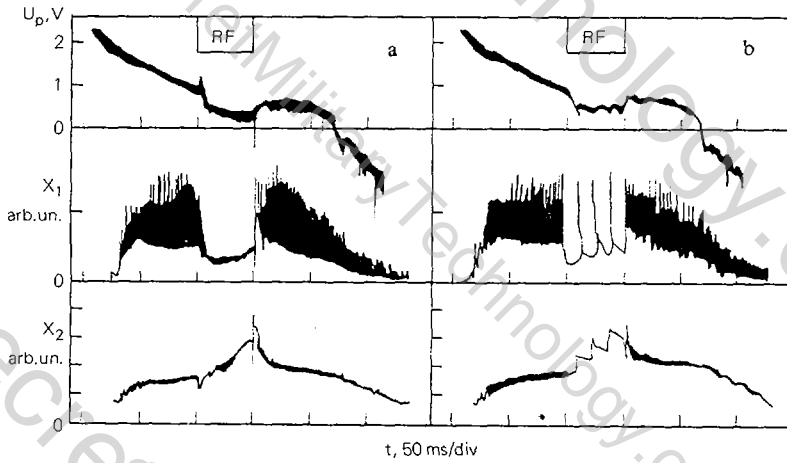


FIG. 7. Oscillograms of discharge voltage and signals from two X-ray probes at (a)  $\Delta\Phi = 90^\circ$  and (b)  $\Delta\Phi = -150^\circ$ .

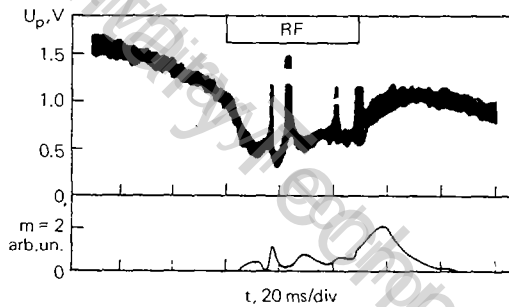


FIG. 8. Oscillograms of discharge voltage and  $m = 2$  mode amplitude in T-7 unstable regime,  $I_p = 230$  kA.

tion function for the electrons results in a substantial current drive, even for a standing wave. The calculation is done with a 2-D Fokker-Planck code which includes terms describing the longitudinal electric field and the diffusion of electrons in RF-oscillations. Collisions are described in accordance with Ref. [9]. As an example, the following conditions are prescribed:  $n_e = 5 \times 10^{12} \text{ cm}^{-3}$ ,  $T_e = 500 \text{ eV}$ ,  $Z_{\text{eff}} = 1$ , energy life-time for electrons  $\tau_{Ee} = 2.5 \text{ ms}$ , loop voltage  $U_p = 1 \text{ V}$ . A level curve of the distribution function for electrons,  $f(v_{\parallel}, v_{\perp})$ , in a quasi-steady state, when only a DC electric field is applied, is shown in Fig. 9a. A level curve after switching on the RF-power, with a specific power of  $\tilde{p} = 0.5 \text{ W} \cdot \text{cm}^{-1}$ , is shown in Fig. 9b. The wave spectrum shown in the same

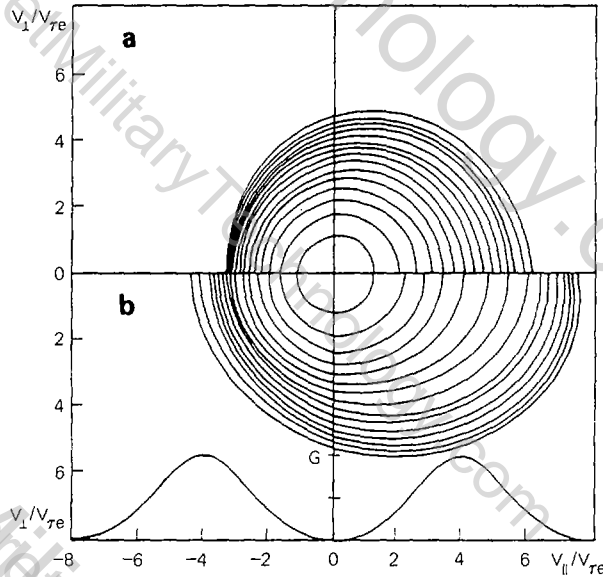


FIG.9. Level lines of  $f_e(v_{\parallel}, v_{\perp})$  electron distribution function: a) electric field only, b) RF-power on. Spectral density of RF-power,  $G(v_{\parallel})$ , is shown below.

figure is chosen to be symmetric with respect to  $v_{\parallel} = 0$  in order to emphasize the role of an initial asymmetry in the electron distribution function.

The distribution is deformed in the direction of the electron current, in spite of the symmetry of the excitation spectrum. The ratio between the diffusion coefficient due to waves,  $D_w$ , and that due to collisions,  $D_c$ , at  $v_{\parallel} \sim 4 v_{Te}$  is about 3 ( $D_w = \tilde{p}/m n_{res}$ , where  $n_{res}$  is the number of resonance electrons); therefore, we see a slight plateau region in the distribution function. The increase in the current, with RF-drive, is about 20%, which is in qualitative agreement with the experimental results.

The dependence of  $-\Delta U_p/U_p$  on  $\bar{n}_e$  at  $\bar{n}_e < 10^{13}$  cm coincides with the dependence  $1/n_e$  (solid line) predicted by theory for the efficiency of current drive by lower-hybrid waves.

The behaviour of the X-ray signals indicates the development of a fan-like instability in the regimes being studied with low plasma density [10–12]. The RF-effect on these signals needs further study. This can be explained by the fact that the dynamics of the fan-like instability is sensitive to the shape of the distribution function for electrons, in the range of some tens of keV. The lower-hybrid wave mainly affects the very energetic part of the distribution function [13].

In conclusion, we should like to note that the transition to current-drive experiments in regimes with more dense plasmas seems to demand an increase in

generator frequency and use of antennas with greater longitudinal wave modulation.

### ACKNOWLEDGEMENTS

The authors wish to thank the T-7 engineering team headed by A.I. Nikonorov and the cryogenics service led by A. Volobuev for support of the experiments, as well as Drs V.V. Parail and G.V. Pereverzev for useful discussions.

### REFERENCES

- [1] FISCH, N., Phys. Rev. Lett. **41** (1978) 873.
- [2] KLIMA, R., LONGINOV, A.B., Fiz. Plazmy **5** (1979) 496.
- [3] YAMAMOTO, T., et al., Phys. Rev. Lett. **45** (1980) 716.
- [4] LUCKHARDT, S.C., et al., Phys. Rev. Lett. **48** (1982) 152.
- [5] STEVENS, J., PLT GROUP, PPPL, in Heating in Toroidal Plasmas (Proc. 3rd Joint Varenna-Grenoble Int. Symp., Grenoble, March 1982) paper D2.
- [6] IVANOV, D.P., et al., At. Ehnerg. **45** (1978) 171.
- [7] PORKOLAB, M., Phys. Fluids **20** (1977) 2058.
- [8] PORKOLAB, M., et al., Phys. Rev. Lett. **38** (1977) 230.
- [9] KILLEEN, J., et al., Methods Comput. Phys. **16** (1976) 389.
- [10] ALIKAEV, V.V., et al., Zh. Tekh. Fiz. **45** (1975) 515.
- [11] PARAIL, V.V., POGUTSE, O.P., Fiz. Plazmy **2** (1976) 228.
- [12] SOKOLOV, Yu. A., Preprint IA Eh-3101, Moscow (1979).
- [13] ALIKAEV, V.V., et al., Fiz. Plazmy **7** (1981) 1282.

### DISCUSSION

B. COPPI: The streaming parameter characteristic of these experiments is relatively large. Have you seen all the experimental features of the slide-away regime before RF injection?

V.S. STRELKOV: It is true that the ratio of current velocity to thermal velocity is high in this regime, but the characteristics of these regimes are unlike those of the so-called runaway regimes.



## FUSION REACTOR PLASMAS WITH POLARIZED NUCLEI

R.M. KULSRUD, H.P. FURTH, E.J. VALEO,  
R.V. BUDNY, D.L. JASSBY, B.J. MICKLICH,  
D.E. POST

Plasma Physics Laboratory,  
Princeton University,  
Princeton, New Jersey

M. GOLDHABER  
Brookhaven National Laboratory,  
Upton, New York

W. HAPPER  
Princeton University,  
Princeton, New Jersey

United States of America

### Abstract

#### FUSION REACTOR PLASMAS WITH POLARIZED NUCLEI.

New techniques of bulk polarization could be used to fuel a reactor with polarized hydrogenic atoms so as to form a plasma of polarized nuclei. Theoretical calculations indicate that, once the nuclei of the plasma are polarized in some preferred state, they can maintain this state with a probability near 100% during their lifetime in the reactor, including possible recycling. There are a number of practical advantages to be gained from the use of polarized plasma in a fusion reactor. The nuclear reaction rates can be increased or decreased and/or the direction of emission of the reaction products can be controlled. The D-T reaction rate can be enhanced by as much as 50%, with the reaction products emitted perpendicular to the magnetic field. Alternatively, it is possible to direct the reaction products primarily along the field, with no enhancement. In the case of the D-D reaction, the theoretical predictions are somewhat less certain. Enhancement of the reaction rate by a factor of 1.5 to 2.5 is to be expected. In a different polarization state, suppression of D-D reactions may be feasible — a possibility that would be of interest for a “neutron-free” D-<sup>3</sup>He reactor. A quantitative discussion of the relevant nuclear physics as well as of the various mechanisms producing depolarization is given.

#### INTRODUCTION

A recent note [1] proposed that the performance of thermonuclear reactors could be improved by injecting fuel

atoms whose nuclear spins are polarized relative to a plasma-confining magnetic field. This injection may be accomplished by gas puffing or by energetic neutral beams. It was pointed out that the nuclei would remain polarized after ionization, even in the extreme environment of the thermonuclear plasma, and even after a number of recycling passes to the wall and back. A number of practical advantages were cited: Nuclear reaction rates could be increased or decreased and/or the direction of emission of the reaction products e.g., alpha particles and neutrons could be modified. If a practical technology of fuel injection can be developed, as now seems likely, the use of polarized fuel will provide fusion reactor engineers with a powerful tool.

In this paper we present theoretical substantiation of the conclusions of Ref. 1, along with some new results. We first review the modifications to be expected in the nuclear reactions D-T, D-D, and D-He<sup>3</sup>. We then discuss the degree of polarization actually to be expected in a reactor and show that it may be close enough to 100% to yield the desired practical benefits.

## I. NUCLEAR REACTIONS

### The DT Reaction

Assume we have a partially polarized plasma. Let  $m_s$  denote the component of nuclear spin along  $\underline{B}$  and let  $t_+$  and  $t_-$  denote the fraction of tritons with  $m_s = 1/2$  and  $-1/2$  respectively. Let the fraction of deuterons with  $m_s = 1, 0, -1$  be  $d_+, d_0$  and  $d_-$ . Let  $a \equiv d_+ t_+ + d_- t_-$ ,  $b \equiv d_0$ ,  $c \equiv d_+ t_- + d_- t_+$ . Let the probability that the D-T reaction goes through the resonant  $3/2^+$  state of He<sup>5</sup> be  $f$  where  $f \sim .95$ . Then a simple application of quantum theory shows that the average total nuclear cross-section is

$$\sigma = \left(a + \frac{2}{3} b + \frac{1}{3} c\right) f \sigma_0 + \left(\frac{2}{3} b + \frac{4}{3} c\right) (1 - f) \sigma_0 \quad (1)$$

while the differential cross-section for alpha particles to be emitted in solid angle  $d\Omega$  (and neutrons in the opposite direction) is

$$\frac{d\sigma}{d\Omega} = \frac{f \sigma_0}{2\pi} \left[ \frac{3}{4} a \sin^2 \theta + \left(\frac{2}{3} b + \frac{1}{3} c\right) \left(\frac{4/f - 3 + 3 \cos^2 \theta}{4}\right) \right] \quad (2)$$

where  $\theta$  is the pitch angle of the velocity vector of the alpha particle. In terms of these equations it is easy to predict the dependence of the nuclear reaction rate on the state of polarization as well as the angular distribution of the emitted alpha particles.

If the nuclei are unpolarized, then  $a = b = c = 1/3$ ,  $\sigma = 2/3 \sigma_0$ , and the differential cross-section is isotropic. If on the other hand the nuclei are nearly polarized along  $\underline{B}$ , then  $d_+ = 1-\epsilon$ ,  $d_0 = \epsilon$ ,  $d_- = 0$ ,  $t_+ = 1-\epsilon$ ,  $t_- = \epsilon$ , where  $\epsilon \ll 1$  represents the lack of total polarization,  $\sigma = \sigma_0 (f - \epsilon/3)$  and  $d\sigma/d\Omega$  is proportional to  $\sin^2\theta + (4\epsilon/9)(1 + \cos^2\theta)$  valid to first order in  $\epsilon$  and  $1-f$ . Thus, the corresponding reaction rate is almost 50% faster and the emission of neutrons and alpha particles is nearly perpendicular to  $\underline{B}$ . An incidental advantage of this mode of polarization is that neutrons will pass through the surrounding walls more nearly perpendicularly than in the unpolarized case, with correspondingly reduced first-wall damage and heating. In the particular case of a mirror machine, the neutron flux to the end plugs can be reduced and the fraction of alpha particles trapped in the mirror field can be enhanced. In an alternate polarization mode  $d_0 = 1-\epsilon$ , where the deuterons are nearly transverse to  $\underline{B}$ , there is no enhancement in  $\sigma$ , but the angular distribution of alpha particles and neutrons is approximately  $(9\epsilon/2) \sin^2\theta + 4(1-f) + (1 + 3 \cos^2\theta)$  so that they are emitted preferentially along  $\underline{B}$ . This mode of polarization may be of particular usefulness in a tokamak reactor, where fusion energy multiplication is less critical than in a mirror machine, so that the enhancement in  $\sigma$  is less important. Parallel emitted alpha particles are easier to contain in a tokamak reactor and make a more favorable contribution to MHD stability. Reduction of the neutron flux striking the small-major-radius side simplifies tokamak blanket design. (A calculation for a tokamak of aspect ratio 3 and square minor cross-section shows that the resulting flux of neutrons to the small radius side of the blanket is 70% of that for an unpolarized reactor). Which mode of polarization is most advantageous is thus seen to depend on the specific practical considerations peculiar to each reactor design.

#### D-D Reactions

The results to be expected for the D-D reaction are more controversial. For the neutron reaction  $D(d,p)He^3$  the various matrix elements for the different spin states have been evaluated by Ad'yasevich and Fomenko [2] from analysis of data

based on a polarized beam of deuterons incident on an unpolarized target.

They found that the most important matrix elements for the reaction  $D(d,p) \text{He}^3$  were from the  $S=0, \ell=0, J=0$ , initial state,  $\alpha_0$ , and from the  $S=1, \ell=1, J=1$  state,  $\alpha_1$ . The matrix elements from all the  $S=2$  states which we denote by  $\delta$  were much smaller. Consider the interaction of two D populations, as for the case of a beam and a target plasma of deuterons, and let  $A_{ij}$  be the fraction of deuteron pairs with  $m_{S1} = i$ ,  $m_{S2} = j$ . Then keeping only these matrix elements, we have for the total average cross-section:

$$\begin{aligned} \frac{2\sigma}{\pi\lambda} = & 2(A_{11} + A_{-1,-1})\delta^2 + A_{00}\left(\frac{4}{3}\delta^2 + \frac{2}{3}|\alpha_0|^2\right) \\ & + (A_{10} + A_{01} + A_{-10} + A_{0,-1})\left(\delta^2 + \frac{3}{2}|\alpha_1|^2\left[\cos^2\theta_0 + \frac{1}{2}\sin^2\theta_0\right]\right) \\ & + (A_{1,-1} + A_{-1,1})\left(\frac{\delta^2}{3} + \frac{2}{3}|\alpha_0|^2 + \frac{3}{2}|\alpha_1|^2\sin^2\theta_0\right) \end{aligned} \quad (3)$$

where  $\theta_0$  is the direction of relative motion before the reaction and  $|\delta|^2 \approx .01$  represents the contribution of the quintuplet state  $S=2$ .

In terms of this we may derive the enhancements of the reaction rate  $E_{ij}$  for  $A_{ij} = 1$  and all other A's zero, relative to the unpolarized case  $A_{ij} = 1/9$ :

$$\begin{aligned} E_{11} = \frac{9\delta^2}{\Delta}, \quad E_{10} = [4.5\delta^2 + 6.75|\alpha_1|^2\left(\frac{1}{2}\sin^2\theta_0\right)]/\Delta \\ E_{1,-1} = (3|\alpha_0|^2 + 6.75|\alpha_1|^2\sin^2\theta_0 + 4.5\delta^2)/\Delta \\ E_{00} = \frac{3|\alpha_0|^2 + 6\delta^2}{\Delta}, \quad \Delta = |\alpha_0|^2 + 3|\alpha_1|^2 + 5|\delta|^2 \end{aligned} \quad (4)$$

Ad'yasevich and Fomenko estimate  $|\alpha_1|^2/|\alpha_0|^2 = .5$ ,  $\delta^2/|\alpha_0|^2 = .01$  at 290 keV bombarding energy. They extrapolate to other energies by letting  $|\alpha_0|^2$  and  $|\delta|^2$  vary as the penetrability of an S-wave through the Coulomb barrier, and  $|\alpha_1|^2$  as the penetrability of a P wave. Table I gives these enhancements at various bombarding energies. It is seen that enhancements in excess of 2 are obtained for  $E_{00}$  and  $E_{1,-1}$  at low energies. Suppressions of order 5 to 10 are obtained for

TABLE I. D-D ENHANCEMENTS

E	50	100	300
$\delta^2/ \alpha_0 ^2$	.01	.01	.01
$ \alpha_1 ^2/ \alpha_0 ^2$	.10	.20	.50
$E_{11}$	.067	.055	.035
$E_{00}$	2.27	1.85	1.20
$E_{10}$	.53 $-.25 \sin^2 \theta_0$	.85 $-.40 \sin^2 \theta_0$	1.34 $-.66 \sin^2 \theta_0$
$E_{1-1}$	2.25 + .5 $\sin^2 \theta_0$	1.84 + .81 $\sin^2 \theta_0$	1.19 $+1.32 \sin^2 \theta_0$

$E_{11}$ . The cases (1,1) and (0,0) apply to reactions in thermal plasma while (10) and (1,-1) apply only to beam-plasma reactions. For the (1,1) case the large suppression would provide an easy test of the polarization concept.

Unfortunately, the relative size of the matrix elements is not at all certain. Hale and Dodder [3] found on analyzing other data that  $\delta^2/|\alpha_0|^2 \approx 1$ , which vitiates the results of Table I. Suppression is small and the maximum enhancement is only 1.7. However, the discrepancy may be due to the fact that the data they analyze is from a thick target. Such data overemphasizes  $\delta^2$ .

### D-He<sup>3</sup> Reactions

The D-He<sup>3</sup> reaction is identical to the D-T reaction with different values of  $\sigma_0$  and  $f$ . It also can be enhanced by 50%. However, if the D are all polarized with  $m_s = 1$ , the D-D reaction is suppressed, according to Table I, so a D-He<sup>3</sup> reactor would be free of neutrons. (This conclusion may not be valid if the Hale-Dodder[3] results are the correct ones.)

## II. POLARIZATION OF THE PLASMA

We now summarize the four processes that could depolarize the nuclei once they are polarized. These processes can operate on the nuclei while they are in the reactor, or during the injection phase, or in a tokamak during the recycling

phase. These four are (a) inhomogeneous fields, (b) collisions, (c) magnetic fluctuations, and (d) the atomic processes: recombination, charge-exchange and ionization. It will appear that the depolarization rates of all these processes are very small.

#### A. Inhomogeneous Fields

As a nucleus moves through a static magnetic field whose direction is changing in space, it can be depolarized if the rate of change of direction is too fast. If the nucleus is nearly polarized in a single spin state (say  $m_s = 1$  for the deuteron), then the change of amplitude of the adjacent state  $\beta$  is given up to a phase factor by

$$\Delta\beta = - e^{i\phi} \left(\frac{I}{2}\right)^{1/2} \int_0^\phi e^{-i\phi'} \frac{d\theta}{d\phi'} d\phi' \quad (5)$$

where  $\phi = \int_0^t \omega_i(t) dt$  is the precession phase,  $\theta$  is the angle of the direction of the field relative to some fixed direction in space, and  $\omega_i(t)$  is the local precession frequency of nucleon  $i$  (D or T). If the magnetic moment of the nucleus is  $g$  nuclear magnetons (a nuclear magneton is  $e\hbar/2m_p c$ ), then  $\omega_i = g_i eB / (2m_p c I) \approx (g_i / I) \Omega_2$ , where  $\Omega_2$  is the deuteron gyration frequency and  $I$  the spin of the nucleus ( $\omega = .86\Omega_2$  for deuterons and  $5.94 \Omega_2$  for tritons). Equation (5) was derived assuming that  $B$  is always in a single plane, but it gives essentially the correct result even for a 3-D field if account is taken of the fact that it is only the left circularly polarized component of the change in  $B$  as seen by the moving nucleon that produces depolarization.

Examination of Eq. (5) shows that the change in  $\beta$  is given essentially by that harmonic of  $\theta(t)$  at  $(g/I) \Omega_2$ . Thus, if  $v/\Omega \approx 1$  cm and the direction of the field varies by  $\delta\theta$  over a typical scale  $\lambda = 10^2$  cm, then the change in  $\beta$  is of order  $\delta\theta \exp(-100)$  and is quite negligible. Equation (5) also applies to the nucleus when it is in the atomic state and being injected into the reactor. For example, it is possible to design a field variation in a neutral beam injector which makes  $(\Delta\beta)^2$  very small ( $< .1\%$ ) during the passage from the neutralizer cell (where  $B$  is necessarily along the direction of acceleration) into the plasma-confinement region of the reactor.

#### B. Collisions

For reactor plasma parameters, nuclei suffer many binary Coulomb collisions per fusion reaction. During a collision, with a moving charge, rapid fluctuating magnetic fields will

TABLE II. CROSS-SECTIONS FOR COLLISIONAL DEPOLARIZATION

$$\left[ r_p = \frac{e^2}{m c^2}, \omega_p^2 = \frac{4\pi n e^2}{m}, p_o = \frac{e^2}{T}, \chi = \frac{\lambda}{mv} \right]$$

Depolarization Mechanism	Cross-Section	For D (cm <sup>2</sup> )	For T (cm <sup>2</sup> )
<u>by electrons</u>			
spin-orbit	$4\pi g^2 r_p^2 \ln(c/\omega_p \chi)/3$	$1.45 \times 10^{-30}$	$1.76 \times 10^{-29}$
spin-spin	$(11/9)\pi g^2 r_p^2$	$.73 \times 10^{-31}$	$.81 \times 10^{-30}$
quadrupole		$7.3 \times 10^{-38}$	
<u>by deuterons</u>			
spin-orbit	$(\pi/3)g^2 r_p^2 \ln(c/\omega_p p_o)$	$3.7 \times 10^{-31}$	$4.4 \times 10^{-30}$
spin-spin	$(\pi/3)g^2 g_2^2 r_p^2$	$1.1 \times 10^{-32}$	$1.3 \times 10^{-31}$
quadrupole		$2.3 \times 10^{-31}$	
<u>by tritons</u>			
spin-orbit	$(\pi/3)g^2 r_p^2 \ln(c/\omega_p p_o)$	$3.7 \times 10^{-31}$	$4.4 \times 10^{-30}$
spin-spin	$(\pi/3)g_3^2 g^2 r_p^2$	$1.2 \times 10^{-31}$	$1.6 \times 10^{-30}$
quadrupole		$2.3 \times 10^{-31}$	

be produced at the nuclei, which can produce depolarization (this is denoted as spin-orbit coupling). In addition, the interaction of the magnetic moments of the colliding particles can produce spin exchange and depolarization (spin-spin coupling). Finally, because the deuteron has a quadrupole electric moment, it can be depolarized by direct electric interaction. However, because of the very short duration of the collisions and the relative weakness of the interactions, the actual amount of depolarization is very small in practice. To quantify this, let us introduce an effective cross-section  $\sigma_i$  for depolarization by each process. Each collision produces a randomly phased change in  $\beta$ , the amplitude of the undesired state. These  $\Delta\beta$  add incoherently. We may write

$$\frac{d(\Delta\beta)^2}{dt} = \sum_i n v \sigma_i \quad (6)$$

where  $\sigma_i$  is the contribution to the cross-section of each process. Values of  $\sigma_i$  are given in Table II.

From inspection of the table we see that the cross sections are very small; those of electrons being comparable to those of ions. Because of the factor  $v$  in Eq. (6), depolarization by electrons predominates. Adding up all the  $\sigma_i$ 's for electrons, we find the total depolarization cross-section is  $1.7 \times 10^{-29} \text{ cm}^2$  for tritons, and  $.7 \times 10^{-30} \text{ cm}^2$  for D nuclei in the  $m_s = \pm 1$  states. (For deuterons in the  $m_s = 0$ , the depolarization cross-section must be doubled since there are two adjacent states to depolarize to.)

The corresponding rates for a reactor with  $n_e = 2 \times 10^{14} \text{ cm}^{-3}$  are  $d(\Delta\beta)^2/dt = 2 \times 10^{-5} \text{ s}^{-1}$  for T, and  $1.75 \times 10^{-6} \text{ s}^{-1}$  for D in the  $m_s = 0$  state and  $.9 \times 10^{-6} \text{ s}^{-1}$  for D in the  $m_s = \pm 1$  states. During a 20-second residence time, a triton will be depolarized by .04% and a deuteron by .004%.

### C. Magnetic fluctuations

According to Eq. (5) any changing magnetic field that the nucleus sees in its frame will produce depolarization. Subsection (A) refers to static externally produced inhomogeneities in the field. Fluctuating currents in the plasma itself are known to produce additional time-dependent fluctuations that the nuclei will see, and they will produce depolarization. If these fluctuations are small, one can evaluate Eq. (5) statistically to obtain the result of many incoherent fluctuations:

$$\frac{d(\Delta\beta)^2}{dt} = \frac{g^2 e^2 I_o(\omega_i)}{4m_p^2 c^2} \quad (7)$$

where  $I_o(\omega_i)$  is the intensity at the precession frequency of left circularly polarized magnetic fluctuations seen by the moving spiralling nucleus,  $(\delta B)^2 = \int I_o(\omega) d\omega$ . One may easily translate this to the intensity spectrum of waves in the laboratory frame  $I(\omega, k_z, k_\perp)$ :

$$\frac{d(\Delta\beta)^2}{dt} = \sum_n \left( \frac{g_i}{2m_p c} \right)^2 J_n^2(k_\perp \rho_\perp) I(\omega_i - k_z v_z - n\Omega_i, k_z, k_\perp) \quad (8)$$

where  $z$  refers to the direction along the field. The argument of the Bessel function is  $k_\perp \rho_\perp \equiv k_\perp v_\perp / \Omega_i$  as usual.

To determine depolarization by magnetic fluctuations from Eq. (8), it is necessary to estimate the fluctuation

intensity. Depolarization by thermal fluctuations can be shown to be extremely small; the main danger is from fluctuations produced by instabilities, for which there is no simple way of predicting the mean level of intensity. For a triton, the resonant frequency for  $n=0$  is  $\omega_3 \approx 6\Omega_2$ . Because parallel propagating waves at this frequency are whistler waves, which are right-circular polarized, it is only the left-circular polarized component of off-angle propagating whistler waves that can produce depolarization. Making use of Eq. (8) we find  $d(\Delta\beta)^2/dt = .45 (\delta B)^2 (\omega_3/\Delta\omega) S^{-1}$  where  $\Delta\omega$  is the band over which  $(\delta B)^2$  is calculated ( $\delta B \approx .05g$ ,  $\Delta\omega \approx \omega_3$  would produce 1% depolarization in 20s).

For depolarization of deuterons with  $n=0$ , one finds  $d(\Delta\beta)^2/dt = 0.1(\delta B)^2 (\omega_2/\Delta\omega)$  (so that  $\delta B \approx .07g$ ,  $\Delta\omega \approx \omega_2$  would produce 1% depolarization in 20 s). For deuterons  $\omega_2 = .86\Omega_2$ , so this frequency is near the ion cyclotron wave band. However, in a plasma consisting of 50% D, 50% T, the waves cut off below  $.833\Omega_2$ ; thus the dangerous waves are relatively fast and their wave lengths have to be rather large. In an inhomogenous field, such as that of a tokamak, the wavelengths may be too large to fit into a localized region where  $\omega_2$  is sufficiently constant to cause an interaction at  $n=0$ .

It might be suspected that the anisotropies generated in the alpha-particle velocity distributions as displayed in Eq. (2) could generate instabilities. Again, it is found that only frequencies very close to cutoff,  $.833\Omega_2$ , can resonate with the alpha particles of sufficiently high energy to be anisotropic. Such waves are also very long. Further, if the polarization mode is chosen so that alpha particles are emitted predominantly along B, the alpha distribution is such as to suppress rather than to amplify these waves.

Finally, one must consider  $n=-1$  in Eq. (8). These waves are at a frequency  $-.14\Omega_2$  and so they are Alfvén waves. If  $k_\perp \rho_1$  is small, the Bessel-function factor greatly reduces their depolarization efficiency. If  $k_\perp \rho_1$  is large, they are subject to substantial ion cyclotron damping and are not likely to reach a large amplitude. In any event, this frequency is considerably larger than drift-wave frequencies, so there is no apparent reason for amplification.

In summary, no specific instability mechanism has been identified thus far that appears to be dangerous to maintenance of adequate polarization. Of course, any heating by externally driven waves, such as ion-cyclotron heating,

must be planned with particular caution if polarization is to be maintained.

#### D. Ionization, Recombination and Charge Exchange

Atomic processes are relatively unimportant while the nucleus is in the hot interior of the reactor. However, during the time between polarization of the nucleus as a neutral atom outside the reactor plasma and its injection into the reactor, either by gas puffing or as an accelerated neutral, several atomic processes may be expected to occur. Further, depending on the particular reactor design, the nucleus may leave the reactor plasma, recombine, and reenter as many as twenty times before being pumped away. If, during this recycling process, a nucleus has a substantial probability of being depolarized, the general level of polarization will be reduced by dilution.

The ionization process is fast enough so that there is little chance for a change in polarization. During recombination or charge-exchange, the bare nucleus will pick up an electron whose state of polarization is either parallel to the nucleus or antiparallel. If it is parallel, there will be no change in polarization. If it is antiparallel, the resulting atomic state will be a superposition of two states, one with the nuclear polarization unchanged and the electron spin opposite to it and a second state of amplitude  $\epsilon_0 = B_C/2B_0$  with the spins exchanged.  $B_C$  is the so-called critical field at which the Zeeman splitting equals the hyperfine splitting due to the interaction of the magnetic moments of the nucleus and the electron in the ground state. ( $B_C \approx 300$  gauss for deuterium and  $10^3$  gauss for tritium).  $B_0$  is the strength of the field in which the recombination occurs. When the atom is reionized the chance of an increase in depolarization of the nucleus is represented by  $\epsilon_0^2$ . Thus, for an arbitrary direction of electron spin we get  $\Delta\beta^2 = 1/2 \epsilon_0^2 = B_C^2/(8B_0^2)$  per recombination event.

In mirror machines, recycling is expected to be unimportant, but in toroidal reactor design it is convenient to let the nuclei recycle about twenty times. If a nucleus goes to the wall, recombines on the surface, and then reenters the plasma twenty times, one can estimate the total depolarization. Assuming a 50 kilogauss field at the wall each deuteron suffers a depolarization of  $.5(300/10^5)^2 \approx .5 \times 10^{-5}$  per recombination or a total depolarization of  $10^{-4} = .01\%$ . For tritons the total figure is  $.1\%$ . The most dangerous process that can occur is that the nuclei embed

themselves in a metal surface. The depolarization relaxation time is then very short (10 ms - 100 ms), so that the depolarization during 100 ms would be 100%. If the surfaces that bound the hot plasma are made of graphite, however, the best estimate for the relaxation time is 100 s [4], so that the depolarization during 100 ms is .1%. These considerations would tend to reinforce the attractiveness of graphite as the optimal material for plasma-contact surfaces.

### III. CONCLUSION

While there are many processes that can reduce the polarization of nuclei in a plasma, our initial studies of these processes indicate they may all be small enough so that polarization in a reactor may be maintainable at close to one hundred percent. It appears that taking account of nuclear spins could lead to fundamental improvements in performance of nuclear fusion reactors.

#### Acknowledgment

This work was supported by the United States Department of Energy, Contract Nos. DE-AC02-76-CHO-3073 and DE-AC02-76-CHO-0016. B.J. Micklich was supported by a Fannie and John Hertz Fellowship.

### REFERENCES

- [1] KULSRUD, R.M., FURTH, H.P., VALEO, E.J., GOLDHABER, M., Princeton Univ., Plasma Phys. Lab. Rep. PPPL-1912 (1982), submitted to Phys. Rev. Lett.
- [2] AD'YASEVICH, B.P., FOMENKO, D.E., Sov. J. Nucl. Phys. 9 (1969) 167.
- [3] HALE, G., DODDER, D., "Few Body Systems and Nuclear Forces", Lecture Notes in Physics, Vol. 2, Springer Verlag (1978) 523; also private communication.
- [4] CARVER, G.P., Phys. Rev. B 2 (1970) 2284.

### DISCUSSION

C.C. BAKER: The neutron flux at the first wall is made up of primary and scattered neutrons, the latter usually being the larger component; thus the effect of reducing the flux on the inside of a torus will probably not be large. What effect will surface processes in recycling have on polarized particles?

R.M. KULSRUD: Recombination on the wall surface leads to very little depolarization (according to theory). However, embedding of the nuclei in the wall can be serious if the wall is metallic. If the wall is of graphite, experiments

indicate that, for residence times of the nuclei in the wall of the order of 100 ms, the depolarization is quite small.

R.S. POST: Is  $\delta B/B$  small enough in the presence of RF heating or neutral beam heating to allow the nuclei to maintain polarization?

R.M. KULSRUD: There is no direct evidence on the magnitude of  $\delta B/B$  for fluctuation resonant with the precession frequency, in the absence of RF heating, but with neutral beams. My impression is that because of ion-cyclotron damping they may not be serious. At the deuteron-cyclotron frequency RF heating is potentially a strong mechanism for depolarization of deuterons. However, it may be possible to heat at the tritium-cyclotron frequency without depolarization.

M. THUMM: How important is depolarization by spin-flip processes during elastic nuclear scattering of deuterons from tritons in the plasma?

R.M. KULSRUD: A rough estimate indicates that depolarization by magnetic interactions during an elastic nuclear scattering is slight. I would guess that a spin flip by nuclear forces would be equivalent to a nuclear reaction, at least for D-D. However, I cannot be certain about this point.

H.L. BERK: Can you give the enhancement factor for other reactions, such as D-D or D-<sup>3</sup>He?

R.M. KULSRUD: For D-<sup>3</sup>He it is the same as for D-T: 50% gain. The D-D reaction is not well known as to its spin dependence. According to results obtained in the Soviet Union, the gain can be as large as 2.5 and the suppression as great as a factor of ten if the correct polarization is chosen. The Los Alamos group gets 1.7 and virtually no suppression.

## CURVATURE-DRIVEN TRAPPED-PARTICLE MODES IN TANDEM MIRRORS

H.L. BERK\*, M.N. ROSENBLUTH\*

Institute for Fusion Studies,  
University of Texas at Austin,  
Austin, Texas

H.V. WONG\*\*

Fusion Research Center,  
University of Texas at Austin,  
Austin, Texas

T.M. ANTONSEN, Jr.†

Department of Physics and Astronomy,  
University of Maryland,  
College Park, Maryland

D.E. BALDWIN††

Lawrence Livermore National Laboratory,  
Livermore, California

B. LANE§

Massachusetts Institute of Technology,  
Cambridge, Massachusetts

United States of America

### Abstract

#### CURVATURE-DRIVEN TRAPPED-PARTICLE MODES IN TANDEM MIRRORS.

The variational structure of the plasma linear response function is used to demonstrate the relation of magnetohydrodynamic (MHD) and trapped-particle instabilities. Although in most systems, where bending energy stabilizes ballooning modes, trapped-particle instabilities have a low growth rate, in tandem mirrors with thermal barriers the trapped-particle instability growth rate can approach that of MHD instabilities. In addition, the kinetic theory yields stabilizing effects due to the difference in electron and ion orbits and destabilizing effects due to the variation of the  $\vec{E} \times \vec{B}$  drift along a field line.

\* Research sponsored by US Department of Energy Contract No. DE-FG05-80ET-53088.

\*\* Research sponsored by US Department of Energy Contract No. DE-AC05-79ET-53036.

† Research sponsored by US Department of Energy Contract No. DE-AC05-79ET-53044.

†† Research sponsored by US Department of Energy Contract No. W-7405-ENG-48.

§ Research sponsored by US Department of Energy Contract No. DE-AC02-78ET-51013.

## 1. INTRODUCTION

Tandem mirrors are characterized by regions of both "good" and "bad" curvature, which are designed to give, with an appropriate pressure weighting, average MHD stability<sup>[1]</sup>. If the "bad" curvature drive is to contribute to instability, it is necessary to isolate perturbations from the good curvature region. In ideal MHD theory this gives rise to bending energy, which stabilizes the mode if the plasma beta is less than the critical ballooning beta limit. If one then considers perturbations without bending energy, as has been done for trapped-particle modes in tokamaks<sup>[2]</sup>, one takes electrostatic perturbations limited to the bad curvature region and finds instability albeit with a greatly reduced growth rate. Recent concepts in tandem mirror theory<sup>[3]</sup> propose an axi-cell thermal barrier, where a simple mirror is superimposed between the central cell and quadrupole field (the MHD anchor). Further, within the axi-cell, electrostatic potentials are established and distribution functions controlled, so that a small fraction of the particles sample both the central cell and the MHD anchor. In this paper we show that particles trapped in the central cell and axi-cell may then drive a trapped-particle mode, which in some circumstances can give MHD-like growth rates. By increasing the fraction of particles sampling the MHD anchor and central and axi-cells, the growth rate can be either reduced or, as a consequence of spatially varying electric fields, even stabilized (when dissipative effects are ignored). An outline of the derivation, as well as the appropriate stability criteria for the various cases, will be discussed in this paper.

## 2. VARIATIONAL PRINCIPLE

In order to treat this problem we have derived a new variational form for the growth rate  $\gamma$ . The starting point is a slight generalization of the works of Antonsen et al.<sup>[3,4]</sup> where additional finite Larmor radius effects are included. In the eikonal approximation, with the assumption that

$$\beta < 1, \quad \omega_b > \omega > \omega^* > \omega_E, \omega_c, \omega_B$$

( $\beta$  is the conventional plasma beta,  $\omega_b$  the particle bounce time in the central cell,  $\omega$  the mode frequency,  $\omega^*$  the drift frequency,  $\omega_E$  the electric field drift,  $\omega_c$  the curvature drift and  $\omega_B$  the magnetic field drift) a variational expression for  $\gamma^2$  can be obtained in terms of two field components,  $\psi$  and  $\chi$ , which is of the form:

$$\gamma^2 = \frac{\int \frac{d\ell}{B} \left[ -\frac{\partial \rho}{\partial \Phi} \langle \omega^* \omega_c (\chi + \bar{\psi})^2 \rangle - k_{\perp}^2 c^2 (b \cdot \nabla \chi)^2 / 4\pi \right]}{\int \frac{d\ell}{B} \left( -\frac{\partial \rho}{\partial \Phi} \right) \left[ \psi^2 - \bar{\psi}^2 + \left\langle \frac{k_{\perp}^2 v_1^2}{\omega_{c1}^2} \right\rangle (\chi^2 + \psi^2 + 2\chi\bar{\psi}) \right]} \quad (1)$$

with

$$\bar{\alpha} = \oint \frac{d\ell}{v_{\parallel}} \alpha / \oint \frac{d\ell}{v_{\parallel}}$$

$$\langle\langle \alpha \rangle\rangle = \sum_j \int d^3v \, q^2 \left[ \frac{\partial F}{\partial E} + \frac{1}{B} \frac{\partial F}{\partial \mu} \right] \alpha / \sum_j \int d^3v \, q^2 \frac{\partial F}{\partial E}$$

$$\langle \alpha \rangle = \sum_j \int d^3v \, q^2 \frac{\partial F}{\partial E} \alpha / \sum_j \int d^3v \, q^2 \frac{\partial F}{\partial E}$$

$$-\frac{\partial \rho}{\partial \Phi} = - \sum_j \int d^3v \, q^2 \frac{\partial F}{\partial E}$$

and we note that the denominator of Eq. (1) is positive definite.

The eigenmode of the system is found by maximizing  $\gamma^2$  with respect to the functions  $\psi$  and  $\chi$ . If the numerator can be made positive, the eigenfunction will normally have  $\psi \rightarrow 0$  as then the denominator will be  $\mathcal{O}(k_{\perp}^2 \rho_{\perp}^2)$  ( $\rho_{\perp}$  is the ion Larmor radius), ensuring a large value for  $\gamma^2$ . This choice of  $\psi = 0$  (or equivalently,  $E_{\parallel} = 0$ ), yields the conventional MHD theory.

As the tandem mirror is designed so that the numerator will be negative for  $\mathbf{b} \cdot \nabla \chi = 0$ , it is necessary to choose a finite  $\mathbf{b} \cdot \nabla \chi$  to isolate the perturbations from the good curvature region. However, this gives rise to the bending energy which is proportional to  $(\mathbf{b} \cdot \nabla \chi)^2$ , and for  $\beta$  less than the critical beta for ballooning stability, stability is predicted.

To obtain instability below the critical beta, we have to eliminate the bending energy and this can be done by choosing  $\chi = 0$  and finite  $\psi$  in regions of bad curvature. As the denominator is positive definite, this expression will always yield instability. Except for the addition of the FLR term, the resulting variational form is the same as obtained by Rosenbluth<sup>[5]</sup> for the Kadomtsev-Pogutse<sup>[2]</sup> trapped-particle mode. We note that when  $\chi = 0$ , and the ambipolar potential can be ignored, this quadratic form is still valid when  $\omega_E \ll \omega \lesssim \omega^*$ . For tokamaks the denominator is  $\mathcal{O}(1)$ , while only the small fraction of trapped-particles in the bad curvature region effectively contribute to the numerator, so that the resulting expression leads to growth rates much below that predicted for MHD.

Now, for tandem mirrors, quite a different situation exists (see Fig. 1). Most particles in the central cell are confined within that region, while only a minority of the particles sample the quadrupole end cell. Hence the perturbation for which  $\psi$  is constant in the central cell and vanishes in the transition region, as shown in Fig. 1, will cause a cancellation of the  $\psi^2$  and  $\bar{\psi}^2$  terms from those particles trapped in the central cell. Only the FLR term and the contribution from the particles turning in the transition and anchor regions will contribute to the denominator. As the perturbation is both confined to the bad curvature region so that the numerator is

TANDEM MIRROR (AXICELL) SCHEMATIC

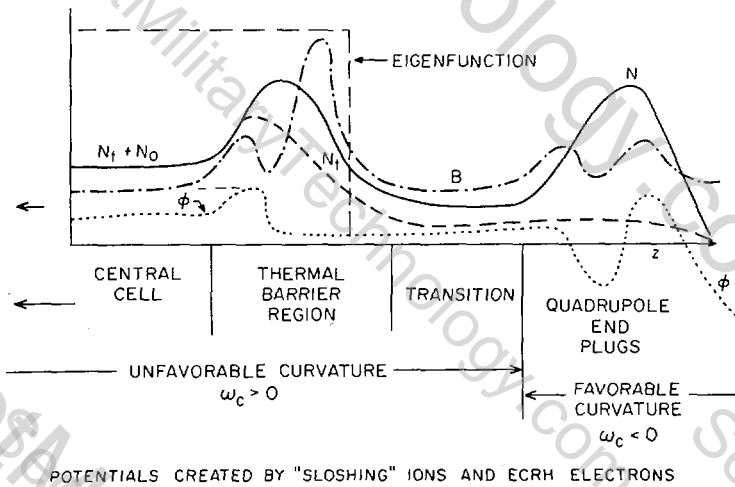


FIG.1. Structure of equilibrium magnetic field, particle density and equilibrium ambipolar potential at the ends of a tandem mirror with a thermal barrier. Also included is the eigenfunction of a destabilizing perturbation.

positive, and annihilates the large elements of the denominator,  $\gamma^2$  is near maximum and hence the perturbation is close to an eigenfunction. Further, the growth rates approach MHD growth rates if

$$P \approx \frac{N_t}{N_o} \frac{L_t}{L_o} \frac{T_o}{T_t} \frac{1}{k_{\perp}^2 \rho_{\perp}^2} \lesssim 1$$

where  $N_t(L_t, T_t)$  and  $N_o(L_o, T_o)$  are the density (length, temperature) of the transition and central region respectively. In particular, the growth rate for  $P \lesssim 1$  is

$$\gamma = \gamma_{MHDC} = \left[ \frac{\int \frac{d\ell}{c} \frac{k_{\perp} \cdot \underline{b} \cdot \nabla (p_{\perp} + p_{\parallel}) (k_{\perp} \cdot \underline{b} \cdot \underline{\kappa})}{\int \frac{d\ell}{c} \frac{\rho k_{\perp}^2}{B^3}} \right]^{1/2} \quad (2)$$

where the integral is only over the central cell and axi-cells,  $\rho$  is the mass density, and  $\kappa$  is the field line curvature.

For  $P \geq 1$ , the growth rate is reduced and the general result obtained from maximizing Eq. (1) is roughly

$$\gamma = \frac{\gamma_{MHDC}}{[1+P]^{1/2}} \quad (3)$$

It has been shown<sup>[6]</sup> that even if  $\gamma > \omega_b$ , and if  $\gamma > \omega^*$ , the growth rate will be even larger than is obtained from maximizing Eq. (1).

### 3. CHARGE SEPARATION STABILIZATION

When the ambipolar potential is considered (a case probably not important in tokamaks, but crucial in tandem mirrors), Eq. (1) needs to be modified when considering  $\omega \approx \omega_* \gg \omega_E$ . Assuming  $\chi = 0$ , a functional dispersion relation of the following form results:

$$\omega^2 A + \omega B + C = 0 \quad (4)$$

where A, B, C are given by

$$A = \int \frac{d\ell}{B} \left( -\frac{\partial \rho}{\partial \Phi} \left[ \langle \psi^2 - \bar{\psi}^2 \rangle + \left\langle \left\langle \frac{k_{\perp}^2 v_{\perp}^2}{2\omega_{ci}^2} \psi^2 \right\rangle \right\rangle \right] \right)$$

$$B = \int \frac{d\ell}{B} \left( -\frac{\partial \rho}{\partial \Phi} \left[ \langle (\omega_* - \omega_D) (\bar{\psi}^2 - \psi^2) \rangle - \langle \bar{\psi}^2 (\omega_* - \omega_D) \frac{k_{\perp}^2 v_{\perp}^2}{2\omega_{ci}^2} \rangle \right] \right)$$

$$C = \int \frac{d\ell}{B} \left( -\frac{\partial \rho}{\partial \Phi} \langle (\omega_* - \bar{\omega}_D) \omega_D \left( 1 - \frac{k_{\perp}^2 v_{\perp}^2}{2\omega_{ci}^2} \right) \bar{\psi}^2 \rangle \right)$$

with  $\omega_D = \omega_E + \omega_c$ . The part of the term B proportional to  $\bar{\psi}^2 - \psi^2$  would vanish if there were no ambipolar potential and if the distribution functions for the electrons and ions were self-similar (as is the case with Maxwellian electrons and ions in conventional tokamak models). However, with an ambipolar potential, the perturbed cross-field displacement will differ for the transiting electrons and ions. The form of the dispersion relation will be:

$$\omega^2(1+P) - \omega\omega_1^*(1+\alpha P) + \gamma_{MHDC}^2 = 0 \quad (5)$$

where  $\alpha \approx 1$  and depends on the detailed structure of the ambipolar potential. For example, present designs allow for reflection of most of the transiting ions near the MHD anchor, and transiting electrons just outside axi-cell, in which case  $\alpha \approx +1$ . Then the conventional FLR term and the new charge-uncovering term add and thus enhance stabilization. The stability condition becomes:

$$P > P_{\text{crit}} \equiv \frac{4}{\alpha^2} \frac{\gamma_{\text{MHDC}}^2}{\omega_i^{*2}} \approx \frac{4}{\alpha^2} \frac{L_c}{L_o} \frac{R_p}{R_c} \quad (6)$$

where  $L_c$  is the length of the bad curvature region and  $R_c^{-1}$  its curvature.

#### 4. RESONANCE AND ELECTRIC FIELD INSTABILITIES

Even when Eq. (6) is satisfied, the system may be susceptible to dissipative and resonant instabilities. For example, the Landau damping drive may be seen from the following structural form. We now assume  $\omega \sim \omega^* \sim \omega_E > \omega_B > \omega_c$  and  $\chi = 0$ . Then the following quadratic form can be derived:

$$4\pi \int_0^\infty \frac{ds}{B} \psi^2 \left\{ \frac{\rho k_\perp^2}{B^2} \left(1 - \frac{\omega_E}{\omega}\right) \left[1 - \frac{(\omega_E + \omega_i^*)}{\omega}\right] + \frac{m^2}{r\omega^2 B R_c} \frac{d}{d\psi} (p_l + p_r)\right\} \\ + 2 \sum_j \frac{4\pi q_j^2}{\omega c^2} \int dE d\nu \left[ \frac{\partial F}{\partial E} + \frac{k \times b \cdot \nabla F}{m_j \omega \omega c_j} \right] \Lambda(\omega, \psi, \psi) \quad (7)$$

where we assumed that the equilibrium and perturbation are even with respect to the midplane (a valid assumption if  $\psi \neq 0$  in the quadrupole MHD anchors) and

$$\Lambda(\omega, \psi, \psi) = \int_0^{t_b} dt' \int_0^{t_b} dt \frac{\partial \psi(t)}{\partial t} \frac{\partial \psi(t')}{\partial t'} \\ \cdot \left[ \sin\left(\int_0^t \Omega dt''\right) \sin\left(\int_0^{t'} \Omega dt''\right) \cot\left(\int_0^{t_b} \Omega dt''\right) - \sin\left(\int_0^{t'} \Omega dt''\right) \cos\left(\int_0^t \Omega dt''\right) \right]$$

$$t_b = \int_0^{s_b} \frac{ds}{|v_\parallel|}, \quad v_\parallel(s_b) = 0, \quad \Omega = \omega - \omega_E, \quad \omega_E = -\frac{ck \cdot \nabla \psi \times b}{B}, \quad \frac{\partial \psi}{\partial t} = v_\parallel \frac{\partial \psi}{\partial s}$$

$$t^> = \max(t, t'), \quad t^< = \min(t, t') \quad (8)$$

With the assumption that  $\Lambda$  is typically large, an approximate solution requires that  $\psi$  be constant in the central cell and axi-cell from say  $-s_R < s < s_R$ , so that the large term from trapped particles may be annihilated. This then leads to the dispersion relation:

$$4\pi \int_0^{s_R} \frac{ds}{B} \left\{ \frac{k_{\perp}^2 \rho}{B^2} \left(1 - \frac{\omega_E}{\omega}\right) \left(1 - \frac{(\omega_E + \omega_1^*)}{\omega}\right) + \frac{4\pi m^2}{r\omega^2 B R_c} \frac{d}{d\psi} (P_{\perp} + P_{\parallel}) \right\} \\ + 2 \int_j \frac{4\pi q_j^2}{\omega c^2} \int dE du \left[ \frac{\partial F}{\partial E} + \frac{k_{\perp} \times b \cdot \nabla F}{m_j \omega \omega_{cj}} \right] \left[ -\sin\left(\int_{t_R}^{t_b} \Omega dt\right) \cos\left(\int_{t_R}^{t_b} \Omega dt\right) \right. \\ \left. + \sin^2\left(\int_{t_R}^{t_b} \Omega dt\right) \cot\left(\int_0^{t_b} \Omega dt\right) \right] = 0 \quad (9)$$

It can be verified that Eq. (9) reduces to Eq. (4) for  $1 \gg \omega_E/\omega$ ,  $\int_0^{t_b} \Omega dt$ . With only the restriction  $\int_{t_R}^{t_b} \Omega dt \approx \epsilon \ll 1$ , Eq. (9) still reduces to Eq. (4), except for an additional dissipative term,  $\mathcal{O}(\epsilon^2)$ , arising from the zeros of  $\cot\left(\int_0^{t_b} \Omega dt\right)$ . Hence, if  $P$  is somewhat larger than  $P_{crit}$ , one of the two stable waves produced when  $P > P_{crit}$  will be destabilized by the dissipative term to give a growth rate  $\gamma \sim \omega_1^{*2}(t_b - t_R)$ . Collisional effects are expected to give a similar destabilization. For  $P \gg P_{crit}$ , further investigation is needed.

Another source of instability can arise from the variation of  $\omega_E$  with position, a possibility also recently noted by Lee et al.<sup>[7]</sup>. We note that Eq. (8) can be unstable for a flute even for  $R_c^{-1} = 0$ . Defining

$$\omega = \bar{\omega}_E + \delta\omega, \quad \omega_E = \bar{\omega}_E + \delta\omega \quad \text{with} \quad \bar{\alpha} = \left( \int_0^{s_R} ds \rho / B^3 \right) / \int_0^{s_R} ds \rho / B^3$$

we find the dispersion relation:

$$\delta\omega^2 - \delta\omega \bar{\omega}_1^* + \frac{\delta\omega_E^2}{\bar{\omega}_E} + \frac{\delta\omega_E \bar{\omega}_1^*}{\bar{\omega}_E} = 0$$

with the instability condition being

$$\frac{\delta\omega_E^2}{\bar{\omega}_E} + \frac{\delta\omega_E \bar{\omega}_1^*}{\bar{\omega}_E} > 4 \bar{\omega}_1^{*2}$$

Clearly, for  $\delta\omega_E^2$  sufficiently large, a flute instability is excited.

## 5. SUMMARY

We have generalized the variational principle for the trapped-particle mode and applied it to the case of tandem mirror stability. This case has several novel features:

1) Due to the potential barriers, the equilibrium may contain regions of very low density in the transition between central cell and stabilizing anchor. In this case we have shown that the growth rate  $\gamma_0$  of electrostatic trapped-particle modes localized away from the anchor may approach that of the unanchored MHD system, even though MHD interchange and ballooning stability criteria are met.

2) However, because of the parallel electric fields in the equilibrium, ion and electron trajectories differ. This leads to a stabilization (effective even for  $m=1$ ) roughly when  $\omega^* > \gamma_0$ , although residual collisional or resonance growth remains.

3) The equilibrium may also be characterized by large variations of the  $E \times B / B^2$  drift frequency. If these are large compared to  $\omega^*$ , a novel type of flute instability is predicted.

## ACKNOWLEDGMENTS

Important discussions with T.K. Fowler, B.G. Logan and L.D. Pearlstein are gratefully acknowledged.

## REFERENCES

- [1] BALDWIN, D.E., LOGAN, B.G., Phys. Rev. Lett. 43 (1979) 1318.
- [2] KADOMTSEV, B.B., POGUTSE, O.P., Nucl. Fusion 11 (1970) 67.
- [3] ANTONSEN, T.M., Jr., LANE, B., RAMOS, J.J., Phys. Fluids 24 (1981) 1465.
- [4] ANTONSEN, T.M., Jr., LEE, Y.C., Phys. Fluids 25 (1982) 132.
- [5] ROSENBLUTH, M.N., Phys. Fluids 11 (1968) 869.
- [6] ROSENBLUTH, M.N., Topics in Plasma Instabilities: Trapped-Particle Modes and MHD, Institute for Fusion Studies, Austin, Texas, Rep. 62 (1982).
- [7] LEE, X.S., CATTO, P.J., AAMODT, R.E., presented at Annual Controlled Fusion Theory Conference, Santa Fe, New Mexico, Paper 1-D-3 (1982).

**Session L**

**STELLARATORS, BUMPY TORI, MULTIPOLES I**

Chairman

H. KAKIHANA

Japan

## PLASMA PROPERTIES AND ION HEATING IN EBT-S\* AND HOT ELECTRON RINGS AT TRW\*\*

F.W. BAITY, L.A. BERRY, L. BIGHEL<sup>†</sup>, J.A. COBBLE,  
R.J. COLCHIN, W.A. DAVIS, H.O. EASON, J.C. GLOWIENKA,  
G.R. HASTE, D.L. HILLIS, S. HIROE, R.K. RICHARDS,  
T. UCKAN, T.L. WHITE, J.B. WILGEN  
Oak Ridge National Laboratory, Oak Ridge, Tennessee

J.D. BARTER, W.F. DiVERGILIO, L.L. LAO, N.H. LAZAR,  
B.H. QUON, T.K. SAMEC, W. WUERKER  
TRW Inc., Redondo Beach, California

F.M. BIENIOSEK, J.H. MULLEN, T.L. OWENS  
McDonnell Douglas Astronautics Corp.,  
St. Louis, Missouri

R.A. DANDL, G.E. GUEST  
AMPC Inc., Encinitas, California

G.A. HALLOCK, L. SOLENSTEN  
Rensselaer Polytechnic Institute,  
Troy, New York

United States of America

### Abstract

#### PLASMA PROPERTIES AND ION HEATING IN EBT-S AND HOT ELECTRON RINGS AT TRW.

The ELMO Bumpy Torus-Scale (EBT-S) has been heated by up to 200 kW of 28-GHz microwave power. Application of this power has greatly extended the operating regime of interest and has allowed scaling over a wider range of plasma temperature and density. Electron temperatures of about 1 keV have been reached at densities of  $0.5-2 \times 10^{18} \text{ m}^{-3}$ . Electron confinement is approximately classical, with  $\tau_E \approx 2-5$  ms. Impurity densities are low, and impurity radiation represents a negligible power loss. Ion heating has been observed with RF in the range 15-50 MHz. High- $\beta$  electron rings provide MHD stability to EBT-S. Measured values of the energy loss agree with calculated values to within a factor of 4, which is within the combined error limits of the calculations and other observations. Multiple-frequency ring

\* Research sponsored by the Office of Fusion Energy, US Department of Energy, under contract W-7405-eng-26 with the Union Carbide Corporation.

\*\* Work supported by US Department of Energy contract DE-AC03-79ET51017.

<sup>†</sup> Deceased.

formation has been studied in the simple mirror device SM-1, and with this technique four-fold increases in the ring stored energy have been observed. These results have been extended in the five-cell STM-1 device to include the formation of hot electron discs and ring-disc combinations. In addition, ion-cyclotron heating of a streaming plasma has been shown to give a large increase in the stored energy in STM-1.

## 1. INTRODUCTION

The ELMO Bumpy Torus-Scale (EBT-S) [1] at Oak Ridge National Laboratory is a 24-sector toroidal device with closed magnetic field lines. The plasma is formed and heated in the steady state by microwaves. Plasma is confined due to the closure of poloidal drift surfaces by particles with drift velocities much higher than the drift associated with the toroidal field gradient [2]. Magnetohydrodynamic (MHD) stability is provided by precessing high-energy electrons [3], which encircle a toroidally circulating core plasma and have sufficient beta to provide  $\phi d\alpha/B$  stabilization. These hot electrons form naturally in ring-shaped regions where the applied microwave frequency is twice the local electron cyclotron frequency. The operating parameters [4] are strongly dependent on the ambient gas pressure  $p_0$ . At high pressure the hot electron rings are very weak, and the core plasma is dense but cold and unstable. This mode, the (cold) C-mode, changes to the (toroidal) T-mode at lower values of  $p_0$ . The T-mode is the regime of greatest interest: the rings have significant  $\beta$  (up to  $\approx 30\%$ ), the core plasma is quiescent and warm (core electron temperature up to 1 keV), and the confinement appears to be neoclassical. At still lower pressure, the ring and core plasmas are both unstable. This is the (mirror) M-mode.

Up to 200 kW of electron cyclotron heating (ECH) power  $P_{\mu}$  at a frequency of 28 GHz has been applied to EBT-S. The use of this power has permitted the study of core plasma confinement with a much broader range of densities and temperatures than was possible with previous lower-power, lower-frequency ECH sources.

The SM-1 at TRW is a simple mirror device with several (up to four) microwave heating sources available. Rings form in a manner analogous to ring formation in EBT-S, and the mirror geometry affords a convenient test bed to study ring formation and ring particle distributions. Recently this device has been expanded into a 5-cell device, STM-1, in which a plasma is formed at high neutral density at one end, then heated in downstream cells.

TABLE I. EBT-S PARAMETERS

$P_{\mu}$ (kW)	$\sim 200$
$T_e$ (eV)	200-1100
$T_{iBULK}$ (eV)	10-20
$T_{iTAIL}$ (eV)	60-600
$\bar{n}(0)$ ( $m^{-3}$ )	$0.5-2 \times 10^{18}$
$n_0$ ( $m^{-3}$ )	$\sim (0.5-1) \times 10^{16}$
$\tau_E$ (ms)	$\sim 2-5$
$\tau_p$ (ms)	$\sim 4-10$

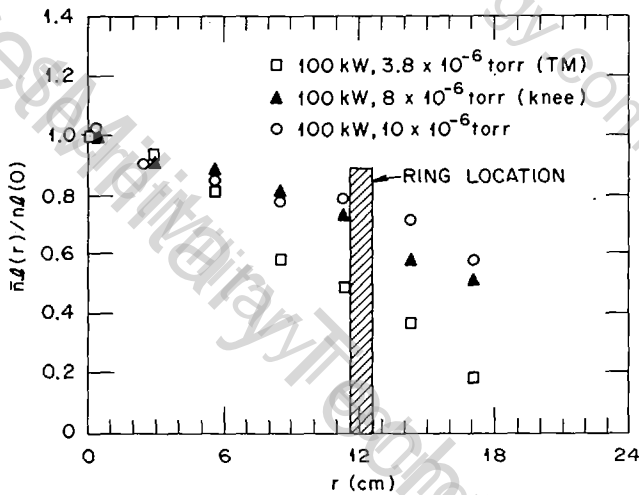


FIG.1. Line integral densities at several radii for three different pressures. These data were obtained from a multichannel microwave interferometer.

Details of the EBT-S core plasma confinement are given in Section 2. Section 3 discusses the results of ion-cyclotron heating (ICH) experiments, with the application of up to 20 kW of steady-state power and 100 kW of pulsed radio frequency (rf) power. The hot electron ring experiments in EBT-S and in SM-1 and STM-1 are discussed in Sections 4 and 5.

## 2. CORE PLASMA CONFINEMENT

Plasma parameters characteristic of T-mode operation are listed in Table I. The chord-averaged electron density  $n$  is determined by a single-channel or a 9-channel 70-GHz microwave interferometer. Data from the 9-channel instrument are shown in Fig. 1. These  $\bar{n}_l$  values have not been Abel-inverted, but

results of inversion show that the central density is constant to within 30% throughout the T-mode. Densities are observed to scale with ECH power as  $n \sim P_\mu^{0.5}$ . By momentarily puffing gas into the plasma, the density can be increased three to four times while maintaining MHD equilibrium through the integrity of the hot electron rings.

The electron temperature  $T_e$  is usually determined by analysis of bremsstrahlung radiation in the energy range 0.2–6.0 keV, using a 5-channel detector. Figure 2 shows that the electron temperature is sensitive to ambient pressure and microwave power, reaching 1 keV at the lowest pressures and highest powers. Very little radial temperature dependence is observed, the temperature being essentially flat out to the radius of the electron rings. The space potential well depth, as determined by means of a cesium ion beam, closely follows these electron temperatures ( $e\phi/T_e \approx \text{const}$ ).

The neutral density is determined by analysis of  $H\alpha$  light emission. Typical  $H^0$  densities are listed in Table I.  $H^0$  Neutral hydrogen atoms have sufficient energy to penetrate the core plasma; the molecules are cold and highly attenuated.

The cavity walls in EBT-S are constructed of aluminum, which is the dominant plasma impurity. Ionization states up to only  $Al^{+5}$  have been observed, implying lifetimes of  $<100 \mu\text{s}$ .

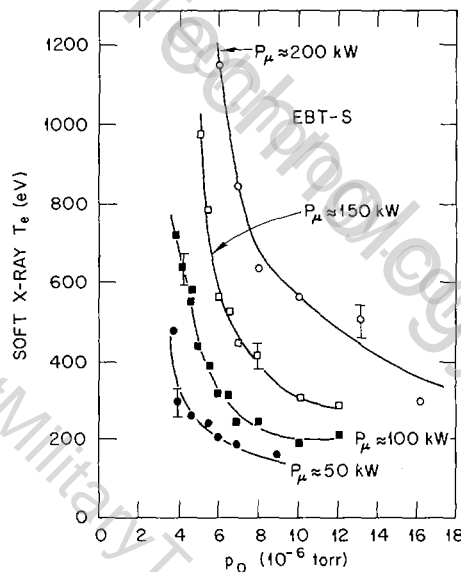


FIG.2. Electron temperature as a function of pressure for applied microwave powers of 50, 100, 150 and 200 kW.

The fractional density of impurities inside the rings is  $n_{\text{imp}}/n < 10^{-3}$ . Low ionization states and low impurity levels result in  $Z_{\text{eff}} = 1.0$ , and line radiation from impurities represents a negligible power loss.

Plasma fluctuations exist at all pressures but are minimal in the T-mode. These peak near or just outside the hot electron rings, and are tentatively identified as drift modes. In the T-mode, and especially near the T-M transition, another instability appears, which results in instability of the hot electron rings. These fluctuations are triggered by the  $n_{\text{core}}/n_{\text{ring}}$  electron density ratio becoming too low and are believed to be responsible for the transition into the M-mode.

For the EBT-S densities, the power flow from electrons to ions due to Coulomb collisions is low, so that the bulk ion temperature is  $\approx 10$ -20 eV. However, non-Maxwellian tail distributions are observed, particularly near the T-M transition, with energies of up to several hundred electron volts. These tail ions, which represent a small fraction of the total ion distribution, may owe their energy to anomalous heating mechanisms.

The basic equation of neoclassical electron scaling in bumpy torus magnetic fields is

$$\langle n \rangle \tau_E \sim T^{3/2} f(\lambda_n, \lambda_T, \lambda_{E_r})$$

where  $f$  is a function of the scale lengths for density ( $\lambda_n$ ), temperature ( $\lambda_T$ ) and radial electric field ( $\lambda_{E_r}$ ). Combining this equation with the defining equation for  $\tau_E$  ( $\tau_E \sim n T_e / P_\mu$ ) gives  $P_\mu \sim n^2 / T_e^{0.5} f$ . Thus, the density is predicted to scale with the square root of the absorbed microwave power, if scale lengths are held constant. Assuming that the absorbed power scales with the applied power, this scaling is observed. Neoclassical scaling further predicts that  $\tau_E / \tau_p \sim \text{const.}$  (if the  $\lambda$ 's are held constant), and this relation is also consistent with the data.

### 3. HEATING EXPERIMENTS IN THE ION-CYCLOTRON RANGE OF FREQUENCIES

Steady-state wave heating experiments have been conducted on EBT-S over a frequency range of 15-50 MHz. In the EBT-S experiments the fast ion-cyclotron wave ( $\omega/\omega_{ci} > 1$ ) is launched from a Faraday-shielded stripline antenna placed in the mid-plane of a single EBT cavity. Detailed measurements of wave dispersion properties verify the existence of the fast wave in the plasma. Coupling efficiencies for fast wave launching greater than 90% have been obtained in the high-density, C-mode plasmas. The ion heating experiments described here have been

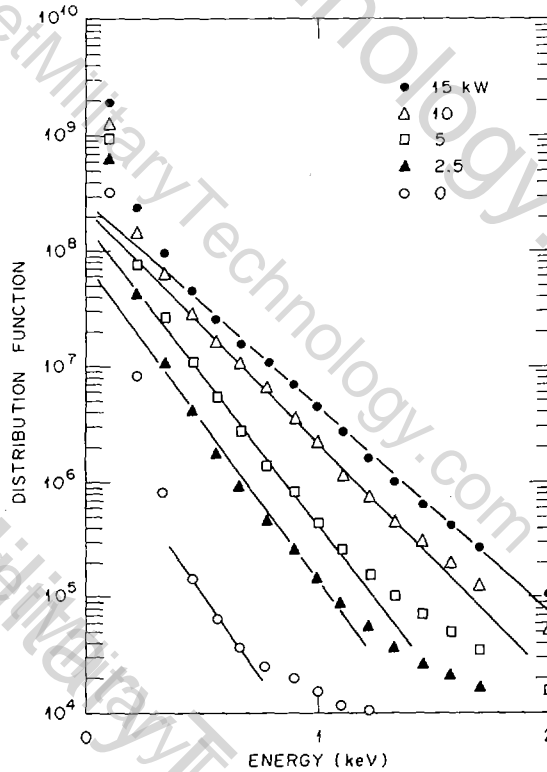


FIG. 3. Deuteron energy distribution functions for several ICRH power levels in a 95%  $D^+$ , 5%  $H^+$  plasma in the T-mode. Wave frequency = 30 MHz. Solid lines are Maxwellian curve fits.

TABLE II. PARAMETERS FOR CURVE FITS IN FIG. 3

Wave Power (kW)	0	2.5	5.0	10.0	15.0
$T_i$ (eV)	160	165	170	215	240
$n_i n_0^2$ ( $\times 10^{21} \text{ eV}^{-0.5} \text{ cm}^{-5}$ )	0.2	2.3	6.2	14.5	18

$\lambda$  is the plasma diameter;  $n_0$  is the neutral density.

conducted in the T-mode, where coupling efficiencies are typically 40-50%. For both the C-mode and the T-mode, the coupling efficiency is maximized at frequencies well above the (mid-plane) cyclotron frequency.

Figure 3 shows the ion distribution function deduced from charge exchange neutral analysis for several rf power levels from 2.5 to 15 kW. In this case, the bulk plasma is composed of 95% D<sup>+</sup> and 5% H<sup>+</sup>. The majority of the heated ions are deuterons as determined from mass analysis of the charge-exchange neutrals. Maxwellian curve fits characterizing the data are shown in the figure, and the corresponding parameters for these fits are given in Table II. From these data, the principal effect of the rf heating is the formation of a 160 to 240-eV tail on the ion distribution function. Assuming an isotropic distribution, the tail density for 15 kW of wave power represents approximately 10-50% of the bulk ion density. If the distribution is anisotropic, this density should be multiplied by  $(T_{\parallel}/T_{\perp})^{0.5}$ .

In addition to ion heating, application of the fast wave in EBT results in a significant enhancement of the relativistic electron annuli. In one case, at a wave power level of 15 kW, the stored energy of the annulus in the cavity adjacent to the fast wave antenna more than doubled. This increase in annulus energy was recorded by a hard x-ray spectrometer and confirmed by diamagnetic loop measurements. This effect represents a new phenomenon with potentially significant implications for future EBT machines.

#### 4. HOT ELECTRON RINGS IN EBT

In the T-mode, the hot electron rings, necessary for the MHD stability of EBT, have a  $\beta$  greater than a critical value. The critical  $\beta$  for the C-T transition is about 3% and does not change appreciably with either  $p_{\theta}$  or  $p_{\mu}$ . The transition pressure varies with power as  $p_{\mu}^{0.5}$ .

The ring volume was determined indirectly by the ratio of the stored energy (determined from diamagnetic loops) to the energy density (determined from bremsstrahlung spectra). The value obtained was  $2 \times 10^{-3} \text{ m}^3$ , or about 15% of the core plasma volume.

The power required to sustain the rings has been compared with the calculated values in two ways: the total power was measured in turn-off experiments, and two of the components of the power loss have been measured - synchrotron radiation and scattering. The accuracy of the experiments is not sufficient to rule out losses in addition to the classical processes [5], but within this uncertainty, classical losses can account for the observed power.

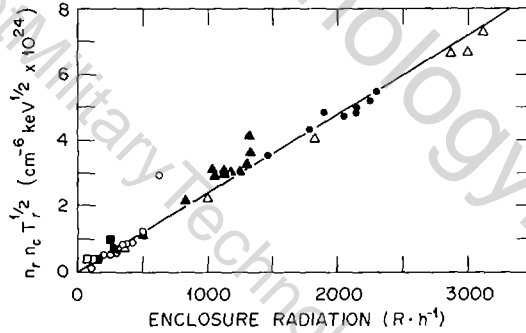


FIG.4. Variation of the X-ray radiation level with the scattering parameter  $n_{core} n_{ring} T_{ring}^{0.5}$ .

The synchrotron spectrum has been measured in the range 80-110 GHz. A featureless spectrum that falls slowly with frequency is observed, in agreement with theoretical expectations. There is a factor of 2 uncertainty in absolute calibration and a second factor of 2 due to the effects of reflections. Within this total factor of 4 the radiated power agrees with that calculated.

The scattering loss is measured indirectly by the bremsstrahlung produced as the scattered electrons strike the chamber walls. The bremsstrahlung should depend on the product of the ring and core densities, times the square root of the ring temperature. Figure 4 shows that this scaling is valid over more than an order of magnitude. The uncertainties in the comparison between the theoretical and experimental intensities (e.g. geometry) are a factor of 4. Recent calculations have shown that the scattering loss should be greater than previously expected [5] and should be the dominant loss process for ring temperatures less than about 2 MeV.

Modulation of the power to a single sector has allowed the determination of the total power to sustain the ring. The total ring energy was determined from the diamagnetic signal. Dividing this energy by the ring confinement time yields the ring power. Unfortunately, the various signals — x-rays, synchrotron radiation, and diamagnetism — give different characteristic times, and are different for buildup and decay. By choosing the shortest of these (buildup of the x-rays) an upper bound to the ring power was obtained, which was four times the theoretical value.

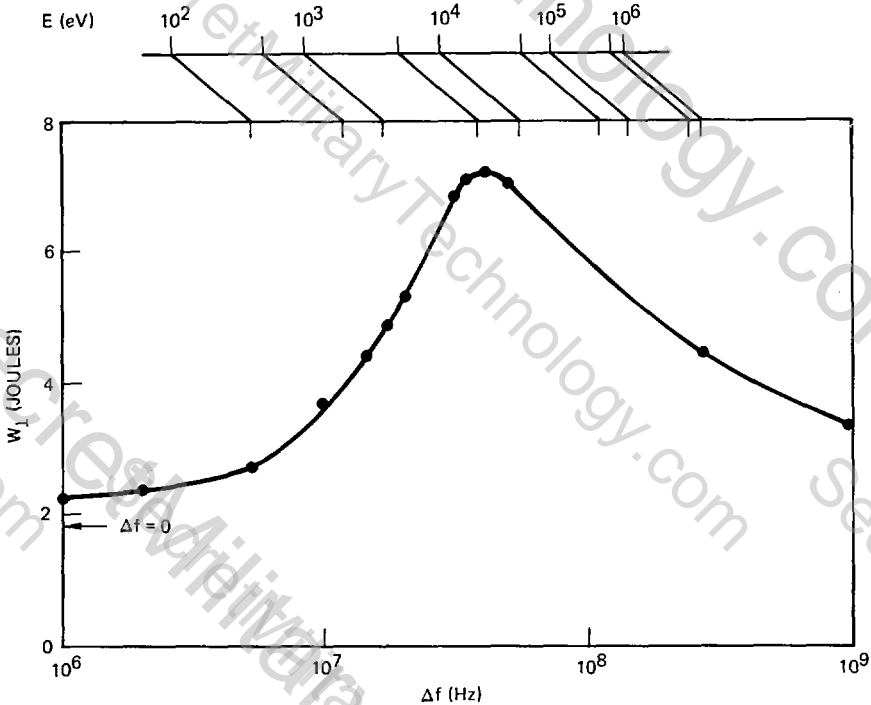


FIG.5. Total stored energy as a function of the frequency separation for two-frequency heating. The scale at the top gives the electron energy for which the bounce frequency is equal to the frequency difference.

## 5. ECRH IN SYMMETRIC TANDEM MIRRORS

The symmetric tandem mirror program at TRW is focused on the study of axisymmetric mirror-confined plasmas in support of both the EBT and tandem mirror efforts. Two novel techniques of controlled electron-cyclotron resonance heating (ECRH) have been demonstrated: (1) use of multiple-frequency ECRH, and (2) the decoupling of stream heating from relativistic electron heating.

In the single-cell SM-1 mirror and in the 5-cell STM-1 facility, a mirror ratio of 2.2:1 results in fundamental resonance heating near the mirror throat and midplane harmonic heating for the same X-band microwave power input.

Multiple-frequency electron-cyclotron heating (MFECH) experiments were carried out in the single-cell SM-1 mirror facility [6]. An array of Hall probes was used to reconstruct the spatial structure of the ELMO ring. The effect of widely

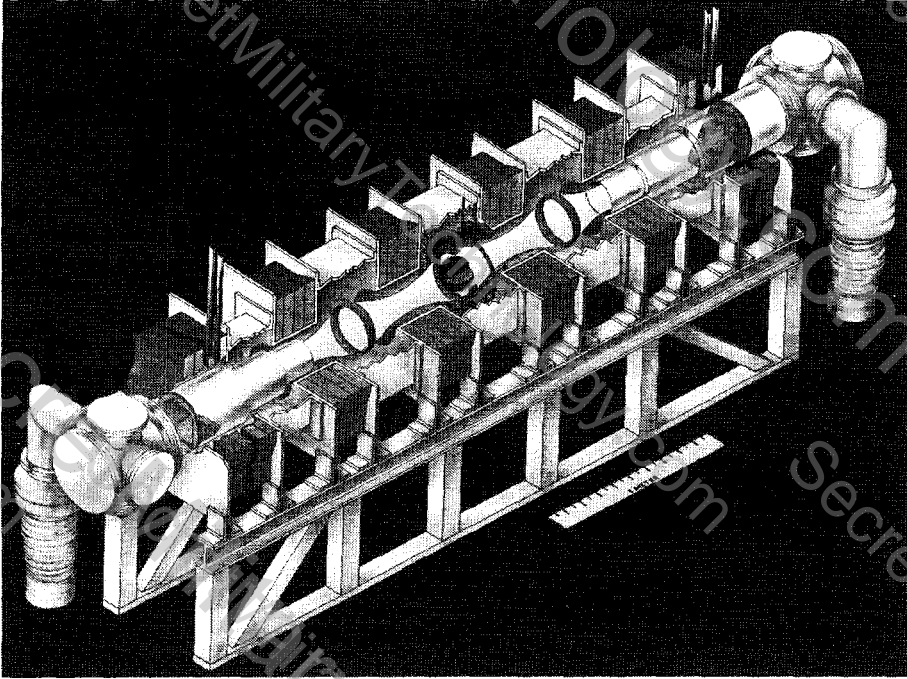


FIG. 6. Perspective drawing of the symmetric tandem mirror facility, STM-1.

spaced MFECH (from 8.2 to 10.5 GHz) on the volume of the ring could then be distinguished from improvements in heating efficiency. This effect is maximized for small frequency separations (Fig. 5) for which the spatial extent of the ring remains unchanged. The four-fold increase in ring stored energy obtained with a frequency separation of only 40 MHz suggests that, in agreement with theoretical models and Monte-Carlo studies [7], the main effect of MFECH is the destruction of superadiabatic behavior in single-wave heating of the intermediate energy electrons (10 keV) that feed the relativistic electron population ( $T_e = 400$  keV). In addition, the application of widely spaced frequencies provides control of the ring thickness due to the spatial spread of the harmonic resonances.

It is also observed that the use of MFECH allows the production of stable plasmas at high microwave input powers. The overall improvement in stored diamagnetic energy is a factor of 7 when single-frequency heating is replaced by 4-frequencies.

By using five adjacent mirror sections, the STM-1 facility (Fig. 6) allows the efficient formation of a cold plasma stream

by ECH breakdown in the high neutral pressure end cell. Then, supplemental heating (both ICRH and ECRH) is applied in the lower neutral density downstream mirror cells. A reduction in neutral density from the end to the center cell by a factor of 14 has been achieved, thus allowing ICRH in a low charge-exchange loss environment. A large increase in stored energy (30 mJ) is observed with ICRH. A perpendicular charge-exchange analyzer indicates the presence of a Maxwellian ion population with  $T_i = 180$  eV, the density of which is, however, too low to account for the rise in stored energy. This result suggests that the ion distribution is anisotropic and that the ion temperatures observed may not represent the entire ion population.

One of the more exciting results is the demonstration of the feasibility of hot electron discs. A skimmer probe is used in the center cell in conjunction with diamagnetic loops to determine the radial pressure profile. By tailoring the strength of the magnetic field along with the spectrum of microwave power, three distinct configurations can be produced: (1) ELMO ring only, (2) ring plus disc, and (3) disc only. In the last case, the flat pressure profile has an on-axis  $\beta$  of 10%.

## 6. SUMMARY

Electron-cyclotron heating has been used in EBT-S and in the TRW mirror devices, SM-1 and STM-1, to produce hot electron populations as well as plasmas with lower electron temperatures. The EBT-S core plasma, in the T-mode, has a low impurity content, electron temperatures in the range of several hundred electron volts, but low ion temperatures. Neoclassical scaling laws for electron density, temperature, and confinement times have been experimentally demonstrated.

RF power, above the ion-cyclotron frequency, has led to ion tail formation, but with "tail" densities that approach the bulk ion density. In addition to this improvement in ion parameters, the stored energy of the hot electron rings was also significantly increased.

The power loss from the hot electron rings has been measured, and found to be consistent — within the uncertainties in the experiments and calculations — with classical processes.

MFEC has shown several beneficial effects. Breaking of the superadiabatic motion results in an enhanced feed into the energetic population, so that the stored energy is much higher — up to a factor of 4. In addition, widely spaced frequencies can increase the ring thickness, simply as a result of the spatial spread of the resonance regions.

Separation of the plasma production region from the supplemental heating region has permitted ICRH in an environment

with low charge-exchange losses in STM-1. The hot electron population can be produced in several combinations of rings and disks by ECH in the downstream cells. These developments have potential impact on the design of tandem mirror devices as well as on the experimental investigation of the MHD stability limits in EBT.

## REFERENCES

- [1] DANDL, R. A., et al., Plasma Physics and Controlled Nuclear Fusion Research (Proc. 7th Int. Conf. Innsbruck, 1978) Vol. 2 (IAEA, Vienna, 1979) 365; DANDL, R. A., et al., Summary of EBT-I Experimental Results, Oak Ridge National Laboratory Report ORNL/TM-6457 (October 1978).
- [2] MOROZOV, A. I., SOLOV'EV, L. S., Reviews of Plasma Physics, Vol. 2 (Consultants Bureau, New York, 1966) 201.
- [3] NELSON, D. B., HEDRICK, C. L., Nucl. Fusion 19 (1979) 283.
- [4] GLOWIENKA, J. C., J. Vac. Sci. Technol. 18 3 (1981) 1088.
- [5] BOROWSKI, S. K., UCKAN, N. A., JAEGER, E. F., and KAMMASH, T., Nucl. Fusion 20 (1980) 177.
- [6] QUON, B. H., et al., submitted to Phys. Fluids; also Proc. 2nd EBT Ring Physics Workshop (Oak Ridge National Laboratory, 1982) 519.
- [7] SAMEC, T. K., et al., Proc. 2nd EBT Ring Physics Workshop (Oak Ridge National Laboratory, 1982) 519.

## DISCUSSION

R.J. TAYLOR: Could you comment on the device potential in EBT? Is it negative or positive, and how does it change with RF heating (ICRF)?

L.A. BERRY: The ambipolar potential is essential to confinement. On EBT-S we find that  $\phi \propto kT_e$  and is negative. With ICRF the potential is increased by only 10–20 volts. This results in a slightly reduced electric field.

## EXPERIMENTAL AND NUMERICAL STUDIES ON PLASMA CONFINEMENT IN NAGOYA BUMPY TORUS (NBT)

M. FUJIWARA, T. KAMIMURA, M. HOSOKAWA,  
T. SHOJI, H. IGUCHI, H. SANUKI, M. TANAKA,  
M. AIZAWA\*, K. TAKASUGI, F. TSUBOI,  
H. TSUCHIDATE, K. MATSUNAGA, K. KADOTA,  
A. TSUSHIMA, K.W. WHANG\*\*, H. IKEGAMI  
Institute of Plasma Physics,  
Nagoya University, Nagoya,  
Japan

### Abstract

EXPERIMENTAL AND NUMERICAL STUDIES ON PLASMA CONFINEMENT IN NAGOYA BUMPY TORUS (NBT).

Experimental and theoretical studies have been made on plasma produced by electron-cyclotron heating in the Nagoya Bumpy Torus (NBT). Hot electron rings are studied for their energy loss mechanism, which is experimentally confirmed to be classical Coulomb drag. Ion-cyclotron heating (ICH) was carried out up to 200 kW input power and the ion temperature was observed to increase by 300 eV. An interesting result associated with ICH is the enhancement of positive electrostatic plasma potentials against the wall. Numerical studies on particle confinement in the bumpy torus configuration reveal that the plasma potential  $\phi$  can confine high-energy particles with energy  $W \lesssim Ae\phi$  through the  $E \times B$  poloidal drift motion. A new bumpy torus configuration using inverse-dee (ID) coils is also proposed, which can achieve aspect-ratio enhancement and improve confinement of passing particles significantly without employing any additional coils. The proposed idea of the ID bumpy torus enables a much smaller bumpy torus fusion reactor to be designed.

### 1. INTRODUCTION

Recent progress in experimental research reports stable confinement of high-temperature plasmas by electron-cyclotron heating (ECH) bumpy tori such as the Nagoya Bumpy Torus (NBT) and the ELMO Bumpy Torus (EBT), Oak Ridge, in which plasmas are generated, heated and stabilized by high-power microwaves of several frequencies from 8.5 GHz to 28 GHz in the steady state. Machine and

\* Permanent address: College of Science and Technology, Nihon University, Tokyo 101, Japan.

\*\* Permanent address: Department of Physics, University of California, Los Angeles, California, USA.

TABLE I. MACHINE AND PLASMA PARAMETERS OF VARIOUS BUMPY TORUS DEVICES

	IN OPERATION			OPERATION IN 1982	PLANNING	
	NBT-1	EBT-1	EBT-S	NBT-1M	EBT-P (S.C.)	NBT-2 (S.C.)
$B_{res}$ (T)	0.3	0.64	1.0	1.0	2.1	2.5-3.5
R (cm)	1.6	1.5	1.5	1.4	4.5	5.0
$f_E$	1.0	1.0	1.0	1.0	1.0	$\leq 1.5$
A	8.0	9.3	9.3	10.0	16	15
$\bar{a}$ (m)	0.1	0.1	0.1	0.1	0.18	0.3
$N_{coil}$	24	24	24	24	36	36
$n$ ( $cm^{-3}$ )	$\sim 10^{12}$	$1.5 \times 10^{12}$	$4 \times 10^{12}$	$4 \times 10^{12}$	$1.7 \times 10^{13}$	$3 \times 10^{13}$
$T_e$ (keV)	0.1-0.2	0.3	0.5	0.5	2	1-2
$T_i$ (keV)	0.05+ $\geq 0.1$ (ICH)	0.06	0.1	0.1	0.4	1-2
$n\tau$ ( $s/cm^{-3}$ )	$\sim 10^9$	$10^{10}$	$2 \times 10^{10}$	$2 \times 10^{10}$	$5 \times 10^{11}$	$\sim 10^{12}$
$f_\mu$	8.5 GHz	18.0	28	28-35	60-110	60-110

plasma parameters of various devices are listed in Table I. The critical issues for stable plasma confinement in an ECH bumpy torus are ring physics, ion heating, and confinement scaling, among others.

In Section 2 we describe experimental studies of the mechanisms of ring production and energy loss. Ion-cyclotron heating (ICH) experiments have been carried out in order to study ion energy transport and its effect on plasma confinement. In Section 3, numerical studies on particle confinement show that bumpy-torus plasmas are composed of both toroidal and mirror plasmas, and that in a vacuum magnetic field they are mostly mirror-like plasmas. The ambipolar potential greatly improves confinement by eliminating the loss cones that characterize mirror-like plasmas. The critical energy of confined particles is given by  $W = Ae\phi$ , where A is the aspect ratio, while  $W \lesssim e\phi$  in the tandem mirror configuration. When we consider fusion plasmas in the bumpy torus, fusion-reacting ions of energy 100–200 keV can be well confined by a plasma potential  $\phi \sim kT/e \sim 10$  kV. But serious problems may arise for the confinement of  $\alpha$ -particles. In Section 4, a new concept, called the inverse-dee (ID) bumpy torus is proposed, which has been developed to reduce the direct loss of high-energy particles like  $\alpha$ -particles without the use of additional coils such as ARE or symmetrizing coils which cause the simplicity of the original bumpy torus structure to deteriorate.

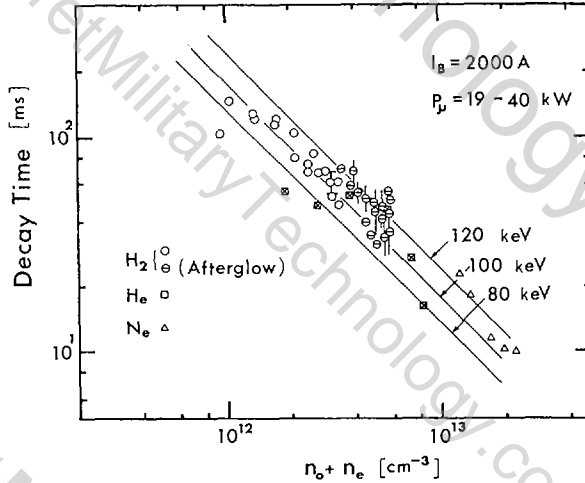


FIG.1. Hot electron ring decay time as a function of number density of target cold electrons. Calculated values with typical hot ring temperature are shown for comparison (solid lines).

## 2. THE EXPERIMENT

The Nagoya bumpy torus (NBT) consists of 24 mirror sectors (mirror ratio 1.9) connected toroidally with the major radius,  $R_0 = 160$  cm, and minor radius,  $a = 20$  cm, at the midplane. Toroidal plasmas are maintained at  $(0.5-1) \times 10^{12} \text{ cm}^{-3}$  by ECH (8.5 GHz; 75 kW maximum) and stabilized by hot electron rings ( $T_h \cong 100$  keV) [1].

The behaviour of the hot electron rings, which is crucial for MHD stability of bumpy-torus plasmas, is studied in detail in NBT and EBT. The energy loss processes are: Coulomb drag by background plasma, synchrotron radiation, and ionization of background neutral atoms. The other mechanisms are non-classical ones such as non-adiabaticity and anomalous scattering by high-power microwave fields.

As shown in Fig. 1, the recent NBT experiment on decay time measurement of the X-band synchrotron emission, which is proportional to the hot-electron energy density, reveals the linear decrease of the decay time with background plasma density, which is well explained by Coulomb drag processes. The stored energy, especially the density  $n_h$  of the hot electron ring, is observed to increase linearly with the input microwave power  $P_\mu$ , but levels off at 4-5 kW input per ring. Several mechanisms are proposed for the levelling off, such as increase of Coulomb drag due to increase in  $n_e$  with  $\sqrt{P_\mu}$ , reduction of heating efficiency  $\eta$  by the increase of  $n_e$  and  $n_h$ , reduction of  $\eta$  due to increase in  $T_e$  or  $T_h$ .

The spatial profile of the rings is also important in the MHD stabilization of the toroidal core plasma. The criterion for the formation of magnetic wells by the

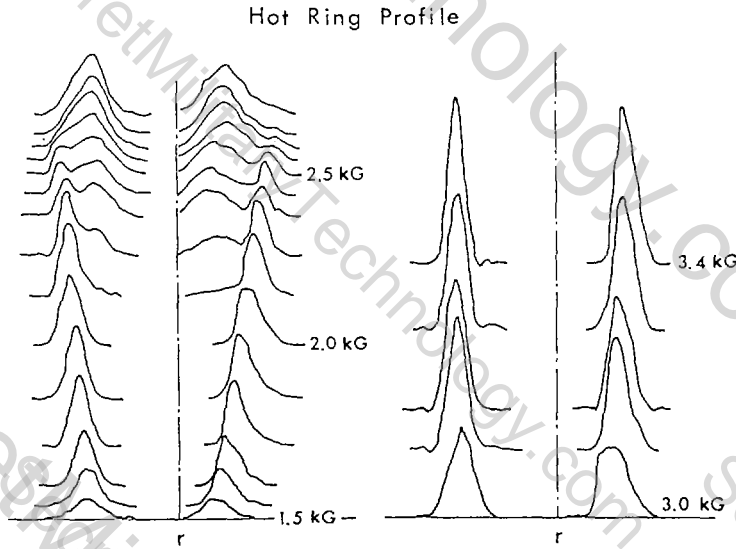


FIG.2. Radial profile of hot electrons measured by skimmer probe.

hot electron ring is given as  $\beta \sim 2\Delta/R_c$  [2], where  $\Delta$  is the ring width and  $R_c$  is the characteristic length of the field gradient. In the NBT, the location and radial profile of the hot electron rings are measured from the change of synchrotron radiation intensity as a skimmer probe is moved radially.

Figure 2 shows the location and shape of the ring for various magnetic field intensities at the midplane. The peak and width of the ring are plotted in Fig. 3, where the horizontal bar corresponds to the half-width of the hot electron distribution. The solid curve indicates the fundamental zone and second-harmonic cyclotron resonance zone with the electron rest mass. As is seen in Fig. 3, the location of the ring does not always coincide with the cyclotron resonance zone, but is somewhere between the resonance zones. Three mechanisms are considered to account for this phenomenon. A series of peaks in the lower magnetic field corresponds to the second cyclotron harmonic resonance zone with relativistic mass effect. The second series in the higher magnetic field may correspond to the region of long confinement time round the toroidal plasma axis. The location of the ring is observed to be determined by the largest product of heating rate and confinement time.

ICH experiments with more than 200 kW of RF power were carried out on NBT-1. At present, ICH experiments are focused on studies of their effects on plasma transport with high ion temperature operation.

A pair of loop antennae (poloidal modes  $m = \pm 1$ ) are mounted near the mirror throat to excite a slow wave mode from a high field side [3]. The RF input power for each antenna can be raised to 250 kW at 6.5 MHz, with 5 ms

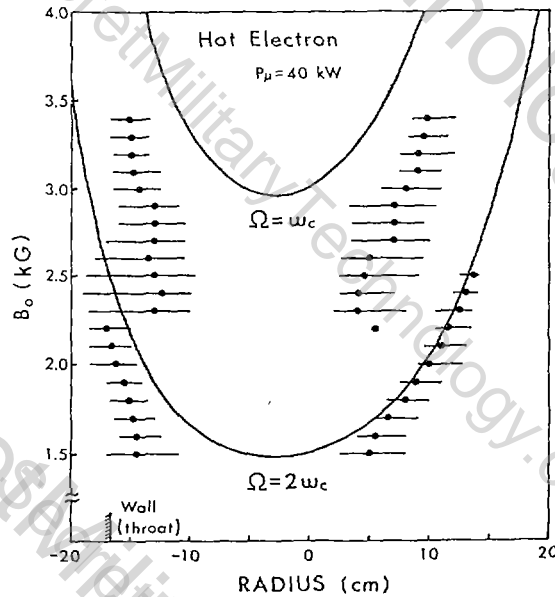


FIG.3. Ring positions as a function of magnetic field intensity. Fundamental and second-harmonic cyclotron resonance points at the midplane are shown.

duration. The ion temperature is measured by a time-of-flight type neutral analyser, which can detect charge-exchanged hydrogen atoms with energies ranging from 50 eV to 1 keV (Fig. 4). The ion temperature is observed to increase with the input RF power and then tends to saturate, as shown in Fig. 5. The observed temperature saturation is associated with a non-adiabatic loss of high-energy ions having a large ratio of ion Larmor radius to magnetic scale length in the weaker field region of the mirror midplane. The effect of ion heating on the ambipolar potential, which is important in plasma transport owing to the resulting  $E_r \times B_t$  poloidal drift motion of plasma particles, is studied by heavy-ion beam probing. Positive potential (radially outward electric field) is observed to be enhanced by ICH (Fig. 4). The mechanism of the change in potential profiles is not clear, although the density decrease observed during ICH implies an enhancement of some anomalous diffusion for electrons.

### 3. NUMERICAL STUDIES ON PLASMA CONFINEMENT IN A BUMPY TORUS

The orbit of a charged particle in a bumpy torus is closed in the poloidal plane by the poloidal drift due to the curvature of magnetic field lines and grad B. The poloidal precessional velocity depends strongly on the pitch angle of the

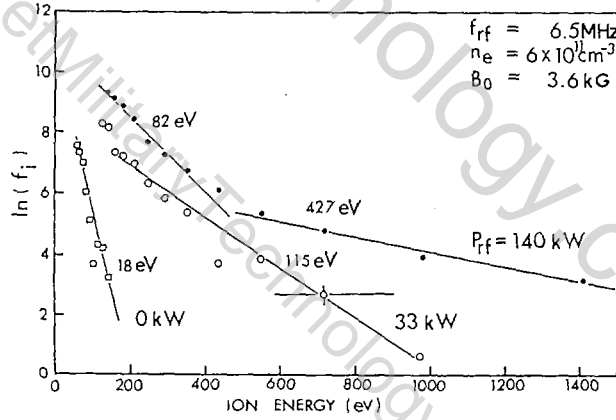


FIG. 4. Energy spectrum detected by time-of-flight energy analyser when ICH is applied to NBT plasmas.

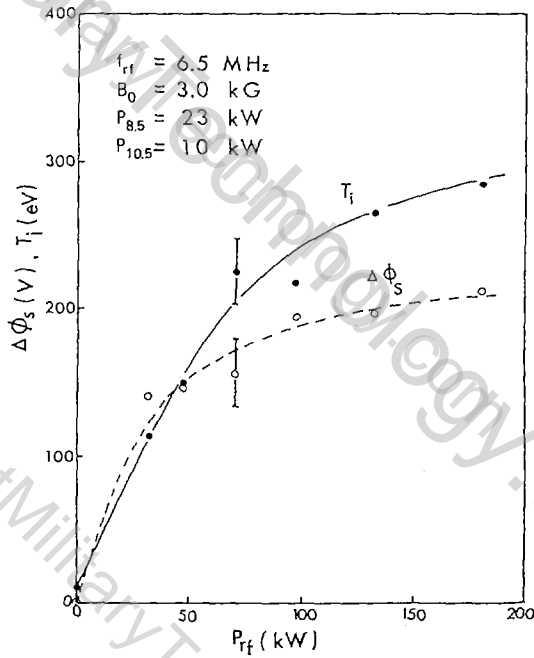


FIG. 5. Increase in ion temperature and enhancement of plasma potential as functions of input ICH power.

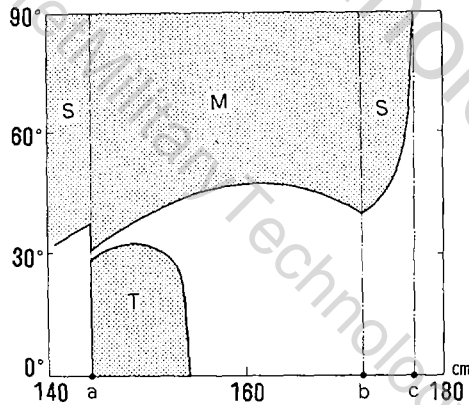


FIG.6. Spatial dependence of the loss cone in NBT-1 without ambipolar potential. The vertical scale is pitch angle  $\theta = \cos^{-1}(v_{\parallel}/v)$ , and the horizontal scale is the radial position in the meridional plane of the torus. Particles in the loss cone are eliminated by hitting the coil throat. Shaded region is confined region.

particle velocity, and, especially for  $v_{\parallel}/v = 1$ , it is one order of magnitude smaller than that of a trapped particle. The orbit of a particle with  $v_{\parallel}/v \cong 1/\sqrt{M}$  (where  $M$  is the mirror ratio) does not close inside the toroidal vessel because the poloidal drift is cancelled out by the positive (at the midplane) and negative (near the mirror throat) curvature of the mirror field lines.

The spatial dependence of the loss cone in velocity space is shown in Fig. 6. The region close to the inside wall of the torus is characterized by both mirror and toroidal confinement of particles with a narrow loss cone at  $v_{\parallel}/v = 1/\sqrt{M}$ , and particle confinement outside the torus is similar to that of an ordinary mirror machine, whose loss cone is at  $v_{\parallel}/v \geq 1/\sqrt{M}$ , except that, in the bumpy-torus configuration, the particle in the loss cone,  $v_{\parallel}/v \geq 1/\sqrt{M}$ , drifts out towards the wall at approximately the toroidal drift velocity, and the loss rate decreases with increasing magnetic field, whereas in an ordinary mirror device the particles are rapidly lost in a transit time of the order of  $L/v$ .

The plasma potential has a strong effect on the confinement characteristics because the  $E \times B$  drift due to the ambipolar potential is comparable to the magnetic drift ( $E_r/B \sim \phi/Ba \sim \kappa T/eBR_c$ ) for particles with thermal energy  $\kappa T$ .

This feature is illustrated in Figs 7(A) and (B). Figure 7(A) shows the loss cone expressed in the perpendicular and parallel energy space for various radial positions in the P-type potential (radially outward electric field), and Fig. 7(B) shows the N-type potential (inward electric field). All these calculations have been carried out for ions. The magnetic drifts tend to be cancelled by the  $E \times B$  drift in the N-type potential, while both drifts are added in the P-type. For electrons, the situation in the N- and P-types is reversed, except for the lack of potential rim in the reversed P-type for electrons. From this figure it is concluded

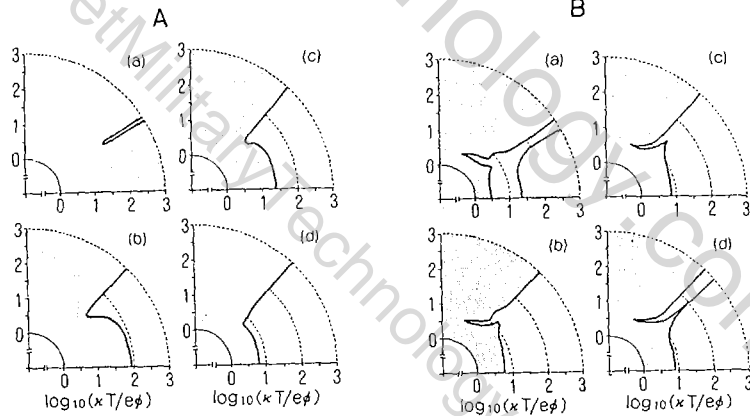


FIG. 7. Loss-cone angle expressed in parallel energy (horizontal axis) and perpendicular energy (vertical axis) space normalized by  $e\phi$  for (A) potential hill (P-type) and (B) potential well (N-type).

that the critical energy boundary  $W_c$  of the confined particles can be estimated by  $W_c = Ae\phi$  which comes from the condition of balance between toroidal drift and  $E \times B$  drift,  $W_c/eR_0B = \phi/aB$  ( $\sim \kappa T/eaB$ ). More precisely, the electron and ion diffusion associated with plasma potential must be calculated in a self-consistent way.

The essential differences between the numerical results described above and conventional neoclassical transport theory [4] are as follows: (1) the available region of neoclassical theory is localized in a narrow space round the drift axis of passing particles; (2) the maximum energy of the confined particle is given by  $W = (e\phi)(R_0/a)$ , where  $\phi$  is either a potential depth for N-type or a potential hill for P-type.

#### 4. INVERSE-DEE (ID) COIL BUMPY TORUS

According to numerical analyses for particle behaviour in a conventional bumpy torus with the use of circular coils,  $E \times B$  drift induced by the radial ambipolar field greatly helps confinement of passing particles for low energies  $W \leq Ae\phi$ . We have still some serious problems in the confinement of  $\alpha$ -particles, however, because the energy of an  $\alpha$ -particle is so high that confinement characteristics are governed by the vacuum magnetic field only [5]. Several ideas involving the use of additional coils, such as ARE or symmetrizing coils, were presented in order to reduce the direct loss of high-energy particles in the bumpy torus of a moderate mechanical size. In this paper a new idea is proposed for obtaining excellent confinement characteristics by using non-circular (i.e. half circle) coils known as inverse-dee (ID) coils [6].

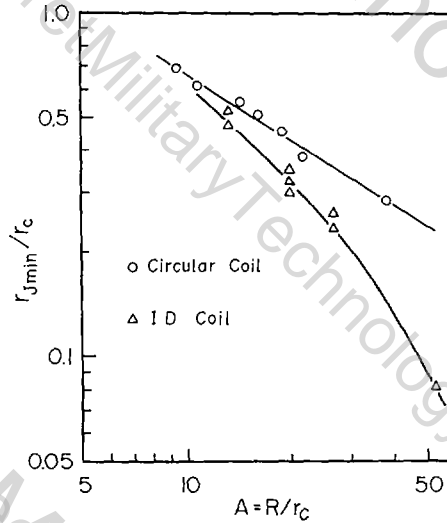


FIG.8. Dependence of  $r_{Jmin}$  normalized by coil radius  $r_c$  on aspect ratio  $A = R/r$  for circular and ID coils.

One very simple index of confinement of passing particles is the position  $r_{Jmin}$ , where the longitudinal invariant  $J_{||}$  of a passing particle ( $v_{||}/v = 1$ ) has minimum value. Figure 8 shows computer results of drift orbit calculations for the relations between  $r_{Jmin}$  and aspect ratio for the circular and ID bumpy torus. Great care has been taken not to change the mirror ratio, since  $r_{Jmin}$  depends on it. It is clear that  $r_{Jmin}$  is reduced with increase of the aspect ratio, but the reduction rate is much larger for the ID bumpy torus than for the circular torus when the aspect ratio is larger than 20.

Analytical studies involving a number of assumptions led to the following equations for evaluating  $r_{Jmin}$  of a non-circular-coil bumpy torus whose coil shape is given by  $r_c = a(1 + \delta_n \cos n\theta)$ :

$$\frac{r_{Jmin}}{r_c} \cong \frac{r_0}{a} \left( 1 + \frac{\Delta_n}{r_0} - (-1)^n \delta_n \right) \quad (1)$$

where

$$\frac{\Delta_n}{r_0} \cong (-1)^n \delta_n \left[ \frac{a}{r_0} \frac{K_n \left( \frac{Na}{R} \right)}{K_1 \left( \frac{Na}{R} \right)} \frac{I_1 \left( \frac{Nr_0}{R} \right) I_1' \left( \frac{Nr_0}{R} \right) + I_1' \left( \frac{Nr_0}{R} \right) I_1 \left( \frac{Nr_0}{R} \right)}{I_1 \left( \frac{Nr_0}{R} \right) I_1' \left( \frac{Nr_0}{R} \right) + \left[ I_1' \left( \frac{Nr_0}{R} \right) \right]^2} \right] \quad (2)$$

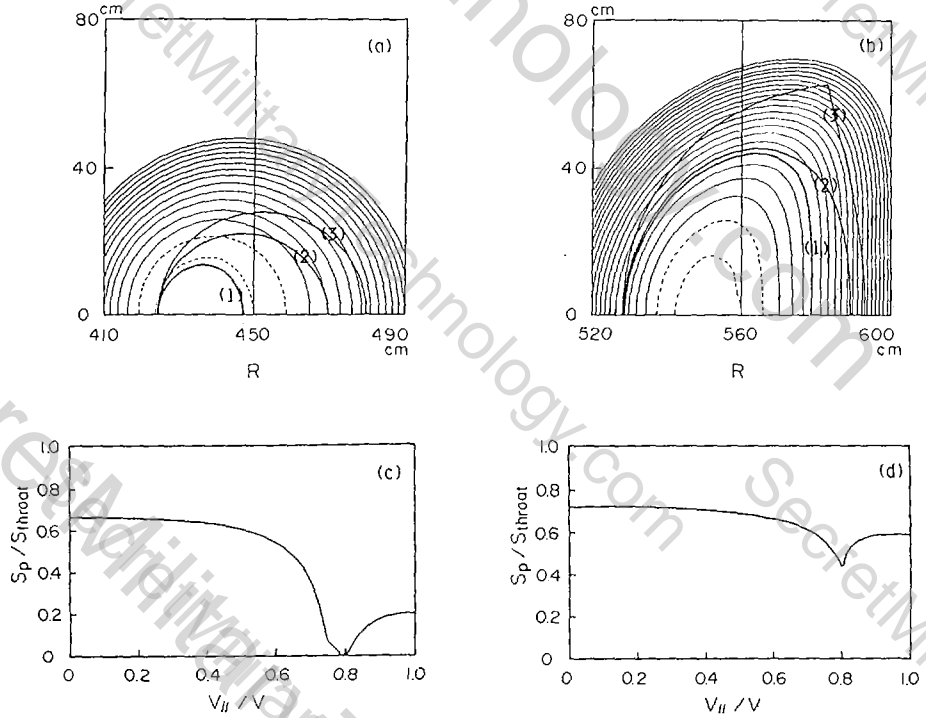


FIG. 9. Drift surfaces of passing particles denoted by curve (1) and trapped particles (2), which are limited by the shadow of the discharge chamber (3), for: (a) EBT-P and (b) corresponding ID bumpy torus. Filling factor  $S_p/S_{\text{throat}}$  is also compared for (c) EBT-P and (d) corresponding ID bumpy torus design.

and  $r_{J\text{min}} = r_0$  for the circular bumpy torus. If we take  $n = 1$  for simplicity, Eq. (1) becomes

$$\frac{r_{J\text{min}}}{r_c} \cong \frac{r_0}{a} \left( 1 - \delta_1 \left( \frac{a}{r_0} - 1 \right) \right) \quad (3)$$

Equation (3) shows that the condition  $\delta_1 > 0$  makes  $r_{J\text{min}}/r_c$  small and that the deformation is more effective for smaller  $r_0$  (i.e. larger aspect ratio), which is already shown in Fig. 8. As an example, the conceptual design and confinement characteristics of a relatively large device using ID coils are shown in Fig. 9.

The drift axis of a passing particle is close to the axis of the drift surface of trapped particles, and subsequently the confinement area increases drastically for passing particles. Particle confinement in EBT-P [7] is compared with that in the proposed design using ID coils in Fig. 9, which shows drift surfaces of passing and trapped particles. The filling factor  $F$ , which is the ratio of the area

$S_p$  surrounded by the outermost drift orbit to the area  $S_{\text{throat}}$  of the mirror throat projected on the midplane, is also compared. The proposed ID-coil bumpy torus gives much better confinement than the conventional circular bumpy torus, i.e. the filling factor  $F$  for  $v_{\parallel}/v = 1$  is three times as large, resulting in the well confined plasma diameter being twice as large as that in the ordinary bumpy torus with almost the same major radius. The ID-coil bumpy torus will enable us to design a much smaller fusion reactor with greater output power than the conventional bumpy torus.

## REFERENCES

- [1] FUJIWARA, M., et al., in Plasma Physics and Controlled Nuclear Fusion Research 1980 (Proc. 8th Int. Conf. Brussels, 1980) Vol. 1, IAEA, Vienna (1981) 845.
- [2] VAN DAM, J.W., LEE, Y.C., Proc. Workshop on EBT Ring Physics, Oak Ridge, 1979, p. 471.
- [3] SHOJI, T., et al., Proc. Int. Conf. Plasma Phys., Göteborg, 1982, paper 9P-II-28.
- [4] Proc. EBT Transport Workshop, Aug. 1979, DOE/ET0112.
- [5] BATHKE, C.G., et al., Los Alamos Sci. Lab. Rep. LA-8882-MS (1981).
- [6] TSUSHIMA, A., et al., IPP-Nagoya Rep., in preparation.
- [7] BOCH, A.L., Oak Ridge Natl. Lab. Rep. ORNL/TM-7191 (1980).

## DISCUSSION

H.L. BERK: The ion temperature appeared to be saturating with power. What do you attribute this to?

M. FUJIWARA: One possible mechanism is related to the anomalous scattering loss due to the increase in  $\rho_i/L$ ; another mechanism may be the enhancement of transport by the RF field.

D. HWANG: What is the  $k_{\parallel}$  spectrum you are launching in the slow-wave heating experiment in NBT?

M. FUJIWARA: Basic experiments on wave propagation using a low-power RF generator show  $k_{\parallel} \sim 0.07$  at  $\omega \sim 0.8 \omega_{ci}$ . The calculated  $k_{\parallel}$  spectrum is affected strongly by the periodic boundary of the bumpy torus device, but we did not measure the excited  $k_{\parallel}$  spectrum in the high-power ICH experiment.



## HELIOTRON STUDIES

K. UO, A. HIYOSHI, T. OBIKI, O. MOTOJIMA, S. MORIMOTO,  
 A. SASAKI, K. KONDO, M. SATO, T. MUTOH, H. ZUSHI,  
 H. KANEKO, S. BESSHOU, F. SANO, T. MIZUUCHI, S. SUDO,  
 K. HANATANI, M. NAKASUGA, I. OHTAKE, M. IIMA,  
 Y. NAKASHIMA, N. NISHINO  
 Plasma Physics Laboratory,  
 Kyoto University, Kyoto,  
 Japan

### Abstract

#### HELIOTRON STUDIES.

Results of recent heating experiments on the Heliotron E plasma are reported in Part I. In the ECRH experiment, a currentless plasma ( $T_e(0) = 1100$  eV,  $T_i(0) = 120$  eV,  $\bar{n}_e = 5 \times 10^{18} \text{ m}^{-3}$ ) was produced with a gyrotron oscillator (28 GHz, 200 kW, pulse length 40 ms). The neutral-beam injection (NBI) heating produced a plasma ( $T_i(0) \approx T_e(0) \approx 660$  eV;  $\bar{n}_e = 3 \times 10^{19} \text{ m}^{-3}$ ) with NBI power of 1.6 MW. The heating efficiency was found to be  $2 \text{ eV} \cdot P_{\text{abs}}(\text{kW}) / \bar{n}_e (10^{19} \text{ m}^{-3})$ , where  $P_{\text{abs}}$  is the absorbed neutral beam power. The central beta value reached about 1%. The electron and ion temperatures were observed to decay during the NBI pulse. Radiative loss seems to play a major role in this evolution.

Part II presents design studies of a heliotron steady-state reactor without Joule current which aims at a commercial reactor. The main objective of this part of the paper is to present a viable design of a heliotron reactor which can be compared with tokamak reactor designs.

### Part I

#### HEATING EXPERIMENT ON HELIOTRON E PLASMA

##### 1. INTRODUCTION

During the last few years, there has been much progress in experiments on helical systems, especially heating experiments and currentless plasma production [1–5]. The energy confinement times essentially follow the drift parameter scaling for Joule-heated discharges, i.e. the confinement time increases as the Joule current is decreased. It has therefore been difficult to obtain a plasma which simultaneously has high temperature and long confinement time, since the Joule input is reduced in the low-current regime. This means that additional heating is necessary to obtain high-temperature plasmas under low-current or currentless conditions. It can be expected that favourable confinement will be obtained in the currentless plasma.

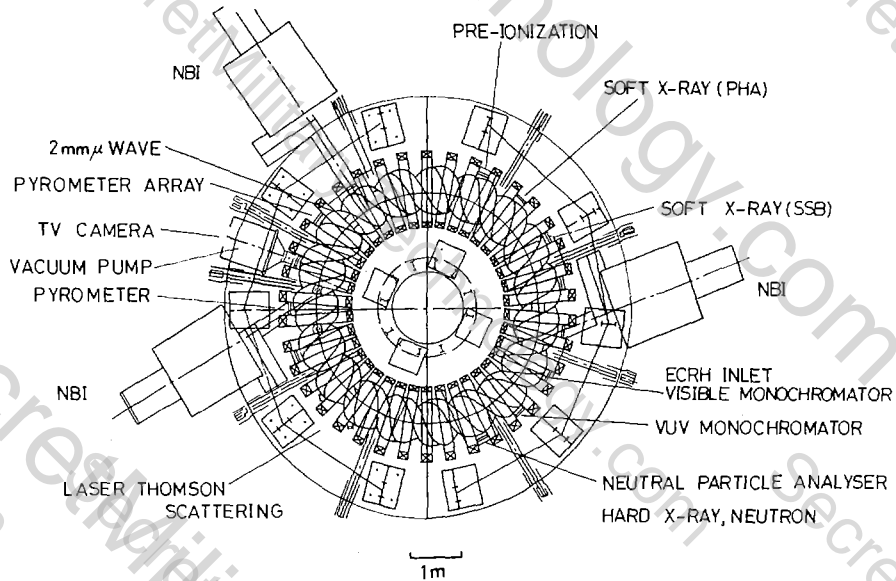


FIG.1. Top view of Heliotron E.

At present, there are two large devices for helical systems: Wendelstein-VII A and Heliotron E. Currentless plasmas have been produced in W-VII A with neutral-beam injection (NBI) and in Heliotron E with ECRH.

In the last two years, studies of Joule, ECRH [2, 3] and NBI plasmas were made in Heliotron E. The Joule plasma was studied as a target plasma for RF and NBI heating. Confinement properties for a wide range of plasma parameters, with and without Joule current, were investigated using the above auxiliary heating systems.

## 2. EXPERIMENTAL SYSTEM

### 2.1. Heliotron E system

Heliotron E is a non-axisymmetric toroidal device with large rotational transform and strong shear. The major and minor radii are 2.2 m and 0.2 m, respectively. The confining magnetic field is produced by a combination of helical ( $\ell = 2$ ), vertical and toroidal field coils. Figure 1 is a schematic of the device. The helical conductor, mounted outside the vacuum chamber, closes itself after two toroidal and nineteen poloidal rotations. The vertical field is necessary to cancel the vertical field produced by the helical coil. The toroidal

field coils are not necessary to produce the confining field but can be used to change such field properties as rotational transform, shear and volume of the confining region. Material limiters are not necessary. An air-core transformer is employed to generate a Joule current. The electrical power to the coils is fed by a 330 MVA AC generator through rectifiers.

## 2.2. ECRH system

Recent development of gyrotron technology has made it possible to supply a high microwave power to plasma confinement devices in order to produce and heat plasmas. The Varian gyrotron VGA-8050A generates 200 kW at 28 GHz. The maximum pulse width is 40 ms.

The  $TE_{02}$  circular mode was transmitted to Heliotron E by a 2.5 inch diameter waveguide coated with silver which contains a flexible joint to avoid mechanical destruction of the gyrotron tube. Fine tuning of the magnetic field and the cathode current of the tube is necessary to achieve the maximum output of the  $TE_{02}$  mode.

## 2.3. NBI system

The NBI system has three beam lines, each with two injectors of a magnetic multicusp type. Two beam lines are arranged in the  $28^\circ$  off-normal injection angle, and one is in the perpendicular (normal) injection angle of the torus in order to investigate the influence of injection angles. Performances of the injector and the beam line are reported in Ref. [6].

The maximum neutral beam power is 2.5 MW at maximum beam energy. The beam line chamber is equipped with four cryopanel to evacuate the neutral gas from the injector. The total pumping speed for the hydrogen gas is about  $10^5$  litre·s<sup>-1</sup> in each beam line.

## 3. EXPERIMENTAL RESULTS OF ECRH

The magnetic field strength is 10 kG, so that the ECR occurs on the magnetic axis. Hydrogen gas is filled 500 ms before the RF pulse. During the RF pulse, additional gas is puffed to keep the density constant. At  $t = 2$  ms after the beginning of the RF pulse, the plasma is considered to be fully ionized because the line-averaged electron density is saturated at that time. The evolution of electron and ion temperature is shown in Fig.2. The central electron temperature continues to increase up to 0.85 – 1.0 keV until  $t = 20$  ms, after which it seems to saturate during the RF pulse. The central ion temperature also saturates at  $T_i = 0.11$  keV around  $t = 20$  ms. The electron temperature decreases rapidly

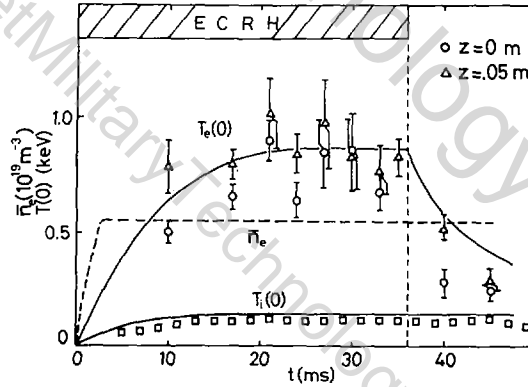


FIG. 2. Temporal evolution of central electron and ion temperature and averaged electron density. RF power is 90 kW. Line-averaged electron density is  $5 \times 10^{18} \text{ m}^{-3}$ . Solid lines indicate electron and ion temperature calculated on the basis of a simple transport model.

to 0.25 keV in 9 ms after the end of the pulse. The calculated central electron and ion temperatures are also shown in Fig. 2, assuming that  $\eta_{\text{PIN-PRAD}}$  ( $\eta$  is the heating efficiency) at the centre of the plasma is  $120 \text{ kW} \cdot \text{m}^{-3}$ , which corresponds to the peaked profile of power deposition, and that the anomaly factors of ion and electron transport, compared with the neoclassical values, are 1 and 6, respectively. The neutral density,  $5 \times 10^{14} \text{ m}^{-3}$ , is calculated from the data measured by a fast-neutral-particle analyser. Although there are many assumptions, the temporal development of the electron and ion temperatures is explained to some extent by this simple calculation. The anomaly factor 6 of the electron thermal conduction is larger than that for the afterglow plasma (less than 3) in the previous experiment [2, 3]. This discrepancy might be attributed to the different wall conditions. The characteristics of the temporal development of the electron internal energy ( $W_e = (3/2)n_e T_e \text{ dV}$ ) is also similar to that of the temperature.

The spatial profiles of electron temperature and density at  $t = 21 \text{ ms}$  under the same conditions as Fig. 2 are shown in Fig. 3. These profiles are measured simultaneously at ten different spatial points by laser Thomson scattering. The averaged radius  $\bar{r}$  is defined as follows:

$$\bar{r} = a\sqrt{(x/0.15)^2 + (z/0.30)^2}$$

where  $a = 0.21 \text{ m}$ , and  $x$ - and  $z$ -axes are in the directions of the shortest and longest radii of the elliptic cross-section of the plasma, respectively. The data are averaged over three plasma shots under the same conditions in order to reduce the experimental errors. The electron temperature profile is more peaked,  $T_e = 1.0 (1 - \bar{r}^2/a^2)^3 \text{ keV}$ , than those of the Joule-heated (low-current)

and NBI-heated plasmas, in which cases the profiles are parabolic. This suggests that the power deposition of the RF pulse may occur more strongly near the central region of the plasma. The profile of the electron density is less peaked,  $n_e = 8.4 \times 10^{18} (1 - r^2/a^2)^{1.5} \text{ m}^{-3}$ , than that of the temperature. If the additional gas is not puffed, the averaged density decreases to about  $2 \times 10^{18} \text{ m}^{-3}$ , while the electron temperature increases up to 1.0 – 1.3 keV. The physical picture of the density decrease is not yet clarified.

The ion temperature saturation phenomenon may be attributed to the charge-exchange loss. To examine this, we changed the working gas from hydrogen to helium. The charge-exchange cross-section of a helium plasma, whose ionized state is mostly  $\text{He}^{++}$ , is very much smaller than that of a hydrogen plasma. Although additional gas puffing is not required in this case, the temporal development of the line-averaged electron density is similar to that of a hydrogen plasma. The power of the RF pulse is 70 kW. The ion temperature is measured by the residual fast hydrogen neutral particles in the helium plasma. In contrast to the case of hydrogen, the ion temperature continues to increase until the end of the RF pulse. The attained temperature is 150 eV, which is higher than that of the hydrogen plasma. Therefore, the charge-exchange loss of ions with neutrals has an evident effect on the ion temperature in the case of hydrogen plasma.

Figure 4 shows the dependence of the central electron temperature on the input power of the RF pulse  $P_{\text{IN}}$ . In this case, the electron density is in the range of  $(4.5 - 6.0) \times 10^{18} \text{ m}^{-3}$ . The plotted temperature is the value during saturation. The ratio  $T_e(0)/P_{\text{IN}}$  is somewhat larger in the case of low power than for high power. The value of  $T_e(0)/P_{\text{IN}}$  is around  $10 \text{ eV} \cdot \text{kW}^{-1}$ , and that of  $W_e/P_{\text{IN}}$  is about  $8 \text{ J} \cdot \text{kW}^{-1}$ . These values represent the central and averaged heating rates due to ECRH, respectively.

These values are compared in Table I with those obtained in tokamaks. It should be noted that ECRH is used in tokamaks only as additional heating to a Joule plasma. The heating rate in Heliotron E is larger by a factor of about two than those in tokamaks.

#### 4. NBI HEATING EXPERIMENT

##### 4.1. Results of NBI heating

In the first stage of the injection heating experiment, the Joule-heated plasma, which has relatively low Joule current and a long confinement time, has been chosen as the target plasma of the injection ( $I_{\text{OH}} \approx 10 \text{ kA}$ ,  $T_e(0) \approx 200 \text{ eV}$ ,  $T_i(0) \approx 100 \text{ eV}$ , and  $\bar{n}_e \approx (1-6) \times 10^{19} \text{ m}^{-3}$ ).

The temperature of the ions and electrons and the density of the neutral particles at the central chord measured by the charge-exchange analyser are

TABLE I. COMPARISON OF HELIOTRON AND TOKAMAK VALUES

	Machine parameters			Plasma parameters with ECH				Heating rate					
	$B_0$ (T)	$\bar{a}$ (m)	R (m)	$f_0$ (GHz)	$P_{EC}$ (kW)	$n_{eo}$ ( $m^{-3}$ )	$\bar{n}_e$ ( $m^{-3}$ )	$T_{eo}$ (eV)	$\Delta T_{eo}$ (eV)	$W_e$ (J)	$\Delta W_e$ (J)	$\Delta T_{eo}/P_{EC}$ (eV/kW $^{-1}$ )	$\Delta W_e/P_{EC}$ (J/kW $^{-1}$ )
ISX-B (Ref.[7])	1.25	0.2	0.93	35	80	$1.6 \times 10^{19}$	$1.0 \times 10^{19}$	1250	400	850	$\approx 300$	5	4
JFT-2 (Ref.[8])	1.0	0.25	0.9	28	110	$8.5 \times 10^{18}$	$6 \times 10^{18}$	1000 (1250) <sup>a</sup>	400	764	421	4 to 6 <sup>a</sup>	4
T-10 (Ref.[9])	1.5	0.25		84	500		$1.5 \times 10^{19}$	1440	460	2000		1	4
H-E	1.0	0.2	2.2	28	90	$9.0 \times 10^{18}$	$5.5 \times 10^{18}$	900	900	700	700	10	8

<sup>a</sup> 1000 eV measured by Thomson scattering; 1250 eV by soft X-rays.

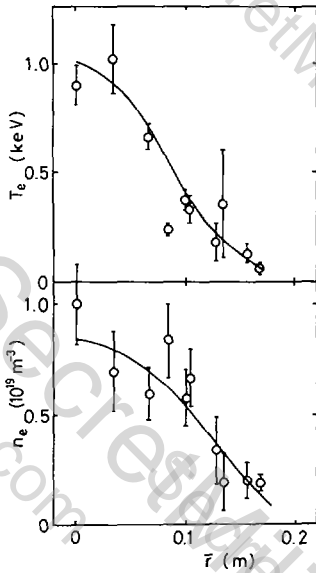


FIG.3. Spatial profiles of electron temperature and density measured by laser Thomson scattering at  $t = 21$  ms.

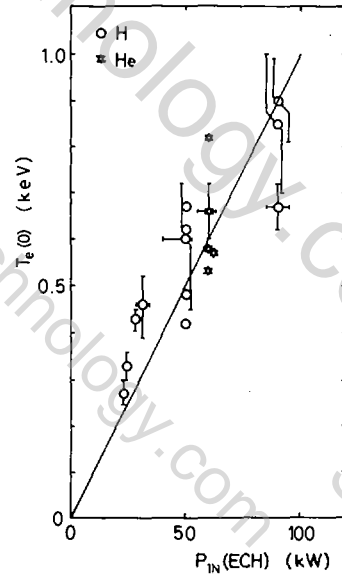


FIG.4. Dependence of central electron temperature on RF power  $P_{IN}$ . The density is fixed in the region  $4.5\text{--}6.0 \times 10^{18} \text{ m}^{-3}$ . The solid line indicates heating rate of  $10 \text{ eV} \cdot \text{kW}^{-1}$ .

plotted as a function of time in Fig.5 (1.35 MW injection power). The electrons and the ions are simultaneously heated by NBI. The maximum obtained ion and electron temperatures are 660 eV at the power level of 1.6 MW. The electron is heated first because the NBI power is mostly absorbed by electrons with low initial temperature. The power absorbed by the ions increases as the electron temperature increases. An increase of the neutral density at the centre by almost one order of magnitude is observed during the NBI pulse. This increase can be roughly explained by the halo neutral-particle deposition due to beam injection.

The ion temperature starts to decrease during the NBI pulse at an NBI power of 1.0–1.6 MW. The drop in the ion temperature can be ascribed to the increase in both plasma density and the impurity concentration at the plasma centre. The temperature decrease during the longer NBI pulse is a crucial problem that needs to be investigated. A soft-X-ray measurement by a 5-channel detector array indicated the enhancement of the radiation mainly at the central plasma region. No line radiation of heavy metals such as tungsten or molybdenum was observed with a vacuum-ultraviolet spectroscope, though emission from iron and titanium was observed. The line radiation of oxygen or carbon also increased with time

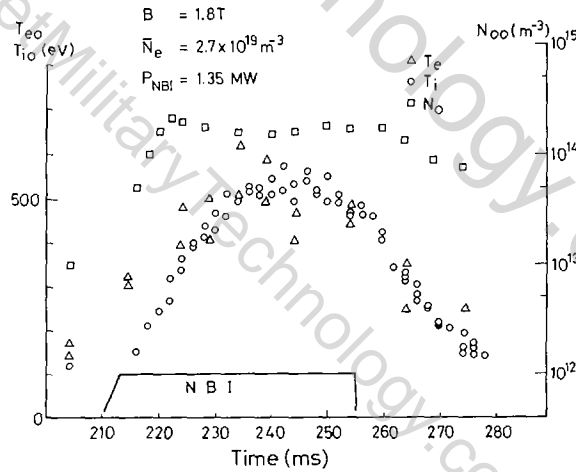


FIG.5. Neutral density at plasma centre; electron and ion temperature as a function of time.

during the NBI pulse. Quantitative estimations of the radiation power have not yet been performed. A fluctuation during the NBI pulse was also observed. Frequencies of several tens of kHz were detected by a magnetic loop. The fluctuation amplitude increased with increasing NBI power. The possibility of this fluctuation being the major cause of the temperature decrease seems to be small, however, since the fluctuation is excited at the beginning of the NBI pulse and the amplitude decreases with time. No major disruptions have been observed which might have had deleterious effects on confinement during NBI heating.

#### 4.2. Heating efficiency and energy balance

A dependence of the temperature rise on the input NBI power is measured for various densities. The input power is varied by changing the number of the injectors while keeping constant the acceleration voltage and the beam current per injector. The ion temperature increment is plotted against the absorbed NBI power  $P_{\text{abs}}$  in Fig.6. The absorbed NBI power is normalized by the averaged electron density in  $10^{19} \text{ m}^{-3}$  units. Absorbed power means the ionized neutral power which is not the exact absorbed NBI power into the plasma. The power loss due to particles of unconfined orbits ( $\approx 10\%$ ) and charge-exchange ( $\approx 10\%$ ) is not subtracted from the ionized power input. The ionization efficiency for the density range of  $(2-6) \times 10^{19} \text{ m}^{-3}$  is between 40% and 60% at an accelerating voltage of 25 kV. As shown in Fig.6, the temperature rise or the heating efficiency using such a definition of the absorbed power then scales as

$$\Delta T = 2 \text{ eV} \cdot P_{\text{abs}} (\text{kW}) / \bar{n}_e (10^{19} \text{ m}^{-3})$$

## NBI EXPERIMENT

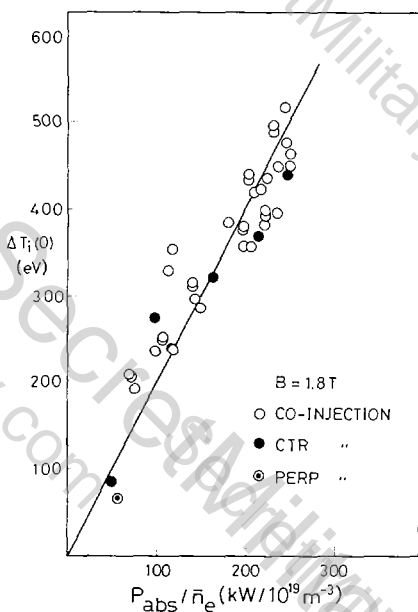


FIG. 6. Dependence of ion temperature increase on the normalized absorbed NBI power.

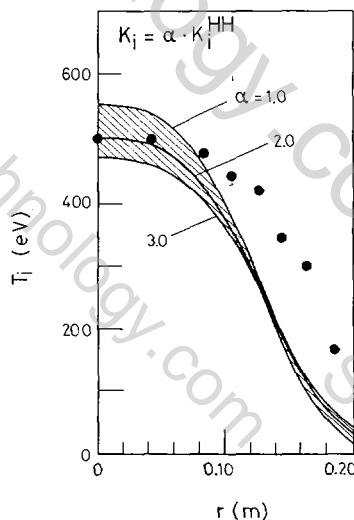


FIG. 7. Ion temperature profiles calculated from ion energy balance and measured ion temperature as a function of normalized plasma radius.

for a wide variety of the NBI power and the plasma parameters. The temperature rise is almost the same for ions and electrons. No saturation is seen at the present power level. It is difficult now to compare the ion heating rate with that of other devices, since the major input of the beam energy is transferred to the electrons. An important feature of NBI heating in Heliotron E is that the heating efficiency is almost the same for co- and counter-injection under a  $28^\circ$  injection angle as well as for perpendicular injection, which is predicted by Monte-Carlo calculation [10]. This implies that the orbit loss of the fast particles is small in the heliotron field even for perpendicular injection. The counter-injection experiment was performed by changing the direction of both magnetic field and plasma current. The absorbed power for perpendicular injection is smaller than that of the  $28^\circ$  injection, since the injection port is smaller than the others.

Plasma energy increases with the increase of absorbed NBI power. The energy content is increased by more than a factor of five, and the central beta value then reaches nearly 1%. At the present power level, we have not observed plasma energy saturation.

An energy balance calculation using a neoclassical-type heat conductivity is made for the plasma ions as shown in Fig. 7. The observed temperature of the

ions is plotted on the calculated temperature profile. A multiplication factor  $\alpha$  of the neoclassical heat conductivity given by Hazeltine and Hinton [11] was used as a variable parameter in the calculation. The absorbed NBI power profile was calculated from the Monte-Carlo code. The calculated temperature agrees with the experimental one in the central region. In the calculation, we used an assumed neutral-density profile obtained from a particle-transport computer code. The multiplication factor of the neoclassical heat conductivity, however, was not so greatly affected by changing the neutral density. The ion energy confinement can be described by the neoclassical plateau scaling, and the major loss channel of the ions seems to be the thermal conduction loss. The observed ion temperature outside  $r = a/2$  is higher than the calculated value provided  $\alpha = 1$ . This discrepancy might be attributed to the fact that the ion temperature determined experimentally in the outer part of the plasma is overestimated, supposing the orbits of the localized particles, heated in the central region, pass through the outer region.

The global energy confinement time of the electrons, defined as the ratio of the total plasma energy to the NBI power absorbed by the electrons, is about 10 ms. This, however, is not the actual energy confinement time, since the radiation power is not subtracted from the absorbed power. The power profile of the radiation has not yet been exactly measured. The energy confinement time will be improved because the radiation power is a substantial fraction of the absorbed power.

## Part II

### DESIGN STUDY OF HELIOTRON STEADY-STATE REACTOR<sup>1</sup>

#### 1. PHYSICAL CONCEPTS

The equilibrium and stability of the heliotron plasma are provided by the current in the helical coil placed outside a plasma. The magnetic field of the heliotron reactor has favourable characteristics in that the field transform  $\kappa$  and the shear  $\Theta$  are very large [12]. The value of  $\kappa$  is greater than unity and  $\Theta$  reaches 0.5. The large transform and shear are thought to be effective in reducing the level of plasma instabilities, which lead to a larger value of the critical  $\beta$  and to the reduction of plasma transport.

A currentless steady-state operation is the basic design concept of the heliotron reactor [13]. The steady-state operation can diminish the severe heat

---

<sup>1</sup> The authors of Part II are O. Motojima, A. Iiyoshi and K. Uo.

TABLE II. PARAMETERS OF HELIOTRON H

Minor radius (m)	1.8
Major radius (m)	21.0
Plasma volume (m <sup>3</sup> )	1343
Average density (10 <sup>20</sup> · m <sup>-3</sup> )	1.17
Average temperature (keV)	10.3
Average beta	0.06
Magnetic field (T)	4.0
Neutron current (MW · m <sup>-2</sup> )	1.3
Thermal power (MW)	3400
Net electrical power (MW)	1190
System power density (MW · m <sup>-3</sup> )	0.41
Thermal conversion efficiency	0.35
Net plant efficiency	0.31

cycle. Based on the experimental results from Heliotron E, we assume that no disruption occurs in the heliotron plasma, which is a serious problem in tokamak reactors [14]. The plasma boundary is determined by the last closed magnetic surface of the helical field (magnetic limiter configuration). The built-in divertor has the important task of exhausting ash from the D-T reaction [15]. One of the primary objectives of our design studies is to make it clear that the above physical concepts improve the reliability and economy of the heliotron reactor.

## 2. DESIGN PARAMETERS OF THE REACTOR

The design parameters of the heliotron commercial reactor (Heliotron H) are given in Table II. The electric output power is about 1200 MW, which is the standard power level of a present-day electric power plant. The magnetic field on the axis is 4 T, based on obtaining a  $\bar{\beta}$  value of 6%. Though the maximum field on the coil surface is almost twice as large as that on the axis, the material of the superconductor can be NbTi, which is well suited to the fabrication of a helical coil system. A poloidal cross-section and top view of the reactor are shown in Fig.8.

The coil system is composed of a continuous helical coil and vertical field coils. The  $\ell$  and  $m$  numbers are 2 and 15, respectively. The helical coil has a winding law  $\theta = m/\ell \phi$ , where  $\theta$  is the poloidal and  $\phi$  the toroidal co-ordinate.

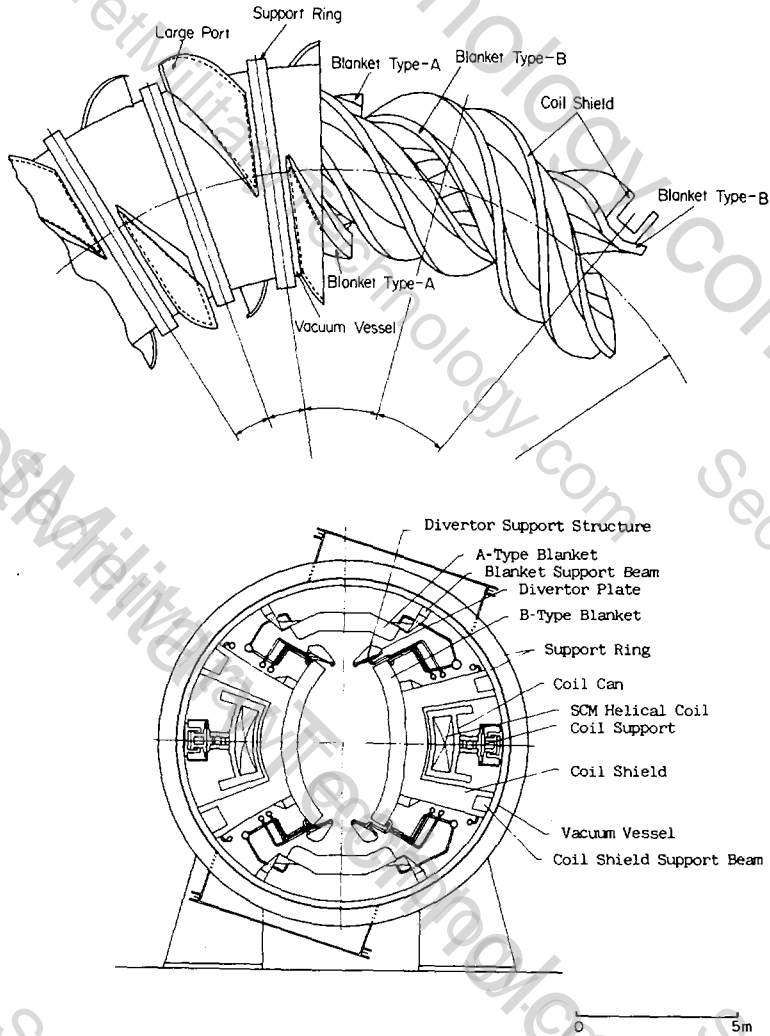


FIG.8. Poloidal cross-section and top view of heliotron reactor.

This is a simple system without toroidal and Joule coils. Since the Joule-heating electric field is not applied to the torus, a poloidal electric break is not necessary. After the plasma is produced by ECRH, additional RF and NBI heating systems are planned in order to increase the temperature up to ignition condition.

Figure 9 shows the functional dependence of the output power and wall loading on the plasma profile factor  $\zeta$ , calculated on the basis of the fully 3-D structure of the heliotron reactor. Here the density and temperature profiles are assumed to have the following form:

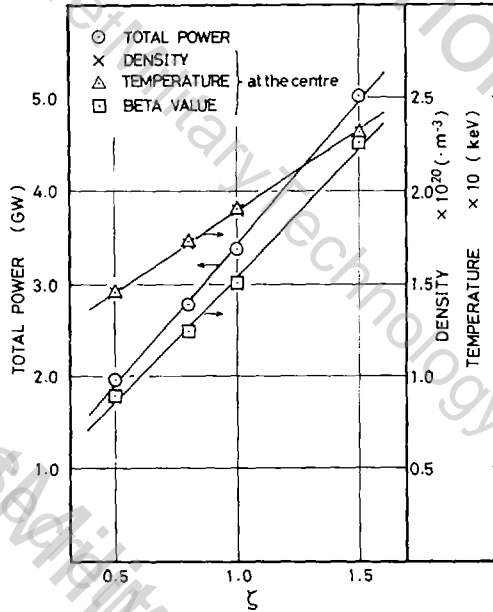


FIG.9. Functional dependence of reactor specification on the profile factor  $\zeta$ .  $N = N_0(1 - (r/a)^2)^\zeta$  and  $T = T_0(1 - (r/a)^2)^\zeta$ .

$$N = N_0(1 - (r/a)^2)^\zeta \text{ and } T = T_0(1 - (r/a)^2)^\zeta$$

In Fig.9 the volume-averaged density and temperature are kept constant. From this calculation it is obvious that the narrow profile is preferable for obtaining a large output power, while keeping the wall-loading low. The problem is how to suppress the instabilities due to the pressure gradient. Since the heliotron has large field transforms and shear, it is at least possible to say that the pressure gradient can be increased so as to be larger than other systems with low transform and shear. In the helical system, which has a large field ripple at the boundary, the trapping efficiency of the  $\alpha$ -particle becomes low at the boundary. In this sense, a peaked profile is preferable for  $\alpha$ -particle heating and confinement. The design parameters of Table II depend on the case of  $\zeta = 1$  (parabolic profile).

### 3. BLANKET STRUCTURE

To facilitate maintenance, a modular system is required. In our design, blankets are modularized so that they can be dismantled. We have designed two types of blankets. One is installed behind the divertor (type A) and is used to

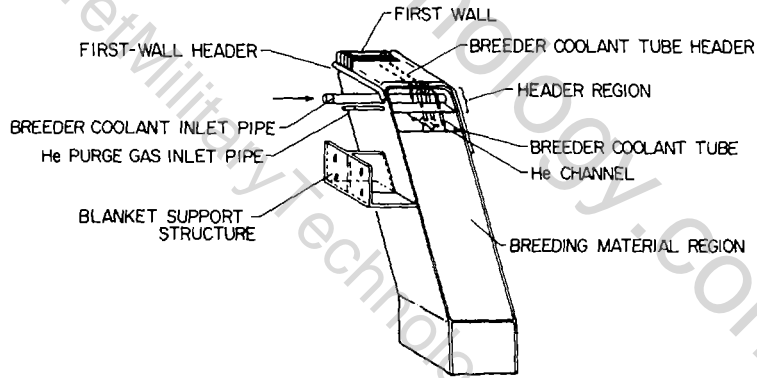


FIG.10. Sketch of type-B blanket module.

TABLE III. TRITIUM-BREEDING RATIO

Case 1	$\text{Li}_2\text{O} (^6\text{Li}-50\%)$	1.05
Case 2	$\text{Li}_2\text{O} (^6\text{Li}-\text{natural})$	1.17
Case 3	$\text{Li}_2\text{O} (^6\text{Li}-50\%, \text{PbO}-5\text{cm})$	1.16
Case 4	$\text{Li}_2\text{O} (^6\text{Li}-50\%, \text{PbO}-10\text{cm})$	1.17

breed tritium. The other (type B) is installed inside the helical coil (see Fig.10). Since there is little space in front of the helical coil, the type-B blanket is designed to be as compact as possible. It is used to breed tritium and to shield the helical coil from the neutron flux. Type A is 1.1 m thick and type B is 0.5 m thick. The blanket material is  $\text{Li}_2\text{O}$ . Both blankets consist of small 3 tonne sections which can be easily fabricated and dismantled. The modules are installed through ports between helical coils, shown in Fig.8. To get a breeding ratio greater than unity, the major part of the tritium should be bred in the type-B blanket.

The tritium-breeding ratio is calculated with a 2-D code that takes into account the structure of heliotron blankets A and B [16] (the result is shown in Table III). DOT-3.5 and MORSE codes are used. The nuclear data are GICX 40(42-n, 21- $\gamma$ ). Table III shows that the breeding ratio can possibly be greater than unity, even though there is little space behind the helical coil. The blanket is composed of 80%  $\text{Li}_2\text{O}$ , 10% SUS, 4% He purging channel, 4% cooling channel and 2% clearance. The burning-up effect is also calculated for the blanket material. It is not so severe as to reduce the breeding ratio for more than ten years. The reduction is less than 1%.

A radiation shield is installed between the type-A blanket and the helical coil to reduce the nuclear heating of the superconductor. The available thickness is only 50 cm. The main structure material is B<sub>4</sub>C and SUS. This thickness is sufficient to limit the nuclear heating to less than  $10^{-5} \text{ W}\cdot\text{cm}^{-3}$ .

#### 4. HELICAL COIL

The continuous helical coil system must be more reliable than the modular coil system. Even a small fault (minor breakdown of the insulation, or small thermal contact) may stop the reactor for a long time. Since our design concept is based on sufficient development of the superconductor, we have chosen NbTi. However, even in modular coils or tokamak toroidal field coils, a small fault is not acceptable in the realization of a reactor. The required tolerance should also be high.

The cross-section of the helical coil is a rectangle  $0.6 \text{ m} \times 1.3 \text{ m}$ ; the minor radius is 3.2 m. The magnetomotive force is  $2.8 \times 10^7$  Ampère-turns. The maximum electromagnetic force is directed to a minor radius, which is an outward radial force of  $4.4 \times 10^3 \text{ t}\cdot\text{m}^{-1}$ . To support this large force under a tolerable deformation, a support ring 100 mm thick is installed every half a pitch length of the helical coil. The expected deformation is 5 mm; the necessary refrigeration power is estimated at 0.1 MW.

#### 5. DIVERTOR STRUCTURE

The divertor plate is installed between type A and B blankets. We expect that more than 95% of the charged-particle loss flows incident to the surface of the divertor plate. It is a typical helical divertor, rotating at the same pitch as the helical coil, with total length 800 m. Since the width of the divertor layer varies along the helix owing to the toroidal effect, the divertor plate must be located precisely with respect to the magnetic field and in a direction oblique to the field line. It is possible to design the wall-loading to be less than  $2 \text{ MW}\cdot\text{m}^{-2}$ . The incident heat flux is simulated, taking into account the practical geometry of the reactor. The charge-exchange neutral particle flux is estimated to be 30–50% of the particle loss. On the first wall behind the helical coil, the heat flux of charged particles is small. Figure 11 is a sketch of the entire divertor plate module. Since the heat flux exceeds  $2 \text{ MW}\cdot\text{m}^{-2}$ , the deterioration of the divertor plate is very large, and it has to be replaced several times during the lifetime of the reactor. We shall have an opportunity to replace it once a year, when the power plant has to be shut down for the annual safety check by the government. There is good accessibility in the direction perpendicular to the helical coil,

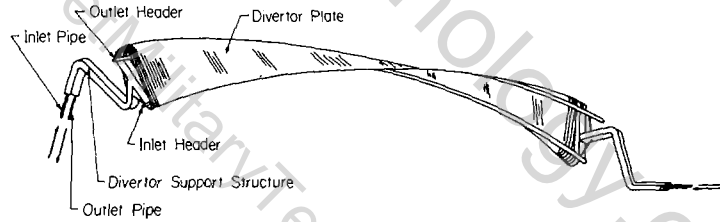


FIG.11. View of divertor plate.

since nothing impedes the outward movement of the divertor plate. We have designed three types of divertor plates, using W, SiC and SUS.

#### NOTE

Recent experimental results of the Heliotron E device verify the reliability of the physical design base of the heliotron reactor [2]. The best confinement scaling of Heliotron E predicts a more compact reactor. We consider the design base of Heliotron H to be conservative. To improve the reliability and economy of heliotron reactors, further design and experimental studies are necessary.

#### ACKNOWLEDGEMENTS

We wish to acknowledge the contribution to the engineering designs of the Mitsubishi group, Messrs R. Saito, N. Ueda, I. Yanagisawa and M. Tomita. We also thank Prof. M. Ohta and Dr. H. Nakashima at Kyushu University for the nucleonics calculations. We are grateful to Messrs M. Nakasuga and Y. Suzuki for help with additional numerical calculations.

#### REFERENCES

- [1] BARTLETT, D.V., et al., in Plasma Physics and Controlled Nuclear Fusion Research 1980 (Proc. 8th Int. Conf. Brussels, 1980) Vol. 1, IAEA, Vienna (1981) 185.
- [2] UO, K., et al., in Controlled Fusion and Plasma Physics (Proc. 10th Europ. Conf. Moscow, 1981) E-1.
- [3] IYOSHI, A., et al., Phys. Rev. Lett. **48** (1982) 745.
- [4] ATKINSON, D.W., et al., in Plasma Physics and Controlled Nuclear Fusion Research 1980 (Proc. 8th Int. Conf. Brussels, 1980) Vol. 1, IAEA, Vienna (1981) 153.
- [5] OHKUBO, K., et al., Nagoya Univ. Research Rep. IPPJ-554 (1980).

- [6] OBIKI, T., SASAKI, A., SANO, F., UO, K., Rev. Sci. Instrum. 52 (1981) 1445.
- [7] GILGENBACH, R.M., et al., Phys. Rev. Lett. 44 (1980) 647.
- [8] LaHAYE, R.J., et al., Nucl. Fusion 21 (1981) 1425.
- [9] ALIKAEV, V.V., et al., in Controlled Fusion and Plasma Physics (Proc. 10th Europ. Conf. Moscow, 1981) H-3.
- [10] HANATANI, K., WAKATANI, M., UO, K., Nucl. Fusion 21 (1981) 1067.
- [11] HAZELTINE, R.D., HINTON, F.L., Phys. Fluids 16 (1973) 1883.
- [12] UO, K., Plasma Phys. 13 (1971) 243.
- [13] IYOSHI, A., UO, K., in Plasma Physics and Controlled Nuclear Fusion Research 1974 (Proc. 5th Int. Conf. Tokyo, 1974) Vol. 3, IAEA, Vienna (1975) 619.
- [14] UO, K., et al., in Plasma Physics and Controlled Nuclear Fusion Research 1980 (Proc. 8th Int. Conf. Brussels, 1980) Vol. 1, IAEA, Vienna (1981) 217.
- [15] MOTOJIMA, O., IYOSHI, A., UO, K., Nucl. Fusion 15 (1975) 985.
- [16] NAKASHIMA, H., OHTA, M., to be published.

### DISCUSSION

S. SUCKEWER: You have a very broad ion temperature profile. Is this related to measurement by charge-exchange?

K. UO: Yes. The charge-exchange measurement is made by changing the chord angle  $\theta$ .

Y.-K.M. PENG: The presence of a small plasma current of about 30 kA in the NBI experiment would normally be expected to enhance the electron energy loss rather than the ion loss. Can you explain why the ions in the ECH experiment do not exhibit anomaly, whereas they do in the NBI experiment on Heliotron E?

K. UO: The  $\tau_{Ee}$  scaling on the heliotron plasma shows a strong  $\xi (\propto I/\sqrt{T_e})$  dependence, namely  $\tau_{Ee} \propto 1/\xi$ . The ECRH plasma has no current, whereas the NBI plasma does have some (about 30 kA). The current might result in rather poor ion confinement.

R. HAWRYLUK: In the ECH experiments, what is the ratio of the heat loss through the ion channel to that through the electron channel?

K.UO: The ion/electron channel heat loss ratio is about 1/6.

R. HAWRYLUK: How well known is the factor of 1/3 multiplying the neoclassical electron energy confinement time?

K. UO: The anomaly factor 1/3 is the best-fitting factor in the simulation.



## PLASMA HEATING AND CONFINEMENT IN THE KHAR'KOV STELLARATORS

A.V. ARSEN'EV, V.E. BYKOV, V.K. BOCHAROV,  
M.P. VASIL'EV, Ya.F. VOLKOV, A.V. GEORGIEVSKIJ,  
Yu.V. GUTAREV, A.G. DIKIJ, V.G. DYATLOV,  
G.V. ZELENIN, A.N. LETUCHIJ, A.S. LOGINOV,  
S.S. KALINICHENKO, V.G. KONOVALOV,  
V.D. KOTSUBANOV, P.G. KRISHTAL',  
A.E. KULAGA, A.I. LYSOJVAN, N.I. MITINA,  
N.I. NAZAROV, O.A. OPALEV, O.S. PAVLICHENKO,  
V.K. PASHNEV, N.F. PEREPELKIN, D.P. POGOZHEV,  
G.N. POLYAKOVA, Yu.F. SERGEEV, A.S. SLAVNYJ,  
K.N. STEPANOV, V.A. SUPRUNENKO,  
V.F. TARASENKO<sup>†</sup>, F.A. TKHORYAK, V.T. TOLOK,  
V.M. TONKOPRYAD, O.M. SHVETS

Institute of Physics and Technology,  
The Ukrainian Academy of Sciences,  
Khar'kov,  
Union of Soviet Socialist Republics

### Abstract

PLASMA HEATING AND CONFINEMENT IN THE KHAR'KOV STELLARATORS.

The latest experimental results on the Khar'kov stellarators Uragan-2, Vint-20 and Uragan-3 in the RF-, Ohmic- and turbulent-heating modes are reviewed.

The present paper reviews the latest experimental results obtained on the Khar'kov stellarators. Reference is made to results obtained on the  $\ell=3$  stellarator Uragan-2 [1] and the  $\ell=1$  torsatron Vint-20 [2], and also to the first data from research on the  $\ell=3$  torsatron with divertor, Uragan-3 [3].

### 1. RF HEATING

One of the main lines of research on the Khar'kov stellarators is the production of a high-density and high-temperature currentless plasma using RF techniques so

<sup>†</sup> Deceased.

that the confining properties of the trap can be studied in the absence of an Ohmic heating current, which distorts the original configuration of the stellarator field and is a source of many plasma instabilities.

ICR plasma heating is achieved by applying electromagnetic waves in the frequency region below or close to the ion cyclotron frequency ( $\omega \lesssim \omega_{ci}$ ), using the effects of local Alfvén, ion-cyclotron and ion-ion hybrid resonances and fast magneto-acoustic waves in the cut-off frequency region. For this purpose, it was necessary to inject 1 MW of RF power into the plasma. This was achieved by means of frame and slot antennas developed at the Khar'kov Physico-Technical Institute [4].

Effective plasma ion heating using ion-cyclotron waves in the Uragan-1 and Uragan-2 racetrack stellarators was observed only when there was a cyclotron region in the toroidal sections. Values of  $n_e = 2 \times 10^{12} \text{ cm}^{-3}$  and  $T_i \lesssim 500 \text{ eV}$  were then recorded in the plasma [5].

Subsequently, a study was made of resonance absorption of Alfvén waves in a dense hydrogen plasma containing a minority of deuterium ions [6]. An anomalously rapid energy transfer was detected between the resonance ions and ions not satisfying the ion cyclotron resonance condition. A plasma was thus obtained with an average ion energy (measured from the spectrum of charge-exchange neutrals) of  $T_i \lesssim 600 \text{ eV}$  and with  $n_e \lesssim 2 \times 10^{13} \text{ cm}^{-3}$ . The RF power input was  $P \lesssim 500 \text{ kW}$  (Fig.1).

## 2. OHMIC HEATING

Despite the success of RF heating, research into the confinement of current-carrying plasma in stellarators remains important in view of the theoretical prediction that rather high bootstrap currents caused by diffusion and heating might be present in the plasma of a stellarator reactor.

We present below the results of research into the quasi-stationary stage of a current discharge on the  $\ell=3$  stellarator Uragan-2 ( $n_e \cong 8 \times 10^{12} \text{ cm}^{-3}$ ,  $T_e \cong 120 \text{ eV}$ ) with a total angle of rotational transform greater than unity ( $\epsilon \lesssim 1.2$ ). In this case, no disruption was observed, although the discharge was accompanied by extensive magnetic-field fluctuations.

The spatial structure of the magnetic-field fluctuations was studied by means of external magnetic pick-up probes. It was established that the largest are magnetic-field fluctuations with wave numbers  $m=2$ ,  $n=1$ ;  $m=n=1$ ;  $m=3$ ,  $n=2$ ; and  $m=1$ ,  $n=0$  (where  $m$  is the azimuthal wave number for the minor torus bypass and  $n$  the number for the major torus bypass. These seem to be tearing-mode oscillations (except for the  $m=1$ ,  $n=0$  oscillations) which develop on the corresponding resonant magnetic surfaces.

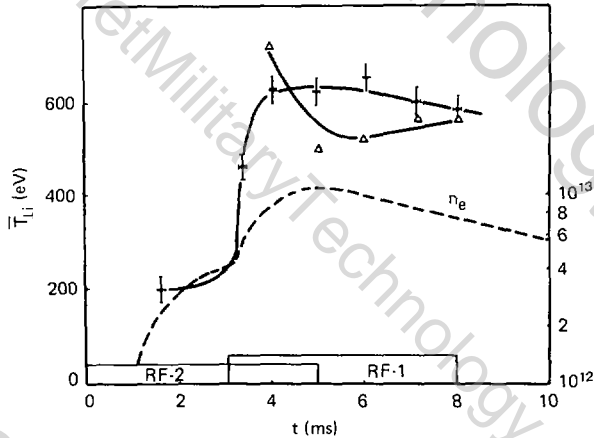


FIG.1. Time dependence of mean energy of hydrogen ions  $\bar{T}_{\perp H}$  (circles) and deuterium ions  $\bar{T}_{\perp D}$  (triangles) and of plasma density  $n_e$  during ion cyclotron heating ( $B_0 = 13.2$  kG).

The amplitude of the magnetic-field fluctuations over the radius of the plasma column was measured by means of a movable magnetic probe. It peaks near the discharge axis (Fig.2) and rises as the ratio of current to stellarator angle of rotational transform,  $t_c/t_{st}$ , or with diminishing shear  $S$  (Fig.3). It should be noted that in our experiments the shear value  $S$  is unambiguously linked to the ratio  $t_c/t_{st}$ , so it is difficult to determine which of the magnetic configuration factors —  $S$  or the  $t_c/t_{st}$  ratio — influences the amplitude of the oscillations.

The absolute value of the energy life-time in the Uragan-2 stellarator is close to the values obtained by applying well-known scaling laws (Alcator [7] or quasi-neoclassical [8]), and  $\tau_E \sim u/v_{T_e}$  as observed by the authors of Refs [9, 10] on other stellarators (Fig.4), where  $u$  is the current velocity and  $v_{T_e}$  the thermal velocity of the electrons. It should be pointed out that in our experiments  $n_e$  and  $T_e$  change insignificantly at the quasi-stationary stage of the discharge, and so the energy life-time dependence can perfectly well be written as  $\tau_E \sim 1/I_p$  (Fig.4), where  $I_p$  is the plasma current.

From the experimental results available, it may be assumed that the magnetic-field fluctuations lead to anomalous energy transfer in the discharge. The flat radial profile of  $n_e(r)$  and  $T_e(r)$  observed in the experiments, which is characteristic of all stellarator experiments, seems to be the result of enhanced transfer in the central regions of the discharge which, in turn, may be ascribed to the presence of magnetic-field fluctuations. The increase in the plasma current in a shear stellarator magnetic configuration leads both to an increase in the  $t_c/t_{st}$  ratio and to a decrease in the shear  $S$ , and, consequently, to an increase in the amplitude of the magnetic-field fluctuations.

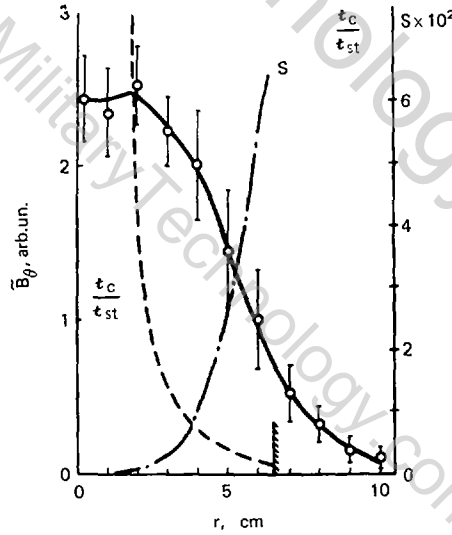


FIG. 2. Distribution across plasma column of amplitude of magnetic-field fluctuations  $\tilde{B}_0$ , shear  $S$  and ratio of current to stellarator angle of rotational transform,  $t_c/t_{st}$ . Dashed line marks the plasma column boundary. Discharge parameters are as follows:  $n_e \cong 6 \times 10^{12} \text{ cm}^{-3}$ ,  $T_e \cong 100 \text{ eV}$ ,  $I_p = 5 \text{ kA}$ ,  $B_0 = 14.4 \text{ kG}$ .

In these experiments, the conditions required for growth of a current-driven convective instability occur at the periphery of the plasma column in the  $n_e$  and  $T_e$  gradient region. This instability can also contribute to anomalous energy losses from the plasma.

In the current plasma of the Uragan-2 stellarator, the main energy losses occur through the electron channel and these losses become greater as the current in the plasma increases. The results confirm the conclusions set out in an earlier paper on RF plasma heating in the Uragan stellarator where it was pointed out that, in the currentless-heating mode, the energy life-time is close to the neo-classical value [5].

The stabilizing influence of shear was also confirmed by research into the electrostatic fluctuations which are associated with the development of intrinsic MHD modes and which give rise to disruptive instability in the  $\ell = 1$  high-shear torsatron Vint-20 (Fig. 5). In these experiments,  $t_c \ll t_{st}$ .

The particle life-time  $\tau_n$  was measured in the Ohmic-heating mode. The dynamics of the radial density distribution profile for atoms of the working gas (hydrogen) was measured by the resonance laser fluorescence technique along the  $H_\alpha$  line. Figure 6 shows the time dependence of the hydrogen density along the discharge axis and at the periphery ( $r = 6.8 \text{ cm}$ ). Figure 7 shows the radial distribution of the hydrogen density along the vertical diameter at  $t = 3.5 \text{ ms}$  from the

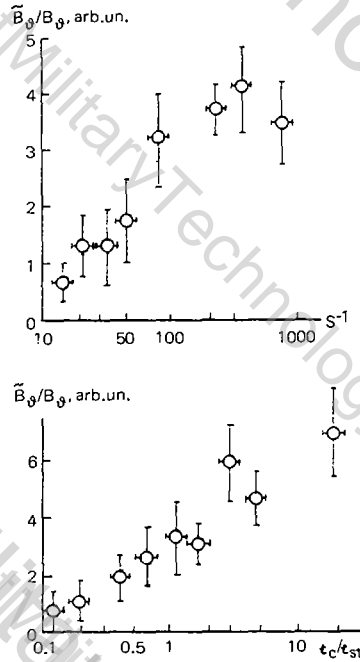


FIG. 3. Amplitude of magnetic-field fluctuations normalized to amplitude of plasma current field,  $\tilde{B}_\theta/B_\theta$ , as a function of  $S$  and  $\tau_c/\tau_{st}$ .

beginning of the discharge. Proceeding from the data on the evolution of the radial distribution of the hydrogen density, combined with measurements of the radial profiles of the electron density and temperature, we can study the charged-particle balance in the stellarator. The measurements have shown that, in the time interval  $t = 1.5 - 2.5$  ms, hydrogen ionization is sufficient to explain the observed rate of growth in the electron density, and the particle life-time is  $\tau_n \cong 1.5$  msec. The subsequent increase in density cannot be ascribed solely to hydrogen ionization, and the effect of impurities has to be taken into account.

### 3. TURBULENT ELECTRON AND ION HEATING

In the Ohmic-heating mode, if there is an increase in the electron temperature  $T_e$  and a slower increase in the density  $n_e$ , the condition  $E/E_{Dr} \sim En/T_e > 1$  may be satisfied even when moderate electric fields are applied. In this case, the Ohmic-heating mode changes smoothly into a turbulent heating mode. A similar situation may also occur at the periphery of the plasma column in other cases.

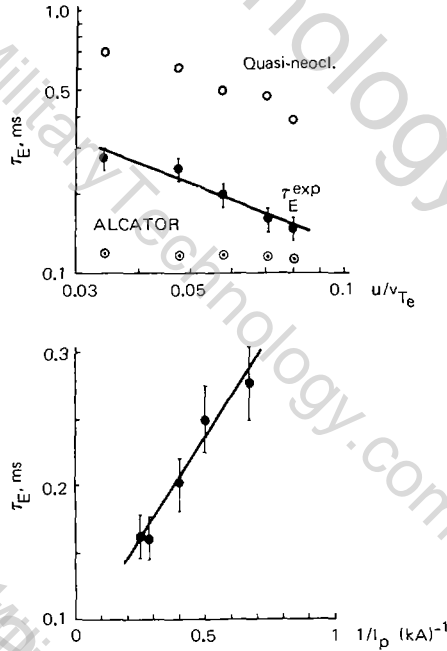


FIG. 4. Energy life-time  $\tau_E$  versus drift parameter  $u/v_{T_e}$  and  $1/I_p$ :

- - experiment;
- ⊙ - theory based on Alcator scaling law [8];
- - theory based on quasi-neoclassical scaling law [9].

Discharge parameters:  $n_e \leq 8 \times 10^{12} \text{ cm}^{-3}$ ,  $T_e \leq 120 \text{ eV}$ ,  $I_p \leq 5 \text{ kA}$ ,  $t_{st} = 1$ ,  $B_0 = 14.4 \text{ kG}$ .

Furthermore, a study of turbulent plasma heating is of considerable interest in itself.

Experiments in turbulent heating of a strongly magnetized plasma in the Uragan-2 stellarator with  $\omega_{ce}/\omega_{pe} = 2-2.5$ ,  $B_0 = 15.8-19.4 \text{ kG}$  and  $t_{st} = 1$  were performed by Perepelkin and co-workers [11] using two short powerful current pulses,  $P_{OH} = 0.25 \text{ MW}$  and  $P_{TH} = 4 \text{ MW}$ . The first pulse was used to obtain a cold, fully ionized plasma ( $n_e = 6 \times 10^{12} \text{ cm}^{-3}$ ,  $T_e^0 = 15 \text{ eV}$ ), and the second to produce turbulent heating. The duration of the pure phase of the high-power discharge was of the order of  $300 \mu\text{s}$  and was limited by the rate of re-cycling and contamination.

The dynamics of high-power discharges is such that, in the high-electric-field mode,  $E \cong E_{Dr} \approx n/T_e$ , turbulent electron heating is accompanied by total stopping of the intense runaway electron flux which occurs in the plasma at the gas ionization stage and at the onset of strong heating. This effect is clearly visible in Fig. 8.

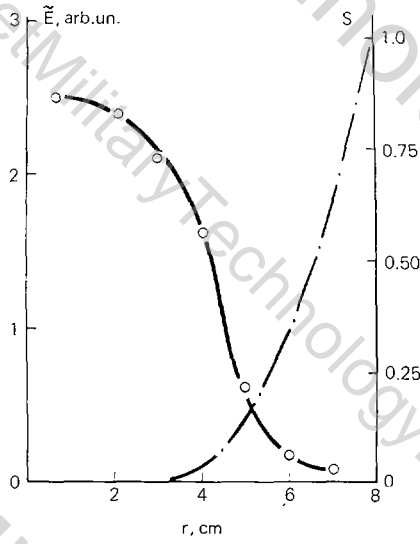


FIG.5. Distribution across plasma column of fluctuation amplitude of electric field  $\bar{E}$  and shear  $S$ .  
 Discharge parameters:  $n_e \cong (1-2) \times 10^{13} \text{ cm}^{-3}$ ,  $T_e \cong 50 \text{ eV}$ ,  $I_p \cong 2 \text{ kA}$ ,  $B_0 = 4 \text{ kG}$ .

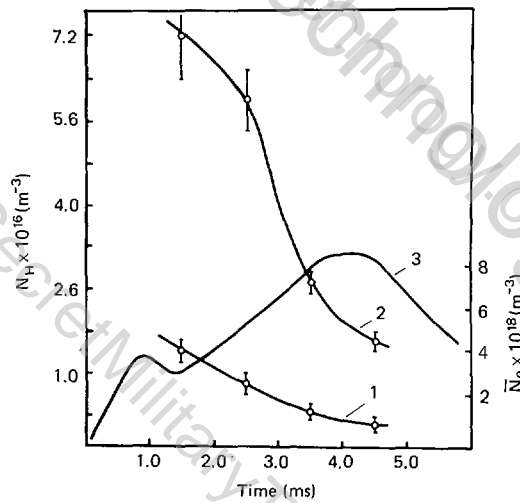


FIG.6. Time dependence of hydrogen atom density at centre (1) and periphery,  $r = 6.8 \text{ cm}$  (2) of plasma column, and time dependence of mean electron density (3).

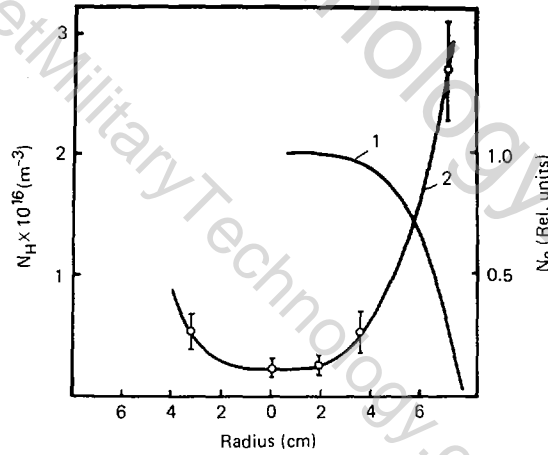


FIG. 7. Radial distribution of hydrogen density at  $t = 3.5$  ms; (1) is the electron density.

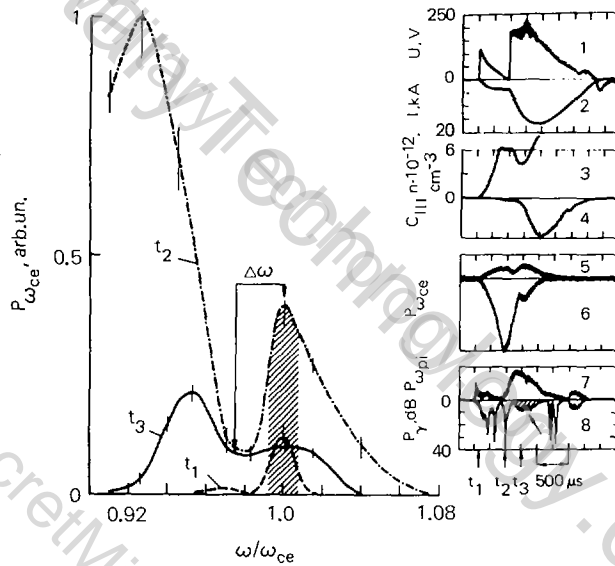


FIG. 8. Radiation spectra at cyclotron frequency and typical discharge oscillograms: 1, 2 – voltage and current; 3 – plasma density; 4 – CIII impurity line (4647 Å); 5, 6 – radiation power at frequencies  $\omega/\omega_{ce} = 0.985$  and  $0.945$ ; 7 – noise intensity near ion plasma frequency  $P_{\omega_p}$ ; 8 – X-ray intensity from local target in plasma,  $P_\gamma$ , over energy range  $\epsilon_e \cong 3\text{--}50$  keV, plotted on logarithmic scale. Shaded area in cyclotron radiation spectra indicates broadening of resonance line due to magnetic-field inhomogeneity in region where radiation is detected on race-track, where  $\Delta B/B = 1.5\%$ .

The radiation spectra near the cyclotron harmonics are complex in shape. The time evolution of the radiation curve is entirely determined by the dynamics of the high-energy 'tail' of the runaway electrons so that it can be used in conjunction with X-ray diagnostics as a reliable method of controlling the electron heating process.

During the gas ionization and electron acceleration stages ( $t_1$  and  $t_2$ ), essentially two peaks are observed in the cyclotron radiation spectrum, including one clearly defined thermal peak near the resonance line  $\omega_{ce}$ , which has a stable frequency, and another non-thermal peak which shifts rapidly along the frequency scale into the 'red' region of the spectrum as the energy of the accelerated electrons increases.

The time at which intense ion plasma noise  $\omega_{pi}$  is generated in the discharge correlates with the disruption of electron acceleration and the disappearance of hard X-rays from the discharge (oscillograms 7 and 8 in Fig.8). The runaway electrons are stopped in a relatively short time (20–25  $\mu$ s). The active stage of the turbulent discharge with  $E > E_{Dr}$  is characterized by the emission of intense, soft X-rays from the target and an intense flux of high-energy charge-exchange atoms, indicating ion heating. Shading and an arrow mark the interval near  $t_3$  in oscillogram 8 (Fig.8) during which soft X-rays are emitted in the thermal energy region,  $\epsilon_e \cong 3-7$  keV. The cyclotron radiation spectrum exhibits a broadened peak with a frequency shift (time  $t_3$ ) which is a characteristic feature of strong electron heating. The resonance line is broadened and its centre shifted relative to the centre of the 'cold' line by  $\Delta\omega/\omega_{ce} = \sqrt{2\pi} T_e/(m_e c^2) = 2-2.5\%$ . This corresponds to an equivalent temperature of 5 keV and is in agreement with the temperature readings from the soft X-ray spectrum.

Figure 9 shows spectra of neutral charge-exchange atoms recorded at the turbulent-heating instant  $t_3$ . The energy content of the ion 'tail' in high fields with  $E > E_{Dr}$  increases with the magnetic field, and the 'tail' temperature,  $T_i \sim I_p \sim B$ , also increases accordingly.

When the Uragan-2 stellarator was operating with high magnetic fields in an optimum mode, the authors observed no limit to the injection of large amounts of Ohmic power into the plasma and no limit to the increase in the electron,  $T_e$ , and ion  $T_i$  temperatures.

#### 4. FIRST EXPERIMENTS AT THE URAGAN-3 TORSATRON

Since impurities have a major effect on the plasma energy balance, methods of reducing their accumulation in the plasma volume are of very great importance. The most effective means of impurity control seems to be the divertor. An experimental device belonging to the next generation, viz. the Uragan-3 with divertor, is now starting operation in Khar'kov. This new experimental device was

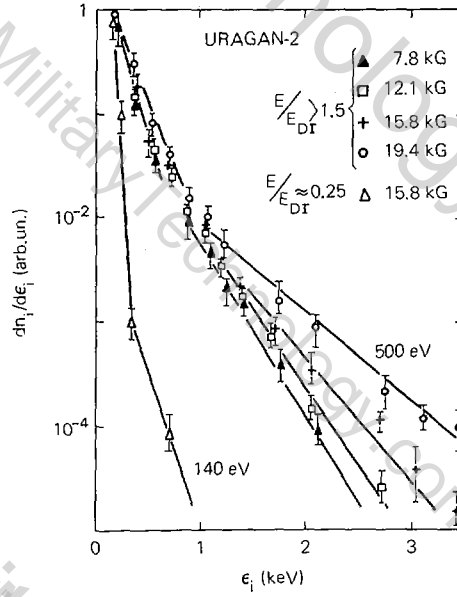


FIG. 9. Charge-exchange neutral-atom spectra recorded during turbulent heating.

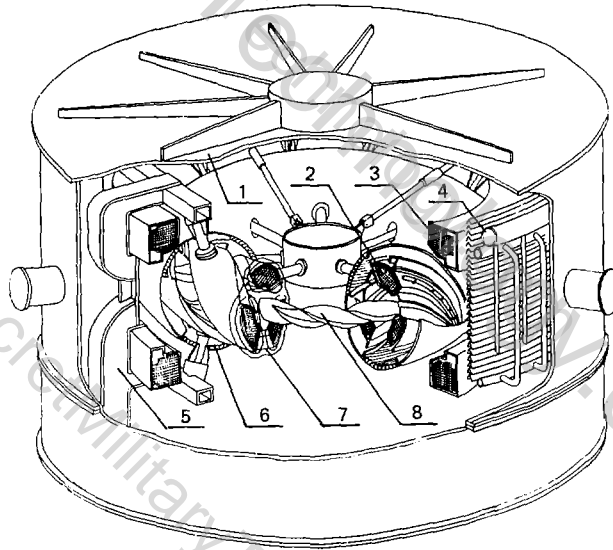


FIG. 10. Diagram of Uragan-3 device: 1 - vacuum tank; 2 - helical winding; 3 - compensating and correcting winding; 4 - cryopanel; 5 - load-bearing frame; 6 - divertor; 7 - divertor flux; 8 - plasma column.

constructed in order to study the operation of a poloidal divertor and investigate the confinement of a currentless plasma in a torsatron over a wide range of collision frequencies.

It consists of an  $\ell = 3$  torsatron with no special toroidal magnetic field winding. A divertor magnetic-field configuration is produced by means of a 'force-free' helical winding with equally inclined turns, combined with a compensating winding consisting of two current rings (Fig.10).

Since the helical winding is, to a large extent, freed from the effect of integral ponderomotive forces, it was possible to design a slimmed-down load-bearing structure which makes access to the useful volume of the plasma comparatively easy. With the addition of a small transverse magnetic field (up to  $\pm 3\%$ ), the torsatron magnetic configuration is such that we can control the main parameters defining the configuration over a wide range with only a slight variation in the radius of the last undestroyed surface.

To produce and heat the plasma, it is intended to use currentless techniques such as RF-heating and heating with fast neutral atoms.

The main parameters of Uragan-3 are given by:

Confining field, $B_0$	25 kg
Major radius of helical winding, $R$	100 cm
Minor radius of helical winding, $a_B$	27 cm
Mean plasma radius, $a$	13.5 cm
Number of field periods, $n_b$	9
Rotational transform angle on the last undestroyed surface, $t_{st}(a)$	0.6
Angle at the axis, $t_{st}(0)$	0-0.25
Shear, $S(a)$	0.15-0.25
Magnetic well, $V'/V'_0$	0-10%

Power of plasma heating sources:

RF-heating	4 MW
Neutral injection	1.5 MW

In the initial experiments on the Uragan-3 torsatron, the magnetic-surface parameters were measured by means of the electron-beam technique.

Data were obtained on the dimensions of the last undestroyed magnetic surface and the thickness of the diverted magnetic flux when a transverse magnetic field was applied in the 'anti-well' mode ( $B_{\perp}/B_0 = -1\%$ ). The lines in Fig.11 mark the magnetic field structure as calculated numerically, and the dots represent the experimental results. There is satisfactory agreement between the measurements and the theoretical predictions.

RF plasma production and heating in the Uragan-3 torsatron is achieved by means of various antennae. Antennae with a broad spectrum of phase velocities

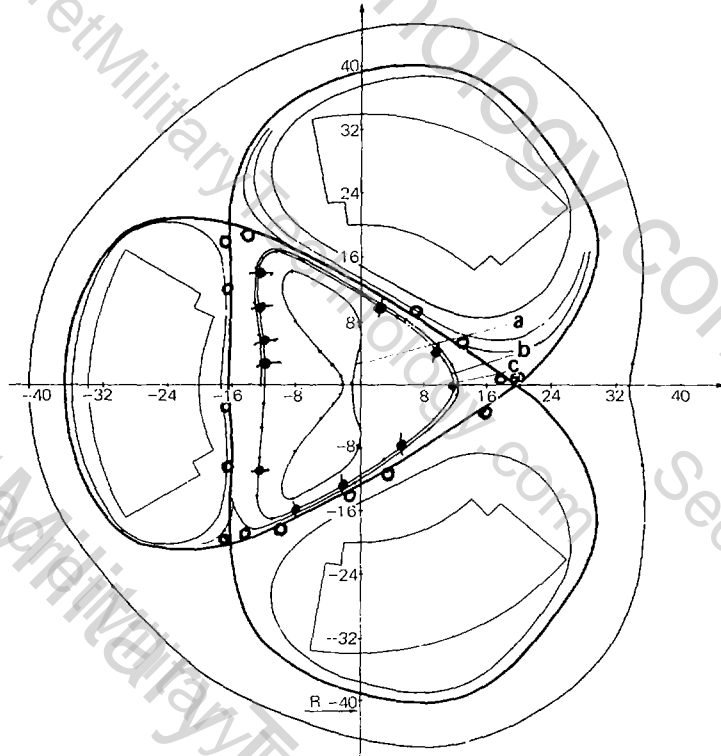


FIG. 11. Magnetic-field lines showing internal (a) and external (b) magnetic surfaces and ergodic layer (c). Dashed line shows the reference separatrix,  $\otimes$  – position of electron gun for the study of the divertor field lines (solid lines).  $\circ$  and  $\bullet$ : experimental points defining geometry of reference separatrix and the last undestroyed surface according to results of single-turn measurements.

$\omega/k_{\parallel}$  are used to produce the plasma. With this technique, it is possible to maintain the local Alfvén resonances  $\omega = k_{\parallel} v_A(r)$  while increasing the plasma density by sequential excitation of toroidal modes  $N = 1, 2, \dots$  (the ‘relay-race’ mode mechanism). In the Uragan-2 stellarator, the same technique yielded a plasma density of  $n_e \approx 10^{13} \text{ cm}^{-3}$  with an RF power input of less than 300 kW (Fig. 12). In the Uragan-3 torsatron, this technique made it possible to maintain RF ionization of hydrogen in the useful volume at an initial pressure  $p_0 \approx 10^{-5}$  torr and an injected power level exceeding 200 kW.

The plasma is then heated by means of antennae covering a comparatively narrow spectrum of phase velocities which maintain Alfvén resonance conditions for the selected plasma density near the discharge axis.

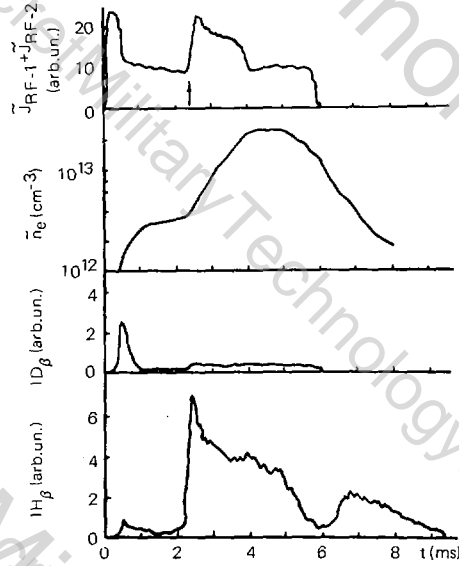


FIG. 12. Currentless hydrogen-deuterium plasma produced by puffing hydrogen (shown by arrow) into a deuterium plasma and running two RF-generators simultaneously ( $P_{1RF} \cong 200$  kW,  $f_1 = 10$  MHz,  $P_{2RF} \cong 300$  kW,  $f_2 \cong 19.3$  MHz,  $B_0 \cong 14$  kG).



FIG. 13. Magnet system module for Uragan-5.

## 5. FURTHER DEVELOPMENT OF THE TORSATRON

A suitable modular design is required in order to develop stellarator systems which can form the basis of a thermonuclear reactor. The authors of Ref. [12] have proposed a modular magnet system for a torsatron. Each module in the system consists of an  $\ell$ -turn helical winding and a multipole compensation winding (the multipolarity  $p$  is determined by the number of circular coils producing the vertical compensating field) which is used as a return circuit. The windings are connected by compensated joints.

A modular torsatron (Uragan-5) is now being developed (Fig. 13) with the following parameters:  $\ell = 3$  helical winding with major and minor radii of 34 cm and 7.1 cm, a multipole ( $p = 6$ ) compensating winding with a minor radius of 8.5 cm and 15 modules matching the number of field periods.

The radius of the last undestroyed surface is  $a \cong 4.5$  cm, and the total angle of rotational transform  $\epsilon_{st} \cong 0.7$ .

## REFERENCES

- [1] AMELIN, V.Z., BIRYUKOV, O.V., VISHNEVETSKIY, V.N., et al., *Ukr. Fiz. Zh.* **21** 3 (1976) 422.
- [2] GEORGIEVSKIY, A.V., SUKHOMLIN, E.A., SUPRUNENKO, V.A., *At. Ehnerg.* **34** 5 (1973).
- [3] Osnovnye fizicheskie zadachi ustanovki "Uragan-3" (Main Physics Problems Associated with the Uragan-3 Device), Khar'kov Physical-Technical Institute Preprint 81-45, Khar'kov (1981).
- [4] KALINICHENKO, S.S., et al., in *Controlled Fusion and Plasma Physics (Proc. 9th Europ. Conf. Oxford, 1979)* Vol.1, Oxford (1979) 19.
- [5] DIKIJ, A.G., et al., *Plasma Phys.* **18** (1976) 577.
- [6] SHVETS, O.M., et al., *Pis'ma Zh. Ehksp. Teor. Fiz.* **34** (1981) 533.
- [7] COHN, D.R., PARKER, R.R., JASSBY, D.L., *Nucl. Fusion* **16** (1976) 31.
- [8] GUTAREV, Yu.V., SUPRUNENKO, V.A., in *Controlled Fusion and Plasma Physics (Proc. 9th Europ. Conf. Oxford, 1979)* A2-7, Oxford (1979) 7.
- [9] UO, K., et al., in *Controlled Fusion and Plasma Physics (Proc. 10th Europ. Conf. Moscow, 1981)* Vol.1, Moscow (1981) E-1.
- [10] ATKINSON, D.W., et al., in *Plasma Physics and Controlled Nuclear Fusion Research (Proc. 7th Int. Conf. Innsbruck 1978)* Vol.1, IAEA, Vienna (1979) 153.
- [11] PEREPELKIN, N.F., et al., in *Controlled Fusion and Plasma Physics (Proc. 10th Europ. Conf. Moscow, 1981)* Vol.1, Moscow (1981) E-12.
- [12] BYKOV, V.E., GEORGIEVSKIY, A.V., SERGEEV, Yu.F., *Tezisy dokladov II Vsesoyuznoj Konferentsii po NPTR (Proc. 2nd All-Union Conf. on Scientific Problems of Fusion Reactors, Leningrad, 1981)* 48.

## DISCUSSION

K. UO: Did you measure the ion temperature in the straight section or the bent section of the Uragan-2 race-track stellarator?

O.S. PAVLICHENKO: We measured the ion temperature in the straight section.

## NEUTRAL-INJECTION HEATING IN THE WENDELSTEIN VII-A STELLARATOR

### *W VII-A TEAM*

G. CATTANEI, D. DORST, A. ELSNER, G. GRIEGER,  
H. HACKER, J. HARTFUSS, H. JÄCKEL, R. JAENICKE,  
J. JUNKER, M. KICK, H. KROISS, C. MAHN, S. MARLIER,  
G. MÜLLER, W. OHLENDORF, F. RAU, H. RENNER,  
H. RINGLER, F. SARDEI, M. TUTTER, A. WELLER,  
H. WOBIG, E. WÜRSCHING, M. ZIPPE

### *NI GROUP*

K. FREUDENBERGER, G.G. LISTER, W. OTT,  
F.-P. PENNINGSFELD, E. SPETH

Max-Planck-Institut für Plasmaphysik,  
Euratom-Association, Garching,  
Federal Republic of Germany

### Abstract

#### NEUTRAL-INJECTION HEATING IN THE WENDELSTEIN VII-A STELLARATOR.

A high-density deuterium plasma with  $\beta(0) \leq 1\%$  at  $B_0 = 3.2$  T,  $n_{e0} \geq 10^{14}$  cm<sup>-3</sup>,  $T_i = 1$  keV,  $T_e = 0.6$  keV, is maintained in the Wendelstein VII-A Stellarator by neutral injection (27 kV, H<sub>2</sub>,  $P_N \approx 1$  MW). This was achieved by increasing the density of the target plasma by the ablation of an injected D<sub>2</sub> pellet. Oxygen is the dominant impurity. Contamination of the plasma has been reduced by various means, lowering the radiation losses, so that the "currentless" phase could be extended from 10 ms to 150 ms. The plasma in the currentless phase shows no instabilities. Analysis of the energy balance describes the ion heat loss in agreement with the neoclassical prediction. The electron conduction loss seems to follow the empirical scaling  $\chi_e \sim 1/nT^{2/3}$ . The beam-heating efficiency as predicted by the ODIN code, especially for the ions, is smaller than its observed value.

### 1. INTRODUCTION

"Currentless" operation of the Wendelstein VII-A Stellarator by neutral-injection (NI) heating was achieved in 1980 [1]. The plasma exhibits very favourable properties:

- (a) No MHD instabilities, which would cause deterioration in the confinement at residual plasma current  $I_p$ , are observed.
- (b) The level of density fluctuations is significantly reduced.

- (c) The improved confinement allows a plasma to be maintained at remarkably high pressure.

However, radiative losses increasing strongly with time restrict the duration of the currentless phase. A detailed analysis of the power balance was uncertain owing to the dominant radiative power losses. In the meantime, significant progress has been made in diminishing the plasma contamination and consequently in extending the duration of the currentless phase [2]. The full NI power  $P_N \approx 1$  MW was applied to heat the plasma.

## 2. MODE OF OPERATION

Four neutral injectors, using  $H_2$ , are available with 200–350 kW power each at an accelerating voltage of 27 kV. The W VII-A Stellarator (main radius  $R = 2$  m; plasma radius  $a = 0.1$  m; main field  $B_0 \leq 3.5$  T; helical windings  $\ell = 2$ ,  $m = 5$ ; shearless external transform  $\epsilon_0 \leq 0.6$ ) with medium-sized geometry, allows only almost perpendicular injection,  $84^\circ$ , to the direction of the magnetic field. Consequently, large losses (orbit losses and shine-through even at high target densities  $fn_{d1} > 1 \times 10^{15} \text{ cm}^{-2}$ ,  $n_{e0} > 10^{14} \text{ cm}^{-3}$ ) must be taken into account.

The deuterium target plasma is produced by Ohmic heating at a maximum line density  $fn_{d1} \approx 0.5 \times 10^{15} \text{ cm}^{-2}$  with 20 kA plasma current, which is programmed down at the start of NI. To avoid catastrophic energy losses due to growing tearing modes, especially (2,1) and (3,2) modes during this transition, the location of the resonance surfaces within the plasma must be controlled. This is mainly done by feedback control of the current in the helical windings with the condition  $\epsilon_0 + \epsilon_p \approx 0.5$  for the total rotational transform at the plasma boundary.

By proper adjustment of the NI power, and of the cold gas flux by programmable gas valves, a fast current reduction (20 ms) a sufficient suppression of the (2,1) tearing mode even at  $\epsilon_0 + \epsilon_p = 0.45 < 0.5$  is possible. The current reduction is the most critical part during the transition to the currentless discharge with a shearless profile of the transform  $t$ .

A residual current of 0.5–3 kA is observed in the parameter range of the W VII-A plasma with resistive voltage kept near zero. This current is higher by an order of magnitude than predicted for bootstrap or Ohkawa current. There may be a number of reasons for this residual current:

- (a) The plasma pressure.  
 (b) Non-stationarity of the plasma parameters may introduce dynamic voltages by positional shift of the plasma column.

(c) Unfortunately there is a large voltage ripple in the primary OH system at zero loop voltage, and the current may therefore result from rectified eddy currents at the plasma boundary.

Apparently the residual current modifies the magnetic configuration and consequently influences the confinement. Further investigations at stationary conditions are necessary to clarify this observation.

(d) Since the particle transport in W VII-A is faster than neoclassical transport, the diffusion-driven currents must also be expected to deviate from neoclassical predictions. An increased particle loss could result in an increased bootstrap current.

### 3. RESULTS

#### 3.1. Parameter range

The refinement of the scenario for the transition to currentless plasma finally leads to improved plasma parameters. Two examples will be described in detail. Figure 1 presents the main parameters of a "clean" standard discharge "A". Starting with the target plasma, the plasma current  $I_p$ , the external transform  $t_0$ , and the edge value  $t_0 + \tau_p$  are plotted. Three injectors are used. By the use of Ti-gettered ion sources, the amount of light impurities in the beam has been significantly reduced [3]. A steady cold gas flux maintains broad density profiles, as seen in Fig. 2. The corresponding electron temperature stays at  $T_e \approx 400$  eV. Figure 1 shows the energy content  $W$ , electron temperature  $T_e$  determined by soft-X-ray measurements, ion temperature  $T_i$  measured by charge-exchange analyser as well as that derived from neutron flux from D-D reactions. An ion temperature profile at  $t = 180$  ms obtained by active charge-exchange analysis using a diagnostic beam is included in Fig. 2. At the boundary region, values for  $T_i$  derived from Doppler width measurements from C V lines are added. Figure 3 shows the time behaviour of the total radiation within the indicated radii measured by bolometer. The distribution of the local radiative power density is plotted for this discharge in Fig. 4. When it is taken into account that the line density is growing steadily, the slight increase of central radiation indicates an effective reduction of the impurity flow compared to previous discharges.

The operation with refined beams and the subsequent reduction of impurity inflow allows the full use of four injectors. In a second example (Fig. 5) a discharge "B" with  $P_N \approx 1$  MW is described. During this discharge at  $t = 124$  ms, a  $D_2$  pellet (0.6 mm diameter,  $500 \text{ m} \cdot \text{s}^{-1}$  velocity) has been ablated. Practically all particles remain in the plasma, which results in density increase by a factor of 2. From

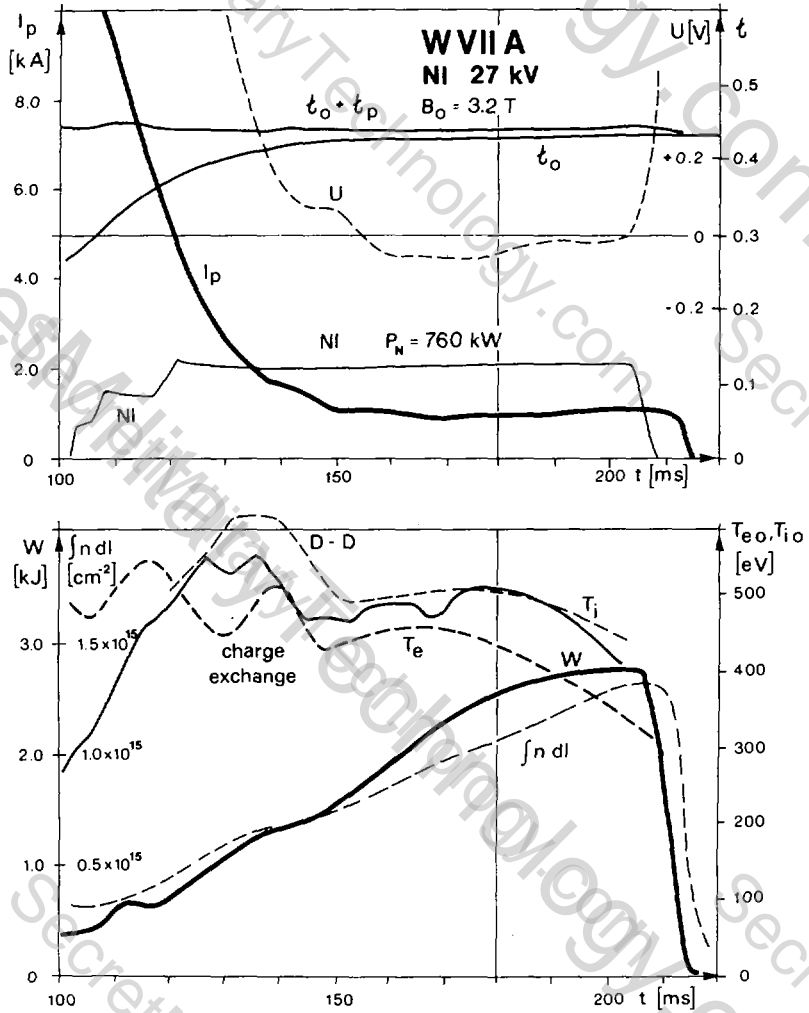


FIG.1. Discharge "A": plasma current reduction  $I_p$ , "currentless" phase with resistive voltage  $U$  during NI,  $P_N = 760$  kW ( $T_i$  gettering). Main parameters:  $t_o, t_o + t_p$ —rotational transform;  $\int n dl$ —line density;  $W$ —energy content;  $T_{e0}$ —electron temperature (soft X-ray);  $T_{i0}$ —ion temperature (charge-exchange, D-D neutrons).

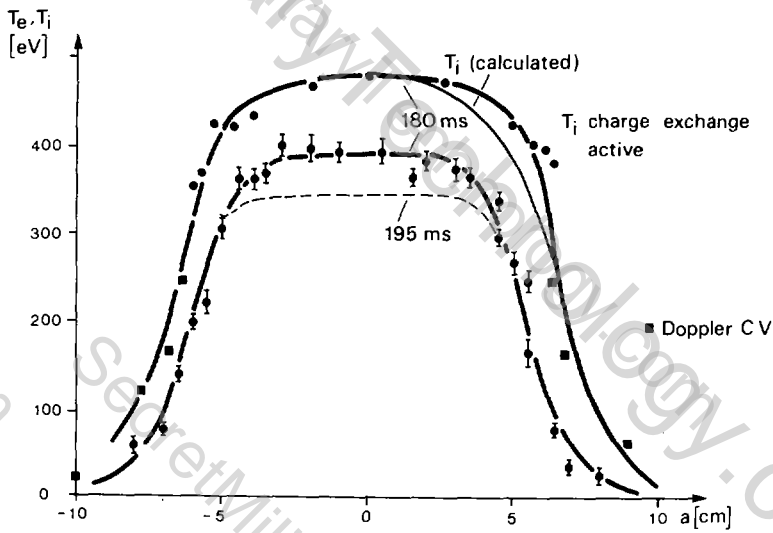
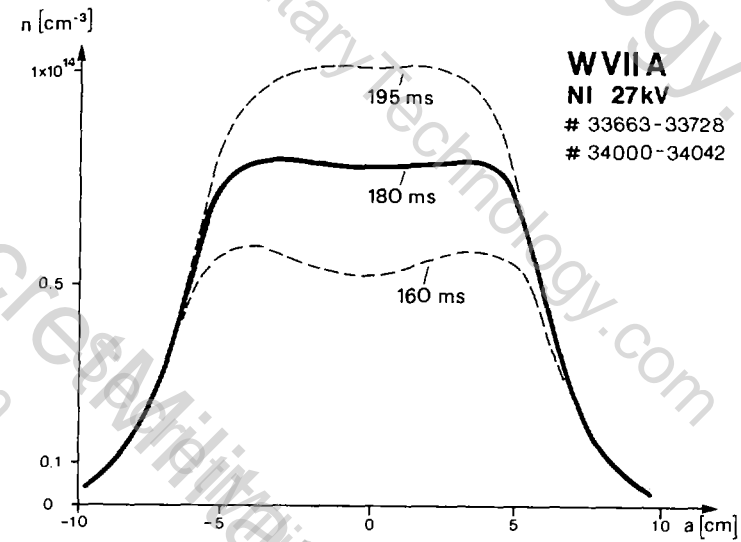


FIG.2. Temperature and density profiles for discharge "A". The approximate  $T_i$  profile (transport analysis) is indicated at  $\Delta t = 180$  ms.

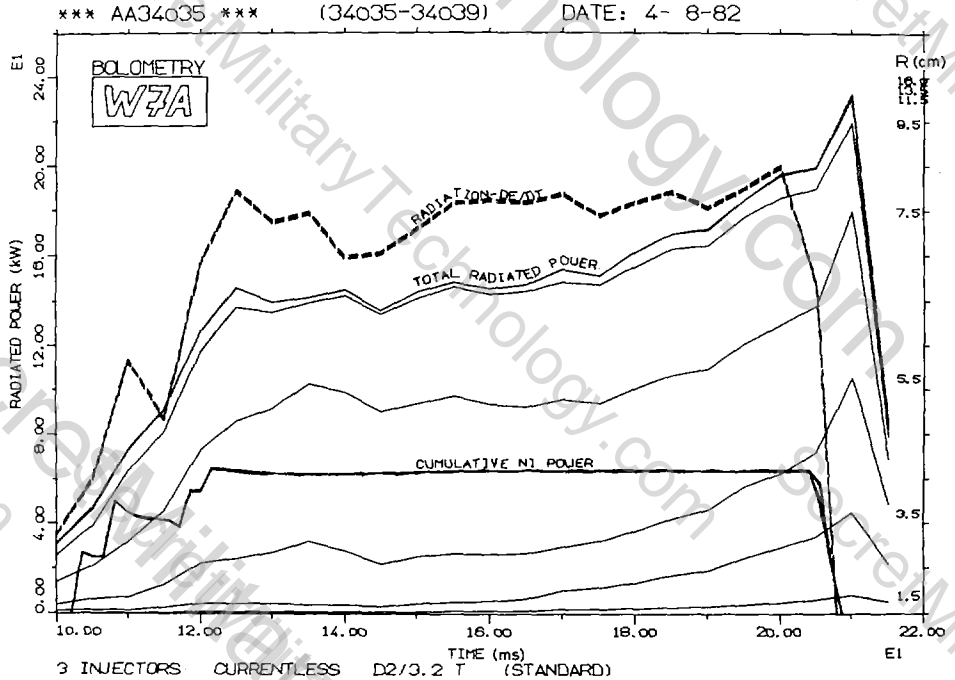


FIG. 3. Total radiative loss  $P_{rad}$  obtained by bolometer ("A"). Integrated values for different radii.  $P_{rad} - W$  is included.

this density increase in the early phase of the currentless discharge, the higher heating efficiency leads to a higher energy content. Addition of the fourth injector drives the ion temperature up to  $T_i \approx 1$  keV. Figure 6 illustrates the temperature and density profiles for this well documented discharge. From the central plasma parameters  $n_{e0} = 1.1 \times 10^{14} \text{ cm}^{-3}$ ,  $T_e = 0.6$  keV,  $T_i = 1$  keV for  $B_0 = 3.2$  T, a central  $\beta(0) = 0.8\%$  is calculated. For singular shots, values exceeding  $\beta(0) \approx 1\%$  have been reached.

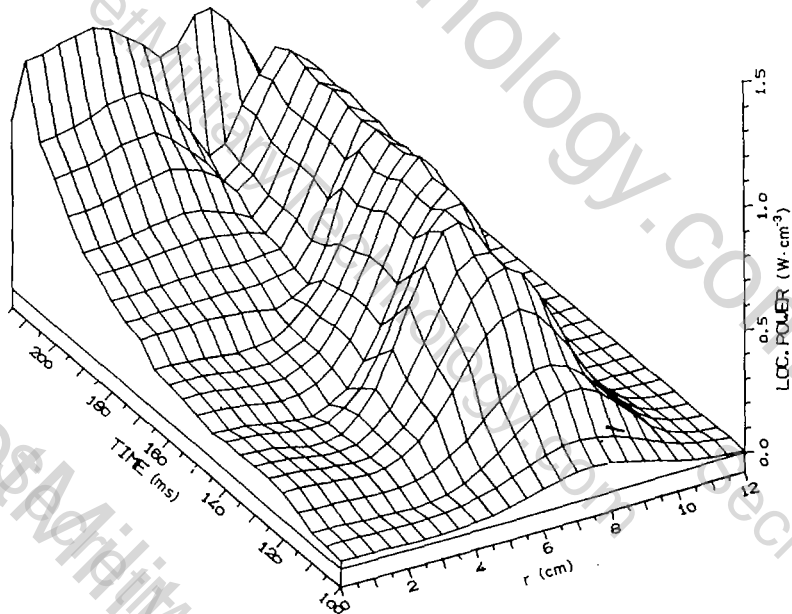
### 3.2. Energy balance

Rough estimates of the energy balance in W VII-A have already been carried out, but the non-stationarity of the parameters, the dominant radiative losses and the uncertainties of the beam power deposition have impeded this analysis. Improvement of the discharge and the diagnostics has now provided a more secure basis.

BOLOMETRY

W7A

SHOTS:  
34035  
34036  
34037  
34038  
34039



DATE: 4- 8-82

3 INJECTORS

CURRENTLESS

DZ/3.2 T

(STANDARD)

FIG.4. Radiative power density profiles for discharge "A".

### 3.2.1. Global energy balance

A numerical code, ODIN [4], modified for application to W VII-A, has been used to calculate the heating efficiencies with measured density and temperature profiles of the plasma. The NI power  $P_N$  can be taken from the response of the internal calorimeters in W VII-A. There is no doubt about the shine-through losses, which are measured and found to be in agreement with the calculation. The orbit losses, however, appear to have been overestimated. The build-up of radial electric fields can lead to better confinement of the hot injected ions. The resulting poloidal rotation has been confirmed by spectroscopic measurements. Doppler-shift measurements of impurity lines during NI are consistent with poloidal velocities  $v \approx 10 \text{ km} \cdot \text{s}^{-1}$ , corresponding to several hundred volts per cm radial field strength. Experimentally, the heating efficiencies can be derived by analysis of the transient behaviour of the plasma during stepwise changes of the injection power. Some results are presented in Fig. 7. For several discharges, including the standard case "A", one additional injector has been used for 10–20 ms. For

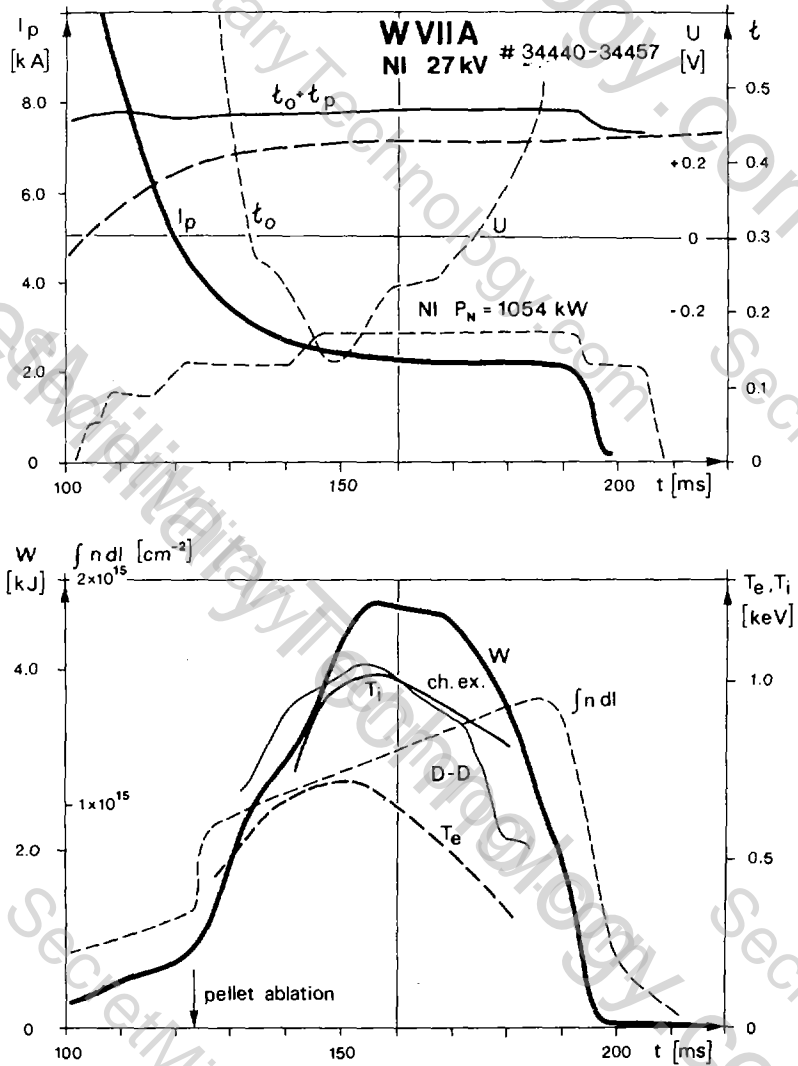


FIG. 5. Discharge "B": neutral injection  $P_N = 1056$  kW. Main parameters as in Fig. 1. Pellet injection at  $\Delta t = 124$  ms ( $D_2$   $\Phi$  0.6 mm,  $500 \text{ m} \cdot \text{s}^{-1}$ ).

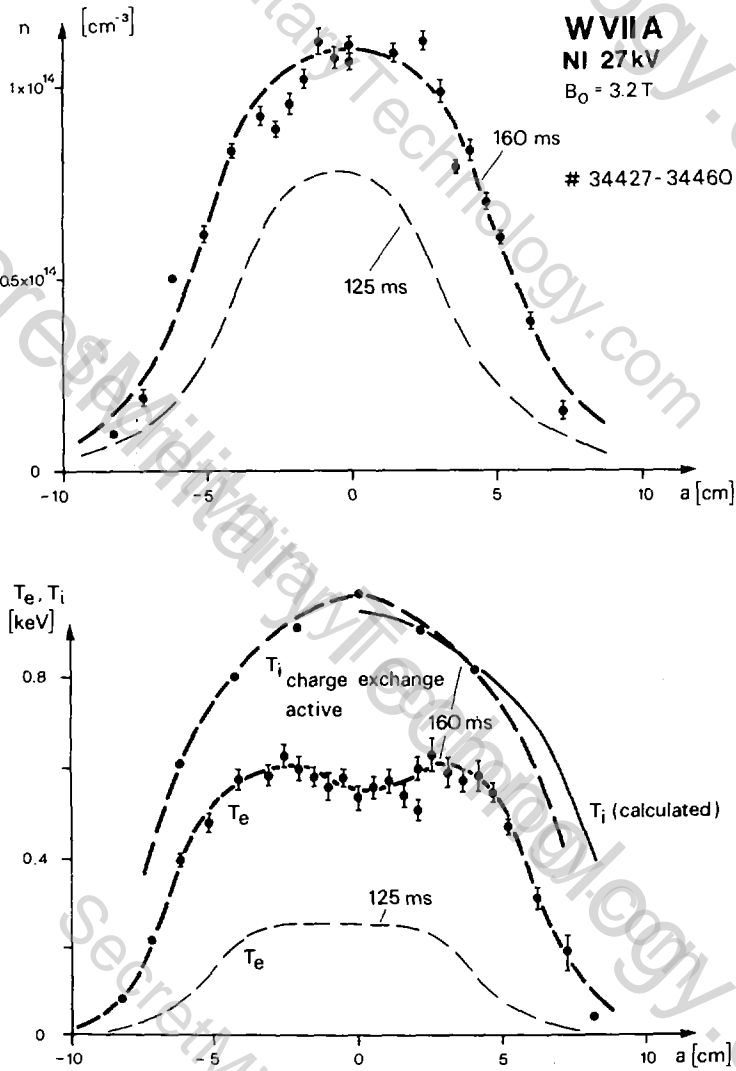


FIG. 6. Temperature and density profile for discharge "B" at 125 ms and 160 ms after pellet injection. The approximated  $T_i$  profile (transport analysis) is included.

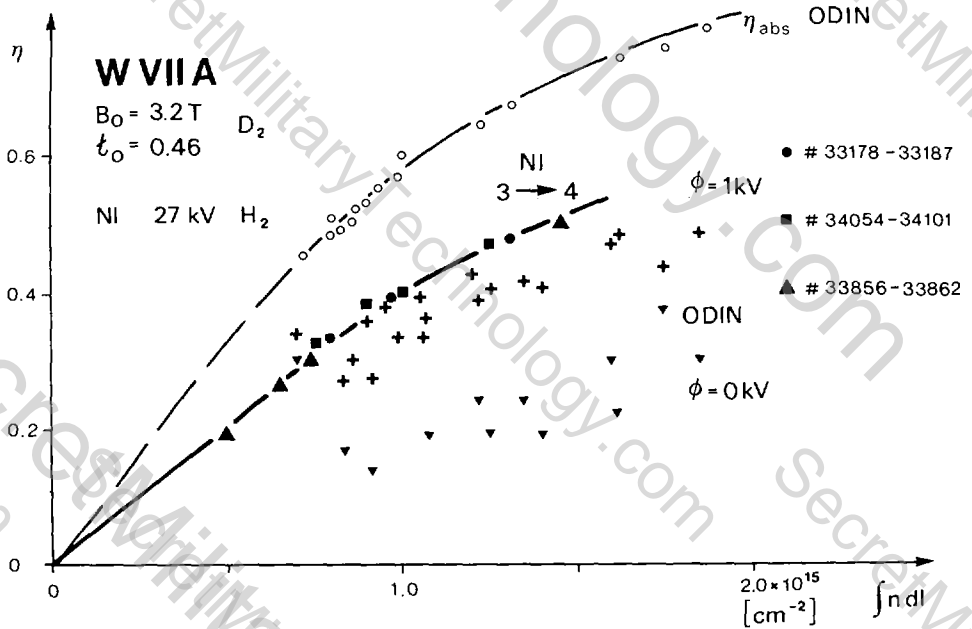


FIG. 7. Total heating efficiency  $\eta$  for NI versus line density  $\int n dl$  for various discharges as calculated by the ODIN code:  $\eta_{abs}$  is trapping efficiency;  $\eta$  corrected for the orbit losses at radial potential difference. For comparison, experimental values for  $\eta$  are plotted. +:  $\phi = 0 \text{ kV}$ . ▼:  $\phi = 1 \text{ kV}$ .

comparison, the heating efficiency from the ODIN calculations, assuming a radial potential difference  $\phi = 0$  or  $\phi = 1 \text{ kV}$ , are also given in Fig. 7. The calculation for  $\phi = 1 \text{ kV}$  agrees with those values for the heating efficiency obtained in the experiment, although for a detailed analysis the different density and temperature profiles have to be taken into account.

For the two selected discharges, the energy replacement time  $\tau_E$  can be calculated at the time of the profile measurements. The time variation of the internal parameters is relatively small:  $\tau_E = W/(P_{IN} - W)$ , where  $W$  is the internal energy and  $P_{IN}$  the effective heating power (see Table I).

The radiative losses  $P_{rad}$ , especially in the internal region  $P_{rad}/5.5 \text{ cm}$  within  $a = 5.5 \text{ cm}$ , reduce the available heating power significantly.  $P_{th}$  is calculated from the transport analysis discussed in the next section.

### 3.2.2. Energy transport analysis

The transport calculations are based on the neoclassical heat conduction  $\kappa_{i,plateau} = n\chi_i \approx n_i T_i^{3/2}$  and the empirical electron heat conduction  $\kappa_e = n\chi_e \approx 1/T^{2/3}$

TABLE I. DISCHARGE PARAMETERS

Discharge	W (kJ)	W (kW)	P <sub>N</sub> (kW)	f <sub>ndI</sub> (cm <sup>-2</sup> )	η <sub>exp</sub>
A	2.6	30	760	1 × 10 <sup>15</sup>	0.4
B	4.7	-10	1054	1.2 × 10 <sup>15</sup>	0.45

Discharge	P <sub>rad</sub> (kW)	P <sub>rad</sub> /5.5 cm	P <sub>th</sub> (kW)	P <sub>IN</sub> (kW)	τ <sub>E</sub> (ms)
A	180	40	260	304	9.0
B	200	100	370	474	10.0

$\kappa_e$  was verified for Ohmic discharges not affected by MHD perturbations [5]. With measured profiles for density, temperature and radiative losses, the unknown quantities in the energy balance are reduced to the beam deposition profiles for ions  $p_{bi}$  and electrons  $p_{be}$ , which can be compared with ODIN code predictions. By trial and error,  $p_{bi}$  is varied until the measured  $T_i$  profiles are approximated. The electron heat conduction equation is solved for  $p_{be}$ , taking into account the measured  $T_e(r)$  and radiation profile. For the classical energy transfer  $P_{ie}$ , the composition of the ion component  $H^+$ ,  $D^+$  and oxygen is included. Heating of electrons by impurity ions and charge-exchange losses are neglected. In Figs 2 and 6 the approximated ion temperature profiles  $T_i$  are indicated for comparison.

The global energy balances for discharges "A" and "B" are presented in Fig.8. The following results are obtained:

- The necessary ion heating  $p_{bi} \lesssim 2.5 - 9 \text{ W} \cdot \text{cm}^{-3}$  is concentrated within  $r \leq a/2$  and exceeds the ODIN calculations even for a radial potential difference of 1 kV.
- The necessary electron heating  $p_{be} < 1 - 1.5 \text{ W} \cdot \text{cm}^{-3}$  peaks at  $r \approx 1/2 - 2/3 a$ .
- The main part of the power is deposited in the centre and transferred to the ions, contrary to the predictions of the ODIN code. The necessary total heating power  $p_{th}$ , however, is fairly consistent with the  $P_{IN}$  predictions.
- In discharges with low central radiative losses, ion heat conduction is the essential loss for the central region, whereas electron heat conduction becomes dominant at the plasma edge.

Within these assumptions, the ions need almost all the heating power available by neutral injection. The electrons are heated by the ions and almost no direct

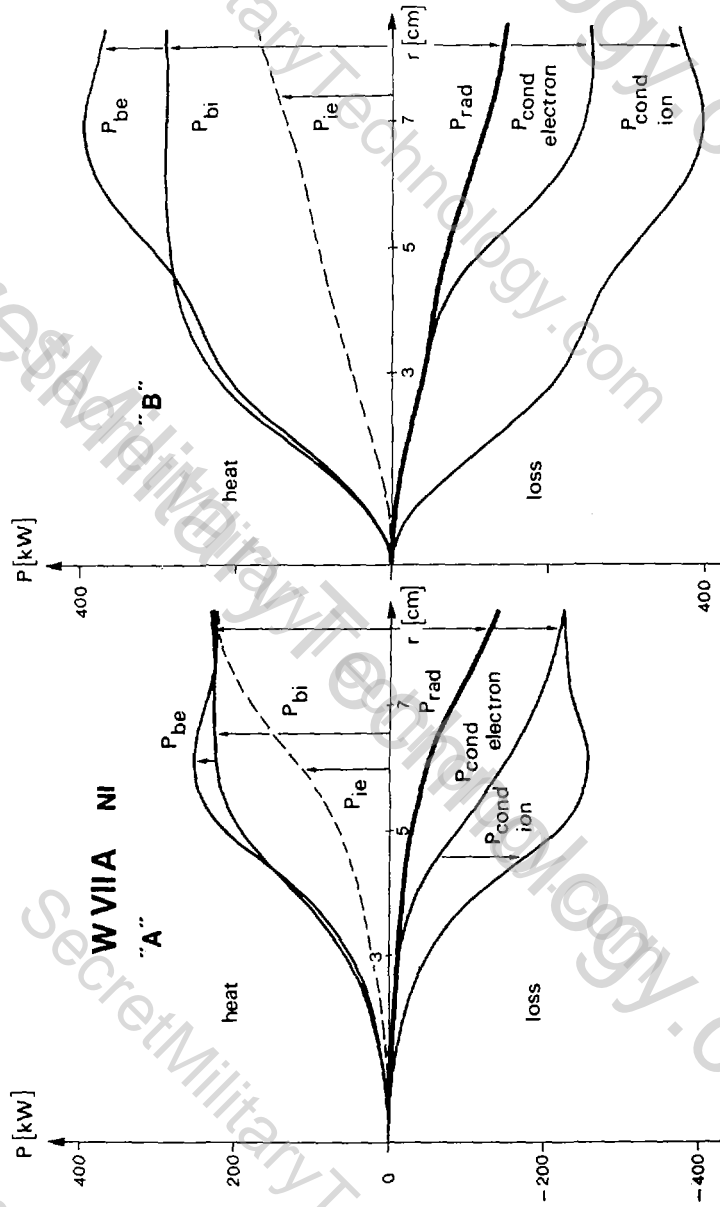


FIG. 8. Global energy balance for discharge "A" at 180 ms and "B" at 160 ms. Measured radiation loss  $P_{rad}$ , calculated conduction loss  $P_{cond}$ , NI heating to electron  $P_{be}$  and to ions  $P_{bi}$  versus radius.

electron heating is necessary. This picture is consistent with the hollow electron temperature profiles of discharge “B” (Fig. 6).

### 3.3. Radiation losses

Towards the end of the “currentless” phase of neutral-beam-heated discharges, a strong increase of the central impurity radiation is usually observed. Local radiation of up to  $3 \text{ W} \cdot \text{cm}^{-3}$  could be deduced from a turnable 10-channel bolometer system. Nearly the same values are obtained from ultrasoft-X-ray measurements with an array consisting of 30 Si diodes which are sensitive to radiation with energy  $\geq 350 \text{ eV}$ . Radiation levels of this order finally exceed the power deposited by NI, and lead to temperature decay and termination of the discharge.

The increase of impurity radiation in time may have several causes:

- (a) improved confinement for all particle species during the “currentless” phase;
- (b) contamination of the neutral beam with oxygen and a very effective trapping of beam impurities by the plasma;
- (c) additional influx of impurities during current decay, as indicated by an increase of the radiation from low ionization stages; the impurities remain trapped during the “currentless” phase.

#### 3.3.1. Density increase and particle confinement

There is strong experimental evidence for substantial increase in particle confinement during the currentless plasma phase. From  $H_\alpha/D_\alpha$  signals at various ports round the machine, beam fuelling is found to be the main source of particle production.

If all beam particles that are trapped, including the fraction of particles introduced into lost orbits and an oxygen impurity content of 5% (see below), are taken as the main particle source, we estimate particle confinement times of the order of 100 ms (assuming 0.7 for the recycling coefficient as found in Ohmically heated discharges), which is less than the neoclassical confinement time by a factor of 5 to 10.

#### 3.3.2. Impurities

The central radiation consists mainly of O VIII and O VII line radiation with wavelengths of 19 Å and 22 Å respectively. This is deduced from the observations of the line radiation in the range 14 – 19.5 Å by crystal spectrometer. The importance of the 22-Å radiation can be roughly estimated from the O VII line at 18.6 Å. Moreover, pulse-height spectra taken with a windowless Si(Li) soft-X-ray detector ( $\Delta E \approx 200 \text{ eV}$ ) during different time intervals show a peak in the distribution at about 650 eV ( $\approx 19 \text{ Å}$ ). To investigate the sources of impurities and the main impurity species in the plasma centre, the following experiments have been made:

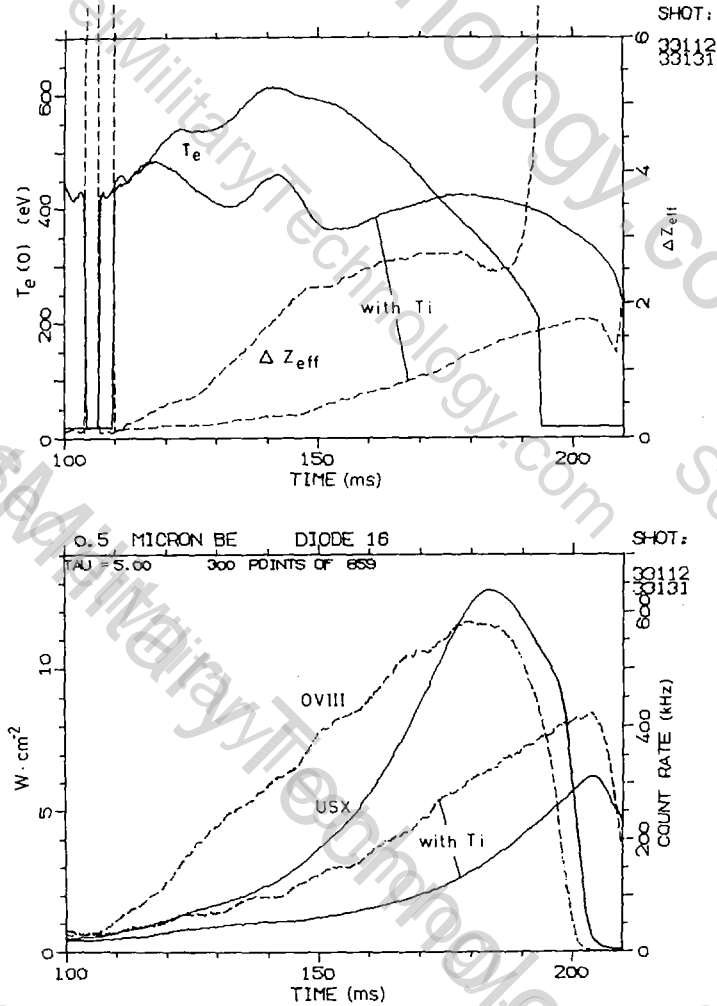


FIG.9. Reduction of  $Z_{eff}$  and electron temperature decay rate in the plasma centre (extracted from X-continuum radiation) for "clean" discharge (upper diagram). The lower diagram shows the corresponding effect on the central soft X radiation ( $>500$  eV) and O VIII line radiation.

(a) Unlike hydrogen, beam-injected oxygen is expected to be absorbed almost completely by the plasma, even at moderate densities. This is confirmed by measurements of sputtered molybdenum in front of the beam dump by laser fluorescence [6]. Because of the high sputtering yield of oxygen, the contribution of the oxygen impurities in the hydrogen beam dominates the Mo sputtering. With plasma, the Mo sputtering is reduced by a factor of 10, whereas for H sputtering a reduction by only a factor of 2 would be expected because about 50% of the

beam power is still transmitted through the plasma. Therefore, oxygen must have been primarily absorbed in the plasma.

(b) In addition, computations with a modified version of the ODIN neutral beam deposition code have shown [7] that a considerable fraction of injected oxygen is thermalized in a high ionization state near the plasma centre (up to 80% within a 5-cm radius). Central deposition is even increased if radial electric fields, which have been shown to exist, are included.

(c) Titanium gettering of the ion sources has led to a considerable reduction of the light-impurity content contamination of the extracted fast ion beam as detected by the mass spectrometric measurements [3].

Figure 9 demonstrates the reduction of the central radiation losses if "cleaned" neutral beams are used and the heating rate of the NI is carefully adjusted to avoid additional impurity influx from the wall via  $m = 2$  islands which may evolve during the current decay. The relative change of both the central USX signal and the O VIII radiation at 19 Å also indicates the important role of the oxygen line radiation.

These optimized discharges also do not show the strong decrease of electron temperature during NI, therefore allowing for a further extension of the duration of the discharge. Moreover, the central  $Z_{\text{eff}}$  value obtained from the central flux of the continuum radiation above about 3 keV is drastically reduced.

(d) A direct method of studying the effect of beam-injected oxygen was applied by using an additional 20-ms injection pulse from a fourth injector with no titanium gettering. Figure 10 shows the effect of additionally running the fourth injector (144–164 ms) on the evolution of the central temperature (measured by the X-ray filter method) and  $Z_{\text{eff}}$  (from X-ray continuum radiation). After an initial rise of the electron temperature (150–160 ms), a faster decrease due to enhanced line radiation is observed.  $Z_{\text{eff}}$  has increased by 0.5 after the end of the 20-ms injection pulse. Assuming that the oxygen injected with the neutral beam is completely deposited inside a radius of 5 cm, a 2.5% oxygen contamination of the ungettered injector can be evaluated. During a 60-ms operation period, with three gettered injectors only, the increase in  $Z_{\text{eff}}$  is about 1, corresponding to 0.6% oxygen content of each beam, well consistent with direct measurements of the beam impurity concentration.

(e) Controlled impurity contamination of the plasma with neon has shown that fast neon neutrals (via injection) are effectively deposited in the plasma centre during the "currentless" phase. Cold neon only penetrates if the gas puff coincides with the plasma current decay [8].

(f) Since iron is also present in the plasma centre, as detected by resonance lines of Fe XVII (15 Å and 17 Å) and Fe XVIII (14.2 Å), the relative contribution

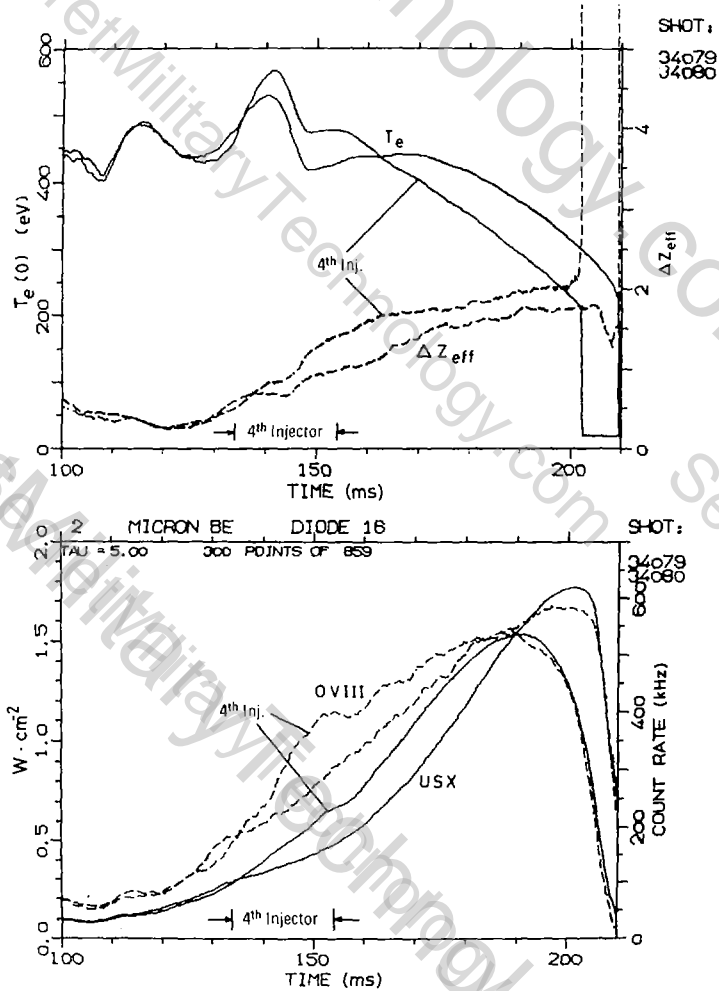


FIG.10. Enhancement of  $Z_{eff}$ , O VIII line radiation (19 Å), USX radiation (>500 eV) and the decay rate of the central electron temperature by use of an additional 20 ms injection pulse.

of Fe line radiation to the whole central radiation (above about 350 eV, USX diodes) was determined by Fe-laser blow-off at different times during the discharge. A strong increase of the Fe XVII radiation was observed just after the Fe ablation, whereas the relative increase of the USX radiation was much smaller (Fig. 11). A contribution of 10–20% of the Fe line radiation to the total central radiation losses can be estimated.

(g) The time behaviour of the central radiation can be well explained by a mixture of O VIII and O VII line radiation, with a shift towards O VII in the case

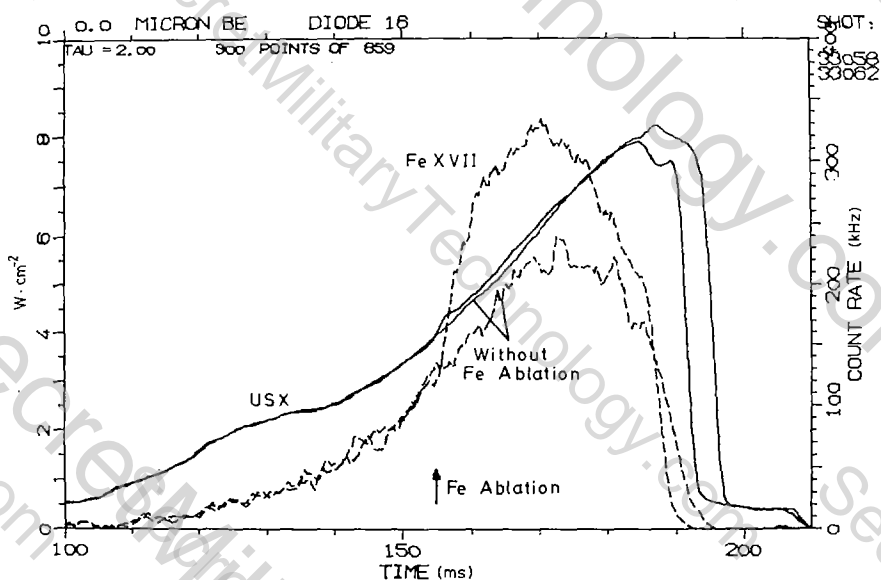


FIG.11. Effect of Fe ablation by laser blow-off at 154 ms on the Fe XVII line radiation (15 Å) and the central USX radiation (>350 eV).

of electron temperature decay below about 400 eV by progressive radiation cooling. About 50 ms after the start of injection, strongly increasing iron radiation is observed which adds to the final radiation level by about 20%. Although radiation from iron is lower than oxygen, the steep increase of Fe XVIII in the centre, even with decreasing temperature, and the simultaneous reduction of the radiation from lower Fe charge states, may be an indication of an inward flow of impurities.

### 3.3.3. Confinement of injected impurities

The laser ablation technique has been used to obtain some information on the confinement of impurities. Si and Fe have been ablated at various times during the discharge.  $3 \times 10^{16}$  particles are estimated to reach the plasma, as compared to the total number of particles ( $\approx 2 \times 10^{19}$ ) present in the plasma.

During the Ohmic-heating phase,  $t < 100$  ms, the intensity of Si XII (499.43 Å) normalized to the line-integrated electron density decays with a time constant of 16 ms (Fig. 4). From radial profile measurements we conclude that Si XII is representative of the central part of the plasma. The same time constant is deduced from the decay of the Fe XVII (15 Å) line radiation for iron ablation.

With NI in the currentless phase, an increase of the time constant by a factor of 2 to 3 is observed. As an example, Si XII/ $f_{ndI}$  versus time is shown during this phase. The electron temperature has been kept constant except for the first 5 ms;

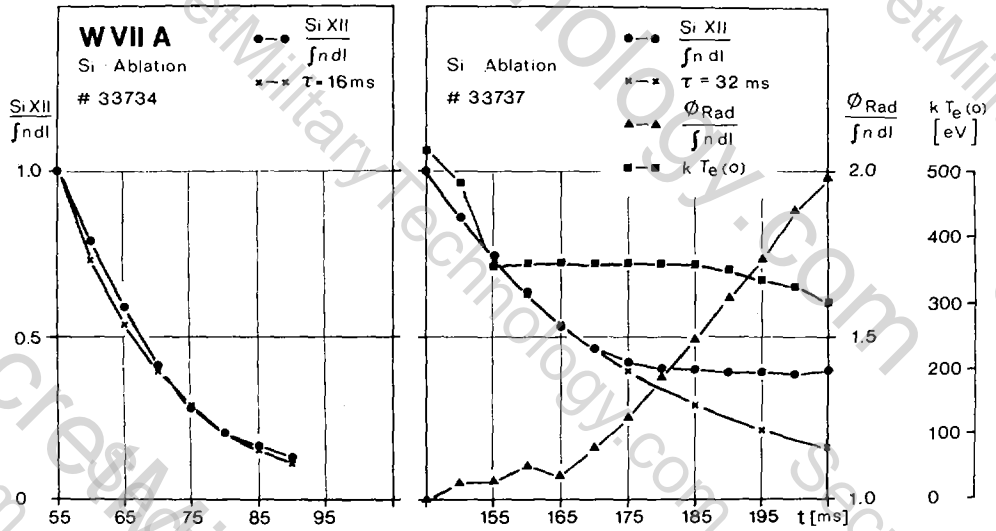


FIG.12. Decay of Si XII/ $f_{ndI}$  signals after ablation (time of ablation 50 ms and 140 ms). Exponential decay curves are given for comparison. Central radiation  $\phi_{rad}/f_{ndI}$  from USX diodes and  $kT_e(0)$  are shown as a function of time.

the time of ablation was 140 ms. In this case, an exponential decay with a 32 ms time constant fits the experimental decay only within the first 25 ms of the decay. Later in time, the decay of the Si XII signal is much longer. This time behaviour is also confirmed by measurements of the continuum radiation as seen by X-ray diodes. From this result, one is led to the conclusion that either the confinement has further improved or a change in the density and temperature profiles during the final stage of the current decay around 145 ms causes a change in the transport of the impurities, resulting in an inward transport. Temperature profiles have been found to change from triangular shape to flat profiles.

Although this inward transport cannot be excluded, there is evidence of improved confinement if a further reduction of density fluctuations, as measured by microwave scattering around 160 ms, is related to the confinement of particles. The central radiation from USX diodes, again normalized to  $f_{ndI}$ , is plotted in Fig. 12 and can be taken as a measure of the impurity content. It is interesting that the observed linear increase starts at about the same time that the exponential decay of the line radiation is considerably reduced. This behaviour is also seen from the line radiation of intrinsic impurities in the plasma.

#### 4. SUMMARY AND CONCLUSIONS

In spite of the geometry of the device ( $a \leq 0.1$  m) and the small effective heating power ( $P_{IN} < 500$  kW), remarkable plasma parameters have been achieved

in W VII-A with NI. So far no saturation due to  $\beta$ -limiting effects has been observed. Certainly the effect of the residual current in the "currentless" phase on the configuration must be carefully investigated. Long pulse operation (a pulse duration  $\Delta t > 150$  ms has already been established) may favour these investigations in excluding dynamic effects resulting from the current decay. Experiments are under way to substitute plasma build-up and heating by RF application for Ohmic heating. This may finally prevent the difficulties, especially during the transition phase to currentless plasma.

The inclusion of radial electric fields seems to explain the reduction of the orbit losses and thus the increased heating efficiency observed. The mechanism for preferential coupling of the beam power to the ions still needs to be investigated. Ion-cyclotron waves, which have been observed in correlation with NI, may turn out to be responsible for this increased ion heating.

The improvement of energy confinement seems to be supported by the disappearance of sawtooth instabilities and tearing modes with vanishing plasma current. It may be concluded from the transport analysis that the electron conduction, even in the currentless case, can be described by the empirical scaling  $\chi_e \approx 1/(nT_e^{2/3})$ , which has been derived from Ohmic discharges. In the case of Ohmic heating, this favourable scaling at high temperatures is not applicable in the whole plasma region as a result of those instabilities. Ion heat conduction seems to be in agreement with neoclassical predictions and becomes dominant for high ion temperatures ( $\chi_i \approx T_i^{3/2}$ ). As a consequence of the weak coupling of the beam to the electrons, the ions must also transfer a large fraction of the power to the electrons operating at high densities. The electron temperature profile is very sensitive to the impurity content and to the coupling to the ions. This coupling mechanism has been investigated at densities low enough for the temperature difference between electrons and ions to be accurately enough documented. Experiments with additional electron heating by a small plasma current are consistent with that picture.

The oxygen contamination of the plasma has been significantly reduced by various means. There is an unavoidable influx of impurities by the beam and from the wall, and in the case of continuous density increase, still observed for the long pulse discharges, this leads to radiative losses exceeding the power input from NI. An accumulation by an increased inward flow of impurities can at present be neither affirmed nor excluded.

#### ACKNOWLEDGEMENTS

The progress of the W VII-A Stellarator experiments would have been impossible without the efforts of the technical staff. Dr. Büchl and Mr. Schiedeck were responsible for pellet injection. Dr. Scherzer contributed by analysing

exposed carbon probes. The support of the Jülich group, especially Dr. Bogen and Dr. Schweer for laser fluorescence measurements, and Dr. Schlüter for preparation of the crystal spectrometer, is gratefully acknowledged.

#### REFERENCES

- [1] W VII-A TEAM, NI GROUP, in Plasma Physics and Controlled Nuclear Fusion Research 1980 (Proc. 8th Int. Conf. Brussels, 1980) Vol. 1, IAEA, Vienna (1981) 185.
- [2] W VII-A TEAM, NI GROUP, in Proc. 3rd Joint Varenna-Grenoble Int. Symp. Heating in Toroidal Plasma, Grenoble, 1982, Vol. 2 (1982) 813.
- [3] OTT, W., et al., *ibid.*, Vol. 1, p. 123.
- [4] W VII-A TEAM, NI GROUP, Proc. 2nd Joint Varenna-Grenoble Int. Symp. Heating in Toroidal Plasma, Como, 1980, Vol. 2 (1980) 789.
- [5] W VII-A TEAM, Bull. Am. Phys. Soc. 26 (1982) 891, 2U 11.
- [6] BOGEN, P., et al., in Proc. 5th Int. Conf. Plasma Surface Interaction in Controlled Fusion Devices, Gatlinburg, 1982.
- [7] LISTER, G.G., et al., in Proc. 3rd Joint Varenna-Grenoble Int. Symp. Heating in Toroidal Plasma, Grenoble, 1982, Vol. 1 (1982) 103.
- [8] W VII-A TEAM, Bull. Am. Phys. Soc. 26 (1982) 891, 2U 10.

#### DISCUSSION

R. GOLDSTON: It seems to me that you could learn a great deal about beam ion thermalization in W VII-A by measuring the charge-exchange energy spectra of the fast ions at a number of angles and poloidal and toroidal locations. Have you done anything along these lines?

H. RENNER: We have analysed slowing-down spectra: the flat energy distribution obtained may indicate increased thermalization. Corresponding predictions of the Monte-Carlo calculations, including radial electric fields or higher collision frequencies, confirm these observations. Unfortunately, the energy resolution of our analyser is rather poor, and access to the plasma is limited.

M. NAGAMI: In tokamak experiments with neutral-beam injection, the electron energy confinement time is proportional to the plasma current, indicating that the intensity of the poloidal field is essential in electron energy transport. Your electron heat conductivity expression for W VII-A shows no  $B_p$  dependence. Have you checked this against experiments?

H. RENNER: In the experiments with Ohmic heating in W VII-A no explicit dependence on the poloidal field has been found for variation of  $1 > t > 0.2$  at  $B_0$  from 2 T to 3.5 T. The currentless operation with a restricted accessible parameter range (3.2 T,  $t_0 \approx 0.5$ ) allows no significant proof.

T.K. CHU: The W VII-A has been used for currentless experiments in which energetic neutral beams were injected with a rotational transform from about 0.25 to greater than 0.5. Are there any experimental results indicating that a high rotational transform is desirable?

H. RENNER: A lower transform allows operation at a higher field value and leads to more circular cross-sections of the plasma column. Hence operation at  $t_0 < 0.5$  is preferred, as long as the dangerous (2, 1) mode can be suppressed during the current reduction.

T.K. CHU: Does improved particle confinement time, and therefore impurity accumulation and radiation loss, appear as a real limitation on steady-state operation of a stellarator?

H. RENNER: Certainly restrictions may occur if no measures are taken against the accumulation. I am hopeful that efficient control of the impurity flow, which may critically depend on the density and temperature profiles, will be possible. Possible measures include gas flow, magnetic perturbations by formation of islands, etc.



**Session M**

**HIGH-BETA SYSTEMS II**

Chairman

**B. BRUNELLI**

Italy

Papers M-2-1 and M-2-2 were presented  
by R.E. Siemon as Rapporteur

Papers M-5-1 and M-5-2 were presented  
by C.K. Chu as Rapporteur

## EXPERIMENTAL INVESTIGATION OF THE SPHEROMAK CONFIGURATION

M. YAMADA, R. ELLIS, Jr., H.P. FURTH, R. HULSE,  
 A. JANOS, S.C. JARDIN, D. McNEILL, C. MUNSON,  
 M. OKABAYASHI, S. PAUL, D. POST, J. SINNIS,  
 C. SKINNER, Y.C. SUN, F. WYSOCKI  
 Plasma Physics Laboratory, Princeton University,  
 Princeton, New Jersey

C. CHIN-FATT, A.W. DeSILVA, G.C. GOLDENBAUM,  
 G.W. HART, R. HESS, R.S. SHAW  
 Laboratory for Plasma and Fusion Energy Studies,  
 University of Maryland,  
 College Park, Maryland

C.W. BARNES, I. HENNINS, H.W. HOIDA,  
 T.R. JARBOE, S.O. KNOX, R.K. LINFORD,  
 J. LIPSON, J. MARSHALL, D.A. PLATTS,  
 A.R. SHERWOOD, B.L. WRIGHT  
 Los Alamos National Laboratory,  
 Los Alamos, New Mexico  
 United States of America

### Abstract

#### EXPERIMENTAL INVESTIGATION OF THE SPHEROMAK CONFIGURATION.

The characteristics of the spheromak configuration have been intensively investigated on the basis of three different formation schemes. Significant progress has been obtained in the areas of control of gross MHD instability and impurity influx. The parameters of spheromak plasmas have been improved and are in the range of  $B_t \cong B_p \lesssim 5$  kG,  $T_e \lesssim 50$  eV,  $3 \times 10^{13} < n_e < 10^{15}$  cm<sup>-3</sup>, with the longest life-time of 1 ms.

#### 1. Introduction

The spheromak configuration, in which a compact-toroid plasma is confined by poloidal and internally generated toroidal magnetic fields, has attracted much interest because of its possible applicability to a fusion reactor.<sup>1,2,3</sup> Recently the spheromak configuration has been successfully generated by three different types of formation schemes:

(1) the coaxial plasma-gun,<sup>4</sup> (2) the field-reversed  $\theta$ -pinch with center column z-discharge,<sup>5</sup> and (3) the electrodeless quasi-static S-1 scheme.<sup>6</sup> The characteristics of this configuration have been intensively investigated in these devices, and significant accomplishments have been obtained in the areas of gross MHD stability and impurity control.

It is evident, at present, that radiation is the dominant plasma energy loss mechanism, and that in order to obtain a long-lived spheromak, it is essential to identify and eliminate major impurity sources. In all formation schemes substantial amounts of low-Z and a detectable amount of high-Z impurities are created primarily due to the interaction of the initial plasma with metallic surfaces of plasma forming units. Impurity radiation due to a plasma of electron density  $n_e$  with impurities of density  $n_I$  is proportional to  $n_e \cdot n_I$ . Since  $n_I$  is often observed to decrease together with  $n_e$ , a substantial reduction of radiation of can be obtained simply by reducing  $n_e$ .

The viability of the spheromak concept as a fusion reactor depends strongly on the capability of controlling the gross MHD instabilities, which have been intensively investigated recently both in theory<sup>1,7-9</sup> and experiments.<sup>4-6</sup> Theoretically, the most dangerous of these instabilities is a nearly rigid  $n = 1$  ideal MHD toroidal mode in which the spheromak tilts its axis against the external field, and/or shifts into a region of weaker magnetic field strength. Experiments have demonstrated the feasibility of stabilizing gross instabilities with loose fitting passive coils as opposed to closely fitting conducting shells. This should make the spheromak concept a more attractive alternative for a fusion reactor.

In this paper we present the major experimental results in terms of plasma parameters, impurity control, and the gross MHD stability of the CTX device at Los Alamos, the PS-1,2 devices at the University of Maryland, and the Proto S-1 devices at the Princeton Plasma Physics Laboratory.

## 2. LANL CTX Spheromak

### 2.1 Plasma Parameters

In the CTX experiment at LANL, spheromaks are generated using a magnetized coaxial plasma source.<sup>4</sup> These spheromaks are stably confined within an 80-cm-diameter oblate flux conserver for the lifetime of the configuration ( $< 1.0$  ms). Similar spheromaks can be formed on either a "short" time

scale (40-75  $\mu\text{s}$ ) or a "long" time scale (150  $\mu\text{s}$ ), depending upon whether the coaxial source is powered by a high-voltage fast bank (3  $\mu\text{s}$  rise time) or a low-voltage slow bank (60  $\mu\text{s}$  rise time). Spheromaks are created and injected into either a vacuum or in a few mtorr of hydrogen gas. The latter case produces cleaner, longer-lived spheromaks.

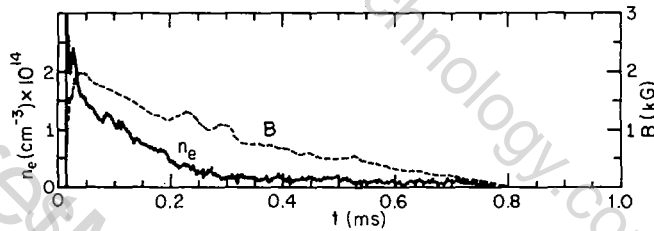


FIG.1. Typical density and magnetic-field histories for the CTX spheromak.

Figure 1 shows typical time histories for the density and magnetic field of spheromaks formed on a short time scale in the case of a few mtorr hydrogen gas present. The density shown is  $\int n_e dl$  from the interferometer divided by the diameter of the flux conserver. At 50  $\mu\text{s}$ , the approximate formation time of the spheromak, the peak electron density reaches  $\sim 1.5 \times 10^{14} \text{ cm}^{-3}$ ; it then falls to a plateau value of  $\sim 2.3 \times 10^{13} \text{ cm}^{-3}$ . The exact plateau value is a linear function of the hydrogen fill pressure. The magnetic field shown in the figure is the axial component of the poloidal field measured on the major axis at a position where the magnetic field energy density equals the average for the whole spheromak. This field component is seen to decay from an initial value of about 2 kG to zero in about 0.75 ms. A typical magnetic field energy decay time is about 0.2 ms. The bumps in the poloidal field during decay are correlated with the appearance of transverse components to the magnetic field on the major axis, all of which is associated with a three-dimensional relaxation of the configuration back towards the Taylor minimum energy state.<sup>10</sup>

## 2.2 Impurity Control

Radial  $T_e$  and  $n_e$  profiles are measured using multipoint Thomson scattering. The temperature tends to be higher where the density is lower. Temperatures as high as 60 eV are measured, but 20-40 eV is more typical. Bolometric and

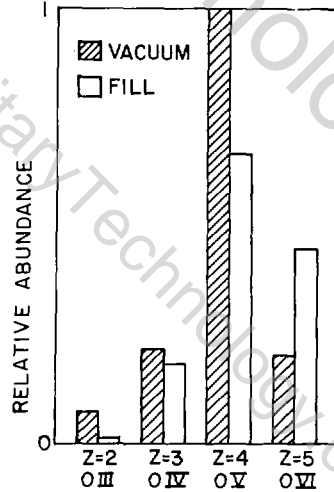


FIG. 2. Relative abundance of oxygen ionization states in CTX for the vacuum and fill cases. The data are normalized to the O V vacuum case. Note both the reduction of radiation and the upward shift in the ionization states for the fill case.

spectroscopic data and power balance considerations indicate that impurity radiation is the dominant energy loss mechanism for the separated spheromak. Immediately following a vacuum opening, carbon is a prominent impurity and the total lifetime for the spheromak configuration is typically 0.2-0.3 ms. After about 100 hours of D.C. glow discharge cleaning there is a large reduction in the carbon radiation and an increase in the total lifetime of the spheromak to about 0.5 ms. At this point oxygen dominates the radiation loss.

After discharge cleaning the total lifetime of the spheromak can be extended to 0.8 ms by use of a background fill of about 8 mtorr hydrogen. Comparable spheromaks have been formed in vacuum and with an 8 mtorr  $H_2$  background. Figure 2 shows the relative abundance of oxygen charge states, determined spectroscopically from resonance lines, for these two cases. For the 8 mtorr  $H_2$  background case the total level of oxygen radiation is lower and the distribution is shifted towards the higher charge states. The presence of the  $H_2$  fill improves the lifetime by providing a particle source to maintain the density at low levels throughout the long life, and by extending the allowable range of most operating parameters which are used to minimize the impurities in the spheromak. Examples of such parameters are (1) the strength of the initial poloidal magnetic field, (2) the delay between

puff gas filling and the initiation of the discharge, (3) the amount of gas puffed in, and (4) the main bank voltage.

Radiation and transport calculations indicate that at  $n_e \sim 10^{14} \text{ cm}^{-3}$  oxygen impurity levels of 1-2% can be overcome by ohmic heating power; however, the present levels appear to be higher because  $T_e$  does not reach the burnout value for oxygen. Steps are being taken to reduce the impurity level and raise the temperature of the spheromaks in CTX.

### 2.3 Gross MHD Stability

In CTX, spheromaks are formed and confined within a close fitting metallic flux conserver. The plasma is injected into the 80-cm-diameter flux conserver through a 30-cm-diameter hole on axis. Various oblate shaped flux conserver geometries have been found which stabilize the tilt and shift instabilities. The presence of an externally applied axial field is destabilizing to the tilt instability, causing the geometry of the flux conserver to become more critical. The presently used flux conserver has a 10 cm wide circumferential slot at the midplane for diagnostic access. Such a slot has been found to stimulate a three-dimensional mode (not studied in detail) which allows the spheromak partially to escape the flux conserver. Twelve metallic conductors bridging the slot reestablished stable confinement within the flux conserver.

## 3. University of Maryland PS Spheromak

### 3.1 Plasma Parameters

In the spheromak experiment at the University of Maryland the compact toroid plasma is formed by a combination of  $\theta$ - and  $z$ - discharges. The experiment was first operated as a fast pinch in which the formation phase took place in approximately one Alfvén transit time across the radius ( $< 1 \mu\text{sec}$ ). The formation method has now evolved to a slow formation scheme (PS-2) with the formation time scale approximately an order of magnitude slower. The poloidal field coil structure has also been changed from a straight field solenoid to a mirror coil permitting the production of nearly spherical shaped plasmas with a separatrix radius of 10 cm. These changes, which were made to make the plasma more stable, have resulted in lower field ( $B < 6 \text{ kG}$ ) as well as lower power input reducing the initial temperature. The initial ion temperature is about 40 eV which quickly ( $10 \mu\text{sec}$ ) drops to 5-10 eV possibly due to radiative loss (densities are typically  $1.3 \times 10^{15} \text{ cm}^{-3}$ ).

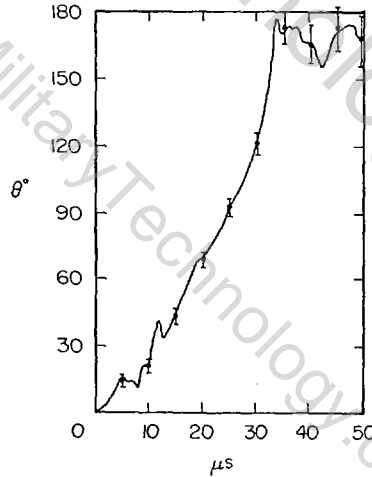


FIG. 3. Tilt angle of PS spheromak as a function of time. The tilt angle is defined by the measured angle of the magnetic field vector with respect to the cylinder axis at the centre of the discharge tube.

### 3.2 Impurity Control

For the present experimental conditions one expects the radiative loss to come mainly from low stages of ionization of the most abundant impurities, carbon and oxygen. These impurities are associated with the dielectric walls necessitated by the fast, resistive, high-power technology of the original system. Increasing the rise time has allowed the insertion of a 50- $\mu\text{m}$  stainless-steel liner inside the glass vacuum chamber. The presence of the liner along with a continuous RF discharge for several hours has resulted in a reduction of CIII radiation by a factor of 20 to 50. However, no change in the magnetic field decay rate is observed. The decay rate for stable plasmas is well described by classical resistivity at 8 eV which is also consistent with Thomson scattering measurements.

### 3.3 Gross MHD Stability

Prior to inserting the metal liner and utilizing the mirror coils in the Maryland experiment, the usual prolate plasmas were found to tilt.<sup>11</sup> In Fig. 3, the measured tilt angle, defined by the direction of the poloidal field vector with respect to the original symmetry axis, is plotted versus time. Two points are of interest here: (1) the rapid growth of the rotation and (2) the fact that the field vector rotates

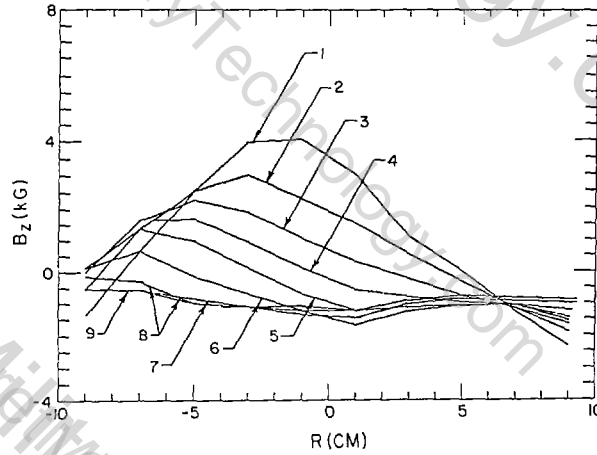
by  $180^\circ$ . By simultaneously observing at  $z = 0$  (midplane) and at  $z = 8$  cm it was determined that in many cases a large part of the configuration rotates as a rigid body aligning its magnetic moment with the externally applied  $B_z$  field which provides toroidal equilibrium. In other cases it appears that after a rotation of less than  $180^\circ$  the externally applied field rapidly diffuses to the axis. In either case the magnetic structure is substantially changed by the time the configuration has rotated  $90^\circ$ .

The situation was greatly improved by superposing a mirror shaped equilibrium field, lining the glass vacuum chamber wall with thin ( $50 \mu$ ) stainless steel, and slowing the reversal field rise-time from  $2 \mu\text{sec}$  to  $\lesssim 10 \mu\text{sec}$ . In this case no immediate tilt was seen, but the plasma shifted radially toward the wall in a randomly oriented direction. This is illustrated in Fig. 4a where we plot the poloidal component of magnetic field in the midplane as a function of distance from the major axis. The symmetry axis (peak poloidal field) is seen to drift into the wall. This data is taken on a single shot with a multicoil probe system. Two types of "Figure-8" stabilization coil systems were used to attempt to stop the drift motion. Two of the four coils of each system are illustrated in Fig. 5a-b. Coils of type (a) were placed inside the liner and found to eliminate the drift motion as shown in Fig. 4b. Type (b) coils were tried on the outside of the glass vacuum chamber and found to be ineffective. They were, however, effective in eliminating the shift when located inside the glass wall but outside of the liner.

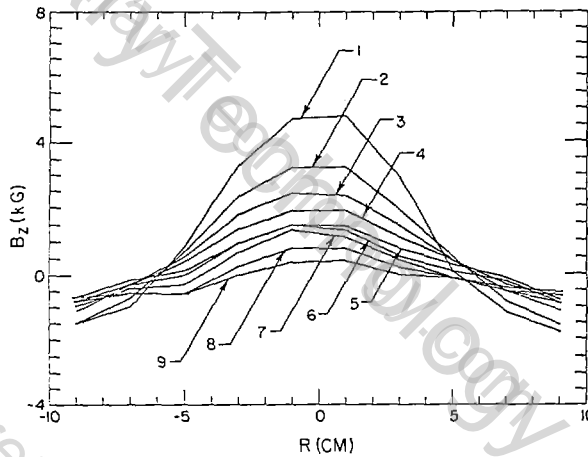
#### 4. Princeton Proto S-1 Spheromak

##### 4.1 Plasma Parameters

Two Proto S-1 devices were constructed to investigate the S-1 spheromak formation scheme<sup>12,13</sup> at PPPL. The formation scheme is based on a transfer of both poloidal and toroidal flux from a toroidal shaped flux core to a forming spheromak plasma without the usage of electrodes. After the Proto S-1A successfully demonstrated the S-1 scheme in 1980,<sup>6</sup> the Proto S-1C, which is twice as large as the Proto S-1A, was constructed to extend the experimental study of the spheromak configuration. In the Proto S-1C device, a spheromak with major radius  $R = 12$  cm and minor radius  $a = 8$  cm has been generated in a slow time scale of  $\tau_{\text{form}} \approx 50 \mu\text{sec}$  and lasts as long as  $100 \mu\text{sec}$ . Toroidal and poloidal plasma currents obtained are  $60$  kA and  $120$  kA, respectively. Plasma temperature and density (Fig. 6) have been measured by laser Thomson scattering together with bolometric and spectroscopic



(a)



(b)

FIG. 4. Radial profiles of the poloidal magnetic field at  $2.5 \mu\text{s}$  intervals for  $20 \mu\text{s}$  (1-9).  
a) Profiles with stainless-steel liner but without coils; b) profiles with both liner and coils (PS).

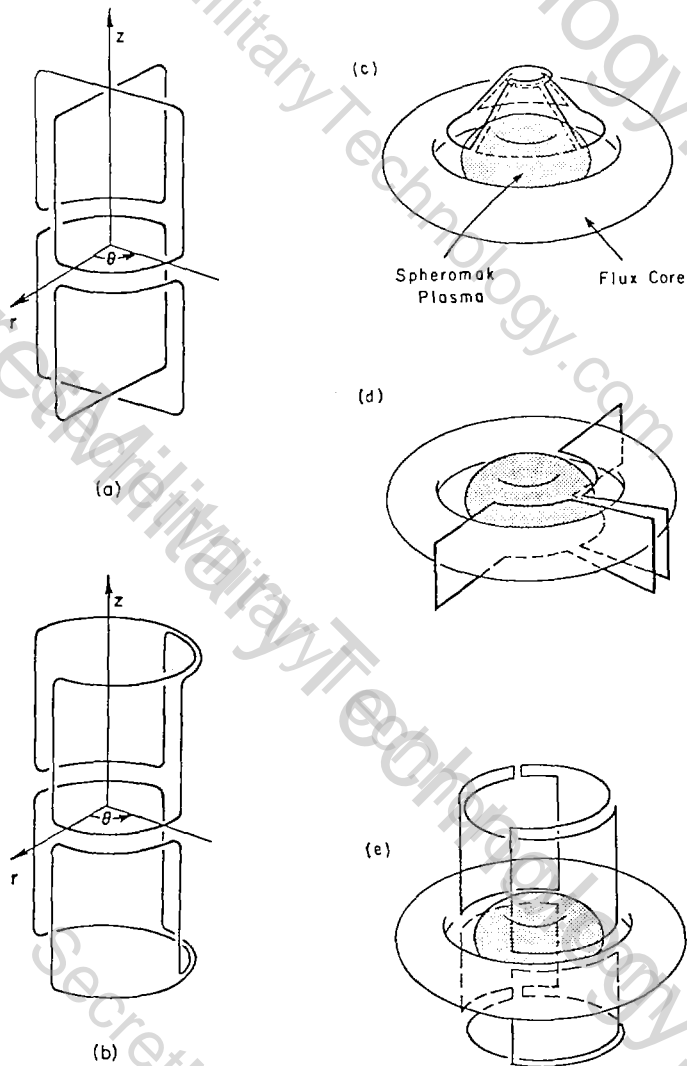


FIG.5. Passive-stabilization coils. Only two of the four coils required for each system are shown. The entire coil system would be obtained by (1) adding a similar pair at  $90^\circ$  (for types a, b, e) or  $180^\circ$  (c) with respect to the pair shown, or by (2) adding a pair on the other side of the midplane of the device. Coil types (a) and (b) are applied to PS-1, 2 at the University of Maryland. Coil types (c), (d), and (e) applied to Proto S-1A, C at PPPL.

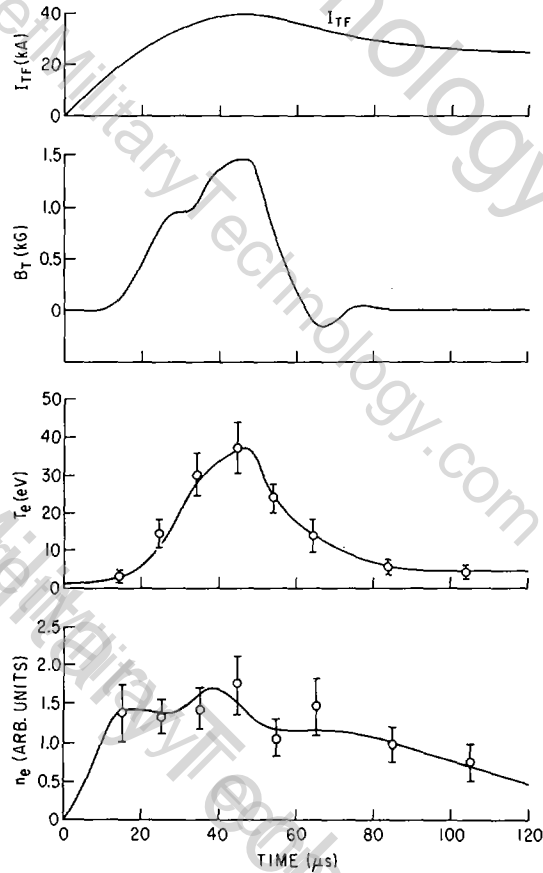


FIG. 6. Electron temperature and density time evolution at  $R = 12$  cm shown with the current  $I_{TF}$  in the toroidal-field coil and the toroidal magnetic field measured at  $R = 12$  cm (Proto S-1 C).

monitoring. By reducing  $n_e$  to less than  $2 \times 10^{14} \text{ cm}^{-3}$ , a  $T_e$  of over 40 eV has been obtained (Fig. 7).

#### 4.2 Impurity Control

In the Proto S-1C device, radiation from low-Z impurities is considered to be the dominant energy loss mechanism. We have identified OII, OIII, OIV, CII, CIII, and CIV lines. The existence of the CIV lines at 5811.98 Å and 5801.33 Å supports the measurement of relatively high temperatures by Thomson scattering ( $\gtrsim 40$  eV). Emission from CV could not be found. Nitrogen, iron, nickel, and titanium radiation (from earlier gettingting) was also identified.

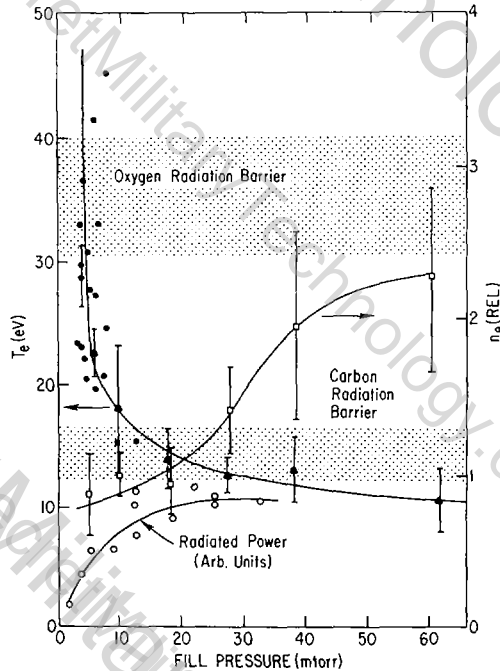


FIG. 7. Fill pressure dependence of electron temperature, density, and total radiated power (Proto S-1 C).

Oxygen and carbon impurity concentrations were estimated, by intentional introduction of known amounts of  $O_2$  and  $C_2H_2$ , to be  $\sim 1-5\%$  oxygen and  $\sim 0.5-3\%$  carbon without discharge cleaning or gettering. (More precise estimates were not possible as it is difficult to correct the data for the effect of changes in  $T_e$  due to the addition of impurities.) Other observations include (1) relative oxygen concentration is reduced by a factor of 2 to 4 by Ti-gettering the vacuum vessel prior to discharges, (2) removing magnetic probes inserted into the plasma decreased the carbon content by a factor of 2 to 4, and (3) the oxygen and carbon impurity levels relative to  $n_e$  did not markedly change at different fill pressures. With the observed amount of low-Z impurities for  $n_e \lesssim 2 \times 10^{14} \text{ cm}^{-3}$ , the radiation loss is estimated to be  $10 \sim 50 \text{ MW}$ , which accounts for most of the ohmic heating input. When the filling-gas pressure is reduced below  $10 \sim 12 \text{ mtorr}$ , the radiated power decreases significantly and  $T_e$  rises (Fig. 7), indicating that the ohmic heating input surpasses the radiation barrier caused by carbon impurities, and almost surpasses that due to oxygen. When the filling

pressure is  $\leq 4$  mtorr, the plasma discharge becomes unstable and nonreproducible.

#### 4.3 Gross MHD Stability

The Proto S-1A device has been primarily used to study gross MHD stability properties of the spheromak configuration.<sup>14</sup> By adjusting the shape of the equilibrium field, spheromak plasmas have been generated in regimes both stable and unstable against the tilting instability. If the flux core currents are adjusted to allow the equilibrium index to become slightly negative ( $n^* \equiv -R/B_{EF} (\partial B_{EF}/\partial R) < 0$ ), a tilting instability occurs. The tilting is very reproducible, apparently due to the magnetic perturbation of the current leads to the core, and proceeds on an axis defined by the leads. Figure 8a shows the time evolution of  $|B_t|$  contours. Immediately after the spheromak formation is completed at  $t \sim 18$   $\mu\text{sec}$ , the plasma begins to tilt and completes its tumbling action when the spheromak toroid has rotated  $90^\circ$  from its original position. The inverse growth rate for this tilting case is  $\gamma^{-1} = 3.6$   $\mu\text{sec}$ , and in general the spheromak configuration is rapidly (2-4  $\mu\text{sec}$ ) disassembled when the tilt angle reaches  $90^\circ$ . This is significantly different from the PS-1,2 results at Maryland. This is probably due to the loss of plasma equilibrium at  $90^\circ$  with the steady-state equilibrium field in the PPPL formation technique.

The shift instability has recently been identified in the Proto S-1C device, when the field index becomes appreciably positive ( $n > 0.1$ ). The growth rate of this mode is observed to be about the same as that of the tilt mode:  $\gamma_S^{-1} \approx 20 \tau_A$ , where  $\gamma_S \equiv (1/R) \partial R/\partial t$  and  $\tau_A \equiv a/v_A \sim 0.1-0.5$   $\mu\text{sec}$ .

Three types of stabilizing coils have been tested<sup>10</sup> as shown in Fig. 5c-e. The design of type (c) coils is based on the computed pattern<sup>6,11</sup> of eddy currents that would appear in nearby conductor walls when a  $n = 1$  rotation/displacement of the spheromak occurs. Type (d)<sup>15</sup> and type (e) coils are effective against tilt and shift instabilities, respectively, while the type (c) coil is effective against both modes.

Figure 8b shows the evolution of  $|B_t|$  contours for the same operational mode as in Fig. 8a, but after addition of Figure-8 coils. The coils were positioned with the outer edges of the coils 6 cm from the midplane of the core (Fig. 7c). It is apparent that the coils have stabilized the tilting of the plasma.

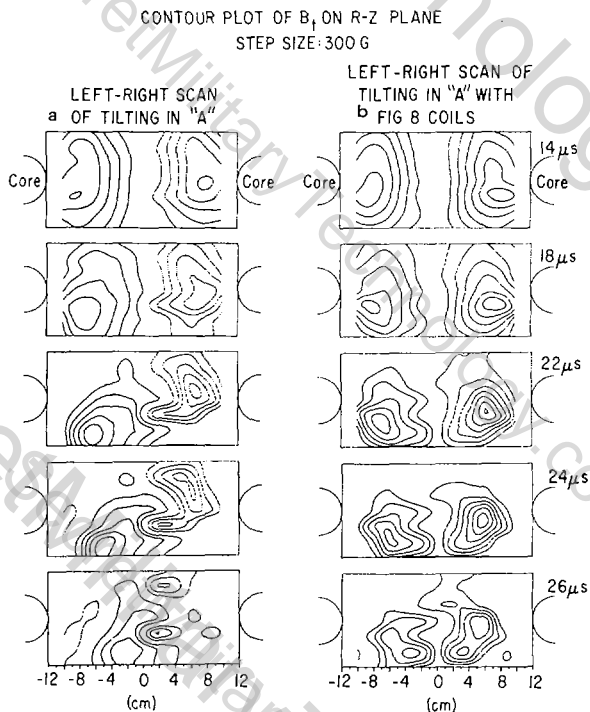


FIG. 8. Time evolution of  $|B_t|$  contours for PS-1A spheromak a) without Figure-of-8 coils, b) with Figure-of-8 coils.

In the Proto S-1C device, spheromak lifetime is reduced to less than 30  $\mu\text{sec}$  even with the figure 8 coils when the fill-pressure is reduced below 10 mtorr. In this condition, the plasma discharge often terminates by a disruption-like phenomenon characterized by a sudden shrinkage in major radius. Figure 9 illustrates a typical case. This disruption has recently been eliminated by inserting an electrically floating 8 cm diameter cylindrical center conductor along the major axis as shown in Fig. 9. The lifetime was thereby extended to over 150  $\mu\text{sec}$ , which is about one-third of the classical resistive decay time. In this case the plasma terminates gently.

##### 5. Conclusion and Discussion

For the past few years, important progress has been made in experimental spheromak research, primarily in the areas of gross MHD stability and impurity control. The parameters of

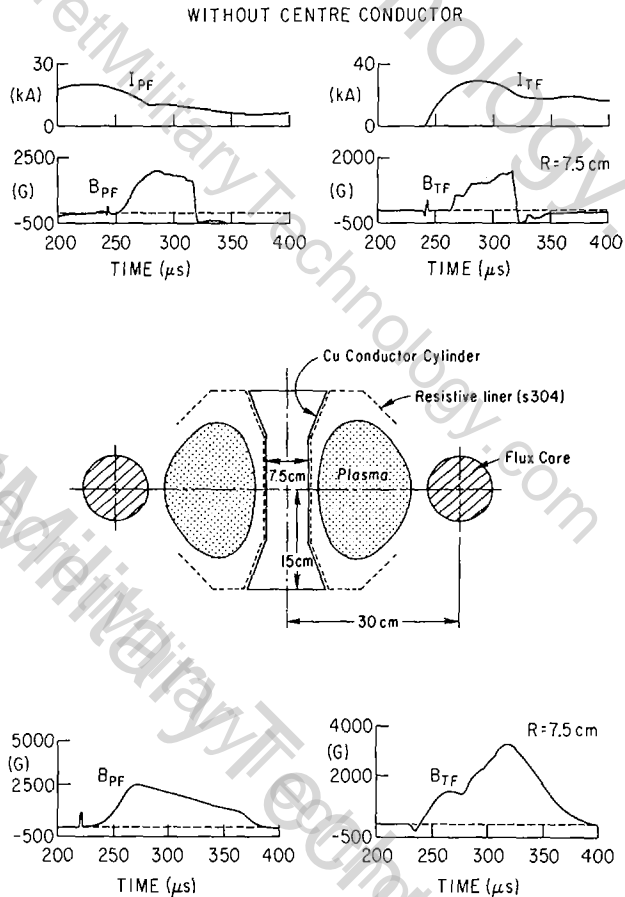


FIG. 9. Elimination of a sudden termination of the spheromak discharge by use of a centre conductor. Shown at the top is the time evolution of flux-core coil currents and poloidal ( $B_{PF}$ ) and toroidal ( $B_{TF}$ ) magnetic fields measured at  $R = 2.5$  cm and  $R = 7.5$  cm in the midplane ( $z = 0$ ), before the centre conductor is installed. Shown in the middle is a schematic diagram for the experimental set-up with a centre conductor. Shown at the bottom is the time evolution of the magnetic fields after installation of a centre conductor.

the three experiments described in this paper have been fairly comparable, with  $B_c \approx B_p \lesssim 5$  kG and  $T_e \lesssim 50$  eV. It was found that, at present, radiation is the dominant plasma loss mechanism. A spheromak generated by the LANL's coaxial gun scheme has been observed to last as long as 1 msec in the 80 cm diameter flux conserver.

Spheromak experiments at the University of Maryland and PPPL are observed to tilt on a time scale of  $\sim (10-20) \tau_A$ .

This is significantly longer than the value based on a simple model, and is probably due predominantly to "line-tying."<sup>16</sup> That is, some magnetic field lines, which contain conductive plasma adjacent to the main spheromak plasma, intersect or wrap around conductors. Furthermore, various simple passive coil systems have been tested in the experiments and proved to be significantly effective in stabilizing the dangerous tilting mode. This demonstration of the feasibility of stabilizing the gross spheromak instabilities with loosely fitting passive coils or with a conductive center rod as opposed to a closely fitting conducting shell should considerably enhance the attractiveness of the spheromak concept for a fusion reactor. While the insertion of the center rod may appear to compromise the principle of the "free plasma entity" of spheromak, the rod is not so restrictive as a surrounding shell nor as a toroidal-field coil system.

The S-1 device currently under construction is expected to produce larger ( $R \approx 0.4$  m,  $a \approx 0.2 \sim 0.3$  m) and hotter ( $T_e > 100$  eV) plasmas. If the S-1 performance can be inferred from performance of the Proto S-1 experiments, the plasma should be able to burn through the carbon and oxygen radiation barriers and permit the exploration of transport-limited high temperature spheromak confinement regimes.

#### REFERENCES

- [1] BUSSAC, M.N., et al., in Plasma Physics and Controlled Nuclear Fusion Research (Proc. 7th Int. Conf. Innsbruck, 1978) Vol.3, IAEA, Vienna (1979) 249.
- [2] H.P. Furth, *J. Vac. Sci. Technology*, **18**, 1073 (1982).
- [3] M.Katsurai and M. Yamada, Princeton University, Plasma Physics Laboratory Report PPPL-1614; to be published in *Nucl. Fusion*, **22** (1982).
- [4] T. Jarboe et al. *Phys. Rev. Lett.* **45**, 1264 (1980).
- [5] G. Goldenbaun et al., *Phys. Rev. Lett.* **44**, 393 (1980).
- [6] M. Yamada et al., *Phys. Rev. Lett.* **46**, 188 (1981).
- [7] M.N. Rosenbluth and M.N. Bussac, *Nucl. Fusion* **19**, 489 (1979).
- [8] J. Finn, W. Manheimer, and E. Ott, *Phys. Fluids* **24**, (1981).
- [9] S.C. Jardin et al., *Nucl. Fusion* **21**, 1203 (1981).  
S.C. Jardin and U. Christensen, *Nucl. Fusion* **21**, 1665 (1981).
- [10] J.B. Taylor, *Phys. Rev. Lett.* **23**, 1139 (1974).
- [11] AN, Z.G., et al., in Plasma Physics and Controlled Nuclear Fusion Research (Proc. 8th Int. Conf. Brussels, 1980) Vol.1, IAEA, Vienna (1981) 493.

- [12] M. Yamada et al. Proc. US-Japan Symposium on Compact Toruses and Energetic Particle Injection, Princeton, N.J., 1979, p. 171.
- [13] S.C. Jardin and W. Park, Phys. Fluids 24, 679 (1981); Lui et al., Phys. of Fluids 24, 673 (1981); Sato et al., to be published.
- [14] C. Munson et al., Proc. 4th Symp. on Compact Toroids at LLL (1981), Livermore, p. 149.
- [15] H. Ikezi, Private Communication (1981).
- [16] J. Finn and A. Reiman, Phys. Fluids 25, 116 (1982).

#### DISCUSSION

I.R. JONES: I wish to refer to the Los Alamos gun experiment: for most of the life-time of the spheromak plasma, the electron density corresponds to the complete ionization of about 0.3 mtorr H<sub>2</sub>. This plasma exists in a neutral background of 8 mtorr H<sub>2</sub>. Would you care to speculate on the role of this very high background of neutral gas?

M. YAMADA: I would not mind speculating on the role of the neutral gas, but I would like first to refer your question to Dr. Sherwood, who is a member of the Los Alamos National Laboratory team.

A.R. SHERWOOD: We do not believe that undisturbed neutral fill gas is present in the spheromak containment region during the life-time of the configuration. A strong shock wave is observed during the plasma filling process, apparently either ionizing or expelling most of the neutrals. If the original density of neutral gas were present in the measured plasma density and temperature, one would expect rapid ionization and an increase in plasma density rather than the observed decrease to a plateau.

M. YAMADA: The mean free path of H<sub>2</sub> molecules penetrating into the Los Alamos spheromak would be a few centimetres before ionization. However, they may reduce the edge temperature of the spheromak and maintain the appropriate current profile. Under these conditions, a cleaner plasma might possibly be produced, because of the reduced rate of sputtering, but this is just speculation.

V. NARDI: One or several toroidal vortices with essentially the same structure as spheromaks are produced in the axial pinch of a focused discharge. The typical radius of a vortex is <1–2 mm, life-time ~10–50 ns, peak density ~10<sup>19</sup>–10<sup>20</sup> cm<sup>-3</sup>, local axial current ≥2 MA, electron temperature ≥1–5 keV, toroidal field ≥100 MG. The self-consistent poloidal field is in the form of filamentary flux tubes which form the vortex wall. In a deuterium discharge a vortex is an intense source of X-rays, neutrons (~10<sup>8</sup> neutrons/vortex life-time) and other particles (see BOSTICK et al., Ann. N.Y. Acad. Sci. 251 (1975) 2;

NARDI et al., Proc. 2nd Conf. Pulsed High-Beta Plasmas, Garching (1972) 163; Physics in High Magnetic Fields, Grenoble, CNRS Symp. No.242 (1975) 129; Energy Storage, Compression and Switching I, Plenum, New York (1976) 175).

Have you made any effort to determine scaling laws for spheromak parameters such as radius, particle density, peak self-consistent field and temperature?

M. YAMADA: No, we have not studied these thoroughly. However, the very small plasmas made in the plasma focusing experiment may well be of the spheromak configuration type. If the total beta value is less than 20% or so in that case, then the same physics as discussed here will be applied. (For example, if  $a \cong 1$  mm,  $B_{t0} = 10^8$  G we can sustain a substantial density of  $\sim 10^{20}$  cm<sup>-3</sup> of several-keV plasmas; the Lawson criterion would tell us that we would need  $\tau_{\text{conf}} \gtrsim 1$   $\mu$ s.) Since we do not at the moment know any *realistic transport scaling*, however, I would rather not comment on scaling.



## EXPERIMENTAL STUDIES OF FIELD-REVERSED CONFIGURATION CONFINEMENT IN FRX-C\*

R.E. SIEMON, W.T. ARMSTRONG, R.R. BARTSCH,  
R.E. CHRIEN, J.C. COCHRANE, R.W. KEWISH,  
P.L. KLINGNER, R.K. LINFORD, J. LIPSON,  
K.F. McKENNA, D.J. REJ, E.G. SHERWOOD, M. TUSZEWSKI  
Los Alamos National Laboratory,  
University of California,  
Los Alamos, New Mexico,  
United States of America

### Abstract

#### EXPERIMENTAL STUDIES OF FIELD-REVERSED CONFIGURATION CONFINEMENT IN FRX-C.

A primary purpose of the large-bore (0.5 m dia.) FRX-C field-reversed theta-pinch experiment is to study the scaling of plasma particle containment time  $\tau_N$  with major radius  $R$  of the field-reversed configuration (FRC). At 20 mtorr fill pressure the FRX-C plasma parameters,  $\bar{n} \approx 4 \times 10^{15} \text{ cm}^{-3}$ ,  $T_e \approx 100 \text{ eV}$ ,  $T_i \approx 150 \text{ eV}$ , are comparable to those obtained in the smaller bore (0.25 m dia.) FRX-B device. Under these conditions, the present measurement of particle confinement time in FRX-C is  $\tau_N \approx 140 \mu\text{s}$ , consistent with the scaling  $\tau_N \propto R^2$ , when compared with the earlier FRX-B results. This favourable scaling has been observed with  $R/\rho_i \approx 30$  ( $\rho_i =$  ion gyroradius), twice as large as in FRX-B, despite theoretical indications that various MHD instabilities would appear as  $R/\rho_i$  was increased. The characteristics of hotter neutron-generating FRC plasma produced at lower fill pressure (5 mtorr), where  $\bar{n} \approx 2 \times 10^{15} \text{ cm}^{-3}$ ,  $T_e \approx 170 \text{ eV}$ ,  $T_i \approx 600 \text{ eV}$ , are also presented. In this plasma regime an accurate determination of  $\tau_N$  is difficult because of the short stable period observed.

### 1. INTRODUCTION

The FRC is an axisymmetric, highly prolate, compact toroid formed with purely poloidal magnetic field, as shown in Fig. 1. Some important distinguishing features of the FRC are the very high volume-averaged plasma beta required by equilibrium in the absence of toroidal magnetic field and the possibility of stable translation inside a conducting cylinder. It appears that these features could be used to significant advantage for fusion power production.

\* Work performed under the auspices of the US Department of Energy.

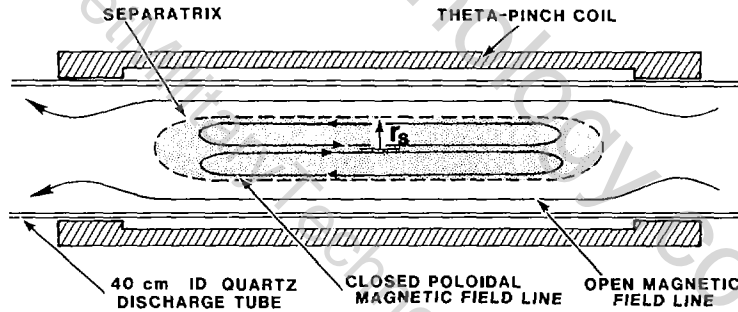


FIG.1. Field-reversed configuration.

A major issue for the FRC is the scaling with size of particle, magnetic flux, and energy containment time. The scaling of particle containment time can be determined using the recent results from FRX-C and the previously reported containment time on FRX-B [1]. A parameter-space study showed that an FRC plasma of very similar density, temperature and magnetic field as produced in FRX-B, but with twice as large a major radius  $R$ , could be produced in FRX-C at a fill pressure of 20 mtorr.

Of the various possible particle loss processes, theoretically predicted lower-hybrid-drift transport appears to agree best with the observed FRC particle confinement time. A model for this transport mechanism has been developed [2] and correctly predicts the measured FRX-B containment time,  $\tau_N \approx 39 \mu\text{s}$ . For FRX-C, the model yields  $\tau_N \approx 160 \mu\text{s}$ , or equivalently,  $\tau_N \propto R^2$ . The data presented in this paper agree with this analytical result.

The increase in FRC confinement time as  $R/\rho_i$  increases is of additional significance because there are MHD instabilities predicted theoretically [3] that have not been observed experimentally. Ion kinetic effects are presumably the explanation, but a detailed understanding does not exist. Possibly a stability limit exists in the ratio  $R/\rho_i$  beyond which MHD modes will affect confinement. If such a limit exists, it must exceed  $R/\rho_i \approx 30$  obtained in the present experimental results.

## 2. DESCRIPTION OF EXPERIMENT

For the measurements reported here, the FRX-C field-reversed theta pinch was operated with the parameters

TABLE I. PARAMETERS OF FRX-C EXPERIMENT

<u>Coil Geometry</u>	
Length	2.0 m
Central Diam. (1.6 m long)	0.5 m
Mirror Region Diam. (0.2 m each end)	0.44 m
Magnetic Mirror Ratio	1.17
Discharge Tube ID	0.4 m
<u>Magnetic Field</u>	
Main Field (vacuum, no bias)	9.5 kG
Rise time ( $\tau/4$ )	4.5 $\mu$ s
Decay time (L/R in vacuum)	300 $\mu$ s

given in Table I. The value of confining magnetic field, reported with the plasma parameters, depends on the reverse bias level (adjustable 0-4 kG) and the significant change in coil inductance that results from the presence of the FRC. The FRX-C main capacitor bank is connected to the coil through two feed slots. Consequently, the applied azimuthal implosion-heating voltage is approximately twice the DC charge voltage applied to the capacitor bank (adjustable from 40 to 50 kV).

An array of 13 magnetic field probes located every 15 cm along the coil between the coil inner surface and outside the discharge tube is used in conjunction with a flux loop surrounding the discharge tube near the midplane to determine the excluded flux radius,  $r_{\Delta\phi}(z)$ , of the FRC [4]. In regions of straight field lines, the FRC separatrix radius can be approximated  $r_s = r_{\Delta\phi}$ . For an equilibrium configuration  $R = r_s/\sqrt{2}$ . A side-on 3.39- $\mu$ m double-pass interferometer is used to measure the time history of  $\Delta\phi$  at the center of the coil. Measurements of  $T_e$  by Thomson scattering are taken with the scattering volume located 5 cm off the coil axis and 10 cm from the coil midplane. Neutron emission is measured with a plastic scintillator and a rhodium foil activation counter. An end-viewing, double-pass, ruby-laser holographic interferometer with a 30-cm field of view is used to measure particle inventory and length-averaged radial density profile. Visible and VUV spectroscopy are used for line intensities and line broadening measurements.

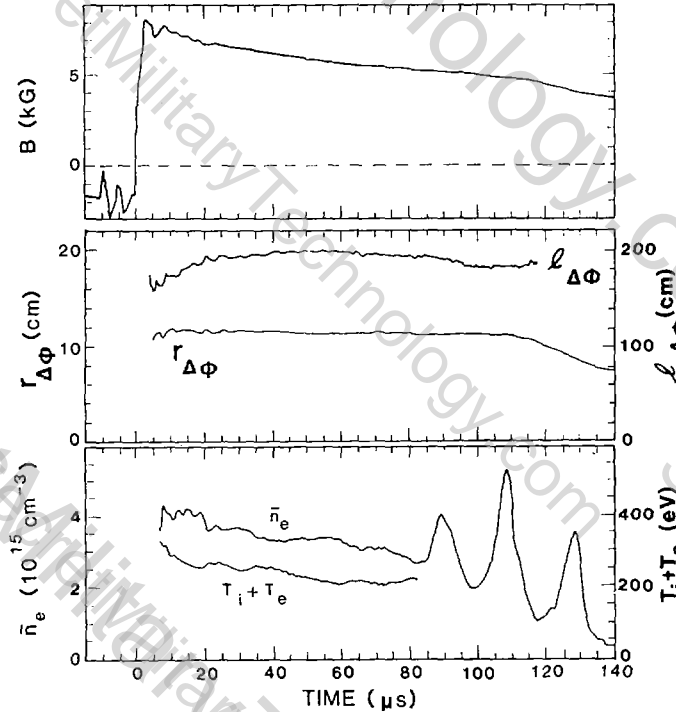


FIG.2. Data on typical discharge at 20 mtorr fill pressure.

### 3. FORMATION PHASE

FRC formation in a field-reversed theta pinch, which encompasses the initial inward radial plasma implosion, magnetic field line reconnection at the plasma ends, and axial contraction of the plasma, has been described elsewhere [1]. The formation on FRX-C has been studied as a function of fill pressure  $p_0$  and bias field  $B_0$  for three magnetic end-mirror configurations:  $M = 1.05, 1.10$  and  $1.17$ . The optimum reverse bias field for plasma reproducibility and lifetime increases with fill pressure, being about 0.8 kG at 5 mtorr and 1.7 kG at 20 mtorr. The FRC length also increases with  $p_0$ , extending from about 1.2 m at 5 mtorr to 1.9 m at 20 mtorr. At 40 mtorr it does not appear that a well-defined, closed-field-line FRC is confined within the 2-m coil. A qualitative observation is that formation is more reproducible and easily achieved at low rather than at high fill pressure.

The primary effect of mirror strength appears to be its influence on field-line reconnection at the plasma ends. With

weak mirrors at 20 mtorr, the FRC shape as deduced from the magnetic probe array often lacks symmetry and indicates an axial drifting of the FRC out of the coil. Similar behavior is found in 2-D MHD simulations [5] if the plasma is given an initial axial momentum. In the experiment, axial drifting of the plasma is possibly a result of non-simultaneous reconnection at the two ends. Asymmetry in the axial contraction following reconnection would result in net FRC momentum. According to simulations, reconnection proceeds more slowly if the mirror strength is reduced or the fill pressure increases. Large mirror ratios reduce the reconnection asymmetry and thus the tendency of the FRC to drift axially. The best performance on FRX-C has been achieved with the largest passive mirror ratio,  $M = 1.17$  (see Table I).

#### 4. PLASMA PARAMETERS AND PARTICLE CONFINEMENT: 20 mtorr

Data obtained on a typical discharge at 20-mtorr fill pressure and 1.7 kG bias field are presented in Fig. 2. The external magnetic field waveform  $B$  is recorded near the coil midplane. The FRC length  $\ell_{\Delta\phi}$  is defined as the distance between the axial end positions where  $r_{\Delta\phi}$  decreases to 65% of its maximum value [6]. The average density is defined as  $\bar{n} = \int n dl / 4r_{\Delta\phi}$ , where  $\int n dl$  is obtained from the side-on interferometer. The value of  $\bar{n}$  for most profiles is very close to the volume-averaged density and differs by no more than 15% for any profile when  $x_s = 0.4$ . The electron temperature measured by Thomson scattering on similar discharges is  $T_e = 100 \pm 20$  eV. The ion temperature is calculated from pressure balance.

The quiescent plasma confinement phase is terminated by a rotational  $n = 2$  instability that begins at about 70  $\mu$ s. The growth of the  $n = 2$  distortion is readily identified in the modulation of the side-on interferometer density data of Fig. 2. End-on holograms also clearly demonstrate the  $n = 2$  nature of the instability.

Small changes in the applied bias field result in insignificant changes of initial FRC temperature and density, but the different bias fields significantly affect the particle and flux decay characteristics. The closed-field-line flux can be approximated as  $\phi_c = (x_s/2\sqrt{2})\pi B r_{\Delta\phi}^2$ . In Fig. 3, the time history of  $\phi_c$  is plotted for six representative shots at 1.7 kG bias, Mode A, and six shots at 1.5 kG bias, Mode B. Clearly, the initial flux decay is slower in Mode A and, as will be shown, this correlates with improved particle confinement.

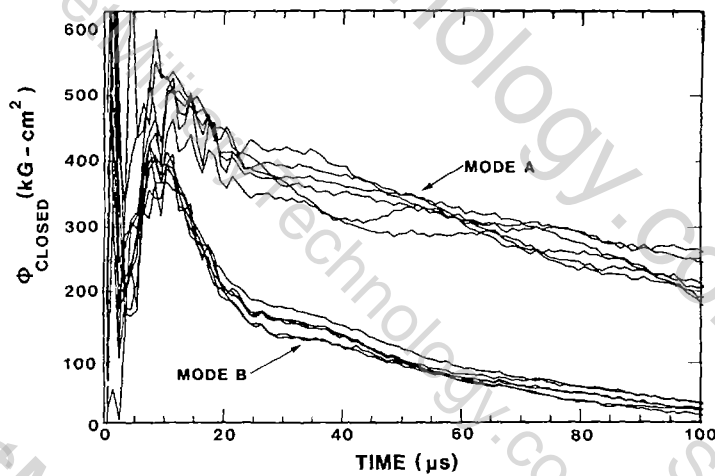


FIG. 3. Time history of closed-field-line flux for 1.7 kG bias, Mode A, and 1.5 kG, Mode B.

From Fig. 2 it can be seen that the FRC length is comparable to the coil length. The smaller bias level in Mode B would result in a slightly longer FRC. The FRC length contracts and then expands slightly as equilibrium is established following reconnection. Perhaps the inferior confinement of Mode B is a consequence of some closed field lines expanding beyond the ends of the coil during the slight expansion.

The particle e-folding time  $\tau_N$  is obtained from two independent measurements of FRC electron inventory time history,  $N(t)$ . First, the density measured by the side-on interferometer is combined with the FRC volume determined from analysis of the axial magnetic-probe array data. Second, the end-on interferograms, obtained with the holographic interferometer, are used to directly determine  $N$  by appropriate integration over the observed interferogram fringe shift profile. A typical end-on interferogram obtained for Mode B operation 30  $\mu$ s after main bank initiation is shown in Fig. 4. Mode A interferograms are not yet available.

Figure 5 presents the particle inventory time histories for Modes A and B. The data points represent analyzed interferograms where each interferogram was recorded separately on a single discharge in Mode B. Superimposed are the inventories determined by side-on interferometry for the same discharges on which the interferograms were taken. A least squares fit to an exponential inventory decay yields the particle decay time  $\tau_N$ .

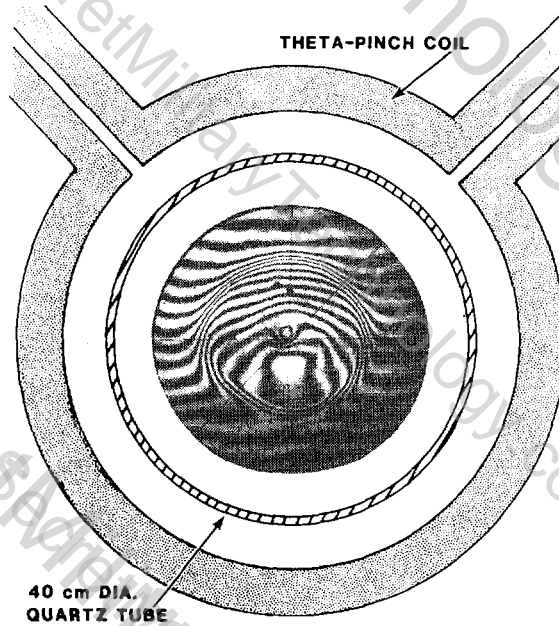


FIG.4. Typical end-on interferogram obtained at 1.5 kG bias and 20 mtorr fill pressure taken 30  $\mu$ s after main bank initiation.

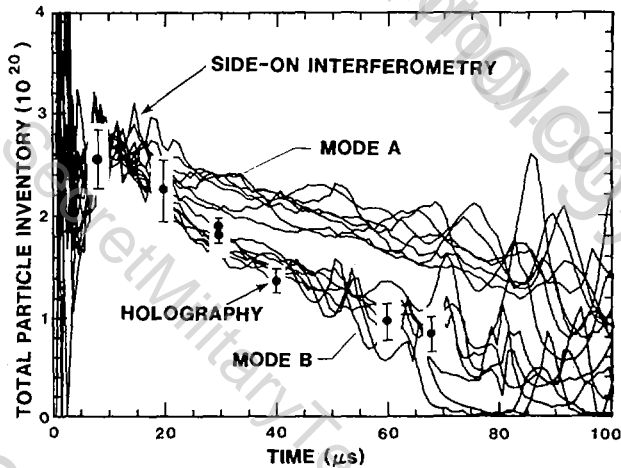


FIG.5. Time history of electron inventory for 1.7 kG bias, Mode A, and 1.5 kG bias, Mode B.

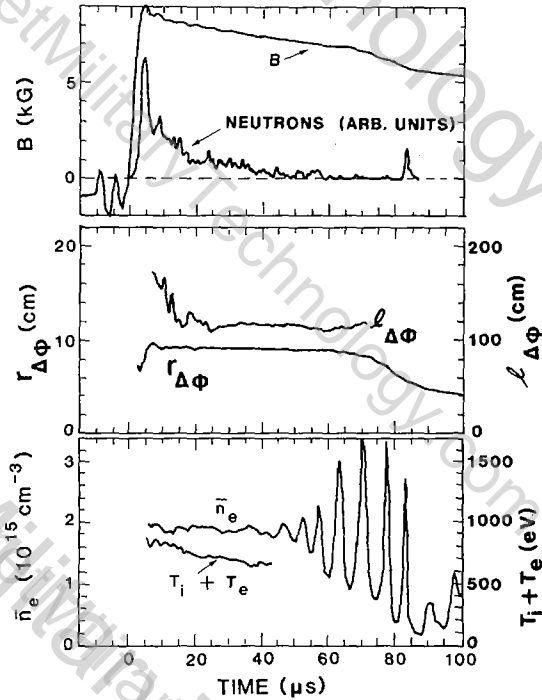


FIG. 6. Data on typical discharge at 5 mtorr fill pressure.

For the low-bias Mode B operation, both measurement techniques give identical decay times,  $\tau_N = 50 \pm 5 \mu\text{s}$ . For the higher-bias Mode A operation the side-on interferometer technique yields  $\tau_N = 140 \pm 30 \mu\text{s}$ .

##### 5. PLASMA PARAMETERS: 5 mtorr

Data obtained at 5 mtorr fill pressure are presented in Fig. 6. Discharges in this regime are characterized by a high degree of reproducibility and significant neutron production (approximately  $3 \times 10^7$  neutron/discharge). The observed reproducibility may be attributed to the small plasma length obtained at this low-fill pressure. Neutron emission combined with density and volume measurements, and assuming a Maxwellian ion velocity distribution, corresponds to a peak ion temperature  $T_i \approx 1.0 \text{ keV}$  at  $\approx 10 \mu\text{s}$ . Line broadening of CV, if interpreted as thermal Doppler broadening, corresponds to  $T_i$  of about five times the pressure balance temperature at  $10 \mu\text{s}$ , dropping to a ratio of two at  $30 \mu\text{s}$ . The temperature  $T_e + T_i$  in Fig. 2 is determined by pressure balance. The pressure balance

temperature is considered the most reliable, but further investigation of this issue is needed. Electron temperature from Thomson scattering is measured on similar discharges to be  $175 \pm 25$  eV.

The quiescent confinement phase is terminated by the rotational  $n = 2$  instability that begins at about  $30 \mu\text{s}$ . The internal flux decays on a much longer time scale, as reported elsewhere [7]. As seen in Fig. 6, the  $n = 2$  distortion grows, resulting in oscillations in the side-on interferometer density measurement, until the plasma touches the discharge tube wall. At that time the confinement is abruptly terminated.

The relatively short quiescent period observed in this fill pressure regime does not allow an accurate determination of  $\tau_N$  using the combined side-on interferometer and magnetic probe technique. End-on interferograms, obtained between 10 and  $45 \mu\text{s}$  after main bank initiation, yield  $\tau_N \approx 68 \mu\text{s}$ .

## 6. DISCUSSION

The particle confinement times reported here are still preliminary in nature and require further confirmation. However, the data obtained to date indicate that the FRC particle confinement time scales approximately with  $R^2$  when the FRC is formed with the optimum bias level.

The transport model that correctly predicts the observed particle containment time [2] also predicts that a substantial increase in  $\tau_N$  is possible if the ratio of separatrix radius to coil radius,  $x_s$ , can be increased to values closer to unity. Field-reversed theta-pinch-generated FRCs so far attain  $x_s$  values of approximately 0.4. Attempts to increase the amount of closed flux, and thus  $x_s$ , by increasing the applied bias above the optimum level at a given fill pressure, result in loss of the closed-field-line configuration. However, by axial translation of the FRC from the theta-pinch coil into a smaller diameter flux conserver, it should be possible to produce FRCs with significantly higher  $x_s$  values. An FRX-C modification is progressing that will allow investigation of this translation process.

The origin of rotation before the onset of the rotational  $n = 2$  mode is not fully understood. A correlation has been proposed between the fraction of particles lost and the onset of the  $n = 2$  mode [8]. In FRX-C about 40% of the particles are lost before the onset of the  $n = 2$ , a somewhat smaller fraction than previously reported [1]. The proposed correlation was

based on the assumption that below a certain threshold value of rotation no instability would occur. However, recent simulations have modified the predicted relationship between rotation and instability [3]. Endshorting, an alternative mechanism to particle loss, has also been suggested as the origin of rotation [9]. Experiments at Nagoya have demonstrated that endshorting does play a role [10].

Regardless of the origin of rotation, recent experiments at Osaka have shown that the  $n = 2$  mode can be suppressed by means of quadrupole fields applied after FRC formation [10]. Quadrupole coils are presently being added to FRX-C.

#### REFERENCES

- [1] ARMSTRONG, W. T., LINFORD, R. K., LIPSON, J., PLATTS, D. A., SHERWOOD, E.G., *Phys. Fluids* 24 11 (1981) 2068.
- [2] TUSZEWSKI, M., and LINFORD, R. K., *Phys. Fluids* 25 5 (1982) 765.
- [3] HARNED, D. S., et al., paper CN-41/M-2-2, these Proceedings.
- [4] TUSZEWSKI, M., *Phys. Fluids* 24 11 (1981) 2126.
- [5] ARMSTRONG, W. T., and MILROY, R. D., Proc. of IEEE Int. Conf. on Plasma Science, Ottawa, Canada, 1982, p. 107.
- [6] SEMENOV, V. N., and SOSNIN, N. V., *Sov. J. Plasma Phys.* 7 2 (1981) 180.
- [7] TUSZEWSKI, M., et al., *Phys. Fluids* (to be published).
- [8] BARNES, D. C., SEYLER, C. E., in Proc. of US-Japan Joint Symp. on Compact Toruses and Energetic Particle Injection (Princeton University, Princeton, New Jersey, 1979) p. 110.
- [9] STEINHAEUER, L. C., *Phys. Fluids* 24 2 (1981) 328.
- [10] MINATO, T., et al., paper CN-41/M-3, these Proceedings.

**COMPACT TOROIDAL PLASMAS:  
SIMULATIONS AND THEORY\***

D.S. HARNED, D.W. HEWETT, C.G. LILLIEQUIST,  
R.W. MOSES, D.D. SCHNACK, J.L. SCHWARZMEIER,  
A.G. SGRO, R.L. SPENCER  
Los Alamos National Laboratory,  
Los Alamos, New Mexico

D.V. ANDERSON, J. KILLEEN, A.A. MIRIN,  
N.J. O'NEILL, A.I. SHESTAKOV, D.E. SHUMAKER  
National Magnetic Fusion Energy Computer Center  
Lawrence Livermore National Laboratory,  
Livermore, California

S.P. AUERBACH, J.K. BOYD, T.A. BRENGLE,  
B.I. COHEN, J.H. HAMMER,  
C.W. HARTMAN, W.C. TURNER  
Magnetic Fusion Energy Division,  
Lawrence Livermore National Laboratory,  
Livermore, California

A. AYDEMIR, D.C. BARNES  
Institute for Fusion Studies,  
University of Texas, Austin, Texas

C. BERNARD  
General Atomic Co., San Diego, California

W.M. TANG  
Princeton Plasma Physics Laboratory,  
Princeton University,  
Princeton, New Jersey

C. SEYLER  
Cornell University, Ithaca, New York

J. TATARONIS  
University of Wisconsin, Madison, Wisconsin  
United States of America

---

\* Work performed under the auspices of the US Department of Energy.

## Abstract

## COMPACT TOROIDAL PLASMAS: SIMULATIONS AND THEORY.

Realistic FRC equilibria are calculated and their stability to the  $n = 1$  tilting mode is studied. Excluding kinetic effects, configurations ranging from elliptical to racetrack are unstable. Particle simulations of FRCs show that particle loss on open field lines can cause sufficient plasma rotation to drive the  $n = 2$  rotational instability. The allowed frequencies of the shear Alfvén wave are calculated for use in heating of spheromaks. An expanded spheromak is introduced and its stability properties are studied. Transport calculations of CTs are described. A power balance model shows that many features of gun-generated CT plasmas can be explained by the dominance of impurity radiation. It is shown how the Taylor relaxation theory, applied to gun-generated CT plasmas, leads to the possibility of steady-state current drive. Lastly, applications of accelerated CTs are considered.

Realistic Field Reversed Configuration (FRC) equilibria have been calculated that satisfy conducting wall boundary conditions inside a cylinder[1]. Solutions exist for a variety of pressure profiles. The choice  $P(\psi) = a + \tanh(b+c\psi+d\psi^3)$  allows for small plasma pressure on the open field lines and can lead to elongated FRCs with flux surfaces ranging from nearly elliptical to highly racetrack. The racetrack cases correspond to sharply peaked current profiles near the separatrix.

In linear stability studies the perturbations are Fourier expanded in the toroidal variable  $\theta$  as  $f=f(r,z)\exp(in\theta)$ . The tilting instability,  $n=1$ , is studied by two approaches: an ideal MHD trial function approach[2], and a resistive MHD initial value code, RIPPLE VI[3]. The calculations show that equilibria with shapes ranging from elliptical to highly racetrack are all unstable to the  $n=1$  tilt mode[2]; the modes with  $n>2$  are even more unstable. For all elongated equilibria the displacements of the tilting mode are primarily axial and are confined to the closed field line region. For elliptical equilibria, each flux surface shifts approximately rigidly, whereas for racetrack equilibria the instability is localized to the large curvature tips of the flux surfaces. For typical FRX-B parameters the growth time is about  $1\mu s$ , while the experiments last for 20-50 $\mu s$ . Furthermore, it appears that this instability does not saturate at a low level. Nonlinear 3-D MHD simulations[4] show that for the case of elliptical flux surfaces the mode grows to an amplitude that would be observable in the experiments. Thus, the observed stability against tilting must be due to effects beyond the ideal MHD model.

For FRCs, both theory[5] and simulations[6] show that the ideal MHD growth times for large  $n$  modes are of the same order as the Alfvén transit times around the closed field lines.

Tang and Catto[7] have generalized ballooning theory to include finite Larmor radius (FLR) effects associated with the diamagnetic and  $\nabla B$  drifts of these modes. When the diamagnetic drift is included in a calculation for a Hill's vortex with parameters modeling the FRX-B plasma, it is estimated that the large- $n$  modes stabilize when  $\rho_i \sim r_{sep}/10$ , a relationship consistent with the experiment. Implementation of the  $\nabla B$  drift is difficult, although it is always stabilizing to the large- $n$  modes.

Recent particle-in-cell simulations[8] show that kinetic effects play an important role in the reconnection processes that occur during the implosion phase of FRC experiments. Streaming ions driven by the magnetic piston are reflected by the bias magnetic field. The reflecting ions drive a gravitational-like mode which forces reconnection at the magnetic null. The self generation of toroidal magnetic field, due to the Hall effect, greatly increases the reconnection rate. After the reconnection phase the toroidal magnetic field (with no net toroidal flux) annihilates and the configuration settles into an FRC equilibrium.

A collisionless, nonresistive kinetic model has been developed to make a detailed study of the reconnection processes discussed in the preceding paragraph. In the simplest case, a Maxwellian plasma approaches an X-point with  $\vec{B} = B_0(x\hat{y} + y\hat{x})$  and  $\vec{E} = E_0\hat{z}$ . It is proven analytically that plasma moving away from the X-point is no longer Maxwellian and has gained energy from the electric field. This nonadiabatic process is verified by numerical computations.

Rotational instabilities are studied with a 2-D ( $r$ - $\theta$ ) massless electron hybrid code[9]. For rigid rotor profiles, the  $n=2$  rotational mode can have substantial growth rates for smaller values of rotation than the instability threshold obtained from FLR fluid theory[10]. Initially non-rotating FRC equilibria satisfying the average  $\beta$  condition are caused to rotate by the particle loss on open field lines[11]. For values of  $S = R/\rho_i > 10$  ( $R$ =radius of o-point,  $\rho_i$ =ion Larmor radius in the external field), the rotation starts near the separatrix, creating a strong velocity shear. The localization of rotation results in considerably less spinup for large  $S$  values than is obtained with rigid rotor profiles. The velocity shear is maintained until the appearance of a large  $n$  number ( $n > 20$ ) instability. The time for the bulk of the plasma to rotate can be increased by increasing  $S$ , increasing  $x_s = r_{sep}/r_{wall}$ , or by decreasing transport losses. The  $n=2$  rotational instability is not observed until the bulk of the plasma is rotating. The increase in the length of time prior to onset of the  $n=2$  instability, for increased values of  $x_s$  and  $S$ , is a possible explanation for the non-observance of rotational modes in the Kurchatov experiment[12] as well as being a favorable result for reactor parameters having  $S > 100$ .

The lower hybrid drift instability is believed to be active near the separatrix of an FRC. As a first step in studying anomalous transport in FRCs, this instability has been simulated in the low drift velocity regime with a finite electron mass hybrid code[13]. The initial growth of the instability obtained from the simulation agrees well with the results of the linear theory.

For the spheromak, the RIPPLE VI code[3] studies a family of force-free equilibria in which the toroidal field functions are linear in  $\psi$  and vanish on a contour inside the separatrix. The configurations differ in the shapes of their poloidal cross-sections (prolate to oblate) and the aim is to determine how these affect the growth rates. The perturbations satisfy conducting wall boundary conditions on a cylinder enclosing the plasma. For the wall positions used, all the equilibria are unstable to the  $n=1$  mode. However, oblateness reduces the growth rate by 40% of the prolate case.

Also studied is the ideal MHD stability of an expanded spheromak, a configuration containing plasma on both the open and closed field lines. The motivation is to study the effect of a reversed toroidal field outside the separatrix. The configuration resembles a reversed field pinch (RFP) of unity aspect ratio and may combine the stability features of the RFP with the attractiveness of the spheromak. In addition line tying[14] might improve the stability of the  $n=1$  mode.

For the simulations, force-free models are used,  $\mathbf{J} = \mu \mathbf{B}$ , where  $\mu$  is almost constant throughout the plasma but vanishes smoothly at the separatrix, and at the plasma edge. The equilibria, obtained from the Grad-Shafranov equation, are tested for stability with a modification of an existing code[15] that minimizes  $\delta W$ . The new code recovers the spheromak results for vacuum outer regions and confirms published work[14]: for an optimized oblate shape, the distance between the wall and the separatrix needed to stabilize the tilting mode is about twice as large with line-tying than without it. In addition, line tying reduces the growth rate. Unfortunately, field reversal is destabilizing; the wall position necessary to stabilize tilting is closer to the current channel under its presence. Finite pressure gradients do not significantly alter the stability limits, except for the onset of an  $n=1$  internal mode above a threshold amount of pressure.

A theoretical study has begun on heating the Los Alamos compact torus (CT) through excitation of the shear Alfvén wave. Assuming low  $\beta$ , the allowed frequencies of the Alfvén wave can be found as eigenvalues of a second-order ordinary differential operator along the equilibrium magnetic field lines[16]. Using profiles characteristic of the CT, the eigenvalue problem is solved numerically and mode coupling is observed. The wave

amplitude is logarithmically singular at the resonant surface making wave absorption and plasma heating possible[17].

The resistive force-free evolution of a spheromak away from an initial state is calculated using a 1-1/2 dimensional transport code with classical resistivity ( $T_e = 7\text{eV}$ )[18]. In experiments the ratio of poloidal to toroidal magnetic field increases monotonically from the constant Taylor value until (presumably) an instability returns the plasma to the Taylor state. The transport code results match the experimental data well until the configuration becomes unstable.

The evolution of a CT on the slow time scale is simulated by the transport code FRT[19]. Calculation of the 2-D equilibrium alternates with the 1-D, simultaneous temporal advancement of the four transport quantities: the particle density, the ion and electron entropy, and the toroidal magnetic flux. The physical processes simulated are: Braginskii transport coefficients, Joule heating, collisional transfer of energy between ions and electrons, radiation cooling of electrons by impurities, and anomalous electron thermal conductivity.

The code has simulated the decay of the CTs produced in the Beta II experiment at LLNL, assuming that the plasma has been injected into the flux conserver. Oxygen impurities of ~1% are included in the calculations. The initial ion density, and ion and electron temperatures are  $10^{15}\text{cm}^{-3}$  and 5eV, respectively. During an initial transient the electron temperature adjusts itself (increasing to approximately 6eV) to maintain a balance between Joule heating and radiation cooling due to the impurities. The electron and ion temperatures are approximately equal. The major power flow is from the magnetic field energy via Joule heating to the electrons, which lose the energy by impurity radiation. The resulting decay of the magnetic flux is approximately linear in time.

A simple power balance model shows that striking features of present coaxial gun generated CT plasmas (finite lifetime, linear current decay, insensitivity to density or magnetic energy) are explained by the dominance of impurity radiation[20]. Analytic estimates are used for magnetic energy and ohmic heating power, and impurity radiation power is fitted with a power law[21],  $P_{\text{rad}} \sim n_e n_I V T^k$  ( $n_e$ ,  $n_I$  = electron, impurity density;  $T$  = electron temperature;  $V$  = plasma volume;  $k$  determined by fitting coronal equilibrium radiation). The magnetic field at the geometric center is shown to obey  $B(t) = B(0)(1-t/t_E)^{1/2\alpha}$ , where  $\alpha = 3/(3+2k)$ . For oxygen  $\alpha = 0.44$ . The extinction time scales as  $t_E \sim (W_B)^{\alpha} R^{2-5\alpha}/(n_e n_I)^{\alpha}$ , where  $W_B$  = initial energy,  $R$  = separatrix radius. Nearly linear current decay and insensitivity to  $W_B$ ,  $n_e$ , and  $n_I$  are thus explained. Burnout of oxygen occurs if  $n_e n_I < 2.6 \times 10^{22} (B(0)/R)^2$ ; typically less than

1% oxygen is needed. Similar results hold for carbon impurities.

Also examined is transport for a high-beta case, an axisymmetric FRC with no toroidal field. In agreement with earlier theory[22], radial simulations of a neutral-beam driven system, using a particle description for the ions and fluid equations for the electrons, demonstrate the necessity of an Ohkawa current in order to achieve field reversal. The simulations extend previous work by including a self-consistent radial electric field which drives significant azimuthal back-currents in the electron fluid.

The reasonable agreement between the Taylor Relaxation theory[23] and the experimental data[24] on CT formation by magnetized coaxial plasma guns raises the possibility that the relaxation mechanism can be used to drive the plasma in a steady state. Supposing that the plasma inside the composite boundary of the gun electrodes plus conducting wall used to contain the CT relaxes to a minimum energy state that conserves helicity, then the total plasma magnetic energy ( $W_B$ ) and helicity ( $K$ ) are related by  $W_B = .5kK/\mu_0$  where  $k$  is a global constant determined by solving the eigenvalue equation  $\nabla \times \mathbf{E} = k\mathbf{E}$ . If a time  $t$  is greater than the initial formation and relaxation phase, and a finite voltage  $V(t)$  is maintained across the gun terminals, then the helicity input to the plasma is

$$K = 2\psi_0 \int_0^t V(t') dt'$$

while  $\dot{W}_B = k\psi_0 V/\mu_0 - P_\eta$ , where  $\psi_0$  is the magnetic flux inside the inner electrode of the plasma gun and  $P_\eta$  is the ohmic loss of magnetic field energy. If a constant voltage  $V = \mu_0 P_\eta / (k\psi_0)$  is maintained across the gun electrodes, then an average current  $I = k\psi_0/\mu_0$  would be drawn from the power supply and  $\dot{W}_B = 0$ . If  $V > \mu_0 P_\eta / (k\psi_0)$ , the plasma magnetic fields could build up on a quasistatic time scale that is slower than Alfvén transit times but faster than ohmic decay times. In practice one expects that a constant voltage applied across the gun terminals would drive the plasma near the gun away from the Taylor minimum energy state. Relaxation would induce a negative voltage spike across the electrodes, bring the composite plasma back to the minimum energy state, and distribute the helicity globally. If the constant voltage electrodes are arranged to draw current down the axis of the experiment, then this scheme is a one bump version of the steady state "Bumpy z-pinch" described by Jensen and Chu[25].

A CT can form the basis of a magnetically driven, collective accelerator. Viewed as a magnetized micropellet, CTs may have  $\sim 10^8$  times the magnetic moment of a magnetized solid pellet while, from the point of view of a collective

accelerator, the CT may contain some  $10^8$  times the ions possible with electrostatic forces. Several accelerator configurations are considered within constraints of maintaining macroscopic stability against the accelerating field slipping by, and against acceleration-driven interchange modes. One configuration accelerates the CT between coaxial electrodes by a  $B_0$  field. If the accelerating force on the CT is normalized to the ring force on the electrodes,  $F_{acc} = \kappa U_{mag}/a$ ,  $a =$  CT minor radius. We find  $\kappa < 1$  for stability against  $B_0$  "slip by" and  $\kappa < \beta_{max}$  for stability against interchange. Typical gun-produced CTs with low mass ions can be accelerated to 10MJ kinetic energy in 100m, limited by the power which can be delivered to the ring ( $10^{12}W$ ). For CTs with high ion mass, accelerator lengths are reduced to 10m. If conical electrodes are used, simultaneous focusing and acceleration can take place.

As applications, rings of low kinetic energy can be accelerated across the confining magnetic field of a fusion reactor to provide fuel, energy or a steady state current-drive. Growth of the tilting instability, however, should lead to eventual reconnection of the ring and reactor fields. This causes deposition of the "cargo" of fuel, the energetic particles, or the magnetic helicity. Global conservation of the helicity leads to an increase in the circulating current following ring injection and hence to the possibility of a current drive. Estimates of the efficiency of this process suggest that a thermonuclear  $Q$  of  $\sim 100$  is possible. At high kinetic energies ( $\sim 10MJ$ ) and with focusing, it appears possible to concentrate very high power densities, short pulses of ion bombardment for purposes of driving an inertial fusion pellet. At high kinetic energies and low mass, rings containing a small fraction of massive nuclei could attain from 1-10MeV/nucleon, useful for the synthesis of transuranic elements.

#### REFERENCES

- [1] HEWETT, D.W., SPENCER, R.L., submitted to Phys.Fluids(1982).
- [2] SCHWARZMEIER, J.L., et.al., to be submitted to Phys.Fluids.
- [3] SHESTAKOV, A.I., et. al., J.Comp.Phys.46(1982)69.
- [4] BARNES, D.C., et al., in Proc. 3rd Symp. on Compact Toroids, in MFE, Los Alamos Report LA-8700-C,134(1980).
- [5] NEWCOMB, W.A., Phys. Fluids23(1980)2296.
- [6] ANDERSON, D.V., BARNES, D.C., J.Comp.Phys.42(1981)288.
- [7] TANG, W.M., CATTO, P.J., Phys.Fluids24(1981)1314.
- [8] HEWETT, D.W., SEYLER, C.E., Phys.Rev.Letters46(1981)1519.
- [9] HARNED, D.S., to appear in J.Comp.Phys.(1982).

- [10] HARNED, D.S., submitted to Phys.Fluids.
- [11] HEWETT, D.W., J.Comp.Phys. 38(1980)378.
- [12] ES'KOV, A.G., et al., in Seventh European Conference on Controlled Nuclear Fusion Research (IAEA, Vienna, 1978) III187.
- [13] HEWETT, D.W., NIELSON, C.W., J.Comp.Phys. 211(1978)219.
- [14] FINN, J., REIMAN, A., Phys.Fluids 25(1982)116.
- [15] BERNARD, L.C., et al., Computer Physics Comm. 24(1981)377.
- [16] KIERAS, C.E., TATARONIS, J.A., to appear in Phys.Fluids.
- [17] KIERAS, C.E., TATARONIS, J.A., submitted to Phys.Fluids.
- [18] SGRO, A.G., SPENCER, R.L., Bull.Am.Phys.Soc. 26(1981)1038.
- [19] SHUMACHER, D.E., et al., J.Comp.Phys. 45 2(1982)266.
- [20] AUERBACH, S.P., to appear in Phys.Fluids.
- [21] POST, D.E., et al., Princeton Plasma Physics Laboratory Rep. PPPL-1352(1977).
- [22] BALDWIN, D.E., RENSINK, M.E., Comments Plasma Phys. Cont. Fusion 4 (1978)55.
- [23] TAYLOR, J.B., Phys.Rev.Lett. 33(1974)1139.
- [24] TURNER, W.C., et al., Lawrence Livermore National Laboratory Rep. UCRL-87004(1982).
- [25] JENSEN, T.H., CHU, M.S., J.PlasmaPhys. 25 3(1981)459.

## DISCUSSION

ON PAPERS IAEA-CN-41/M-2-1 AND M-2-2

H.A.B. BODIN: Have you any evidence whether the plasma is rotating before you see rotating flutes? Suppose it is rotating much earlier, is this likely to affect the various calculations of stability and transport you reported?

R.E. SIEMON: We have not measured the rotation in FRX-C. In other, similar experiments there is evidence for rotation before onset of the  $n = 2$  mode obtained by Doppler shift measurements on impurity atoms. In general, the calculations of stability and transport do not include rotation effects, but you may be correct in suggesting that centrifugal force terms are important, because the rotational velocity is of the same order of magnitude as the growth rate predicted by MHD analysis.

H.L. BERK: Is it clear that the plasma is not rotating at the onset of formation of an FRC?

R.E. SIEMON: Measurements have not been carried out on FRX-C to determine the rotational speed of the plasma, so it is not clear that the FRC is not rotating. In the case of a conventional theta pinch without bias field, experiments have shown that the implosion phase does not impart much angular momentum to the plasma (see Phys. Fluids 23 (1980) 1832).

H.L. BERK: What is the pressure-scale length near the separatrix compared with the ion Larmor radius in both theory and experiment?

R.E. SIEMON: In both theory and experiment the density-scale length near the separatrix is a few ion Larmor radii.

H.H. FLEISCHMANN: I have a comment regarding the tilt stabilization of Spheromak-CT rings. So far, only rather closely fitting shells or feedback coils have been mentioned, which are likely to limit the respective reactor designs. Stabilization by large-orbit high-energy particles has been proposed, and first results of experiments (by my group at Cornell) as well as of theoretical work (by Professor Sudan's group) indicate good prospects in this direction. What do you think about this possible stabilization method?

R.E. SIEMON: I agree that energetic particle beams offer interesting possibilities for stabilizing the tilt mode in a spheromak or for providing other beneficial effects in either the spheromak or the FRC configuration.

T.S. GREEN: In early experiments on reversed field configurations we observed axially propagating area waves following the formation of the configuration. Do you observe these, and is it possible to use the measurement of the wave characteristics as a diagnostic to study plasma rotation?

R.E. SIEMON: The area wave in current experiments is less pronounced than in earlier work, perhaps because the ratio of final field to initial bias is typically much smaller. The idea of using the wave as a diagnostic for rotation is new to me and I thank you for the suggestion.



## EXPERIMENTAL STUDIES ON CONFINEMENT OF FIELD-REVERSED-CONFIGURATION PLASMA

T. MINATO, M. TANJYO, S. OKADA, Y. ITO, M. KAKO,  
S. OHI, S. GOTÔ, T. ISHIMURA, H. ITÔ  
Plasma Physics Laboratory,  
Osaka University, Osaka

Y. NOGI, S. SHIMAMURA, Y. OSANAI, K. SAITO,  
K. YOKOYAMA, S. SHIINA, S. HAMADA, H. YOSHIMURA  
College of Science and Technology,  
Nihon University, Tokyo

Y. ASO, C.H. WU\*, S. HIMENO\*\*, M. OKAMOTO, K. HIRANO  
Institute of Plasma Physics,  
Nagoya University, Nagoya

Japan

### Abstract

#### EXPERIMENTAL STUDIES ON CONFINEMENT OF FIELD-REVERSED- CONFIGURATION PLASMA.

Compact toroids with field-reversed configuration (FRC) generated by theta pinch have been studied in three laboratories in Japan. Parameters of FRC plasmas produced in these laboratories are  $T_i = 0.1$  to  $1$  keV;  $T_e = 0.1$  to  $0.25$  keV;  $n_e = (2 - 6) \times 10^{15} \text{ cm}^{-3}$ ; and  $\tau_Q$  (lifetime) =  $15$  to  $70 \mu\text{s}$ . The stable period  $\tau_s$  of the FRC plasma is always limited by the  $n = 2$  rotational instability. Using the experimental data obtained so far, an empirical scaling of  $\tau_s \propto \bar{n}_e r_s \ell_p L_c$  was found. Here  $\bar{n}_e$ ,  $r_s$ ,  $\ell_p$  and  $L_c$  are mean electron density, plasma radius, plasma length and coil length, respectively. By delaying the time when escaping plasma reaches the vacuum tube wall by auxiliary guide fields extending away from the confinement region,  $\tau_s$  is improved from  $20 \mu\text{s}$  to  $30 \mu\text{s}$ . The results partly support the theoretical view that the end-shortening effect causes plasma rotation and, consequently,  $n = 2$  rotational instability. The instability is suppressed by applying a quadrupole field of about  $0.1$  T field strength at  $r = r_s$ , which is much smaller than the confinement field. From the stability analysis with the condition of pressure balance on the surface of the deformed plasma column, the field strength necessary to suppress the instability is obtained, which agrees fairly well with the experiments.

\* On leave from Institute of Physics, Academia Sinica, Beijing, Peoples' Republic of China.

\*\* On leave from Energy Conversion Research Institute, Hokkaido University, Sapporo, Japan.

## 1. INTRODUCTION

High-temperature plasmas produced by theta pinch in the negative bias field mode are confined for several tens of  $\mu\text{s}$  in the field-reversed configuration (FRC) in which no toroidal field is contained [1, 2]. In the latter half of the confinement period, injurious  $n = 2$  rotational instability occurs and grows so that the plasma column is heavily distorted. One of the most important problems in the FRC plasma research is extension of the stable period by delaying the onset time of the instability or by suppressing its occurrence. This paper presents experimental results on confinement of FRC plasma obtained in three laboratories in Japan: Osaka University (PIACE-I and II), Nihon University (NUCTE-I and II) and Nagoya University (STP-L).

## 2. SCALING LAW OF THE STABLE PERIOD

The stable period  $\tau_s$  of FRC plasma, which is defined as the period between the formation of FRC plasma and the onset time of the  $n = 2$  rotational instability, is considered one of the most important parameters in FRC plasma confinement. We have tried to find an empirical scaling of  $\tau_s$  by examining the experimental data obtained in the machines at the three laboratories mentioned above, and propose the following scaling:

$$\tau_s = c n_e r_s l_p L_c \quad (c = \text{const.}) \quad (1)$$

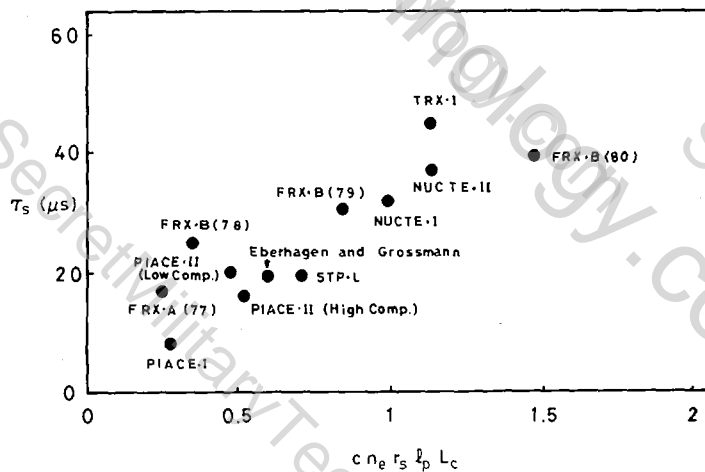


FIG.1. Empirical scaling of stable period.

where  $n_e$ ,  $r_s$ ,  $\ell_p$  and  $L_c$  are electron density, separatrix radius, plasma length, and coil length, respectively [3]. We also referred to the experimental data reported so far and confirmed that the scaling was plausible. Figure 1 shows  $\tau_s$  plotted as a function of  $n_e r_s \ell_p L_c$  from all data available at present. The constant  $c$  is  $9 \times 10^{-21} \cdot s^{-1}$  in this figure.

The scaling is explained here on the assumption that the plasma rotation and the resulting instability are induced by the particle loss with the preferential angular momentum [4]. The particle loss is estimated not from the particle flow across the separatrix but from that in the open field region. Conservation of the diffusing particles gives the relation:

$$2\pi r_s \ell_p \Gamma_r = 4\pi r_s \Delta \Gamma_z \quad (2)$$

where  $\Gamma_r$  and  $\Gamma_z$  are the radial and axial particle flux, respectively, and  $\Delta$  is the sheath width over which the plasma extends outside the separatrix. The particle confinement time  $\tau$  can be expressed by

$$\tau = N/4\pi r_s \Delta \Gamma_z \quad (3)$$

where  $N$  is the total particle number ( $\pi r_s^2 \ell_p n_e$ ). The axial particle flux is  $\Gamma_z = D_{||} dn/dz \sim D_{||} 2n/L$ , where  $L$  is the length of the open field line along which the particles flow. Assuming the diffusion coefficient  $D_{||}$  is the ambipolar one with classical collision frequency, Eq.(3) becomes

$$\tau = 1.7 \times 10^{-22} Z_{\text{eff}}^2 n_e r_s \ell_p L / \Delta (T_i) (T_e)^{3/2} \quad (4)$$

where  $T_e$  and  $T_i$  are expressed in eV and others in m.k.s. units. Thus we obtained an expression similar to Eq.(1) except for factors such as  $\Delta$ ,  $T_i$  and  $T_e$ . On NUCTE-I,  $\tau$  becomes  $49 \mu s$ , which is comparable to  $\tau_s$  of  $30-35 \mu s$  [5] on the assumptions that  $\Delta$  is equal to the ion Larmor radius, that  $Z_{\text{eff}} = 2$  and  $L = 1.2 L_c$ . The empirical scaling and its physical explanation suggest that the plasma particle loss makes some contribution to the onset of the instability.

### 3. EXPERIMENTAL EVIDENCE OF END-SHORTING EFFECT

The experiment in STP-L has been focused on the study of the  $n = 2$  rotational mode through the control of end-shortening conditions by the plasma guiding field (GF) [6]. The main discharge is fired when the expanding fronts of  $D_2$  gas injected by the puffs at the centre of the pinch coil reach the coil ends. It may therefore be expected that the hot plasma escaping from the confinement region expands into the vacuum along the GF up to the ends of

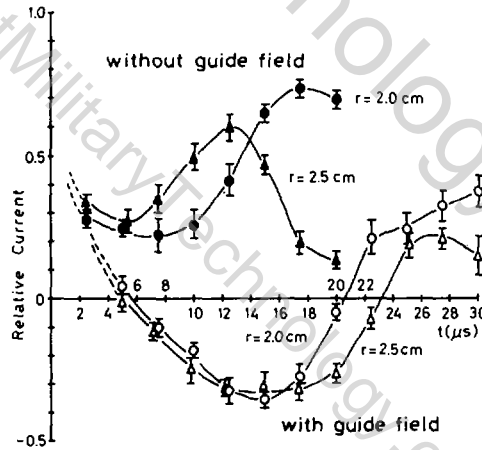


FIG. 2. Ion currents measured by directional probe. The relative current is proportional to the rotation velocity. The positive direction denotes that of the ion diamagnetic current.

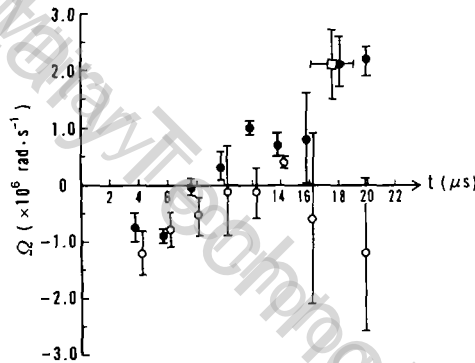


FIG. 3. Angular velocity of the FRC obtained by Doppler shift of the  $C V$  line aiming at the neutral point from side-on positions. ●: operation without GF; ○: operation with GF; □: rotation frequency of the  $n = 2$  deformation.

the apparatus and that end-shortening effects are eliminated before the plasma tips hit the end wall. Typical operating parameters in the present study are as follows:  $B_{\max} = 1$  T;  $r_s \cong 1.8$  cm;  $T_i \cong 300$  eV;  $T_e \cong 120$  eV; electron density  $\bar{n}_e \cong 5 \times 10^{15}$  cm $^{-3}$ ; and the averaged beta  $\langle \beta \rangle \cong 1$ . We measured the rotation of the external plasma by a directional probe and that of the FRC plasma by Doppler shift of the  $C V$  line using a 1 metre J-Y spectrometer focused on the neutral point. The results are given in Figs 2 and 3, where the positive direction denotes that of the ion diamagnetic current. We consider

that the C V measurement precisely reflects the rotational angular velocity  $\Omega$  of the FRC plasma after  $12 \mu\text{s}$ . This is based on the observation that the inward flow of C V ions turns into outward flow at  $12 \mu\text{s}$ . In the earlier phase, flow analysis shows that  $\Omega$  should be much more negative than for the C V ions.

We can see in Figs 2 and 3 that at the early phase the external plasma is rotating positively and the FRC negatively. These results are consistent with our hybrid code simulation, in which the initial randomly distributed rotation is ordered so that the average canonical angular momentum ( $mrv_{\theta} + reA_{\theta}$ ) tends to be zero after about 600 ns from the start of the discharge. Streak photographs clearly show that the onset time of the  $n = 2$  mode is delayed about  $10 \mu\text{s}$  when the GF is applied [6]. Figure 2 may suggest the importance of the end-shorting effect in the delay, because the time derivative of the rotation is seen to become positive shortly after the expanding plasmas hit the wall. The  $\Omega$  of the FRC, on the other hand, is monotonic, as shown in Fig.3. In the case without GF, the maximum  $\Omega$  is limited by the appearance of the  $n = 2$  mode. The maximum  $\Omega$  agrees fairly well with the angular velocity  $\omega$  of the  $n = 3$  deformation. If we estimate the diamagnetic drift frequency  $\Omega^*$  by  $\langle j_0 \rangle T_i / en_e r_s (T_i + T_e)$ , we have  $\Omega^* \cong 2.3 \times 10^6 \text{ rad} \cdot \text{s}^{-1}$ . Consequently, the critical ratio  $\alpha (= \Omega / \Omega^*)$  for the  $n = 2$  mode takes the value of about 1 and the  $\omega$  becomes equal to  $\Omega^*$ .

#### 4. SUPPRESSION OF $\bar{n} = 2$ INSTABILITY BY QUADRUPOLE FIELD

The effect of the quadrupole field on the  $n = 2$  rotational instability has been studied on the PIACE-II machine [7]. Under typical operating conditions of the machine in this study, a deuterium plasma with a reversed bias magnetic field of 0.2 T is compressed by the fast-rising magnetic field of 0.8 T at its maximum with risetime  $1.4 \mu\text{s}$  and decay time  $70 \mu\text{s}$ . During the early period of confinement,  $\bar{n}_e$ ,  $T_e$ ,  $T_i$ ,  $r_s$  and  $\ell_p$  are  $2.8 \times 10^{15} \text{ cm}^{-3}$ , 100 eV, 300 eV, 3.5 cm and 60 cm, respectively. The compression coil is 100 cm long and has 14.8 cm inner diameter; the discharge tube, made of quartz, has 12.3 cm inner diameter.

The quadrupole field has  $6 \mu\text{s}$  risetime and  $100 \mu\text{s}$  decay time. The quadrupole field is applied  $5 \mu\text{s}$  after switching on the compression field, when the FRC plasma is already formed, in order to generate FRC plasmas with the same parameters with and without the quadrupole field. The effect of the quadrupole field was studied by measuring the time history of  $n_e \ell$  (line integral of electron density) along the central chord of the plasma cross-section at the axial midplane. After the onset of the instability, the plasma column suffers rotational elliptic deformation.

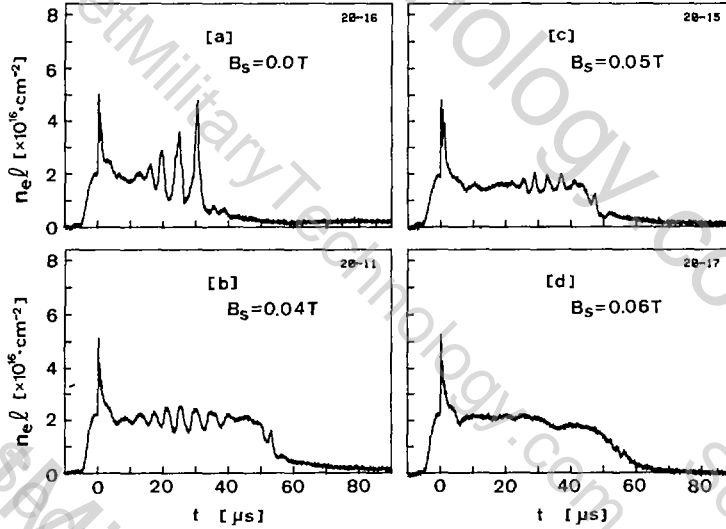


FIG. 4. Time histories of  $n_e l$  measured along the central chord of the plasma cross-section at the midplane. Plasma compression starts at time  $t = 0$ .  $B_s$  is the strength of the quadrupole field at  $r = r_s$  ( $= 3.5$  cm) without plasma column.

A time history of  $n_e l$  without the quadrupole field shown in Fig.4(a) shows the evidence of the occurrence and growth of the instability. Figures 3(b), (c) and (d) show the time histories of  $n_e l$  for field strengths  $B_s$  of 0.04, 0.05 and 0.06 T, respectively.  $B_s$  denotes the strength of the quadrupole field at  $r = r_s$  ( $= 3.5$  cm) without the plasma column. With the increase of the field strength, growth of the instability is at first suppressed (Fig.4(b)); the time of its occurrence is delayed Fig.4(c); and, finally, it is completely suppressed (Fig.4(d)). It was also observed from streak photographs that the quadrupole field effectively suppresses the instability.

A stability analysis based on MHD approximation was made on the effect of the quadrupole field in suppressing the instability. The magnetic pressure of the quadrupole field at each point on the elliptically deformed plasma surface was calculated on the assumption that the plasma was a perfect conductor. Since the magnetic pressure at each point changed in time owing to the plasma rotation, we used time-averaged magnetic pressure as the effective means to suppress the instability. From the pressure balance condition on the plasma surface and the equation of motion for the plasma fluid, we obtained a dispersion relation and the following stability condition:

$$B_s > \frac{|\Omega| r_s}{2} \sqrt{\mu_0 \rho} \quad (5)$$

where  $\rho$  is the plasma mass density. Using the experimental data and assuming that  $\Omega$  was equal to the modal frequency of the  $n = 2$  perturbation ( $|\Omega| = 1.7 \times 10^6 \text{ rad} \cdot \text{s}^{-1}$ ), we obtained  $B_s \approx 0.1 \text{ T}$  as the theoretical threshold value. This value agrees fairly well with the experimental field strength of  $0.06 \text{ T}$  in the case shown in Fig.4(d), where the instability is eliminated.

## 5. CONCLUSIONS

Efforts have been made to establish methods to control the  $n = 2$  rotational instability and to obtain FRC plasma with a long stable period. The empirical scaling suggests that a great plasma length is associated with a long stable period. The guide field is effective in delaying the occurrence of end-shortings and, as a result, in extending the stable period. The  $n = 2$  rotational instability is completely suppressed by applying the quadrupole field, the strength of which agrees fairly well with that predicted by the theoretical stability condition.

Thus, no serious difficulty remains in the control of  $n = 2$  rotational instability. Further efforts should be directed to the reduction of particle and energy losses of FRC plasma in order to attain long-lasting plasma confinement in the FRC.

## REFERENCES

- [1] ARMSTRONG, W.T., et al., Phys. Fluids 24 (1981) 2068.
- [2] ES'KOV, A.G., et al., in Plasma Physics and Controlled Nuclear Fusion Research 1978 (Proc. 7th Int. Conf. Innsbruck, 1978) Vol.2, IAEA, Vienna (1979) 187.
- [3] NOGI, Y., et al., in Proc. 4th Symp. Physics and Technology of Compact Toroids, Lawrence Livermore National Lab., 1981, paper A3.
- [4] TUSZEWSKI, T., LINFORD, R.K., Phys. Fluids 25 (1982) 765.
- [5] NOGI, Y., et al., in Proc. US-Japan Workshop on Compact Toroids, Osaka, 1981, p.29.
- [6] ASO, Y., et al., Nucl. Fusion 22 (1982) 843.
- [7] OHI, S., et al., Proc. US-Japan Workshop on Compact Toroids, Osaka, 1981, p.11.

## DISCUSSION

H.A.B. BODIN: You report results on the use of a quadrupole field to control instabilities of an already rotating plasma. Many years ago, one of the favoured mechanisms for inducing rotation was a transverse field, e.g. of the quadrupole type. The application of a quadrupole induced rotation and generally made the plasma rotationally unstable. What is different in your case, where the quadrupole fields evidently help?

T. ISHIMURA: In our experiment, the quadrupole field was applied after the formation of the FRC plasma, the electron temperature of which was about 100 eV. Therefore the field did not penetrate into the plasma column, because of its thin skin depth, and the Hall current inducing plasma rotation could not flow in the plasma. The quadrupole field exerts higher magnetic pressure on the extended part of the distorted plasma column and thus helps to restore the plasma column to its normal state.

H.A.B. BODIN: Did you check this by putting on the quadrupole field earlier?

T. ISHIMURA: We tried firing the quadrupole field and the main compression field simultaneously; in this case, the plasma decayed soon after its formation, so we did not obtain any valuable information from this trial.

R. GOLDSTON: It is commonly found in tokamak work that a non-axisymmetric magnetic perturbation can prevent an  $m = 2$  tearing mode from rotating without preventing it from growing and eventually causing a major disruption. What evidence do you have that your  $m = 2$  distortion has stopped growing as well as rotating when you apply the quadrupole field?

T. ISHIMURA: We took stereoscopic streak photographs of the plasma column and confirmed that the distortion of the plasma column did not occur in the case with the 0.06 T quadrupole field. The rotational velocity of the plasma column was not measured. However, the period of the visual oscillation of the plasma column did not change with the strength of the quadrupole field. It is therefore probable that the rotational velocity of the plasma column did not change either.

## MERGING EXPERIMENT AND SIMULATION OF COMPACT TOROIDS

K. WATANABE, K. IKEGAMI, M. NAGATA,  
M. NISHIKAWA, A. OZAKI, N. SATOMI, T. UYAMA  
Faculty of Engineering, Osaka University, Suita,  
Osaka

T. SATO, S. OTSUKA, T. HAYASHI, K. NISHIKAWA,  
Institute for Fusion Theory, Hiroshima University,  
Hiroshima  
Japan

### Abstract

#### MERGING EXPERIMENT AND SIMULATION OF COMPACT TOROIDS.

Experimental and numerical spheromak studies are reported.—Part I presents the confinement and merging of spheromaks by co-axial-gun experiments. Titanium gettering on the electrodes and inner walls is found to significantly increase the life-time, say, from 400 to 800  $\mu$ s. Experiments on successive injection of two spheromaks into a flux conserver have demonstrated stable merging; the merged toroidal flux is almost doubled while the poloidal one remains nearly the same, which is in good agreement with the simulation.—Part II presents numerical simulation results of spheromak merging in two dimensions and tilting disruption in three dimensions for a slow-induction method. Merging simulations have shown that during the merging process the total magnetic helicity is conserved while the magnetic energy decreases to a relatively large extent. Three-dimensional simulations have demonstrated that the created spheromak disrupts as a result of tilting instability. The disruption mechanism is found to be due to three-dimensional reconnection.

#### GENERAL INTRODUCTION

We present the first experimental and numerical demonstrations of merging and some other important processes occurring in spheromaks. The possibility of merging can provide us with a certain amount of flexibility in designing a compact toroid reactor as far as fuel and current supplies are concerned. It is, therefore, a timely and important task to study the merging process of spheromaks.

Experiments were carried out by the CTCC-1 facility of Osaka University. Two spheromaks were successively injected into a flux conserver by a single co-axial gun. The merging process was observed by measuring the temporal evolution of the toroidal and poloidal fluxes, the magnetic field and the plasma density.

Separately, numerical simulations of spheromak merging were done by using a 2-D MHD simulation code, adopting the Princeton slow-induction method. Three-dimensional spheromak creation and tilting disruption were also studied in detail by a 3-D MHD simulation code (MAGIC3C).

## PART I: OSAKA COMPACT TOROID EXPERIMENT

(K. Watanabe, K. Ikegami, M. Nagata, M. Nishikawa, A. Ozaki, N. Satomi, T. Uyama)

### 1.1. Experimental development

The Osaka Compact Toroid (CT) experiment using a magnetized co-axial gun started with the CTCC-1 machine in autumn 1980 as the first experiment of a Compact-Toroid-Collision-and-Compression project. Figure 1a shows a schematic view of the CTCC-1 machine. Plasma ejected from the gun stretches out the radial field lines generated by a poloidal coil. These elongated field lines reconnect themselves and form a closed poloidal field. Consequently, a CT is formed in

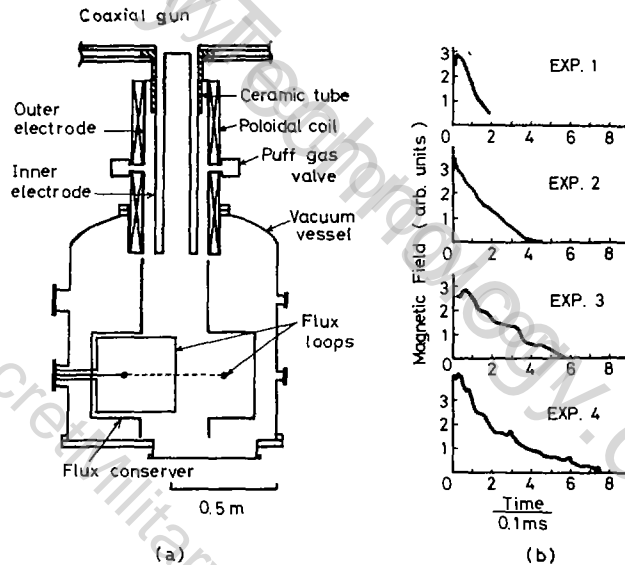


FIG.1. (a) Schematic diagram of CTCC-1; (b) time evolution of CT magnetic field in four kinds of experiments; exp.1: initial experiment; exp.2: application of improved electrode; exp.3: use of titanium gettering on co-axial electrode surfaces; exp.4: use of titanium gettering on inner wall of flux conserver.

which the poloidal field is confined together with the toroidal field generated by the gun current [1]. Details of the facility are described elsewhere [2]. Earlier, we succeeded in creating an oblate CT in a copper flux conserver (FC) which has a plasma life-time ( $\tau_{\text{life}}$ ) of about 250  $\mu\text{s}$  ( $\tau_{\text{e-folding}} = 110 \mu\text{s}$ ) [3, 4]. The electron temperature was, however, observed to be below 10 eV.

For the purpose of further heating and current sustainment, a CT plasma merging experiment was conducted by using CTCC-1. Simultaneously, we tried to lower the impurity content in the CT by titanium coating.

Recently, we carried out more than five trial experiments on the improvement of CT production in order to achieve long confinement. Figure 1b shows four typical examples of time evolution of the magnetic field in the CT, obtained in four different trial experiments. The top diagram shows the evolution in an early experiment. The second diagram corresponds to the case where an improved inner electrode with protruding circular edges at intervals of 1 cm on the inner electrode surface was used. Note that the life-time was increased up to 400  $\mu\text{s}$ . In experiment 3, titanium gettering on some fraction of both inner and outer electrode surfaces was introduced. In addition, successive double gun firing with 2 – 5  $\mu\text{s}$  delay time was used which led to a further increase in life-time. The attained life-time was 600  $\mu\text{s}$ . On the basis of this success, we applied titanium gettering on the inner wall of the flux conserver, but not on the electrodes. The background pressure was lower than  $4 \times 10^{-8}$  torr. This experiment showed remarkable improvement in confinement. The life-time was longer than 0.8 ms. The e-folding time of the magnetic-field decay turned out to be more than 400  $\mu\text{s}$ , specifically, 413  $\mu\text{s}$  (see bottom diagram of Fig.1b). Moreover, a substantial rise in the plasma temperature was found. Unfortunately, however, disruption of the plasma was observed frequently; it appeared to be associated with the magnetic-field fluctuations which might have been excited by the plasma injection processes.

## 1.2. CT merging experiment

An experiment using CTCC-1 was performed to study the possibility of CT merging and further heating. The CT merging was performed by shooting two plasmas into the flux conserver successively, with 80  $\mu\text{s}$  time delay, by using the same plasma gun. The gun was driven by two capacitor banks, which were constructed by dividing a 68  $\mu\text{F}$  capacitor bank.

In the normal-operation experiment, we have found that the CT plasma in the flux conserver is trapped in the force-free magnetic-field configuration, a fact which is consistent with the analytic solution [2, 3]. To study the global behaviour of the CT during the merging process, we measured both the poloidal and toroidal fluxes,  $\Psi_p$  and  $\Psi_t$ , using two kinds of one-turn loop, i.e. a circular loop with a radius of 25 cm which nearly coincides with the magnetic axis and a rectangular loop as is shown in Fig.1a. Oscillograms of both  $\Psi_p$  and  $\Psi_t$  are shown in Fig.2a.

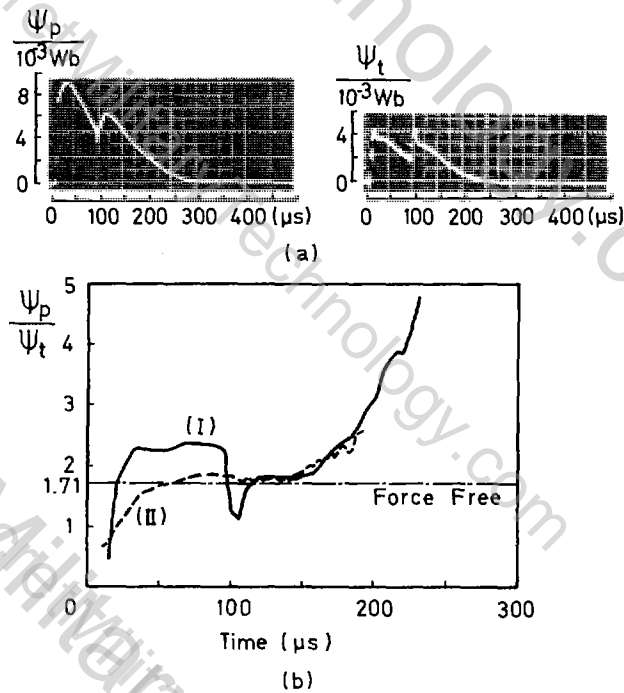


FIG.2. (a) Oscillograms of poloidal ( $\Psi_p$ ) and toroidal ( $\Psi_t$ ) flux; (b) time evolution of flux ratio ( $\Psi_p/\Psi_t$ ). (I) is obtained in merging and (II) in normal operation. Dot-dash line indicates the value for the fundamental force-free field configuration.

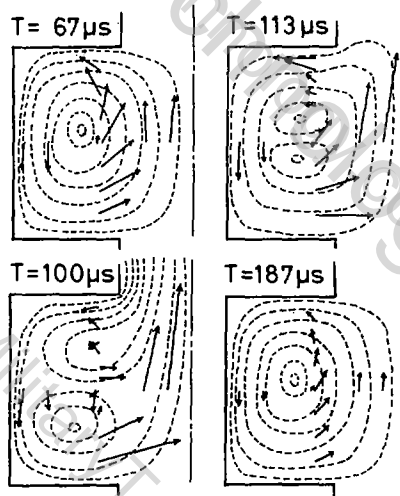


FIG.3. Patterns of poloidal magnetic field lines drawn from data of magnetic-field measurement in R-Z plane. Second plasma is injected at  $T = 80 \mu\text{s}$ .

When the plasma which is injected as the second one enters the flux conserver at  $80 \mu\text{s}$ ,  $\Psi_t$  increases rapidly and nearly reaches the additive value of the toroidal fluxes contained in the two plasmas. On the other hand,  $\Psi_p$  first decreases rapidly and then increases because of the flux carried by the plasma injected as the second one. Hence, there is a definite tendency for  $\Psi_p$  to increase and for  $\Psi_t$  to decrease faster than in the normal-operation case with the  $68/2 \mu\text{F}$  bank. Figure 2b shows the temporal development of  $\Psi_p/\Psi_t$ ; here, the dot-dashed line gives the value for the fundamental mode of the force-free configuration. After the first CT is injected,  $\Psi_p/\Psi_t$  becomes approximately the force-free value (the dot-dashed line). When the second plasma is injected into the flux conserver where the first target CT is situated,  $\Psi_p/\Psi_t$  decreases rapidly, first below the force-free value, and then is restored up to the force-free value; then it is constant for a while. After such a plateau period,  $\Psi_p/\Psi_t$  increases rather rapidly. The increase of  $\Psi_p/\Psi_t$  in the latter phase was found in the normal-operation case, as well (see broken line in this figure). Thus, the increase in  $\Psi_p/\Psi_t$  is considered to be due to the shift of the configuration arising from the change of the  $\beta$  value.

To study the merging process in detail, we have measured the magnetic fields at twenty positions on the symmetric axis (Z-axis), the midplane and a Z-line at radius of 19.5 cm by shot-to-shot scanning of a magnetic probe. From these data, we can graphically represent the poloidal-field configuration at different times. Typical patterns are presented in Fig.3. As is illustrated in this figure, the second plasma enters the flux conserver with a velocity of the order of  $10^7 \text{ cm}\cdot\text{s}^{-1}$  and starts to merge. At this time, the target CT is pushed toward the wall and a neutral x-point is formed at the position of the initial magnetic axis of the target CT. The peripheral field lines of the two plasmas reconnect within  $10 \mu\text{s}$ , while the complete reconnection of the core field lines takes about  $80 \mu\text{s}$ .

## PART II: NUMERICAL SIMULATIONS OF SPHEROMAK CREATION, MERGING AND TILTING

(T. Sato, S. Otsuka, T. Hayashi, K. Nishikawa)

The emergence of the concept of 'compact toroids' has stimulated us to develop dynamic simulation codes since many of the advantages of the compact toroid lie in its dynamic behaviour. The idea of developing simulation codes is to guide choice and design of future experiments. Our goal is, therefore, to work out a reliable MHD dynamic simulation code whereby many important features inherent to compact toroids can be studied adequately before the experiments are actually carried out. In this simulation, we have paid particular attention to the Princeton S-1 spheromak [5]. First, we present a simulation of spheromak merging performed by the 2-D MHD simulation code which was

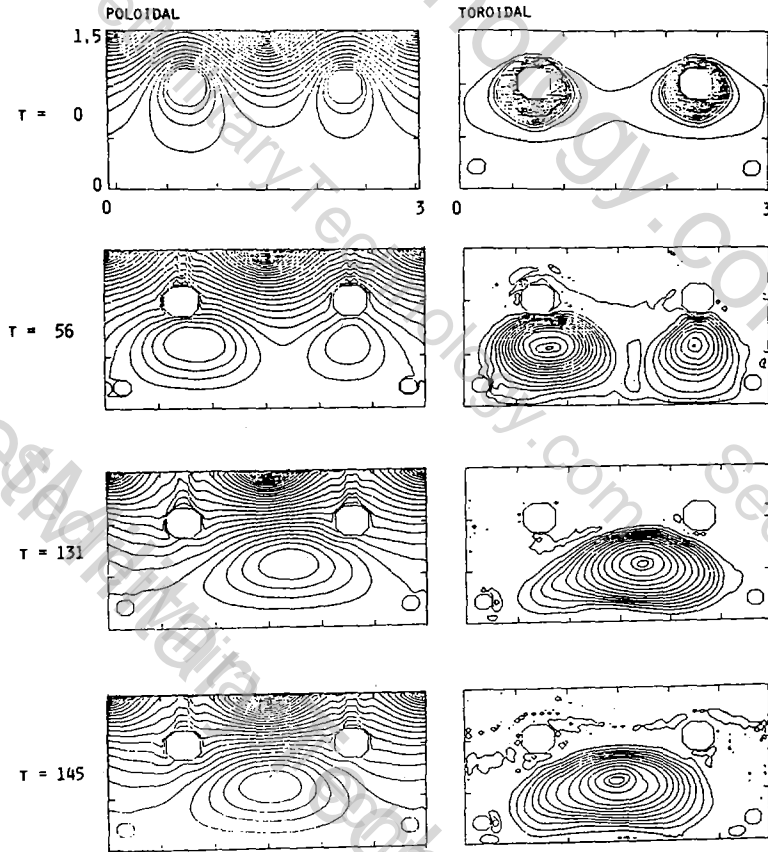


FIG.4. Example of merging simulation of two spheromaks with different sizes. Left-hand column represents poloidal-flux contours and right-hand one toroidal-flux contours (octagons show flux cores).

used successfully for single-spheromak formation [6]. We then briefly describe our recent simulations of spheromak tilting performed by a 3-D MHD code (MAGIC3C).

### 2.1. Spheromak merging

To create a merging simulation of spheromaks, we adopt the Princeton formation scheme which has already been proven to be numerically tractable [6–8]. We set up a simulation model in such a way that, in a cylindrical vacuum vessel, two toroidal flux cores are placed, having a certain distance along the cylindrical

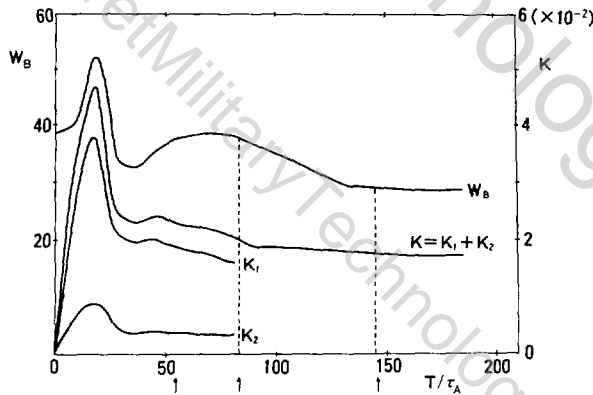


FIG.5. Time evolution of total magnetic field ( $W_B$ ) and helicities ( $K_1$ ,  $K_2$ ) of two merging spheromaks. Merging starts at left-hand dashed line and ends at right-hand line. Leftmost arrow indicates time when two spheromaks are created independently.

axis. Three toroidal coils which produce the vertical field are wound around just outside the vacuum vessel (two of them are placed just at the ends of the cylinder and one is at the middle). The middle external coil carries  $(-)$ 560 Ka and the other two carry  $(-)$ 400 Ka and  $(-)$ 380 Ka, respectively.

Since we are not only interested in demonstrating the possibility of merging, but also in deriving a quantitative relationship between the poloidal and toroidal fluxes before and after merging, we must set up a model that can separately create two spheromaks of arbitrary size. The model we have used for this purpose is the following: if initially different currents are supplied to the toroidal coils in the two flux cores (e.g. 500 and 400 Ka) and if they are crowbarred at a certain value (e.g. at  $(-)$ 100 Ka), two different spheromaks can be formed independently in front of each flux core.

Here, we present a case where two spheromaks with different fluxes are formed separately and approach each other so as to merge into one. Figure 4 shows the whole process of creation and merging of two different spheromaks in front of the flux cores (octagonal shape). The left-hand diagrams show the poloidal-flux contours and the right-hand ones those of the toroidal flux. Figure 5 shows the temporal changes in the total magnetic energy  $W_B$  of the two spheromaks and their helicities ( $K$ ). An interesting observation is that during the merging process (the period marked by two dashed lines) the total helicity is almost conserved while the magnetic energy decreases to a relatively large extent [9]. Incidentally, the poloidal fluxes of the two spheromaks before merging were 0.260 and 0.487 Wb, respectively, and the toroidal fluxes were 0.087 and 0.215 Wb, respectively, whereas the merged poloidal and toroidal fluxes were 0.488 and 0.301 Wb, thus

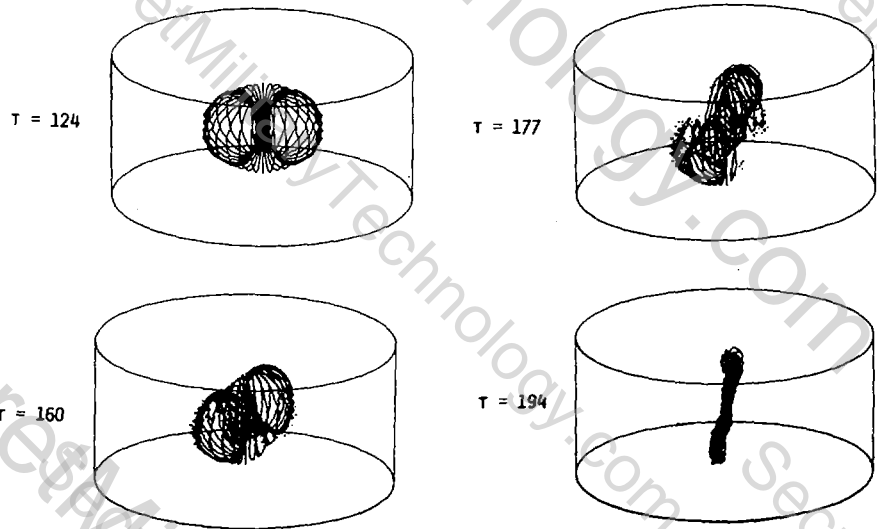


FIG. 6. 3-D display showing spheromak tilting and disruption.

indicating  $\Psi_T = \Psi_{T1} + \Psi_{T2}$  and  $\Psi_P = \max(\Psi_{P1}, \Psi_{P2})$ , which is in good agreement with the Osaka experiment. We note that the consistency of these flux relations with the conservation of helicity is due to the fact that the merged spheromak has spread along the cylindrical axis.

## 2.2. Spheromak tilting

A three-dimensional MHD simulation code (MAGIC3C) is developed and applied to the Princeton S-1 spheromak. The whole life of the spheromak, from its creation up to the tilting disruption, is successfully followed by the MAGIC3C code.

Figure 6 shows a 3-D display of how the three-dimensionally created spheromak undergoes a tilting instability and leads to disruption. The figure shows the assembly of contour lines of the azimuthal component ( $B_\theta$ ) of the spheromak magnetic field ( $B_\theta = 1$  kG). The growth rate of the tilting instability is found to be roughly  $20 \tau_A$ , which agrees surprisingly well with the Princeton experiment [10].

Another interesting finding is the disruption of the tilted spheromak. When the spheromak begins to tilt, its toroidal symmetry is broken because of the presence of the vertical field. More specifically, when the spheromak tilts, the toroidal field develops a component parallel to the vertical field on the one half

and an anti-parallel one on the other one. Thus, the spheromak field reconnects with the vertical field on the anti-parallel side whereby the tilted spheromak is one-sidedly eroded by the vertical field. This erosion leads to an abrupt disruption of the tilted spheromak.

#### REFERENCES

- [1] ALFVÉN, H., et al., J. Nucl. Energy, Part C: Plasma Physics **I** 116 (1960).
- [2] WATANABE, K., et al., in Compact Toroids (Proc. 2nd US-Japan Workshop, Osaka University) Osaka, Japan (Feb. 1981) 66.
- [3] WATANABE, K. et al., J. Phys. Soc. Japan **50** (1981) 1823.
- [4] WATANABE, K., et al., 4th Symp. Physics and Technology of Compact Toroids and 3rd US-Japan Workshop on Compact Toroids (Lawrence Livermore National Lab.) Livermore, California, USA (Oct. 1981).
- [5] YAMADA, M., et al., Phys. Rev. Lett. **46** (1981) 188.
- [6] SATO, T., et al., to be published.
- [7] LUI, H.C., et al., Phys. Fluids **24** (1981) 673.
- [8] JARDIN, S.C., PARK, W., Phys. Fluids **24** (1981) 679.
- [9] TAYLOR, J.B., Phys. Rev. Lett. **33** (1974) 1139.
- [10] YAMADA, M., et al., paper IAEA-CN-41/M-1, this volume.



## HIGH-BETA TOKAMAK PLASMA PHYSICS STUDIES\*

C.K. CHU, A.V. DENIZ, D.J. ELKIN, G. ERLEBACHER,  
R.A. GROSS, R. IZZO\*\*, S. JOHNSTON, C. KOSTEK,  
F. LEVINTON†, M. MACHIDA††, T.C. MARSHALL,  
R.L. MERLINO§, G.A. NAVRATIL, D. OEPTS§§  
Plasma Physics Laboratory,  
Columbia University,  
New York, N.Y.,  
United States of America

### Abstract

#### HIGH-BETA TOKAMAK PLASMA PHYSICS STUDIES.

Experimental and theoretical research at Columbia University on the physics of high-beta tokamaks is summarized. Data obtained from multipoint Thomson scattering and multichannel magnetic probes show  $\beta_0 \approx 42\%$ ,  $\langle \beta \rangle \approx 13\%$ ,  $n_e(0) \approx 2 \times 10^{21} \text{ m}^{-3}$ , and  $T_e \approx 80 \text{ eV}$ . A toroidal diamagnetic well is clearly observed as well as an outward shift in the peak of the pressure profile, amounting to 40% of the minor radius and indicating  $\epsilon\beta_p > 1$ . Growing density fluctuations characteristic of low-n MHD instability are observed on the outer (large major radius) edge of the pressure profile. Spectroscopic measurements of poloidal and toroidal flows indicate a velocity of about  $1.6 \times 10^6 \text{ cm-s}^{-1}$  in each direction. Simulation of the formation and equilibrium of Torus II are described, as well as a more general treatment of high-beta tokamak stability from bifurcation theory.

#### 1. TORUS II EXPERIMENT

The actual behavior of high-beta tokamak plasmas ( $\epsilon\beta_p > 1$ ) remains an outstanding plasma physics problem critical to the economic operation of a tokamak fusion reactor. The high-beta tokamak, Torus II, was designed to explore the equilibrium and stability properties of high-beta plasmas. It consists of a pyrex glass toroidal vacuum vessel of rectangular cross-section,  $b/a = 2$ ,  $R_0 = 0.225 \text{ m}$ ,  $2a = 0.13 \text{ m}$ , and operates with a  $Z = 2$ , helium plasma  $n_e \approx 2n_i \approx 2 \times 10^{21} \text{ m}^{-3}$ . The peak electron and ion temperatures are approximately 80 eV with a 3.5 kG toroidal

\* Research supported by US Department of Energy contract DE AC02 76 ET 53016.

\*\* Present address: Princeton Plasma Physics Laboratory.

† Partial support: Natl. Sci. and Engineering Research Council of Canada.

†† Partial support: CNPq of Brazil.

§ Present address: University of Iowa.

§§ FOM - Institute Plasma Fysica, Jutphaas, Netherlands.

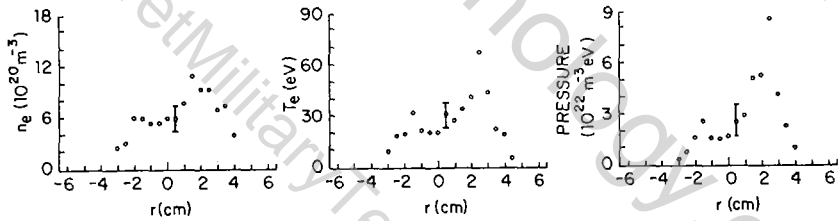


FIG.1. Radial profiles of electron density and electron temperature measured by multipoint Thomson scattering 9.5  $\mu$ s after the heating phase. The radial profile of the total pressure is calculated assuming  $T_e = T_i$ .

field, yielding a central beta,  $\beta_0 \sim 42\%$ , and a volume average,  $\langle \beta \rangle \sim 13\%$ . The plasma is pre-heated by the formation of a toroidal z-pinch followed by an intense heating phase (100 MW to 200 MW input to the plasma) where a rapid reversal of the toroidal field (1.7  $\mu$ sec) both heats and converts the plasma into a tokamak configuration with  $q > 1$  at the plasma edge. The formation of the high-beta equilibrium occurs on a faster time scale (5  $\mu$ sec) than the expected MHD instability growth time ( $>10 \mu$ sec), allowing the generation of a wide range of equilibria from stable to highly unstable whose subsequent evolution can then be observed.

Further details of the heating scheme and of Torus II are discussed in Refs 1-3. Described here are the results of detailed studies of the important plasma parameters as measured with a well developed set of diagnostics, including simultaneous measurement at many spatial locations of electron density and temperature by Thomson scattering, local values of magnetic fields by multi-channel magnetic probes, and fluctuations in the line-integrated electron density by dual beam  $\text{CO}_2$  laser scattering.

The radial pressure profiles were determined in Torus II from the measurement of the local value of electron density and temperature simultaneously at ten spatial locations by multi-point Thomson scattering. The Thomson scattering system [4] consists of an 8 Joule, 300 MW ruby laser beam directed across the midplane of the torus and toward the major axis. The scattered light is collected at  $90^\circ$  and imaged onto a coherent fiber optic array which transfers the light to the input of a triple-grating spectrometer patterned after the Los Alamos design [5]. The blue-shifted wing of the Thomson-scattered signal is detected with a multi-anode microchannel plate tube with a 10

by 10 anode array on the output. This detector system provides a measurement of 10 wavelength channels at each of 10 spatial locations across the midplane of the torus. The data is then digitized and processed for display by computer. Shown in Fig. 1 are the observed profiles of electron density and temperature during the equilibrium phase at  $9.5 \mu\text{sec}$  after the heating phase. Also shown in Fig. 1 is the computed pressure profile from this data assuming  $T_e = T_i$ . The profiles of density and temperature both show a substantial (approximately 40% of the minor radius) shift of the position of the peak toward the outside (large major radius) as expected for values of  $\epsilon\beta_p > 1$ . A computation of the peak and volume average beta from these profiles yields values of 42% and 13% respectively. The equilibrium lasts for approximately  $15 \mu\text{sec}$  and is lost apparently because of the decay in the external equilibrium fields.

Measurements of the electron density and electron density fluctuations during the equilibrium phase were made using single- [3] and double-beam [6]  $\text{CO}_2$  laser forward scattering with both

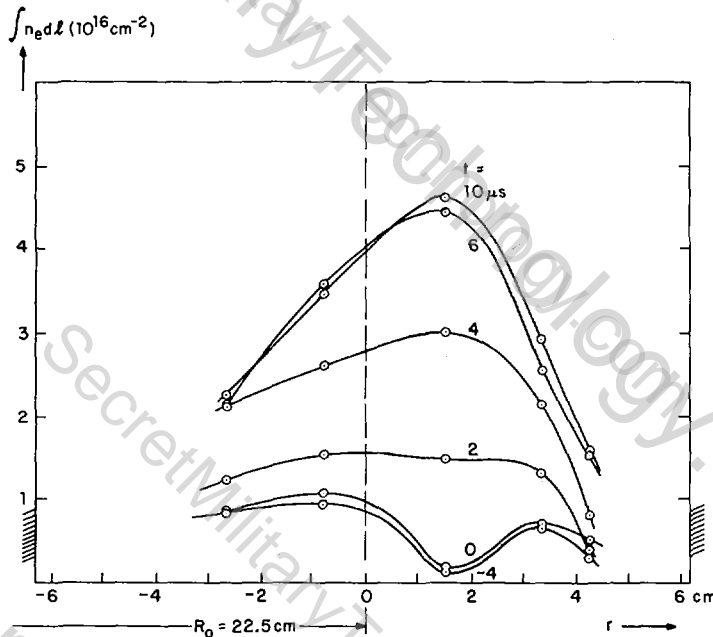


FIG.2. Radial profiles of the line-integrated electron density. The heating phase begins at  $t = 0$  and an equilibrium is achieved at  $t = 5 \mu\text{s}$ .

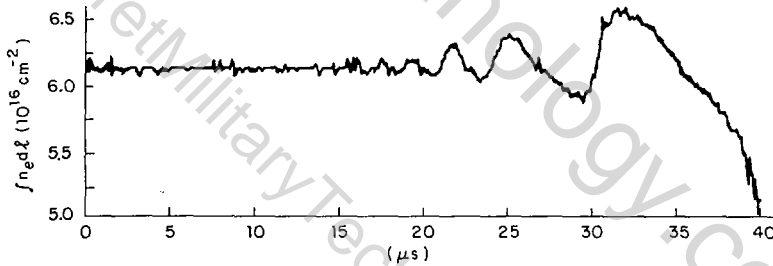


FIG.3. Time-dependence of the line-integrated electron density as determined by two-beam  $\text{CO}_2$  scattering 3.5 cm outside the minor axis.

homodyne and heterodyne detection [7]. When the scattering system was operated as an interferometer, the time evolution of the line-integrated density profile was measured and is shown in Fig. 2. The outward shift of the position of the peak in the density profile is in agreement with the Thomson-scattering observations. The density fluctuation measurements were performed using two parallel laser beams, one inside the major radius and the other outside. We observe a growing density fluctuation on the outside part of the profile with a growth rate and frequency in the range expected for MHD instabilities. In Fig. 3 we show the time-dependent density determined by use of the two independent beams to determine the absolute phase shift introduced by the plasma as a function of time along one chord. This technique removes ambiguities which may be introduced by refraction and Doppler shifting of the transmitted beam. The growing fluctuation can be clearly seen but the equilibrium is lost before the effects of this fluctuation could be determined. The measured and calculated parameters for this instability are given below. Because of the large amplitude seen in the fluctuating line-integrated density, the mode numbers must be low, with  $n \approx m < 8$ :

$$\omega \approx 2 \times 10^6 \text{ sec}^{-1} < \omega_{ci} \approx 1.6 \times 10^7 \text{ sec}^{-1}$$

$$\gamma \approx 10^5 \text{ sec}^{-1} \text{ vs } \gamma_{\text{max}} \approx \frac{c_A}{q_0 R_0} \approx 10^6 \text{ sec}^{-1}$$

$$n \text{ and } m \lesssim 8$$

$$\rho_i \approx 0.2 \text{ cm}, \quad k_{\text{radial}} \rho_i \approx 1$$

The magnetic field structure in Torus II has been studied by a magnetic probe consisting of a single small tube inserted radially or vertically, containing two orthogonal coils at each of six locations. Data was recovered, stored and processed by the computer data acquisition system. The probe surface is quartz and 6 mm in diameter. Measurements from Thomson scattering show that the presence of the probe in the plasma tends to lower the electron temperature but the beta remains roughly unchanged.

The diamagnetic well in the toroidal field has been observed and is shown in Fig. 4. The maximum toroidal beta was observed to be in the range of 40% to 50%, in good agreement with the results shown in Fig. 1 and previous measurements of the ion temperature [2] using the Doppler-broadened line HeII at 4686 Å. The width of the diamagnetic plasma was 6 cm to 8 cm and the height was 12 cm to 15 cm. The diamagnetic well remains for several microseconds, showing nearly constant toroidal beta. Measurement of the vertical magnetic field component permits a rough calculation of the toroidal current density (approximately 250 A/cm<sup>2</sup>) which is also shown in Fig. 4, and total current (about 30 kA) as well as  $q$  with  $q(0) \approx 1$ .

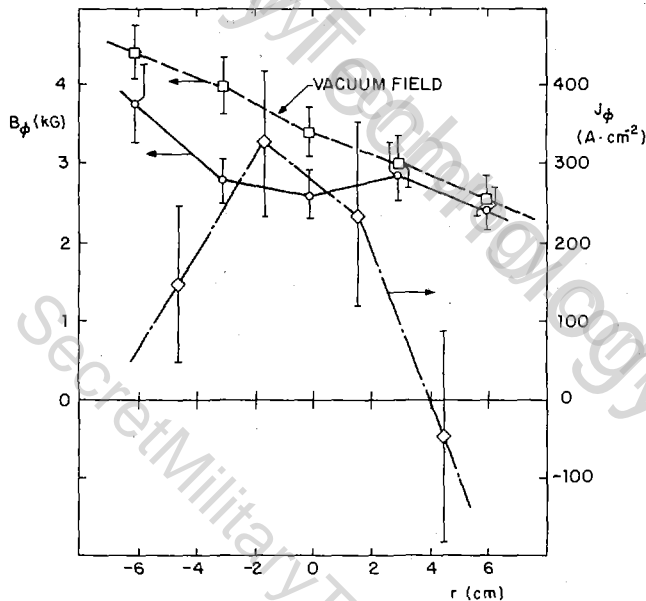


FIG.4. Radial profile of the toroidal magnetic field in the vacuum case and with plasma 5.5  $\mu$ s after the heating phase. Also shown is the computed toroidal current profile on the same shot.

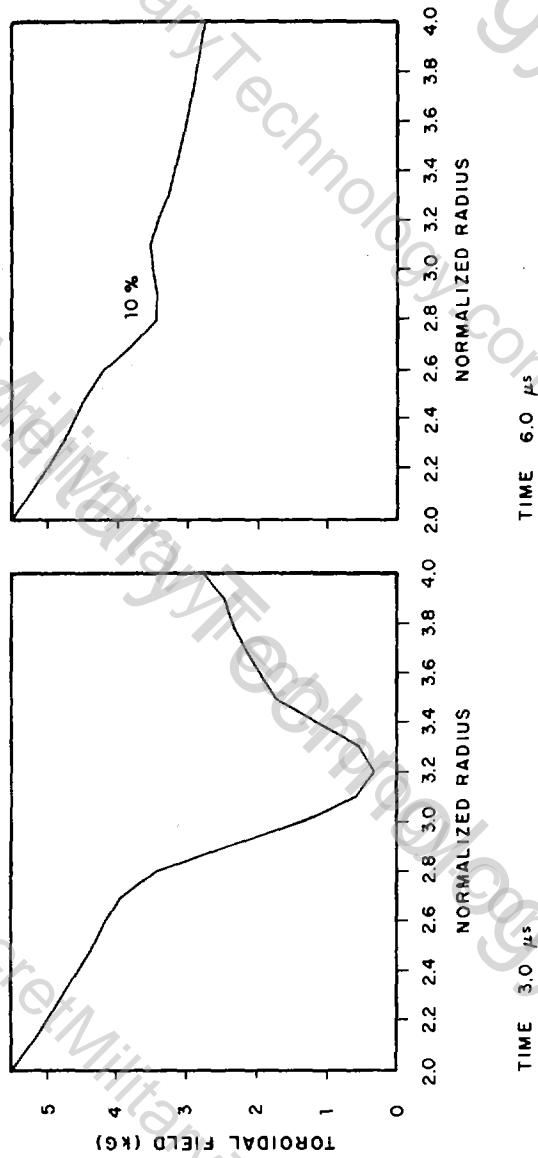


FIG.5. Radial profile of the toroidal magnetic field determined from computational simulation of the start-up phase of Torus II for 3  $\mu$ s and 6  $\mu$ s after the beginning of the heating phase.

Toroidal and poloidal rotation of the plasma has been observed [8] from observations of the HeII 4686 Å line. The toroidal flow was  $1.6 \times 10^6$  cm/sec (about 30% of  $v_{th,i}$ ) in the direction of the toroidal current, and a poloidal flow of the same magnitude follows the ion diamagnetic direction. The measurement of the toroidal flow can be compared with neoclassical transport theory in the collisional regime, but the poloidal motion is dominated by an  $E \times B$  drift. A positive radial electric field of approximately 50 v/cm is inferred by comparing data with the theory. The flow motion decays as the plasma cools, which suggests that it is a feature of the equilibrium.

In summary, the experimental results from Torus II demonstrate the achievement of a high-beta tokamak equilibrium with  $\epsilon\beta_p > 1$  and finite rotation speed for approximately 15  $\mu$ sec. A low-n MHD instability is observed at the outer part of the pressure profile. Modification of the experiment to allow extension of the operating pulse beyond 100  $\mu$ sec is in progress as part of an overall plan to upgrade the Torus II device.

## 2. THEORY AND COMPUTATION

The start-up phase of the Torus II plasma has been simulated [9] with our two-dimensional initial-value code, which provides detailed information on the heating of the plasma. Since the code employs toroidal and poloidal flux functions as boundary conditions, whereas actually the known parameters are the coil currents, we used inductance codes to obtain the boundary flux functions from these currents. At the end of the intense Ohmic heating phase ( $\sim 6 \mu$ sec), the plasma has achieved radial equilibrium, but is still seeking equilibrium in the axial direction. The plasma is still elongated (4:1), the plasma current ranges between 40-60 kA, and the edge  $q$  is between 1.5 and 2. Assuming ion-acoustic anomalous resistivity [10], the soaking-in of the toroidal field is shown in Fig. 5 at 3 and 6  $\mu$ sec after the main heating current. Despite the fast rise of the current, we found at all times Ohmic heating to be the dominant term in the energy equation (>90%), while compression and shock heating is below 10%. With proper choice of the vertical field, as used in our present experiments, calculations show that the plasma never hits the side walls. However, with the present coil geometry, a significant portion of the plasma leaks through the corners of the cross-section. Calculations have been made for upgrading Torus II in which the coil geometry has been changed to treat this problem.

The long-term diffusion and decay of the plasma is studied with a one-dimensional diffusion code (no inertial terms), in which we assume steady-state coronal equilibrium for the radiation, classical thermal conductivity, and various impurity levels. Starting with a plasma of 70 eV, we readily see that silicon is the controlling radiating agent at the early times (or at higher temperatures), and oxygen takes over at later times. For impurities of 0.5% oxygen and 0.5% silicon, which are realistic levels for a quartz vessel, a hot plasma can be readily maintained for 40  $\mu$ sec. Higher levels of impurities (for example, either oxygen or silicon exceeding 2%) result in greatly shortened plasma life below 20  $\mu$ sec.

A zero-dimensional atomic physics code is used to augment computed MHD results to include ionization and recombination physics. We follow these processes (radiative and three-body) for the helium gas as well as for oxygen and silicon. Treating the electrons and ions separately, we compute the Ohmic heating input, electron-ion energy exchange, bremsstrahlung losses, line radiation, classical transport losses, and ion-acoustic turbulent heating. We find that Torus II can achieve peak  $T_e$  of 50 to 100 eV. Due to the turbulent heating, temperature equilibration occurs within 10  $\mu$ sec.

Axisymmetric equilibria have been simulated using the free-boundary PEST code, as well as a fixed boundary triangular-mesh code developed here. Equilibria have been obtained which roughly model the experimental parameters with  $\langle \beta \rangle \approx 13\%$ ,  $\beta_0 \approx 42\%$ , magnetic axis shift of approximately 40% of the minor radius, and edge  $q \approx 2$ .

Bifurcation of ideal MHD equilibria at high beta is being investigated [11] analytically and by computing, using global parameters representing poloidal beta and shear. Axisymmetric bifurcations of a Grad-Shafranov equilibrium having nonlinear profiles occur at low beta and at high beta for modest values of shear. They are modeled by a pair of cusp catastrophe surfaces that are joined smoothly. The middle fold of the surface corresponds to an equilibrium unstable to axisymmetric modes. Various stable pathways in parameter space leading to high-beta stable equilibria are deduced from the model. The procedure is being generalized to nonaxisymmetric bifurcations (specifically those associated with high-n ballooning modes).

## REFERENCES

- [1] AYDEMIR, A., et al., "Experimental and Theoretical Studies of High-Beta Tokamaks", Plasma Physics and Controlled Nuclear Fusion Research 1978 (Proc. 7th Int. Conf. Innsbruck, Austria, 1978) Vol. II, IAEA, Vienna (1978) p 105.
- [2] GEORGIU, G. E., MARSHALL, T. C., WEBER, P. G., Phys. Fluids 23 2085 (1980).
- [3] CHU, C. K., et al., "High-Beta Tokamak Stability Studies", Plasma Physics and Controlled Nuclear Fusion Research 1980 (Proc. 8th Int. Conf. Brussels, Belgium, 1980) Vol. II, IAEA, Vienna (1981) p 339.
- [4] LEVINTON, F. M., and NAVRATIL, G. A., to be published in Review of Scientific Instruments and Columbia Plasma Physics Laboratory Report No. 86 (1982).
- [5] SIEMON, R. E., Applied Optics 13 697 (1974).
- [6] MACHIDA, M., OEPTS, D., NAVRATIL, G. A., Columbia Plasma Physics Laboratory Report No. 85, (1981).
- [7] SLUSHER, R. E., and SURKO, C. M., Phys. Fluids 23 472 (1980).
- [8] KOSTEK, C., and MARSHALL, T. C., Columbia Plasma Physics Laboratory Report No. 87 (1982).
- [9] IZZO, R., Columbia Plasma Physics Laboratory Report No. 84 (1981).
- [10] MARSHALL, T. C. and LUI, H. C., Phys. Fluids 19 1417 (1975).
- [11] ELKIN, D., and JOHNSTON, S., 1982 Sherwood Theory Conference, paper number 2D17.



## BETA INCREASE IN A BELT-PINCH PLASMA BY FAST MAGNETOSONIC WAVE HEATING

V. ERCKMANN, A. MAYER, G. MÜLLER,  
K. SCHWÖRER, M. THUMM, R. WILHELM  
Institut für Plasmaforschung,  
University of Stuttgart,  
Stuttgart,  
Federal Republic of Germany

### Abstract

#### BETA INCREASE IN A BELT-PINCH PLASMA BY FAST MAGNETOSONIC WAVE HEATING.

Additional heating of strongly elongated high- $\beta$  plasmas by fast magnetosonic wave absorption at the second harmonic of the ion cyclotron frequency ( $\omega = 2\omega_{ci}$ ) was investigated in the belt-pinch HECTOR. Fast Alfvén waves with toroidal and poloidal mode numbers  $n=0$  and  $m=0$ , respectively, were launched radially into the plasma ( $k \perp B$ ) by modulating the confining magnetic field with a frequency of 1.2 MHz during 5  $\mu$ s. The experiments were performed under various plasma and resonance conditions in regimes where the ion gyroradii are comparable to the perpendicular wavelength ( $k_{\perp}r_{ci} \approx 1$ ). When the resonance layer is located in the plasma centre, very efficient wave absorption with an energy flux of about  $50 \text{ MW} \cdot \text{m}^{-2}$  was observed. The  $\beta$ -value on the magnetic axis increased from 30% to 70%, indicating a localized power deposition. The ion temperature grew nearly linearly with increasing incident wave power up to  $T_i(r=0) = 250 \text{ eV}$  at a modulation degree of  $\delta B/B \approx 0.2$  ( $P_{in} \approx 200 \text{ MW}$ ). The electron temperature is unaffected by the wave and remains almost constant. When the resonance surface is shifted from the magnetic axis towards the plasma boundary the plasma heating is reduced by a factor of 2 and the central  $\beta$  remains constant during the RF heating pulse. In corresponding hydrogen discharges, where the resonance region  $\omega = 2\omega_{ci}$  is located outside the plasma, no heating was observed. During the RF heating process and the subsequent energy decay, the plasma passes through a sequence of flux-conserving equilibria. This was demonstrated by numerical calculations starting from experimental input parameters using a free-boundary 2-D equilibrium code.

### 1. INTRODUCTION

In several belt-pinch experiments the confinement of tokamak-like high- $\beta$  plasma equilibria was investigated extensively [1–4]. These experiments demonstrated the possibility of suppressing at least the fast-growing MHD instabilities such as external kink, ballooning and vertical displacement modes by means of highly elongated flux surfaces, poloidal  $\beta$ -values in the range of the aspect ratio  $A$ , and appropriate poloidal field configurations. Owing to the

pulsed operation and the unavoidable energy losses, these shock-heated plasmas are non-stationary on a time scale shorter than 100  $\mu\text{s}$ .

In this situation an effective additional heating of the plasma is of interest, such as the coupling of fast magnetosonic waves into the toroidal system. At the second harmonic of the ion cyclotron frequency  $\omega = 2\omega_{ci}$ , strong wave absorption is expected, especially in the high- $\beta$  case, where the perpendicular wavelength is in the order of the ion gyroradius. Mode conversion processes to backward-wave ion Bernstein modes are expected to become very efficient [5, 6]. For typical experimental conditions in belt-pinch plasmas the value of  $k_{\perp} r_{ci}$  is on the order of 1, which is a great improvement on the usual second-harmonic ion cyclotron frequency heating in tokamaks [7], where the ion gyroradii remain small in comparison with the perpendicular wavelength ( $k_{\perp} r_{ci} \ll 1$ ). After a short description of the Stuttgart belt-pinch experiment HECTOR (Highly Elongated Cross-section TORus) and a summary of its typical plasma parameters in Section 2, the results on fast magnetosonic wave heating at  $\omega = 2\omega_{ci}$  under various plasma and resonance conditions are given in Section 3.

During the RF heating pulse and the subsequent energy decay time, negligible magnetic field diffusion occurs, and a nearly flux-conserving sequence of equilibria should be passed through by the plasma. This special aspect of fast plasma heating of high- $\beta$  tokamak equilibria is discussed in Section 4.

## 2. EXPERIMENTAL SET-UP AND PLASMA PARAMETERS BEFORE RF HEATING

The belt-pinch HECTOR produces strongly elongated diffuse high- $\beta$  plasmas by fast shock-wave compression. The coil system consists of two concentric cylindrical coils (height  $2b^c = 1.18$  m; inner coil radius  $R_i^c = 0.19$  m; outer coil radius  $R_a^c = 0.43$  m) with helically twisted windings [8]. Thus the toroidal and poloidal magnetic fields necessary for equilibrium are generated simultaneously. Magnetic shock compression is accomplished by a fast-rising magnetic field generated by pulse-charged Blumlein transmission lines (poloidal peripheral voltage  $U_{\max} = 200$  kV; toroidal magnetic field  $B_{t\max}(r=0) = 0.16$  T; energy content  $W = 25$  kJ; risetime  $t_r = 0.5$   $\mu\text{s}$ ). Stability with respect to vertical displacement modes and a clear separation of the plasma ends from the wall is achieved by means of passive multipole windings at the top and bottom of the compression coil. The initial plasma for fast magnetic compression is generated in two stages: an RF predischARGE (frequency  $f = 85$  MHz; charging voltage  $U = 30$  kV; pulse length  $t = 50$   $\mu\text{s}$ ; power  $P = 1$  MW) is used to ignite a toroidal preheating discharge ( $f = 16$  kHz;  $B_t(0) = 0.1$  T;  $W = 65$  kJ) which produces a homogeneous plasma with an ionization degree of about 30% at low filling pressures ( $p_0 = 0.1$  to 0.2 Pa). The pre-ionization was optimized with respect

TABLE I. PLASMA PARAMETERS BEFORE FAST MAGNETOSONIC WAVE HEATING

Major plasma radius,	$R(0)$	=	0.32 m
Plasma height,	$2b$	=	1.0 m
Plasma width,	$2a$	=	0.11 m
Radial compression ratio,	$a^c/a$	=	1.7
Toroidal plasma current,	$I_t$	=	85 kA
Plasma beta,	$\beta(0)$	=	0.30–0.75
Poloidal plasma beta,	$\langle \beta_p \rangle$	=	3.5
Plasma q-value,	$q(a)$	=	3.3
Plasma density,	$\langle n_e \rangle$	=	$10^{20} \text{ m}^{-3}$
Electron temperature,	$T_e(0)$	=	50 eV
Ion temperature,	$T_i(0)$	=	150 eV
Impurity content,	$\alpha_C$	=	0.4%
	$\alpha_o$	=	0.3%

to the ionization degree and impurity content [4]. Characteristic plasma parameters in the post-compression phase before supplementary RF heating are listed in Table I. The toroidal vacuum field decays with a crowbar L/R time of 70  $\mu\text{s}$ . The pulse time of the toroidal plasma current is about 35  $\mu\text{s}$ .

Radial profiles of the toroidal and poloidal magnetic fields  $B_t(r, t)$  and  $B_p(r, t)$ , the toroidal current density  $j_t(r, t)$  and the plasma pressure  $p(r, t)$  were obtained from simultaneous measurements with internal multiple probes. The  $\beta$ - and q-values are also evaluated from these measurements and from measurements of the toroidal diamagnetic flux, of the poloidal fields outside the discharge vessel and from calculations using a 2-D equilibrium code (see Section 4). The electron temperature  $T_e(r, t)$  was determined by 90° Thomson scattering of ruby laser light and by UV-spectroscopy of impurity lines (C, O). The axial electron line density  $\bar{n}_e(r, t)$  was measured by end-on CO<sub>2</sub> laser interferometry, and the radial profile of  $n_e(r, t)$  in the torus midplane by Thomson scattering. The radial ion temperature profile  $T_i(r, t)$  was determined spectroscopically from Doppler broadening measurements of the D $_{\alpha}$  (656.1 nm) line and the He II (468.6 nm) line (2% helium was added to the filling gas) using a Fabry-Perot polychromator and was also derived from the pressure balance. The impurity content was measured spectroscopically.

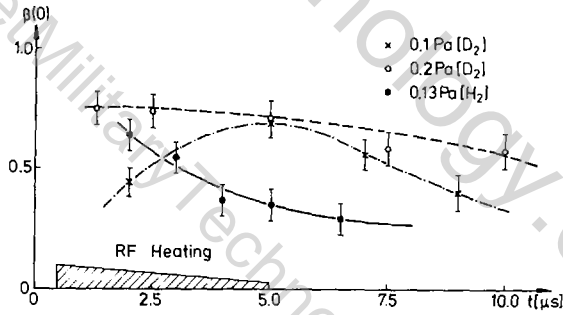


FIG.1. Time evolution of plasma  $\beta$  on the magnetic axis for central resonance zone ( $\omega = 2\omega_{ci}$  ( $p_0 = 0.1$  Pa;  $D_2$ ), resonance layer close to the plasma boundary ( $p_0 = 0.2$  Pa;  $D_2$ ), and resonance region outside the plasma ( $p_0 = 0.13$  Pa;  $H_2$ ).

### 3. FAST MAGNETOSONIC WAVE HEATING

For supplementary RF heating, the confining external magnetic field is modulated with a frequency of 1.2 MHz during a time interval of about  $5 \mu\text{s}$ . This modulation is generated by standing waves excited in the Blumlein transmission lines after crowbaring the main field coil. The modulation degree drops during the RF pulse and is chosen by varying the time at which the crowbar is activated. All values quoted below refer to the time average. As a consequence of this modulation, fast Alfvén waves ( $\vec{k} \perp \vec{B}$ ) are launched radially into the plasma with toroidal and poloidal mode numbers  $n = 0$  and  $m = 0$ , respectively. During the plasma production through fast shock compression, fast anomalous magnetic field diffusion depends on the plasma density [8]. The internal magnetic field and the spatial position of the resonance layer  $\omega = 2\omega_{ci}$  can therefore be modified by varying the filling pressure. When the resonance zone is located in the plasma centre ( $p_0 = 0.1$  Pa; filling gas,  $D_2$ ) very efficient wave absorption is observed. The propagation of the wave was measured by magnetic multiple probes. The trajectories of constant phase show an inward propagation to the plasma core where the wave is damped out [4]. The wave carries an energy flux on the order of  $50 \text{ MW} \cdot \text{m}^{-2}$ . A pronounced increase in the plasma  $\beta$  was measured. The  $\beta$ -value on the magnetic axis grew from 30% to 70% as shown in Fig.1. The electron temperature is unaffected by the wave and remains almost constant during heating. For the given plasma parameters, ion-electron heat transfer can be neglected in the  $10 \mu\text{s}$  time-scale considered here. The ion heating was measured for different modulation degrees of the magnetic field. The ion temperature grows almost linearly with increasing incident wave power from  $T_i(0) = 150$  to  $250$  eV at  $P_{in} \approx 200 \text{ MW}$  ( $\delta B/B = 0.2$ ), as shown in Fig.2.

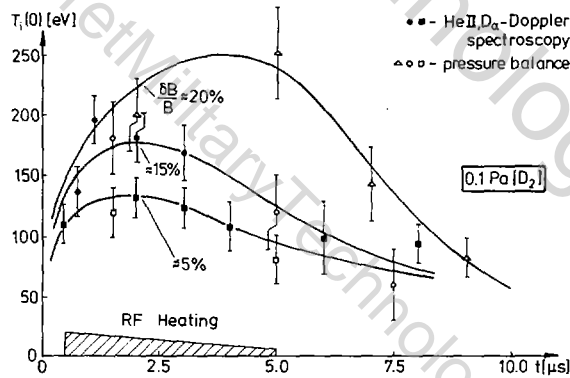


FIG.2. Time evolution of the central ion temperature during RF heating with different wave amplitudes for resonance layer  $\omega = 2\omega_{ci}$  on the magnetic axis ( $p_0 = 0.1 \text{ Pa}$ ;  $D_2$ ).

The high values of the ion-heating power needed to raise  $\beta$  and the fast-ion temperature drop after heating can be explained by ion energy losses due to limited ion confinement. This result is characteristic for shock-heated high- $\beta$  plasmas with ion gyroradii comparable to the typical gradient length [4].

By increasing the filling pressure ( $p_0 = 0.2 \text{ Pa}$ ;  $D_2$ ) the magnetic field in the plasma centre is lowered, the resonance layer splits, and the two regions with  $\omega = 2\omega_{ci}$  are shifted from the magnetic axis towards the inner and outer plasma boundaries. In this case the plasma heating is reduced by a factor of 2 and the central  $\beta$  remains constant during the RF heating pulse, as can be seen from Fig.1. The outward shift of the resonance surface results in a broadening of the energy deposition.

In comparable hydrogen discharges ( $p_0 = 0.13 \text{ Pa}$ ;  $H_2$ ), where the resonance region  $\omega = 2\omega_{ci}$  is placed outside the plasma, no heating was observed. The corresponding  $\beta$ -value decreases rapidly even during the RF pulse, as shown in Fig.1.

#### 4. SEQUENCE OF FLUX-CONSERVING EQUILIBRIA

The duration of the RF heating pulse and the associated  $\beta$ -increase as well as the subsequent energy decay time of the plasma is short compared to the diffusion time of the magnetic field. Thus the total magnetic flux is expected to remain approximately constant during the change of  $\beta$ , and the plasma should undergo a sequence of flux-conserving equilibria. Such FCT equilibria were extensively investigated in theory for strongly heated high- $\beta$  tokamaks [9]. Equilibrium  $\beta$ -values up to 28% were reported.

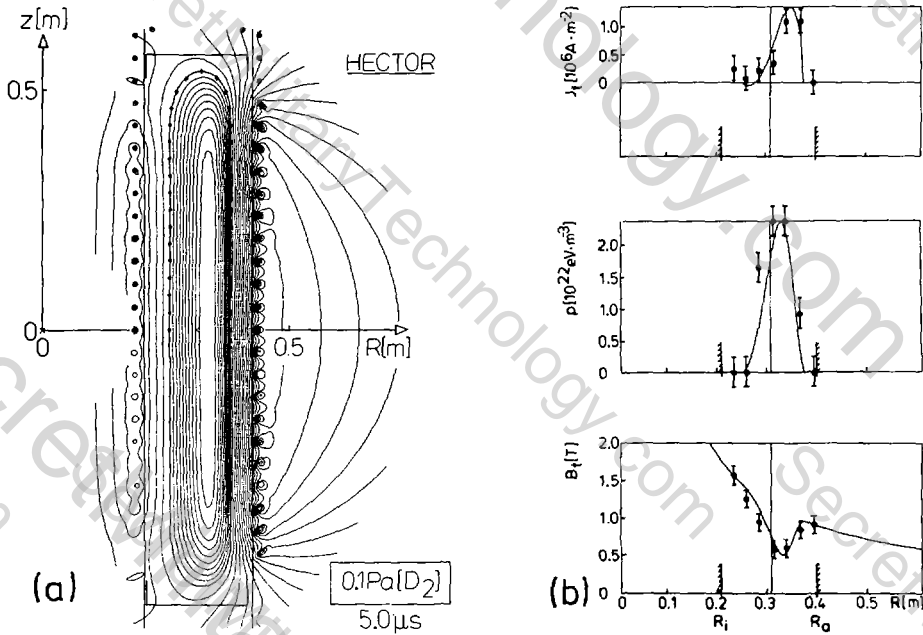


FIG.3. Calculated poloidal flux contours (a) and comparison of calculated and experimental radial profiles (b) of  $B_t$ ,  $p$  and  $j_t$  after RF heating ( $t_2 = 5 \mu\text{s}$ ) for central resonance layer  $\omega = 2\omega_{ci}$  ( $p_0 = 0.1 \text{ Pa}$ ;  $D_2$ ).

The HECTOR equilibria are studied by means of a two-dimensional free-boundary equilibrium code [10]. Input parameters of the calculations are the plasma surface shape, the radial distribution of the toroidal current density within the plasma, the vacuum toroidal magnetic field distribution and the geometrical positions of the toroidal conductors which carry the externally applied currents. The toroidal plasma current density distribution  $j_t(r)$  is prescribed by the expression:

$$j_t = c_1 r + c_2 (\psi - \psi_c) r + \frac{c_3}{r} + \frac{c_4 (\psi - \psi_c)}{r}$$

in the plasma region and by  $j_t = 0$  outside the plasma.  $\psi(r)$  and  $\psi_c$  are the poloidal flux functions inside the plasma and at the plasma surface, respectively. The constants  $c_i$  ( $i = 1, 2, 3, 4$ ) are related to the plasma pressure and to the poloidal current function, respectively.

The output parameters of the calculations that are compared to the experimental data are the radial distributions of the plasma pressure  $p(r)$  and

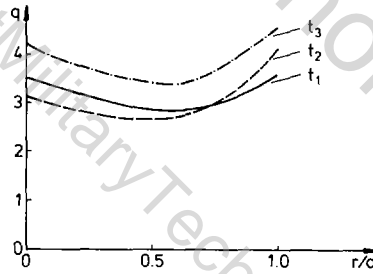


FIG.4. Time evolution of the calculated radial  $q$ -profile during central resonance RF heating ( $t_1 = 2 \mu s$  to  $t_2 = 5 \mu s$ ) and during the subsequent plasma cooling ( $t_2 = 5 \mu s$  to  $t_3 = 9 \mu s$ ).

the toroidal field  $B_t(r)$ , the distributions of the external poloidal field along the  $z$ -direction  $B_{z1}(z)$  and  $B_{z2}(z)$ , as well as the magnitude of the toroidal currents required in the external coils. The radial distribution of the safety factor  $q(r)$ , the poloidal flux function  $\psi(r)$ , and the values of  $\beta$  and  $\beta_p$  are also calculated. The code is applied in a "trial and error" way.

By varying the four constants  $c_i$  in the current density distribution and slightly modifying the plasma contour within the experimental uncertainties, a set of input data had to be found such that the output parameters fit the experimental data. As an example, Fig.3 shows the results of the calculations for the equilibrium at the end of the RF heating pulse and a comparison with the measured profiles. During wave heating and the subsequent cooling of the plasma, the distribution  $q(\psi)$  remains constant within the uncertainties in fitting experimental data, as can be seen from Fig.4. This is also valid for the total poloidal flux inside the plasma. Owing to the free-boundary condition, the plasma moves slightly inside the discharge vessel. Thus fluxes and  $q$ -profiles are conserved in a system moving together with the plasma, indicating a FCT sequence of plasma equilibria.

As can be seen from Fig.5, the experimentally determined plasma current density peaks strongly towards the outer region of the pressure profile as  $\beta$  increases during strong central wave heating, and it flattens when the plasma energy decays after heating. The time behaviour of the normalized profiles  $j_r^*(r)$  and  $p^*(r)$  (normalization with respect to the plasma width  $2a$  at  $t_2 = 5 \mu s$ ) is in good qualitative agreement with the FCT calculations made by Dory and Peng [9].

## 5. CONCLUSIONS

Effective additional heating of highly elongated toroidal high- $\beta$  plasmas by fast magnetosonic wave absorption at the second harmonic of the ion

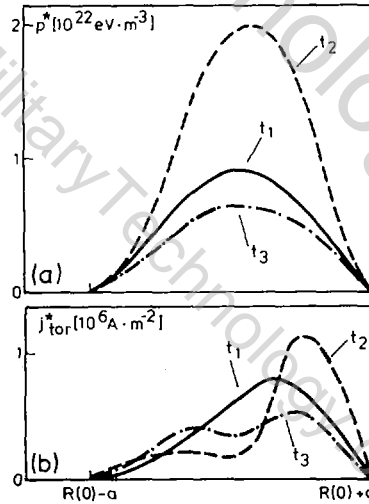


FIG.5. Time evolution of the normalized, experimentally determined pressure (a) and current density (b) profiles during FCT heating from  $t_1 = 2 \mu\text{s}$  ( $\langle\beta\rangle = 0.34$ ;  $\beta_p = 3.5$ ) to  $t_2 = 5 \mu\text{s}$  ( $\langle\beta\rangle = 0.46$ ;  $\beta_p = 4.0$ ) and during the subsequent plasma energy decay until  $t_3 = 9 \mu\text{s}$  ( $\langle\beta\rangle = 0.22$ ;  $\beta_p = 1.9$ ).

cyclotron frequency was demonstrated in the Stuttgart belt-pinch HECTOR. According to the plasma  $\beta$ -values above 30% and  $k_{\perp} r_{ci} \approx 1$ , heating in this experiment differs from present-day ion cyclotron frequency heating in tokamaks, where the ion gyroradii remain small in comparison with the perpendicular wavelength ( $k_{\perp} r_{ci} \ll 1$ ). As expected from wave theory including hot plasma dispersion, absorption and mode conversion to electrostatic ion Bernstein modes near the resonance surface  $\omega = 2\omega_{ci}$  [5, 6], very effective ion heating was observed. For the central resonance layer  $\omega = 2\omega_{ci}$  in particular, a strong increase in the plasma  $\beta$  within a few microseconds was obtained, indicating a localized power deposition. Under these optimum conditions the  $\beta$ -value in the plasma centre is almost doubled while the central ion temperature rises from 150 to 250 eV. The high values of ion heating power ( $\approx 50 \text{ MW} \cdot \text{m}^{-3}$ ) needed to raise  $\beta$  and the fast-ion energy decay after RF heating can be explained by ion energy losses due to the large gyroradii which are comparable to the density gradient length [4].

During the fast heating process and the subsequent plasma energy decay, a sequence of flux-conserving equilibria is passed through by the plasma which was established by free-boundary 2-D equilibrium calculations starting from measured plasma parameters and profiles. FCT sequences for increasing plasma  $\beta$  with a maximum averaged  $\beta$ -value of  $\langle\beta\rangle = 0.46$  ( $\beta_p = 4.0$ ) could be shown for the first time in the present experiments.

## REFERENCES

- [1] BECKER, G., GRUBER, O., KRAUSE, H., MAST, F., WILHELM, R., Nucl. Fusion **18** (1978) 1653.
- [2] GRAFFMANN, E., HOENEN, F., KALECK, A., KÖNEN, L., KORTEN, M., SCHLÜTER, J., in Controlled Fusion and Plasma Physics (Proc. 8th Europ. Conf. Prague, 1977) Vol.1, Prague (1977) 77.
- [3] CHU, C.K., et al., in Plasma Physics and Controlled Nuclear Fusion Research 1980 (Proc. 8th Int. Conf. Brussels, 1980) Vol.2, IAEA, Vienna (1981) 339.
- [4] ERCKMANN, V., MÜLLER, G., SCHWÖRER, K., SINGETHAN, J., THUMM, M., WILHELM, R., in Controlled Fusion and Plasma Physics (Proc. 10th Europ. Conf. Moscow, 1981) Vol.1, Moscow (1981) Contributed Paper L-10; IPF Stuttgart Rep. IPF-81-8 (1981).
- [5] PERKINS, F.W., Nucl. Fusion **17** (1977) 1197.
- [6] SCHARER, J.E., BEYER, J.B., BLACKFIELD, D.T., MAU, T.K., Nucl. Fusion **19** (1979) 1171.
- [7] COLESTOCK, P.L., DAVIS, S.L., HOSEA, J.C., HWANG, D.Q., THOMSON, H.R., in Heating in Toroidal Plasmas (Proc. 2nd Joint Grenoble-Varenna Int. Symp. Como, 1980) Vol.1, CEC Brussels (1981) 471.
- [8] SÖLDNER, F., Phys. Fluids **21** (1978) 1036.
- [9] DORY, R.A., PENG, Y.-K.M., Nucl. Fusion **17** (1977) 21.
- [10] BECKER, G., LACKNER, K., Nucl. Fusion **17** (1977) 903.



## DISCUSSION

ON PAPERS IAEA-CN-41/M-5-1 AND M-5-2

B. COPPI: If my estimate is correct, the experimental value of  $q$  on the magnetic axis of the Torus II experiment is well below unity. Our work at MIT indicates that there is a second stability region for  $m = 1$  internal modes. Is it possible that your experiment shows evidence for this?

C.K. CHU: It is possible, although our equilibria calculations so far all show  $q(0)$  very nearly equal to 1. We shall look for this stability region in future experiments and equilibria calculations.



## SUPPRESSION OF LOSSES IN A COMPACT TORUS WITH PROGRAMMED SHAPING OF THE MAGNETIC STRUCTURE

V.V. BELIKOV, V.M. GOLOVIZNIN, V.K. KORSHUNOV,  
A.P. KRESHCHUK, R.Kh. KURTMULLAEV, Ya.N. LAUKHIN,  
A.I. MALYUTIN, A.P. PROSHLETSOV, O.L. ROSTOVTSSEV,  
V.N. SEMENOV, V.F. STRIZHOV  
I.V. Kurchatov Institute of Atomic Energy,  
Moscow, Union of Soviet Socialist Republics

*Presented by V.P. Smirnov*

### Abstract

#### SUPPRESSION OF LOSSES IN A COMPACT TORUS WITH PROGRAMMED SHAPING OF THE MAGNETIC STRUCTURE.

The role of the functional elements of the compact torus system in suppressing energy and particle losses from the plasma is demonstrated. Experiments are carried out using the TOR and BN facilities with  $B = 7-11$  kG,  $n = (2-4) \times 10^{15} \text{ cm}^{-3}$  using compensated diamagnetic loops, radially inserted magnetic probes, neutron and X-ray detectors and an He-Ne laser interferometer ( $\text{Jnd}\ell$ ). It is established that power losses of magnetic flux and energy develop under conditions of spontaneous shaping of the closed structure or when the control elements are partially utilized. A marked improvement in all the characteristics of the compact torus is observed when programmed operation of the control elements is optimized (in accordance with the compact torus concept developed at the Kurchatov Institute). An appreciable increase in energy inside the separatrix is observed when the start of the longitudinal wave is delayed; the evolution of the geometrical dimensions and parameters of the plasma during compression satisfactorily agrees with two-dimensional MHD calculations assuming zero losses. When the external field is reduced, an increase in the radius and length of the compact torus is observed, which to within measurement error obeys the adiabatic law. An ion temperature of  $T \approx 1.4$  keV is achieved, and the collisionless nature of the heating ( $\lambda_{ii}/L \approx 50$ ) is confirmed. It is established that an unfavourable torus structure which initiates losses may be self-sustaining.

1. The present paper reports experimental results which demonstrate the role of the functional elements of the compact torus in optimizing a shaped trap and, particularly, in reducing the losses. The experiments were carried out using the TOR and BN facilities with  $B \sim 7-11$  kG and  $n \sim (1-3) \times 10^{15} \text{ cm}^{-3}$  without crowbarring.

Unlike traditional reversed-field theta pinches, the compact torus has facilities for programming the closure process of the anti-parallel configuration.

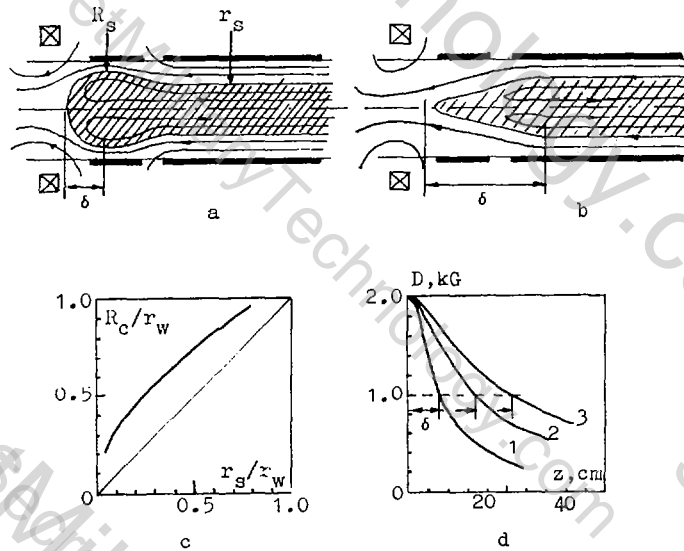


FIG. 1. Pre-compressional magnetic field structure: a) controlled; b) non-optimal or spontaneous reconnection; c) marginal separatrix radius  $R_c$  for balloon mode of operation; d) poloidal piston width  $\delta$  in various regimes: (1) optimized compact torus; (2) non-optimized regime; (3) uncontrolled shaping. The notation (1, 2, 3) is used throughout the figures.

Depending on the orientation of the field generated by the mirror coils, two control sequences are possible [1, 2]: a) using an intermediate stable cusp structure followed by stimulated reconnection and b) using a so-called 'balloon' structure. In the second case, formation of a poloidal piston and delayed compression is achieved by means of initial bulging of the end regions of the closed configuration (Fig. 1a). As a result, this structure is stable with respect to longitudinal compression whilst its expansion is impeded by the magnetic mirrors. An irreversible compression mechanism is initiated by pre-accumulation of magnetic flux in a trigger coil. The starting time is determined by passage of the separatrix through the critical radius  $R_s = R_c$ ; according to estimates, we have  $R_c = 2r_w / ((1 + 16r_w^2/r_s^2)^{1/2} - 1)^{1/2}$  (Fig. 1c). Optimization of the process generally requires a special type of magnetic control pulse [3] although broadly the same result can be achieved with a sinusoidal trigger field by selecting the amplitude, duration and delay  $\tau$ , as was done in the present case ( $\tau$  is the delay in the growth of the trigger field relative to the inversion time).

2. Various dependences related to changes in  $\tau$  are demonstrated in Fig. 2. A systematic improvement in the qualitative characteristics of the process can

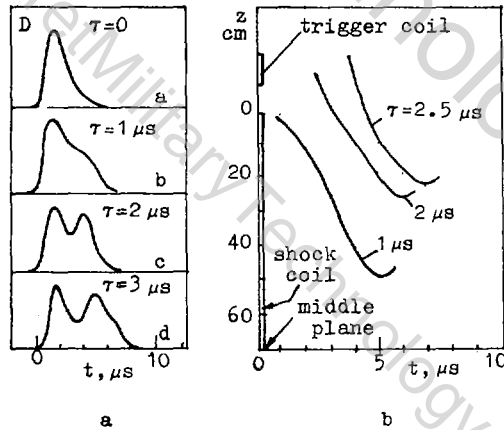


FIG.2. Transformation of diamagnetic signal at the end of the shock coil and  $z$ - $t$  diagram of poloidal piston motion for various  $\tau$ .

be identified as  $\tau$  increases: the delay of the piston increases, the wave front is clearly separated even at the edge of the shock coil (Fig. 2a), and the piston formation zone is shifted from the edge of the shock coil into the trigger coil (Fig. 2b). As a result, a larger initial plasma volume is involved in the process, and the starting and final lengths of the torus increase. It is important to note that, at the same time, the thickness of the poloidal piston decreases (Fig. 1d). The structure of the piston at the wave starting time is shown qualitatively in Fig. 1 for large (a) and small (b) delays.

The mirror coils play an important part in these processes. If the amplitude of the mirror field goes outside the optimum range, this severely disrupts the process, resulting in the evolution of tearing below the trigger coil or in premature starting of the wave.

By optimizing the controlled shaping and reducing the losses in the end zones of the torus, it is possible to alter the ratio of the lengths of the pulsed coils (i.e. to decrease  $l_{sc}/l_{tc}$ ) whilst keeping the optimum proportions of the torus unaltered.

3. Results obtained with a shortened shock coil are shown in Fig. 4. The relative shifts of the signals observed in the compression phase and also the general behaviour of the parameters (Fig. 4a) are confirmed by two-dimensional MHD calculations. The high efficiency of relaxation of the longitudinal plasma flow ( $\tau_R \sim 2 \mu s$ ) should be noted. For comparison, the classical time is  $\tau_{ii} = 2.1 \times 10^6 T_i^{3/2}/n \approx 90 \mu s$ , the mean free path is  $\lambda_{ii} \sim 20$  m, and the ratio of these to the transit parameters is  $\tau_{ii}/\tau_{tr} \sim 50$ ,  $\lambda_{ii}/L \sim 50$ . This result to a certain

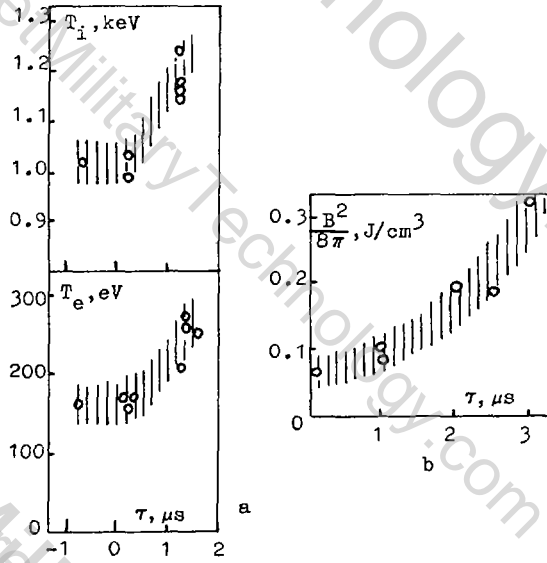


FIG.3. Ion and electron temperatures after cumulation and magnetic pressure in shock front as a function of  $\tau$ .

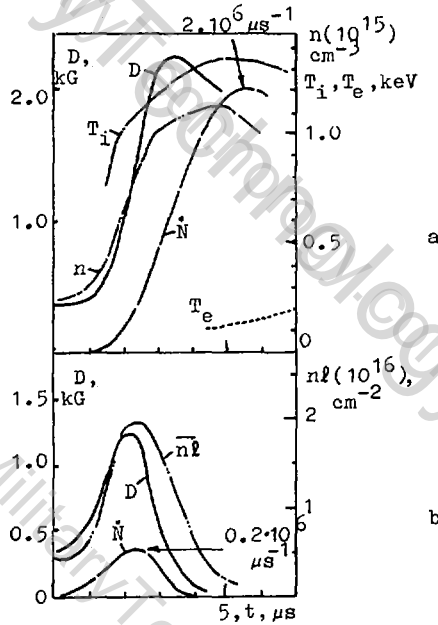


FIG.4. Time behaviour of plasma parameters in middle plane (cumulation) (a) and in shock wave front (b).

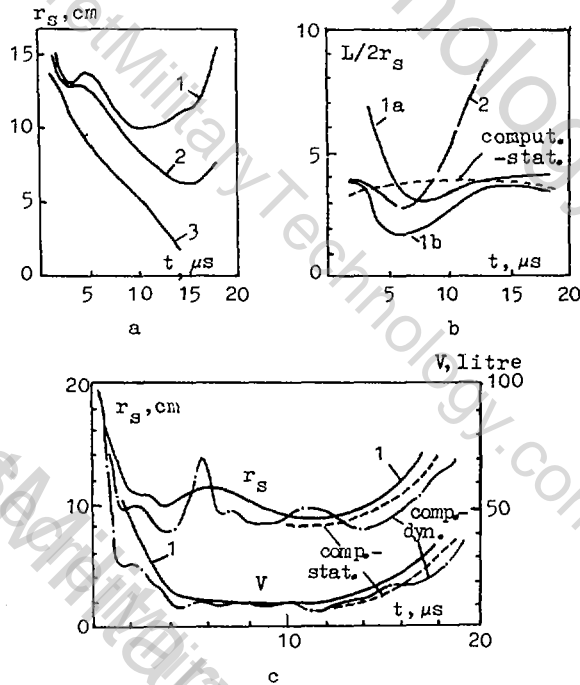


FIG.5. Compact torus evolution influenced by alternating external field and losses: a) separatrix radius; b) ellipticity  $L/2r_s$  (1a, 1b are experimental curves for compact tori of different length); c) comparison of experiment and MHD computer calculations. "dyn." = dynamic and "stat." = quasi-steady-state calculations.

extent simulates thermonuclear conditions: for  $T_1 = 8$  keV,  $n = 3 \times 10^{16} \text{ cm}^{-3}$ ,  $\tau_{ii}/\tau_{tr} \sim 30$ ,  $\lambda_{ii}/L \sim 30$ .

A clear dependence of the plasma temperature on  $\tau$  is observed (Fig. 3a). Measurements of the diamagnetism (plasma pressure) in the shock wave show complete agreement with this behaviour (Fig. 3b). These dependences are a logical consequence of the idea of triggered delay of shock compression in order to shift the process towards higher values of the field. The characteristics of the travelling wave (Fig. 4b) and the temperature in the shock front determined from this ( $T_1 \sim 500$  eV) together with Fig. 4a characterized the ratio of thermal and directional energies in the shock flux.

4. The evolution of the non-equilibrium closed configuration in an alternating external field following the reconnection phase is shown in Figs 5 and 6 for three types of experimental system: (1) a compact torus with programmed shaping, (2) a system where the functional elements of the compact torus are not fully utilized and their phasing is non-optimal, and (3) a reversed-field theta pinch. The results are compared with calculated values obtained by

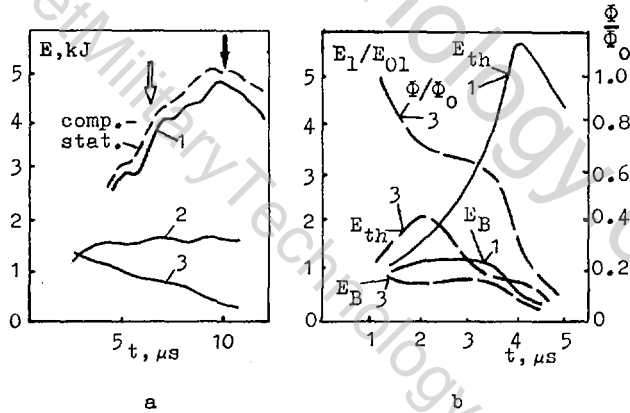


FIG. 6. Time dependences of total ( $E_{th} + E_B$ ) (a) and normalized-line (b) energy content in a closed region.  $\Phi/\Phi_0$  is the normalized closed flux for regime 3.

using a two-dimensional MHD model which takes into account the main experimental parameters assuming no losses. The dependences  $r_s(t)$ ,  $V(t)$ ,  $L/2r_s(t)$  and  $E(t)$  can be used to assess the relationship between the competing processes: heating during longitudinal and transverse compression, and magnetic flux and energy losses. The following should be noted in particular: 1) the increase in the cumulative discontinuity of  $r_s$  and in its equilibrium value in the optimum system (Fig. 5a). 2) The increase in  $L/2r_s$  (Fig. 5) in system (2) shows that magnetic-flux annihilation predominates in the loss balance; on the other hand, a steady-state value close to the calculated level is typical of the optimum compact torus regime. Figure 5 b shows two cases of the compact-torus regime having slightly different initial conditions. 3) Agreement between the experimental dependence of the energy content  $E(t)$  (Fig. 6a) and the calculated behaviour. Here,  $E(t)$  is the sum of thermal and magnetic energies within the separatrix. In the other systems, up to two thirds of the energy (2) or more (3) may be lost during the establishment of an equilibrium configuration. 4) The level of dissipative processes in the compression phase is satisfactorily modelled in the calculations by selecting the viscosity, as is indicated by the agreement between the calculated cumulative parameters and the experimental values (Fig. 4a); see also Fig. 5c. However, after cumulation, relaxation is found to be considerably more efficient in the experiment. The efficiency with which magnetic energy is converted to thermal energy in the programmed compression regime and also the clearly defined dissipative character of the process with high losses under conditions of spontaneous shaping of the closed configuration are also noted. (Fig. 6b; the data were obtained from multi-channel measurements using miniature magnetic probes.) Measurements of the electron density in these regimes also reveal appreciable plasma losses from within the separatrix. Moreover,

characteristic features of the dissipative regime include the conservation of sections of high field gradient in the plasma, a rapid decrease in the trapped flux  $\Phi$  and a correlation between  $d\Phi/t$  and bursts of X-ray emission.

5. The experimental results show that in unfavourable regimes the losses do not cease when shaping of the closed structure is completed. Thus, the common features of the topology of closed traps such as those shown in Figs 1a and b by no means imply universality with regard to heating and losses. An analysis shows that, of the various mechanisms of anomalous dissipation during the shaping phase of the closed configuration, an important role may be played by ion-acoustic turbulence. In unfavourable regimes, anomalous transport mechanisms (annihilation, energy losses) may be self-sustaining in the end regions of an elongated torus or may even extend over the total longitudinal dimension. In addition, appreciable losses may arise from contamination of the plasma and these increase particularly when the shaping process is uncontrolled. In the presence of a high carbon concentration (2%), local annihilation of the magnetic field may occur within  $10^{-6}$  s. These losses are suppressed by forming a structure of the type shown in Fig. 1a during the initial phase and sustaining this throughout the process, combined with radial expansion of the plasma under conditions of high-power shock heating of the ions.

#### REFERENCES

- [1] ES'KOV, A.G., KURTMULLAEV, R.Kh., MALYUTIN, A.I., SEMENOV, V.N., CHERNYAKOV, A.L., in *Controlled Fusion and Plasma Physics (Proc. 6th Europ. Conf. Moscow, 1973)* 595.
- [2] ES'KOV, A.G., et al., in *Plasma Physics and Controlled Nuclear Fusion Research (Proc. 7th Int. Conf. Innsbruck, 1978) Vol. 2, IAEA, Vienna (1979)* 187.
- [3] KURTMULLAEV, R.Kh., MALYUTIN, A.I., SEMENOV, V.N., *Reactor Aspects of the Compact Torus Fusion System with a Self-Contained Combustion Chamber (Proc. 2nd All-Union Conf. Engineering Problems of Fusion Reactors, Leningrad, 1981)*.

#### DISCUSSION

M. TUSZEWSKI: What limits the plasma confinement to a few micro-seconds? Is an equilibrium ever reached?

V.P. SMIRNOV: The principal task in this paper was to find the optimum conditions for the formation of a compact torus. For this reason, the experiments were conducted without a crowbar, and this also determined the confinement time. As to the achievement of equilibrium, the rise time  $\tau_s \sim L/2c_s$  is less than the characteristic time of the process, T, although there is no great margin in the parameter  $\tau_s/T$ .



**Session N**

**INERTIAL CONFINEMENT III**

Chairman

T.F. GODLOVE

USA

Papers N-6-1 and N-6-2 were presented  
by H. Herold as Rapporteur

## INERTIAL FUSION RESEARCH BASED ON PULSED POWER

G. YONAS

Sandia National Laboratories,  
Albuquerque, New Mexico,  
United States of America

### Abstract

#### INERTIAL FUSION RESEARCH BASED ON PULSED POWER.

PBFA II, with design parameters of 3.5 MJ and 100 TW, is being designed to allow inertial fusion ignition experiments using imploding foils or light ion beams. Flexibility is being retained to implode a cylindrical foil through magnetically insulated power concentration at 30 MA or to drive one or more ion diodes operating in the 10 MV range. In both cases the goal is to deliver  $100 \text{ TW}\cdot\text{cm}^{-2}$  and 1 MJ to a target in order to investigate ignition and possibly breakeven. Imploding foil data on Proto II have demonstrated that electromagnetic energy can be efficiently converted into foil kinetic energy with the output increasing as the square of the foil current. Experiments at Sandia National Laboratories have reached 60 kJ at 5 MA with the foil imploding in 80 ns and stagnating in 10 ns. This implosion demonstrates adequate stability, and modelling has shown that this behaviour should extrapolate to higher currents if the implosion time is less than 100 ns. To extend the scaling data to 8 MA, Proto II has been modified by extending magnetic insulation to inhibit insulator flashover. One-TW proton diodes have delivered about  $2 \text{ TW}\cdot\text{cm}^{-2}$  to 3 mm diameter targets using ballistic focusing limited by beam divergences of typically 20 mrad. This divergence is induced by instabilities in the electron-ion flow, non-uniformities in the anode plasma, or a combination of these effects. Further increases in intensity can be achieved with increases in voltage and ion mass, as well as with beam bunching. Analytical models indicate that beam focusing increases with the square of the voltage and that heavier ions such as  $\text{C}^{+2}$  or  $\text{Li}^{+1}$  are required to obtain the correct stopping power at  $>10 \text{ MV}$ . Correlation with analytical scaling models and electromagnetic code simulations is continuing. PBFA II will be capable of operating over a wide voltage range to accommodate the different options, with scaling experiments on PBFA I providing the basis for the selection.

### INTRODUCTION

Given success in efficient energy absorption, avoidance of preheat, and achievement of symmetric and stable implosions, ICF breakeven will probably require a 1-MJ,  $\sim 100\text{-TW}$  driver. Pulsed power devices, developed initially as low-cost, relativistic electron beam accelerators, have been converted with minor modifications and minimal energy losses into light ion beam accelerators and imploding foil drivers. Such devices are being used to investigate the power concentration issues that must be resolved before ignition experiments can be carried out.

Sandia National Laboratories' HydraMITE and Proto I (1 TW), Proto II (10 TW), and PBFA I (30 TW) are being used to establish the relevant scaling laws. PBFA II will have sufficient flexibility to operate as either a foil driver or as a light ion accelerator. Additional ion beam experiments are underway at the Naval Research Laboratory (NRL) and at Cornell University. These experiments should permit the selection of the optimum PBFA II approach in 1984—operation beginning in 1986.

Unlike the situation with lasers, energy deposition is not a principal physics question. The stopping power of light ions has been calculated, including the effects of bound and free electrons.<sup>[1]</sup> Confirmation of this classical deposition behavior has been obtained at 500 kA/cm<sup>2</sup> using measurements of target hydrodynamic response,<sup>[2]</sup> and at 50–250 kA/cm<sup>2</sup> using neutron time-of-flight.<sup>[3]</sup> Since roughly a factor-of-ten higher current densities will be needed for ignition, we must consider questions of possible streaming instabilities that might lead to anomalous effects such as acceleration of background electrons to high velocities. A review of linear stability theory of ions propagating through homogeneous media has shown no destructive effects.<sup>[4]</sup> Stopping power estimates for various species show that 3-MeV protons, 25-MeV lithium, or 60-MeV carbon will provide the needed stopping power to carry out ignition experiments; moreover, the PBFA II voltage range will accommodate these ion species. Thus, our emphasis is to demonstrate production and focusing of the requisite beam onto the target.

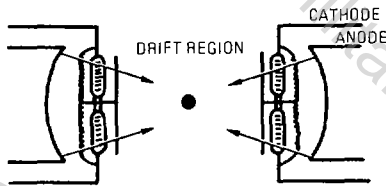
A similar situation applies to the imploding foil approach. Here, we expect to be able to couple the energy from a pulsed power device directly to a foil at a power density  $>10^{12}$  W/cm<sup>2</sup>, using magnetic self-insulation in vacuum. The foil kinetic energy can be converted to thermal radiation during the plasma stagnation phase. The radiation is then used to ablatively implode a nearby spherical pellet. Again, the issue appears to be that of concentrating the output power rather than that of energy deposition: the dominant physics question is the stability of the imploding foil.

We plan to investigate the required scaling of power concentration with foils up to 130 kJ on Proto II and with ions up to 300 kJ on PBFA I before proceeding with one option toward the goal of ignition at the megajoule level on PBFA II. In preparation for these ignition experiments we expect to carry out preliminary target experiments on Proto II and PBFA I. Target design and long-term target fabrication technology are being developed in collaboration with the Los Alamos and Lawrence Livermore National Laboratories.

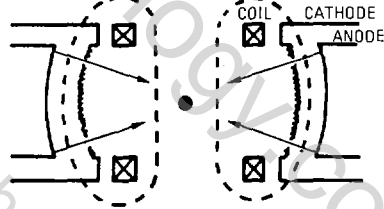
#### DISCUSSION

In 1979 Sandia made the decision to change program emphasis from electron beams to light ions and imploding foils. Even though we had obtained confirmation of enhanced magnetic stopping of electrons, target design calculations still indicated

(a) AMPFION DIODE (ADDITIONAL FIELD FROM SELF-EXCITED COIL)



(b) APPLIED FIELD (ADDITIONAL FIELD FROM EXTERNALLY EXCITED COIL)



(c) PINCH REFLEX (SELF-MAGNETIC FIELD)

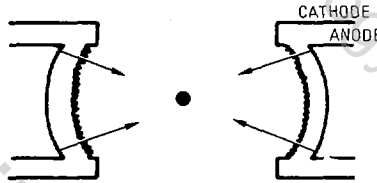


FIG.1. Three ion diodes are being investigated to determine optimum approach for PBFA II. The cylindrical geometry employed on PBFA I is shown.

substantial energy penalties because of excessive preheat. The scaling for both the ion and foil approaches, however, formed a more promising basis for projecting ignition. Substantial progress has subsequently validated that decision.

Our approach to ion beam concentration on PBFA II will be through the use of ballistic focusing. Although beam transport over distances of several meters is necessary for repetitive pulse application, it is not essential for demonstrating ignition. Thus, our attention is being directed toward obtaining beams of high intensity with sufficiently low divergence and creating force-free drift conditions between the cathode and the target to permit beam convergence. All of the diodes being investigated utilize a magnetic field tangential to the anode in order to increase the path length for electrons relative to that of the ions and thereby to increase the ion-to-electron current ratio. These ion diodes differ in the detailed methods for applying the magnetic field and for providing the plasma that supplies the ions. Three specific diode types are under investigation: (1) Ampfion, [5] (2) applied field, [6] and (3) pinch reflex [7] (Fig. 1). Before explaining the status of each diode we first define the criteria used in evaluating their performance.

A suitable diode must have a dense, stable, high-purity, and spatially uniform anode plasma. The magnetic field must trap an electron cloud that can act as a virtual cathode to extract the ion beam at high current density. Finally, we must provide a plasma to charge and current-neutralize the beam during transit

from the cathode to the target. The intensity on target is given by the product of the beam-bunching factor, the beam power brightness ( $\beta$ ), the fraction of the solid angle subtended by the diode surrounding the target (approximately one half), and the fraction of ions that hit the target (approximately one half). For example, a beam with a 10-mrad divergence could be focused onto a 0.5-cm radius target from a distance of 50 cm. Beam bunching with such a geometry can afford a factor-of-two-to-four increase in beam intensity, which should compensate for the low angular distribution and the portion of the solid angle not available. Thus,  $\beta$  should be between one and four times the desired intensity on target, depending on the degree of bunching.

In order to implode targets at the MJ level in 10 ns with ablation velocities of  $2 \times 10^7$  cm/sec, 20 MJ/g must be deposited. With particle ion ranges of 20 mg/cm<sup>2</sup>, we require a beam intensity of 40 TW/cm<sup>2</sup>. The beam brightness,  $\beta$ , equals  $J_D V / \theta^2$ , where  $J_D$ ,  $V$  and  $\theta$  are the current density, accelerating potential, and divergence half angle at the diode. An example of postulated PBFA II diode conditions would be  $J_D = 10^3$  A/cm<sup>2</sup>,  $V = 10^7$  V,  $\theta = 10$  mrad, giving a  $\beta \approx 100$  TW/cm<sup>2</sup> rad<sup>2</sup>. Several proton diodes have already demonstrated local divergences of approximately 20 mrad at an operating voltage of  $\approx 1$  MV. The most pressing issue is to determine the scaling of the beam divergence angle with voltage and mass. For instance, if the divergence results from simple magnetic deflection or irregularities in the anode plasma, the needed level of brightness should be reached at  $10^7$  V by extrapolation from existing data.

Focusing experiments are under way on Proto I and PBFA I in the 1- to 2-MV range. In order to operate PBFA I as an ion accelerator, we have reversed the polarity of half of the modules in the pulse-forming section and connected the output vacuum transmission lines in a series-parallel arrangement with a single, barrel-shaped diode connected to this "current manifold".

The Ampfion diode uses a self-excited field coil that provides a spatially uniform magnetic field in the accelerating gap. This coil (shown integral with the cathode in Fig. 1a) limits the spatial extent of the magnetically nonneutralized region and consequently minimizes beam deflection. In Ampfion experiments on PBFA I employing a dielectric flashover plasma source, initial data at  $\approx 0.8$  MV has given a beam brightness of  $\approx 1$  TW/cm<sup>2</sup> rad<sup>2</sup>. By injecting plasma into the drift region, excellent current neutralization was demonstrated. Attempts to scale these results to higher voltage have shown a high sensitivity to low levels of prepulse. Parallel experiments on HydraMITE using plasma erosion switches to eliminate prepulse have shown a 0.5-cm diameter damage pattern on a target placed at the 20-cm design focal length of the diode, indicating reproducible and stable beam behavior. Additional steps are being introduced on PBFA I to further reduce the prepulse level before further scaling studies are undertaken.

If the applied field is allowed to enter the drift region, Fig. 1b, it can impede the co-moving flow of current neutralizing

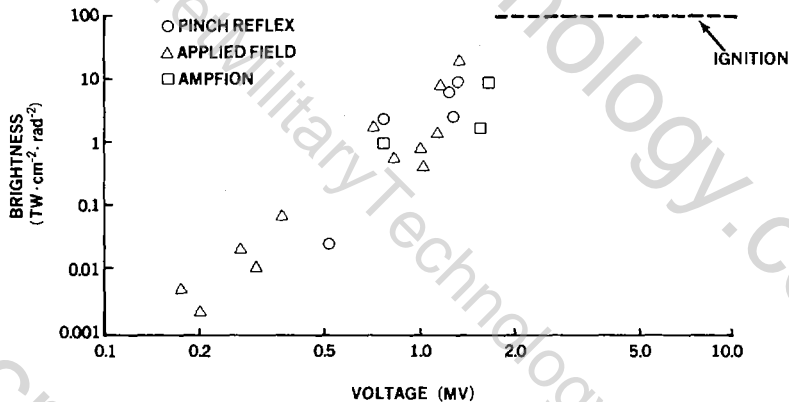


FIG.2. A compilation of data for the three candidate diode approaches showing that beam brightness has improved with voltage and the introduction of improvements in diode design.

electrons. Experiments on Proto II, with transport in a vacuum drift region of ion beams above the Alfvén current demonstrated that focusing was extremely limited. A drift region filled with argon at  $\approx 4$  torr has now been employed with a 4.5-cm radius diode on Proto I, demonstrating 90% current neutralization and well-behaved ballistic focusing onto 3-mm-diam targets giving  $\approx 2$  TW/cm<sup>2</sup> and radiation temperatures of 30–40 eV.<sup>[8]</sup> The intrinsic beam brightness is  $>10$  TW/cm<sup>2</sup> rad<sup>2</sup> at 1.4 MV, and this diode looks promising for application on PBFA I and PBFA II.

The pinch reflex diode (Fig. 1c) has no field coils but relies on the combined self-magnetic field of the leakage electron and ion flow to limit the total electron current. Current neutralization is provided by a gas-filled region separated from the vacuum diode by a thin foil. This diode has been extensively studied in the coaxial geometry at NRL, and a 25-cm diam barrel-shaped geometry is being jointly developed by Sandia and NRL for its use on PBFA I.<sup>[9]</sup> Experiments at 8.0 TW and 2.0 MV have shown a brightness of  $\approx 1.0$  TW/cm<sup>2</sup> rad<sup>2</sup>, based on a local divergence of approximately 60 mrad. The macroscopic scaling agrees with existing models, but large-scale nonuniformities indicate irregular anode plasma formation. Steps are being taken to provide an improved ion source for this diode.

Thus all three diodes have given promising brightness data at  $\approx 1$  MV. We have used simple analytical models to describe the potential causes of divergence, and we expect the brightness of these diodes to scale with the square of the voltage. Figure 2 is a collection of brightness data which is not inconsistent with at least quadratic scaling. Unfortunately, in view of the extremely extremely varied conditions represented, we cannot as yet conclusively resolve the scaling issue. In addition, our simple models cannot deal with microscopic instabilities that may introduce

surprises as we extend our voltage range. Electromagnetic particle codes are now being developed that could have a dramatic effect in helping to elucidate these phenomena.[10]

Even given the needed level of diode stability to achieve adequate brightness levels, we must also produce several thousand  $\text{cm}^2$  ion sources with densities of  $10^{13}$  -  $10^{16}/\text{cm}^3$ . Our studies with active devices such as plasma guns or arrays of capacitively driven plasma arcs are emphasizing the production of adequate plasma purity, density and uniformity. In our early tests of multiple plasma arcs we found that neutrals were being ionized in the diode, leading to rapid impedance collapse. A new source has used time-of-flight separation to solve this problem, and an adequate  $\text{C}^{+2}$  source as needed for Ampfion on PBFA II is now available.[11]

The simpler, passive dielectric flashover sources have been used in applied field diodes for several years. Using lithium nitrate in the heated anode of this type of diode, we have produced 300-kA lithium beams with a proton impurity level of  $< 10\%$ . [12] This approach has also been extended to the Ampfion geometry and may be employed on PBFA I. Because of the rather high second ionization potential of lithium, we should also be able to obtain high charge state purity. If sufficient uniformity can be obtained over large areas, the flashover source will be the most straightforward to use. Nevertheless, the dense anode plasma from such a source is not optimal. A lower density plasma used with a large-radius diode would permit magnetic pressure to increase the anode-cathode gap during the pulse, leading to voltage-ramping and beam-bunching without the use of special pulse-forming techniques. The passive and active ion source approaches are under continuing development, and we are investigating other methods.

Imploding-foil research has progressed rapidly since its inception at the Air Force Weapons Laboratory in 1973. As a result of an extensive series of scaling experiments on Proto II over the last few years, we have found that the output from the imploded plasma scales with the square of the current. A 10-ns radiation pulse has been produced with an 80-ns, 5-TW input pulse.[13] This behavior is consistent with limited growth of the hydromagnetic instability. Estimates indicate that adequately stable implosions and short thermalization times will require drive times less than a few hundred ns and possibly less than 100 ns.[14] A possible extension of this operating range may be possible using a modest gas fill for stabilization.[15] Experiments are beginning on Proto II at the 10-TW level, using a low-inductance diode that requires self-magnetic flashover inhibition[16] of the vacuum interface to accomplish the needed level of power concentration. If these experiments are successful, an additional factor-of-four higher current will still be needed for ignition experiments on PBFA II.

With 36 modules PBFA II will operate at a voltage level of 4 MV, but reconnection of the multiple modules will permit a wide range of operating conditions from 2-16 MV at greater than

90 TW<sup>[17]</sup>. Higher voltages of up to 26 MV will be available at somewhat reduced output power. New technologies used in PBFA II, including laser-triggered switching and "double-bounce" charging, are to be first tested in a single-module test-bed. A new laboratory building to house PBFA II is under construction, and we plan to continue operation of PBFA I until PBFA II becomes operational in 1986.

Both the ion and foil approaches to ignition will have an inherently low experimental data acquisition rate because of damage to nearby diode components. This situation would be undesirable for a high-gain Target Development Facility and would prevent future energy applications. For these reasons we have been studying methods of transporting beams over several meters in a background gas. The gas in the chamber would provide wall protection from xrays and debris, and studies indicate that a wall structure can be designed to withstand the blast loading.<sup>[18]</sup> The transport approach that has received the most attention is beam confinement in preformed, current-carrying plasma channels. Wire and laserinitiated channels and wall-confined discharges, studied at Sandia and NRL, have shown that beam brightness can be maintained over several meters, given reasonable channel conditions. Other approaches which could considerably simplify reactor concepts would require beams of high brightness from either high-voltage single-stage or multiple-stage ion accelerators.<sup>[19]</sup> Under suitable conditions it is conceivable to propagate a magnetically self-confined beam or even transport a beam ballistically. These long-term issues should emerge more clearly as the immediate questions of power concentration are answered.

#### CONCLUSION

Light ions and imploding foils appear to be capable of creating the required drive conditions for ignition experiments on PBFA II. Scaling of these approaches on Proto II and PEFA I is providing the information necessary to proceed with the final design of PBFA II. Once the power concentration issues are resolved on PEFA II, we expect that the challenging problems of implosion hydrodynamics can be confronted with sufficient diagnostics to determine the feasibility of ignition.

#### REFERENCES

1. MEHLHORN, T. A., J. Appl. Phys. 52 (1981) 6522.
2. WIDNER, M. M., MEHLHORN, T. A., PERRY, F.C., BURNS, E. J. T., and FARNSWORTH, V. A., Jr., Comments on Plasma Phys. 2 4 (1982).
3. YOUNG, F. C., GOLDSTEIN, S. A., STEPHANAKIS, S. J., and MOSHER, D, 8th IEEE Int. Conf. on Plasma Science, Santa Fe, NM (1981).

4. SWEGLE, J. A., Sandia National Laboratories, SAND-82-0072 (1982).
5. MENDEL, C. W., MILLER, P. A., QUINTENZ, J. P., SEIDEL, D. B., and SLUTZ, S. A., 4th Int. Topical Conf. on High Power Electron and Ion Beam Research and Technology, Palaiseau, France (1981).
6. JOHNSON, D. J., BURNS, E. J. T., QUINTENZ, J. P., BIEG, K. W., FARNSWORTH, A. V., MIX, L. P., and PALMER, M. A., J. Appl. Phys. 52 (1981) 1968.
7. COOPERSTEIN, G., MEYER, R. A., MOSHER, D., OLIPHANT, W. F., SANDEL, F. L., STEPHANAKIS, S. J., YOUNG, F. C., and KAROW, H. U., *ibid.* Ref. 5; and OLSEN, J. N., ROSENTHAL, S. E., MIX, L. P., LEEPER, R. J., ANDERSON, R. J., DREIKE, P. L., SEIDEL, D. B., and QUINTENZ, J. P., Sandia National Laboratories (private communication).
8. JOHNSON, D. J., BURNS, E. J. T., SLUTZ, S. A., DREIKE, P. L., and FARNSWORTH, A. V., Sandia National Laboratories (private communication).
9. OLSEN, J. N., ROSENTHAL, S. E., MIX, L. P., LEEPER, R. J., ANDERSON, R. J., DREIKE, P. L., SEIDEL, D. B., and QUINTENZ, J. P., Sandia National Laboratories (private communication).
10. DROBAT, A., Science Applications, Inc., and POUKEY, J. W., Sandia National Laboratories (private communication).
11. MILLS, G. S., Sandia National Laboratories (private communication).
12. ANDERSON, R. J., Sandia National Laboratories (private communication).
13. MCDANIEL, D. H., Sandia National Laboratories (private communication).
14. HUSSEY, T., and MCDANIEL, D. H., Comments Plasma Phys. Controlled Fusion 6 5 (1981) 177.
15. HUSSEY, T., Sandia National Laboratories (private communication).
16. VANDEVENDER, J. P., MCDANIEL, D. H., NEAU, E. L., MATTIS, R. E., and BERGERON, K. D., J. Appl. Phys. 53 6 (1982) 4441.
17. VANDEVENDER, J. P., and MARTIN, T. H., Sandia National Laboratories (private communication).
18. MOSHER, D., HOVINGH, J., COOK, D., FRANK, T., MOSES, G., Nucl. Tech. Fusion 1 (1981) 302.
19. HUMPHRIES, S., Jr., ANDERSON, R. J., FREEMAN, J. R., LOCKNER, T. R., POUKEY, J. W., RAMIREZ, J., J. Nuc. Instrum. Methods 187 (1981) 289.

## LIGHT-ION INERTIAL CONFINEMENT FUSION RESEARCH AT NAVAL RESEARCH LABORATORY\*

G. COOPERSTEIN, R.J. BARKER\*\*, D.G. COLOMBANT,  
A. DROBOT\*\*\*, Shyke A. GOLDSTEIN\*\*, R.A. MEGER\*\*,  
D. MOSHER, P.F. OTTINGER\*\*, F.L. SANDEL\*\*\*,  
S.J. STEPHANAKIS, F.C. YOUNG  
Naval Research Laboratory,  
Washington, D.C.,  
United States of America

### Abstract

#### LIGHT-ION INERTIAL CONFINEMENT FUSION RESEARCH AT NAVAL RESEARCH LABORATORY.

High-brightness proton beams (0.4 MA, 1 MV) have recently been extracted from 20 cm<sup>2</sup> axial pinch-reflex diodes (PRDs) mounted on the NRL Gamble II generator. A source power brightness of  $\geq 10 \text{ TW}\cdot\text{cm}^{-2}\cdot\text{rad}^{-2}$  was achieved in these experiments. A new barrel-shaped equatorial PRD that can be coupled to PBFA II has also been operated on Gamble II and has demonstrated 50% proton efficiency with predominantly azimuthally symmetric charged-particle flow. In other experiments the stopping power of deuterons in hot plasmas was measured using a PRD on Gamble II. Results show about 40% increase in stopping power over that in cold targets when the beam was focused to about  $0.25 \text{ MA}\cdot\text{cm}^{-2}$ . Research is also being performed on transporting ion beams in large-diameter channels ( $\geq 2.5 \text{ cm}$ ) and on a post-transport plasma-filled magnetic focusing section to bring the beam to pellet dimensions.

### 1. INTRODUCTION

Recent NRL experiments and theory have investigated key aspects of two ignition-system configurations for light-ion-drivers on Sandia's PBFA II [1]. The first configuration uses groups of modules to drive small-area disc-like axial ion diodes each of which focuses a beam into a z-discharge transport channel about 2 m long and a few cm in diameter [2]. Each channel is terminated in a short, higher-current discharge which magnetically focuses the beam onto the pellet [3], and

---

\* Work supported by US Department of Energy, Washington, D.C., and Defense Nuclear Agency, Washington, D.C.  
\*\* JAYCOR Inc., Alexandria, Virginia.  
\*\*\* Science Applications Inc., McLean, Virginia.

thus allows larger-diameter beams to be transported and then focused. Such a system is schematically illustrated in Fig. 1. The second configuration ties all 36 modules to a single barrel-shaped radial ion diode with 1 m dimensions surrounding the pellet located on the diode axis of symmetry.

Section 2 will review recent high-brightness diode experiments on Gamble II. The new barrel-shaped equatorial PRD concept and preliminary Gamble II results will be reviewed in Section 3. Section 4 will discuss the energy-loss experiments of deuteron beams in subrange Mylar and aluminum targets. Finally, transport considerations in large-diameter channels, and final focusing concepts and experiments, will be discussed in Section 5.

## 2. ION BEAM BRIGHTNESS STUDIES

Beam power brightness at the diode imposes the ultimate limit on the ability to focus ion beams onto targets. The PRD, which has been previously described [4,5], has been studied with respect to its performance as a source of high-current-density, low-divergence ion beams. Electron-filamentation instabilities, which may occur in the electrode plasmas and vacuum gap are currently under investigation. Changes in diode geometry and electrode materials are being investigated experimentally in order to determine their effects on the instabilities.

In recent 1-TW diode experiments on Gamble II, .6 TW proton beams were extracted from 20-cm<sup>2</sup>-area anode foils. The ion beam brightness was measured crudely by a shadowbox technique [5,6] that uses multiple pinhole images of the ion beam. With the multiple hole shadowbox one can reconstruct the ion source pattern and its divergence. The ion source exhibited 10 to 20 beamlets 1 cm in diameter for this small-radius diode. The beam divergence changed drastically when the gap,  $\Delta$ , between the anode and the cathode inner foil was changed. The half angle of the diverging beam cone,  $\delta\theta$ , was measured to be  $\approx .1$  rad at a gap of 1.5 cm and  $\approx .05$  rad at a gap of .5 cm.

A simple calculation to explain beam divergence versus gap width was performed assuming that the total ion beam current (450 kA) was distributed equally among 15 sources each having a diameter of 1 cm. Self-pinching of these ion beamlets by self-magnetic fields would result in  $\delta\theta = .08\Delta/\sqrt{V}$  for protons at a voltage  $V$  measured in MV. The experimental results at  $V = 1.2$  MV show that  $\delta\theta$  agrees well with the predicted value at the

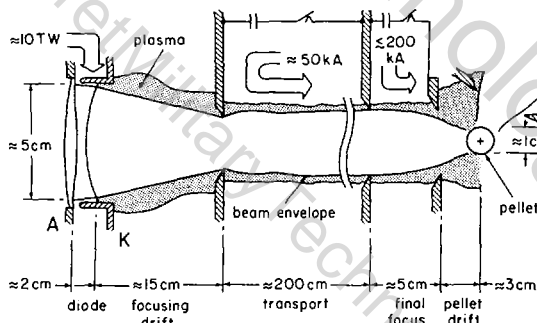


FIG. 1. Schematic of modular light-ion ICF system.

larger gap of  $\Delta=1.5$  cm. At the smaller gap, however, the experimental divergence cannot be explained by this magnetic self-pinching effect.

Two other mechanisms which could increase the beam divergence have been identified. The first is associated with plasma hydrodynamics when the anode plasma is formed at discrete spots and expands in a two-dimensional manner, generating bulges on the anode. Such spotty structure is clearly seen in the shadowbox pinhole images. The second mechanism is filamented electron beam flow. The resultant space charge structure introduces azimuthal and radial components to the electric field in addition to the axial field. The filamented electron flow could also result in azimuthal magnetic deflections of the beam ions.

The beam brightness ( $JV/\delta\theta^2$ ) observed for  $V = 1.2$  MV,  $J = 20$  kA/cm<sup>2</sup> and  $\delta\theta \approx .05$  rad is  $\approx 10$  TW/cm<sup>2</sup>rad<sup>2</sup>. Holding  $J$  constant, scaling up the voltage to 3 MV, reducing  $\delta\theta$  appropriately ( $\delta\theta \approx 1/\sqrt{V}$ ), and assuming a factor-of-4 bunching during transport without brightness loss, leads to a modular-beam brightness of about 250 TW/cm<sup>2</sup>rad<sup>2</sup>. If 40% of the solid angle surrounding a pellet is subtended by final-focus exit apertures, on-target modular power densities approaching 100 TW/cm<sup>2</sup> might then be achievable with existing PRDs.

### 3. EQUATORIAL-PINCH-REFLEX DIODE (PRD)

A new version of the NRL PRD has been designed to operate on the radial triplate geometry of Sandia's PBFA I. A conceptual schematic is shown in Fig. 2. This diode produces two cylindrically symmetric sheet beams of electrons which flow from top and bottom by self-magnetic pinching and reflexing

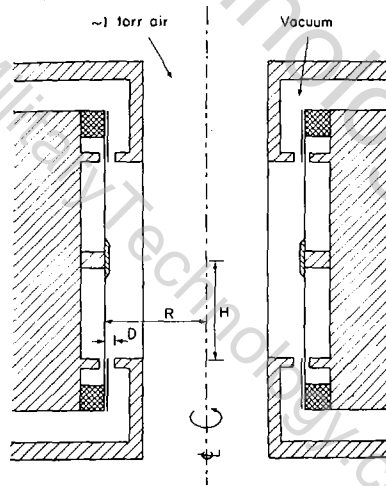


FIG.2. Equatorial pinch reflex diode.

action on the anode foil to a common line pinch around the equator of the diode, hence the name equatorial-pinch-reflex diode (EPRD).

Although this diode appears to be a simple topological variation of the conventional PRD, there are basic conceptual differences. There is no electron-space-charge-density enhancement as occurs with the conventional axial PRD because there is no radially converging electron flow towards the diode axis. This lack of electron convergence leads to a constant ion current density rather than one that increases inversely with the distance from the diode axis as in the axial PRD; hence the EPRD has better focusing properties.

Another major difference and advantage of the EPRD over the conventional PRD is that the ratio of ion current to electron current,  $I_i/I_e$ , is decoupled from the diode impedance  $Z$ . For a given anode-cathode gap spacing,  $D$ , and diode radius,  $R$ , the impedance of an EPRD of height  $H$  is proportional to  $D/R$  as with the conventional PRD, however,  $I_i/I_e$  is proportional to  $H/D$  (i.e. the electron path length/the ion path length) and is independent of diode radius or diode impedance. Thus, for any current equal to or above the critical current, the ion production efficiency can be made arbitrarily large by increasing the separation between the two disc cathodes. These properties were verified using a particle-in-cell code [7].

The EPD has been tested on NRL's Gamble II generator by driving only the upper half of the diode shown in Fig. 2 in a coaxial-feed geometry. The anode radius was 7 cm and typical anode-cathode gaps were 3.5 to 6 mm. Initial experiments [8] have shown the diode to be an efficient ion source and a good electrical match to the accelerator. Net ion currents on the order of 400 kA have been measured with diode impedances of 1.5-2  $\Omega$ . Predominantly azimuthally symmetric electron and ion current flow has been observed. The diode impedance has been shown to be a linear function of anode-cathode gap but practically independent of diode axial height as predicted by theory. Shadowbox results show a time-averaged half-angle divergence of 1-2° from areas not containing filaments. Experiments to reduce beam filamentation are in progress. Sandia National Laboratory is presently testing a high-power diode of similar design on PBFA-I [9].

#### 4. ENERGY-LOSS EXPERIMENT

Theoretical research [10] indicates that, at the ionization levels of ICF pellet plasmas, the stopping power of light ions may be enhanced by a factor of two over that in the cold target. In this section, measurements of the energy loss of MeV deuterons in plasmas formed by focusing intense Gamble II ion beams (1 MeV, .2 MA, 20 ns) onto subrange-thick targets are presented. The results demonstrate that the stopping power of the heated target is enhanced over that of the cold target.

For these energy-loss measurements, a spherically contoured PRD is used to produce a 250-kA/cm<sup>2</sup> focused deuteron beam while a planar anode foil version of the diode is used to produce a 50-kA/cm<sup>2</sup> deuteron beam. The .01 cm thick plastic anode foil is coated with deuterated polyethylene (CD<sub>2</sub>) to provide the deuterons.

The experimental technique for determining the deuteron-energy loss uses neutron time-of-flight (TOF) with a multilayered target [11]. The target consists of a subrange stopping foil sandwiched between .3- $\mu$ m and 1.0- $\mu$ m-thick layers of CD<sub>2</sub>. Measurements of the d-d neutron TOF from the two CD<sub>2</sub> targets are used to determine both the incident deuteron energy and the deuteron energy loss in the stopping foil on each shot. The thickness of the stopping foil is adjusted so that neutrons from the two CD<sub>2</sub> targets can be resolved. In these experiments, 6.4- $\mu$ m Mylar and aluminum stopping foils are used. The time interval between the peak of the ion power and the peak of the first neutron pulse determines the neutron

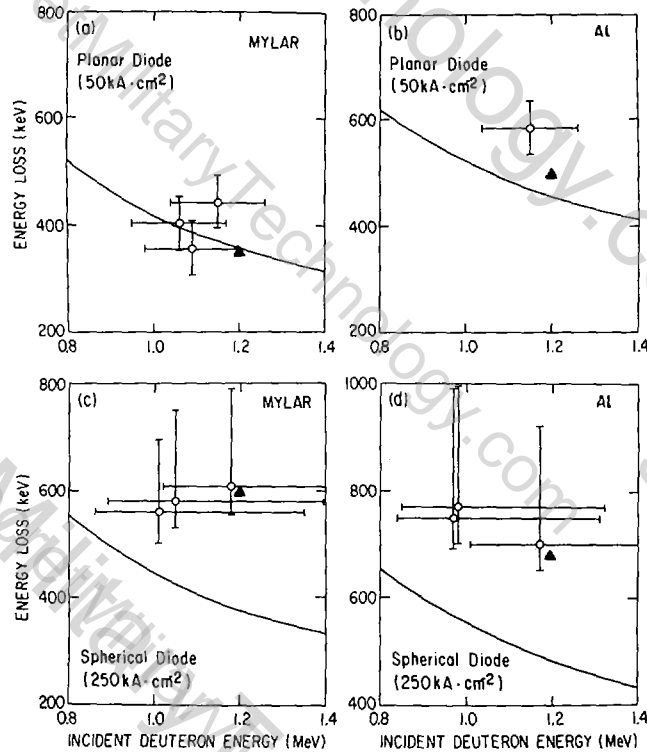


FIG. 3. Comparison of energy loss measurements with planar (a and b) and spherical (c and d) diodes with energy-loss curves calculated for cold target.  $\blacktriangle$ : calculated energy losses at peak power.

energy from the front  $\text{CD}_2$  target and, by kinematic calculation, the incident deuteron energy. The time separation of the two neutron peaks provides a direct measure of the deuteron energy loss in the stopping foil.

The results of stopping-power measurements using both planar and spherical diodes are presented in Fig. 3. For each case, the measurements are compared to the cold-target energy loss deduced from measurements of stopping cross-sections by Andersen and Ziegler [12]. The measured energy losses are significantly larger than cold-target values in all cases except for the planar diode with a Mylar target. In this case, the measurements are consistent with cold-target values.

The deuteron energy losses deviate from that in a cold target when sufficient ionization occurs in the stopping

medium. Hydrocode calculations which model this experiment [13] indicate that the target has expanded to about 2 mm thickness at the peak of the power pulse, and that the electron temperature is 4 to 5 eV at 50 kA/cm<sup>2</sup> and 13 to 17 eV at 250 kA/cm<sup>2</sup> for an aluminum stopping foil. Similar results for Mylar are  $\approx$ 3 eV at 50 kA/cm<sup>2</sup> and 9 to 11 eV at 250 kA/cm<sup>2</sup>. The calculated energy losses at peak power are shown as solid triangles in Fig. 3, and are in reasonable agreement with the measurements. For the experimental conditions where a significant number of free electrons are produced in the stopping foil, the measured deuteron stopping is enhanced (Fig. 3b, c and d). If the energy deposition produces less ionization, the measured energy loss is consistent with cold-target stopping (Fig. 3a).

##### 5. TRANSPORT AND FINAL FOCUSING

Intense light-ion beam transport in z-discharge channels provides accelerator standoff from ICF targets and allows time-of-flight bunching of the beam to higher intensity. Stability constraints [14] combined with channel expansion and beam-energy loss constraints [15] define an operational window for ion transport. Results show that a larger operational window exists for the higher-atomic-weight species. This is a consequence of their lower currents at equivalent transported power levels. Raising the channel density somewhat above the optimum for minimum beam-energy loss during transport relaxes the two-stream and channel-filamentation stability constraints and the channel-expansion constraint while only slightly modifying the energy-loss constraint. Increasing the beam radius relaxes the two-stream stability constraint and considerably reduces the channel-expansion and beam energy-loss constraints.

It is determined that multi-terawatt beams can be transported a few meters in large-radius channels with beam divergence half angles of .1 to .2 radians. Such angles are presently attainable with PRDs. If time-of-flight bunching during transport and final focusing after transport are employed, less than 10 (and as few as 4) channels are required to deliver the power needed to ignite a pellet.

Theoretical results show factor-of-ten increases in final-focused ion-current density for beams transported in hollow channels. Channels which carry discharge current in the channel interior result in beam-brightness loss during transport and hence cannot be compressed as well by the final

focusing cell. Focusing cells which are  $1/8$  of an ion-betatron-wavelength long focus the beam an additional  $1/8$ -wavelength beyond the exit of the focusing cell. This 1-2 cm drift length is the stand-off distance separating the cell exit from the pellet. High plasma densities can be employed in the short-focusing cell without excessive beam-energy loss in order that the plasma-MHD response can be minimized.

A final-focus system was designed and fielded on the Gamble II accelerator [16]. A discharge of  $\approx 100$  kA was initiated by an external capacitor bank along the Lexan insulator which was filled with 5-10 torr of air. Channel currents were chosen to match a  $1/4$  betatron wavelength for the ions with the 8-cm channel length. A convex pinch-reflex type anode was used to partially offset the self-pinching of the ion beam in the diode and provide a nearly parallel trajectory injected ion beam. When aluminum witness plates were used, focusing was evidenced by rear-surface spall which only appeared over the exit-aperture region when the focusing current was turned on. Further experiments with shadowboxes placed downstream of the exit aperture confirmed that a well defined focal position existed and that no large-scale mixing of the ion orbits in the  $1/4$ -betatron-wavelength focusing cell occurred during focusing. Results agree well with theoretical predictions. Eventually, experiments will be performed with this final-focusing system placed at the exit of the transport system.

#### REFERENCES

- [1] KUSWA, G.W., QUINTENZ, J.P., SEIDEL, D.B., JOHNSON, D.J., MENDEL, Jr., C.W., BURNS, E.J.T., FEHL, D., LEEPER, R.J., PERRY, F.C., MILLER, P.A., WIDNER, M.M., and FARNSWORTH, Jr., A.V., in the Proceeding of the 4th Int. Conf. on High-Power Electron and Ion-Beam Research and Technology, Palaiseau, France (1981) p.3.
- [2] SANDEL, F.L., STEPHANAKIS, S.J., YOUNG F.C., and OLIPHANT, W.F., *ibid.*, p. 129; MOSHER, D., COLOMBANT, D.G., GOLDSTEIN, S.A., and OTTINGER, P.F., *ibid.*, p. 19; GOLDSTEIN, S.A., COLOMBANT, D.G., MOSHER, D., OTTINGER, P.F., and SANDEL, F.L., *ibid.*, p. 113.

- [3] OTTINGER, P.F., GOLDSTEIN S.A., and MOSHER, D., 1980 IEEE Int. Conf. on Plasma Science, Madison, Wisconsin (1980) p. 95.
- [4] GOLDSTEIN, S.A., COOPERSTEIN, G., LEE, R., MOSHER D., and STEPHANAKIS, S.J., Phys. Rev. Lett. 40 1504 (1978).
- [5] COOPERSTEIN, G., GOLDSTEIN, S.A., MOSHER, D., BARKER, R.J., BOLLER, J.R., COLOMBANT, D.G., DROBOT, A., MEGER, R.A., OLIPHANT, W.F., OTTINGER, P.F., SANDEL, F.L., STEPHANAKIS, S.J., and YOUNG, F.C., in Laser Interaction and Related Phenomena, edited by H. Schwarz, H. Hora, M. Lubin and B. Yaakobi, Vol. 5 (Plenum, New York, 1981), p. 105.
- [6] STEPHANAKIS, S.J., GOLDSTEIN, S.A., OTTINGER, P.F., MOSHER, D., Bull. Am. Phys. Soc. 26 921 (1981).
- [7] BARKER, R.J., and GOLDSTEIN, S.A., Bull. Am. Phys. Soc. 26 921 (1981).
- [8] SANDEL, F.L., private communication.
- [9] OLSEN, J.N., private communication.
- [10] MEHLHORN, T.A., J. Appl. Phys. 52 6522 (1981); NARDI, E., PELEG, E., and ZINAMON, Z., Appl. Phys. Lett. 39 46 (1981); MOSHER, D., in ERDA Summer Study of Heavy Ions for Inertial Fusion LBL-5543, 1976, p. 39.
- [11] YOUNG, F.C., 1982 IEEE Int. Conf. on Plasma Science, Ottawa, Canada (1982), p. 27.
- [12] ANDERSEN, H.H., and ZIEGLER, J.F., The Stopping and Ranges of Ions in Matter, Vol. 3, Pergamon Press, New York (1977).
- [13] MEHLHORN, T.A., private communication.
- [14] OTTINGER, P.F., GOLDSTEIN, S.A., and MOSHER, D., NRL Memo Report 4548, July 1981.
- [15] MOSHER, D., COLOMBANT, D.G., and GOLDSTEIN, S.A., Comments Plasma Physics 6 101 (1981).
- [16] MEGER, R.A., GOLDSTEIN, S.A., OTTINGER, P.F., MOSHER, D., STEPHANAKIS, S.J., and YOUNG, F.C., Bull. Am. Phys. Soc. 26 921 (1981).

## DISCUSSION

S. WITKOWSKI: You used electrodes a few centimetres from the target to get the necessary energy density on the latter. Do you think the required high-energy densities could also be reached with more distant electrodes?

G. COOPERSTEIN: Dr. Shyke A. Goldstein has put forward ideas for generating the required magnetic field and plasma parameters in close proximity to a pellet in a reactor environment. One concept involves the possible use of a long-pulse CO<sub>2</sub> laser to generate the hot electrons and plasma blow-off from the surface of the pellet. Another concept involves electrode structures as an extension to the pellet design. The current to these electrodes could be fed through plasma channels created by laser ionization.

C. YAMANAKA: Of the three diodes, pinch reflex, Ampfion, and applied B-fields, which yields the best performance in terms of figure of merit for brightness, divergence, deflection and neutralization? Which is best for your ICH machine?

G. COOPERSTEIN: At the present time it is difficult to choose between these diode concepts because they have all obtained similar power brightnesses and each has different advantages and disadvantages. More research and better understanding will be needed before a definite choice can be made between them. However, it is encouraging that such different diode concepts all work so well.

## RESEARCH PROGRESS IN INTENSE ION BEAM PRODUCTION FOR INERTIAL CONFINEMENT FUSION AT CORNELL UNIVERSITY\*

H. BLUHM<sup>†</sup>, J.B. GREENLY, D.A. HAMMER,  
B.R. KUSSE, J. MAENCHEN, A. MANKOFSKY,  
J. NERI<sup>†</sup>, R. PAL, T.J. RENK, G.D. RONDEAU,  
R.N. SUDAN

Laboratory of Plasma Studies,  
Cornell University,  
Ithaca, New York,  
United States of America

### Abstract

#### RESEARCH PROGRESS IN INTENSE ION BEAM PRODUCTION FOR INERTIAL CONFINEMENT FUSION AT CORNELL UNIVERSITY.

Recent results obtained in the generation of intense pulsed light ion beams and their application to inertial confinement fusion are described. Studies of time-integrated and time-dependent beam divergence using a magnetically insulated ion diode with a "flashboard" anode at  $\lesssim 10^{11}$  W diode power show a directionality which is apparently due to electron dynamics in the diode. Nevertheless, ion beams having divergence angle as small as  $0.5^\circ$  have been produced at  $>10^8$  W·cm<sup>-2</sup>. In another experiment with a similar diode, the anode plasma formation time varied with the detailed anode configuration, the diode voltage and the insulating magnetic field, with the longer times obtained at lower voltage and higher insulating magnetic field strength. The anode plasma density was determined to be in the  $10^{15}$ /cm<sup>-3</sup> density range and to move away from the anode at  $\approx 2$  cm· $\mu$ s<sup>-1</sup> in another similar experiment. Preliminary experiments performed on a  $10^{12}$  W accelerator show reasonable power coupling to a magnetically insulated ion diode, with  $>10^9$  W·cm<sup>-2</sup> beams at  $\approx 1.5$  MV being generated. Computer simulations suggest that if such a beam can be focused into a plasma channel, most of its energy can be delivered to a pellet one to two metres away. In experiments on the applied  $B_\theta$  diode, microwave radiation, ion production efficiency, and ion beam fluctuations all reach a maximum when the insulating magnetic field is about 1.4 times the critical field for magnetic insulation. Finally, relatively pure beams of heavy ions have been produced by making the anode with hydrocarbon-free dielectric material which contains the desired species together with other ions having substantially higher ionization potential. The sum of these results suggests that flashboard anodes operated at the few-MV level can be used to produce beams with properties suitable for inertial confinement fusion experiments on sufficiently powerful pulsed power generators.

\* Research supported by US Department of Energy Contract No. DE-AC02-77ET53005 and by Sandia National Laboratories, Albuquerque.

<sup>†</sup> Present address: Institut für Neutronenphysik und Reaktortechnik, Kernforschungszentrum Karlsruhe, Fed. Rep. Germany.

<sup>+</sup> Present address: Naval Research Laboratory, Washington, D C.

## 1. INTRODUCTION

Light-ion-beam-driven inertial confinement fusion requires the delivery of  $\geq 10^{13}$  W/cm<sup>2</sup> of beam power density to a  $\leq 1$  cm size pellet in a 10-30 ns pulse. This, in turn, requires that the beam source be capable of producing a low divergence angle beam ( $\approx 1^\circ$  mean angle) at  $10^9$ - $10^{10}$  W/cm<sup>2</sup>. The Cornell University program has been addressing this problem systematically by studying ion beam characteristics (uniformity, divergence, etc.) and the properties of the ion diode anode and cathode plasmas, as a function of operating parameters and diode configuration, first at power levels of  $10^{10}$ - $10^{11}$  W followed by scale up to  $10^{12}$  W on the recently installed LION accelerator. In this paper we report recent results of experiments performed at  $\leq 10^{11}$  W which have investigated the anode plasma turn-on rate and density, time-integrated and time-dependent properties of ion beams, and microwave emission, all from magnetically insulated diodes (MIDs) [1]. We also present preliminary experimental results obtained at  $\geq 3 \times 10^{11}$  W, and a brief description of the techniques required to produce heavy ion beams with MIDs. Finally, we address the question of the transport of an ion beam from the source to the pellet in a plasma channel with a brief discussion of computer simulation results.

The anode plasma ion sources in all of the experiments to be described here have been "flashboards", solid dielectric material mounted on the positive electrode of the MID either in the form of dielectric strips, or a dielectric sheet having an array of holes drilled in it, either with or without metal pins inserted in the holes. In either case, the dielectric discontinuities distort the electric field when the high voltage pulse is applied to the diode, thereby inducing a "surface flashover". It is intended that the resultant plasma will spread over the entire anode surface and provide an ion beam current density  $j_i$  given by the space charge limited flow value

$$j_i \approx 50 A^{-1/2} v^{3/2} d^{-2}, \text{ A/cm}^2 \quad (1)$$

where  $A$  is the ion mass relative to the proton mass,  $v$  is the diode voltage (megavolts) and  $d$  is the accelerating gap spacing (cm). Magnetic insulation, which prevents electron current from dominating diode power flow, requires that the applied magnetic field exceed the value

$$B^* = \left(\frac{2mV}{e}\right)^{1/2} (1 + eV/2mc^2)^{1/2} / d \quad (2)$$

where  $m$  and  $e$  are the electron mass and charge, respectively, and  $c$  is the speed of light, and all quantities are in mks units. Magnetically insulated diodes with flashboard anodes have been used to produce ion beams at  $>2 \text{ kA/cm}^2$  for 30 ns [2]. Results presented in this paper include the production of ion beams with divergence angle as small as  $0.5^\circ$  at power density in excess of  $10^8 \text{ W/cm}^2$  with a diode voltage of  $\leq 1 \text{ MeV}$ . This suggests that "flashboards" operated at higher voltage on a very high power generator can be used to achieve the necessary ion beam characteristics to demonstrate ion-beam-driven ICF.

## 2. ION BEAM QUALITY EXPERIMENTS

An extensive series of experiments on ion beam uniformity and divergence as a function of the details of the anode and cathode configurations, the diode voltage, and the insulating magnetic field strength, has been carried out using the diode shown in Fig. 1. This diode is similar to that described by Maenchen et al. [3] except that electrons emitted by cathode vanes (see Fig. 1) form a "virtual cathode" by  $E \times B$  drifting over the anode surface. The active anodes consisted of epoxy-filled groove structures having different groove widths and spacings, and oriented either parallel or perpendicular to the magnetic field. The diode was powered by  $\approx 100 \text{ ns}$  pulses at  $0.5\text{--}1.0 \text{ MV}$ , with total diode currents ranging from 50 to 110 kA. The ion current fraction ranged from 0.3 to 0.7, depending upon anode structure, voltage and insulating magnetic field strength. The ion beam was typically half protons and half singly charged carbon, as determined by nuclear diagnostics (carbon activation and prompt  $\gamma$  measurements), foiled Faraday cups and a Thomson parabola energy and  $q/m_i$  analyzer ( $q = \text{ion charge}$  and  $m_i = \text{ion mass}$ ).

Beam divergence was studied with both time-integrated and time-dependent diagnostics. The time integrated measurements using a screen mesh imaged on a damage target showed divergence angles typically ranging from  $0.5\text{--}1.5^\circ$ , depending upon the anode used and the shot parameters. Beam power brightness ( $j_i V / \theta^2$ , where  $\theta$  is the divergence angle) in excess of  $1 \text{ TW/cm}^2/\text{Sr}$  was achieved for higher voltage, better insulated shots. However, the time-dependent measurements, made using a metal plate with three pinholes followed by a scintillator which was viewed by a streak camera, showed that the beam had a time-dependent directional aiming error that degraded the beam brightness and which had its source in the diode. Figure 2 illustrates the following observations.

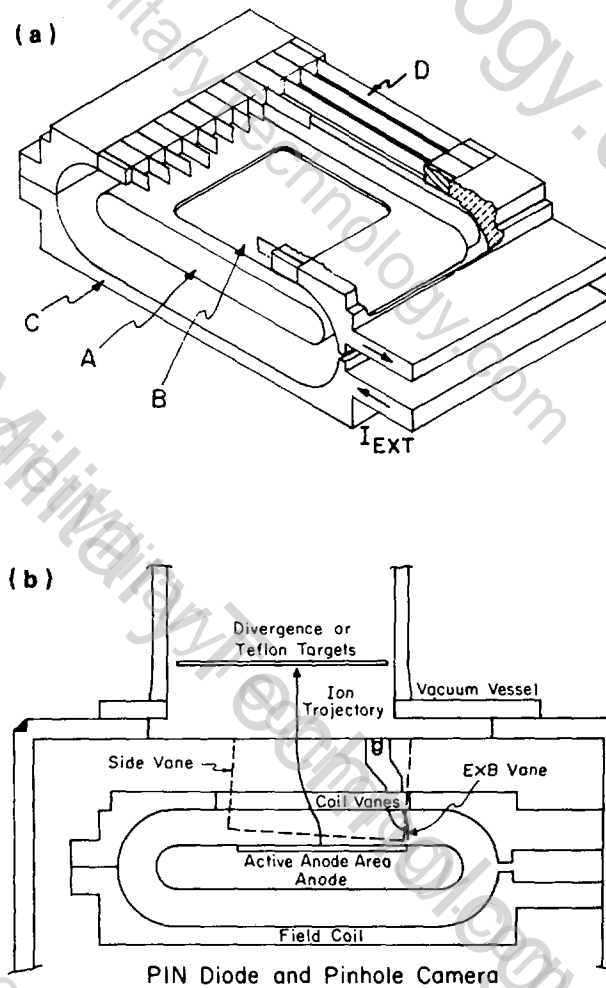


FIG.1. Two views of the diode used for time-integrated and time-dependent beam quality measurements.

(a) A cutaway view showing: A, the aluminium anode; B, the active anode (epoxy-filled groove) area; C, the cathode-coil which carries the current,  $I_{\text{ext}}$ , to produce the magnetic insulation field; and D, copper vanes to allow extraction of the ion beam.

(b) End view illustrating the vanes which inject electrons into the diode to form the virtual cathode and showing diagnostic locations and a typical ion trajectory.

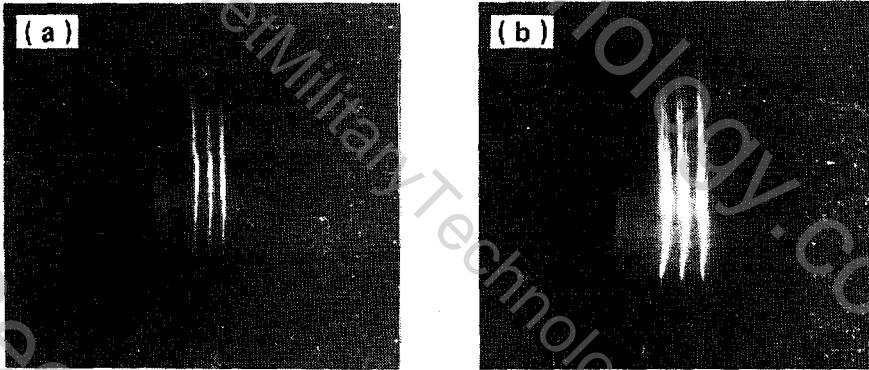


FIG.2. Two streak camera photographs illustrating the difference between the ion beam motion parallel (a) and perpendicular (b) to the applied magnetic field direction. The full visible streak time in both photographs is about 100 ns (magnifications are different).

Parallel to the applied magnetic field  $\vec{B}$ , the streak photographs showed single reasonably straight streaks with time-dependent width which is taken to be indicative of the beam divergence angle. Parallel to  $\vec{E} \times \vec{B}$  the beam exhibited time-dependent "aiming errors" which showed up on the streak photographs as oscillations and multiple beamlets within each streak. However, individual beamlets were narrower than those in the direction parallel to  $\vec{B}$ .

The directionality of the aiming error of the beam is believed to be due to the virtual cathode electron injection vane structure in the present diode. (It was not affected by a change in orientation of the epoxy-filled grooves in the anode.) The directionality in the beam divergence behavior was confirmed by the time-integrated targets. However, the angles which would be inferred from time-averaging the streaks were significantly larger than those obtained from the time-integrated targets. Time-of-flight of the ion beam from the diode to the scintillator and the relative sensitivity of the scintillator to protons and carbon ions indicate that the streak photographs were produced by the proton component of the beam. The beam component responsible for the low time-integrated divergence angles is believed to be the carbon ions, which would be substantially less sensitive to the beam's self-magnetic fields and/or electric fields produced by virtual cathode dynamics.

### 3. ANODE PLASMA STUDIES

Two experiments, also using MIDs similar to that of Maenchen et al. [3], have investigated the characteristics of the anode plasma. In one, the time evolution of the light from several epoxy-filled groove anode configurations was observed by fast streak and framing photography. Experiments were performed in the 300-600 kV voltage range with a 60 ns (fwhm) pulse having a 30 ns (10-90) rise time. It was found that the initial appearance, intensity, and rate of spread of light over the anode surface depended upon the width of the epoxy-filled grooves, their orientation with respect to the applied magnetic field, the applied field strength, and the accelerating voltage. Turn-on times varied from 20 to 40 ns, with the longer times occurring at the lower voltages and the higher insulating magnetic fields. Framing photographs suggested that the anode plasma did not fully cover the metal area between epoxy-filled grooves in the 50 ns pulse used in this experiment. Furthermore, the overall results implied that the surface flashover anode plasma formation process required electron bombardment of the anode surface in addition to electric field distortion, and that induced diamagnetic currents in the anode plasma played an important role in the early plasma formation process. Beam divergence measurements were also made on this experiment. The directionality of results was consistent with those in the previously discussed experiment. In addition, time-integrated measurements indicate that the groove edges caused the ions emitted there to have aiming errors of order  $10^\circ$ , consistent with the framing camera observation that the anode light (and presumably the plasma) did not fully cover the metal area between grooves.

The second anode plasma experiment involved the determination of the time evolution of the plasma density using visible light emission spectroscopy. The broadening of the  $H_\beta$  line (4861.3 Å) of neutral hydrogen has been measured as a function of time and distance from the anode surface. Since in the plasma density and temperature range of interest ( $<10^{16}/\text{cm}^3$  and  $\approx 1$  eV) Stark broadening is the predominant mechanism, the plasma electron density may be inferred from the line width. For one series of shots, the diode was operated at 400 keV peak voltage, an accelerating gap of 5 mm, and a 7.5 kG insulating magnetic field ( $B/B^* \approx 1.5$ ) which yielded an ion current density of  $\approx 120$  A/cm<sup>2</sup>. The electron density as a function of position in the diode at several different times is shown in Fig. 3. The uncertainty in determining the time in the data analysis was  $\pm 5$  ns, and the density uncertainty is  $\pm 0.5 \times 10^{15}/\text{cm}^3$ . Plasma light was first observed 10-15 ns after the start of the voltage pulse, consistent with the

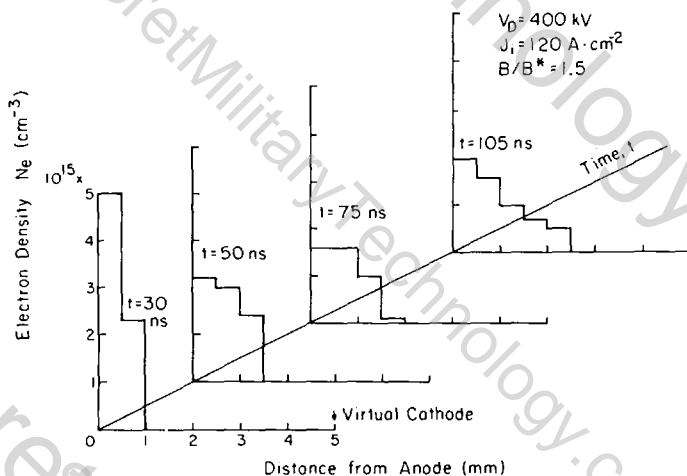


FIG.3. Anode plasma density as a function of distance from the anode at four times. The initial physical gap spacing is 5 mm, and the voltage pulse begins to fall at about 75 ns.

start of emission of ion current (from Faraday cups). At early time (30 ns), the plasma is  $\leq 1$  mm thick, expanding into the gap at about  $2 \text{ cm}/\mu\text{s}$ . From the intensity of the  $H_{\beta}$  line, the electron temperature in the anode plasma near 1 eV and a neutral hydrogen density of  $10^{16}/\text{cm}^3$  were estimated, assuming Saha equilibrium. This diagnostic can easily be applied to the higher power density levels relevant to ICF applications.

#### 4. PRELIMINARY HIGH POWER EXPERIMENTS

A new MID configuration has been operated on the LION accelerator, a  $10^{12}$  W (450 kA, 1.8 MV, 40 ns pulse) PBFA-I module, for a limited number of shots. This diode, similar in configuration to that of Greenly [4], utilizes a radial applied magnetic field together with the self-field of the ion beam to provide the necessary total magnetic insulation field strength. An annular  $50 \text{ cm}^2$  epoxy-filled groove copper anode is used. Operating with a 5 mm gap and  $B/B^*$  between 1 and 2, 30-50% of the LION power has been coupled into the diode. Although diagnostic ablation has prevented a quantitative current density measurement, it is believed to be  $> 2 \text{ kA}/\text{cm}^2$ . From Thomson parabola ion energy analyzer measurements, the peak proton energy is between 1.2 and 1.6 MeV.

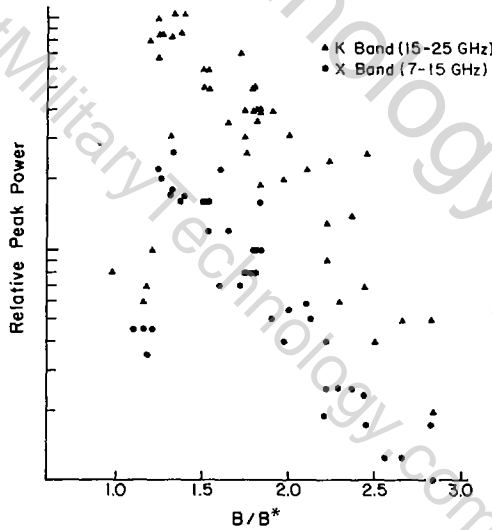


FIG. 4. Microwave power produced by the applied  $B_{\theta}$  diode as a function of  $B/B^*$ .

##### 5. MICROWAVE EMISSION STUDIES FROM A MID

Recent studies using the applied- $B_{\theta}$  diode [5] have correlated the microwave activity of the electrons in the cathode sheath with ion beam behavior. The frequency spectrum, which spans at least 1-80 GHz, sharply peaks in the 5-10 GHz range. Figure 4 illustrates the behavior of the microwave radiation as a function of  $B/B^*$ . In particular, the radiation intensity peaks at about  $B/B^* = 1.4$  (in all bands). This dependence is in qualitative agreement with the theoretical arguments presented by Sudan [6], which suggested that microwave activity should peak slightly above  $B/B^* = 1$ . The ion beam current density also peaks near this value of  $B/B^*$ , although it falls much more slowly for smaller  $B/B^*$ . Using the pinhole plate-scintillator-streak camera technique described in Sec. 2, it is found that the ion beam undergoes (nonreproducible) fluctuations (intensity and aiming error) which also appear to peak near  $B/B^* = 1.4$ . However, local divergence shows no significant correlation with  $B/B^*$ . In earlier experiments by Maron [7], performed using a  $\approx 0.5$  ms MID, local correlations were found between microwave and x-ray emissions as well as with ion beam fluctuations.

## 6. HEAVY ION BEAM PRODUCTION

It is now possible to produce substantial current densities (30-50 A/cm<sup>2</sup> at 200-300 keV) of ions other than protons by the use of anode flashboards containing the desired species together with other ions which have a higher ionization potential. For example, a BaF<sub>2</sub> anode has been used to produce 30 A/cm<sup>2</sup> of Ba<sup>+</sup> and Ba<sup>++</sup> at  $\leq 300$  keV, with negligible fluorine (or proton) contamination. In order to eliminate a proton component, it was necessary to eliminate all hydrocarbon contamination, including even very low vapor pressure diffusion pump oil. Similarly, a Na<sup>+</sup> beam was produced using an NaCl anode. Given the low divergence results described in Sec. 2 which were ascribed to C<sup>+</sup> ions at  $>10^8$  W/cm<sup>2</sup> at the source, there is reason to believe that the light ion species which best matches the high power accelerator used for ICF experiments to a particular pellet design can be produced using flashlight anodes.

## 7. CHANNEL TRANSPORT SIMULATIONS

Two and one-half dimensional ( $r, z, v_r, v_\theta, v_z$ ) hybrid simulations of ion beam transport in preformed z-pinch plasma channels have been performed using the CIDER code[8]. In this code, beam and background ions are represented by particles, while electrons are represented by an inertialess thermal fluid. The electron energy equation includes collisional beam energy deposition, Ohmic heating and optically thin radiation due to impurities. Fields are solved for in the quasineutral Darwin approximation.

The formation phase of the z-pinch discharge is not simulated. Instead, a self-consistent z-pinch equilibrium is initiated by specifying profiles for plasma density  $n(r)$ , neutral density  $n_0(r)$ , and electron temperature  $T_e(r)$ . The magnetic field is then obtained from pressure balance and Ampère's law. Typical parameters are  $n(0) = 2 \times 10^{18}$  cm<sup>-3</sup> (hydrogen),  $n_0(0) = 1 \times 10^{17}$  cm<sup>-3</sup>, and  $T_e(0) = 6$  eV, resulting in a channel current of 36.5 kA. Initial transients are allowed to die out, after which the beam is injected over a number of timesteps.

Simulations of the injection and propagation of 3-7 MeV, 1-2 MA proton beams in 0.6 cm radius hydrogen channels show that about 93% of the initial beam energy can be transported over distances of 1 m, indicating that transport efficiencies in the 75% range are possible in 4 m channels. This figure is

consistent with one-dimensional fluid simulations[9]. Current neutralization is found to be in excess of 99%. Increasing the injected energy of the beam  $E_{inj}$  from 5.0 MeV to 7.6 MeV in 25 ns results in a 30% spatial bunching of the beam 1 m downstream from the injector. No gross axisymmetric instabilities are observed.

Average beam divergence on axis  $\langle \Delta\theta_{rz} \rangle$  at the channel exit is measured to be less than  $2^\circ$  in most cases for an initial  $\langle \Delta\theta_{rz} \rangle$  in the  $1.5^\circ$  range. We also find it necessary to impart a small azimuthal velocity spread ( $\Delta v_\theta / \sqrt{2E_{inj}/m} \lesssim 0.05$ ) to the beam ions so that their nonzero  $p_\theta$  will force them away from the  $r = 0$  axis. In this way, Ohmic beam energy losses and channel expansion are reduced by decreasing the beam current density, and the channel return current density near the axis.

## 8. CONCLUSION

The sum of these results, together with recent results with magnetically insulated diodes obtained at Sandia Laboratories, Albuquerque, suggest that flashboard anodes can produce low divergence beams of a variety of different light ion species at  $>10^9$  W/cm<sup>2</sup>. Operated at the few MV level on the most powerful pulsed power generators, the resultant beams should be capable of being used for interesting ICF pellet experiments.

## REFERENCES

- [1] See, for example, HUMPHRIES, S., Jr., Nucl. Fusion 20 (1980) 1549.
- [2] JOHNSON, D. J., et al., Phys. Rev. Lett. 42 (1979) 610.
- [3] MAENCHEN, J., et. al., Phys. Fluids 22 (1979) 555.
- [4] GREENLY, J. B., Cornell University Laboratory of Plasma Studies Report 286 (1980).
- [5] GREENSPAN, M. A., et al., Appl. Phys. Lett. 37 (1980) 248.
- [6] SUDAN, R. N., Proc. 4th Int. Top. Conf. on High Power Electron and Ion Beam Research and Technology (Palaiseau, France, 1981) Vol. I, p. 389.
- [7] MARON, Y., manuscript in preparation.
- [8] MANKOFSKY, A., SUDAN, R. N., DENAVIT, J., Bull. Am. Phys. Soc. 26 (1981) 1014.
- [9] FREEMAN, J. R., BAKER, L., COOK, D. L., Nucl. Fusion 22 (1982) 383.

## DISCUSSION

M.G. HAINES: Can you comment on the stability of the Z-pinch used for the ion beam transport? In the simulation, the  $m = 0$  mode would be allowed and finite-Larmor-radius effects of the background plasma would be small if the pinch radius is greater than the Larmor radius of the ion beam particles.

D.A. HAMMER: The model does permit the  $m = 0$  mode, but it does not have time to grow during the  $\approx 100$  ns duration of the simulations. Experimentally one would, presumably, inject the beam into the channel before significant distortion would have time to build up.

T.F. GODLOVE (*Chairman*): Are your channel propagation theory results in general agreement with those of the US Naval Research Laboratory?

D.A. HAMMER: The code used in our simulations was  $2\frac{1}{2}$ -D, as compared with 1-D in the NRL work, and all ions were treated as particles. Nevertheless, our results are in general agreement with those of NRL.

R.N. SUDAN: This  $2\frac{1}{2}$ -D analysis in general confirms the 1-D analysis in that no anomalous  $2\frac{1}{2}$ -D effects are noted. "Sausaging" cannot be seen because it is only 2-D, and pinching is not seen because the beam pulse time is much shorter than the growth time of any MHD instability of the channel. So, in general, beam transport in channels looks very promising.



## LIGHT ION BEAM FUSION RESEARCH IN JAPAN

K. IMASAKI, S. MIYAMOTO, S. HIGAKI, T. OZAKI,  
K. NISHIHARA, S. IDO, S. NAKAI, C. YAMANAKA  
Institute of Laser Engineering,  
Osaka University,  
Suita, Osaka

K. YATSUI, K. MASUGATA, M. MATSUI  
Technological University of Nagaoka,  
Nagaoka, Niigata

Japan

### Abstract

#### LIGHT ION BEAM FUSION RESEARCH IN JAPAN.

In inertial confinement fusion research by light ion beams, the important issues to be investigated are the development of pulse power technology, beam generation and concentration of power, beam transport, development of diagnostics, interaction of the beam with the solid target, and implosion dynamics. At ILE, Osaka, the  $10^{12}$  W machine, REIDEN IV, has successfully generated light-ion beams at 1 MV. It has been modified to generate 3 MV pulses by the addition of an impedance-transforming line. Pinch reflex diode experiments were performed on REIDEN IV with an ion power of  $0.2 \times 10^{12}$  W. The beam species and energies were measured by a Thomson parabola analyser. The dependence of beam divergence on diode current density and self-focusing property in the pinch reflex diode was investigated. The focused beam was injected into the CO<sub>2</sub> laser guided plasma channel and the transport property was investigated by measuring the ions emitted from the plasma channel. The results were in good agreement with the computer orbit calculation. Diagnostics for a focused proton beam were developed which gave an image of the focal spot of the protons. The deposition profiles of deuteron beams were determined by analysis of neutron and incident beam spectra. Beam-target coupling physics and scaling of the ablation pressure on beam intensity were investigated by measuring the foil acceleration using a N<sub>2</sub> laser shadowgraph and the recently developed method of neutron energy analysis. At the Technological University of Nagaoka, beam technology was developed by means of magnetically insulated ion diodes. Channel propagation experiments with focused beams were also performed.

#### 1. INTRODUCTION

On the basis of the conceptual design of a reactor, ROKKO I [1], and pellet implosion simulation, the key issues in research and development for a light ion beam inertial confinement fusion system have been analysed and experiments systematically performed at ILE, Osaka, on:

- (a) Pulse power technology;

- (b) Beam generation and focusing;
- (c) Beam transport through a laser-guided plasma channel;
- (d) Development of diagnostics;
- (e) Beam-target coupling physics and scaling of ablation pressure on beam intensity; and
- (f) Implosion simulation and pellet design.

Developments in beam technology at Nagaoka covered beam generation and focusing in magnetically insulated ion diodes and channel propagation of focused beams.

## 2. PROGRESS TOWARD FUSION WITH LIGHT ION BEAMS AT ILE, OSAKA

### 2.1. Developments in pulse power and beam technology

Developments in pulse power technology were made on the  $10^{12}$  W, 100 kJ machine, REIDEN IV [2], which consists of a 2.5 MV, 150 kJ Marx generator, an intermediate storage capacitor, a  $1 \Omega$  pulse-forming line and a transmission line. REIDEN IV delivered a 1 MV pulse with total machine efficiency of 40% into the matched load. It has been modified to generate a 3 MV pulse by the addition of an impedance-transforming line, which is a coaxial tapered line for impedance transform from  $1 \Omega$  to  $9 \Omega$  with 70% efficiency. Figure 1 is a photograph of REIDEN IV.

Pinched e-beam and pinch reflex ion diode [3] experiments were performed. 4 mm thick polyethylene or 100  $\mu\text{m}$  thick Mylar was used as an anode ion source. For deuteron-beam experiments, the surface of the anode was coated with deuterated polyethylene. The hollow-type cathode was 50 mm in diameter. Experiments were performed with ion-beam current in the range of 30–200 kA and ion production efficiency of 20–40%.

The generation and focusing, or divergence, of the beam were extensively investigated by:

- (a) Thomson parabola analyser, to measure ion species and energies and the divergence of each species as a function of diode current;
- (b) Shadow-box, to measure beam divergence as a function of the ion-emitting region on the anode or ion energy or diode current;
- (c) X-ray image of the anode to obtain information about the anode plasma or surface current;
- (d)  $\alpha$ -particle pinhole image of the focused proton beam on a boron target.

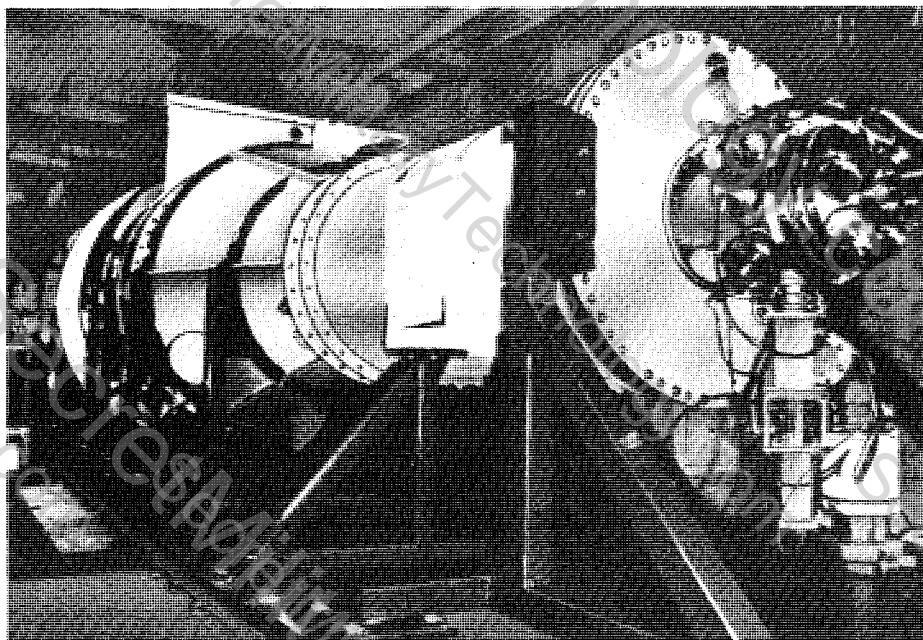


FIG.1. REIDEN IV, with impedance-transforming line.

The time-integrated focal spot size of 1 cm is much larger than that expected by  $f\Delta\theta$  using measured local divergence of the beam  $1^\circ$  and focal length  $f$  of 5 cm. The discrepancy may be explained by the axial shift of the focal point due to the time-varying diode current and the position of the ion-emission region and its movement on the anode, both depending on the ion species.

Figure 2 shows the effective divergence of the larger-mass ion species to be smaller in the case of carbon than for the proton in the region of high diode current.

Figure 3 shows the similar behaviour of divergence increase at higher diode current. Figure 3(a) shows that the higher electron current density causes stronger beam divergence. Figure 3(b) shows the spread of the focusing angle due to the time-varying self-B-field as a function of radial position. The broken line is the predicted value for the diode current of 500 kA and the ion current of 120 kA. The experimental results are in good agreement with the predicted values except at small radius, which may be due to the strong divergence in the REB pinch region. Experimental results show that the average source beam brightness is  $2 \text{ TW}\cdot\text{cm}^{-2}\cdot\text{rad}^{-2}$ . The heavier ions, such as carbon, are shown to be suitable for providing narrower focus owing to their smaller divergence and because they are less sensitive to magnetic deflection at high current density operation.

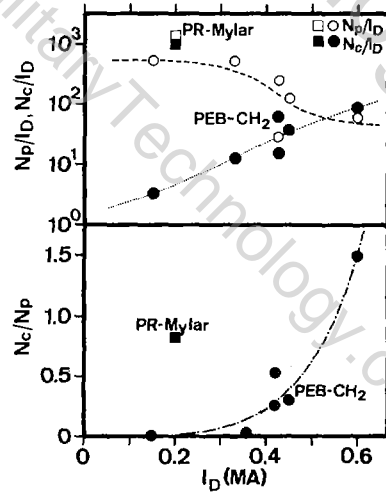


FIG.2. Particle measurement by Thomson parabola analyser with double entrance apertures.  $N_p$  and  $N_c$  are the detected numbers of protons and  $C^A$  (including the recombined  $C^{3-1+}$  ions) for the energy of  $E/Z = 500-600$  keV, respectively. Circles and squares are the data obtained using 4 mm thick polyethylene and 100  $\mu$ m thick Mylar anodes, respectively. The increase of  $N_c/N_p$  with the diode current  $I_D$  may be due to difference in beam divergence between proton and carbon because  $N$  is proportional to  $I_D/(\Delta\theta)^2$ .  $N_p/I_D$  and  $N_c/I_D$  therefore show the inverse square of the beam divergence.

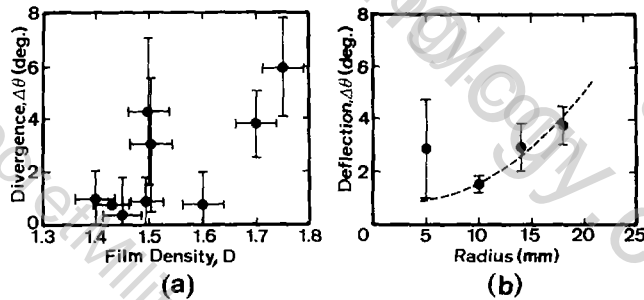


FIG.3. (a) Measured local divergence in the pinch reflex diode as a function of density of the X-ray pinhole camera image. (b) Time-varying self focus angle as a function of the radial position of the pinhole.

Focused ion beams were transported through a CO<sub>2</sub> laser guided plasma channel. Details about channel-plasma formation by CO<sub>2</sub> laser guide in C<sub>2</sub>H<sub>4</sub> gas have been reported in Ref. [4]. The channel electron densities and their profile were measured by N<sub>2</sub> laser interferometry as  $n_e \approx 5 \times 10^{17} \text{ cm}^{-3}$  at the channel centre with 30 kA and 20 mbar C<sub>2</sub>H<sub>4</sub> gas. The focused proton beams ( $5 \times 10^9 \text{ W}\cdot\text{cm}^{-2}$ ) were injected axially to the plasma channel. The beam energy loss was estimated to be 150 keV at the injection proton energy of 750 keV, achieved by measuring the average ion energy at input and output of the 40 cm long channel by the B-N activation method. This is consistent with the collisional loss suffered by the plasma particles in the channel.

The dynamics of ion-beam transport in the plasma channel were investigated by measuring the emitting angles of protons from the channel end. The radial profiles of emitted protons were obtained as a function of the ion energy [5]. The ion orbits and the angular distribution of ions emitted from the channel end were calculated for the three different current distributions in the plasma channel, as shown in Fig.4. The observed distribution was consistent with that of the current centre. Control of current distribution in the plasma channel may be useful for efficient beam transport, which may be possible in a laser guided plasma channel.

## 2.2. Developments in diagnostics

New diagnostics which can be used for target irradiation experiments with focused beams have been developed. Diagnostics which measure light ion beam parameters are:

- (a) The B-N activation method to measure the mean energy of proton beams;
- (b) Thomson parabola analyser using a nuclear track detector (CR39) to measure the species and energy spectra of beam ions;
- (c)  $\alpha$ -particle pinhole camera using B<sup>11</sup>(p, $\alpha$ )2 $\alpha$  reaction to measure the focal spot size and profile of the proton beam [6];
- (d) Determination of beam current density by time-resolved D-D neutron detection.

Diagnostics that measure the target behaviour are (a) four-channel shadowgraphy and interferometry using a N<sub>2</sub> laser with 7 ns pulse width, and (b) determination of energy deposition profile by analysis of neutron and incident beam spectra.

## 2.3. Target interaction and ablation pressure scaling

To investigate the energy deposition of ion beams in the target, we have devised a new diagnostic method of obtaining the deposition rate,  $dE/dX$ , as a function of ion energy. The principle of this measurement is as follows. We suppose,

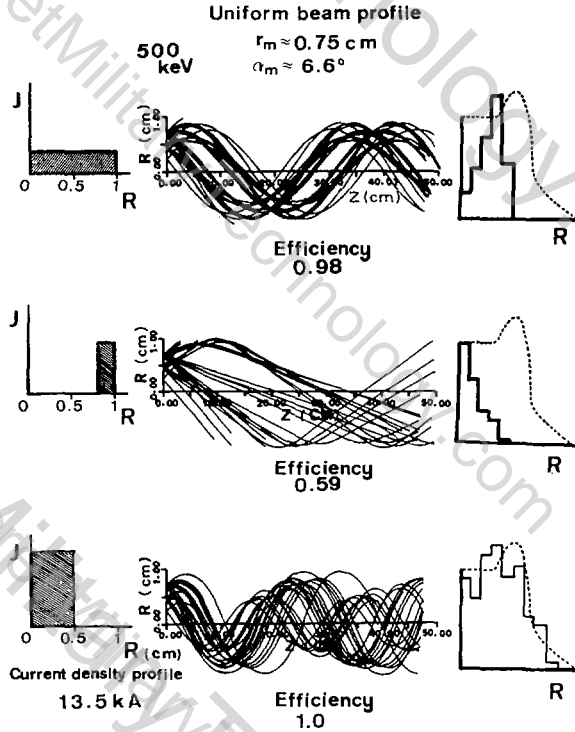


FIG. 4. Ion orbits in the transport channel and the distribution of ions emitted from the channel end for three different channel current distributions. Dashed lines in the emitted ion distribution are measured curves.

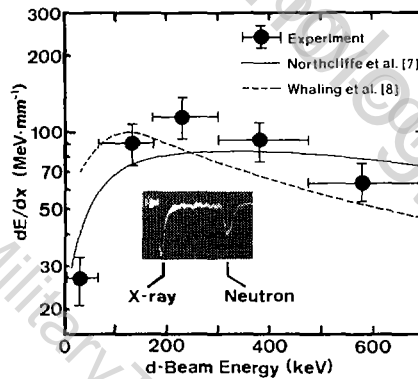


FIG. 5. Measured  $dE/dx$  as a function of deuteron beam energy using neutron time-of-flight analysis. Inset waveform is the detected neutron signal 15 m from the target. Solid lines are theoretical predictions [7]; dashed line represents experimental data [8].

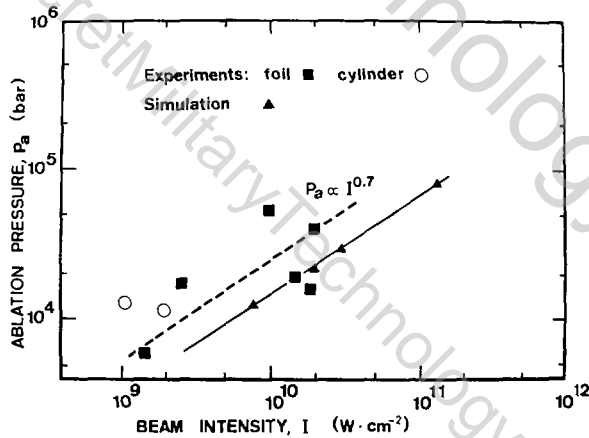


FIG. 6. Scaling of ablation pressure to incident beam intensity.

for simplicity, that a monoenergetic D-beam impinges on the target. Beam ions are slowed down, mainly owing to the interaction with electrons. Only a small part of the D-beam undergoes the  $D(d,n)^3H$  reaction. If  $dE/dX$  is small at certain values of ion energy, such ions can travel a longer path with small loss of energy. They have therefore a greater chance of D-D reaction. The generated neutrons carry information on the ion energy at the reaction. By measuring the energy distribution of the neutron, we can estimate the  $dE/dX$  of the D-beam as a function of deuteron energy. The method can be applied even if the incident beam has an energy spread, by introducing into the calculation the necessary information on the energy distribution of the beam ions. The ion energy distribution was measured by a Thomson parabola analyser and the neutron energy was derived from time-of-flight measurements.

The experiments for measuring the deposition profile were performed for the low beam intensity region (about  $10^9$  W·cm<sup>-2</sup>). In this region, plasma effects on the deposition profile were not expected. The measured  $dE/dX$  as a function of ion energy  $E$  is shown in Fig. 5 with the detected neutron signal. The results of  $dE/dX$  are in good agreement with the theoretical prediction [7] and the other experimental data [8]. This method has now been extended to the high power density region where the effect of the plasma is no longer negligible.

The dynamic behaviour of a foil target irradiated by focused proton beams up to  $2 \times 10^{10}$  W·cm<sup>-2</sup> was studied. The ablation pressure on the target was estimated from the acceleration of the target measured optically by a N<sub>2</sub> laser. The results in Fig. 6 show the ablation pressure scaling as  $P_a = 3 \times 10^{-3} I^{0.7}$  bar ( $I$  in W·cm<sup>-2</sup>) [9]. This experimental dependence was in good agreement with computer simulation, where flat deposition of beam energy over the ion range was assumed. The ion temperature of 2.1 eV was measured by two-channel charge

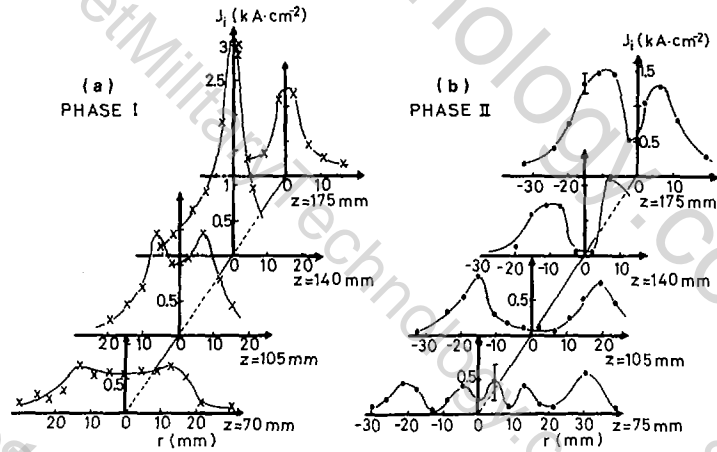


FIG. 7. Ion current density distribution at  $V_b$  (beam voltage)  $\approx 650$  kV.  $I_i$  (total ion current)  $\approx 12$  kA;  $\tau_b$  (beam pulse width)  $\approx 80$  ns (FWHM). As reported elsewhere, owing to an impedance mismatch between pulse-forming line and diode, a voltage reflection appeared; the diode works at a relatively high impedance in phase I, while the impedance decreases in phase II owing to the presence of a residual anode sheath plasma.

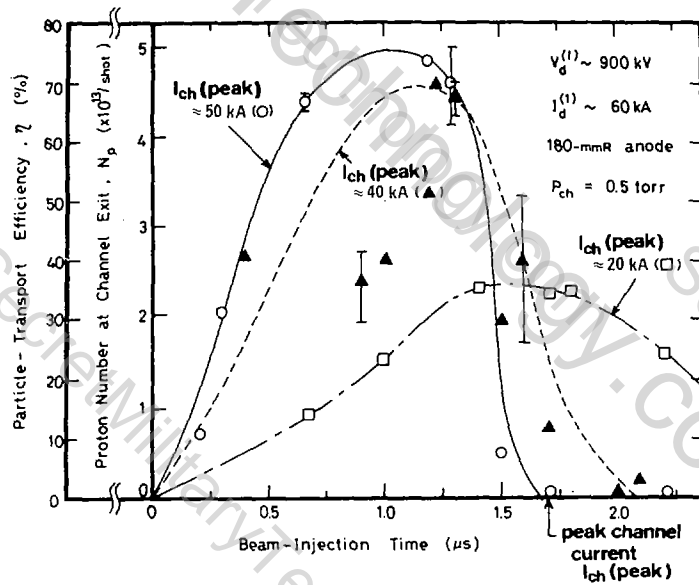


FIG. 8. Particle transport efficiency versus beam injection time after closure of the channel switch.

collectors. Assuming uniform dissipation over the classical range of ions in a  $CD_2$  target, the ion temperature of the ablated plasma was estimated to be 2.0 eV, which corresponded quite well with the measured value. Cylinder targets were also used and the results are shown in Fig.6.

The experimental dependence of ablation pressure on the proton beam intensity predicts that the required intensity of the ion beam is  $10^{14} \text{ W}\cdot\text{cm}^{-2}$  in order to get an ablation pressure of  $2 \times 10^7$  bar so that pellet compression can achieve significant burn of the fuel.

### 3. DEVELOPMENT OF BEAM TECHNOLOGY AT NAGAOKA

#### 3.1. Geometric focusing of light ion beams in magnetically insulated diodes [10, 11]

The geometric focusing properties of proton beams in magnetically insulated ion diodes have been studied in detail on the 15 kJ light ion beam generator, ETIGO-I. Figure 7 shows the distribution of an ion current density measured by a biased ion collector. After being extracted from a spherical plastic anode 110 mm in diameter, the beam is focused at the focusing point with focal spot radius  $r^* \approx 16$  mm, where  $r^*$  denotes the radius at which half the total ion current is involved. This gives the total divergence angle as about  $6^\circ$ . The local divergence angle, observed by shadow-box to be about  $1^\circ$ , has a slighter effect on focusing. On the other hand, deviation of ion trajectories from the ideal ones (or aberration) is found to be  $1.7^\circ$  to  $3^\circ$ , which strongly affects the focusing. An annular distribution in phase II is explained by ion trajectory calculation as being due to a non-uniform space-charge effect. From comparison of experiment and theory in the ion current distribution, the space-charge neutralization factor is estimated to be more than 99.9%. The central region appears to be less charge-neutralized than the outer region, although the reason for this is uncertain.

#### 3.2. Light ion beam transport through wall-stabilized plasma channel

Beam transport was studied experimentally through a wall-stabilized plasma channel one metre long. An 800 keV proton beam is injected into the channel produced by a 60 kV,  $1.9 \mu\text{F}$  capacitor bank. The channel and the maximum injection radii are  $R = 10$  mm and  $a = 6$  mm, respectively, and the maximum injection angle is  $\theta_m \approx 0.311$  rad. Maximum transport efficiencies (energy and particle number) of more than 85% have been obtained at  $I_{ch}$  (channel current)  $\approx 52$  kA. Transport efficiencies increased with increasing channel current or decreasing channel pressure, in good agreement with existing theories.

Figure 8 shows particle-transport efficiency measured by the carbon activation technique, where peak channel current is a parameter. At  $I_{ch}(\text{peak}) \approx 20$  kA

the beam transport attains maximum efficiency at the peak of the channel current ( $t \approx 1.7 \mu\text{s}$ ) and decreases gradually with the channel current. At  $I_{\text{ch}}$  (peak)  $\approx 40$  kA, however, the transport ceases to exist after the current peak, which may indicate the presence of some plasma instabilities.

#### REFERENCES

- [1] IMASAKI, K., et al., IAEA Technical Committee Meeting and Workshop on Fusion Reactor Design and Technology, Tokyo, 1981 (Proc. in preparation).
- [2] IMASAKI, K., et al., in Plasma Physics and Controlled Nuclear Fusion Research 1980 (Proc. 8th Int. Conf. Brussels, 1980) Vol.2, IAEA, Vienna (1981) 391.
- [3] GOLDSTEIN, S.A., et al., Phys. Rev. Lett. **40** (1978) 1504.
- [4] IMASAKI, K., et al., in Proc. 4th Int. Top. Conf. on High-Power Electron and Ion-Beam Research and Technology, Palaiseau, 1981, paper 1A2.
- [5] OZAKI, T., et al., Jpn. J. Appl. Phys. **21**(1982) L81.
- [6] MIYAMOTO, S., et al., ILE, Osaka, Research Rep. ILE 8102T (1981).
- [7] NORTHCLIFFE, L.C., et al., Nuclear Data Table A7 (1970) 233.
- [8] WHALJING, W., Handbook, Phys. **34** (1958) 195.
- [9] MIYAMOTO, S., et al., Jpn. J. Appl. Phys. **21** (1982) L83.
- [10] MASUGATA, K., et al., Jpn. J. Appl. Phys. **20** (1981) L347.
- [11] YATSUI, K., et al., Proc. 4th Int. Conf. on High-Power Electron and Ion-Beam Research and Technology, Palaiseau, 1981, p.27.

#### DISCUSSION

S. WITKOWSKI: How did you measure the ablation pressure?

K. IMASAKI: We used the shadowgraph method with  $\text{N}_2$  lasers and charge collectors in front of and behind the target.

## STATUS OF RELATIVISTIC-ELECTRON-BEAM-GENERATOR-DRIVEN INERTIAL-CONFINEMENT FUSION

L.E. ARANCHUK, M.V. BABYKIN, K.A. BAJGARIN,  
 N.U. BARINOV, A.V. BARTOV, S.L. BOGOLYUBSKIJ,  
 V.V. BULAN, V.D. VIKHAREV, V.S. VOLKOV,  
 Yu.M. GORBULIN, E.M. GORDEEV, V.V. GOREV,  
 E.V. GRABOVSKIJ, A.V. GUBAREV, S.A. DAN'KO,  
 S.K. DOLOTOV, V.I. ZAJTSEV, D.M. ZLOTNIKOV,  
 Yu.G. KALININ, V.N. KISELEV, Yu.V. KOKA,  
 V.D. KOROLEV, P.V. KUKSOV, V.I. LIKSONOV,  
 V.I. MIZHIRITSKIJ, S.L. NEDOSEEV, G.M. OLEJNIK,  
 L.I. RUDAKOV, V.A. SKORYUPIN, V.P. SMIRNOV,  
 E.A. SMIRNOVA, E.Z. TARUMOV, M.V. TULUPOV,  
 S.D. FANCHENKO, V.Ya. TSARFIN, A.S. CHERNENKO,  
 R.V. CHIKIN, A.Yu. SHASHKOV, Yu.I. SHESTAKOV,  
 I.R. YAMPOL'SKIJ, V.V. YAN'KOV  
 I.V. Kurchatov Institute of Atomic Energy,  
 Moscow,  
 Union of Soviet Socialist Republics

### Abstract

#### STATUS OF RELATIVISTIC-ELECTRON-BEAM-GENERATOR-DRIVEN INERTIAL-CONFINEMENT FUSION.

The Angara inertial-confinement fusion programme of the I.V. Kurchatov Institute of Atomic Energy is briefly discussed. Research is mainly going on in two directions: REB-generator application to liner acceleration and target irradiation by high-current electron beams. The latest experimental data on liner implosion and e-beam focusing aiming at the preparation of the Angara 5-1 experimental programme are reported.

### 1. INTRODUCTION

A device for demonstration experiments based on pulsed generators is being constructed in the framework of the Angara programme at the I.V. Kurchatov Institute of Atomic Energy. At present, research is going on at the Angara 5-1 experimental module and other devices. The main point of the programme is fuel heating as a result of either liner magnetic acceleration [1] or target irradiation by a focused relativistic electron beam (REB) [2]. Any scheme of pulsed-generator

energy transfer to a target, including the light-ion beam approach studied mainly in the USA, is based on identical methods of electromagnetic-power transport along vacuum lines with magnetic self-insulation (MIVL). The transition from one mode of operation to another would simply require replacement of some relatively simple output devices. In comparison with the ion beam approach, the electron beam approach has the advantage of direct energy transport to the target surface used as anode at the MIVL output. This enables a large-scale model experiment on single e-beams. The necessary  $2 \times 10^7 \text{ J} \cdot \text{g}^{-1}$  level of energy input into thin shells can be attained by the experimentally discovered anomalous energy deposition in matter by electrons orbiting in beam-produced magnetic fields, which increases the efficiency of heating.

The highly efficient irradiation of the target in a cloud of relativistic electrons accumulated in a magnetic trap whose dimensions are by an order of magnitude greater than those of the target may be considered to be an alternative approach to direct target irradiation by focused REB in the demonstration experiment.

According to calculations, the breakeven conditions in the liner approach can be reached at a lower energy level than with e-beams. The main problem is to concentrate the energy in the magnetic field near the shell surface, which requires the use of low-inductive-output devices and MIVL and an increase in output generator current.

## 2. ELECTRON BEAM FOCUSING IN THE DIODE

In the first experiments on REB focusing in diodes with up to 180 kA current in the Triton and Ural devices making use of conical and pin cathodes, a current density of about 10 to 20  $\text{MA} \cdot \text{cm}^{-2}$  was attained which was explained by the fact that the accelerating gap was filled with the plasma created either by the pre-pulse or the main pulse [3, 4]. In Angara-I, with a current of 150–300 kA, a beam current density of up to 30  $\text{MA} \cdot \text{cm}^{-2}$  and a power flow of up to  $10^{13} \text{ W} \cdot \text{cm}^{-2}$  were achieved. This became possible by the use of a ring edge cathode with a deep conical hole at the centre. The nature of the damage done to the anode permits the suggestion that separate current channels drifting towards the axis and merging into a common current channel with a diameter of 1 to 1.5 mm are formed [5]. In contrast to the Triton data with the pre-pulse plasma, in the Angara-I experiments a long delay between voltage and current resulting in energy loss was noted.

Since the diodes studied had a small aspect ratio, we must, to explain the observed current values, assume that the plasma, partially or completely, fills an accelerating gap. As was noted earlier with the Angara-I experiments, the diode current flows in a Z-pinch-type plasma channel with the current velocity exceeding the ion sound velocity. In such conditions, small-scale instabilities and turbulent

resistance may develop. The model of such a turbulent diode was suggested by L.I. Rudakov. The parameters of the plasma channel may be estimated from the Bennett equation, with the assumption that current velocity in the channel cannot substantially exceed the ion sound velocity [2]. Unfortunately, this model does not allow a determination of the current channel radius. The diode impedance predicted by the model is  $\geq 4\Omega$  for  $V \sim 1$  MV, which corresponds to the optimum focusing conditions observed in the experiments. Further research on focusing in the diodes aims at elucidating the diode physics and at developing low-impedance diodes with a short current delay relative to the voltage and a high efficiency of anode foil heating.

Enhanced electron energy deposition in the anode foil due to electron orbiting in the beam self-magnetic field occurs during the high-current foil heating. The possibility of such an effect was pointed out in Ref.[6]. In 1976, in the Triton device, the enhanced heating was first observed in a 5  $\mu\text{m}$  thick foil, which was less thick than the range of a single electron [7]. Calculations based on L.I. Rudakov's theoretical model, with averaging over the beam area, show that the deposition enhancement factor is given by  $3/2 (I/I_A)$  [2], where  $I_A = 17000 \beta\gamma A$ , A, and is very sensitive to the total beam current and the electron energy ( $\beta\gamma$ -factor). The foil deposition power over the focal spot surface is given by

$$P = \frac{dE}{d(\rho x)} \rho \delta \times \frac{3}{2} \frac{I}{I_A} \frac{I}{e}$$

where  $\delta$  is the thickness. In a realistic system, the foil deposition power increases with growing current and is limited in time by the electric power drop as a result of diode short-circuit or voltage switch-off. In the Angara-I experiments, the enhancement factor reaches eight to ten at the end of a pulse when the diode current attains large values and the electron energy begins to fall off. Preliminary plasma production in the diode by a controlled pre-pulse in Angara-I allowed achievement of an earlier diode current start and of an increase in the total energy input to the diode. The temperature of a foil was not, however, raised substantially, because of poor focusing.

In Angara-I, also the dependence of the diode characteristics on the longitudinal magnetic field of the diode current flowing through a 1-cm diam. coil with three to four turns was studied. The magnetic field in the diode gap is a superposition of the diode current field and the coil-produced diverging field; it reached  $10^5$  G. An earlier (about 20 ns, Fig.1) start of the soft-X-ray emission and an increase in temperature (up to 35–40 eV) were observed.

In Kalmar I, the angular distribution of the anode bremsstrahlung was measured by an M3-3-type film and thermoluminescent LiF probes. It turned out that the electrons hit the anode mainly at angles  $\geq 40$ – $50^\circ$  with respect to the axis [8].

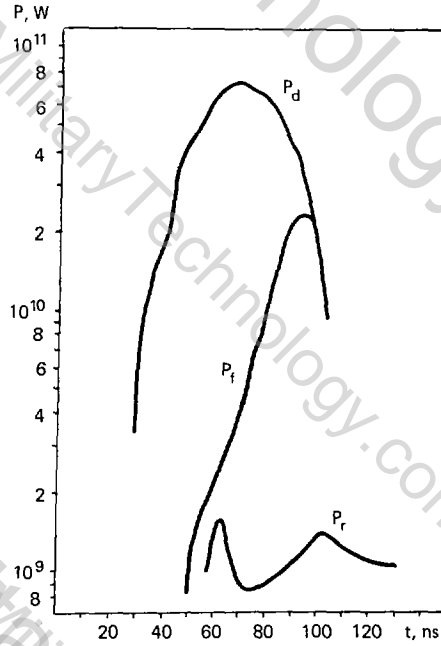


FIG.1. Change of input power in foil,  $P_f$ , and of soft radiation,  $P_r$ , in the presence of magnetic field in the diode. Foil heating and radiation begins earlier near maximum power in the diode,  $P_d$ . On radiation power curve, second maximum is also observed as usually near maximum of  $P_f$ .

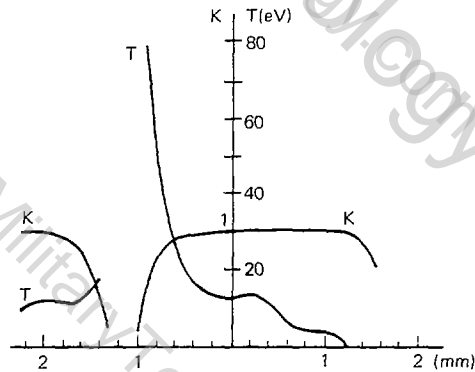


FIG.2. Temperature distribution  $T$  and absorption coefficient  $K$  along diode axis.

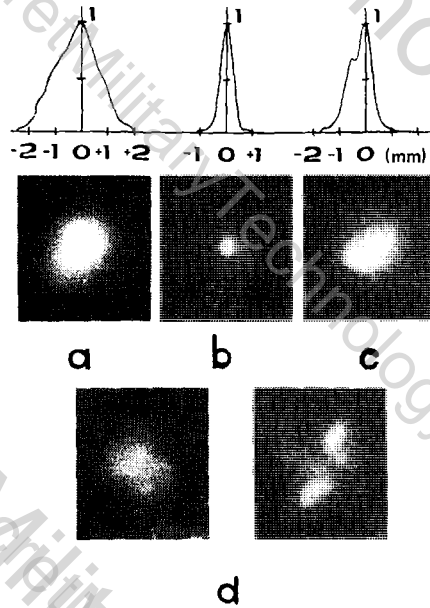


FIG.3. X-ray photograph of electron focal spot and distribution of its intensity. a – time-integrated curve, b – 45 ns after current start, c – 70 ns after current start, d – current channel destruction on several separate filaments.

At the Mirage device, work [9] was continued, and an attempt was made to determine instantaneous temperature profiles along the diode axis by measuring the absolute radiation power with an image-converter streak camera. The measurement was carried out at a wavelength of 532 nm, selected by a monochromator. The coefficient of absorption at the same wavelength was determined from plasma shadowgraphs on the second harmonic of a YAG:Nd laser. These data were used to calculate the temperature according to Kirchhoff's law. Laser radiation attenuation due to refraction was eliminated by applying a lens collecting the refracted rays. The absence of refraction was checked in a special schlieren photography experiment. The experimental temperature data along the diode axis are shown in Fig.2.

The focal spot in the bremsstrahlung was also photographed ( $E \geq 40 \sim 60$  keV) for this device [10] by means of a pinhole camera and an image-converter camera in which a microchannel plate was used both as cathode and intensifiers. Figure 3 shows the difference between the half-width of a time-integral frame picture and a 5-ns exposure frame up to 50–60 ns. The calculated instantaneous current density exceeded the integral density by more than an order of magnitude and reached  $80 \text{ MA} \cdot \text{cm}^{-2}$ , the power density amounting up to  $6 \times 10^{13} \text{ W} \cdot \text{cm}^{-2}$ . In some shots, however, a complex X-ray image structure was observed as had also



FIG. 4. Diode plasma luminescence photograph, 25 ns after current start in the line. Exposure time: 5 ns.

been noted in previous experiments. Sharp focusing at one or several spots was observed only up to 50–60 ns from the start of the current. The current density decrease to values comparable with the integral measurements took place at a later time.

We may suggest that the de-focusing of the beam is a result of the current instability developing in the diode. In particular, the high-frequency oscillations on the current oscillograms (with a period of several nanoseconds) increase abruptly in the last stage of the pulse. A comparison of data obtained by means of time-resolved and time-integrated measurements suggests that the beam is sharply focused during its existence but migrates over the time-integrated spot image, with instantaneous heating of small foil areas. If the anode foil has not yet expanded up to the moment of heating, then, after the beam displacement off the heated spot, the latter will cool off as a result of the fast expansion during a time comparable to the heating time. Hence, an underestimated mean temperature is observed.

In the thin layer of foil material plasma produced in the short time of 5 to 10 ns, the increase in energy deposition due to magnetic stopping should not be substantial since the Larmor radius is comparable to the layer thickness. To verify this assumption and, furthermore, to develop the above described measurements, experiments on heating pre-expanded plasma by a focused beam were carried out at the Mirage device. A plasma of  $10^{20} \text{ cm}^{-3}$  density was produced by the explosion of a 3.5- $\mu\text{m}$ -thick gold foil brought about by an auxiliary current. The diode gap was isolated from the plasma layer by a tantalum foil of a thickness of 2 to 20  $\mu\text{m}$ . The experiment showed a significant increase in radiation power.

The plasma dynamics in a diode at the MIVL output was studied at the MS-M accelerator ( $R_d = 2\Omega$ ) (Fig.4). The diameter of the electrodes at the line output was 10 and 6 mm, respectively, the accelerating gap 1 to 3 mm. The formation of current-carrying plasma streams and channels in the accelerating gap was observed by image-converter photography of the plasma glow and by laser diagnostics.

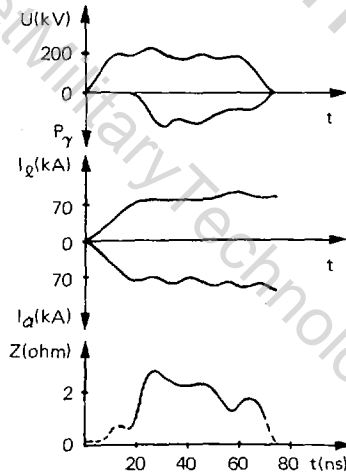


FIG.5. Voltage  $U$  and  $I_0$  - current at the input of the line,  $I_a$  and  $P_\gamma$  - current and X-ray radiation from the anode,  $Z$  - diode impedance.

The estimated plasma density in the channels did not exceed  $10^{17} - 10^{18} \text{ cm}^{-3}$ , the diameter of the channels was 0.2–0.3 mm, and the plasma flow velocity at the front amounted to  $(2 - 5) \times 10^7 \text{ cm} \cdot \text{s}^{-1}$ . The appearance of the channels is apparently connected with the formation of cathode spots in the region of the MIVL edge, which emit plasma streams that are magnetically confined by the stream current field. The streams propagate along the negative electrode up to the accelerating gap and form either one or several channels. The sharpness of focusing and the diode impedance are defined by the plasma channel quality and its formation time. Pinhole photographs of the anode show that the beam is fixed in the channels. In principle, each channel can form a turbulent pinch [2].

An important diode parameter in the self-focusing regime is its operation time before the gap is filled by dense layers of near-electrode plasma. To increase this time and shorten the beam current delay we may inject plasma into the diode from an external source, thus preparing the channel formation conditions for large cathode-anode gaps. This method must be more effective than plasma production during the pre-pulse.

The plasma was created by an erosion source placed within the cathode  $10^{-6} - 10^{-5} \text{ s}$  before the pulse. The measurements showed that an initial gap in optimum conditions increased more than three times and the diode operation time increased 1.5–2 times, in comparison with the regime of the optimum diode operation time without plasma injection. The efficiency defined from a comparison of the currents at the MIVL input  $I_0$  (Fig.5) and the anode  $I_a$  was more than 90%. In these experiments, a beam focusing down to 2 mm diameter was observed.

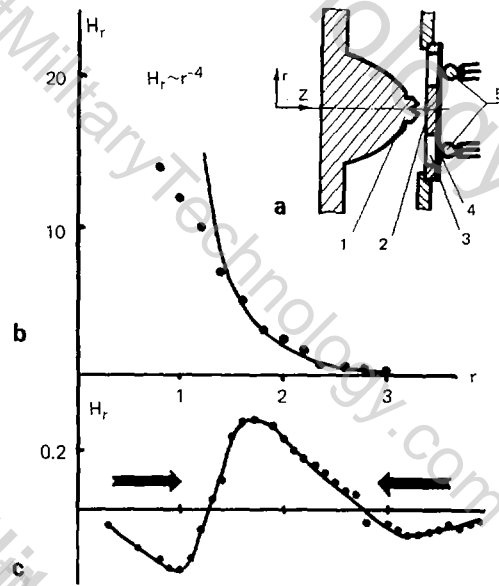


FIG. 6.  $H_r$  component of magnetic-field measurement scheme: a) Kalmar-1 diode: 1 – cathode, 2 – anode (2 mm thick), 3 – radial split, 2 mm wide and 20 mm long, 4 – vacuum seal, 5 – magnetic probe; b)  $H_r$  versus radius near inner anode surface (model measurements with solenoid coil on diode axis), source frequency: 40 MHz; c)  $H_r$  value measured by probe near outer anode surface. Arrows show split length.

At the Kalmar device an attempt was made to detect a longitudinal magnetic field in the beam due to the development of a screw-type current instability [11]. In this case,  $H_r \neq 0$  should be observed at the anode surface. To detect this field against the background of the  $H_\phi$  field narrow radial slits were produced in the metallic anode. Magnetic probes (Fig. 6) were placed behind these slits. In 30% of the shots,  $H_r$ ,  $H_z$  fields were observed. The  $H_r$  field appears when the diode has an active resistance and X-ray radiation appears. The  $H_r$  pulse always has a front of no more than 10 ns. The  $H_z$  field in the plasma reached  $10^{-1}$  of the  $H_\phi$  field at the current column boundary. No changes in the diode impedance were found during the appearance of the  $H_z$  field.

The physical model of the diode must explain the following facts: high excess over the Alfvén current, focusing, mechanism of plasma channel resistance. For a small aspect ratio of  $R/d \approx 1$ , the current can exceed the Alfvén limit sufficiently only if almost the entire diode gap is filled with plasma and we have a Z-pinch. The main question is the reason for pinch stability during the hundreds of Alfvén times,  $\tau = R/v_A$ , where  $v_A$  is the Alfvén velocity.

In our opinion the properties of such a Z-pinch are connected with the drift effect of the magnetic field by the electron current [12]. From the Bennett

equation for our parameters ( $I = 200$  kA,  $T = 700$  keV) it follows that  $u/v_A \approx 3-5$  ( $u$  is the electron current velocity). We remember that the usual mono-fluid hydrodynamics can be applied for  $u/v_A \ll I$ . From this condition, we may suppose that the ions are at rest and consider a steady flow of electrons. If we assume the magnetic field to be frozen in the electrons we can show that along the current line the value of  $nr^2$  is constant, where  $n$  is the electron density, and  $r$  the radius. In this case, the current is a function of  $nr^2$ . No sausage-type instability can develop in such a pinch because its development is usually connected with a decrease of  $nr^2$  due to plasma loss through the neck and it would contradict the conservation of  $nr^2$  along the current line in the present conditions.

The diode electrical resistivity in this model is the result of the work needed for compression of the electron flow. The magnetized electron flow in the diode should become self-focused upon entering a denser plasma region.

For  $u/v_A \approx 3-5$ , small-scale instabilities may develop, resulting in substantial anomalous resistivity if the effective collision frequency reaches  $\nu \approx \omega_{pe}(R/L)\sqrt{(T/mc^2)}$ , where  $L$  is the pinch length.

### 3. GENERATION OF DISC-TYPE RELATIVISTIC ELECTRON BEAMS

At the Ural device, model experiments on target irradiation in a relativistic electron cloud inside a cusp-geometry magnetic trap are going on. For this purpose, thin disc-type REB generation in a high magnetic field ( $B \leq 15$  kG) at  $U = 200$  kV,  $I_{max} = 60$  kA and  $\tau = 100$  ns was studied [13]. The beam was generated by means of an 'edge'-type stainless-steel ring cathode with an inner diameter of  $2R_c = 140-144$  mm and thicknesses of  $h_0 = 0.5; 1; 2$  mm, placed in the median plane of the cusp magnetic trap. A cylindrical stainless-steel foil of 0.2 mm thickness was used as the anode. The initial gap  $d_0$  between the anode foil and the cathode edge varied from 3 to 5 mm. The measured current is described by a formula obtained by A.V. Gordeev for a vacuum diode with a knife-type cathode and a plane anode, placed in a high longitudinal magnetic field:

$$I_e = \frac{17}{\pi} \frac{R_c}{d_0 - vt} (\gamma - 1) \sqrt{\frac{\gamma - 1}{\gamma + 1}} \text{ (kA)}$$

where  $v$  is the dense-cathode-plasma velocity.

The maximum diode current was 60 kA, which is almost twice the calculated value of  $I_e$ . Obviously, the diode impedance was virtually independent of  $B$ , which varied from 3 to 13 kG. The disc beam thickness measured from X-ray pinhole photographs of the anode beam trace is well described by the formula  $h = h_0 + 22E_1/B^2$ , where the normal vacuum electric field at the cathode surface  $E_1$  is in  $V \cdot cm^{-1}$  and  $B$  is in G (Fig.7). The measured beam thickness at  $h_0 = 0.5$  mm



FIG. 7. X-ray pinhole photograph of anode beam trace. Trace length: 3 cm ( $h_0 = 2$  mm,  $B = 13$  kG). Separate current channels are to be seen.

and  $B = 13$  kG was 0.6 mm. The anode erosion trace and the X-ray pinhole photograph of the anode beam show that the disc-type beam consists of many current channels (four to five channels per 1 cm length of the beam trace).

#### 4. LINER IMPLOSION

The development of pulsed-power technology at a level of  $\sim 10^{13}$ W power, 1–3 MV voltage and  $(0.5-1) \times 10^{-7}$  s pulse duration, combined with MIVL, permits a novel approach to electrodynamic liner acceleration. The implosion rate for a cylindrical liner with an initial radius of 1–2 cm and a mass of some milligrams can be of the order of  $2 \times 10^7$  cm $\cdot$ s $^{-1}$ , in these conditions. Thus, a liner can be treated as an intermediate power amplifier in a 'driver-target' system. A liner is a low-inductance (the initial inductance is 1–2 nH), low-impedance load which must be matched with the output impedance of the generator. The current needed to drive the liner with sufficient acceleration should be 30–50 MA. Then the liner will be exploded and the thickness of the imploding plasma shell will appreciably exceed the initial liner thickness. In our experiment, we used plastic and metal wire liners of  $(0.2-2.0) \times 10^{-3}$  g mass and currents of up to 1.5 MA. A significant azimuthal and axial non-uniformity in the plasma shell density after the liner explosion was found. Satisfactory uniformity of the plasma shell was reached after about 200 ns. At this moment, the plasma filled the volume inside the liner. We think that currentless pre-ionization of the liner will ensure higher azimuthal uniformity and radial compactness of the imploding shell.

#### 5. CONCLUSIONS

The experiments on e-beam focusing in diodes demonstrated the existence of plasma channels in the cathode-anode gap that are responsible for the quality of focusing. The diode characteristics are improved by plasma production either by a pre-pulse or by injection from outside. In the latter case, a lower and almost constant impedance during the main pulse was obtained. The results of the

experimental investigation into the diode phenomena call for the development of a theoretical model and the establishment of scaling laws.

Research on a possible effective irradiation of the target in a relativistic electron cloud accumulated inside the electromagnetic trap to be used in the Angara-5 demonstration experiment device is going on.

The preliminary experimental results on liner compression in the diode may be used to determine the optimum conditions of electrodynamic acceleration of the foils at the Angara-5 device. Present-day diagnostics can be used to obtain the necessary information on many aspects of liner implosion and associated physical phenomena.

### REFERENCES

- [1] ALIKHANOV, S.G., et al., *Pis'ma Zh. Tekh. Fiz.* **5** (1969) 1395.
- [2] RUDAKOV, L.I., *Fiz. Plazmy* **4** (1978) 72.
- [3] LIKSONOV, V.I., et al., *Pis'ma Zh. Ehksp. Teor. Fiz.* **19** (1974) 516.
- [4] KOKA, Yu.V., et al., in *Plasma Physics and Controlled Nuclear Fusion Research (Proc. 5th Int. Conf. Tokyo, 1974) Vol.2, IAEA, Vienna (1975) 337.*
- [5] BABYKIN, M.V., et al., *Technology of Inertial Confinement Experiments (Proc. Advisory Group Meeting Dubna, 1976), IAEA, Vienna (1977) Techn. Doc. IAEA 200, 41.*
- [6] BECKNER, E.M., et al., in *Controlled Fusion and Plasma Physics (Proc. 6th Europ. Conf. Moscow, 1973) Vol.2, Moscow (1974) 200.*
- [7] BOGOLYUBSKIY, S.L., et al., *Pis'ma Zh. Ehksp. Teor. Fiz.* **24** (1976) 202.
- [8] GORDEEV, E.M., et al., *Fiz. Plazmy* **7** (1981) 790.
- [9] CHICHIN, R.V., et al., in *Controlled Fusion and Plasma Physics (Proc. 10th Europ. Conf. Moscow, 1981) 1, Rep.F-2b.*
- [10] GORBULIN, Yu.M., et al., *Pis'ma Zh. Ehksp. Teor. Fiz.* **35** (1982) 333.
- [11] GORDEEV, E.M., et al., *Pis'ma Zh. Tekh. Fiz.* **6** (1980) 1450.
- [12] CHERNOV, A.A., YAN'KOV, V.V., *Voprosy Atomnoj Nauki et Tekhniki, Ser: Termoyadernyj Sintez.* **1** (1982) 61.
- [13] DOLOTOV, S.K., TARUMOV, E.Z., *4th All-Union Symp. High-Current Electronics, Novosibirsk, Theses of Reports, 1* (1982) 159.

### DISCUSSION

G. YONAS: In the plasma-filled diode, is the current carried by the discharge in the plasma or by energetic electrons?

M.V. BABYKIN: I think the way a diode with external plasma injection works can be explained by the turbulent-diode model.

V.P. SMIRNOV: I should like to add that measurements have shown that under optimum conditions the intensity and dose of hard X-rays remain roughly the same as when there is no plasma injection. This suggests that most of the current is carried by high-energy electrons.



## INVESTIGATION OF THE NEUTRON PRODUCTION PHASES OF A LARGE PLASMA FOCUS DEVICE

H. HEROLD, L. BERTALOT, R. DEUTSCH, W. GRAUF,  
U. JÄGER, H.J. KAEPELER, F. LEPPER,  
T. OPPENLÄNDER, H. SCHMIDT, R. SCHMIDT,  
J. SCHWARZ, K. SCHWÖRER, M. SHAKHATRE  
Institut für Plasmaforschung,  
University of Stuttgart, Stuttgart

A. HAYD, M. MAURER, P. MEINKE  
Neue Technologie, MAN München  
Federal Republic of Germany

### Abstract

#### INVESTIGATION OF THE NEUTRON PRODUCTION PHASES OF A LARGE PLASMA FOCUS DEVICE.

Plasma dynamic behaviour and neutron production in large focus devices with pinch currents of approximately 1 MA have been studied by theoretical and experimental methods. For treating turbulent plasma motion, a hybrid code based on the analytical computer algorithm REDUCE was developed. Experimental diagnostics include schlieren photographs, reaction proton localization with pinhole cameras and neutron measurements with Ag counters and scintillators. Calculated and measured data concern the 280 kJ, 60 kV operational mode of the Poseidon plasma focus. It is shown that for large pinch currents ( $> 500$  kA), neutron emission also appears before  $m = 0$  onset in the intermediate phase. This part of the neutron production becomes predominant for very large currents. The lifetime of this intermediate phase strongly increases with increasing current. According to theory, the late phase of the focus is governed by strong turbulence phenomena. The lifetime of the turbulence packets is approximately 150 ns and seems to explain the long-lasting neutron emission in this phase.

### 1. INTRODUCTION

Theoretical and experimental studies on neutron production phenomena of plasma foci at high energy levels were carried out and compared with earlier results from smaller devices. For the calculation of plasma focus (PF) dynamics and turbulence phenomena, a newly developed hybrid code [1-3] was employed. This code is based on the analytical computer algorithm REDUCE. The complete non-linear two-fluid equations with viscosity are used to describe PF behaviour.

The experiments were carried out on the newly installed Poseidon PF device (500 kJ, 80 kV) at energy levels of 120 to 380 kJ and  $I_{\max}$  of 1.8 to 3.2 MA.

## 2. CALCULATION OF TURBULENT PLASMA FOCUS DYNAMICS AND NEUTRON PRODUCTION

The calculation procedure is described in detail in Ref.[2]. The two-fluid equations are formulated in cylindrical co-ordinates by REDUCE. The essential feature of the further calculation is a description of dynamical phenomena in  $\omega, \vec{k}$  space. This is accomplished by introducing a plane wave assumption:

$$\psi(\vec{r}, t) = \psi_0(\vec{r}, t_0) + \tilde{\psi}(\vec{r}, t)$$

$$\tilde{\psi} = \sum_{\ell=1}^m \epsilon^\ell \tilde{\psi}_\ell, \quad \epsilon < 1$$

$$\tilde{\psi}_\ell = \frac{1}{2\pi} \int \hat{\psi}_\ell \exp[i(\vec{k} \cdot \vec{r} - \omega t)] d^3k d\omega$$

and solving the system of equations for the  $\tilde{\psi}_\ell$  by sorting according to powers of  $\epsilon$ . Here,  $\psi_0$  is an initial value for the dynamical variable  $\psi$  at time  $t_0$  and  $\tilde{\psi}(\vec{r}, t)$  is a generalized "perturbation value" which also contains an incremental part. The oscillatory behaviour of the dynamical variables, as well as turbulent circulation, is expressed through the vorticity  $\vec{\zeta}$ :

$$\vec{\zeta} = \text{rot } \vec{v} = -\nabla^2 \vec{a}$$

where  $\vec{a}$  is the vector potential of the velocity field. A separate equation is also formulated for the electrical vorticity  $\vec{\zeta}_e$ :

$$\vec{\zeta}_e = \text{rot } \vec{j}$$

where  $\vec{j}$  is the local current density. The degree of turbulence is expressed by the character and magnitudes of these vorticities as well as the fluid and magnetic Reynolds numbers.

To obtain the plasma parameters as functions of space and time, a retransformation from  $\omega, \vec{k}$  space to  $\vec{r}, t$  space is carried out, smoothing over the high-frequency oscillatory part of the respective dynamical variables. Avoiding the well known difficulties with steep gradients in numerical calculations, the retransformation into  $\vec{r}, t$  space is made analytically using the Fourier development:

$$f(x) = -\frac{1}{2\pi} \sum_{n=0}^m \left\{ \left( \frac{1}{ix} \right)^{n+1} e^{ikx} \frac{\partial^n \tilde{f}(k)}{\partial k^n} \right\}$$

where  $\tilde{f}(k)$  is the Fourier transform of  $f(x)$ . The analytical differentiation is made by REDUCE, followed by summing the series consisting of  $m$  members. Numerical evaluation employs FORTRAN computer language.

Calculations to date were made for the compression phase, intermediate phase (from maximum density to  $m=0$  onset), instability and late phase of the PF.

Because the dispersion relation is established by REDUCE from the basic equations without any simplification, all instabilities driven by macroscopic plasma motion and drifts (instabilities due to co-ordinate space non-uniformity) are included.

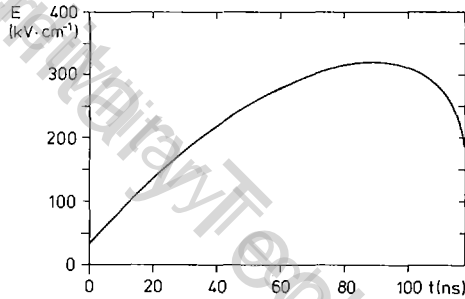


FIG.1. Electric field versus time during the intermediate phase of the Poseidon plasma focus ( $t=0$  for maximum compression).

For the intermediate phase, the theory yields an unstable behaviour if the pinch current exceeds 500 kA. A Rayleigh-Taylor-like rippling occurs with fluting growth being damped out shortly before  $m=0$  onset (see next section). Simultaneously, a current filamentation occurs. The local electric field in quasi-solitons, travelling along the filaments, increases (Fig.1) and leads to acceleration of deuterons, which in turn causes neutron production from d-d reactions. Number density and energies of accelerated ions are calculated by solving the Vlasov equation. Neutron yield is computed using a beam-target model. For pinch currents  $I_p \leq 500$  kA, no neutron production from acceleration mechanisms occurs during the intermediate phase. The lifetime of the intermediate phase increases with pinch current.

During the  $m=0$  instability, the vorticity is purely oscillatory and a rotational part develops only after the  $m=0$  flow field has decayed. Turbulence packets

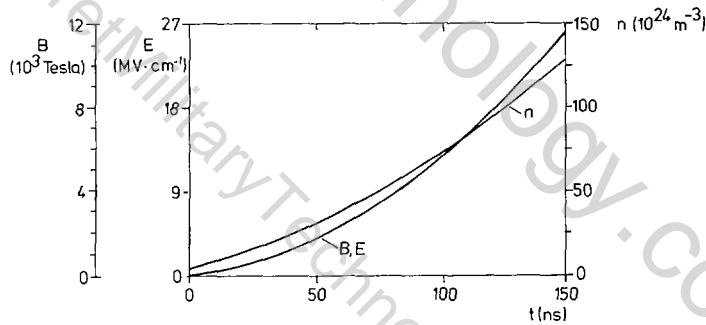


FIG.2. Magnetic field  $B$ , electric field  $E$  and density in the turbulence packets versus time  $t$ , in the late phase of the Poseidon plasma focus.  $t=0$  corresponds to the onset of the  $m=0$  instability.

are formed, behaving as solitons. The density and the electric and magnetic fields (Fig.2) in these solitons increase rapidly to very high values. Deuterons are accelerated and neutron production from d-d reactions occurs. The surrounding plasma decays rapidly. The contraction time of the  $m=0$  instability is approximately 13 ns and the late phase with the turbulence packets lasts for approximately 140 to 170 ns, both being almost independent of the magnitude of the pinch current.

### 3. COMPARISON OF THEORY AND EXPERIMENT

Most of the experiments with Poseidon were carried out at 280 kJ/60 kV, with deuterium filling pressures of 3 to 4 mbar for optimum neutron production. The electrode dimensions were: inner radius 65.5 mm; outer radius 100 mm. The maximum total current was 2.9 MA and the pinch current  $I_p \lesssim 1.1$  MA. The calculations were performed for this operational mode.

Experimentally, the correlation between focus dynamics and neutron production was studied by five-frame schlieren pictures, by neutron measurements with Ag counters and scintillators, and by reaction proton source localization with pinhole cameras.

A typical experimentally obtained signal of the neutron emission is shown in Fig.3. For these measurements the field of view around the focus pinch was restricted to 12 cm diameter by a paraffin collimator. Thus, scattered neutrons and neutrons produced far away from the pinch were eliminated. The calculated neutron emission is shown in Fig.4. It becomes evident from such curves that a strong pre- $m=0$  neutron emission does occur during the intermediate phase, as predicted by the theory for pinch currents  $I_p > 500$  kA. The neutron

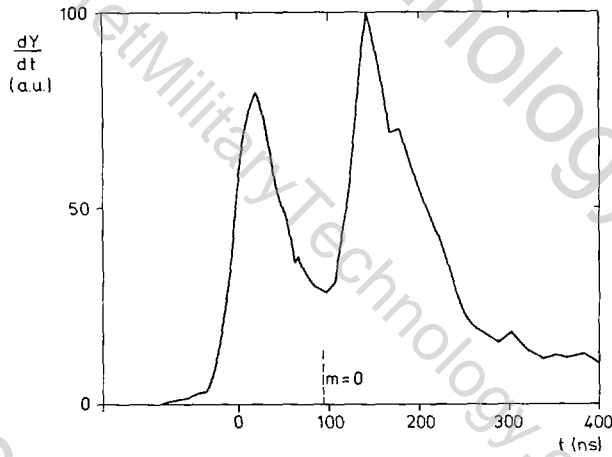


FIG. 3. Typical measured neutron signal of the Poseidon focus.  $t=0$  refers to the maximum compression,  $t_{m=0}$  to the onset of the  $m=0$  instability.

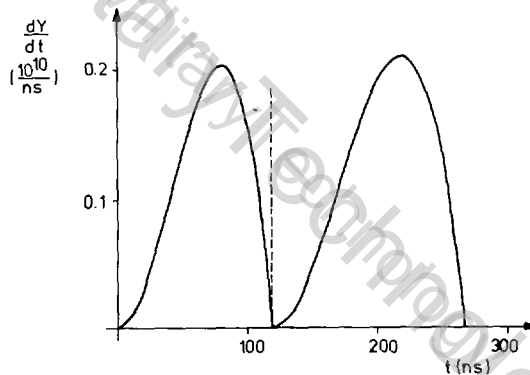


FIG. 4. Calculated neutron production rates in the intermediate (0 to  $\approx 120$  ns) and late ( $> 120$  ns) phases of the Poseidon plasma focus.

yield observed in this phase,  $Y_{ip} \approx 2 \times 10^{10}$ , cannot be explained by thermal neutron production for the "normal" plasma parameters ( $T_i \approx 700$  eV from compressional heating,  $\tau \approx 90$  ns and plasma volume from schlieren pictures,  $n \approx 3 \times 10^{18}$  cm $^{-3}$ ). Hence, acceleration processes or anomalous ion heating must already take place in the focus plasma before the  $m=0$  onset. In previous experiments at smaller PF devices with pinch currents  $I_p \leq 500$  kA, no neutron production was detectable before  $m=0$  break-up [4], nor was it predicted by the above calculations [2].

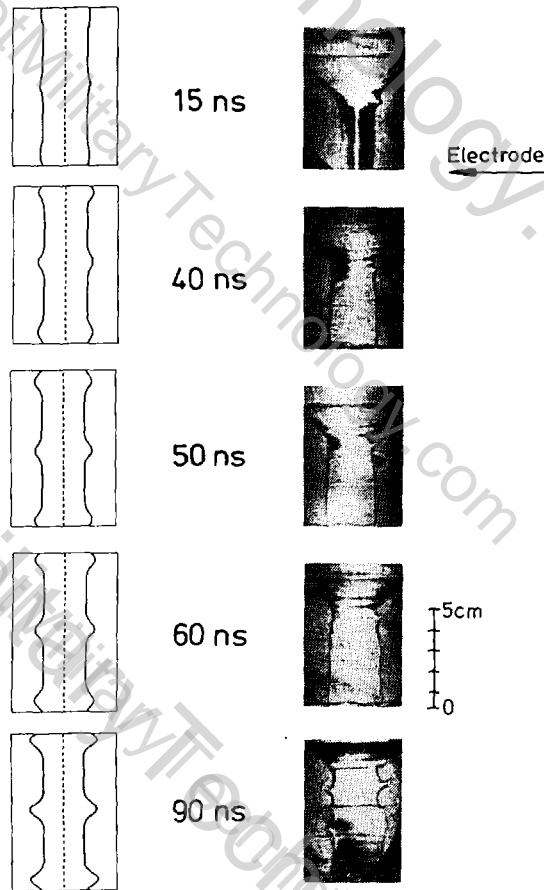


FIG.5. Comparison of calculated plasma geometry during the intermediate phase with schlieren pictures, taken from one Poseidon discharge (exposure  $\approx 1$  ns).

Schlieren pictures taken in sequences during the intermediate phase demonstrate that the plasma remains radially well contained in cylindrical configurations with slightly rippled surface. In Fig.5 these pictures are compared with theoretically obtained shapes.

The lifetime of the intermediate phase  $\tau_{ip}$  is of considerable importance for further focus development, and it increases strongly with increasing pinch current. This is checked for the data of different experiments in Fig.6 and appears to be well in accordance with theory, which yields a scaling like  $\tau_{ip} \propto I_p^{3/2}$ . In the case of a "break-even" PF, this lifetime is calculated to be approximately  $10 \mu\text{s}$  for  $I_p \approx 20$  MA. Furthermore, the theory shows that for very high pinch currents

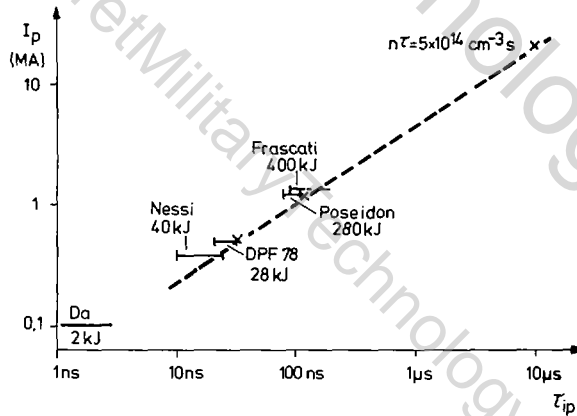


FIG.6. Theoretical prediction (X) of the lifetime of the intermediate phases  $\tau_{ip}$  (maximum compression until  $m=0$  onset) as function of the pinch current  $I_p$  compared with experimental observations for several plasma focus devices.

the neutron production in the intermediate phase becomes much more effective than in the late phase (Fig.7).

For the late phase of the PF, the theory predicts the existence of relatively long-living turbulence packets of rather small size ( $\approx 0.25$  mm radius), which are the source of fast ions and of subsequent neutron emission. There is some experimental evidence for such post- $m=0$  macroscopic turbulence phenomena. In previous experiments one or two small sources of fast ions ( $E_d \geq 2$  MeV) were regularly observed in the discharges by pinhole techniques [4]. They were located on the z-axis of the pinch. Their size (0.3 to 0.5 mm diameter) agrees well with the value calculated for a turbulence packet. Furthermore, the FWHM of the post- $m=0$  neutron emission ( $\approx 100$  ns) is in accord with the lifetime of the turbulence packets (135 ns). The values in brackets refer to the Poseidon experiment. In particular, this long-lasting neutron emission from the pinch region in the presence of a fast decaying plasma could not be satisfactorily explained until now.

Time-integrated pinhole pictures of the reaction protons were taken at Poseidon using CR-39 films as detectors. This method gives a considerably improved space resolution compared to the usual source localization techniques by neutron collimators or neutron pinholes. The distortion of the proton trajectories by the focus magnetic field can be corrected mathematically, and methods for that purpose have been developed [5]. Figure 8 is an example of such proton pictures. The geometrical features of the proton source in Fig.8 may well be interpreted as the superposition of a large source of pinch dimensions (intermediate phase emission) by rather small axially located sources (late phase emission). The spatial resolution in this case was 3 mm.

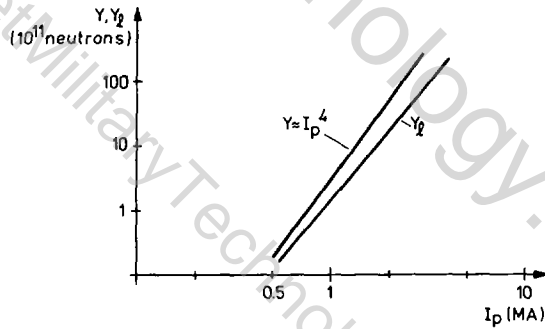


FIG. 7. Calculated total neutron yield  $Y$  and neutron yield during the late phase  $Y_L$  as function of pinch current  $I_p$ .

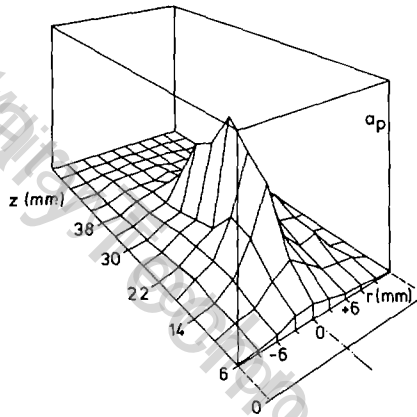


FIG. 8. Pinhole picture of reaction protons from Poseidon at 40 kV, 125 kJ,  $p_{02} = 30$  mbar,  $D_2$ .  $a_p$  = number of proton tracks per  $\text{mm}^2$ ;  $r$  = pinch radius;  $z$  = pinch length,  $z=0$  anode tip.

#### 4. CONCLUSIONS

Strong neutron production is already observed from the well contained focus plasma before the onset of  $m=0$  instability. The neutron yield occurring in a separate pulse is about a factor  $10^3$  higher than "thermal" production. According to the calculation, this is due to non-linear phenomena such as current filamentation, the occurrence of slowly decaying wave packets and high electric fields ( $300 \text{ kV} \cdot \text{cm}^{-1}$ ) leading to acceleration of deuterons. For small pinch currents  $\leq 500 \text{ kA}$ , these phenomena do not occur.

The lifetime of this intermediate phase increases with the pinch current (there is agreement between theory and experiment). For the 20 MA level, necessary for break-even, the delay of the  $m = 0$  instability onset is calculated to be  $\approx 10 \mu\text{s}$ . Furthermore, the neutron production becomes dominant in the intermediate phase compared to that of the post- $m = 0$  phase, while the total yield still scales favourably as  $Y \propto I_p^4$ . These preliminary results are certainly highly attractive for fusion reactors. However, some experimental features (curved pinch,  $B_{z0}$  field, photon emission) not yet considered in the theory and, particularly, microscopic turbulence, require further investigation.

#### REFERENCES

- [1] HAYD, A., KAEPPELER, H.J., MEINKE, P., Inst. Plasmaforschung, Stuttgart, Rep. IPF-82-1 (1982).
- [2] HAYD, A., KAEPPELER, H.J., MAURER, M., MEINKE, P., Inst. Plasmaforschung, Stuttgart, Rep. IPF-82-7 (1982).
- [3] HAYD, A., KAEPPELER, H.J., MAURER, M., MEINKE, P., in Proc. Int. Conf. Plasma Physics, Göteborg, 1982, p.64, Paper 12 b:3.
- [4] BERTALOT, L., et al., in Plasma Physics and Controlled Nuclear Fusion Research 1980 (Proc. 8th Int. Conf. Brussels, 1980) Vol.2, IAEA, Vienna (1981) 161.
- [5] JÄGER, U., Inst. Plasmaforschung, Stuttgart, Rep. IPF-80-8 (1982).



## EXPERIMENTAL PROGRESS IN PLASMA DYNAMICS AND GENERATION OF ENERGETIC PARTICLES IN DENSE PLASMA FOCUS

M. YOKOYAMA, Y. KITAGAWA, Y. YAMADA,  
M. OKADA, Y. YAMAMOTO, C. YAMANAKA  
Institute of Laser Engineering,  
Osaka University, Suita, Osaka

K. HIRANO, Y. KONDOH, K. SHIMODA,  
T. YAMAMOTO, M. HATTORI, M. SATO  
Department of Electronic Engineering,  
Gunma University, Kiryu, Gunma  
Japan

### Abstract

#### EXPERIMENTAL PROGRESS IN PLASMA DYNAMICS AND GENERATION OF ENERGETIC PARTICLES IN DENSE PLASMA FOCUS.

The progress of recent experiments in dense plasma focus at Osaka University and Gunma University is described. Correlation between macroscopic behaviour of focused plasma and neutron yield in two Mather-type devices, A and B, are presented. A Filippov-type device, C, was used to observe plasma dynamics including current sheet, imploding and reflected shock wave. In device A, nuclear activation is used for measuring deuteron intensity, energy spectrum and angular distribution. Cellulose nitrate particle-track detectors are used for high-energy protons. Spatial and temporal locations of generation of high-energy ions are observed by ruby laser holographic interferometry. Ion pinhole cameras are used for determining the localization of high-energy ion generation. Experimental results show that energetic ions are produced and accelerated by a plasma diode. Ion temperatures in focused plasma are estimated from measurement of the D-D/D-<sup>3</sup>He reaction ratios in a D<sub>2</sub>-<sup>3</sup>He mixture gas experiment. In the upstream and downstream directions with respect to the discharge current, electrons and ion beams were observed in device B. A simultaneous measurement using the streak-mode interferometer and the Thomson analyser showed that the neutrons were generated by a "moving plasma diode mechanism". According to the measurement performed with a multi-framing interferometer for device C, the highest collapse of the current sheet was attained at the collision between the collapsing current sheet and the reflected shock wave.

### 1. INTRODUCTION

The plasma focus is not only one of the complementary fusion devices between the low- $\beta$  tokamak and high compression inertial fusion, but it is also

very suitable for detailed studies of non-classical processes in the absorption of intense lasers. There has recently been considerable interest in generating intense high-energy electron and ion beams in plasma focus devices for inertial confinement fusion.

In this paper, correlation between plasma dynamics (including shock generation and growth of macroscopic instabilities) and the neutron yield in plasma focus devices is investigated. Neutrons and high-energy ions produced in the focus phase are also investigated in the low- and high-pressure modes.

## 2. APPARATUS

Two Mather-type (A[1] and B[2]) and one Filippov-type (C[3]) plasma focus devices were used. The devices were operated at 30 kV for stored energy of 18 kJ at 1.5 torr  $D_2$  (low-pressure mode), and 5 torr  $D_2$  (high-pressure mode), respectively.

A condenser bank of  $24 \times 2.32 \mu F$  was used to energize devices B and C. For device A, radioactivity induced in graphite, aluminium and copper targets provided the deuteron intensity, energy spectrum and angular distribution. The experimental set-up and target parameters are shown in Fig. 1. High-energy protons were also measured by cellulose nitrate particle track detectors.

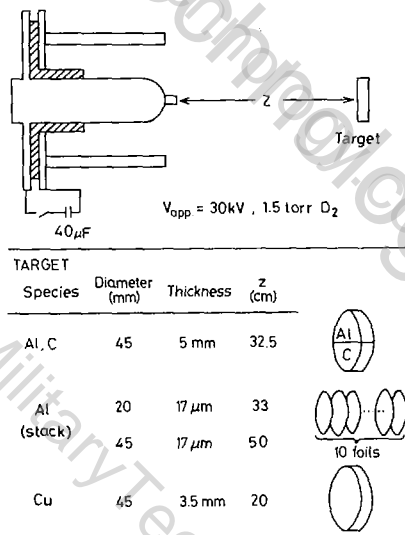


FIG.1. Device A: experimental set-up for nuclear activation and target parameters.

To see the spatial and temporal location of the generation of high-energy ions on and off the axis of the inner electrode of the plasma focus device, a three-channel ruby laser holographic interferometry (2 ns exposure time) was used. Ion generation was localized by two ion pinhole cameras located in the radial and axial directions. The ion temperature was estimated from measurement of the  $D-D/{}^3\text{He}$  reaction ratio in the  $D_2-{}^3\text{He}$  mixture plasma-focus discharge.

For device B, a Thomson analyser was used for measuring the charged-particle beam generated from the focused plasma [4]. Six scintillator (NE 102A) photomultiplier combinations were used for the time-dependent measurement for each energy band of 10 keV. For the time-integrated band, CN film (Kodak CN85) was used as detector.

To investigate the correlation between the dynamic behaviour of the focused plasma and the acceleration mechanism of the ion beam, a streak-mode interferometric measurement and a time-dependent measurement of the ion beam were carried out simultaneously. In the interferometer, the plasma was observed through a slit (0.2 mm wide) which covered up to 2.5 cm of the electrode face along the axis.

For device C, a multiframing interferometric study was carried out [5].

### 3. EXPERIMENTAL RESULTS AND DISCUSSIONS

For device A, stacks of 10 aluminium foils were used to measure the deuteron energy spectrum. In the low-pressure mode of  $D_2$ , the main energy component was up to 2 MeV and the high-energy tail ranged from 2 MeV to more than 3 MeV. The energy spectrum of protons measured by CN film technique had also been shown to consist of two exponentially decaying components [6]. The main component was less than 1 MeV and the high-energy tail extended to more than 2 MeV [7].

The angular distribution of the deuteron was measured by placing 19 graphite targets above the anode at various angles. The intensity of the high-energy deuterons fell by a factor of two for a  $20^\circ$  displacement from the axis. The angular distribution of the deuteron beam ( $E_d > 330$  keV) was  $\lesssim 30^\circ$  in the low-pressure mode. In the high-pressure mode, distribution was shown to be multistructure, and two peaks were observed at  $\lesssim 20^\circ$  and  $\approx 60^\circ$ . The results of angular distribution of the deuterons in the low (1.5 torr  $D_2$ ) and high (5 torr  $D_2$ ) pressure modes are shown in Fig. 2. The angular distribution of protons was also measured by CN films with Al foils.

A holographic interferogram showed time-sequential pinch images for deuterium fill-gas pressure of 1.5 torr. At 0 ns, when the hard X-ray and high-energy ion beams are generated, the pinched column is cut 1 mm below the anode

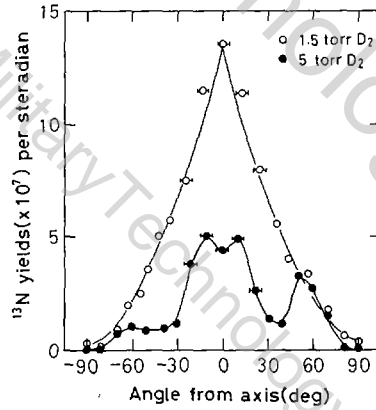


FIG. 2. Angular distribution of deuteron in low-pressure mode (1.5 torr D<sub>2</sub>) and high-pressure mode (5 torr D<sub>2</sub>).

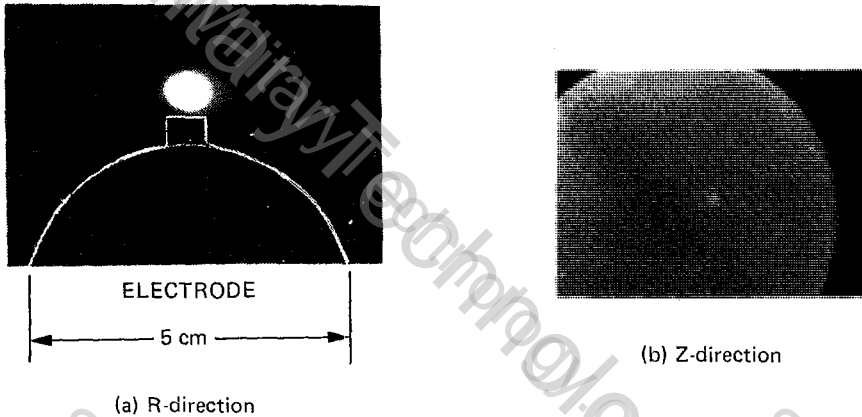


FIG. 3. Deuteron pinhole images in (a) the radial and (b) the axial directions for 30 kV, 18 kJ and 1.5 torr D<sub>2</sub>.

tip, forming a plasma diode. At 10 ns, the anode plasma begins to blow off in the downflow direction. For hydrogen gas we also observed such a cut for the low pressure of 4 torr, while for the high-pressure region we could observe no such cut in the pinched column.

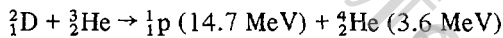
In the ion pinhole camera the pinhole was made of 2 mm thick lead and the film was Kodak CN85. The film on the z-axis was filtered with 17 μm thick Al. Figure 3 shows the deuteron images in the radial and axial directions. The axial

TABLE I. ION TEMPERATURES ESTIMATED FROM D<sub>2</sub>-<sup>3</sup>He EXPERIMENT

D <sub>2</sub> + <sup>3</sup> He	D-D/D- <sup>3</sup> H	T <sub>i</sub>	
		Thermonuclear (keV)	Beam-accelerated (keV)
4 torr (1:1)	14	5.0	42
4 torr (1:2)	13	5.2	43
1.5 torr (1:1)	3	11	74

location agrees with that of the pinched column cut observed in time-sequential holographic interferograms. The experimental results show that energetic ions are produced and accelerated by a plasma diode.

The ion temperature was estimated from measurement of the D-D/D-<sup>3</sup>He reaction ratio. The plasma focus device was operated at 30 kV with a gas mixture of D<sub>2</sub> and <sup>3</sup>He. The reactions were:



D-D neutrons were measured by an Ag-coated GM counter; D-<sup>3</sup>He protons were measured by an activation technique using the <sup>63</sup>Cu(p,n)<sup>63</sup>Zn reaction. The threshold for protons is 4.21 MeV.

During operation of atomic or molecular mixtures of D<sub>2</sub> and <sup>3</sup>He, in the high- and low-pressure modes, ion temperatures and directed kinetic energies are estimated depending on the assumptions of thermonuclear and beam target models [8]. The results are shown in Table I.

The major results obtained by device B are the following. When a hollow inner electrode was employed, the only deuteron beam was observed in the direction downstream with respect to the discharge current. The time-integrated measurement of the ion beam showed that the energy was distributed mainly from 100 keV to 400 keV and its maximum was higher than 1 MeV. In the upstream direction only the electron beam with energy spread from 0.1 MeV to 1 MeV was observed.

Figure 4(a) and (b) shows typical examples of time-distance plots for X-rays, neutrons and energy-analysed deuteron beams, respectively. The scintillation detectors in the Thomson analyser were located on the axis and 160 cm from the electrode face. The detector for X-rays and neutrons was placed 90° from the axis and 350 cm from the point of intersection of the electrode face and its axis.

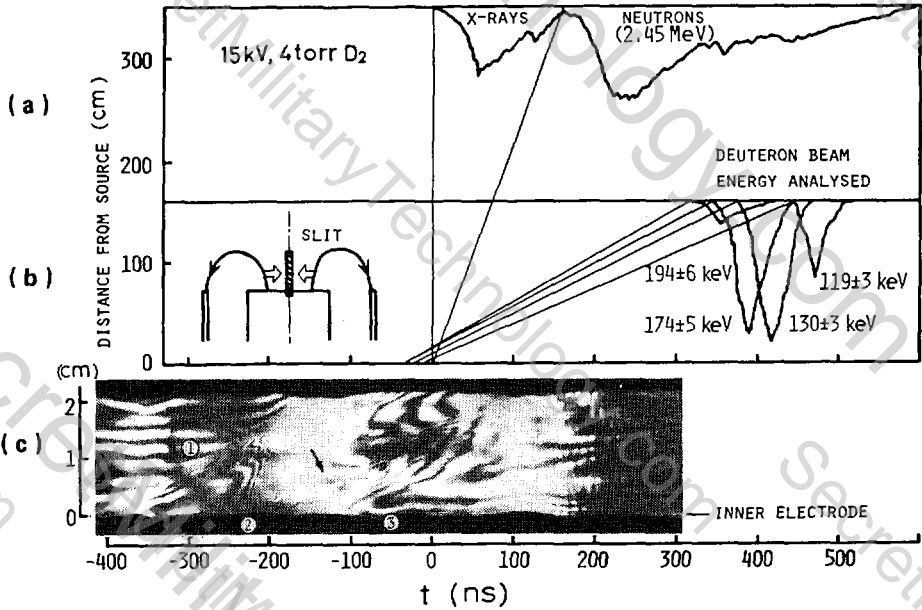


FIG.4. Device B: time-and-distance plots of (a) X-rays and neutrons; (b) energy-analysed deuteron beams; and (c) interferogram in the streak mode.

Figure 4(c) shows streak-mode interferometry in which the slit was aligned to view the plasma column along the axis. The time-and-distance zeros in the plots are taken to be the onset of X-rays and the electrode face, respectively. In Fig.4(c), points 1 and 2 show the imploding shock front and the collapsing current sheet. Since propagation of the shock and the collapse of the current sheet occur in a funnel shape, the fringe shift starts from the neighbourhood of the electrode face and propagates along the axis. Then the electron density, except in a certain region, rises rapidly because of the collapse, and the plasma induces a ruby laser cut-off. The region indicated by the arrow shows that the  $m=0$  instability occurs about 1 cm from the electrode. Then the plasma becomes transparent again. This is ascribed to the current disruption which originates about 0.5 cm from the electrode face.

The disruption region moves in the downstream direction for about 100 ns, as shown by point 3 in Fig.4(c). It can be easily seen from the time-distance plot that the deuteron beam, X-rays and neutrons are generated in this phase. Therefore the neutron yield can presumably be understood in terms of a "moving diode model".

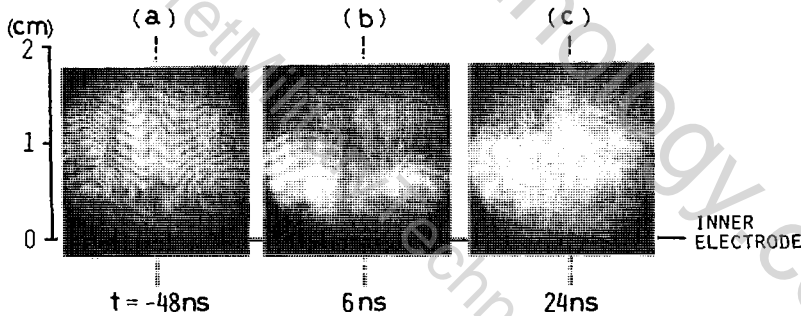


FIG. 5. A typical example of interferograms in the framing mode obtained with device C. Discharge voltage, 15 kV; working gas, 2.5 torr  $D_2$ .

A typical example of the interferometric observation carried out using device C is shown in Fig. 5. In Fig. 5(a), an imploding shock front, which seems to be part of a hypercycloid, appears. The velocity of the shock front is approximately  $5 \times 10^6 \text{ cm} \cdot \text{s}^{-1}$ . The frame shows that the fringes shift considerably behind the front. According to measurements using a magnetic probe, this part is considered to be the current sheet that carries the plasma current. The front collides in part with the electrode axis, and a reflected shock wave is generated. The electron density behind the incident shock is found to be approximately  $4 \times 10^{18} / \text{cm}^3$ . The electron density behind the reflected shock front can be understood in terms of an  $N_2$  laser cut-off. At the time of frame (b) in Fig. 5 the reflected shock front collides with the collapsing current sheet and a very dense plasma column is formed. Frame (b) shows the highest collapse. After the highest collapse, an MHD instability, which seems to be an  $m = 0$  mode, is generated abruptly as shown in frame (c), and then the plasma column decays. It should be noted that the plasma does not show a cut-off in this frame again. A computer simulation using an MHD code and the experimental results showed good agreement except for the electron density behind the reflected shock. The excessive electrons in this region may be understood to be due to an evaporation of the electrode material.

#### REFERENCES

- [1] YOKOYAMA, M., KITAGAWA, Y., YAMADA, Y., YAMANAKA, C., HIRANO, K., in Plasma Physics and Controlled Nuclear Fusion Research 1980 (Proc. 8th. Int. Conf. Brussels, 1980) Vol. 2, IAEA, Vienna (1981) 187.
- [2] HAMADA, F., SHIMODA, K., HIRANO, K., Phys. Fluids 22 (1979) 1217.
- [3] HIRANO, K., HATTORI, M., SHIMODA, K., KIDO, G., MIURA, N., CHIKAZUMI, S., J. Phys. Soc. Jpn. 51 (1982) 297.

- [4] YAMANO, T., KONDOH, Y., SHIMODA, K., HIRANO, K., *Jpn. J. Appl. Phys.* **21** (1982) 659.
- [5] HIRANO, K., SHIMODA, K., EMORI, S., *Rev. Sci. Instrum.* **50** (1979) 1236.
- [6] KITAGAWA, Y., YAMADA, Y., SAIBARA, H., YOKOYAMA, M., YAMANAKA, C., in *Proc. IEEE Int. Conf. Plasma Science, Santa Fe, 1981*, p.119 (Paper 5c4).
- [7] YAMADA, Y., KITAGAWA, Y., YOKOYAMA, M., YAMANAKA, C., *Phys. Letters* **83A** (1981) 9.
- [8] YOKOYAMA, M., KITAGAWA, Y., YAMADA, Y., YAMANAKA, C., in *Proc. 10th Europ. Conf. on Controlled Fusion and Plasma Physics, Moscow, 1981*, Paper D-5.

## DISCUSSION

ON PAPERS IAEA-CN-41/N-6-1 AND N-6-2

J.P. RAGER: With regard to the D-<sup>3</sup>He experiment by the Osaka group, the 40–50 keV deuteron beam energy derived from the relative reaction rate of the D-D and D-<sup>3</sup>He nuclear reactions is certainly too small, in view of some essential properties of neutron emission, such as the end-on line shift of the neutron spectra and the absolute yield for a large plasma focus. There could be three explanations:

(a) The D-D reaction rate is measured by Ag activation, and the detectors monitoring the D-D or D-<sup>3</sup>He reaction rate present a very different aspect in relation to the source.

(b) We know at Frascati that the nuclear data which are normally used to support the D-<sup>3</sup>He reaction rate measurement through copper activation by 14.3 MeV protons are not reliable. In our experiment we performed copper activation calibration and used neutron activation to monitor the D-D reaction rate. Taking all these precautions, we found a mean beam energy of 70–80 keV, much closer to the deuteron energy usually derived from neutron emission properties.

(c) We have also observed a change in the character of the MHD activity when the <sup>3</sup>He is introduced.

I should also like to comment on the theoretical work presented by the Stuttgart plasma focus group. Their new theoretical approach is surely promising, provided it is fully backed up by experimental findings. I see two major problems:

(a) Although we at Frascati have also observed a change in the respective weight of the neutron emissions before and after the onset of MHD instability when the energy level is increased, it must be borne in mind that even in a low-energy system, neutron emission can be observed before this onset. It has also been reported that some plasma foci have neutron yield without any MHD activity at all.

(b) The plasma focus neutron emission properties, especially the spectral ones, vary little when  $I_p$  is modified and even when the filling pressure is changed within reasonable limits, though for the latter case the character of the MHD instabilities varies considerably.

What, therefore, are the main changes in the character of the plasma focus physics when the 500 kA limit in  $I_p$  is exceeded?

H. HEROLD: The calculations show that at low pinch currents the strong non-linear processes and, consequently, the strong pre- $m = 0$  neutron emission, do not occur; this is consistent with experiments in which a precise chronology was carried out. At high currents very large vorticity is introduced into the plasma and strong local E fields appear, giving rise to ion acceleration and strong neutron emission.

**Session O**

**TECHNOLOGY AND REACTOR CONCEPTS II**

Chairman

V.T. TOLOK

USSR

Papers O-2-1 and O-2-2 were presented  
by K. Yoshikawa as Rapporteur

## TASKA – A TANDEM MIRROR FUSION ENGINEERING TEST FACILITY

TASKA-TEAM

P. KOMAREK (*Compiler*)  
Kernforschungszentrum Karlsruhe GmbH,  
Karlsruhe,  
Federal Republic of Germany

University of Wisconsin,  
Madison, Wisconsin,  
United States of America

Abstract

### TASKA – A TANDEM MIRROR FUSION ENGINEERING TEST FACILITY.

TASKA is a fusion engineering test facility based on the tandem mirror principle with an inboard thermal barrier. The aim of the design is to demonstrate that all key technologies for a fusion reactor can be well integrated into one machine, similar to studies based on toroidal confinement. – The main parameters of TASKA are an 86-MW, DT power level, a neutron wall loading of  $1.5 \text{ MW} \cdot \text{m}^{-2}$ , and an overall tritium breeding ratio of 1.0. A barrier magnetic field of 20 T is provided by a hybrid coil (14 T by a superconducting coil and 6 T by an inserted normal conducting coil). The injected power is 117 MW, which is composed of 40 MW of ICRF, 15 MW of ECRH, and 62 MW of neutral-beam power. The length of the central cell is about 20 m; the overall machine length is about 80 m and the plasma radius is 0.32 m. – The preliminary design has shown that TASKA could provide meaningful tests of heating technologies, superconducting magnets, remote maintenance equipment, etc. as well as blanket and material tests and that all these reactor-relevant technologies could be integrated into one machine of moderate size with relatively low cost.

### 1. INTRODUCTION

The favourable expectations for successfully designing and operating a major DT fusion experiment have initiated considerable efforts spent on studies on the next step which is envisaged to be an engineering test facility with all the key technologies required for a 'DEMO'. A worldwide endeavour aiming at such a conceptual design is the study of the International Tokamak Reactor, INTOR. Recent advances in the physics of tandem mirrors have induced us to examine the potential of a tandem mirror device with thermal barriers serving as such an engineering test facility.

We, therefore, focused our study TASKA (*Tandem Spiegelstudie Karlsruhe*) on the maximum reasonable step beyond the next generation of large mirror machines (AMBAL, TMX-Upgrade, GAMMA-10, TARA, and MFTF-B). The objective of the study is to demonstrate that all key technologies required for this step (and later for DEMO) can be integrated into one machine and tested adequately. Thus, TASKA has to serve as a test bed for the technologies of plasma engineering, superconducting magnets, existing materials, plasma heating (neutral-beam and RF-heating), breeding and test blankets, tritium technology, and remote handling. It has to prove that such a facility can operate safely and reliably as a DT burner. In this respect, the objectives of TASKA are similar to the technological ones of INTOR.

Thus, the TASKA study allows a comparison of the technologies required for a tokamak-based solution with a solution based on the tandem mirror with thermal barriers and may prove or disprove whether the favourable expectations set on a mirror solution are justified from an engineering point of view.

The physics concept is based on tandem mirror confinement with a thermal barrier. The level of validity of such a concept is still a major issue brought up by critics of the tandem mirror concept. Certainly, this is an item only partially verified in experiments, but it is expected that several near-term devices (TMX-Upgrade, GAMMA-10, MFTF-B, etc.) can, by the middle of this decade, demonstrate the thermal-barrier mode of operation in a parameter range broad enough for confidence. Thus, the study has used the validity of this present-day physics model as a premise.

## 2. GENERAL DESCRIPTION OF THE TASKA DEVICE

### 2.1. Physics basis

The tandem mirror physics concept has been verified on GAMMA-6 [1] and TMX [2]. The key experiment to demonstrate operation with thermal barriers on a tandem mirror will be performed in 1982–83 on TMX-U. This device will also advance the understanding of electron heating and the central-cell region will be operated in the collisionless-diffusion regime.

The MFTF-B in its axicell modification [3], currently under construction, should demonstrate long-pulse operation (30 s) in the TMR thermal-barrier mode in the 1985–86 time period. The limits on central-cell beta will also be investigated in that device. High-power, continuous (30 s) 80 keV neutral beams will be used to achieve a D–T equivalent  $Q \approx 1$  in the same time period. Thus, we assume these physics concepts to form a reasonable basis for an engineering design of a technology test facility as a next-step machine; they are, therefore, used for TASKA. Figure 1 shows the operating regime for TASKA in comparison with other tandem mirror devices on a  $n\tau$ -versus- $T_i$  (central cell) diagram.

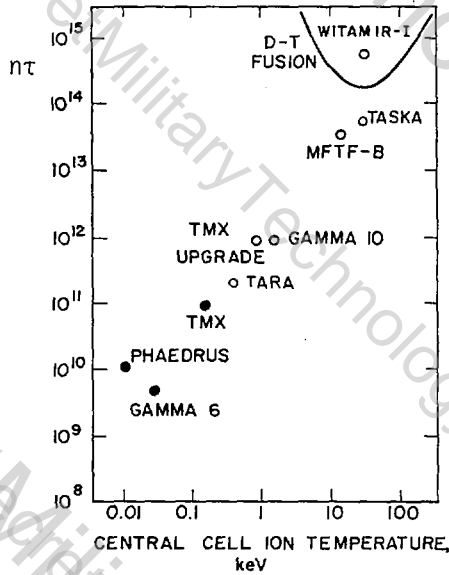


FIG. 1.  $n\tau$  versus central-cell ion temperature for present (●) and future (○) tandem mirrors.

## 2.2. Basic reactor parameters of TASKA [4]

The design uses existing technologies or those which may be expected to be available in the near future. A net power gain is not required; therefore,  $Q$  is not an important parameter and will be slightly less than unity. However, a main consideration is that the neutron wall loading should be high enough to provide a significant neutron flux and fluence for materials and blanket tests. The central-cell length is minimized because of the modest requirements of the test blankets, thus reducing cost without losing scalability. A tritium breeding ratio of 1.0 or more is foreseen, so that there will be no net tritium consumption over the lifetime of the machine. Electric power production, direct energy conversion, or fission fuel breeding are options that can be examined during the life of TASKA.

A schematic view of TASKA is shown in Fig. 2. A selective list of TASKA general operating parameters is given in Table I. In Fig. 3, the confining magnetic fields and electric potentials are shown. The end plugs consist of an inside thermal barrier and a minimum-B yin-yang coil set. There are three central-cell solenoids.

## TASKA-TEAM

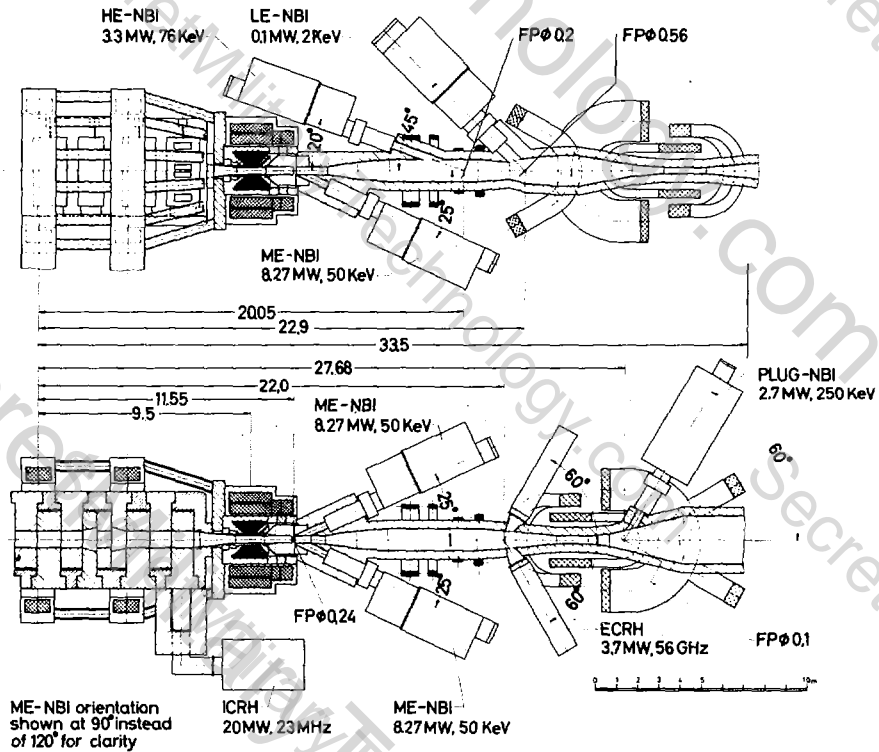


FIG. 2. TASKA overview.

Some key features of TASKA are listed below:

The low power level of 86 MW greatly eases the tritium requirements and reduces the overall cost, compared to previous test devices.

The relatively high wall loading of  $1.5 \text{ MW} \cdot \text{m}^{-2}$  will allow reactor-relevant testing to be performed in both blanket and materials modules.

One of the key features of the machine that allows such a favourable performance is the use of a high-field, room-temperature copper insert which raises the field in the barrier coil from 14 T produced by the superconducting coil to 20 T.

The tritium for this device is provided by circulating a  $\text{Pb}_{83}\text{Li}_{17}$  alloy in HT-9 ferritic-steel tubes. The overall breeding ratio is 1.0 so that no net tritium consumption is incurred over the life of the machine. The low solubility of  $\text{T}_2$  in  $\text{Pb}_{83}\text{Li}_{17}$  results in only a 20 g inventory in the blanket.

There are two modules devoted to blanket testing and one module devoted to materials testing. These test modules are placed between the central-cell coils for ease of access and maintenance.

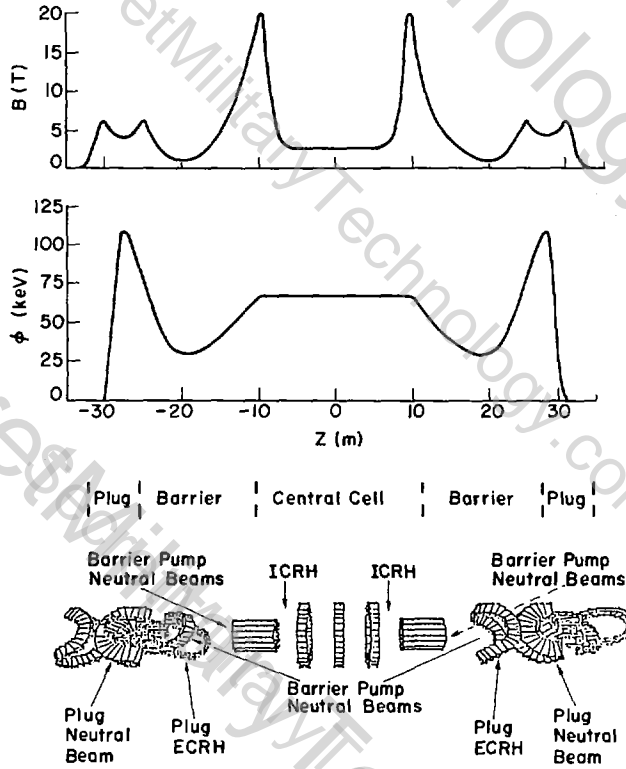


FIG. 3. Magnet and electrostatic configuration of TASKA.

TABLE I. GENERAL OPERATING PARAMETERS – TASKA

DT power level	86 MW
First-wall neutron wall loading	$1.5 \text{ MW} \cdot \text{m}^{-2}$
Total heating power	117 MW
Central-cell magnetic field (on-axis)	2.7 T
Central-cell length	19.2 m
Test modules:	
Number/total volume of test modules	1-material/493 litres 2-blanket/5700 litres
Structure/breeder	HT-9/ $\text{Pb}_{83}\text{Li}_{17}$

### 2.3. The central cell

The central cell of TASKA consists of a long cylindrical structure which surrounds the plasma and is made up of blanket, vacuum vessel, reflector and shield. This cylindrical structure fits inside three superconducting solenoids which provide the confining field with the central cell. On either end of the central cell, there is an ICRF heating section, each consisting of four launching antennae. These antennae are recessed within the first wall and, therefore, do not intersect the path of charged particles streaming out toward the end plugs. The central-cell coils are supported independently of the blanket/shield and are capable of being translated axially on tracks, to provide access for blanket modules located within the bore of the coils. Table II summarizes the main parameters.

Two important blanket types were investigated in the TASKA study: permanent breeding blankets and test blankets. Two blanket modules are designated as blanket test modules, all others as breeding blankets. The inner surfaces of blanket modules adjacent to the test blankets are tapered. This was done to enhance and more uniformly distribute the neutron flux to the material test module REGAT (*Reduced Damage Gradient Test*) [5].

The blanket modules are surrounded by a vacuum vessel made of 4 cm thick 316 stainless steel. The vacuum vessel is followed by a 28 cm thick reflector zone consisting of water-cooled 316 stainless steel. Each blanket module has the vacuum vessel wall combined with the reflector as the module closure which seals against the flange. This portion of the reflector is attached to and is a permanent part of the blanket module.

The last element in the central cell is the biological shield which is needed to protect the central-cell solenoids and personnel during hands-on operations at the fusion device, which might be possible during shut-down periods. The shield is 25 cm thick and is composed of ferritic steel structure, B<sub>4</sub>C, Pb and water cooling. The shield part adjacent to the blanket module closure is also attached to the module.

### 2.4. Plasma heating systems

As indicated in Fig. 2, neutral-beam injection (NBI) is used as the primary means for plasma heating, plasma fuelling, and selective ion charge-exchange pumping in the TASKA design. ECRH and ICRF are used for maintaining the plug electron temperature and the central-cell ion temperature, respectively.

#### 2.4.1. Neutral-beam injection and its influence on the overall design

Computational studies of the equilibrium plasma parameters needed to attain the desired neutron wall loading of  $1.5 \text{ MW} \cdot \text{m}^{-2}$  in the central cell yield

TABLE II. MAIN PARAMETERS OF THE TASKA CENTRAL CELL

A) Physics parameters	
Fusion power	86 MW
14-MeV neutron wall loading	$1.52 \text{ MW} \cdot \text{m}^{-2}$
Overall tritium breeding ratio	1.0
Density	$1.9 \times 10^{14} \text{ cm}^{-3}$
Ion temperature	30 keV
Electron temperature	11.5 keV
Beta	0.5
$(n\tau)_{ic}$	$5.4 \times 10^{13} \text{ cm}^{-3} \cdot \text{s}$
$(n\tau)_{ec}$	$5.3 \times 10^{13} \text{ cm}^{-3} \cdot \text{s}$
Q	0.74
B) Engineering parameters	
Magnet system	3 NbTi solenoids
Inner coil bore	5.6 m
Magnetic field on the axis	2.7 T
at the coil	<6 T
Length of central cell	19.2 m
Length of permanent breeding blanket	8.76 m
Inner bore of blanket	0.92 m
Blanket thickness	1.00 m
Thickness of shield and reflector	0.53 m
Area of first wall for blanket test	$5.84 \text{ m}^2$
Area of first wall for materials tests	$1.44 \text{ m}^2$
Blanket structural material	HT 9
Blanket coolant and breeding material	$\text{Li}_{17}\text{Pb}_{83}$

the NBI-design and heating requirements listed in Table III. For simplicity in present parameter studies, each neutral beam is assumed to consist only of the full energy component.

The NBI performance parameters are based upon a present capability or scaling of existing ion source technology. However, the application to steady-state D-T operation for TASKA will require a further level of special technological development, particularly in the following areas:

The design of high-power level steady-state NBI/ion sources with high reliability and compatibility with remote NBI component changeout. Operation of NBI hardware in a high neutron fluence with a tritium-loaded system will also require some form of remote handling for maintenance (the aim is for a minimum of 1 year normal life-time before required maintenance).

Special cooling technology will be required because of locally high beam power loading on the charged ion dump, on the remnant neutral beam dump, on associated diagnostics, on the ion source grids, and on the machine end walls. The development of steady-state vacuum pumping schemes for the H<sub>2</sub>, D<sub>2</sub> or D<sub>2</sub>/T<sub>2</sub> gas flow in the ion source and neutralizer is required. Sufficient local pumping speed is required to reduce the line density of gas beyond the ion dump to low enough values to limit re-ionization loss to less than 10% and eliminate duct choking. The low injection angles for the high- and medium-energy pump beams tend to require long ducts and careful baffling to avoid direct beam impingement on the walls. The cooling of duct walls (to avoid any thermal desorption) is also essential. Initial studies with a long-duct NBI system possessing a small thermal desorption term of 0.005 torr·L·s<sup>-1</sup>·kJ<sup>-1</sup>, revealed that we may have a duct-choking problem. To overcome this, present plans call for H<sub>2</sub>, D<sub>2</sub> and T<sub>2</sub> gas pumping using panels of solid getter material arranged in a full-surface-folded panel configuration which allows cyclic regeneration. A short cold-wall/hot-exit neutralizer is being considered to reduce the neutralizer gas flow.

The relatively high plug-NBI energy requirements and the need to avoid neutron production in the plugs call for the use of H<sup>0</sup> injection at 250 keV. This will require H<sup>-</sup> ion source technology for a reasonable neutralization efficiency. Such a source is also desirable for other fusion devices.

Magnetic shielding for the NBIs in the high fringe magnetic field of TASKA (particularly for beam lines at low injection angles) is required. While such shielding is difficult to include in the small space allowed, it is feasible.

It is obvious that TASKA represents a challenge to NBI technology, but no insurmountable problems have been identified. Testing of advanced neutral-beam injectors and heating systems in an integrated system can be one of the key applications for TASKA.

TABLE III. PARAMETERS FOR THE NEUTRAL-BEAM INJECTION SYSTEM OF TASKA

Location	Injection angle	Species	$V_0$ (kV)	NBI power per injector (MW)	Number of ion sources per injector	Total number of injectors
Plug-NBI	60°	H <sup>0</sup>	250	2.7	1	2
High-energy-NBI (barriers)	20°	D <sup>0</sup> + T <sup>0</sup>	76	3.3	1	2
Medium-energy-NBI (barriers)	25°	D <sup>0</sup>	50	8.3	3	6
Low-energy-NBI (barriers)	45°	D <sup>0</sup>	2	0.1	1	2

One of the most difficult problems faced in the TASKA study was finding a suitable means of pumping out ions which become trapped in the barrier region. The most straightforward means is to inject neutral beams at 25° into the barrier loss cone so that charge-exchange events will give ions which travel into the central cell, simultaneously solving the plasma fuelling problem (medium-energy beams). Additional beams were, however, necessary to pump the barrier region.

It turned out that the most power-saving solution was a combination of the high-energy beams injected into the bottom of the barrier at 20° and the low-energy beams located to inject into a region of the thermal barriers at 45° where the plasma potential is such as to allow the low-energy beams to pump out the higher-energy trapped ions: 'two stage pumping'. Since the neutral-beam injection angles, dictated by plasma physics requirements, are small the present magnet design is the result of a trade-off between the magnetic fields from the plasma physics requirements and the access requirements for neutral-beam injection. To fulfil these requirements, the barrier coil is built up from several parts with different thicknesses and different current densities. In addition, the end plug has been moved away from the barrier coil to facilitate NBI access. However, the minimum field in the thermal barrier region is then lower than the required 0.8 T. This requires that field-shaping coils (in this case, normally conducting ones) be placed on each end of the device to increase the field up to the required level.

Injection of neutral beams into the plug is somewhat easier in terms of access, but achieving the required energy is very difficult without invoking negative-ion technology. High energy is required to overcome the effective potential  $(\phi_c + \phi_e)/R_p \sin^2 \theta_{in} - 1 = 114 \text{ keV}$ .  $R_p$  is the beta-corrected plug mirror ratio. For reasonable plug beam input power, neutral-beam energies higher than 200 keV are required. An injection angle  $\theta_{in}$  of  $\sim 60^\circ$  is also critical since a sloshing-ion distribution is necessary for plug microstability.

A special feature of TASKA is that  $H^0$ -injection can be used for the MHD-anchors since they are well isolated from the central cell. Maintenance of the source will be easier because of the reduced neutron bombardment and tritium contamination.

#### 2.4.2. RF-heating systems

The plug electrons are maintained at a temperature of 59 keV with 7.5 MW of ECRH power per plug. The frequency chosen is 56 GHz, which corresponds to resonance at a magnetic field of 2 T. The resonance surface is located between the minimum field point in the barrier and the mirror throat of the plug. The 56 GHz frequency corresponds to the upper limit of high power cw gyrotron sources considered to be available on the TASKA time-scale.

The ECRH power is delivered to the plasma using a quasi-optical offset Cassegrain beam waveguide transport system. Using a set of hyperbolic-parabolic mirrors, the microwave power is reflected and focused onto the plasma at the desired angle. An array of gyrotrons feeds a single launcher system. Two launcher systems are required per plug.

Forty megawatts of ICRF heating of central-cell ions are used to maintain the ion temperature at 30 keV; this allows a considerable reduction of the neutral-beam energy and power required for pumping of the thermal barrier. The fundamental deuterium frequency at the beta-corrected magnetic field in the central cell is 15 MHz. In this frequency range, and because of the 32 cm hot-plasma radius, we are constrained to using antennae to couple the ICRF power to the plasma. To improve antenna coupling, second-harmonic heating (at 30 MHz) is used. To protect the antennae from alpha-particle bombardment and to improve the coupling to the hot plasma, a warm-plasma halo between the hot plasma and the antennae is proposed. The antennae are located at each end of the central cell in order to leave the central region free for test modules. The antennae are austenitic stainless steel with a high-conductivity copper surface layer and cooled by water. The Faraday shields are made of molybdenum and radiation-cooled.

### 3. MAJOR STUDY RESULTS

The study has shown that TASKA can provide meaningful tests of major fusion technologies (materials, blankets, magnets, etc.) and that all these reactor-relevant technologies can be integrated into one machine of moderate size and relatively low cost. In particular, the following main statements can be made:

The low DT-power level of 86 MW (620 MW in INTOR) eases the tritium requirements and reduces the overall cost compared to previous test devices. (The estimations gave direct cost of less than US \$800 million based on the same cost algorithms as are used in INTOR.)

The wall loading of  $1.5 \text{ MW} \cdot \text{m}^{-2}$  allows reactor-relevant testing of blanket and material modules. In particular, the materials testing capabilities are very attractive. A large volume ( $>300$  litre) of high-damage-level (up to  $\sim 100$  dpa) testing space is available in TASKA and can accommodate all the specimens needed to qualify alloys and non-metallic materials for a demonstration plant operating around the turn of the century.

The DC-nature of tandem mirror magnets is a big advantage compared with pulsed magnets or DC-magnets with transient pulse load as in tokamaks. Consequently, fatigue is not a limitation.

The technology of the central-cell magnets and the end-plug magnets is available today. This is shown by big bubble chamber magnets and the successful yin-yang test at Livermore.

The technology of the barrier coils needs further development with respect to  $\text{Nb}_3\text{Sn}$  conductor and insulation technology in conjunction with hybrid coil inserts.

The proposed solutions for beam and RF-heating are extrapolations of existing technologies which have to be further developed.

The overall engineering including maintenance and remote handling looks very reasonable and simpler than in many other systems.

This study is being continued in order to optimize the system with respect to reducing cost, but keeping the constraints of a powerful technology test device to the most reasonable extent possible.

### ACKNOWLEDGEMENT

The study has been carried out jointly by the Nuclear Research Centre Karlsruhe (KfK) and the University of Wisconsin [4] with further contributions by Lawrence Livermore National Laboratory. The contributions and donation of scientific staff from many other institutions were also important to the success

of the study. These were from Grumman Corporation, Hanford Engineering Development Lab., Babcock and Wilcox Corporation in USA, as well as from IPP-Garching, KFA-Jülich, INTERATOM and Siemens Co. in the Federal Republic of Germany.

#### REFERENCES

- [1] MIYOSHI, S., et al., in Plasma Physics and Controlled Nuclear Fusion Research (Proc. 7th Int. Conf. Innsbruck, 1978) Vol.2, IAEA, Vienna (1979) 437.
- [2] SIMONEN, T.C., UCRL-53120, Lawrence Livermore National Laboratory.
- [3] THOMASSEN, K.I., KARPENKO, V.N., An Axicell Design for the End Plugs of MFTF-B, UCID-19318 (April 1982).
- [4] ARENDT, F., et al., TASKA – Tandem Spiegelmaschine Karlsruhe – a Tandem Mirror Fusion Engineering Test Facility, KfK-3311 (1982) and UWFDM-500.
- [5] KULCINSKI, G.L., et al., J. Nucl. Mater. 103–104 (1981) 67–72.

## KARIN-I: CONCEPTUAL DESIGN OF A MOVING-RING REACTOR

KARIN-I WORKING GROUP\*

Institute of Plasma Physics,  
Nagoya University, Nagoya,  
Japan

### Abstract

KARIN-I: CONCEPTUAL DESIGN OF A MOVING-RING REACTOR.

The 500 MW(e) D-T fusion reactor KARIN-I has ten moving plasma rings which are produced by relativistic electron beam injection, heated by major radius compression, and conveyed in a linear cylindrical burning section by an annular liquid lithium flow outside a SiC first wall. The liquid lithium not only stabilizes the tilting motion of the rings but also works as a tritium breeder and coolant. The energies of ash-accumulated rings are efficiently recovered by expansion. The linear alignment of the reactor components provides simple maintainability of the system.

### 1. INTRODUCTION

Many physical and technological problems represent obstacles to the realization of the actual extraction of power from thermonuclear fusion. One of the key problems is compatibility between confinement of a burning plasma and maintenance of the reactor. The problem of plasma confinement may presumably be solved by toroidal geometry, but fusion reactors with toroidal geometry are expected to encounter maintenance problems. A reactor with linear geometry, on the other hand, is easier to maintain, although confinement may be rather poor. These considerations led to the construction of the steady-state moving-ring reactor KARIN-I, with linear geometry, containing a number of toroidal plasma rings similar to the concept at PPPL [1].

- \* A. MOHRI, Y. FUJII-E, K. IKUTA, H. MOMOTA, H. NAITOU, Y. NOMURA,  
Y. TOMITA (IPP, Nagoya University)  
M. OHNISHI, K. YOSHIKAWA (Kyoto University)  
S. INOUE, M. NISHIKAWA (Osaka University)  
S.-INOUE ITOH (Hiroshima University)  
K. KITAMURA (Technical University of Toyohashi)  
S. NAGAO (Chubu Institute of Technology)  
M. IWAMOTO (Mitsubishi Elect. Corp.)  
Y. GOMAY, M. KUMAGAI (Toshiba Corp.)  
Y. KAWAKITA, Y. SUZUKI (Nisshin Elect. Corp.)  
K. OKAMOTO (ULVAC Corp.)  
H. MATSUNAGA, S. YOSHIZAWA (Toyo Information System Co. Ltd.)

TABLE I. PLASMA PARAMETERS

	Formation	Burning	Recovery
Major radius	4.5 m	1.5 m	6.0 m
Minor radius	1.5 m	0.5 m	2.0 m
Fuel density	$1.9 \times 10^{19} \text{ m}^{-3}$	$4.8 \times 10^{20} \text{ m}^{-3}$	
Temperature	1.64 keV	9.3 keV	
Ring current	2.45 MA	7.2 MA	
$\beta_p(a)/B_p(a)$	0.23	0.43/2.88 T	
$\beta_t(0)/B_t(0)$	0.22	0.39/3.04 T	
Averaged beta	0.16	0.36	
Axial field	0.11 T	1.2 T	

	Case 1	Case 2
Total plasma energy	103 MJ	103 MJ
Toroidal magnetic energy	14 MJ	11 MJ
Plasma current energy	73 MJ	72 MJ
Plasma thermal energy	16 MJ	20 MJ

$E_{\text{REB}} = 25 \text{ MeV}$	Fusion power:	$P_{\text{rec}} = 72 \text{ MW}$
$I_{\text{REB}} = 1.7 \text{ MA} \times 4$	$P_{\alpha} = 370 \text{ MW}$	$\tau_{\text{rec}} = 0.35 \text{ s}$
$\tau_{\text{REB}} = 100 \text{ ns}$	$P_n = 1480 \text{ MW}$	Effective pumping
Total energy = 17 MJ	No. of rings: 10	speed (two sets)
$\tau_{\text{comp}} = 0.25 \text{ s}$	Burn time 10 s	$10^6 \text{ litres} \cdot \text{s}^{-1}$
$P_{\text{comp}} = 90 \text{ MW}$	Ring velocity $5 \text{ m} \cdot \text{s}^{-1}$	

## Blanket and shield structure:

Axial length	50 m
First-wall radius	2 m
Thickness of SiC	0.02 m
Thickness of Li layer	0.25 m
Neutron wall loading	$2.4 \text{ MW} \cdot \text{m}^{-2}$
Li inlet/outlet temperature	$450^\circ\text{C}/500^\circ\text{C}$
Li temperature difference	$47^\circ\text{C}$
Inlet-outlet pressure drop	6.4 atm
Expected energy deposition	$\approx 90\%$
Tritium breeding ratio	$\approx 1$
Shield material	Concrete
Shield coolant	Water/borated water
Total thickness of shield	1.8 m

This report describes the conceptual design of KARIN-I, whose main objectives are to evaluate the feasibility of a moving-ring reactor and to clarify R&D problems inherent in KARIN-I. The following design targets have been adopted:

- (1) A D-T reactor with a tritium breeding blanket;
- (2) A commercial reactor with 500 MW(e) net electric power output.

Much progress in physics and technology is expected during the next few decades.

KARIN-I has three main components: the formation, burning and recovery sections. Their functions and the evolution of the plasma are discussed separately.

## 2. FORMATION SECTION

Current-carrying plasma rings ( $R = 4.5$  m;  $a = 1.5$  m;  $I = 2.45$  MA) are produced at intervals of one second by the injection of four pulsed intense relativistic electron beams, each of 25 MeV, 1.7 MA, 100 ns. The ring-plasma formation, and heating through beam-plasma interaction, are attained in as short a time as a few microseconds.

Magnetic compression follows in order to heat the plasma to a burning condition in 0.25 seconds by increasing the external vertical or axial magnetic field from 0.11 T to 1.2 T. The power required is estimated as 90 MW, and the average plasma temperature as 9.3 keV, as shown in Table I.

The most dangerous tilting instability is suppressed by a central stabilizing conductor in addition to a resistive side wall.

Since we must satisfy the Mercier criterion for stability, a suitable  $q$ -profile is also chosen so that the poloidal beta value 0.43 becomes attainable. Further study of other instabilities is necessary, however.

## 3. BURNING SECTION

A ring is then pushed into the burning section by means of a magnetic field gradient. At its entrance, liquid lithium is pumped into the blanket region at  $17 \text{ m}^3 \cdot \text{s}^{-1}$  through 30 subdivided flow channels in order to reduce MHD drag, and flows in annulus at a speed of  $5 \text{ m} \cdot \text{s}^{-1}$ . The poloidal magnetic field of the plasma ring can easily permeate into the lithium flow with the help of insulation separators, and it is then frozen. The ring is thus conveyed axially [2]. The flowing liquid lithium serves also as a tritium breeding material and as a coolant.

Eddy currents induced in the twisted coils wound on the first wall and in the lithium layer serve to suppress the tilting instability of both rapid and slow modes, if they occur.

## KARIN-I WORKING GROUP

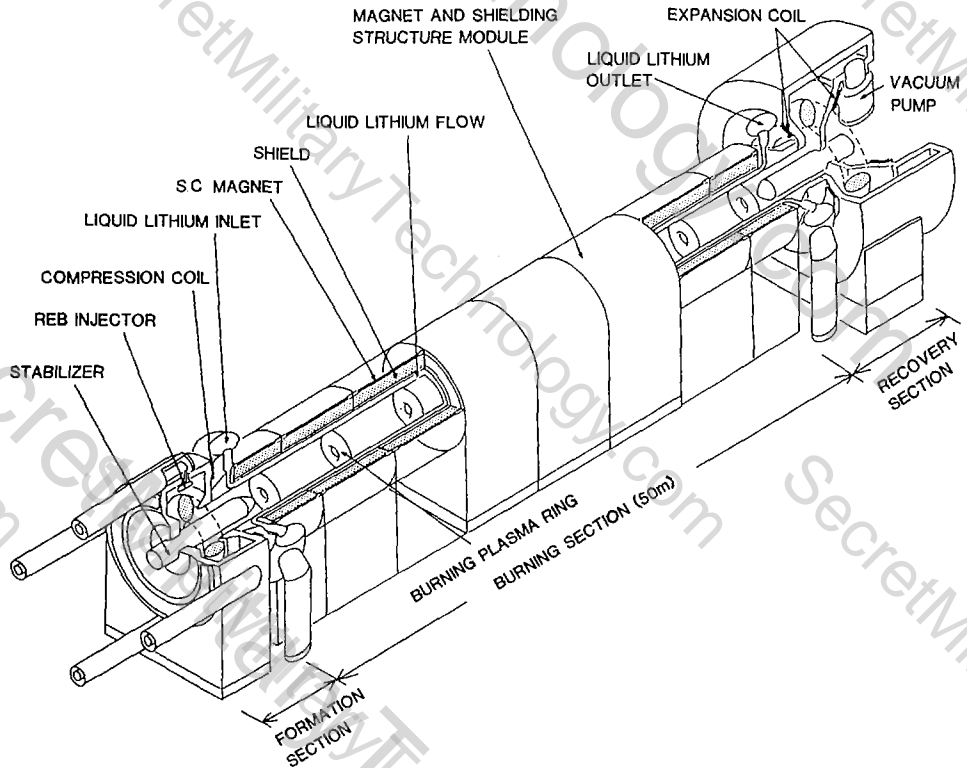


FIG.1. Layout of the moving-ring reactor system KARIN-I.

Burn control to suppress the thermal instability is also applied by a major radius compression-decompression feedback control. In the 50 m long burning section ten plasma rings yield a total fusion power of 1850 MW(th) and an average wall loading  $2.4 \text{ MW} \cdot \text{m}^{-2}$ . When a highly conducting metal is used for the first wall under these conditions, an unacceptable pressure drop, Joule dissipation and stresses due to MHD effects could appear. To reduce these MHD effects, SiC was chosen as a first-wall material in the design. Owing to the problem of compatibility, however, it will be necessary to coat the outer surface of the SiC first wall in order to avoid fatal damage by chemical reaction with lithium at about  $500^\circ\text{C}$  operation temperature.

#### 4. RECOVERY SECTION

At the exit of the burning section, a method similar to that used at the entrance is applied to disconnect the coupling between the liquid lithium flow

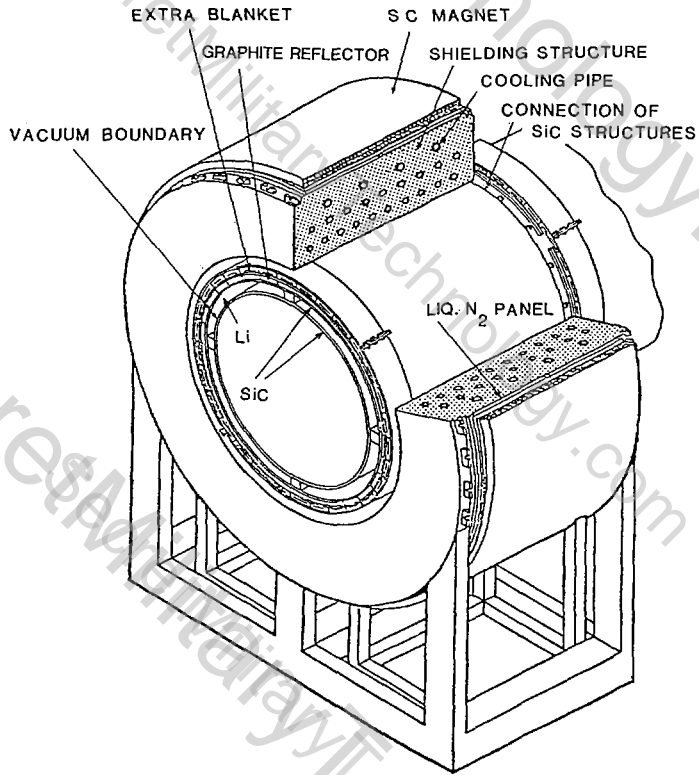


FIG.2. Blanket assembly and single module of shielding and magnet structures.

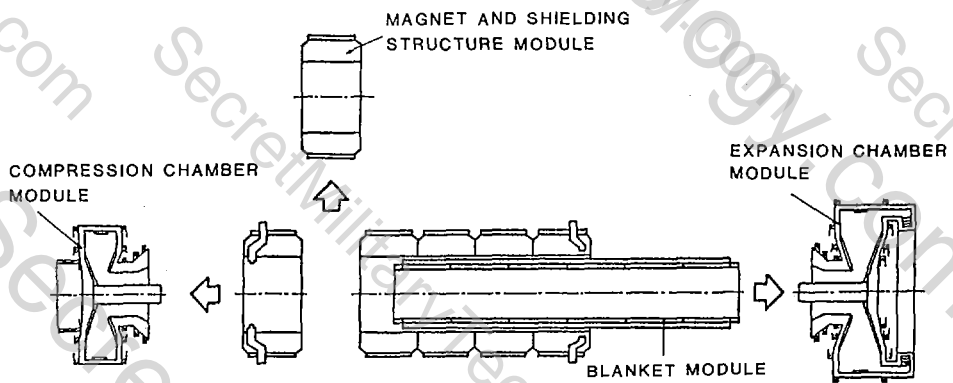


FIG.3. Scheme of reactor disassembly.

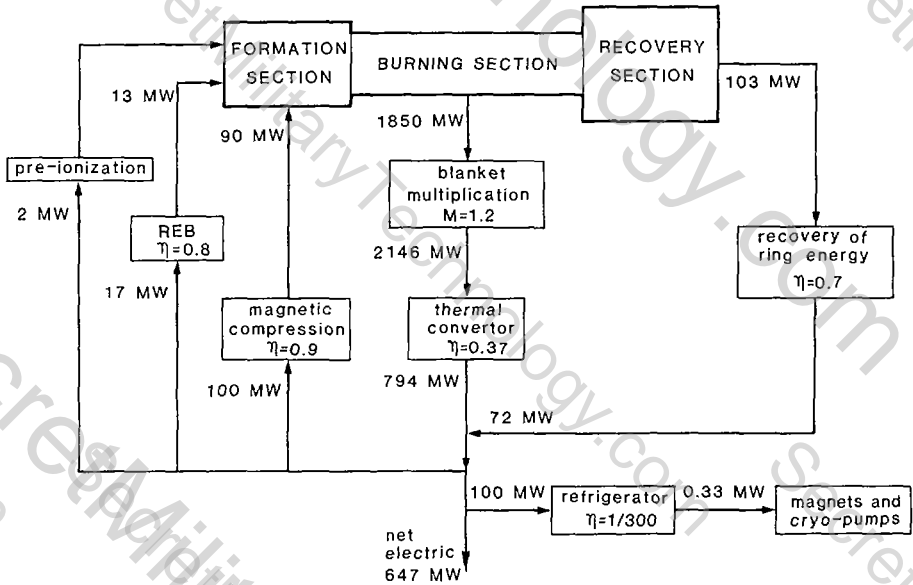


FIG.4. Energy flow in the moving-ring reactor system KARIN-I.

and the plasma ring. The plasma ring is then introduced into the recovery section. The plasma ring at the exit still has about 100 MJ electromagnetic energy, which is sufficient to damage the wall seriously when collapse of the ring is uncontrolled. Energy is therefore recovered by the outer recovery (control) coils through expansion of the major radius. As much as 70% of the recovery efficiency is estimated to be attainable. Particles are then pumped out by two cryogenic vacuum systems with an effective evacuation speed of  $10^3 \text{ m}^3 \cdot \text{s}^{-1}$  each.

## 5. TOTAL PLANT AND POWER BALANCE

The reactor system layout is shown in Fig. 1. The blanket assembly and a single module of shielding and magnet structure are illustrated in Fig. 2.

The scheme of the reactor disassembly, sketched in Fig. 3, is as follows. First, the compression chamber module is detached from the full line of the moving-ring reactor structure. Manipulators then decompose the connection of the liquid lithium inlet pipings. This procedure is repeated for the expansion chamber module. The blanket module is then extracted in the axial direction. The shielding and magnet structure modules in the burning section are then ready to be dismantled in the direction normal to the axis. Since there are only 60 pipe

connections in this reactor and since the linear cylindrical blanket module can be extracted and replaced in a simple manner, maintainability can be greatly improved by virtue of the reactor's linear geometry.

As shown in Table I, the gross total fusion output is 1850 MW(th) (Fig. 4). With a neutron multiplication factor for the blanket ( $M$ ) of 1.2 and a conventional thermal converter efficiency of 0.37, the gross total electric power is 866 M. (e), including 72 MW(e) from direct energy recovery. Subtracting the 219 MW(e) needed for plasma-ring formation, the cryogenic pump system and other auxiliary systems, the net electric power output is 647 MW(e), resulting in overall efficiency of 30%.

## 6. CONCLUSIONS

It is demonstrated in this design that the remarkable features of toroidal plasmas combine well with a linear geometry system towards a feasible fusion reactor. The following R&D issues inherent in KARIN-I have been found to require investigation in the future:

- (1) Transport of particles and energies of spheromak plasma, and establishment of reliable scaling laws;
- (2) MHD stability of the plasma ring;
- (3) Control of parameter profiles in the plasma ring;
- (4) Ash exhaust from the plasma ring in the burning section;
- (5) First-wall material satisfying the requirements of fabrication, heat removal, mechanical strength, thermal stress, thermal fatigue, activation and tritium breeding.

## ACKNOWLEDGEMENTS

The working group on this conceptual design was organized as a subgroup of the Working Group on Fusion Reactors in the Research Information Centre, IPP, Nagoya University. The authors are greatly indebted to Professor S. Hayakawa for encouragement and valuable suggestions. This work was supported by the Grant-in-Aid for Fusion Research of the Ministry of Education, Japan.

## REFERENCES

- [1] KATSURAI, M., YAMADA, M., Princeton Plasma Physics Lab. Rep. PPPL-1614 (1980).
- [2] TOMITA, Y., MOHRI, A., Jpn. J. Appl. Phys. 20 (1981) 1723.



## CONCEPTUAL DESIGN OF A MOVING-RING REACTOR\*

A.C. SMITH Jr., C.P. ASHWORTH, K.E. ABREU  
Pacific Gas and Electric Co.,  
San Francisco, California

G.A. CARLSON, W.S. NEEF Jr.  
Lawrence Livermore National Laboratory,  
University of California, Livermore, California

H.H. FLEISCHMANN  
Cornell University, Ithaca, N.Y.

K.R. SCHULTZ, C.P.C. WONG, D.K. BHADRA, R.L. CREEDON,  
E.T. CHENG, G.R. HOPKINS  
General Atomic Co., San Diego, California

W. GROSSMAN Jr.  
New York University, New York, N.Y.

D.M. WOODALL  
University of New Mexico, Albuquerque, N.M.

T. KAMMASH  
University of Michigan, Ann Arbor, Michigan

United States of America

### Abstract

#### CONCEPTUAL DESIGN OF A MOVING-RING REACTOR.

A design of a prototype Moving-Ring Reactor has been completed. The fusion fuel is confined in current-carrying rings of magnetically field-reversed plasma ("compact toroids"). The plasma rings, formed by a coaxial plasma gun, undergo adiabatic magnetic compression to ignition temperature while they are being injected into the reactor's burner section. The cylindrical burner chamber is divided into three "burn stations". Separator coils and a slight axial guide-field gradient are used to shuttle the ignited toroids rapidly from one burn station to the next, pausing for one third of the total burn time at each station. D-T-<sup>3</sup>He ice pellets refuel the rings at a rate which maintains constant radiated power. The first wall and tritium-breeding blanket designs make credible use of helium cooling, SiC and Li<sub>2</sub>O to minimize structural radioactivity. "Hands-on" maintenance is possible on all reactor components outside the blanket. The first wall and blanket are designed to shut the reactor down passively in the event of a loss-of-coolant or a loss-of-flow accident. Helium removes heat from the first wall, blanket and shield, and is used in a closed-cycle gas turbine to produce electricity. Energy residing in the plasma ring at the end of the burn is recovered via magnetic expansion. Electrostatic direct conversion is not used in this design. The reactor produces a constant net power of 99 MW(e).

---

\* Work performed for the Electric Power Research Institute under contract RP-922.

## 1. INTRODUCTION

The object of this work was to design a prototype fusion reactor in which the ignited fusion fuel is confined in current-carrying rings of magnetically field reversed plasma ("compact toruses"). "Prototype" signifies an intermediate step between an experimental pilot plant and a lead commercial plant. We sought a design that showed promise for upgrading for commercial use.

There are several important reasons why the design calls for moving plasma rings with stationary burn cells:

(a) The plasma burn chamber is separated from the ring-formation/heating and ring-exhaust/expansion sections. This minimizes the neutron fluence in regions outside the burner and physically segregates reactor functions, avoiding multipurpose reactor component designs.

(b) The peristaltic and adiabatic magnetic compression brings the rings to ignition in a way which is potentially very efficient (and is insensitive to the low-energy ring formation efficiencies).

(c) Some variations in reactor power output can be accommodated by varying the number of identical burn modules. Because the rings are shuttled rapidly between burn stations, adjustment of their "residence time" in each of the burn stations does not introduce significant time-varying thermal power to the walls.

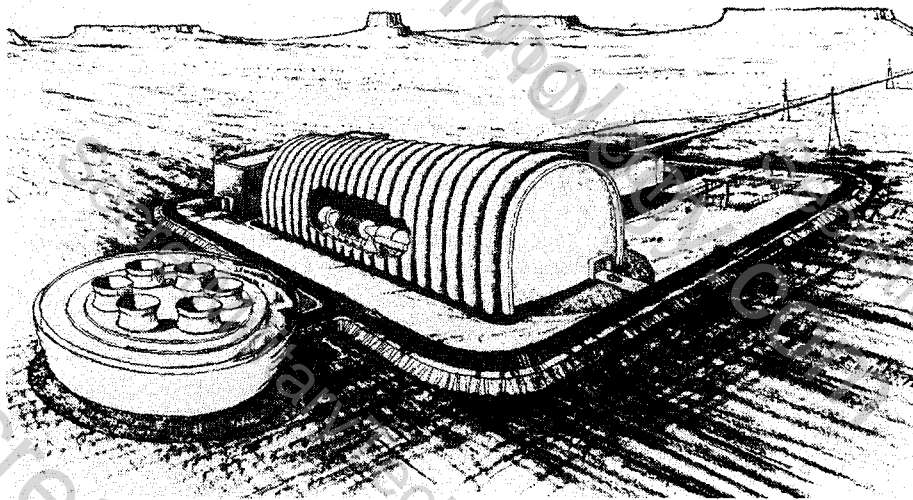


FIG.1. Sketch of the 99 MW(e) prototype Moving-Ring Reactor fusion power plant.

(d) Use of multiple moving plasma rings permits effective utilization of the ring generator and exhaust ring recovery equipment.

(e) Moving the rings through the reactor greatly simplifies the discharge of burn products. The reactor's linear geometry also provides an inherent divertor action.

The set of physics, and the technology and mechanical design criteria needed to make this concept attractive can be used as targets for experiments and technology programmes.

Six major criteria guided the prototype design. The prototype must: produce net electricity decisively ( $P(\text{net}) \geq 70\%$  of  $P(\text{gross})$ ), with  $P(\text{net}) \approx 100 \text{ MW(e)}$ ; be physically small (low project cost) but have a design that can be scaled up to an attractive commercial plant; have all features required of commercial plants; avoid unreasonable extrapolation of technology and of the known physics data base; minimize nuclear issues substantially, i.e. accident and waste issues of public concern; be modular (to permit repetitive fabrication of parts); and be maintainable with low occupational radiological exposures.

The design succeeded in meeting all these criteria except small physical size. Figure 1 is an artist's sketch of the power plant.

## 2. THE REACTOR

The Moving-Ring Reactor [1] consists of three cylindrical in-line sections: a plasma ring generator and compressor, a central burner section, and a spent-ring exhaust section. The details are shown in Fig. 2.

### 2.1. Ring generator, compressor and expander

A hollow, coaxial plasma gun generates the compact toroids in the relatively low magnetic field ( $\approx 0.26 \text{ T}$ ) 15.5 m beyond the first ring burn station. New rings are injected at intervals of about two seconds. The hole through the inner gun electrode permits plasma diffusing from the burning rings to escape along field lines to the plasma dump and vacuum pumps located in the tank housing the gun.

The plasma rings are forced peristaltically into the 6.5 T magnetic field of the burner section by sequentially energizing compression "push coils" located between the plasma gun and the first burn station.

Compression scaling laws from MHD compact toroid equilibrium codes [2] were used to design the compressor. The principal scaling laws were  $T_1 \propto B$  and  $\langle R(\text{ring}) \rangle^2 \propto B^{-1}$ . The design calls for 20 coils in the compressor. The coil radii range from 65 cm near the throat of the burner section to 320 cm near the plasma

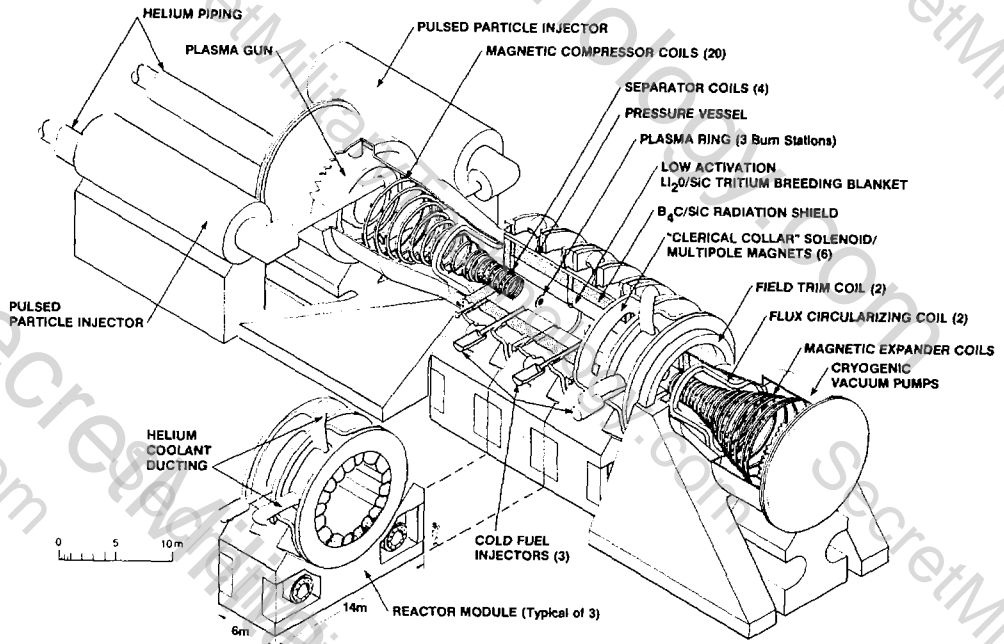


FIG.2. Design details of the prototype Moving-Ring Reactor.

gun. The ring compression will require about 2 to 5 ms. Pulsed compressor coil currents range from 0.5 to 2.0 MA. Overall compressor efficiency is calculated to be  $\approx 75\%$ .

If the initial plasma temperature is assumed to be  $\approx 3$  keV, the field compression ratio of  $\approx 25$  will bring the plasma to the initial ignition ion temperature of  $\approx 75$  keV. Slotted conducting walls are located just outside the compressor coils. These walls stabilize the plasma ring dynamically during compression against precessional/radial instabilities.

Rings of the type proposed in this reactor have been observed experimentally to "tilt" under some conditions. One of the schemes for stabilizing the tilt currently being considered is to replace some of the ring's plasma current with axis-encircling particles, since this instability is not observed in purely Astron-like experimental configurations (e.g. [3]). This reactor design therefore includes an option to "hybridize" the plasma ring with axis-encircling particles before compression heating [4].

We assume that tilt-stabilization can be done with about 20% of the ring current carried by axis-encircling particles (i.e. "fast-particle" field reversal  $\approx 40\%$ ).

If protons are used,  $\approx 0.8$  MJ beams of  $\approx 20$  MeV trapped particles would be required. A generation/trapping efficiency of about 40–50% is assumed. The gun plasma combines with the particle ring in the region between the gun muzzle and the first compressor coil (see Fig. 2).

We calculate the overall injection and compression process efficiency (including the axis-encircling particles) to be about 70%.

Thermal and magnetic energy in the plasma rings at the end of the burn is recovered magnetically by 20 recovery coils in the expander section. We calculate the magnetic direct conversion efficiency of the expander to be  $\geq 75\%$ .

## 2.2. Pulsed plasma burn calculations

The 1-D Fokker-Planck transient plasma burn analysis used to model the fusion plasma has been described elsewhere [1]. We have assumed that the energy and particle confinement times are equal to the classical ion energy confinement time and that the electrons have an energy confinement time which is one tenth of the ion energy confinement time.

The range of compact toroid characteristics that can be accommodated in the 2.5 m bore prototype reactor is limited by first-wall radiation loading and/or ring physical size. The reference design plasma is assumed to be a field-reversed mirror type of plasma ring with some Spheromak-like imbedded toroidal magnetic field. We presume a magnetic/thermal energy ratio of 1/3 and an average  $\langle \beta \rangle = 0.67$  (peak  $\beta = 1.0$ ). The supposed presence of the imbedded toroidal field permits credible investigation of a wide range of possible plasma sizes for use in the reactor.

The relative fraction of tritium in the plasma fuel mixtures was varied in order to investigate the increased direct conversion output (for a given wall load) and the relaxed tritium breeding ratios possible with plasma burns "poor" in tritium. Reactor power balance considerations limited the scope of our interest to ignited plasma burns lasting long enough to achieve a fusion energy gain of  $Q = 30$ . As the relative fraction of tritium in the burns is decreased, the trade-offs are: (a) whether the increased initial plasma sizes required for ignition lead to plasmas that no longer fit inside the first wall at the end of the burn; and (b) increased total bremsstrahlung production because of higher temperatures and larger plasmas.

On this basis, our burn model and assumptions predict that the prototype reactor could accommodate a burn with no less than 20% tritium. The reference design fuel mixture at the start of the burn is 20% T, 73% D and 7%  $^3\text{He}$ . (The  $^3\text{He}$  is in equilibrium recycle concentration to maximize the production of charged particles.) Initial plasma ion (electron) temperatures are 75 (50) keV, with an initial (final) plasma average radius of 39 (57) cm. The burn time to reach  $Q = 30$  is 5.9 seconds. The fusion power per ring is  $\approx 105.5$  MW.

The physical design of the reactor could accommodate poorer energy confinement than our base assumptions by up to a factor of 5 if the initial tritium concentration in the burn is increased to about 50% T. Under these conditions, fuel mixtures "poorer" than  $\approx 50\%$  tritium would require plasma rings too big to fit in the 2.5 m reactor bore at the end of the plasma burn.

### 2.3. Axial ring transport

The use of electrically insulating materials throughout the first wall, blanket and shield greatly simplifies the plasma ring transport mechanism. An axial guide-field gradient of  $\approx 0.005 \text{ T} \cdot \text{m}^{-1}$  provides force to move the rings, which are held in place at the burn stations (and stably separated from one another) using aluminium "separator coils" located at the midplane between burn positions.

At intervals of about two seconds, each ring is rapidly ( $\approx 0.01 \text{ s} - 0.1 \text{ s}$ ) shuttled to the next burn station (and the last ring exhausted into the expander) by sequentially tailoring the currents in the separator coils. This "musical chairs" ring translation permits the reactor to accommodate a wide range of plasma burn times without introducing the complication of time-varying wall loads.

There is an electromagnetic drag on the rings when they are moved. This arises from eddy currents induced in the superconducting coil cases and the metallic pressure vessel located radially just inside the superconductor coils. This drag has been calculated and is negligible.

### 2.4. Low-activation first wall, blanket and shield

#### 2.4.1. Materials

Silicon carbide was selected as the primary component of the first wall, blanket and shield to minimize induced radioactivity, to eliminate the possibility of first wall/blanket meltdown in the event of a loss-of-coolant accident (LOCA), and to eliminate the presence of electrically conducting materials near the rings to minimize the electromagnetic drag when the rings are translated. SiC is stable under neutron irradiation, has high thermal conductivity, and has low tritium permeability at temperatures below  $1000^\circ\text{C}$ .  $\text{Li}_2\text{O}$  is the tritium breeding material. High-pressure helium (28 atm) is the high-temperature coolant because of its chemical inertness and transparency to neutrons.

#### 2.4.2. Blanket and shield design; heat removal system

Twenty-four wedge-shaped lobes (each 0.9 m long) nest inside the cylindrical coolant pressure vessel to make up the first wall, blanket and shield structure in each of the three 6 m long burner modules (see Fig. 2). Figure 3 gives a cutaway view of one of the lobes.

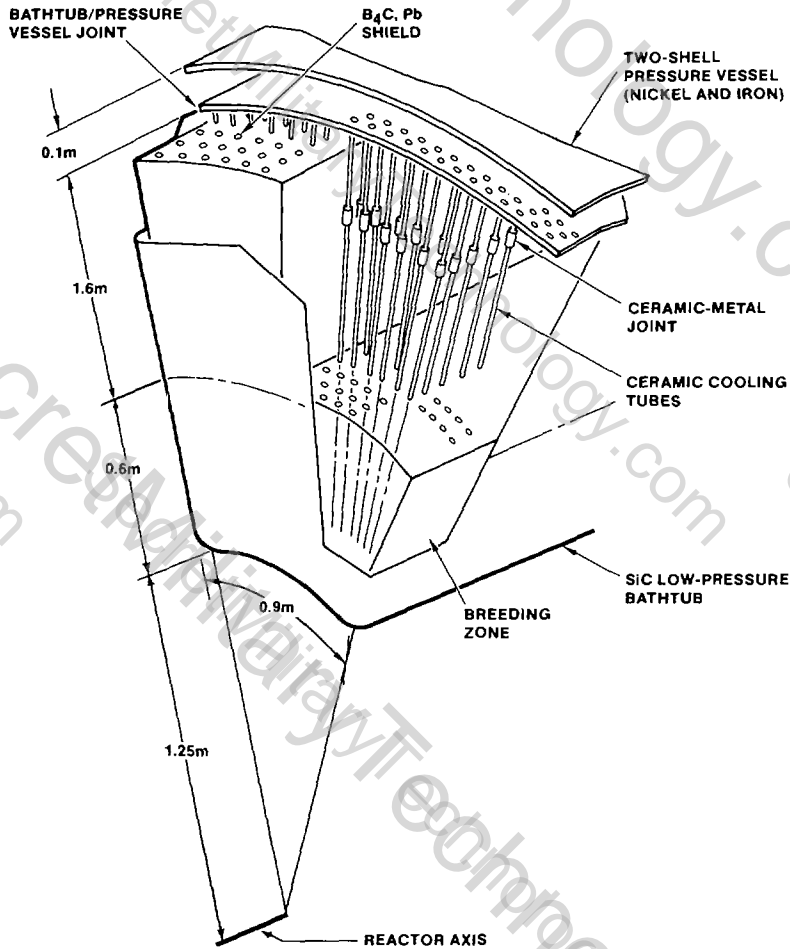


FIG.3. Low-activation blanket/shield module.

The 1.4 m thick SiC/B<sub>4</sub>C shield is secured to the pressure vessel. Penetrating through the shield into the front region of the lobe is a "forest" of small (2.1 cm diameter), concentric feed, high-pressure SiC coolant tubes, 3.5 cm centre to centre. These tubes remove the heat from the Li<sub>2</sub>O while an independent 1 atm helium stream purges the tritium from the 0.6 m thick breeding zone. The blanket shield assembly is encased in a SiC "bathtub" clamped at its base to the pressure vessel. The "bathtub's" curved first-wall surface is 0.6 cm thick and the sidewall is 2.0 cm thick. The use of ceramics in this fashion is credible because the large SiC structure supports little load beyond its own weight.

The 1.4 m SiC/B<sub>4</sub>C shield thickness is more than adequate to protect the superconducting magnet throughout the life of the reactor. Occasional annealing of the Cu stabilizer is not necessary.

Helium coolant ducts loop over the axial sections of the "clerical collar" guide-field coils to provide the coolant routing to the main helium piping located in the base of each reactor module.

#### 2.4.3. Neutronics

The Li<sub>2</sub>O/SiC breeding zone is 0.6 m thick with a 0.2 m thick SiC reflector. The Li<sub>2</sub>O high-temperature zone has a volume fraction of about 57%. The total blanket energy multiplication is 1.19 while the tritium breeding ratio is 1.09 (considerably more than the 0.9 T/n required for the 20% tritium plasma burn).

The impurity level in the materials was assumed to be about 1 ppm. The average wall load of 1.7 MW·m<sup>-2</sup> results in a dose rate just outside the breeding zone of ≈0.4 mrem·h<sup>-1</sup> and a dose rate just outside the shield of <<2.5 mrem·h<sup>-1</sup>, the maximum dose rate permitted for "hands-on" maintenance, one day after shut-down. Therefore, "hands-on" maintenance is possible on all components outside the blanket. The dose rate inside the vacuum chamber is ≈0.2 rem·h<sup>-1</sup>, making contact maintenance in this region impossible.<sup>1</sup>

#### 2.5. Magnetic field design

The graded axial guide-field in the reactor's burner section is produced by a set of six NbTi superconducting coils. A radial magnetic well is produced by adding a set of eight alternating bends to the coils. We have dubbed the resulting shape the "clerical collar" coil. The rectangular superconductor current bundles are 0.45 m × 1.74 m and the average coil radius is 5 m. The 1.9 m longitudinal segments used in this design provide the radial magnetic well. With the separator coils energized, the radial well depth is ≈0.4% at ≈1 m. The axial field is nominally 6.5 T, with an axial gradient of ≈0.005 T·m<sup>-1</sup>.

The elliptical magnetic flux bundles leaving the reactor are circularized by auxiliary superconducting coils located at each end of the guide-field coil set.

The four separator coils which maintain the plasmas in their burn positions have an average radius of 1.5 m. The water-cooled conductor bundles are 18 cm × 18 cm. The coils are encased in a 25 cm thick SiC neutron shield such that the afterheat generated from induced radioactivity would be low enough to prevent afterheat meltdown of the aluminium-alloy conductor in the event of a LOCA/LOFA.

<sup>1</sup> 1 rem = 1.00 × 10<sup>-2</sup> sievert.

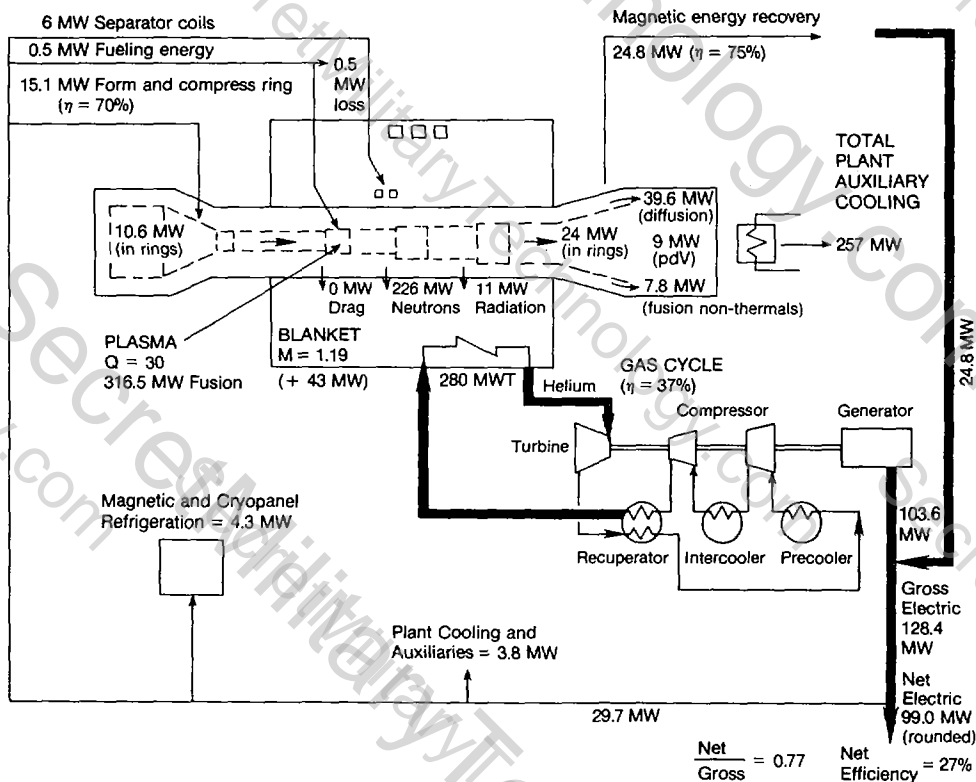


FIG.4. Prototype reactor power flows.

2.6. Vacuum system

Arrays of liquid-helium-cooled cryopanel vacuum-pump the reactor. These panels, located in the two end tanks, are specially designed to pump helium as well as deuterium and tritium. The hydrogen isotopes are cryocondensed. The helium is cryotrapped in argon sprayed directly onto the cryopanel.

Different amounts of pumping are required at the two ends of the reactor. The refuelled plasma rings are ignited and confine the fusion fuel well. Large amounts of gas will be released in the exhaust end of the reactor as the rings complete their burns. On the other hand, the injector end of the reactor must pump only half of the effluent that has diffused out of the rings during the burn.

We calculate the molecular gas loads to be 2 and 15 torr litre  $s^{-1}$  at the injector and exhaust ends of the reactor, respectively. The optimum argon spray rate for our design is  $\approx 30$  argon atoms/helium atoms pumped. The total cryopanel

areas required are 13 m<sup>2</sup> and 89 m<sup>2</sup> at the injector and exhaust ends, respectively. At any one time, two thirds of the cryopanel are pumping while the remaining one third are defrosting.

### 2.7. Pellet refuelling

The plasma rings are continuously refuelled with D-T-<sup>3</sup>He pellets at a rate which maintains constant total radiated power/ring (neutrons + bremsstrahlung). The relative concentrations of D-T-<sup>3</sup>He in the refuelling pellets are identical with the fuel composition of the plasma at the start of the burn. The average plasma density of  $\approx 5 \times 10^{14}$  cm<sup>-3</sup> and temperature of  $\approx 75$  keV require a pellet velocity of  $\approx 10^7$  cm·s<sup>-1</sup>. The 0.09 cm radius pellets are accelerated by ablation using a CO<sub>2</sub> laser. The total refuelling power is  $\approx 0.14$  MW/ring.

### 2.8. Power conversion system

Electricity is produced from the reactor's thermal output by a closed-cycle gas turbine. The thermal power cycle lends itself to dry-cooling without economic penalty. The hot high-pressure helium (750°C, 28 atm) is ducted to the gas turbine located behind a shield wall inside the containment.

The reactor power flows are summarized in Fig. 4. The reactor nets 99 MW(e) with an overall efficiency  $\eta$  of about 27%. Clearly, slightly better performance (i.e.  $\eta \approx 33\%$ ) could be obtained by electrostatic direct conversion of the effluent plasma stream. However, since this does not turn out to be necessary for attractive performance of the commercial upgrading of this reactor, we decided not to add this feature (and complexity) to the prototype design.

## 3. REACTOR SAFETY ISSUES

Reactor safety played a major role in the prototype reactor design. The chief safety elements in the design are:

- (a) First-wall overheating from a LOCA/LOFA will terminate the fusion plasma burn passively by melting silicon safety plugs in the SiC first wall.
- (b) Meltdown of the first wall and blanket is precluded by design and choice of materials – even under total loss of convective cooling. Meltdown of the aluminium alloy separator coils is avoided by the 25 cm thick SiC radiation shield which completely encases the coils, thus reducing the neutron flux and afterheat level.
- (c) Single high-pressure SiC coolant tube failure will not cause chain failure during operation if coolant flow can be maintained. The resulting lobe pressurization can be handled by safety-release-and-shut-down systems.

(d) Hands-on maintenance can be performed outside the blanket of a removed burner module when plasma chamber end-shields are in place.

(e) SiC is an excellent tritium barrier for temperatures less than 1000°C, thus reducing the exposure of the public to tritium.

(f) No high-level waste is produced.

#### 4. REACTOR DESIGN SUMMARY

The prototype reactor met all the design criteria except small physical size. With out present knowledge of materials and the requirement that the moving plasma rings should not be close to electrically conducting structures, we could not satisfy *simultaneously* the needs for minimal radiological hazard in the reactor and small physical size.

Based on the current plasma burn model and assumptions, the initial fraction of tritium in the prototype plasma burn can be no less than 20% because of the dual constraints of permissible ring physical size and surface wall loading. We view this fuel mixture as a step toward larger-bore commercial reactors. Fuel mixtures poorer in tritium may require direct cooling of the first wall to handle bremsstrahlung surface loading.

The current plasma burn model and assumptions indicate that acceptable prototype reactor performance requires near-classical confinement of the ion energy (assuming the electron energy confinement is no worse than  $1/10 \times$  classical ion energy confinement).

The step-wise translation of the plasma rings allows the reactor to accommodate a wide range of plasma burn characteristics (such as burn time and  $\beta$ ).

The reactor design achieves several features of importance to potential users:

The  $\approx 99$  MW(e) net output is a reasonable stepping-stone reactor size in a development programme leading to a larger commercial upgrade plant.

It makes credible use of ceramics to minimize nuclear issues (minimal component radioactivity; no possibility of meltdown; no high-level wastes).

The commercial upgrade has the potential of increased direct conversion output for a given thermal size.

Use of dry cooling in the thermal power cycle permits flexibility in reactor siting.

The direct gas cycle cuts containment building pressure by a factor of about 10.

The reactor's linear modular design simplifies maintenance.

## REFERENCES

- [1] SMITH, A.C., et al., The Moving-Ring Reactor, Electric Power Research Inst. Final Project Report, Contract RP922 (1981), to be published.
- [2] GROSSMAN, W., Jr., et al., to be published.
- [3] PHELPS, D.A., et al., Phys. Fluids 17 (1974) 2226.
- [4] FLEISCHMANN, H.H., et al., in Proc. Joint US/Japan Symposium on Compact Toroids, Princeton (1979).

## DISCUSSION

ON PAPERS IAEA-CN-41/O-2-1 AND O-2-2

P. KOMAREK: Does the pulsed operation create thermal or mechanical fatigue problems for the wall/blanket area, and do AC field problems associated with the moving rings occur?

K. YOSHIKAWA: Yes, effects due to the pulsed operation were our greatest concern in the early design stage. After detailed numerical calculations, however, we found that both thermal and mechanical undesirable effects on the component characteristics due to the transient behaviour, including thermal fatigue, could be readily suppressed within the practical range by a suitable choice of electrically non-conducting material of small thickness and large thermal conductivity (3 cm SiC), a high ring velocity ( $5 \text{ m} \cdot \text{s}^{-1}$ ), a considerably longer compression time (250 ms), and a suitable arrangement of the electrically conducting structures.

A.C. SMITH Jr.: In the US moving-ring reactor design, the plasma rings are shuttled very rapidly from one burn station to the next ( $\tau_{\text{transit}} \approx 0.01 \text{ s}$ ) and spend virtually all the burn time residing in the burn stations. Moreover, by design, the rings are refuelled at a rate such that the total radiated power per ring is constant. Therefore the first wall 'sees' virtually no radiation (or thermal) transients of concern to materials as the rings move, in 'musical chairs' style, through the burner section.



## DEVELOPMENT OF HYDROGEN PELLETT INJECTORS AND PELLETT FUELLING EXPERIMENTS AT OAK RIDGE NATIONAL LABORATORY

S.L. MILORA, S.K. COMBS, C.A. FOSTER, W.A. HOULBERG,  
J.T. HOGAN, D.D. SCHURESKO, S.E. ATTENBERGER  
Oak Ridge National Laboratory\*,  
Oak Ridge, Tennessee

G.L. SCHMIDT  
Plasma Physics Laboratory,  
Princeton University,  
Princeton, New Jersey

M.J. GREENWALD, S. WOLFE, J. PARKER  
Plasma Fusion Center,  
Massachusetts Institute of Technology,  
Cambridge, Massachusetts

United States of America

### Abstract

#### DEVELOPMENT OF HYDROGEN PELLETT INJECTORS AND PELLETT FUELLING EXPERIMENTS AT OAK RIDGE NATIONAL LABORATORY.

The introduction of high-speed hydrogen and deuterium pellet injectors of multipellet capability has allowed pellet fuelling experiments to progress beyond the demonstration stage. The paper describes various aspects of the Oak Ridge National Laboratory Pellet Fueling Program, including the development of pneumatic and mechanical (centrifugal) injector types, plasma fuelling experiments, and the numerical results of pellet ablation and transport studies.

#### 1. INTRODUCTION

The Department of Energy (DOE) national pellet fueling program consists of collaborative efforts between the Oak Ridge National Laboratory (ORNL) and the various plasma fusion laboratories in the United States that operate major magnetic confinement experiments.

The objectives of the development program which is centered at ORNL are two-fold: (1) the short-term development of pellet

---

\* Sponsored by the Office of Fusion Energy, US Department of Energy, under contract W-7405-eng-26 with the Union Carbide Corporation.

fueling systems based on the pneumatic and mechanical acceleration approaches for use in the national experimental magnetic confinement program and (2) the long-term development of one or more practical systems that will meet the anticipated deuterium-tritium pellet fueling needs of the class of proposed fusion devices typified by the Fusion Engineering Device (FED). The experimental efforts that are currently supported by this program include pellet fueling experiments on the Impurity Studies Experiment (ISX-B), the Poloidal Divertor Experiment (PDX), and the Alcator-C device. The various aspects of these activities with particular emphasis on recent developments and experimental results are described in this paper.

## 2. PERFORMANCE OBJECTIVES - EXTRAPOLATION OF THEORY

There are no data on pellet penetration for electron temperatures above  $\sim 1$  keV. Consequently, the requirements for future fueling systems cannot be determined with certainty until experiments have been performed on devices such as the Tokamak Fusion Test Reactor (TFTR). For guidelines in the development program we have relied on extrapolations of pellet ablation theory and empirical tokamak transport models to obtain reference values for pellet velocity, size, and repetition rate. The respective values of 2 km/s, 4-mm diameter, and 20 pellets/s evolved from past pellet fueling simulations ( $1\frac{1}{2}$ -D WHIST transport code calculations with empirical transport scaling), which were performed for reactor design studies such as the International Tokamak Reactor (INTOR), the Engineering Test Facility (ETF), and the FED. The pellet evaporation model used for these projections is based on the theory of neutral gas shielding [1-3]. This model has been benchmarked on the ISX-B [4] and PDX [5] pellet injection experiments in the electron temperature regime of  $\sim 1$  keV and with modest amounts of auxiliary heating (neutral injection). In Fig. 1, the WHIST code simulation of the PDX single-pellet injection experiment (1-mm  $H_2$  pellet injected at  $\sim 800$  m/s) is compared with the temporal evolution of line density and central temperature (electron cyclotron emission) measurements. For present plasma conditions the available models appear to be adequate.

The pellet parameters chosen as goals for the development program form a consistent set. The fueling rate in equivalent atoms/s is comparable to the expected total ionization rate ( $\sim 5 \times 10^{22} \text{ s}^{-1}$ ) for a single atomic species from all combined particle sources (gas injection, recycle, and makeup pellet fueling) needed to support the FED and INTOR operating density level. Thus, the feed rate chosen could, in principle, accommodate a low recycle (such as magnetic divertor) option.

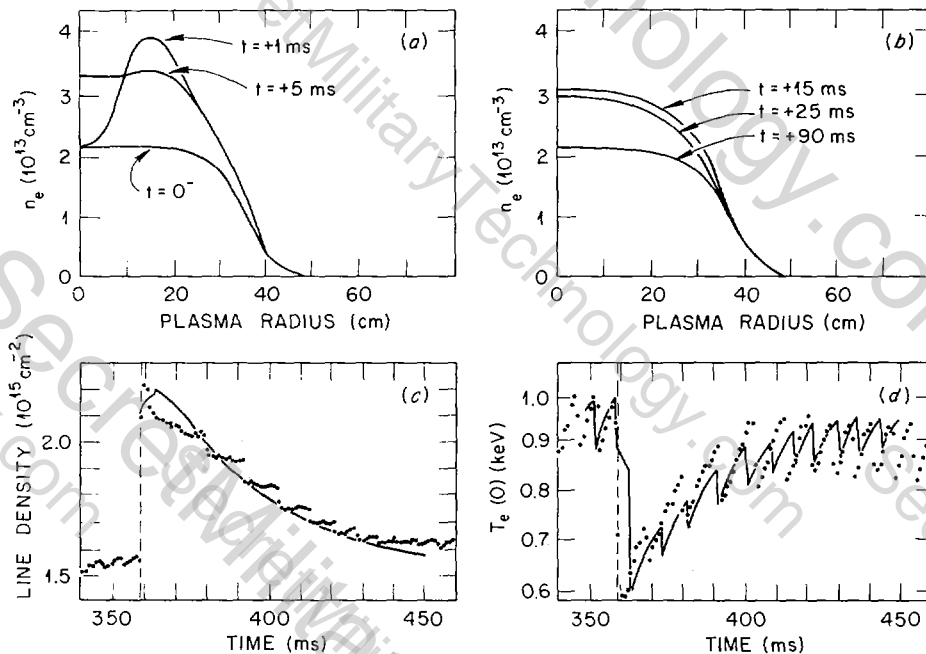


FIG.1. (a) Calculated response of density profiles on PDX (Ohmic discharge with divertor) to single-pellet injection using the WHIST code with empirical transport and the neutral gas pellet evaporation model.

(b) Comparison of the calculations for experimental line density and central electron temperature with measurements.

The 2 km/s velocity is a compromise between the need to provide adequate penetration and the desirability of minimizing technological risk. For FED the tradeoff in pellet size and velocity is shown in Fig. 2. Roughly two-thirds of the plasma volume will be accessible to pellets having the reference values stated above (as compared to  $\sim 5\%$  for gas injection and recycle). Only marginal improvements will result at velocities a factor of 10 greater than those considered here.

### 3. MECHANICAL INJECTOR DEVELOPMENT

Acceleration of pellets by centrifugal forces was first demonstrated in 1978 at ORNL. Steady-state operation at 150 pellets/s and a velocity of  $3 \times 10^2$  m/s was attained in the prototype device which utilized a 30-cm-diam. steel acceleration arbor fed by a constant-rate, high-speed, piston-type extruder.

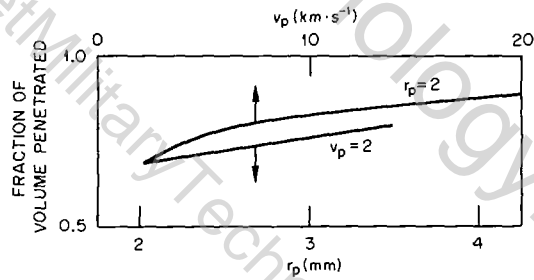


FIG.2. WHIST code calculation of pellet penetration in FED showing weak dependence on pellet velocities above  $2 \text{ km} \cdot \text{s}^{-1}$ .

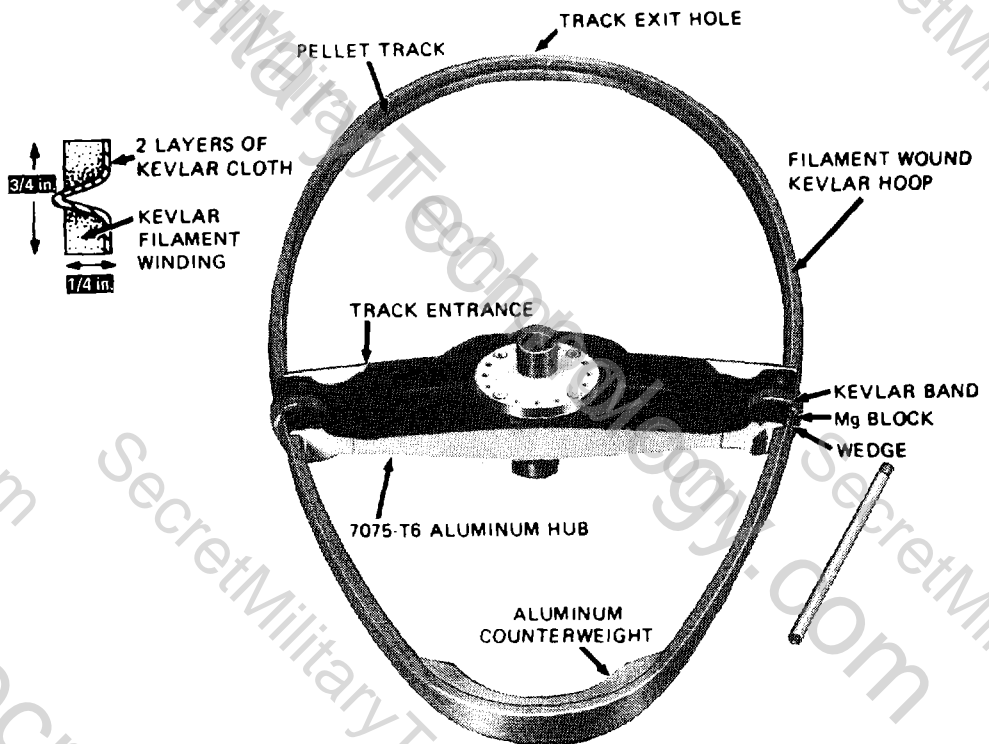


FIG.3. AMI composite accelerator.

The Advanced Mechanical Injector (AMI), which became operational in January 1982, will extend the performance of the centrifugal acceleration concept to velocities in the range of 1-2 km/s. The accelerator stage is illustrated in Fig. 3. The design utilizes a central aluminum hub of roughly the same diameter as the prototype device that accepts pellets from the variable-rate pellet feed mechanism (electromagnetic punch) and accelerates them in an undercut groove to  $\sim 300$  m/s. Acceleration to 1 km/s is accomplished in a "V" groove molded into the filament-wound Kevlar-49/epoxy hoop. Pellets exit tangentially through an orifice at the end of the hoop at twice the hoop tip speed. Details of the cryogenic extruder are discussed in Section 5.

To date, the facility has been operated with pellets of nominal 1-mm diameter at 1-km/s pellet speed (150-Hz arbor rotational speed) and a delivery rate of  $40 \text{ s}^{-1}$  for several seconds duration. The composite hoop has been tested to 1 km/s tip speed; the injector is therefore capable of 2 km/s performance.

#### 4. PNEUMATIC PELLET INJECTOR RESEARCH

The ORNL prototype single-pellet injector (circa 1978) [6], which was used extensively on ISX-B and PDX, has been upgraded to 1.6-mm pellet diameter capability and equipped with additional diagnostics, an improved fast propellant valve, and a low-conductance guide-tube-type pellet injection line to reduce gas-handling problems associated with the use of high-pressure gaseous propellants. The facility is being used to support the development of advanced pneumatic injector concepts in particular and pellet injector vacuum systems in general.

The performance characteristics of the device are summarized in Fig. 4(a). The velocity trends are consistent with a simplified analytical gun model (unsteady gasdynamic expansion). To date, velocities as high as 1200 m/s have been attained at operating pressures of  $\sim 50$  bar with room-temperature helium. The details of the gun operations are illustrated in Fig. 4(b). The rise time of the pressure in the breech has been reduced to 0.3 ms by an improved electromagnetic propellant valve and drive circuit. The pressure measured at the muzzle is  $\sim 6\%$  of the breech pressure maximum. This is about half the value predicted by the idealized theory: the difference can be explained by the parasitic effect of friction in the gun barrel. An improved interior ballistics code has been developed that includes the effects of friction, heat exchange, finite chambrage, and nonzero valve opening time. The calculated pressure history inside the gun mechanism for the conditions shown in Fig. 4 is presented in Fig. 5.

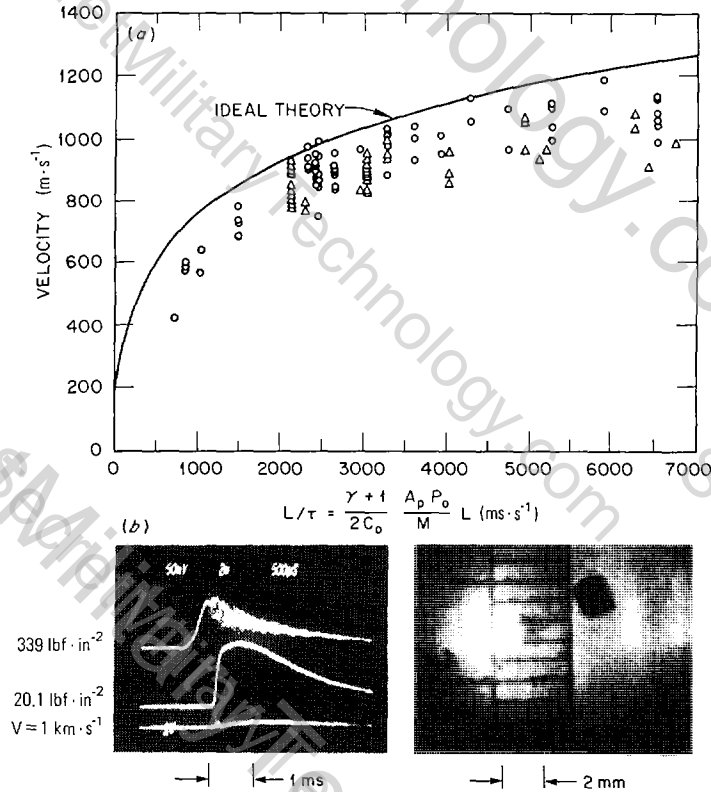


FIG.4. (a) Performance characteristics of 1.6 mm bore single-pellet pneumatic injector. The theory neglects friction, heat exchange and finite gun chamber length.  $L$  = gun barrel length (0.16 m);  $\gamma = 5/3$  (helium);  $C_0 = 1000 \text{ m}\cdot\text{s}^{-1}$ ;  $M$  = pellet mass;  $A_p$  = pellet base area;  $P_0$  = peak chamber pressure.

(b) Left: oscillograms of breech pressure (fast valve exhaust), muzzle pressure, and pellet detection photo-diode (muzzle). Right: shadowgraph of pellet at exit of 1 m  $\times$  3 mm ID quartz guide tube.

The reliability of this system has been greatly improved by the addition of a 1-m-long  $\times$  3-mm-ID quartz guide tube located a few centimeters downstream of the gun muzzle. The tube ensures that all pellets that exit the gun enter the target plasma and greatly reduces the flow of propellant gas into the torus. The shadowgraph in Fig. 4(b) was taken at the tube exit. There is no evidence of serious degradation in pellet mass or velocity.

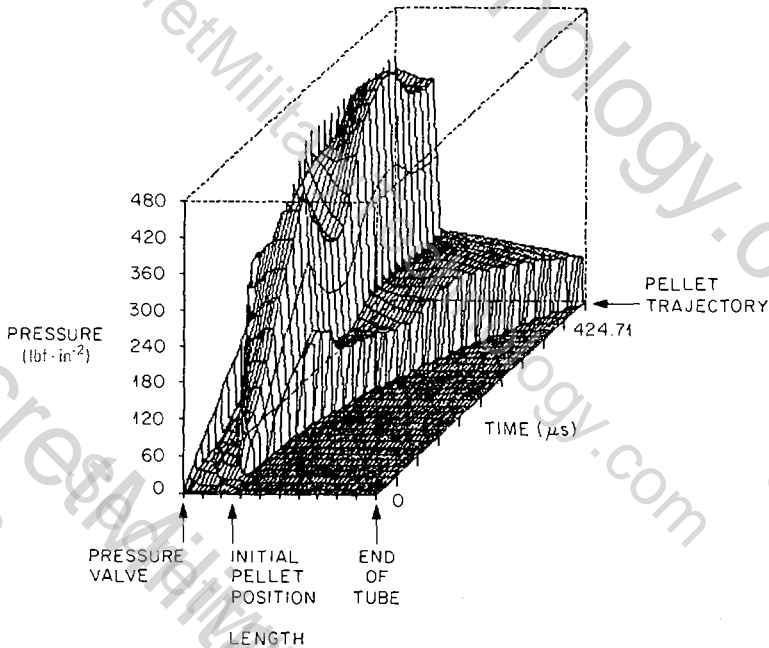


FIG.5. Results of interior ballistics code.

## 5. REPEATING PNEUMATIC INJECTOR DEVELOPMENT

The technologies described above have been incorporated into the design of a facility to test repeating pneumatic injector concepts. This recently completed facility will combine the solid hydrogen extrusion and pneumatic acceleration technologies developed at ORNL to demonstrate acceleration of 2-mm deuterium pellets at up to 2 km/s repetitively ( $10 \text{ s}^{-1}$ ). Design details of the extruder feed and the gun mechanism are illustrated in Fig. 6. The extruder piston forces a ribbon of solid hydrogen between the propellant valve and a reciprocating hollow die (punch). The inward motion of the die chambers a pellet, which is subsequently driven from the gun by the propellant.

The design of the extruder is similar to that of the AMI. It consists of a motor-driven screw press which actuates a piston running in a brass sleeve. The sleeve is brazed at both ends to OFHC copper blocks. The upper block serves as a liquifier and storage reservoir while the lower block freezes the hydrogen charge. Both blocks are convectively cooled by liquid helium.

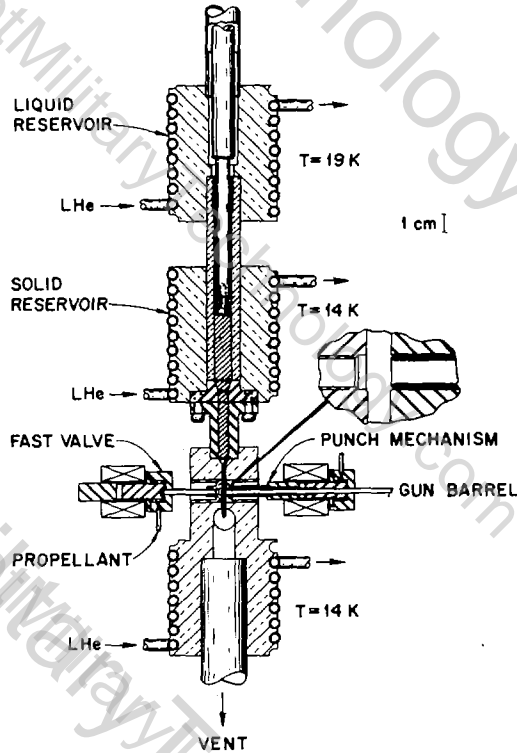


FIG.6. Design details of the API. Actuation time for the electromagnetic punch (chambering mechanism) is  $\approx 6$  ms. Actuator and valve operate repetitively at up to  $20 \text{ s}^{-1}$ . (LHe = liquid helium.)

## 6. EXPERIMENTAL APPLICATIONS

The experiments in progress on PDX and those planned for Alcator-C and ISX-B utilize a pneumatic device developed at ORNL that is capable of delivering four pellets into a single plasma discharge. The design of the Alcator-C/ISX-B version of this injector is illustrated in Fig. 7. It consists of four gun barrel and fast propellant valve units incorporated into a common cryogenic gun mechanism. Individual pellets are formed in situ by freezing liquid hydrogen in cylindrical cavities located on a rotatable wheel interposed between the valve and gun barrel subassemblies. The four pellets are chambered simultaneously by rotating the wheel until the frozen plugs align with the gun barrels. The prototype unit which is installed on PDX produces nominal 1-mm pellets at velocities between 500

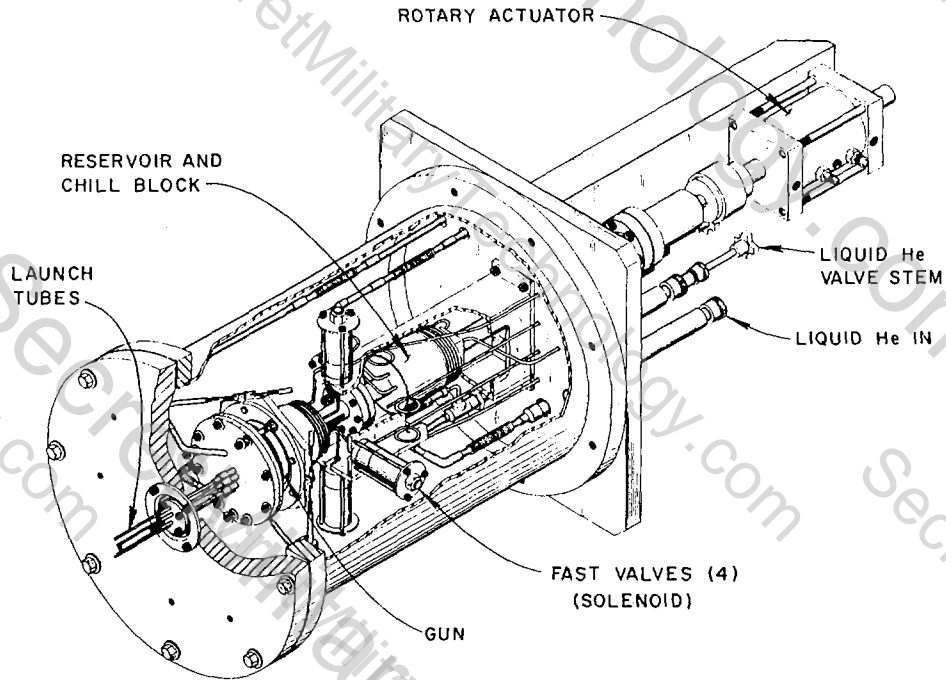


FIG. 7. Four-pellet pneumatic injector. Alcator-C/ISX-B version is shown.

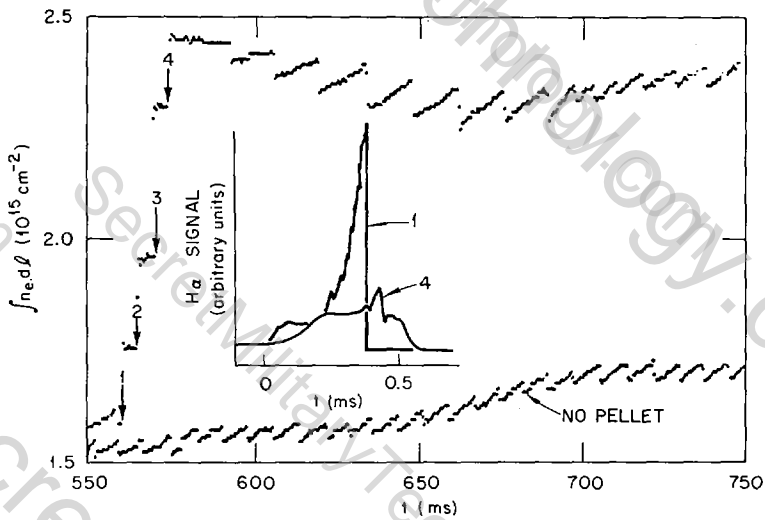


FIG. 8. Response of central line density in PDX plasma to four pellets injected within 20 ms.

and 700 m/s with helium propellant at a pressure of 18 bar. The Alcator-C/ISX-B version has been operated at up to 1 km/s.

Initial results from the PDX device are shown in Fig. 8. The four pellets were injected into an Ohmically heated discharge at 5 ms intervals. As in previous single pellet experiments, the plasma recovers stably from the  $\sim 50\%$  density increase. The duration of the hydrogen light emission ( $H_{\alpha}$  signal) from the pellets, which is an indication of the absolute penetration, increases with each successive pellet ( $\sim 50\%$  penetration to  $\sim 75\%$  penetration). Cooling of the outer regions of the plasma by the addition of fresh fuel is possibly responsible for this result.

#### REFERENCES

- [1] PARKS, P. B., TURNBULL, R. J., FOSTER, C. A., Nucl. Fusion 17 (1977) 539.
- [2] PARKS, P. B., TURNBULL, R. J., Phys. Fluids 21 (1978) 1735.
- [3] MILORA, S. L., FOSTER, C. A., IEEE Trans. Plasma Sci. PS-6 (1978) 578.
- [4] MILORA, S. L., FOSTER, C. A., THOMAS, C. E., BUSH, C. E., et al., Nucl. Fusion 20 (1980) 1491.
- [5] MILORA, S. L., SCHMIDT, G. L., FONCK, R., FOSTER, C. A., et al., Bull. Am. Phys. Soc. 25 (1980) 927 (complete paper to be published).
- [6] MILORA, S. L., FOSTER, C. A., Rev. Sci. Instrum. 50 (1979) 482.

## BLANKET AND SHIELD EXPERIMENTS IN FUSION NEUTRONICS SOURCE (FNS)

T. NAKAMURA, H. MAEKAWA  
Division of Reactor Engineering,  
Japan Atomic Energy Research Institute,  
Tokai-mura, Ibaraki-ken,  
Japan

### Abstract

#### BLANKET AND SHIELD EXPERIMENTS IN FUSION NEUTRONICS SOURCE (FNS).

An intense neutron source based on the D-T reaction was recently completed at the Japan Atomic Energy Research Institute to investigate the neutronics characteristics of various components in a fusion reactor system, especially of blanket and shield. Two blanket experiments and one shield integral experiment have been carried out at the FNS since its initial D-T neutron production in August 1981. — Spatial distributions of the tritium production rate are measured by the liquid scintillation method and by the self-irradiation method with thermoluminescence dosimeters in a spherical lithium oxide assembly with a graphite reflector. Time-of-flight experiments are performed on lithium oxide slab assemblies to obtain the angular dependence of leakage spectra of fast neutrons. — A duct streaming experiment is carried out by utilizing an L-shaped personnel access way in a thick concrete wall of the target room. Neutron and gamma-ray doses in the duct are measured with a neutron dose ratemeter and thermoluminescence dosimeters, respectively; fast-neutron and gamma-ray spectra are obtained by an NE 213 liquid scintillation spectrometer. — The analyses of the experiments are carried out with one- and two-dimensional transport calculations for the blanket and with a three-dimensional Monte-Carlo method for duct streaming. As a whole, the calculations represent the experimental values fairly well.

### 1. INTRODUCTION

The nuclear performance of blanket and shield in a fusion reactor based on D-T burning — the first to be realized for power production — will have a substantial influence on the system design since about 80% of the energy generated in the plasma region is released onto them in the form of 14-MeV fast neutrons. It is, therefore, important to accumulate data on tritium breeding, shield capability, nuclear heat deposition, induced radioactivity, etc. in integral experiments and to verify the nuclear data and calculational methods that will be used in the nuclear design of a fusion experimental or demonstration reactor.

An intense 14-MeV neutron source was recently installed at the Japan Atomic Energy Research Institute to be utilized for the study of the items mentioned above. The Fusion Neutronics Source Facility (FNS) allows a wide

range of experiments with good accuracy by its various neutron production modes and by a well-designed arrangement of target locations, experimental equipment and ports imbedded at suitable positions in the building shield structure.

Two blanket experiments and one shield experiment have been carried out since the initial D-T neutron operation in August 1981. The tritium production rate and other reaction rate distributions were measured in a pseudo-spherical lithium oxide system with a graphite reflector as the first in a series of blanket benchmark experiments. Second, time-of-flight measurements were conducted for the angle-dependent flux spectra of the fast neutrons emitted from the surface of lithium oxide slab assemblies of various thicknesses.

A large-scale duct streaming experiment was performed by using a personnel access tunnel to the target room; dose and spectrum distributions were obtained for neutrons and gamma-rays in the duct.

The purpose of these experiments was to provide experimental data to be used for a check of the calculational techniques applied in the prediction of nuclear performance in a fusion experimental reactor design at JAERI [1]. Especially, there have been no integral experiment data on lithium oxide, which is a promising candidate as blanket material, owing to high Li atom density, in order to achieve a high tritium breeding gain; hence, it has been adopted in the design.

An outline of the experimental facility is presented in Section 2. Descriptions of the experiments and analyses are given for blanket and shield in Sections 3 and 4, respectively.

## 2. EXPERIMENTAL FACILITY

The FNS basically consists of a high-current electrostatic deuteron accelerator, tritium metal target assemblies, tritium handling and processing devices, experimental equipment and a building which, with its shield structure and its ports, plays an important role in the experimental programme [2, 3].

The 400-keV Cockcroft-Walton-type accelerator has two ion sources — for high and low current —, pre- and post-acceleration pulsing devices and two drift tubes in the directions of  $0^\circ$  and  $80^\circ$  with respect to the axis of acceleration. Each beam transport line leads to a separate target room surrounded by a thick concrete shield: a  $15\text{ m} \times 15\text{ m}$  large target room (#1) for the  $80^\circ$  beam line and a small  $5\text{ m} \times 5\text{ m}$  target room (#2) for the  $0^\circ$  beam line. Four types of tritium metal target assemblies have been prepared: LLL-type rotating, small-sized rotating, water-cooled stationary and air-cooled stationary targets.

A variety of source conditions for experiments can be realized by suitable choice of ion sources, beam lines, operation modes — DC and pulse — and target types; a high-intensity continuous source with an initial yield up to  $5 \times 10^{12}\text{ n}\cdot\text{s}^{-1}$  for

a sample irradiation in target room #2 or a 2-ns neutron pulse with peak intensity of  $10^{13} \text{ n} \cdot \text{s}^{-1}$  in target room #1, for example. The performance characteristics of the FNS generator are summarized in Table I.

All tritium gas released from the target into the vacuum system is transferred to a tritium removal and monitoring unit via leak-free lines. Tritium-containing exhaust gas is kept in a storage tank and then re-circulated through the reactor for oxidation and a molecular sieve dryer where tritium is fixed in the form of water.

The FNS is provided with a lot of experimental equipment as, e.g.: 1) a time-of-flight tube facility with detector stations at 11 and 36 m; 2) a  $25 \times 25$  matrix structure where the experimental media are assembled in various shapes and sizes; 3) a movable deck to carry the experimental system on and locate it in the desired position relative to the target; 4) a dual rotatable measuring deck which bears a collimator and a detector shield and rotates around the target from  $0^\circ$  to  $110^\circ$  with respect to the direction of the  $d^+$  beam and 5) a pneumatic sample transfer system between target and measuring rooms. Fig. 1 illustrates the main part of the FNS facility. The absolute source yield is determined by measuring the associated alpha-particles emitted to back angle with a small SSD incorporated in the beam line. Auxiliary monitors are a long counter and Th-fission chambers.

### 3. BLANKET EXPERIMENT

#### 3.1. $\text{Li}_2\text{O}$ spherical system

The system for the first blanket experiment was a pseudo-spherical lithium oxide assembly with a graphite reflector ( $\text{Li}_2\text{O-C}$ ). It was the same assembly that was used to measure the absolute fission rate distributions in an experiment performed previously with a PNS-A neutron source [4].

The  $\text{Li}_2\text{O-C}$  assembly was constructed by loading  $\text{Li}_2\text{O}$  and graphite blocks into stainless-steel drawers, which in turn were inserted into a stainless-steel lattice matrix. The horizontal section across the centre of the assembly is shown in Fig. 2. Figure 3 shows the model adopted for calculation; the homogenized nuclide densities of respective regions are presented in Table II. To observe the spectral change, absolute fission rates were measured by a set of micro-fission  $^{232}\text{Th}$ ,  $^{238}\text{U}$ ,  $^{237}\text{Np}$  and  $^{235}\text{U}$  chambers, in the same way as was reported in Refs [4, 5]. The present results reproduce the previous values within the experimental error, ensuring, thus, a good correlation of the data taken by the two facilities [6].

The tritium production rate was measured by a liquid scintillation method using an  $\text{Li}_2\text{CO}_3$  pellet [7] and by the self-irradiation method of  $\text{LiF}$  thermoluminescence dosimeters (TLD) proposed by Maekawa [8]. The  $\text{Li}_2\text{CO}_3$  pellets

TABLE I. PERFORMANCE CHARACTERISTICS OF FNS

Acceleration voltage : 400 kV					
Beam characteristics :					
DC Mode	A beam line	B beam line	Pulse mode	Bunching	Sweeping
Max. Beam current	23 mA	3.0 mA	Pulse width	1.6 ns	20ns-8 $\mu$ s
Target type	23 cm $\phi$ RT*	HSWCST**	Interval	0.5-256 $\mu$ s	2-512 $\mu$ s
<sup>3</sup> T amount	1,000 C <sub>i</sub>	25 C <sub>i</sub>	Peak current	45 mA	3.0 mA
Max. Neutron yield	5 $\times$ 10 <sup>12</sup> n/s	5 $\times$ 10 <sup>11</sup> n/s	On/off ratio	4 $\times$ 10 <sup>5</sup>	2 $\times$ 10 <sup>5</sup>

\* : Rotating Target,

\*\* : High-Speed Water-Cooled Stationary Target

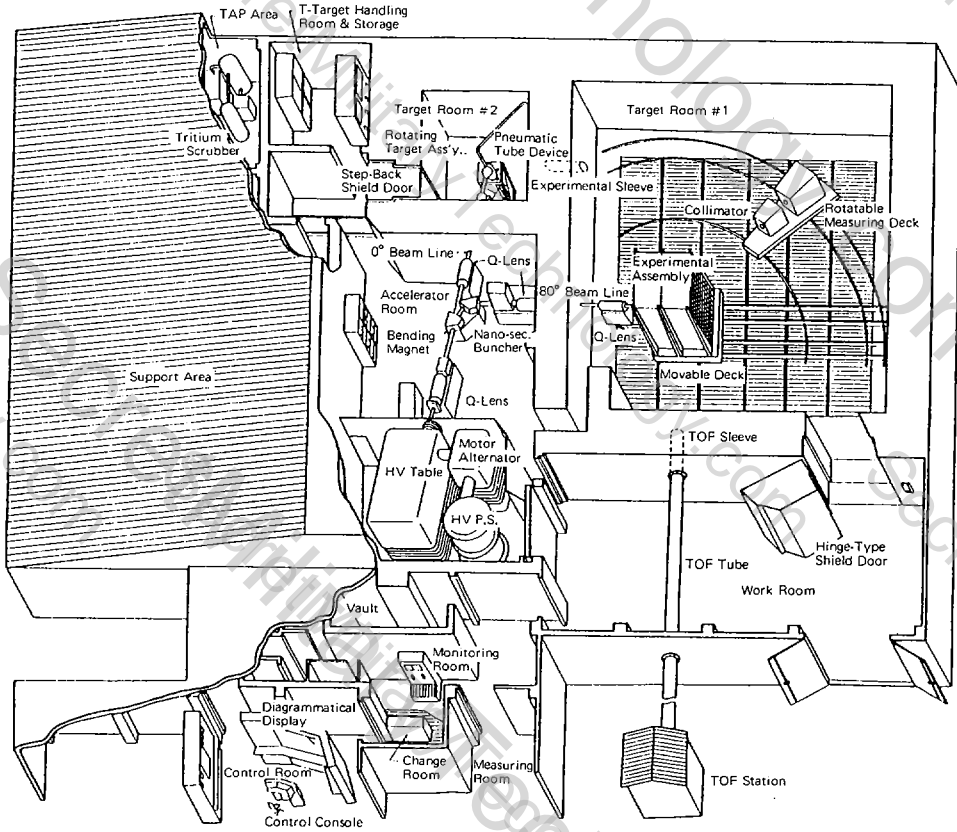


FIG.1. Bird's eye view of Fusion Neutronics Source Facility.

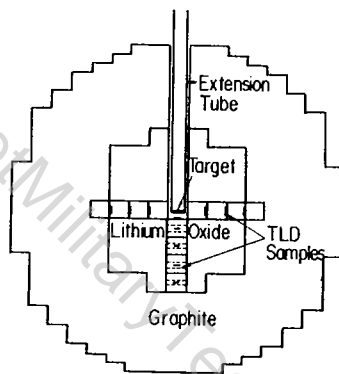


FIG.2. Horizontal section across centre of  $\text{Li}_2\text{O}-\text{C}$  assembly.

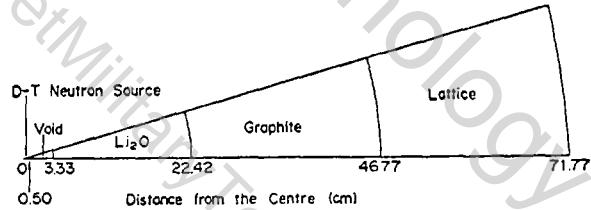


FIG.3. Calculational model of  $\text{Li}_2\text{O-C}$  assembly.

TABLE II. NUCLIDE DENSITIES IN INDIVIDUAL REGIONS

Nuclide	Nuclide density ( $10^{24}$ atoms/cm <sup>3</sup> )			
	Void	Li O	Graphite	Lattice
${}^6\text{Li}$		$3.355 \times 10^{-3}$		
${}^7\text{Li}$		$4.1855 \times 10^{-2}$		
O		$2.2605 \times 10^{-2}$		
C			$6.9298 \times 10^{-2}$	
Cr	$1.751 \times 10^{-3}$	$1.935 \times 10^{-3}$	$1.751 \times 10^{-3}$	$1.161 \times 10^{-3}$
Mn	$8.185 \times 10^{-5}$	$9.632 \times 10^{-5}$	$8.185 \times 10^{-5}$	$5.632 \times 10^{-5}$
Fe	$6.349 \times 10^{-3}$	$7.030 \times 10^{-3}$	$6.349 \times 10^{-3}$	$4.159 \times 10^{-3}$
Ni	$7.303 \times 10^{-4}$	$8.106 \times 10^{-4}$	$7.303 \times 10^{-4}$	$4.821 \times 10^{-4}$

(10 mm  $\phi$   $\times$  5 mm,  $\sim$  0.7 g) of natural abundance and enriched in  ${}^7\text{Li}$  (99.952 atom percent) were placed in  $\text{Li}_2\text{O}$  blocks having holes of 16.6 mm  $\times$  16.6 mm along the  $0^\circ$  direction with respect to the incident  $d^+$  beam. After irradiation in the assembly, the samples were taken out, treated chemically and measured by the liquid scintillation method. The total neutron yield during the irradiation was  $4.5 \times 10^{15}$  neutrons.

TLD-600 ( ${}^6\text{Li}$ : 95.62%) and TLD-700 ( ${}^7\text{Li}$ : 99.993%) powders as manufactured by Harshaw Chemical Co. Ltd. were sealed in 2 mm  $\phi$   $\times$  12 mm glass ampoules. Two pairs of TLD-600 and TLD-700 were set along the  $0^\circ$  and  $90^\circ$  directions with respect to the incident  $d^+$  beam as is shown in Fig. 2. The

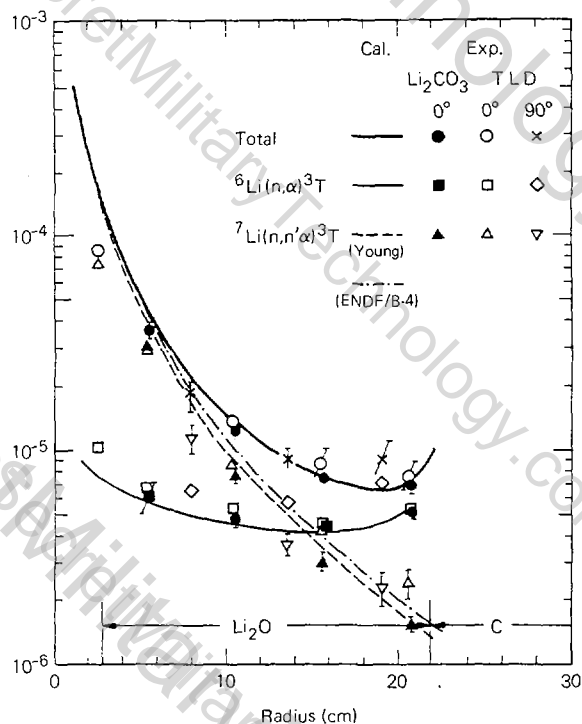


FIG.4. Tritium production rate distribution in  $\text{Li}_2\text{O}-\text{C}$  assembly.

TLDs were annealed twice at  $400^\circ\text{C}$  for one hour after a cooling period of thirteen days introduced to wait for complete decay of induced activities except for tritium and then kept in a special low-background storage for 2215 hours – about three months. The thermoluminescence caused by the self-irradiation due to beta rays from tritium decay during the keeping were measured by a TLD reader.

The tritium production rates were calculated by ANISN [9] with  $P_5-S_{16}$  using a 135-group neutron and 21-group gamma-ray coupled cross-section set, GICX-FNS [10], that was obtained from ENDF/B-IV except for C and  ${}^7\text{Li}$ . The data of ENDF/B-V and Young [11] were adopted for C and  ${}^7\text{Li}$ , respectively.

The measured tritium production rate distributions of the total, the  ${}^6\text{Li}(n, \alpha){}^3\text{T}$  and the  ${}^7\text{Li}(n, n'\alpha){}^3\text{T}$  reactions are shown in Fig. 4, together with the results of calculations. The experimental values of TLD were normalized to those of  $\text{Li}_2\text{CO}_3$  at the point of 5.3 cm. The results achieved by two different methods were in agreement with each other. The  ${}^7\text{Li}(n, n'\alpha){}^3\text{T}$  data were better represented by Young's evaluation than by ENDF/B-IV used previously. To confirm this fact, the cross-section of  ${}^7\text{Li}(n, n'\alpha){}^3\text{T}$  was measured at 14.9 MeV by

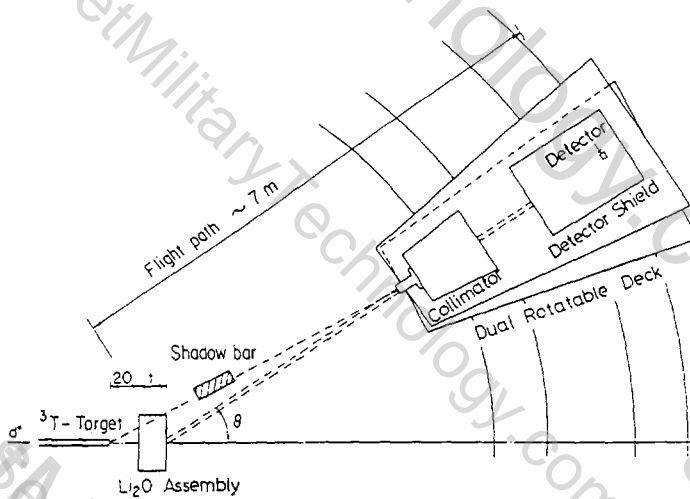


FIG. 5. Layout of TOF experiment.

irradiating  $\text{Li}_2\text{CO}_3$  in the source spectrum field of the FNS. The value obtained was  $(0.290 \pm 0.025)b$ , which agreed well with Young's evaluation.

### 3.2. $\text{Li}_2\text{O}$ slab system

In the case of the fusion blanket, all types of scattering in neutron transport calculations have to be treated more precisely than that in the fission reactor analysis. A good deal of effort is being devoted to an improvement of the calculation methods and the cross-section sets. The present experiment was designed to provide data on angular-flux distributions due to multiple scattering.

The system chosen for this purpose was a set of lithium oxide slab assemblies of 62.8 cm equivalent diameter and 5.05, 20.24 and 40.48 cm in thickness. In this series, lithium oxide blocks were stacked without drawers and lattice to form a pancake cylinder in a frame composed by stacking thin-walled aluminium square tubes of the same size with the blocks for each assembly.

The target was located 20 cm from one side of the slab, and fast-neutron flux spectra leaking from the central area of the other side were measured by a time-of-flight method making use of a fast-neutron detector at angles of  $0^\circ$ ,  $12.2^\circ$ ,  $24.9^\circ$ ,  $41.8^\circ$  and  $66.8^\circ$ . The detector was an NE 213 liquid scintillator of 5.08 cm  $\Phi \times$  5.08 cm size and was located 7.6 m away from the target. Absolute detector efficiency, collimator performance and effect of background were measured and evaluated before the experiment. The layout of the experiment is shown in Fig. 5.

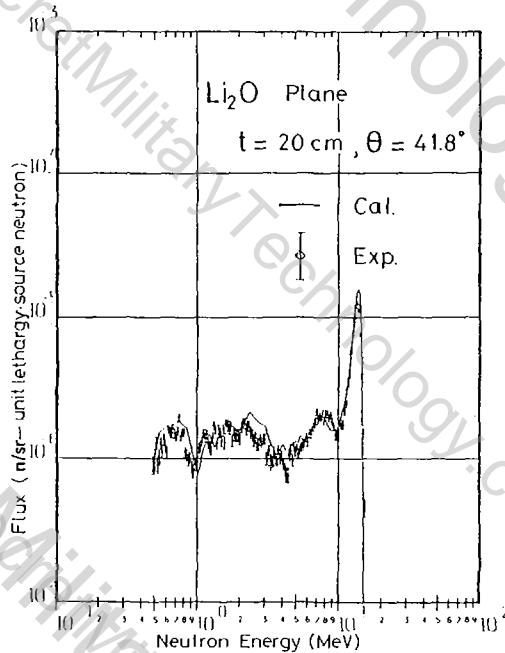


FIG. 6. Typical angle-dependent neutron leakage spectrum from  $\text{Li}_2\text{O-C}$  assembly.

A typical observed angular-flux spectrum is shown in Fig. 6, along with the calculated one. The analysis has been carried out by the two-dimensional transport code DOT 3.5 [12] with  $\text{P}_5\text{-S}_{16}$ , using the GICXFNS cross-section set. Figure 7 shows the angular dependence of the ratios of calculated to experimental fluxes above 0.5 MeV for the three assemblies. A systematic deviation is observed, thus indicating that the present data could be used to judge the accuracy of nuclear data and the treatment of anisotropy in scattering in different calculation methods.

#### 4. SHIELD EXPERIMENT

A duct streaming experiment was carried out in the L-shaped personnel access tunnel in the thick shield wall between the accelerator and the target rooms [13]. This experiment had two goals; one was to confirm the shield capability of this maze structure that had been designed on the basis of a rather simple semi-empirical formula, and the other was to provide reliable data for evaluating the accuracy of shield design methods for large-scale openings as the neutral-beam injector and the vacuum exhaust ports.

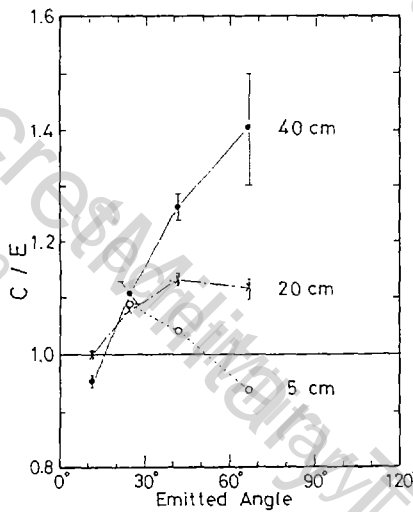


FIG. 7. Angular dependence of ratio of calculated to experimental flux above 0.5 MeV.

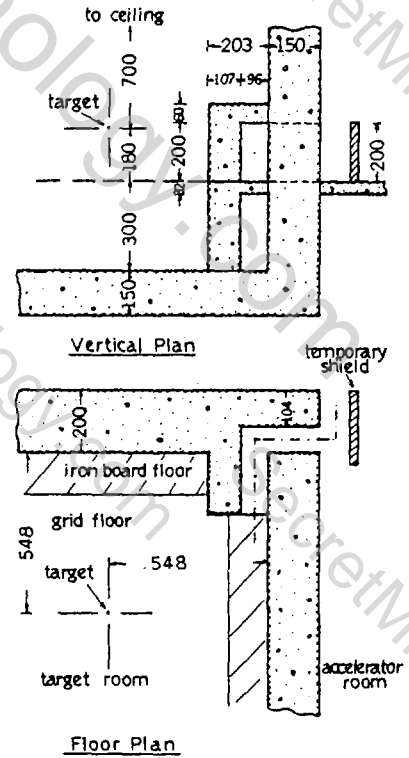


FIG. 8. Duct streaming experiment layout (personnel access way).

The access tunnel used in the present experiments is 200 cm high and 96 cm wide; it is constructed of ordinary concrete. The length of the first maze leg is 250 cm and that of the second one 200 cm. The neutrons from the target located at a height of 180 cm from the floor impinge on the duct mouth at an angle of about  $135^\circ$  with respect to the  $d^+$  beam direction. A temporary polyethylene shield was prepared to minimize the influence of parasitic neutrons from the beam line and to define the geometrical boundary at the exit. The details of the maze are given in Fig. 8, relative to the neutron source position.

The distributions of total neutron dose equivalents, fast-neutron dose equivalents, thermal-neutron flux and gamma-ray exposure dose were measured by using a rem-counter (Studsвик 2202D), a spectrum-weighting function technique with an NE 213 scintillation detector [14], pairs of Cd-covered  $^6\text{LiF}$  and  $^7\text{LiF}$  TLDs and  $\text{CaSO}_4(\text{Tm})$  TLDs covered with a gamma-ray filter so as to have the energy response proportional to that of air from 30 keV to 10 MeV, (UD-200S: Matsushita Electric Co. Ltd.), respectively.

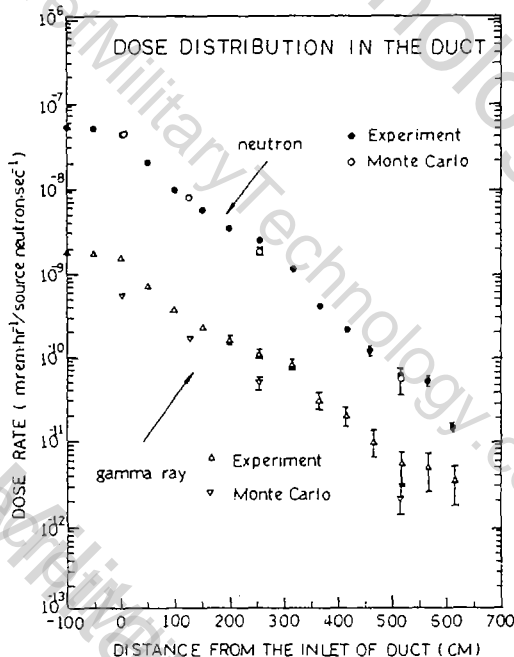


FIG.9. Dose distributions in personnel access way (duct).

The fast-neutron and gamma-ray energy spectra were measured at the four detector locations at the central duct axis. The detector used was of vertical-type, 5.08 cm  $\Phi$   $\times$  5.08 cm NE 213 liquid scintillator mounted on an RCA 6810-A phototube. Pulses due to neutrons and gamma-rays were separated by a pulse shape discrimination method using a rise-time-to-height converter and were recorded simultaneously in separate memory sections of a multi-channel pulse-height analyser. Each pulse height was unfolded with the FORIST code [15] to reconstruct the energy spectrum by using response functions as prepared by Ingersoll [16].

A three-dimensional Monte-Carlo calculation was carried out by MORSE Code [17], using a fairly accurate representation of the target room and the maze structure [18]. A 28-group neutron and 7-group gamma-ray coupled cross-section set, from the GICX40 [19] set using ANISN, was employed. A total of 33 000 source particles were followed in the calculation.

The measured and calculated dose distributions are shown in Fig. 9, and the spectra for fast neutrons and gamma-rays at each location are shown in Figs 10 and 11, respectively. In the case of neutrons, the dose distribution yielded good

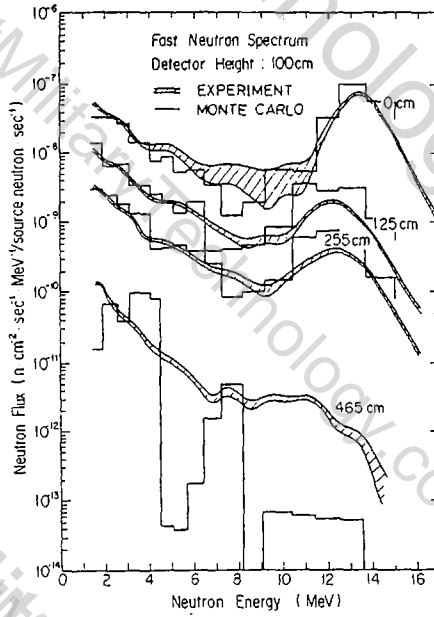


FIG.10. Fast-neutron spectrum in personnel access way (duct).

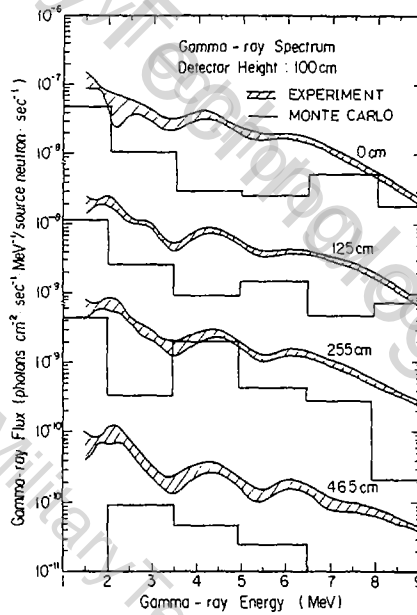


FIG.11. Gamma-ray spectrum in personnel access way (duct).

agreement; the calculation represented the spectral shape fairly well, except for the outermost point where the statistics was quite poor. As for the gamma-rays, the calculation underestimated the results, owing to insufficient data in the gamma-ray generation cross-section in the file used.

## 5. SUMMARY

Useful data were obtained on the tritium production rate and the angle-dependent flux spectrum in two lithium oxide systems. The detailed dose distribution and the spectra were measured for neutrons and gamma-rays in a large-scale bent-duct streaming experiment. Generally, reasonable agreement was observed between calculations and experiments. For a detailed discussion, it is, however, required to add experimental data and to make the calculation more accurate. Through these experiments, it has been demonstrated that the FNS is a powerful experimental tool in fusion neutronics research.

## REFERENCES

- [1] SAKO, K., et al., Conceptual Design of a Gas-Cooled Tokamak Reactor, Nucl. Fusion, Special Suppl., Fusion Reactor Design Problems, 27 (1974); JAERI-M 5502 (1973); JAERI-M 7300 (1977) (in Japanese).
- [2] NAKAMURA, T., et al., Fusion Neutronics Source (FNS), (Proc. 3rd Symp. Accelerator Science and Technology, Aug. 27-29, 1980), Osaka Univ. Osaka, Japan, 55, 56.
- [3] Reactor Engineering Division Annual Report, JAERI-M 9672 (1981) 137-153.
- [4] MAEKAWA, H., et al., J. Nucl. Sci. Technol. **16** (1979) 377.
- [5] MAEKAWA, H., SEKI, Y., J. Nucl. Sci. Technol. **14** (1977) 97.
- [6] NAKAMURA, T., et al., Integral Experiments on Lithium Oxide Spherical Assembly with Graphite Reflector and on Duct Streaming, 3rd IAEA Technical Committee Meeting and Workshop on Fusion Reactor Design and Technology, Tokyo, Oct. 5-16 (1981).
- [7] DIERCKX, R., Nucl. Instrum. Methods **107** (1973) 397.
- [8] MAEKAWA, H., A Method for Obtaining the Tritium Production Rate Distribution with a LiF Thermoluminescence Dosimeter, JAERI-M 6055 (1975) (in Japanese); UCRL-TRANS-11196 (1977).
- [9] ENGLE, W.W., Jr., A User's Manual for ANISN, K-1693, (1967), Oak Ridge National Laboratory.
- [10] SEKI, Y., et al., to be published in JAERI-M.
- [11] YOUNG, P.G., Trans. Am. Nucl. Soc. **39** (1981) 272.
- [12] RHOADES, W.A., MYNATT, F.R., The DOT III Two-Dimensional Discrete Ordinates Transport Code, ORNL/TM-4280 (1979).
- [13] TANAKA, S., et al., A Benchmark Experiment on D-T Neutrons and Secondary Gamma Rays Streaming through a Concrete Bent Duct (to be published in JAERI-M).
- [14] OYAMA, Y., TANAKA, S., Neutron Dosimetry by the Spectrum Weighting Function Method with an NE213 Liquid Scintillator, JAERI-M 9982 (1981) (in Japanese).

- [15] Radiation Shielding Information Center, Oak Ridge National Laboratory, PSR-92.
- [16] INGERSOLL, D.T., et al., Radiation Energy Spectra Unfolding, ORNL/RSIC-40, 47 (1976).
- [17] STRAKER, E.A., et al., The MORSE Code – A Multigroup Neutron and Gamma-Ray Monte Carlo Transport Code, ORNL-4585 (1970).
- [18] SEKI, Y., et al., to be submitted to 6th Int. Conf. Radiation Shielding, Tokyo, Japan (May 1983).
- [19] SEKI, Y., IIDA, H., Coupled 42-Group Neutron and 21-Group Gamma Ray Cross Section Set for Fusion Reactor Calculations, JAERI-M 8819 (1980).

### DISCUSSION

B. BRUNELLI: Could you comment on the level of stability of the neutron source needed in your blanket experiments and on the system for monitoring the neutron yield per unit time (neutron/s)?

T. NAKAMURA: The time variation of the source intensity was continuously monitored by the associated particles method using an SSD incorporated in the drift tube. The neutron yield showed exponential decays with half-lives of  $\sim 10$  h and  $\sim 20$  h for steady beams of 3 mA and 2 mA, respectively, on the high-speed water-cooled stationary target used in this blanket experiment.

## FEEDBACK CONTROL OF THERMAL INSTABILITY BY COMPRESSION AND DECOMPRESSION

M. OKAMOTO, M. OHNISHI\*, K. HIRANO, T. AMANO  
Institute of Plasma Physics,  
Nagoya University,  
Nagoya, Japan

### Abstract

#### FEEDBACK CONTROL OF THERMAL INSTABILITY BY COMPRESSION AND DECOMPRESSION.

Active feedback control of the fusion output power by means of plasma compression-decompression is considered with the purpose of achieving steady-state plasma ignition in a tokamak. A simple but realistic feedback control system is modelled and zero-dimensional energy balance equations are solved numerically by taking into account the errors in the measurements, a procedure that is necessary for the feedback control. It is shown that the control can stabilize the thermal runaway completely and maintain steady-state operation without any significant change in major radius or thermal output power. Linear stability is analysed for a general type of scaling law, and the dependence of the stability conditions on the scaling law is studied. The possibility of load-following operation is considered. Finally, a one-dimensional analysis is applied to the large-aspect-ratio case.

### 1. INTRODUCTION

To overcome the thermal instability in an ignition D-T tokamak plasma [1], a scheme making use of plasma compression-decompression was proposed by Borrass et al. [2]. In this paper, we consider active feedback control of the thermal fusion output power (number of neutrons) in order to stabilize the thermal runaway. A feedback control system which regulates the vertical magnetic field is modelled. The fusion output power is chosen as the object to be controlled, and the errors in measurement necessary for feedback control are included. Numerical calculations show that feedback control can suppress thermal runaway completely and maintain steady-state plasma ignition without changing the major radius significantly. Stability conditions are obtained for a general type of scaling law. The possibility of varying the thermal-fusion output power level during the operation by moving the plasma back and forth along the ignition equilibrium curve is demonstrated by a numerical example. Finally, it is shown that one-dimensional numerical analysis assuming circular

---

\* Institute of Atomic Energy, Kyoto University, Uji, Kyoto, Japan.

cross-sections of the magnetic surfaces supports the results based on the point reactor model.

## 2. FEEDBACK CONTROL SYSTEM AND NUMERICAL RESULTS FROM A POINT REACTOR MODEL

To stabilize the thermal runaway, we compress or expand the plasma by applying the vertical magnetic field:  $B_v = \{B_{10} + \tilde{B}_v(t)\} \times (R_0/R)^n$ , where  $R$  is the major radius,  $R_0$  its ignition equilibrium position,  $n$  the field decay index,  $B_{10}$  the equilibrium vertical magnetic field corresponding to  $R_0$ , and  $\tilde{B}_v$  the controlled vertical field.  $\tilde{B}_v$  is given, so as to reduce the deviation of the controlled object from a specified reference value, by

$$\dot{\tilde{B}}_v + \frac{\tilde{B}_v}{\tau_D} = -\frac{GB_{10}}{\tau_D} \left\{ P(t-\delta t) + \frac{1}{T_I} \int_{t_0}^{t-\delta t} P(t') dt' + T_D \dot{P}(t-\delta t) \right\} \quad (1)$$

$$P(t) = Q_F(t)(1+\epsilon \cdot r)/Q_{F0} - 1 \quad (2)$$

The right-hand side of Eq. (1) is the PID controller, and the left-hand side represents the rise of  $B_v$  with characteristic time  $\tau_D$ .  $G$  is the gain,  $\delta t$  the dead time,  $t_0$  the starting time of the control, and  $T_I$  and  $T_D$  are time constants of the integral and differential circuits, respectively. The object to be controlled is the fusion output power:

$$Q_F \propto \int \frac{1}{4} n^2 \langle \sigma v \rangle_{DT} dV$$

In Eq. (2),  $\epsilon$  is the relative error (say,  $\epsilon = 15\%$ ), and  $r$  is a uniform random number between  $-1$  and  $1$ . In this paper, we choose the following typical values for the gain and characteristic time constants:  $G = 0.3-5$ ,  $\delta t = 10-50$  ms,  $\tau_D = 0.1-2$  s,  $T_I = 1-2$  s and  $T_D = 0-0.2$  s. When  $B_v$  is applied to the plasma, the major radius  $R$  instantly equilibrates, according to the Shafranov equation [3]. It is assumed that the plasma parameters change according to adiabatic scaling laws for the major radius [4].

On the basis of a point reactor model, the dynamic plasma behaviour is followed numerically from start-up to steady-state burning, taking an INTOR-like

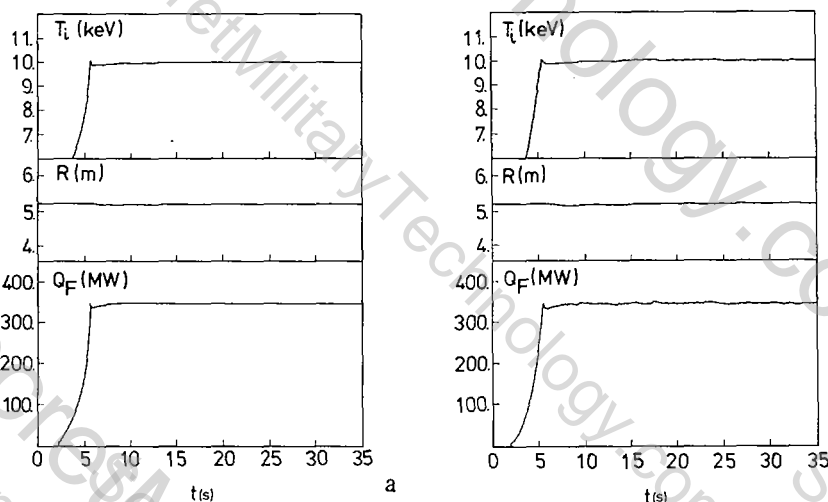


FIG.1. Time evolution of  $T_i$ ,  $R$  and  $Q_F$  (point reactor model). When  $Q_F$  attains  $Q_F^0 = 344$  MW, NBI stops and control starts: (a)  $\epsilon = 0$ ; (b)  $\epsilon = 15\%$ .

tokamak as an example. The initial plasma parameters are:  $R = 5.2$  m,  $a = 1.3$  m,  $I_p = 3.5$  MA,  $n = 1.56 \times 10^{20} \text{ m}^{-3}$ , and  $B_t = 5.5$  T. To attain an ignited plasma, neutral beams are injected and the Alcator scaling law is used for the electron transport. The total number of particles is assumed to be constant. Figures 1(a) and (b) show the time evolution of ion temperature  $T_i$ , major radius  $R$  and fusion output power  $Q_F$  for the cases of  $\epsilon = 0$  and 15%, respectively. After neutral-beam injection (NBI) has heated the plasma up to a point near the self-igniting equilibrium curve, it is turned off, and feedback control is started. We see that feedback control can lead the plasma automatically up to a point on the ignition curve which corresponds to  $Q_F^0$  from the sub- or super-igniting region where NBI is stopped. During this dynamic process, the plasma is compressed or expanded, accompanying the variation in  $R$  which scales as  $\Delta R/R \sim -\Delta n/2n$ . This change becomes smaller when the starting point, where the NBI heating is stopped, is closer to the ignition curve. Once the plasma has found the critical point, the feedback control can continue to maintain its critical point, suppressing the thermal runaway completely, and steady-state burning is obtained. Variations in  $R$  and  $Q_F$  remain quite small while the control maintains the steady state:  $\Delta R/R \cong \pm 0.11\%$ ,  $\Delta Q_F/Q_F \cong \pm 0.55\%$ , when  $\epsilon = 15\%$  (Fig. 1(b)).

The load-following operation can be easily attained by changing the reference value  $Q_F^0$ . A numerical example is shown in Fig. 2. The variation in  $R$  is roughly given by  $\Delta R/R \sim (1/3) \Delta Q_F/Q_F$ . The obtainable change in thermal output power depends on the tolerable major radius variation determined by the reactor design to be realized.

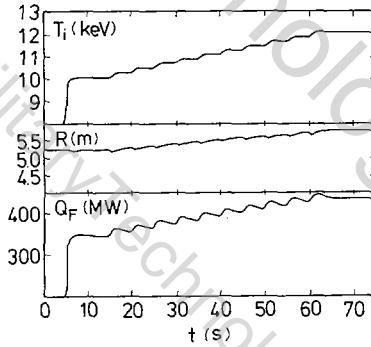


FIG.2. Load-following operation (point reactor model). Operation point moves along ignition equilibrium curve by changing  $Q_{F0}$  from 344 to 440 MW.

### 3. LINEAR STABILITY ANALYSIS

In this section, the linear stability of thermal runaway is analysed for an igniting plasma under feedback control. We assume that the total number of particles  $N$  is constant and  $T_e = T_i = T$ . The linearized total energy balance equation including the effect of major-radius compression becomes

$$\frac{\delta \dot{T}}{T_0} = \gamma_T \frac{\delta T}{T_0} - \frac{4}{3} \frac{\delta \dot{R}}{R_0} - \zeta \frac{\delta R}{R_0} \tag{3}$$

$$\left. \begin{aligned} \gamma_T &= \frac{E_\alpha}{12} n_0 \frac{d}{dT_0} \langle \sigma v \rangle_{DT} - \frac{1}{\tau_{E0}} \left( 1 - T_0 \frac{\partial}{\partial T_0} \ln \tau_{E0} \right) - \frac{1}{3N} \frac{\partial Q_{R0}}{\partial T_0} \\ \zeta &= \frac{1}{\tau_{E0}} \left( 2 - R_0 \frac{\partial}{\partial R_0} \ln \tau_{E0} \right) + \frac{Q_{R0}}{3NT_0} \left( 2 + \frac{R_0}{Q_{R0}} \frac{\partial Q_{R0}}{\partial R_0} \right) \end{aligned} \right\} \tag{4}$$

where  $Q_R$  is the radiation loss and variables with subscript zero are equilibrium quantities. We linearize Eqs (1) and (2), neglecting the integral and differential parts, the dead time  $\delta t$  and the error  $\epsilon$ , to obtain

$$\frac{\ddot{\tilde{B}}_V}{\tilde{B}_{\perp 0}} + \frac{\dot{\tilde{B}}_V}{\tau_D \tilde{B}_{\perp 0}} = -\frac{G}{\tau_D} \left( -2 \frac{\delta R}{R_0} + c \frac{\delta T}{T_0} \right) \tag{5}$$

where  $c = (T_0 / \langle \sigma v \rangle_{DT}) d \langle \sigma v \rangle_{DT} / dT_0$ . Assuming that  $|B_{\perp 0}| \gg |\tilde{B}_v|$ , we linearize the Shafranov equilibrium equation to obtain

$$-n \frac{\delta R}{R_0} + \frac{\tilde{B}_v}{B_{\perp 0}} = -\xi_R \frac{\delta R}{R_0} + \xi_T \frac{\delta T}{T_0} \tag{6}$$

$$\xi_R = 2 - \xi_T \left(1 + \frac{1}{2\beta_{p0}}\right), \quad \xi_T = \frac{\mu_0 I_p}{4\pi R_0 B_{\perp 0}} \beta_{p0} \tag{7}$$

We note that  $\xi_R > 0$  and  $\xi_T > 0$ . By assuming a time dependence of the form  $\exp(-i\omega t)$  for  $\delta T$ ,  $\delta R$  and  $\tilde{B}_v$ , Eqs (3), (5) and (6) give

$$\omega^2 + i \left\{ \frac{1}{\tau_D} - \gamma'_T + \frac{G}{\tau_D \xi} \left(2 + \frac{4}{3}c\right) \right\} \omega + \frac{\gamma'_T}{\tau_D} - \frac{G}{\tau_D \xi} (-2\gamma_T + c\zeta) \tag{8}$$

$$\xi = (\xi_R - n) \left(1 + \frac{4}{3}\eta\right), \quad \gamma'_T = \frac{\gamma_T - \eta\zeta}{1 + 4\eta/3}, \quad \eta = \frac{\xi_T}{\xi_R - n} \tag{9}$$

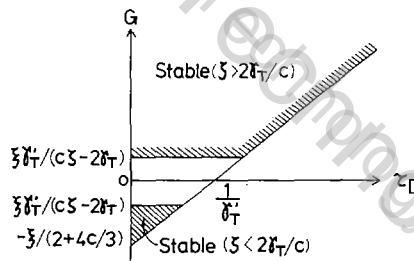


FIG.3. Stable region where feedback control stabilizes thermal runaway.  $G$ : gain,  $\tau_D$ : time lag of control system. Other parameters are defined in Section 3.

It is noticed that for  $\zeta > 0$ ,  $\gamma'_T$  is reduced and the thermal runaway will be passively stabilized with a sufficiently large  $\zeta$  [5]. The stability region given by Eq. (8) is sketched in Fig. 3. We note that feedback control is achievable even if the time lag of the system  $\tau_D$  is longer than the thermal runaway time. It is clear that the control is easier as  $\gamma'_T$  decreases. However, the gain  $G$  increases as  $\zeta$  decreases and  $G = \infty$  when  $\zeta = 2\gamma_T/c$ . As can be seen from Eq. (4),  $\zeta$  is mainly determined by the dependence of  $\tau_E$  on  $R$ . It is concluded that control becomes

difficult for a type of transport scaling where  $\tau_E$  is strongly improved as the plasma moves in the R-direction because of the temperature perturbation. The Alcator scaling is not valid in this case since  $\zeta = 3/\tau_E$ , and  $2\gamma_T/c = 2(1-1/c)/\tau_E$  in the case when  $\tau_E \sim na^2$  if we neglect the radiation loss in Eq. (4).

When, instead of  $Q_F$ , the ion temperature is chosen as the object to be controlled, stability is obtained in a way similar to that shown in Fig. 3 [6]. However, the scheme using the measured major-radius variation [2] yields a very small stability region in the present analysis.

#### 4. ONE-DIMENSIONAL NUMERICAL STUDY

The tokamak transport equations averaged over the magnetic surface  $\rho = \text{const}$  are given by [7]

$$\begin{aligned} \frac{\partial}{\partial t} \left[ \frac{3}{2} p_{e,i} \left( \frac{\partial V}{\partial \rho} \right)^{5/3} \right] &= - \left( \frac{\partial V}{\partial \rho} \right)^{2/3} \frac{\partial}{\partial \rho} \left\{ \frac{\partial V}{\partial \rho} \langle |\nabla \rho|^2 \rangle \right. \\ &\times \left. \left[ n \chi_{e,i} \frac{\partial T_{e,i}}{\partial \rho} + \frac{5}{2} D T_{e,i} \frac{\partial n}{\partial \rho} \right] \right\} + \left( \frac{\partial V}{\partial \rho} \right)^{5/3} \langle Q_{e,i} \rangle \end{aligned} \quad (10)$$

where  $V$  is the specific volume,  $D$  and  $\chi$  are the particle and thermal diffusion coefficients, respectively,  $Q$  is the input power from NBI and alpha heating, and  $\langle \rangle$  denotes the average over the magnetic surface. We assume that  $\partial [n(\partial V/\partial \rho)]/\partial t = 0$  for the particle conservation equation. For simplicity, we solve these equations in the case of a large aspect ratio, assuming circular cross-sections of the magnetic surfaces. The major radius changes according to Eq. (1). For numerical calculations, we adopt the Alcator scaling law assuming that  $D = 2 \times 10^{19}/n \text{ (m}^{-3}\text{)}$ ,  $\chi_e = 5D$  and  $\chi_i = 3 \times \text{neo-classical}$ . Figure 4 shows the result for  $\epsilon = 0$ . The NBI is switched off at  $t = 5.1$  s, and the control is applied at  $t = 5.7$  s. During this dead time, the temperature profiles distorted by the additional heating are relaxed into the profiles by alpha heating only. This rearrangement of profiles is important for reducing the major-radius variation. During the process approaching the critical igniting state,  $\Delta R/R \lesssim 1.15\%$  in Fig. 4. While the control keeps the steady state burning, the major radius does not change significantly. If the errors in neutron measurement are taken into account,  $\Delta R/R \lesssim 0.6\%$  and  $0.95\%$  when  $\epsilon = 10\%$  and  $20\%$ , respectively, during the steady state.

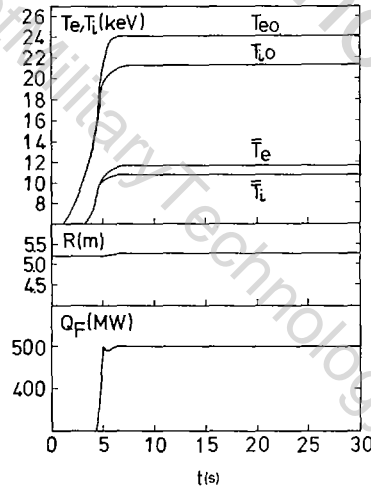


FIG.4. Time evolution of  $T_e$ ,  $R$  and  $Q_F$  (one-dimensional case).  $T_{e0}$ ,  $T_{i0}$ ,  $\bar{T}_e$  and  $\bar{T}_i$  are central electron and ion temperatures, averaged electron and ion temperatures, respectively. NBI stops at  $t = 5.1$  s and control starts at  $t = 5.7$  s.

## 5. SUMMARY

The feedback control of fusion output power with compression-decompression has been shown to be effective for the burn control. Even when the errors in neutron measurement are taken into account, the thermal runaway is suppressed without bringing about any significant change in  $R$  and  $Q_F$ . This is due to the fact that the integral part of the PID controller works well. We have, however, considered the case of constant total number of particles, assuming complete re-cycling and fuelling. The case of imperfect re-cycling should be treated in the future. A one-dimensional analysis assuming concentric circular magnetic surfaces has supported the usefulness of the present method.

## REFERENCES

- [1] OHTA, M., YAMATO, H., MORI, S., in Plasma Physics and Controlled Nuclear Fusion Research (Proc. 4th Int. Conf. Madison, 1971) Vol. 3, IAEA, Vienna (1971) 423.
- [2] BORRASS, K., GRUBER, O., LACKNER, K., MINARDI, E., NEUHAUSER, J., WILHELM, R., WUNDERLICH, R., BROMBERG, L., COHN, D.R., in Plasma Physics and Controlled Nuclear Fusion Research (Proc. 8th Int. Conf. Brussels, 1980) Vol. 1, IAEA, Vienna (1980) 619.

- [3] SHAFRANOV, V.D., in *Reviews of Plasma Physics*, Vol. 2 (translated from the Russian) Consultants Bureau, New York (1966) 124.
- [4] FURTH, H.P., YOSHIKAWA, S., *Phys. Fluids* **13** (1970) 2593.
- [5] BROMBERG, L., COHN, D.R., *Nucl. Fusion* **21** (1981) 201.
- [6] OKAMOTO, M., OHNISHI, M., HIRANO, K., IPP Research Report Nagoya University, IPPJ-573 (March 1982).
- [7] HINTON, F.L., HAZELTINE, R.D., *Rev. Mod. Phys.* **48** (1976) 239.

**Session V**  
**POSTER SESSION**



## LOW- $m$ MAGNETIC-MODE ACTIVITY, DISRUPTIONS IN TOKAMAK DISCHARGES AND THEIR CONTROL

M. COTSFTIS

Association Euratom-CEA sur la fusion,  
Département de recherches sur la fusion contrôlée,  
Centre d'études nucléaires,  
Fontenay-aux-Roses,  
France

### Abstract

LOW- $m$  MAGNETIC-MODE ACTIVITY, DISRUPTIONS IN TOKAMAK DISCHARGES AND THEIR CONTROL.

The problem of tokamak discharge disruptions is tackled by demonstrating that it naturally constitutes a special case of the more general problem of the dynamics, throughout the entire discharge life-time, of drift tearing low- $m$  magnetic modes. This dynamics is represented by a system of equations whose main characteristics are analysed. It is shown that, for a particular mode, three levels exist: non-existence (linear stability), periodic limit cycle (linear instability, but non-linear stability), and disruption (non-linear instability). Analytic expressions for linear and non-linear stability limits are given as well as the amplitude of the limit cycle; the results compare well with various experimental results. — If the 'trajectory' of a mode is known, it is possible to propose a control, that acts on it on a slow time scale, typical of global parameters, as  $n_e(t)$ ,  $I_p(t)$  or  $\alpha$  and  $B_T$ , in order to prevent the mode from reaching the third level, the only dangerous one. This simply implies a slow, but sufficiently early reduction of the plasma current  $I_p$ , as has already been observed previously. This 'slow' control is added to the 'direct' one done by feedback, which is only activated where the mode exceeds the amplitude of the limit cycle; the slow control can, thus, be maintained at reasonable power requirements, when the periodic structure of the (non-linear) mode is taken into account.

### 1. INTRODUCTION

One major reason why, nowadays, tokamak performance is rather limited, is the existence of 'disruptions' which, as is observed in many experiments, can brutally stop the life of discharges. These events are all the more dangerous for future large, long-pulse experiments as they are unpredictable in that no visible precursor announces the plasma modification leading to the disruption. Various modes — mainly the  $m = 2$ ,  $n = 1$  mode — are, however, observed to grow when this disruption phenomenon is imminent.

Two main types of major disruptions can occur [1]:

- 1) disruptions taking place when the critical density is exceeded:

$$n_{\text{crit}} \cong \frac{10 B_T \sqrt{A_i}}{qR Z_{\text{eff}}} \quad (10^{13} \text{ cm}^{-3}, T, m)$$

- 2) disruptions occurring if the critical current is surpassed, in general, for  $q(a) \cong 2.2$ , but this limit may be lower in some experiments.

This situation indicates that disruptions are sensitive to 'global' parameters such as the current  $I_p(t)$  or the density  $n_e(t)$ , a fact which justifies studying a global model for this problem. This is the more appropriate as a control that acts directly on the massively developing  $m = 2, n = 1$  mode would be too late and require a very large amount of power, probably not acceptable in large future machines.

Moreover, it is a common observation in discharges that low- $m$  magnetic modes ( $m = 1, 2, 3; n = 1$  or  $2$ ) are created at the end of the current rise and continue with a very slowly varying amplitude and an almost perfect oscillatory time behaviour (Fig 1). In this case, there is no real instability but the effect of drift of the main parameters, on a *slow* time scale. Also this phenomenon calls for a global approach in order to include this important component of mode structure evolution, from which disruptions arise.

In the following, a system of equations describing, throughout the discharge, the evolution of various modes will be set down; analytic criteria for their stability, showing a good agreement with experiments, will be formulated. This will then allow us to predict the mode evolution and to find a control for these modes, based on global parameters, i.e. on the slow-timescale variation. Such a control will be easy to realize, as has already been seen in several experiments.

## 2. DRIFT-TEARING-MODE EQUATIONS

A) Laboratory plasmas are examples of open systems in a thermodynamical sense [2]. As such, they exchange fluxes with the 'outside' (particles, heat) because they are out of equilibrium and the channels by which they are kept in this stage play a privileged role ( $\nabla n, \nabla T$ ). These systems only exist at the expense of these fluxes and evolve when the parameters change, along a sequence of *branchings*, due to bifurcations that are compatible with the boundary conditions and obey the principle of highest stability.

Such branchings are found from variational equations which are, in turn, derived from the equations describing the dynamics of the system.

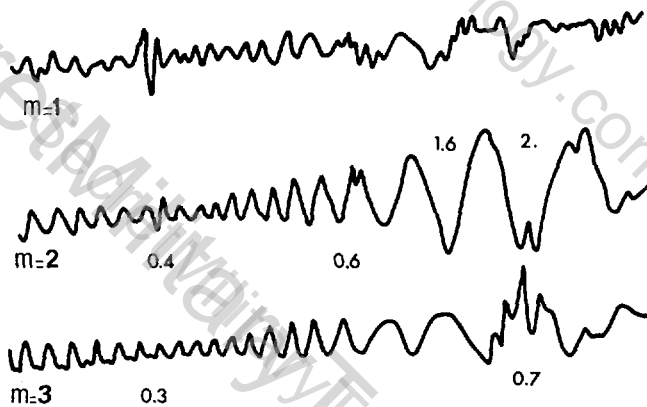
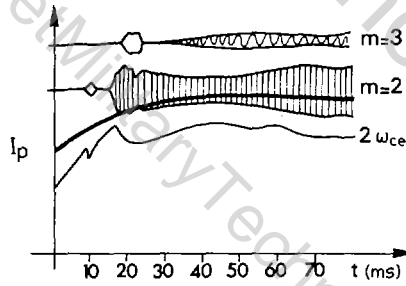


FIG.1. Oscillatory behaviour of  $m = 2$ ,  $n = 1$  toroidal mode, including its two neighbouring satellites. Numbers refer to island size just before disruption.

For a plasma, the first branching corresponds to pure *MHD modes*, which, in a hydromagnetic time  $\tau_H \cong 1$  ms, destroy the configuration. In a toroidal plasma, these modes are forbidden by the Kruskal-Shafranov condition,  $q > 1$ . The next branching occurs in a much softer way and corresponds to the *drift-tearing modes* ('tearing' because the residual magnetic energy is used around the rational surfaces available after the MHD modes have been stabilized; 'drift' because this energy is, via the electrons, coupled with the outfluxes in the channels — density and temperature gradients — because of which the system is out of equilibrium). For high azimuthal wave numbers ( $m \gtrsim 30$ ), these modes may produce anomalous transport that is very unfavourable for effective performance. If we restrict ourselves, here, to low azimuthal wave numbers ( $m = 1, 2, 3$ ), we may say that there is a weakening of the magnetic structure through island creation, which, as will be shown in the following, causes the disruption of the discharge by a sequence of branchings.

B) The basic system of equations which will be used to describe the drift-tearing modes and which includes the drift effects responsible for the remarkable *self-stabilizing behaviour* of the system, on top of the usual geometrical and magnetic field couplings, is given by:

$$\left( \frac{\partial}{\partial t} + \vec{v}_{Di} \cdot \nabla_p \right) \vec{U} + \vec{V} \cdot \nabla_p U = \lambda^{2\alpha} \{ \bar{R}^2 (\vec{B} \cdot \nabla) \vec{J} + \beta_p \bar{R}^3 \nabla \cdot (\nabla \vec{p} \times \vec{e}_\varphi) \} \quad (1a)$$

$$\frac{\partial}{\partial t} \Psi + \vec{V} \cdot \nabla_p \Psi = \lambda^{\alpha-1} \bar{\eta} J + \bar{R}^2 (\vec{B}_0 \cdot \nabla) \Phi \quad (1b)$$

with  $\vec{B} = (1/\bar{R}) [\vec{e}_\varphi + \nabla \Psi \times \vec{e}_\varphi]$ ,  $\vec{V} = \bar{R} \nabla \Phi \times \vec{e}_\varphi$ ,  $J = \bar{R}^2 \nabla_p \cdot (1/\bar{R}^2) \nabla_p \Psi$ ,  $U = \bar{R}^2 \nabla_p^2 \Phi$ ,  $\lambda = \tau_R/\tau_H$ ,  $\bar{R} = R/R_0$ ;  $\vec{v}_{Di}$  the ion drift velocity, and  $\alpha$  a free normalized number. For simplicity, incompressibility has been assumed first. (As is well known [3], including this effect will improve the stability of the system.) Then, the modes are represented by their two potentials,  $\Psi$  and  $\Phi$ , for magnetic and velocity perturbations. Equation (1b) also takes the form  $\partial \Psi / \partial t = \lambda^{\alpha-1} \bar{\eta} J + \bar{R}^2 (\vec{B} \cdot \nabla) \Phi$ , showing that the total operator  $(\vec{B} \cdot \nabla)$  plays an important part in this system. However, because of the operator  $\vec{B}_0 \cdot \nabla$  – which, for unperturbed closed field lines, corresponds to a singularity – and as is observed experimentally, it is only in the form of a few low- $m$  modes of a well defined pattern that a perturbation manifests itself, mainly of the  $(m = 1, n = 1)$ ,  $(m = 2, n = 1)$ , and  $(m = 3, n = 1)$  modes, which appear on magnetic surfaces for which  $q = m/n$ . So Fourier-transforming the potentials  $\Psi$  and  $\Phi$  to give  $X(\psi, \chi, \varphi, t) = \sum_{m,n} X_{m,n}(\psi, t) \cdot \exp i(m\chi - n\varphi)$ , with  $(\psi, \chi, \varphi)$  a triple of intrinsic magnetic co-ordinates related to the unperturbed field, Eqs (1a) and (1b).

become a system of (non-linear) equations for all the components  $\Psi_{m,n}$ ,  $\Phi_{m,n}$ .

As was already mentioned, an important property of the solutions should, in agreement with observations, be an oscillatory periodic behaviour, with a slowly varying amplitude. This behaviour can be incorporated by taking:

$$X_{m,n}(\psi, t) = \sum_{\ell} X_{m,n}^{\ell}(\psi, t_1) \exp[i(m+\ell)\omega t] \quad (2)$$

where the fast oscillatory behaviour is represented by the exponential term, and the remaining slow part, on the time-scale of the main plasma parameters, is included in the  $t_1 = \delta t$  dependence, with  $\delta \ll 1$ . Then, Eqs (1a) and (1b) reduce to a system depending on  $\psi$  and  $t_1$ , with the set  $\{\Psi_{m,n}^{\ell}, \Phi_{m,n}^{\ell}\}$  to be determined order by order. Though complicated in general, the resulting system exhibits an interesting property, due to the same  $m$ -dependence in the

poloidal and time variations of its solutions as is shown by expression (2). Collecting the Fourier transforms, we can write the solution of Eqs (1a) and (1b) in the form:

$$X(\psi, \chi, \varphi, t) = \sum_{m,n} \left\{ X_{m,n}(\psi, \chi, t_1) \exp(in\varphi) \exp(im\omega t) \right\} \quad (3)$$

where the term between the brackets represents a natural 'toroidal' mode of the system, with  $X_{m,n}(\psi, \chi, t_1) = \sum_{\ell} X_{m,n}^{\ell}(\psi, t_1) \exp[i(m+\ell)\chi]$ .

In other words,  $\exp(im\omega t) \exp(in\varphi)$  is still an exact eigenmode of the complete non-linear system (lab), whereas, owing to the toroidal and poloidal field couplings,  $\exp(im\chi)$  is not and should be replaced by the sum above, which represents a set of components on the main surface,  $q = m/n$ , and on the neighbouring surfaces,  $q = (m+\ell)/n$ . This situation is illustrated by Fig.1, where the main ( $m = 2, n = 1$ ) and its two neighbouring ( $m = 1, n = 1$ ) and ( $m = 3, n = 1$ ) components are shown; they all oscillate with the *same* frequency,  $\omega_2 \cong 2\omega_*$ .

C) In the case where  $\epsilon = a/R_0 \ll 1$ , it is possible to carry out expansions in this parameter because now, typically,  $X_{m,n}^{\ell} \cong \epsilon^{\ell} X_{m,n}^0$ . Thus, dropping the index 0, we obtain, to lowest order, the following system:

$$\left( -i \frac{\partial}{\partial t_1} + \omega + \omega_{*i} \right) U_{m,n} = \lambda^{2\alpha} \left\{ F_{mn} J_{mn} + \frac{\partial J_0}{\partial \psi} \Psi_{mn} \right\} + NL_1 \quad (4a)$$

$$\left( -i \frac{\partial}{\partial t_1} + \omega \right) \Psi_{mn} = F_{mn} \Phi_{mn} - i \lambda^{\alpha-1} \frac{\bar{\eta}_m}{m} J_{mn} + NL_2 \quad (4b)$$

where  $q_{mn} = m/n$ , and

$$F_{mn} = \frac{1}{q} - \frac{1}{q_{mn}} - \frac{1}{q} \frac{d\Psi_0}{d\psi}$$

with

$$\begin{aligned} & |\nabla\psi|_0^2 \frac{d^2\Psi_0}{d\psi^2} - (\beta\bar{p}' + \overline{TT}') \frac{d\Psi_0}{d\psi} \\ &= -\frac{i}{\lambda^{\alpha-1}\bar{\eta}_0} \frac{d}{d\psi} \sum_m m(\Phi_m \Psi_m^* + \text{c.c.}) \end{aligned} \quad (5)$$

and the resistivities are obtained from kinetic analysis [4] in the form:

$$\frac{\bar{\eta}_m}{m} = \left\{ \frac{8k_0^2 R_0^2 \omega}{3\sqrt{\pi}} \int_0^\alpha dt \exp(-t^2) t^4 \left\{ \omega - \omega_* \left[ 1 + \eta_e (t^2 - 3/2) \right] \right\} \right\}^{-1} \quad (6)$$

$$\omega \left( \frac{\nu_e - i\omega}{m} \right) \alpha_1 + i \frac{k_\parallel^2 v_e^2 t^2}{3m^2}$$

and

$$\bar{\eta}_0 = \left\{ \frac{8k_0^2 R_0^2}{\sqrt{\pi} \nu_e} \left[ \omega - \omega_* \left( 1 + \frac{5}{2} \eta_e \right) \right] \right\}^{-1}$$

with

$$\eta_e = \frac{d \ln T_e}{d \ln n_e}$$

$$\omega_* = \frac{cRT}{qen_e} \frac{dn_e}{d\psi}$$

$\nu_e$  the collision frequency, and

$$\frac{k_\parallel}{m} = \frac{\bar{T}}{\{|\nabla\psi|_0^2 + \bar{T}^2\}^{1/2}} \frac{1}{R_0} \left( \frac{1}{q} - \frac{1}{q_{mn}} \right)$$

$\alpha_1$  is given recursively [5]. Higher-order terms, including coupling and non-linear terms, are, for the moment, represented symbolically by  $NL_1$  and  $NL_2$ . Finally, to lowest order, i.e. supposing that toroidal geometric and poloidal field couplings are of the same order  $\epsilon$ , we obtain:

$$J_{m,n} = \mathcal{H}_m \Psi_{mn}, \quad U_{m,n} = \mathcal{H}_m \Phi_{m,n}$$

with the operator:

$$\mathcal{H}_m = |\nabla\psi_0|^2 \frac{d^2}{d\psi^2} - (\beta\bar{P}' + \bar{T}\bar{T}') \frac{d}{d\psi} - \frac{m^2 \bar{T}^2}{q^2 |\nabla\psi|_0^2}$$

Without the  $NL_1$  and  $NL_2$  terms, Eqs (4a) and (4b) represent, in the large-aspect-ratio case, equations for purely oscillatory drift-tearing modes in general toroidal geometry.

This system has, on top of the usual couplings, a 'renormalizing' term  $(-1/q) d\psi_0/d\psi$  in the expression for  $F_{mn}$  which is, as was indicated earlier, due to the role of the operator  $\vec{B} \cdot \nabla$ . From Eq.(5) this term is purely imaginary and contributes to the removal of the singularity  $q = q_{mn}$  in Eqs (4a) and (4b) by a sort of dissipative term, which, together with the usual dispersive-type terms, reads as  $-i \lambda^{\alpha-1} (\bar{\eta}_m/m) J_{mn}$ . It is plausible that this term, being of lower order, can contribute to the saturation of the mode amplitude, giving a periodic oscillatory solution, i.e. a limit cycle with amplitude-dependent frequency, as was observed in experiments. So, the problem should be solved as a non-linear eigenvalue problem to obtain the (real) frequency amplitude depending on  $\omega$ . This is known to imply solving the 'internal'-layer problem around  $q = q_{mn}$ , owing to the large value of  $\lambda \gg 1$ , and matching the result with the 'outer' solution [6] to get the (non-linear) dispersion relation of the (m,n) mode – here  $(m = 2, n = 1)$  –, which plays the dominant role.

### 3. STABILITY CRITERIA

A) It follows directly from the previous discussion that there is a sequence of three levels for an (m,n) mode:

- 1) the basic level where the mode does not exist;
- 2) the intermediate level where the mode is linearly unstable, but non-linearly stable, which corresponds to the oscillatory behaviour; and
- 3) the final level where the mode becomes non-linearly unstable.

These three stages correspond to the experimental observations. Thus, to know, for the purpose of control, to which domain in the parameter space of the plasma discharge each stage corresponds, it is only necessary to determine the common boundaries of these domains, in other words, to establish the *linear* and *non-linear* stability criteria corresponding to passing from stage 1 to stage 2 and from stage 2 to stage 3.

Moreover, it is also important to know the amplitude of the non-linear limit cycle in stage 2, a task that is much less demanding than obtaining the frequency since it only requires solution of the 'outer' problem, for which the simplified equation

$$F_{mn} J_{mn} + \frac{\partial J_0}{\partial \psi} \Psi_{mn} = 0 \quad (7)$$

is sufficient, on the assumption that the  $t_1$ -variation is slow as has been observed experimentally. In the linear case, i.e. without the  $\Psi_0$  term, the solution  $\Psi_{mn}$  can be obtained as the product of an approximate solution  $\bar{\Psi}_{mn}$  which is

uniformly valid everywhere across the plasma — and not only around the singularity, as is usually the case — and a 'restoring' function  $\Psi_{mn}$ , which is, in general, very smooth for sufficiently regular profiles  $J_0(\psi)$ . It is found that

$$\Psi_{mn} = \frac{\Gamma(\alpha)\Gamma(\beta)}{\Gamma(1+\alpha+\beta)} F\left(\alpha, \beta, 1+\alpha+\beta; \frac{\psi}{\psi_s}\right) \psi^{m/2}$$

in the interval  $(0, \psi_s)$ , with  $q(\psi_s) = m/n$ , and a combination of such functions in the interval  $(\psi_s, 1)$ , where  $F$  is the hypergeometric Gauss function, with  $\alpha + \beta = m$ ,  $\alpha\beta = -J'_0 \{(1/q)'\}^{-1}|_s$ , evaluated at  $\psi = \psi_s$ .  $\bar{\Psi}_{mn}$  is regular at the origin, and its derivative shows the usual logarithmic behaviour at  $\psi = \psi_s$ .

Hence, the exact linear  $\Delta'_L$  takes the form:

$$\Delta'_L = \pi\alpha\beta \frac{A+1}{A-1} \cotg \pi\beta \quad (8)$$

where  $A$  is a complicated expression involving the matching at the plasma boundary  $\psi = 1$ . The remarkable fact here is that, except for specific cases for which  $A = 1$ , i.e. when the wall location  $\psi_W = 1$ , there is a zero for  $\Delta'_L$  when  $\cotg \pi\beta = 0$ , i.e. a change of sign corresponding to a stability limit. Since  $\beta = 0$  for  $J'_0 = 0$ , the first limit occurs where  $\beta = -1/2$ , with  $J'_0 \{(1/q)'\}^{-1}|_s > 0$ . From the definition of  $\beta$ , we obtain the linear stability limit for mode  $m$ :

$$J'_0 = \left(\frac{1}{q}\right)' \frac{1}{2} \left(m + \frac{1}{2}\right) \Big|_s \quad (9)$$

B) In the non-linear case, we may approximate the function  $(1/q) d\Psi_0/d\psi$  by its value at the singular surface, keeping only the  $\psi$  variation in the singular part  $(1/q) - (1/q_{mn})$  of  $F_{mn}$ , which is justified as long as  $\lambda$  is large enough. The only difference from the previous case is that now the normalizing flux in  $\bar{\Psi}_{mn}$  is not longer  $\psi_s$ , but  $\psi_s - i\zeta_s$ , where

$$\zeta_s = \left[\left(\frac{1}{q}\right)'_s\right]^{-1} \sum_m \frac{m(\Phi_{mn}\Psi_{mn}^* + \text{c.c.})}{2q_s\psi_s\bar{n}_{0s}}$$

giving the new  $\Delta'_{NL}$ :

$$\Delta'_{NL} = \Delta'_L + \pi\alpha\beta\zeta_s \quad (10)$$

With the further approximation that, in the case of stationarity, the dissipative term balances the singular term in  $F_{mn}$ , the components  $\Phi_{mn}$  and  $\Psi_{mn}$  can be evaluated at  $\psi = \psi_s$ , and we obtain the approximate non-linear stability limit:

$$J'_0 = \left(\frac{1}{q}\right)' \left[ \frac{1}{2} \left(m + \frac{1}{2}\right) - \frac{m+1}{\pi} \frac{\Delta_{mn}}{a} \frac{1-A}{1+A} \frac{1}{\psi} \right]_s \quad (11)$$

where  $\Delta_{mn}$  is the size of the (m,n) island. For regular bell-shape  $J_0$  profiles,  $\alpha\beta < 0$ , and, from Eqs (8) and (10),  $\Delta'_L < 0$  implies  $\Delta'_{NL} < 0$ ; conversely, there exists a domain for which  $\Delta'_L > 0$ , but  $\Delta'_{NL} < 0$ , giving non-linear stability in between the two limits (9) and (11).

For completeness, we remark that the amplitude of the mode in the non-linear stability domain can easily be obtained from  $\Psi_{mn}|_s$ , and is given by

$$\frac{\delta B_m}{B_\theta} = \frac{q(1)}{k_0 a} \left( \frac{2\psi_s \nu_e}{m\omega} \right)^{1/2} \left( \frac{1}{q} \right)' \left( \frac{\omega}{\omega - \omega_*} \right)^{1/2} \frac{\Delta_{mn}}{\ell_{mn}} \quad (12)$$

where  $\ell_{mn}$  is a typical gradient of the magnetic perturbation, so  $\Delta_{mn}/\ell_{mn}$  is a form factor of the order of  $\cong 1$ .  $\delta B_m/B_\theta$  can be related to  $\Delta_{mn}/a$  when we suppose the perturbation  $\Psi_{mn}$  to vary in the domain  $\psi > \psi_s$  in the same way as in the vacuum domain, giving

$$\Delta_{mn}/a = \left\{ \frac{2}{m} \frac{\delta B_m}{B_\theta} \left( \frac{\psi_L}{\psi_s} \right)^{m/2} \right\}^{1/2}$$

where  $\psi_L$  is the location of the measuring loops, allowing for the substitution in expression (11).

#### 4. MECHANISM OF DISRUPTIONS AND THEIR CONTROL

Equations (9), (11) and (12) are the main results of the present analysis. Given a current profile  $J_0(\psi)$ , we may plot the limit of linear and non-linear stability which is obtained as the locus of the parameters for which the  $\psi_{lim}$ , giving equal signs in expressions (9) and (11), coincides with the  $\psi_s$  for which  $q(\psi_s) = m/n$ . This has been done with the typical profile  $J_0(\psi) = (1 - \psi)^j$  [7]. The stability lines in the  $\{j, q(a)\}$  plane for  $m = 2$  are shown in Fig.2. What remains to be done is to make sure that these stability criteria are relevant from a physics point of view. Two examples from well-documented TFR experiments [8] are shown in Fig.2; disruption has been verified to occur when the limit (11) is crossed, whereas expression (12) gives the correct amplitude

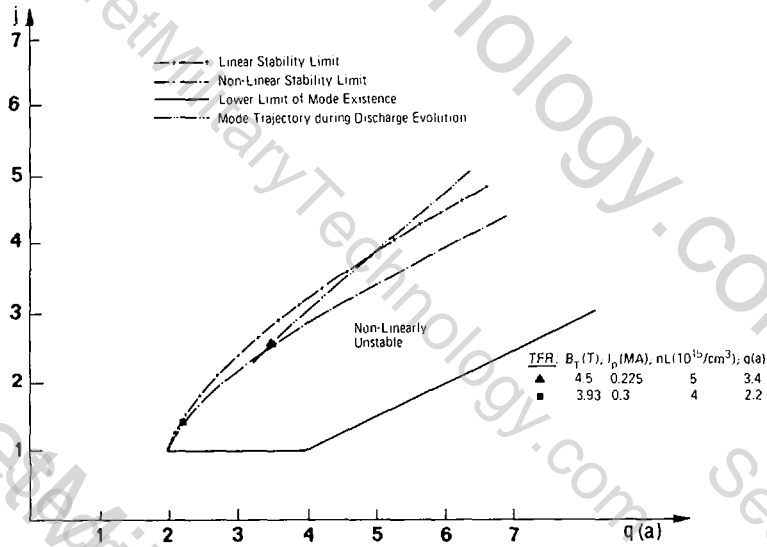


FIG. 2. Stability domain of  $m = 2, n = 1$  mode for  $J_0(\psi) = (1 - \psi)^j$ .

( $\cong 0.8\%$ ) at the limit cycle. Other cases, from other experiments, have been also considered; the same kind of agreement was found.

So, in this analysis, disruption appears to be due to a 'crossing' of non-linear stability under the influence of the (slow) variation of the main plasma parameters rather than to the occurrence of a brutal and violent instability. In fact, it may be verified that the typical amplitude of the mode for which overlapping with neighbouring satellites occurs is about three times that given by expression (12). This explains why the plasma discharge can stay so long within oscillatory modes and can, on the other hand, be destroyed so violently when it crosses the limit (11). This observation implies an important consequence for control because it suggests that one should try to maintain the mode at the limit cycle stage instead of suppressing it totally as is usually proposed. From this, two advantages result: (a) the evolution is now on a *slow* time-scale (easier detection, much lower power level); (b) it is possible to use global parameters like  $n_e(t)$  and  $I_p(t)$ ,  $a$ ,  $B_T$ , as control parameters, because they vary on the *same* time-scale (as is, in fact, already done at the beginning of a discharge during the current rise). As is seen in Fig. 2 from the mode trajectory, further analysis indicates that a simple and efficient control is to reduce the total current  $I_p(t)$ , *slowly but early enough*, with a variation  $I_p(t) \cong (n_l(t))^{-1/3}$ , where  $n_l$  is the line average density. This will, on the diffusion time-scale of the current, which is now sufficient, prevent the surface  $q(\psi_s) = 2$  from crossing the

limit (11). There is already experimental evidence [9], for slow current decline preventing disruption.

Such a control is the more efficient as, in future large machines, the main parameters will vary slowly and precisely. Moreover, it is possible to complement this 'global' control by a feedback fast loop acting directly on the ( $m = 2, n = 1$ ) mode when it performs an excursion above the threshold limit (12). This is the easier as the mode behaves as a pure oscillation, which makes synchronous detection and resonating feedback with a large amplification factor possible and lowers the power requirements down to reasonable values [10].

In conclusion, we may state that disruptions are easy to avoid by this double, slow and fast, control, so that the discharges can reach a high level of thermonuclear performance.

#### REFERENCES

- [1] HUGILL, S.G., NET-INTOR Workshop on Disruptions, IPP Garching (Nov. 1981).
- [2] NICOLIS, G., PRIGOGINE, I., Self-Organization in Non-Equilibrium Systems, J. Wiley and Sons, New York (1977).
- [3] WESSON, J.A., Nucl. Fusion 18 (1978) 87.
- [4] DRAKE, J.F., LEE, Y.C., Phys. Fluids 20 (1977) 1341.
- [5] DRAKE, J.F., GLADD, N.T., LIM, C.S., CHANG, C.L., Phys. Rev. Lett. 44 (1980) 994.
- [6] COTSAFTIS, M., Report UCLA/ENG-8146 (1981).
- [7] HASTIE, R.J., SYKES, A., TURNER, M., WESSON, J.A., Nucl. Fusion 17 (1977) 515; COTSAFTIS, M., Report EUR-CEA FC 1139 (1982).
- [8] TFR GROUP, Disruptions in TFR 600 (to appear).
- [9] FT Group Frascati, Report 81-1 (1981); HAMMETT, G., McGUIRE, K., Report PPPL-1854 (1982).
- [10] COTSAFTIS, M., Resonant Feedback Control of Low-m Magnetic Modes (to appear).



## RF CURRENT DRIVE IN TOKAMAKS AND COMPACT TORI

E. CANOBBIO, R. CROCI  
Max-Planck-Institut für Plasmaphysik,  
Euratom-Association,  
Garching,  
Federal Republic of Germany

### Abstract

#### RF CURRENT DRIVE IN TOKAMAKS AND COMPACT TORI.

The quasilinear Fokker-Planck equation for a Lorentz electron gas in the presence of travelling electrostatic waves is solved analytically. The current generated and the power dissipated into the plasma are calculated in the two limits of low and high RF field strength. Some incorrect assumptions and results in the current literature are corrected. A quantitative comparison with LH current drive experiments is made. The occurrence of a density cutoff is related to the presumably unstable situation where the RF current profile has a sharp maximum at the very edge of the plasma.

### 1. INTRODUCTION

We solve analytically the quasilinear Fokker-Planck equation which describes the interaction of a travelling electrostatic wave (whose  $k$ -spectrum is kept constant by external sources) with a Lorentz electron gas. We calculate the current generated and the power dissipated into the plasma by a rectangular  $k$ -spectrum wave in the two limits of low and high RF field strength.

As we neglect electron-electron collisions, the present paper might be considered a step backwards from existing works, which include the linear theory of the full QLFP equation [1, 2] and numerical studies of the two-dimensional QLFP equation in the high field limit [3] which confirm the original one-dimensional calculation for  $j$  and  $P$  [4]. A few critical comments, however, are appropriate at this point as an introduction to our work.

The classical Legendre polynomial expansion of the linear perturbation of the distribution function  $f^*$  is used in Ref. [1] for a monochromatic  $k$ -spectrum (from which the general case can be produced by linear superposition); the QLFP equation is solved analytically in the Lorentz gas approximation and numerically in its full form, neglecting (it is claimed) the time derivative of the velocity distribution function. This derivative, however, has to be included if only to calculate consistently the power deposition into the plasma. Indeed the Legendre expansion

of the Lorentz term has no spherically symmetric part. Thus the same must be true of the rest of the QLFP equation. As the spherically symmetric part of the QL diffusion term is different from zero if power is absorbed, the time derivative of the spherically symmetric part of the velocity distribution function has to be retained.

The model e-e collision term used in Refs [3] and [4] does not conserve energy, so that the power the plasma absorbs is actually  $P = P(QL) + P(FP)$ . The variation of  $P(QL)$  and  $P(FP)$  with time is computed numerically in Ref. [3]. A steady state is found asymptotically ( $t \rightarrow \infty$ ):  $P(FP) = -P(QL)$ .

What we do in this paper is to write  $f_e = f^0(t, v) + f^*$  with  $\int_1^1 d\xi f^* = 0$  and to consider situations where  $|\partial f^*/\partial t| \ll |\partial f^0/\partial t|$  so that the current – a functional of  $f^*$  – is driven adiabatically by the wave, while the power – a functional of  $(f^0 + f^*)$  – accumulates gradually into the electron gas. The opposite situation would be essentially time-dependent (“runaway” distributions, etc.). We first of all solve the linearized QLFP equation apart from the discontinuity surface (either directly as in this paper or through a bilinear expansion in Legendre polynomials [5]) and then we match the solutions on both sides of each discontinuity surface by multiplying the equation by a function of the pitch-angle variable  $\xi = v_z/v$  and integrating over  $\xi$  across the discontinuity surface.

## 2. THE QLFP EQUATION AND ITS SOLUTION

In the presence of an electrostatic wave

$$E(\bar{z}, t) = \int dk E_k \cos(kz - \omega t)$$

the QLFP equation for the Lorentz electron gas is

$$\partial \phi / \partial \tau = C_w(\phi) + C_e(\phi)$$

where

$$\phi = \phi(\tau, \vec{u}); \quad \vec{u} = \vec{v}/v_e; \quad v_e^2 = 2kT_e/m_e; \quad \tau = Z\omega t/2$$

$Z$  is the charge of the ion background;

$$\omega = 4\pi e^4 m_e \ln \Lambda / m_e^2 v_e^3$$

$$C_w(\phi) = \partial(D(\omega)\partial\phi/\partial w)/\partial w; \quad w = \xi u = v_z/v_e$$

$$D(\omega) = \int dk D_k (\nu Z / \nu_e) / ((\nu Z / 2\nu_e)^2 + (k\omega - \omega/\nu_e)^2)$$

$$D_k = (e E_k / m_e)^2 / 2Z \nu \nu_e^3$$

$$C_e(f) = \partial((1-\xi^2) \partial f / \partial \xi) / \partial \xi u^3$$

In the rectangular spectrum case,

$$E_k^2 = E_0^2 \{ \theta(k-k_2) - \theta(k-k_1) \} / (k_1 - k_2) \equiv E_0^2 \hat{\theta} / \Delta k$$

where  $\theta(x)$  is the Heaviside step function,

$$\Delta k = (\omega_2 - \omega_1) \omega / \nu_e \omega_1 \omega_2 ; \omega_{1,2} = \omega / \nu_e k_{1,2}$$

$$D(\omega) = D_0 \int dk 2\pi \delta(k\omega - \omega/\nu_e) / \Delta k = 2\pi D_0 \hat{\theta} / \Delta k \omega$$

$$D_0 = (e E_0 / m_e)^2 / 2Z \nu \nu_e^3$$

We set

$$f(\tau, \vec{u}) = f^0(\tau, u) + f^*$$

with

$$\int_{-1}^1 d\xi f^* = 0$$

and anticipate that

$$|\partial f^* / \partial \tau| \ll |\partial f^0 / \partial \tau|$$

The QLFP equation thus becomes

$$C_w(f) + C_e(f) = \partial f^0 / \partial \tau = \frac{1}{2} \int_{-1}^1 d\xi C_w(f) \equiv \bar{Q}(u; \tau) \quad (1)$$

where  $\tau$  is simply a parameter and  $\int_0^\infty du u^2 \bar{Q} = 0$  as required by particle conservation.

For the rectangular spectrum case we write

$$f = \theta_{<} f_{<} + \hat{\theta} \hat{f} + \theta_{>} f_{>} \quad (2)$$

where

$$\theta_{<} \equiv \theta(w_1 - w); \quad \theta_{>} \equiv \theta(w - w_2); \quad \theta_{<} + \hat{\theta} + \theta_{>} = 1$$

$f_{<}$  and  $f_{>}$  are solutions of

$$\partial((1-\xi^2)\partial f/\partial\xi)/\partial\xi = u^3 \bar{Q}(u)$$

Excluding the infinities, which can be negative, we have

$$f_{<} = \alpha_{<}(u^2) - u^3 \bar{Q} \ln H_1; \quad H_1 = (1-\xi)/(1-w_1/u) \quad (3)$$

with  $\bar{Q}(w_1) < 0$ , and

$$f_{>} = \alpha_{>}(u^2) + u^3 \bar{Q} \ln H_2; \quad H_2 = (1+w_2/u)/(1+\xi)$$

with  $\bar{Q} = Q(u) \theta(u-w_1)$ .

The solution in the resonance region  $\hat{f}$  will be given later and only in the two limits of low and high field strength, or  $D_0 \rightarrow 0$  and  $D_0 \rightarrow \infty$ .

The jump conditions at  $w = w_1$  and  $w = w_2$  are found by considering the integrals (see Eq. (1)):

$$\int_{w_{1,2}/u - \epsilon}^{w_{1,2}/u + \epsilon} d\xi g(\xi) (C_w + C_e - \bar{Q}) = 0 \quad (4)$$

where

$$C_w = \frac{2\pi D_0}{\Delta k} \left( \xi \frac{\partial}{\partial u} + \frac{1-\xi^2}{u} \frac{\partial}{\partial \xi} \right) \left\{ \frac{\hat{\theta}}{w} \left( \frac{\partial \hat{f}}{\partial w} + \delta_1 (\hat{f} - f_{<}) + \delta_2 (\hat{f} - f_{>}) \right) \right\}$$

and  $\delta_{1,2} \equiv \delta(w - w_{1,2})$ , a Dirac function.

Equation (4) has the form  $A_{1,2}g'_{1,2} + B_{1,2}g_{1,2} = 0$  (the prime indicates derivative with respect to  $\xi$ , and the subscript means "evaluated at  $w = w_{1,2}$ ") and produces four conditions:  $A_{1,2} = 0$  and  $B_{1,2} = 0$ . The former imply the continuity of  $f$ , i.e.  $[f]_{1,2} = 0$  (where  $[f]_{1,2}$  is the jump of  $f$  at  $w = w_{1,2}$ ), while the latter imply

$$\frac{2\pi D_0}{\Delta k w_{1,2}} \left\{ \pm \frac{\partial \hat{f}}{\partial w} + \frac{1}{2} \left[ \frac{\partial f}{\partial w} \right] - \frac{1}{2u} \left[ \frac{\partial f}{\partial \xi} \right] \right\}_{1,2} + \left( \left( 1 - \left( \frac{w}{u} \right)^2 \right) \left[ \frac{\partial f}{\partial \xi} \right] \right)_{1,2} = 0 \quad (5)$$

When the complete solution is known we can calculate the absorbed power density:

$$P = \int d^3 \vec{v} \frac{1}{2} m_e v^2 \partial f / \partial t = \pi m_e v_e^5 \nu Z \int_{w_1}^{\infty} du u^4 Q \quad (6)$$

and the electric current density:

$$-j = e \int d^3 \vec{v} v_{||} f = 2\pi e v_e^4 \int_0^{\infty} du u^3 \int_{-1}^1 d\xi \xi f$$

For simplicity we take throughout this paper  $\delta \equiv w_2 - w_1 \ll w_1$ . Then to lowest order in  $\delta$

$$-j = 2\pi e v_e^4 \int_{w_1}^{\infty} du \left\{ w_1 u^5 Q + \frac{1}{2} u^3 \left( 1 - \left( \frac{w_1}{u} \right)^2 \right) (\alpha_+ - \alpha_-) \right\} \quad (7)$$

### 3. THE LOW FIELD LIMIT

We linearize Eq. (1) by setting  $f = f_M$ , the Maxwell distribution, in  $C_W(f)$  and retain only terms of lowest significant order in  $\delta$ . Then we have

$$\hat{f} = -u^3 Q \ln H_1 + \frac{4\pi D_0}{\Delta k} u^4 \left( \xi - \frac{w_1}{u} \right) f_M + \hat{\alpha}(u^2) - \frac{1}{2} \hat{\beta}(u^2) \ln H$$

$$H = (1 - \xi)(1 + w_1/u)(1 + \xi)^{-1} (1 - w_1/u)^{-1} \quad (8)$$

$$Q = \frac{2\pi D_0 \psi_M}{\Delta k u} \left\{ (w_2^2 + 1 - u^2) \theta(u - w_2) - (w_1^2 + 1 - u^2) \theta(u - w_1) \right\}$$

The four functions  $\alpha_<$ ,  $\hat{\alpha}$ ,  $\alpha_>$  and  $\hat{\beta}$  are related to  $f_M$  by the jump conditions:

$$\alpha_< = \hat{\alpha} = \psi_M; \quad \alpha_> = \psi_M + \frac{4\pi D_0 u \psi_M \delta}{\Delta k (1 - (w_1/u)^2)} \quad (9)$$

$$\hat{\beta} = \frac{4\pi D_0 u^2 (w_1^2 + 1 - u^2)}{\Delta k} \psi_M$$

with

$$\Delta k \equiv \omega \Delta N_{||} / c \approx \omega \delta / v_e w_1^2$$

The absorbed power density is

$$P / m m_e v_e^2 \nu Z = \frac{\sqrt{\pi} D_0}{\Delta k} (e^{-w_1^2} - e^{-w_2^2}) \approx \frac{2\sqrt{\pi} D_0}{\Delta k} \delta w_1 e^{-w_1^2} \quad (10)$$

and the current density

$$-j / e m v_e = \frac{4\sqrt{\pi} D_0}{\Delta k} \delta A(w_1) \quad (11)$$

with

$$A(w_1) = \left( 2w_1^3 + \frac{3}{4}w_1 \right) e^{-w_1^2} + \frac{3}{4} (2w_1^2 + 1) \text{Erfc}(w_1) \quad (12)$$

$$\lim_{w_1 \rightarrow 0} A(w_1) = 3\sqrt{\pi}/8, \quad \lim_{w_1 \rightarrow \infty} A(w_1) = 2w_1^3 e^{-w_1^2}$$

$$\lim_{w_1 \rightarrow 0} (-j/P) = (e/mv_e \circ Z) (3\sqrt{\pi}/4 w_1) \quad (13)$$

$$\lim_{w_1 \rightarrow \infty} (-j/P) = (e/mv_e \circ Z) 4 w_1^2$$

Equations (10) to (13) agree with the corresponding equations of Ref. [1], where it is erroneously claimed that the time derivative of the distribution function has been neglected. Notice that our distribution function is positive everywhere, whereas the distribution function in Ref. [1] tends to  $-\infty \delta(u-w_1)$  for  $\xi \rightarrow 1$ .

Finally, condition  $|\partial f^*/\partial \tau| \ll |\partial f^0/\partial \tau|$  is obviously satisfied as  $f^* \cong O(D_0 f^0)$ .

#### 4. THE HIGH FIELD LIMIT

Under the assumption  $D_0 \rightarrow \infty$ , the solution of Eq. (1) in the inner region is

$$\hat{f} = \frac{1}{2} M(P^2) (w^2 - w_1^2) + N(P^2) + O(D_0^{-1}) \quad (14)$$

with  $P^2 = (v_1/v_e)^2 = u^2(1-\xi^2)$ . The continuity requirement at  $w = w_{1,2}$ , with  $\delta \ll w_1$ , gives

$$M = 0; \quad \alpha_<(u^2) = N(u^2 - w_1^2); \quad \alpha_>(u^2) = N(u^2 - w_2^2) \quad (15)$$

To the next order ( $D_0^{-1}$ ) we find

$$\frac{2\pi D_0}{\Delta k} \hat{f}_{D_0^{-1}} = -\left( \frac{e}{m} \frac{\partial f}{\partial u} \right)_1 (w-w_1)^2 (w+w_1/2) / 3 + \frac{m}{2} (P^2) (w^2 - w_1^2) + m(P^2)$$

Conditions (5) then require

$$u^2 m_1 = (1 - (w_1/u)^2) \left\{ 2 u w_1 (\partial N / \partial u^2)_1 + u^3 Q / (1 - w_1/u) \right\}$$

$$u^2 m_2 = (1 - (w_2/u)^2) \left\{ 2 u w_2 (\partial N / \partial u^2)_2 - u^3 Q / (1 + w_2/u) \right\} + u^2 \delta \left( \frac{e}{m} \frac{\partial f}{\partial u} \right)_1$$

With  $N(u^2 - w_1^2) = f_M$  it follows that

$$Q = \frac{\delta}{2u^2} \frac{\partial}{\partial u} (m_1 w_1 \theta(u - w_1)) = -\delta \left(\frac{w_1}{u}\right)^2 \frac{\partial}{\partial u} \left(\frac{f_M}{u} (1 - (w_1/u)^2) \theta(u - w_1)\right) \quad (16)$$

so that

$$P = m m_e v_e^2 \nu Z \delta B(w_1) \quad (17)$$

with

$$B(w_1) = \frac{2w_1^2}{\sqrt{\pi}} \left\{ (1 + 2w_1^2) \text{Erfc}(w_1) - w_1 e^{-w_1^2} \right\}$$

$$\lim_{w_1 \rightarrow 0} B(w_1) = w_1^2 \quad \text{and} \quad \lim_{w_1 \rightarrow \infty} B(w_1) = e^{-w_1^2} / \sqrt{\pi} w_1$$

From Eq. (7) the current density is

$$-j = e m v_e \delta C(w_1) \quad (18)$$

with

$$C(w_1) = \frac{w_1}{\sqrt{\pi}} \left\{ (1 + 3w_1^2) e^{-w_1^2} - 3w_1^4 \Gamma(0; w_1^2) \right\}$$

$$\lim_{w_1 \rightarrow 0} C(w_1) = \frac{w_1}{\sqrt{\pi}} \quad \text{and} \quad \lim_{w_1 \rightarrow \infty} C(w_1) = 4w_1 e^{-w_1^2} / \sqrt{\pi}$$

For the efficiency figure we find

$$\lim_{w_1 \rightarrow 0} (-j/P) = (e/m_e v_e \nu Z) / \sqrt{\pi} w_1 \quad (19)$$

$$\lim_{w_1 \rightarrow \infty} (-j/P) = (e/m_e v_e \nu Z) 4 w_1^{-2} \quad (20)$$

The  $\lim_{w_1 \rightarrow \infty} (-j/P)$  coincides with the value obtained in the linear approximation (see Eq. (13)).

Finally, we define a critical value  $D^*$  of the QL diffusion coefficient by equating the large  $w_1$  expressions of  $(-j)$  obtained for high and low RF field amplitudes (Eqs (11) and (18)):

$$D^* = \Delta k / 2\pi w_1^2 \quad (21)$$

Equation (21) coincides with the Fisch criterion  $w_1^3 D = 1$  [3, 4].

At last, the condition  $|\partial f^*/\partial \tau| \ll |\partial f^0/\partial \tau|$  is satisfied in the  $D_0 \rightarrow \infty$  limit when  $f^* \equiv O(\delta f^0) \ll f^0$  (adiabaticity condition).

## 5. INTERPRETING THE LH EXPERIMENTS

Unambiguous demonstration of LH wave-driven current in tokamaks below some critical density has been reported by several groups [6–8]. In Versator II, for example, the current rise depends linearly on the transmitted power and is approximately independent of density for  $n \lesssim 6 \times 10^{12} \text{ cm}^{-3}$ , but above this density RF current apparently cannot be driven. In this section we want to show that these facts are in agreement with theory, including the occurrence of a density cutoff which, we suggest, corresponds to the presumably unstable situation where the RF current profile has a sharp maximum at the very edge of the plasma.

First, we relate the wave electric field, which is parallel to  $\vec{B}_0$ , to the amount of power transmitted to (but not necessarily absorbed by) the plasma  $P_t$ , by taking for the electric energy density (see Refs [9] and [10] for a LH wave review)  $\mathcal{E} = \epsilon_0 E_{\parallel}^2 \omega_p^2 / 2(\omega^2 - \omega_{LH}^2)$ . This implies that  $\omega^2$  be sufficiently in excess of  $\omega_{LH}^2 = \omega_{p_i}^2 / (1 + \omega_p^2 / \omega_e^2)$  to avoid linear mode conversion for any  $N_{\parallel}$  within the plasma and that, within the plasma,  $\vec{E}$  be essentially electrostatic. Then we have in  $\text{V} \cdot \text{cm}^{-1}$

$$\vec{E} \approx 2.1 \left( (1 - \omega_{LH}^2 / \omega^2) \right)^{1/2} P_t / V m \quad (22)$$

Here and hereafter  $P_t/V$  is in  $\text{MW} \cdot \text{m}^{-3}$ ,  $f$  is in GHz, and  $n$  is in  $10^{13} \text{ cm}^{-3}$ . Moreover,  $(\omega/\omega_{LH})^2 \approx 2.2 f^2 (n^{-1} + B^{-2})$ , with  $B$  in tesla. Notice, incidentally, that  $\vec{E}$  is much smaller than the nominal values of typical LH antennae. Considering,

for simplicity, only the case  $w_1^2 = 255.9/TN_{||}^2 \gg 1$  (here and hereafter  $T$  is in keV), the low field (or high density) value of the electric current in MA (see Eq. (11)) is

$$I_e \approx 7.6 \frac{TP_E}{ZmR} (1 - (\omega_{LH}/\omega)^2) w_1^5 e^{-w_1^2} \equiv d P_e / m \quad (23)$$

while the high field (or low density) value is (see Eq. (18))

$$I_h \approx 13.2 T m a^2 \Delta N_{||} w_1^3 e^{-w_1^2} \equiv b m \quad (24)$$

where  $a$  and  $R$ , the minor and the major plasma radii, are in metres. A convenient interpolation is  $I = d P_e n (n^2 + d P_e / b)^{-1}$  with  $I_{\max} = \frac{1}{2} (d b P_e)^{1/2}$  at  $n_*^2 = d P_e / b$  or

$$I_{\max} \approx 5.1 a T ((1 - \omega_{LH}^2 / \omega^2) P_e \Delta N_{||} / Z R)^{1/2} w_1^4 e^{-w_1^2} \quad (25)$$

$$n_* \approx 0.8 ((1 - \omega_{LH}^2 / \omega^2) P_e / N Z \Delta N_{||})^{1/2} w_1 \quad (26)$$

Moreover

$$(\partial I / \partial P)_{\max} = \frac{1}{4} (d b / P)_{\max}^{1/2} = (I / 2 P_e)_{\max} \quad (27)$$

and

$$E_* \approx 2.2 (\Delta N_{||} Z \ell m)^{1/2} / w_1$$

while the absorbed power density when  $n = n_*$  is

$$P_a^* \approx 0.16 P_e w_1 e^{-w_1^2} \quad (28)$$

Now our suggestion is that in view of Eq. (20) RF current drive is efficient only as long as  $n_* > n(a)$ . If  $n(0) \geq n_*$ ,  $I \cong I_{\max}$ , which is independent of  $n$  (see Eq. (25)) and is proportional to  $P_e$  (see Eq. (27)). If  $n(0) < n_*$  the current is weaker (see Eq. (24)) unless slideaway or runaway effects dominate.

For a quantitative comparison with the experiments, we have somehow to compensate for the fact that e-e collisions have been neglected. Following Ref. [2], we prescribe replacing  $Z$  by  $(Z+5)$ .

The parameters of Versator II tokamak are (see Fig. 2 in Ref. [6]):  $P/V \cong 0.3$ ;  $T \cong 0.2-0.35$ ;  $\Delta N_{||} \cong 3-9$ ;  $a = 0.13$ ;  $R = 0.4$ . The measured value  $I \cong 3 \times 10^{-3}$  is recovered from Eq. (25) for  $w_1^2 \leq 6$ . Then Eq. (26) gives  $n_* = 0.6$ . A confirmation of the assumption that the measured  $I$  value corresponds to  $I_{\max}$  is provided by the fact that Eq. (27) gives  $\partial I/\partial P \cong 1/20$  to  $1/25$ , in good agreement with the experimental value in a broad parameter range. Equally satisfying although less detailed is comparison with the available data from PLT [7] and other tokamaks [8].

Unfortunately, if our interpretation of the present experiments is correct, the prospects of LH wave current drive for reactor purposes look poor. This is due to the weak dependence of the critical density  $n_*$  upon the transmitted (and absorbed) power density as given by Eq. (26).

#### ACKNOWLEDGEMENTS

It is a pleasure to acknowledge a discussion with D. Pfirsch at an early stage of this work and comments by J.G. Cordey, D.F.H. Start and M. O'Brien.

#### REFERENCES

- [1] J.G. CORDEY, et al., Plasma Phys. **24** (1982) 73.
- [2] N.J. FISCH, A.H. BOOZER, Phys. Rev. Lett. **45** (1980) 720.
- [3] C.F.F. KARNEY, N.J. FISCH, Phys. Fluids **22** (1979) 1817.
- [4] N.J. FISCH, Phys. Rev. Lett. **41** (1978) 873.
- [5] E. CANOBBIO, R. CROCI, in Proc. 3rd Joint Varenna-Grenoble Int. Symp. on Heating in Toroidal Plasmas, Grenoble, 1982, Vol. 3, p. 835.
- [6] S.C. LUCKHARD, et al., Phys. Rev. Lett. **48** (1982) 152.
- [7] W. HOOKE, et al., Bull. Am. Phys. Soc. **26** (1981) 975.
- [8] T. YAMAMOTO, et al., Phys. Rev. Lett. **45** (1980) 716.
- [9] S.Y. YUEN, et al., Nucl. Fusion **20** (1980) 159.
- [10] D.A. EHST, et al., J. Fusion Energy **2** (1982) 83.



## RESISTIVE BALLOONING MODES IN THREE-DIMENSIONAL CONFIGURATIONS

D. CORREA-RESTREPO

Max-Planck-Institut für Plasmaphysik, Euratom-Association,  
Garching, Federal Republic of Germany

### Abstract

#### RESISTIVE BALLOONING MODES IN THREE-DIMENSIONAL CONFIGURATIONS.

Resistive ballooning modes in general three-dimensional geometries are studied on the basis of the equations of motion of resistive MHD. Assuming small resistivity and perturbations localized in the neighbourhood of a closed field line, a stability criterion is derived in the form of coupled system of two second-order ordinary differential equations. This criterion is rather general and contains several limiting cases, in particular, the ideal-ballooning-mode criterion and criteria for the stability of symmetric systems. Making use of multiple-length-scale expansion techniques, analytical results are obtained without imposing any of the usual restrictions, e.g. symmetric configurations, circular plasma cross-sections, large aspect ratio. In particular, a tearing-mode-like dispersion relation for each closed field line is derived. In case of instability, growth rates scaling as fractional powers of the resistivity are found.

### 1. INTRODUCTION

It is generally accepted that resistive ballooning modes are of crucial importance for the stability properties of high- $\beta$  magnetically confined plasmas. In particular, recent experiments in ISX-B have led to speculations that pressure-driven, high- $n$  modes are responsible for the observed deterioration of the energy confinement time.

Here, resistive ballooning modes in general three-dimensional configurations are studied on the basis of the equations of motion of resistive MHD. As in the ideal case [1], the introduction of localized perturbations makes it possible to reduce the calculations to the neighbourhood of any particular, closed field line. The two coordinates which define this field line then only enter the problem as parameters and the calculations are reduced to a one-dimensional problem along each closed field line. Even with the considerable simplification thus achieved, the stability criterion obtained is, in general, rather implicit since its evaluation requires the solution of a system of two coupled second-order ordinary differential equations on each closed field line. However, assuming small growth rates, it is possible

to obtain general, analytical results. In particular, the criterion contains several limiting cases, e.g. the ideal ballooning mode criterion [1] (and thus Mercier's criterion) and the condition  $D_R > 0$  [2] for instability with respect to resistive interchanges.

In Sect. 2. we introduce the model and derive the resistive ballooning mode equations. In Sect. 3. we study these equations on the assumption of small growth rates, making use of multiple-length-scale expansion techniques and derive a dispersion relation for the growth rate. In Sect. 4. we discuss this dispersion relation and in Sect. 5. we summarize the results.

## 2. DERIVATION OF THE RESISTIVE BALLOONING MODE EQUATIONS

We start with the following linearized equations of resistive MHD [3]:

$$\rho \gamma^2 \vec{\xi} = -\nabla(\tilde{p} + \delta \vec{B} \cdot \vec{B}) + (\vec{B} \cdot \nabla) \delta \vec{B} + (\delta \vec{B} \cdot \nabla) \vec{B} \quad (1)$$

$$\delta \vec{B} = \nabla \times \vec{\xi} \times \vec{B} + (\eta/\gamma) \Delta \delta \vec{B} \quad (2)$$

$$\tilde{p} = -\vec{\xi} \cdot \vec{\nabla} p - \gamma_H p \vec{v} \cdot \vec{\xi} \quad (3)$$

Here,  $\gamma$  is the growth rate and  $\gamma_H$  the ratio of the specific heats. All other symbols have their usual meaning.

On the basis of the lowest-order equilibrium (in an  $\eta$ -expansion), we introduce coordinates  $v, \theta, \phi = \zeta - q \theta$ , where  $v, \theta, \zeta$  are Hamada coordinates [4] and  $q_0 = M/N$  ( $M, N$  integers) is the safety factor of a reference rational surface  $v = v_0$  [1]. In these coordinates, the physical quantities satisfy the following periodicity conditions:

$$\phi(\theta, \phi) = \phi(\theta, \phi + 1) = \phi(\theta + 1, \phi - M/N) = \phi(\theta + N, \phi) \quad (4)$$

and are thus periodic in  $\theta$  with period  $N$ , and in  $\phi$  with period 1. The equilibrium magnetic field  $\vec{B}$  and the gradient along a field line can be expressed as

$$\vec{B} = \dot{\chi} [\nabla \phi \times \nabla v + (q - q_0) \nabla v \times \nabla \theta] \quad (5)$$

$$\vec{B} \cdot \nabla = \dot{\chi} [\partial_\theta + (q - q_0) \partial_\phi] \quad (6)$$

with  $q = \dot{\Psi}/\dot{\chi}$ .  $\Psi$  and  $\chi$  are the longitudinal and transverse magnetic fluxes respectively. Dots mean derivatives with respect to the volume.

As in the ideal case [1], we look for solutions of Eqs. (1) - (3) which are localized around a closed field line  $v = v_0$ ,  $\phi = \phi_0$ , and which have finite gradients along the field, i.e.  $B \cdot \nabla / \chi \sim 0(1)$ .

Setting

$$t = (v - v_0)/v_0 \epsilon^3, \quad x = (\phi - \phi_0)\epsilon^3 \quad (7)$$

with  $\epsilon \ll 1$ , we look for perturbations with  $\partial_t \sim \partial_x \sim 0(1)$ . Derivatives transverse to the field are thus large, being of the order  $\epsilon^{-3}$ . Furthermore, the perturbations are required either to vanish or to be negligible for  $|v - v_0| \geq v_0 \epsilon^2, |\phi - \phi_0| \geq \epsilon$ .

Taking into account Eq. (2) and the fact that  $\nabla \times \nabla \times \sim \epsilon^{-6}$ , we require  $\eta \sim 0(\epsilon^6)$  and set

$$\eta = \eta^* \epsilon^6 \equiv \eta^* / k_{\perp}^2 \quad (8)$$

$\epsilon$  is a dummy parameter and is treated here as a kind of tag indicating the magnitude of the term of which it is a factor.

We expand the equilibrium quantities in a Taylor series around the closed field line  $v = v_0, \phi = \phi_0$ :

$$A(v, \theta, \phi) = A(v_0, \theta, \phi_0) + \frac{\partial A}{\partial \phi}(v_0, \theta, \phi_0)(\phi - \phi_0) + 0(\epsilon^2) \quad (9)$$

set

$$\vec{\xi} = U \nabla \theta \times \nabla \phi + T \nabla v \times \nabla \theta + S \vec{B} \quad (10)$$

$$\delta \vec{B} = w \nabla \theta \times \nabla \phi + \tau \nabla v \times \nabla \theta + \mu \vec{B} \quad (11)$$

and expand the perturbations  $U, T$  etc. in a series of the form

$$U = U_0 + U_1 \epsilon + U_2 \epsilon^2 + U_3 \epsilon^3 + \dots \quad (12)$$

Taking into account the condition  $\nabla \cdot \delta \vec{B} = 0$  on the perturbed magnetic field, we obtain  $\partial_t W + v \partial_t \tau = 0$ , which implies  $W_0 = v \partial_x a, \tau_0 = -\partial_x a$ . Expanding Eqs. (1) to (3) in  $\epsilon$ , we obtain from the  $0(\epsilon^{-3}), 0(\epsilon^{-2})$  and  $0(\epsilon^{-1})$  equations  $(\tilde{p} + \delta \vec{B} \cdot \vec{B})_i = 0$  and  $\partial_t U_i + v \partial_t T_i = 0$ , with  $i = 0, 1, 2$ . We shall only need  $(\tilde{p} + \delta \vec{B} \cdot \vec{B})_0 = 0$  and  $\partial_t U_0 + v \partial_t T_0 = 0$ , i.e.  $U_0 = v \partial \phi, T_0 = -\partial \phi$ . We cross Eq. (1) twice with  $\vec{B}$  to obtain  $\xi_{\perp}$ , the component of  $\vec{\xi}$  perpendicular to  $\vec{B}$ . From the  $\nabla \theta \times \nabla \phi$  and  $\nabla v \times \nabla \theta$  components of the resulting  $0(1)$  equations we can eliminate  $(\tilde{p} + \delta \vec{B} \cdot \vec{B})_3$  and obtain

$$\rho\gamma^2 (\dot{\chi}^2/B^2) v_o^2 \Delta^* \Phi = 2 \left[ v_o \kappa_v \partial_x (\delta \vec{B} \cdot \vec{B})_o - \kappa_\phi \partial_t (\delta \vec{B} \cdot \vec{B})_o \right] + v_o^2 (\vec{B} \cdot \nabla) * (\dot{\chi}^2/B^2) \Delta^* a \quad (13)$$

with

$$\Delta^* = \frac{|\nabla v|^2}{v_o^2} \partial_{tt} + 2 \frac{\nabla v \cdot \nabla \phi}{v_o} \partial_{tx} + |\nabla \phi|^2 \partial_{xx} \quad (14)$$

$$(\vec{B} \cdot \nabla) * = \dot{\chi} \left[ \partial_\theta + v_o \dot{q} t \partial_x \right] \quad (15)$$

Here, the equilibrium quantities only depend on  $\theta$ , the variable along the localization line.  $\kappa_v$  and  $\kappa_\phi$  are covariant components of the curvature. Explicitly, they are

$$\kappa_v = \frac{1}{2\dot{p}} \left[ \frac{\dot{p}^2}{B^2} + \ddot{\Psi} I - \ddot{\chi} J - \dot{q} \dot{\chi}^2 \sigma + \dot{p} \vec{B} \cdot \nabla \left( \frac{\vec{B} \cdot \nabla \theta \times \nabla \phi}{B^2} \right) \right] \quad (16)$$

$$\kappa_\phi = -(\dot{\chi}/2\dot{p}) \vec{B} \cdot \nabla \sigma \quad (17)$$

where  $J$  and  $I$  are, respectively, the longitudinal and transverse components of the current and  $\sigma = \vec{j} \cdot \vec{B}/B^2$ .

Multiplying by either  $\nabla v$  or  $\nabla \phi$  and integrating the resulting equation, we obtain from the  $O(1)$  Eq. (2)

$$a - (\eta^*/\gamma) \Delta^* a = (B \cdot \nabla) * \Phi \quad (18)$$

Multiplying Eqs. (1) and (2) by  $\vec{B}$ , taking into account Eq. (3) and the condition  $(\dot{p} + \delta \vec{B} \cdot \vec{B})_o = 0$  and eliminating  $S_o$  yields

$$\begin{aligned} (\vec{B} \cdot \nabla) * & \left( \frac{1}{B^2} \left[ (\vec{B} \cdot \nabla) * (\delta \vec{B} \cdot \vec{B})_o - \dot{p} v_o \partial_x a \right] \right. \\ & - \rho\gamma^2 \frac{(\gamma_H \dot{p} + B^2)}{\gamma_H \dot{p} B^2} \left[ (\delta \vec{B} \cdot \vec{B})_o - \dot{p} v_o \partial_x \Phi \right] \\ & + \rho\eta^* \gamma \frac{1}{B^2} \Delta^* (\delta \vec{B} \cdot \vec{B})_o \\ & \left. - 2\rho\gamma^2 (v_o \kappa_v \partial_x \Phi - \kappa_\phi \partial_t \Phi) \right) = 0 \end{aligned} \quad (19)$$

To solve Eqs. (13), (18), (19), we make the ansatz [1]

$$\begin{aligned} \Phi(t, \theta, x) = f(\epsilon t, \epsilon^2 x) e^{i\alpha x} \cdot \sum_{m=-\infty}^{\infty} \exp \{2\pi i(m/N)\theta\} \\ \times \int_{-\infty}^{\infty} [\exp\{-i(2\pi(m/N) + \alpha \dot{q} v_o t)y\}] F(y) dy \end{aligned} \quad (20)$$

where  $f$ ,  $f_x$ ,  $f_t$  vary slowly with both  $t$  and  $x$  and are assumed either to vanish or to be negligible for  $|t| \geq \epsilon^{-1}$ ,  $|x| \geq \epsilon^{-2}$ .  $\alpha \sim O(1)$

is an arbitrary constant and  $F \in L_2$  in  $-\infty < y < \infty$ . (Representations of periodic functions through functions  $F \in L_2(-\infty, \infty)$  are treated in standard books on the theory of approximation of functions [5], [6], [7].) For  $a$  and  $(\delta \vec{B} \cdot \vec{B})_0$  we make a similar ansatz with  $\tilde{a}(y)$  and  $b(y) \in L_2(-\infty, \infty)$  respectively. Multiplying Eqs. (13), (18) and (19) by  $f^* \exp\{i\alpha(v_0 t \theta - x)\}$  ( $f^*$  is the complex conjugate of  $f$ ), integrating with respect to  $t$  between  $-\epsilon^{-1}$  and  $\epsilon^{-1}$  and with respect to  $x$  between  $-\epsilon^{-2}$  and  $\epsilon^{-2}$ , one obtains (to lowest order in  $\epsilon$ )

$$\rho \gamma^2 \frac{\dot{\chi}^2}{B^2} \vec{C}^2 F = - \frac{2i}{v_0 \alpha} (\kappa_v + \kappa_\phi \dot{q} y) b + \frac{d}{dy} \frac{\dot{\chi}^3}{B^2} \vec{C}^2 \tilde{a} \quad (21)$$

$$(1 + (\alpha^2 \eta^* / \gamma) \vec{C}^2) \tilde{a} = \dot{\chi} (dF/dy) \quad (22)$$

$$\begin{aligned} \frac{d}{dy} \frac{\dot{\chi}^2}{B^2} \left[ \frac{db}{dy} - \frac{i\alpha}{\dot{\chi}} v_0 \tilde{p} \tilde{a} \right] - \rho \gamma^2 \frac{(\gamma_{HP} + B^2)}{\gamma_{HP} B^2} (b - i\alpha v_0 \tilde{p} F) \\ - \frac{\alpha^2 \eta^*}{B^2} \gamma \rho \vec{C}^2 b - 2i\alpha v_0 \rho \gamma^2 (\kappa_v + \kappa_\phi \dot{q} y) F = 0 \end{aligned} \quad (23)$$

with

$$\vec{C} = \nabla \phi - \dot{q} y \nabla v \quad (24)$$

Solving for  $\tilde{a}$  from (22) and substituting in (21) and (23), multiplying (21) by  $i\alpha(pv_0/\dot{\chi}^2) \cdot (\alpha^2 \eta^* / \gamma)$ , subtracting this from (23) and setting

$$b = i\alpha p v_0 (F + D) \quad (25)$$

we finally obtain the following resistive ballooning mode equations (valid in any geometry and not restricted to symmetric configurations):

$$\begin{aligned} \frac{d}{dy} \left[ \frac{\vec{C}^2}{B^2 \left[ 1 + (\alpha^2 \eta^* / \gamma) \vec{C}^2 \right]} \frac{dF}{dy} \right] + \frac{2\dot{p}}{\dot{\chi}^4} (\kappa_v + \dot{q} y \kappa_\phi) F - \frac{\rho \gamma^2}{\dot{\chi}^2 B^2} \vec{C}^2 F \\ = - \frac{2\dot{p}}{\dot{\chi}^4} (\kappa_v + \dot{q} y \kappa_\phi) D \\ \frac{d}{dy} \left[ \frac{1}{B^2} \frac{dD}{dy} \right] - \frac{\rho \gamma^2}{\dot{\chi}^2} \frac{(\gamma_{HP} + B^2)}{\gamma_{HP} B^2} D \\ - \frac{\rho \alpha^2}{\dot{\chi}^2 B^2} \eta^* \gamma \vec{C}^2 D - \frac{2\dot{p}}{\dot{\chi}^4} \frac{\alpha^2 \eta^*}{\gamma} [\kappa_v + \dot{q} y \kappa_\phi] D \\ = \frac{2\rho}{\dot{p} \dot{\chi}^2} \left( \frac{\dot{p}^2 \alpha^2 \eta^*}{\dot{\chi}^2 \gamma \rho} + \gamma^2 \right) \cdot (\kappa_v + \dot{q} y \kappa_\phi) F \end{aligned} \quad (27)$$

The stability criterion is thus as follows: the system is unstable with respect to resistive ballooning modes if there are solutions  $F, D \in L_2(-\infty, \infty)$  with  $\text{Re } \gamma > 0$ , with  $\text{Re } \gamma$  the real part of the growth rate.

### 3. ANALYSIS OF THE RESISTIVE BALLOONING MODE EQUATIONS

#### 3.1. $\eta^*/\gamma = \gamma = 0$ (ideal marginal stability)

If we set  $\eta^*/\gamma = \gamma = 0$ , we obtain the ideal marginally stable case. This has been treated elsewhere [1,8,9,10,11]. Here we assume that the equilibrium is stable in the ideal case. By taking resistivity into account we then introduce the possibility of new instabilities, as in [2,12,13,14].

#### 3.2. $\gamma_H = 0$

If we assume that the perturbed pressure (Eq.(3)) is determined by convection alone and neglect the effect of the compressibility term by setting  $\gamma_H = 0$ , (26) and (27) then reduce to  $D=0$  and

$$\frac{d}{dy} \left[ \frac{1}{B^2} \frac{\tilde{C}^2}{(1+(\alpha^2 \eta^*/\gamma) \tilde{C}^2)} \frac{dF}{dy} \right] + \frac{2\dot{p}}{\tilde{\chi}^4} (\kappa_v + \dot{q}y\kappa_\phi) F - \frac{\rho\gamma^2}{\tilde{\chi}^2 B^2} \tilde{C}^2 F = 0 \quad (28)$$

In axisymmetric systems, (28) is essentially the same equation as was derived in [15], but contrary to [15], we do not find in this case instabilities with growth rates proportional to the resistivity. The results obtained there are due to the fact that the dependence of the integrals in (20), (21) of [15] on both  $\gamma$  and  $\eta$  was ignored. In order to solve (28), we assume that the growth rate  $\gamma$  is real and small (in all the following cases we assume  $\gamma$  to be real, this being consistent with the solutions found) and make use of the two variable expansion procedures described in [16].

Introducing  $\delta \ll 1$  as a dummy parameter indicating the magnitude of the term of which it is a factor, we set  $\rho\kappa_v \sim \rho\kappa_\phi \sim \gamma^{3/2} \sim \delta^3$  (the consistency of the scaling is verified by the results) and take  $y$  and  $z = \delta^{1/2}y$  as the two different length scales. We then make the ansatz

$$F(y) = F_0(y, z) + \delta^{1/2} F_1(y, z) + \delta F_2(y, z) + \dots \quad (29)$$

$$F_i(y + N, z) = F_i(y, z), \quad (30)$$

$$i = 0, 1, 2, \dots$$

$$\frac{dF}{dy} = \frac{\partial F}{\partial y} + \delta^{1/2} \frac{\partial F}{\partial z} \quad (31)$$

and solve (28) order by order.

From the lowest-order equation we obtain  $F_0 = F_0(z)$ . Thus  $F_0$  does not depend explicitly on  $y$ . From the next two orders we obtain  $F_1(y, z)$  and a solubility condition for  $F_2$  in the form of a second-order differential equation for  $F_0$ , the condition for solutions  $F_0 \in L_2(-\infty, \infty)$  being

$$2p \langle \kappa_v \rangle + q \chi^2 \left( \langle \sigma \rangle - \frac{\langle \sigma B^2 \rangle}{\langle B^2 \rangle} \right) > 0 \quad (32)$$

(the brackets denote mean values on the localization line), which is the same as the condition  $D_R > 0$  of [2] for configurations with small  $p$ . Solving this equation leads to an infinite sequence of modes with growth rates scaling as  $\eta^{*1/3}$ :

$$\gamma_n^3 = \frac{\alpha^2 \eta^*}{\rho \chi^2 \langle |\nabla v|^2 / B^2 \rangle} \left[ \langle \sigma^2 B^2 \rangle - \frac{\langle \sigma B^2 \rangle^2}{\langle B^2 \rangle} + \frac{\langle B^2 \rangle}{q^2 \chi^4 (1 + 2n)^2} \left\{ 2p \langle \kappa_v \rangle + q \chi^2 \left\{ \langle \sigma \rangle - \frac{\langle \sigma B^2 \rangle}{\langle B^2 \rangle} \right\} \right\}^2 \right] \quad (33)$$

$$3.3. \quad \gamma_H \neq 0, \quad \eta^*/\gamma \sim \gamma^2 \sim \delta \ll 1$$

Here, contrary to the preceding case, we set  $\gamma_H \neq 0$  and take the effect of the compressibility term in Eq. (3) into account. We also drop the requirement of small driving term made in 3.2 and assume that resistivity and inertia are small and equally important. If we define

$$Q_0^3 = \frac{q \chi^2 \langle B^2 \rangle \alpha^2 \eta^*}{\rho \langle B^2 / |\nabla v|^2 \rangle M}$$

$$M = \langle B^2 / |\nabla v|^2 \rangle \cdot \left[ \langle |\nabla v|^2 / B^2 \rangle + \frac{1}{\beta^2} \left\{ \langle \sigma^2 B^2 \rangle - \frac{\langle \sigma B^2 \rangle^2}{\langle B^2 \rangle} \right\} \right]$$

$$Q = \gamma / Q_0, \quad Y_0^2 = \frac{\langle B^2 / |\nabla v|^2 \rangle}{q^2 \langle B^2 \rangle} \frac{Q_0}{\alpha^2 \eta^*} \quad (34)$$

then the conditions of small  $\eta^*/\gamma$  and  $\gamma$  can be expressed as

$$1/y_0^2 Q \ll 1, \quad Q/y_0 \ll 1 \quad (35)$$

We now go back to (26), (27). Since  $\vec{c}^2 = |\nabla\phi|^2 - 2qy\nabla v \cdot \nabla\phi + \dot{q}^2 y^2 |\nabla v|^2$ , it is clear that resistivity and inertia only play a role for large  $|y| \sim \delta^{-1/2}$ . There are thus different regions. When  $|y| \ll \delta^{1/2}$ , resistivity and inertia may be neglected and (26), (27) become the same equations as in the ideal marginal case, with asymptotic solutions  $D = 0$  and

$$F = a_1 |y|^s + a_2 |y|^{-1-s}, \quad |y| \rightarrow \infty, \quad \text{where } s = -\frac{1}{2} \\ + \left[ \frac{1}{4} + H^2 - H - D_R \right]^{1/2} \quad (36)$$

and  $H$  and  $D_R$  are defined as in [2].

In the outer region ( $|y| \geq \delta^{-1/2}$ ), resistivity and inertia must be taken into account. In order to study this region, we make use of the two-length-scale expansion techniques employed before and make an ansatz similar to (29) - (31) for the functions  $F$  and  $D$ . From the two lowest-order equations in the  $\delta^{1/2}$  expansion one then obtains  $F_0 = F_0(z)$ ,  $D_0 = D_0(z)$ , and explicit expressions for  $F_1$  and  $D_1$ . To next order, we obtain a solubility condition for  $F_2$  and  $D_2$  in the form of a coupled system of two second-order ordinary differential equations for  $F_0$  and  $D_0$ :

$$\frac{d}{dx} \left( \frac{x^2}{1+x^2} \frac{dF_0}{dx} \right) + \frac{H(1-H)}{(1+x^2)^2} F_0 - \frac{H(1+H)x^2}{(1+x^2)^2} F_0 \\ + D_R F_0 - Q^3 x^2 F_0 = -H \frac{d}{dx} \left( \frac{x}{1+x^2} D_0 \right) + \frac{H^2}{1+x^2} D_0 - D_R D_0 \\ \frac{d^2 D_0}{dx^2} + \left[ \frac{H^2}{1+x^2} - KQ^3 \left( F^* + \frac{x^2}{1+x^2} H^2 \right) - Q^3 x^2 - GQ^3 - D_R \right] D_0 \\ = (1 + KQ^3) \left[ D_R F_0 - \frac{H^2}{1+x^2} F_0 - H \frac{x}{1+x^2} \frac{dF_0}{dx} \right] \quad (38)$$

Here,  $x^2 \equiv (1/y_0^2 Q) y^2$  and  $G$ ,  $K$  and  $F^*$  are the same as the  $G$ ,  $K$  and  $F$  of [2].

We now consider, for simplicity, the case of large  $G$  (the conclusions drawn in this case are more pessimistic than those obtained with  $G \sim O(1)$ .) It then follows from (38), that  $D_0 = 0$  and one is left with an equation for  $F_0$  alone, with the solution

$$F_0 = |x|^s \exp\{(1+s-H)x^2/2\} \cdot \frac{d}{dx^2} \left\{ \exp\left[\frac{(H-1-s-Q^{3/2})x^2}{2}\right] P(r) \right\} \quad (39)$$

$$P(r \equiv Q^{3/2} x^2) = \frac{\pi}{\sin \pi \nu} \left[ \frac{{}_1F_1(a^*; \nu; r)}{\Gamma(1+a^*-\nu)\Gamma(\nu)} - r^{1-\nu} \frac{{}_1F_1(1+a^*-\nu; 2-\nu; r)}{\Gamma(a^*)\Gamma(2-\nu)} \right]$$

Here,  $\Gamma$  is the gamma function,  $\nu = 1/2 + s$ ,  
 $a^* = (1/4) \cdot (Q^{3/2} + 2\nu - D_R/Q^{3/2})$  and  ${}_1F_1(a^*; \nu; r)$  is Kummer's  
 function  ${}_1F_1(a^*; \nu; r) = 1 + \frac{a^*}{\nu} r + \frac{a^*(a^*+1)}{\nu(\nu+1)2!} r^2 + \dots$

In order to construct a solution valid in the ideal and resistive regions, we must match the ideal solution for  $|y| \rightarrow \infty$ , (36) to the resistive solution, (39) for  $|x| \rightarrow 0$  [16], [17]. If we set  $\Delta' \equiv a_2/a_1$  (with  $a_1, a_2$  from (36)) and

$$\Delta \equiv \frac{4y_0^{1+2s} Q^{(5-2s)/4}}{\{Q^3 - (1+s-H)^2\}} \frac{\Gamma[1/2 + s]}{\Gamma[-1/2 - s]} \cdot \frac{\Gamma[(1/4) \cdot (Q^{3/2} + 3 - 2s - D_R/Q^{3/2})]}{\Gamma[(1/4) \cdot (Q^{3/2} + 1 + 2s - D_R/Q^{3/2})]} \quad (40)$$

then the condition for matching the resistive to the ideal solution is  $\Delta = \Delta'$ . (In order to be able to carry through the matching for both positive and negative  $y$  values, the quantity  $\Delta'$  must be constructed from the solution in the ideal region in such a way that it is the same for  $y \rightarrow +\infty$  and  $y \rightarrow -\infty$ .)

#### 4. DISCUSSION OF THE DISPERSION RELATION

When studying the dispersion relation  $\Delta = \Delta'$ , it is necessary to keep in mind the restrictions imposed by the assumptions of small resistivity and growth rate, (35). We now consider different cases, according to the sign of the driving term  $D_R$ .

##### 4.1. $D_R > 0$

When  $D_R$  is positive, the gamma functions in (40) have an infinite sequence of poles owing to the term  $(-D_R)/Q^{3/2}$ .  $\Delta$  alternately vanishes and diverges, passing through all values. For a given  $\Delta'$ , there are infinitely many  $Q$ 's which satisfy  $\Delta = \Delta'$ .

Since  $y_0$  scales as  $(\eta^*)^{-1/3}$ , the factor  $y_0^{1+2s}$  is large. Thus, the roots of  $\Delta = \Delta'$  will be near the poles of the gamma function in the denominator of (40), i.e.  $Q_n^{3/2} \approx -(1/2 + s + 2n) + \{(1/2 + s + 2n)^2 + D_R\}^{1/2}$ . Since  $\gamma \sim (\eta^*)^{1/3Q}$ , the actual growth rate  $\gamma$  scales as  $(\eta^*)^{1/3}$ .

#### 4.2. $D_R = 0$

In this case the term  $D_R/4Q^{3/2}$  no longer appears in the argument of the gamma functions and  $\Gamma(a^*)$  has no poles. As can be derived from (39), it is required that  $s < 1/2$  (for  $s > 1/2$ , the function  $F_0$  does not have the correct form for matching to the ideal solutions, since  $x^{1-2s} \gg x^0$  for  $x \rightarrow 0$ , and no unstable solution can be constructed unless  $a_1 = 0$ , i.e.  $|\Delta'| \rightarrow \infty$ .)

Taking into account that  $-1/2 < s < 1/2$ , we can derive the following properties of  $\Delta$ : when  $0 \leq Q^3 \leq (1+s-H)^2$ ,  $\Delta$  is positive and takes all values between 0 and  $+\infty$ . There is therefore always an instability when  $\Delta' > 0$  since in this case  $\Delta = \Delta'$  can always be satisfied (for small  $Q$ ,  $\Delta$  vanishes as  $Q^{(5-2s)/4}$ ,  $Q$  is then proportional to  $y_0^{(4+8s)/(2s-5)}$ , which is consistent with condition (35),  $1/y_0^2 \ll Q$ . Then, for small  $Q$ , the actual growth rate scales as  $\gamma \sim (\eta^*)^{(3+2s)/(5-2s)}$ . When  $(1+s-H)^2 \leq Q^3 \leq \infty$ ,  $\Delta$  takes all values between  $-\infty$  and 0, vanishing as  $1/Q^{1+2s}$  for large  $Q$ . Taking into account that the results must be consistent with the condition  $Q \ll y_0$ , there is an instability only if  $\Delta' \rightarrow -\infty$ . (This is the ideal marginal limit. After careful examination it can be seen that this corresponds to subsequently making  $\eta^*/\gamma$  and  $\gamma$  small.)

#### 4.3. $D_R < 0$

This is the most interesting case since  $D_R < 0$  stabilizes positive  $\Delta'$ -values which are not too large. First we observe, as in the case  $D_R = 0$ , that there are no instabilities if  $s > 1/2$ , i.e., unless  $|\Delta'| \rightarrow \infty$ , we can construct an unstable solution only if the condition  $(1/2 - H)^2 - D_R < 1$  is satisfied.

For  $Q^3 \geq (1+s-H)^2$  we have the same situation as in the case  $D_R = 0$ , i.e. there are instabilities only when  $\Delta' \rightarrow -\infty$  (ideal case). As for  $D_R = 0$ ,  $\Delta$  is also positive for  $Q^3 \leq (1+s-H)^2$ . The crucial difference arises for  $Q \rightarrow 0$ : when  $Q$  becomes small, the terms  $-D_R/4Q^{3/2}$  in (40) become large and  $\Delta \sim (y_0^2 Q)^{1/2} + s$ . When  $\Delta'$  is positive, the resulting growth rates are so small that they are not consistent with the assumption (35) ( $1/y_0^2 \ll Q$ ) unless  $\Delta'$  is large. We can estimate how large  $\Delta'$  must be in order that the condition  $Q y_0^2 \gg 1$  be satisfied: when  $Q$  decreases, the term  $|D_R|/4Q^{3/2}$  changes the behaviour  $\Delta \sim Q^{(5-2s)/4}$  to  $\Delta \sim Q^{1/2} + s$ .

Defining  $Q_c$  as the transition point at which this change of behaviour in  $\Delta(Q)$  occurs, we obtain

$$\Delta_c = \Delta(Q_c). \quad (41)$$

If  $\Delta > \Delta_c$ , the consistency condition  $Qy_0^2 \gg 1$  is satisfied. Thus, in the range  $0 \leq Q^3 \leq (1+s-H)^2$  there is an instability only if  $\Delta' > \Delta_c$ . The exact value of  $Q_c$  is somewhat arbitrary. However,  $|D_R|/Q^{3/2} \approx 1$  seems to be a good approximation, since the behaviour of

$$\frac{\Gamma[(1/4) \cdot (Q^{3/2} + 3 - 2s + |D_R|/Q^{3/2})]}{\Gamma[(1/4) \cdot (Q^{3/2} + 1 + 2s + |D_R|/Q^{3/2})]}$$

is already well represented by  $(|D_R|/Q^{3/2})^{1/2-s}$  for values of  $|D_R|/4Q^{3/2}$  moderately larger than 1.

## 5. CONCLUSION

Localized resistive ballooning modes in general geometries have been studied on the basis of the linearized equations of motion of resistive MHD and a stability criterion has been derived in the form of a coupled system of two second-order ordinary differential equations (Eqs. (26), (27)).

Neglecting compressibility and assuming small growth rates (Sect. 3.2.), we obtain instability only when the condition (32) is satisfied, the growth rates scaling as  $\gamma \sim (\eta^*)^{1/3} = (k_{\perp}^2 \eta)^{1/3}$ . This contradicts the statement made in [15], according to which, under the same circumstances, an axisymmetric system is always unstable with growth rates proportional to  $\eta^*$ .

In Sect. 3.3., (26), (27) have been considerably simplified by assuming small resistivity and inertia (condition (35)). Making use of two-length-scale expansion techniques, one obtains the averaged equations (37), (38). Neglecting the effect of compressibility in these equations (i.e. assuming  $G \gg 1$ ) decouples them. This leaves only one non-trivial equation which can be solved exactly. Satisfying the boundary conditions for this equation leads to a tearing-mode-like [2] dispersion relation for each closed field line

$$\Delta' = \Delta(Q, \eta^* \equiv k_{\perp}^2 \eta, H, D_R)$$

$\Delta'$  being determined from the asymptotic behaviour for large values of the independent variable of the solution of the ideal, marginal-ballooning-mode equation. As in [2], there are always instabilities for  $D_R > 0$ . For  $D_R = 0$  and  $\Delta'$  finite there are no instabilities if  $1/2 + s > 1$ . If  $1/2 + s < 1$  and  $D_R = 0$ , there are

instabilities if either  $\Delta' > 0$  or if  $\Delta' \rightarrow -\infty$ , the case  $\Delta' \rightarrow -\infty$  corresponding to an ideally unstable configuration. For  $D_R < 0$  there are no instabilities if  $1/2 + s > 1$ , unless  $|\Delta'| \rightarrow \infty$ . For  $D_R < 0$ ,  $1/2 + s < 1$  and  $\Delta' > 0$ , there are instabilities only if  $\Delta' > \Delta_c$  ( $\Delta_c$  given by (41)). For  $\Delta' < 0$  there are only instabilities if  $\Delta' \rightarrow -\infty$ , i.e. the system is ideally unstable.

## ACKNOWLEDGEMENT

The author would like to thank J. Nührenberg for many useful discussions.

## REFERENCES

- [1] CORREA-RESTREPO, D., Z. Naturforschung 33a 7 (1978) 789.
- [2] GLASSER, A.H., GREENE, J.M., JOHNSON, J.L., Phys. Fluids 18 7 (1975) 875.
- [3] JOHNSON, J.L., GREENE, J.M., Plasma Phys. 9 5 (1967) 611.
- [4] HAMADA, B., Nucl. Fusion 2 1 (1962) 23.
- [5] TIMAN, A.F., Theory of Approximation of Functions of a Real Variable, Pergamon Press, London 1963.
- [6] LACHIESER, N., Vorlesungen über Approximationstheorie, Akademie-Verlag, Berlin 1967.
- [7] BUTZER, P.L., NESSEL, R.J., Fourier-Analysis and Approximation, Vol. I, Birkhäuser Verlag, Basel 1971.
- [8] CONNOR, J.W., HASTIE, R.J., TAYLOR, J.B., Phys. Rev. Lett. 40 6 (1978) 396.
- [9] DOBROTT, D., NELSON, D.B., GREENE, J.M., GLASSER, A.H., CHANCE, M.S., FRIEMAN, E.A., Phys. Rev. Lett. 39 15 (1977) 943.
- [10] LORTZ, D., NÜHRENBURG, J., Nucl. Fusion 19 9 (1979) 1202.
- [11] LORTZ, D., NÜHRENBURG, J., Sherwood Meeting, Austin, Texas, 1981.
- [12] FURTH, H.P., KILLEEN, J., ROSENBLUTH, M.N., Phys. Fluids 6 4 (1963) 459.
- [13] COPPI, B., GREENE, J.M., JOHNSON, J.L., Nucl. Fusion 6 2 (1966) 101.
- [14] CHANCE, M.S., DEWAR, R.L., FRIEMAN, E.A., GLASSER, A.H., GREENE, J.M., GRIMM, R.C., JARDIN, S.C., JOHNSON, J.L., MANICKAM, J., OKABAYASHI, M., TODD, A.M.M., in Plasma Physics and Controlled Nuclear Fusion Research (Proc. 7th Int. Conf. Innsbruck, 1978) Vol. 1, IAEA, Vienna (1979) 677.
- [15] BATEMAN, G., NELSON, D.B., Phys. Rev. Lett. 41 26 (1978) 1804.
- [16] COLE, J.D., Perturbation Methods in Applied Mathematics, Blaisdell Publishing Company, Waltham, Mass., 1968.
- [17] MURRAY, J.D., Asymptotic Analysis, Clarendon Press, Oxford 1974.

## FILAMENTARY STRUCTURES IN TOKAMAKS AND THEIR IMPORTANCE TO ANOMALOUS ELECTRON ENERGY LOSS

M.G. HAINES, F. MARSH\*  
The Blackett Laboratory,  
Imperial College of Science and Technology,  
London,  
United Kingdom

### Abstract

#### FILAMENTARY STRUCTURES IN TOKAMAKS AND THEIR IMPORTANCE TO ANOMALOUS ELECTRON ENERGY LOSS.

This theoretical paper speculates on the possible existence of fine-scale filamentary structures in magnetically confined plasmas. These structures would be the result of non-linear development of the electrothermal instability and are predicted to occur with a wavelength of a few ion Larmor radii. The linear growth rate is essentially of the order of the heating or cooling rates (e.g. Ohmic heating equipartition, radiation loss rates) and is small compared to MHD instability growth rates. However, the structures could be generated early on in the time history of the discharge, and be steadily maintained by the current as quasi-stationary filaments. A non-linear time-dependent model shows the creation from random noise of narrow current filaments in which the electron temperature is increased locally by a factor of 10 or more with a corresponding drop in density. Saturation of the thermal instability occurs following the triggering of ion-acoustic turbulence in the filament because the local electron drift velocity exceeds the sound speed locally. There is enhanced electron resistivity in the filament, but the high-energy ion tail (produced by direct heating of the ions by the ion-acoustic turbulence and necessary to achieve its saturation) is distributed over a larger volume because of the large Larmor excursions of these hot ions. This increases the amount of direct heating of the ions so as to maintain a fraction  $(m_e/m_i)^{1/4}$  of the ions in the filamentary region at approximately the local electron temperature. The resulting energy balance indicates that a significant fraction of the Ohmic heating goes directly into the ion species, the hot ions mainly losing their energy classically to the colder bulk ions. This might remove the need to postulate an anomalous electron thermal conduction. Ion neo-classical thermal conduction (and radiation loss) would then remove the energy from the plasma.

### 1. INTRODUCTION

The linear theory of the electrothermal instability has been studied for a strongly magnetised plasma ( $\Omega_e \tau_e \gg 1$ ) by Tomimura and Haines [1] for a plasma in which the current is essentially parallel to the magnetic field (as in a tokamak) and

\* Supported by Culham Laboratory, Abingdon, Oxon., UK.

for a wave vector orthogonal to the current and magnetic field. This and the earlier theory of Haines [2] are distinguished from other theories [3] in having the electron and ion species decoupled and ion motion included. For  $\vec{k} \perp \vec{B}$  it results in a comparatively short wavelength  $\approx a_e (m_i/m_e)^{1/2}$  of the fastest growing mode, determined by the damping of shorter wavelengths by the comparatively small transverse electron thermal conduction and of longer wavelengths by Faraday's law. Growth for the  $k_{\perp}$  mode occurs provided  $\beta$  is less than 1 and provided that  $T_e/T_i$  is greater than 1.32 for an equilibrium in which Ohmic heating of electrons is balanced solely by equipartition to the ions. The critical threshold of  $T_e/T_i$  for onset of the instability is reduced if other losses such as radiation are included, and indeed the growth rate is enhanced. The inclusion of ion motion in the theory reduces the threshold  $T_e/T_i$  from 1.5 due to the higher-temperature regions expanding through  $v_p$ , though this expansion across the field lines leads to induction of current and a  $\vec{J} \times \vec{B}$  force which slows down the expansion.

## 2. STEADY-STATE FILAMENTARY MODEL

In a recent paper Haines and Marsh [4] have shown that the non-linear steady state of the electrothermal instability consists of sharply peaked filamentary structures for electron temperature and current density, with corresponding sharp minima for density so that the pressure profile is smooth. In the current peaks the condition for the onset of ion-acoustic instability can easily be satisfied, and also runaway conditions can occur, but were not included in the model itself. This theory showed that a steady state was possible only if the applied electric field was below the critical value  $E_c$  given by

$$E_c = \frac{0.278 \text{ ep}}{(m_i k)^{1/2} \alpha T_i^2}$$

where the electrical conductivity is  $\sigma = \alpha T_e^{3/2}$  and the total pressure is  $p$ . Inclusion of bremsstrahlung could raise  $E_c$  by up to a factor of 2.2. For an electric field  $E < E_c$  there are two possible steady states, one homogeneous and the other filamentary. The possibility of a filamentary steady state was shown by Tomimura and Haines [5], when it was also shown that momentum and energy equilibria lead to an incompatibility between the ideal wall boundary conditions  $n, T_e, T_i \rightarrow 0$  and those dictated by the equations. For this reason the work to be reported here only considers a periodic spatial region containing one filament, which is justified since this region is

much smaller than the total plasma radius for the plasmas under consideration. The actual amplitude of the spatial oscillations of electron temperature could not be determined from the steady-state theory, which only gave a maximum possible amplitude for a given applied electric field. Therefore it was considered appropriate to consider the time-dependent initial value problem.

### 3. TIME-DEPENDENT 1-D SIMULATION

The linear dispersion equation [1,6] is a quintic in the growth rate, and in order to get rid of the fast time scales in the simulation, yet retain the essential physics, the inertial term was removed in the momentum equation. A one-dimensional simulation with the unperturbed current  $j_z$  driven by  $E_z$  in a magnetic field  $B_z$  was considered in slab geometry. In order that periodic boundary conditions could be applied, the magnetic field component  $B_y$  was ignored. This is a valid approximation if the total periodic mesh does not exceed the wavelength of the fastest growing mode found in the more complete linear dispersion theory. The model equations employed are:

$$\text{Faraday's law:} \quad \frac{\partial E_y}{\partial x} = -\frac{1}{c} \frac{\partial B_z}{\partial t} \quad (1)$$

$$\text{Ampère's law:} \quad \frac{\partial B_z}{\partial x} = -\frac{4\pi}{c} j_y \quad (2)$$

$$\text{Pressure balance:} \quad \frac{\partial p}{\partial x} = \frac{j_y B_z}{c} \quad (3)$$

$$\text{Ohm's law:} \quad E_y - \frac{v_x B_z}{c} = \frac{j_y}{\sigma} \quad \text{and} \quad E_z = \frac{j_z}{\sigma} \quad (4)$$

$$\begin{aligned} \text{Electron energy:} \quad & \frac{3}{2} nk \frac{\partial T_e}{\partial t} + \frac{3}{2} nk v_x \frac{\partial T_e}{\partial x} + nk T_e \frac{\partial v_x}{\partial x} \\ & = \frac{\partial}{\partial x} \left[ \frac{\kappa}{1 + \omega_e^2 \tau_e^2} \frac{\partial T}{\partial x} \right] + \frac{j^2}{\sigma} \\ & - \frac{3n^2 e^2 k}{m_i \sigma} (T_e - T_i) - \beta_r n^2 T_e^{\frac{1}{2}} \end{aligned} \quad (5)$$

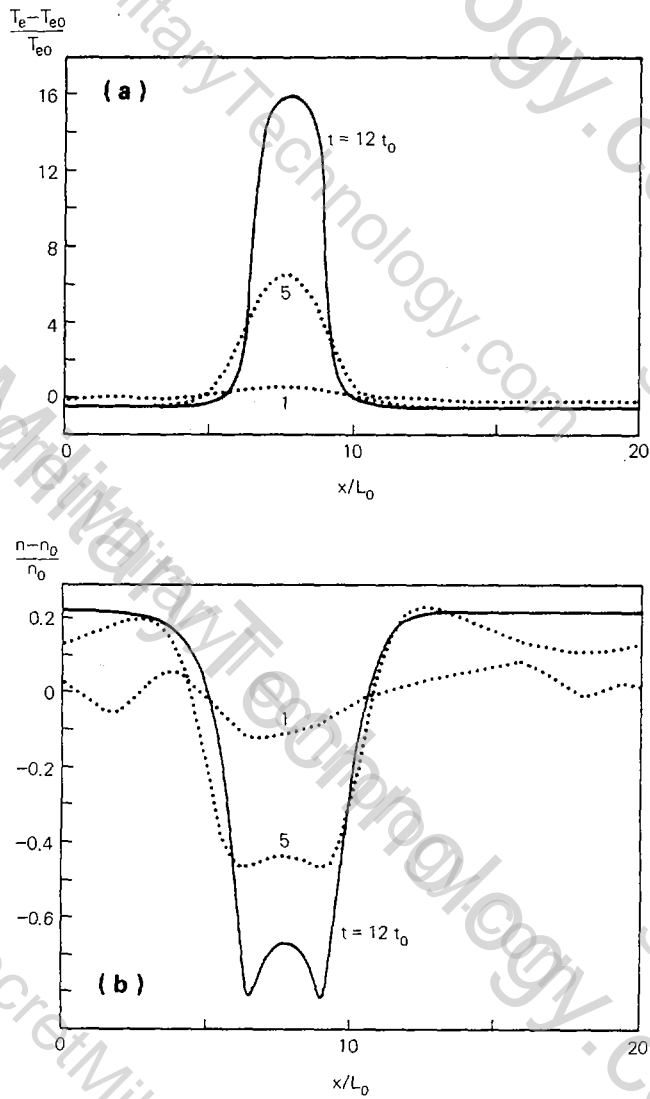


FIG.1. Electron temperature profiles (a) and number density profiles (b) at times  $t = t_0$ ,  $5 t_0$  and  $12 t_0$  for a spatial period of  $20 L_0 = 14 a_i$ .

Continuity:

$$\frac{\partial n}{\partial t} + n \frac{\partial v_x}{\partial x} + v_x \frac{\partial n}{\partial x} = 0 \quad (6)$$

These were written in dimensionless form and solved, using the appropriate length scale  $L_0$  and time scale  $t_0$  for electrothermal instabilities given in terms of initial parameters by

$$L_0 = a_{e0} \left( \frac{m_i}{m_e} \right)^{\frac{1}{2}} = \left( \frac{kT_{e0}}{m_i} \right)^{\frac{1}{2}} \frac{m_i c}{eB_{z0}} \quad (7)$$

$$t_0 = \frac{m_i \sigma_0}{n_0 e^2} \quad (8)$$

A second-order Crank-Nicholson scheme was employed to integrate these non-linear coupled partial differential equations. A small random perturbation was used to start the programme from an initial steady state. Always the longest wavelength mode permitted dominated the solution after a few time-steps.

If the overall boundary condition is constant applied electric field, a self-similar solution for  $T_e$  and  $j_z$ , increasing indefinitely in time, dominates. Clearly a more reasonable boundary condition is constant total current, because the externally applied voltage always adjusts in a tokamak so as to reduce current change. The initial steady state in dimensionless units is completely specified by giving the initial values of  $T_i/T_{e0}$ ,  $\beta_e = 8\pi n_0 kT_{e0}/B_{z0}^2$  and  $\omega_e \tau_e$ , the Hall parameter. If bremsstrahlung is included the initial temperature must be given. For  $T_i/T_{e0} = 0.5$ ,  $\beta_e = 4.338 \times 10^{-3}$  and  $(\omega_e \tau_e)_0 = 6.14 \times 10^6$ , a case was run for slab width of  $20 L_0$  corresponding to the linear fastest-growing mode. The temperature and density profiles for  $t/t_0 = 1, 5$  and  $12$  are shown in Fig. 1(a) and (b). At  $t = t_0$  the profiles are determined by the initial random perturbation but by  $2t_0$  the longest-wavelength mode dominates. However, no steady state is achieved, the electric field continuously drops at later times, and the profiles steepen until the electron fluid approximation  $a_e d(\ln T_e)/dx \ll 1$  breaks down. Before this occurs the conditions for onset of ion acoustic instabilities occur in the temperature peaks. If a slab width of  $7 L_0$  or smaller is employed, a steady state is reached, with  $\partial E_z/\partial t \rightarrow 0$  and the temperature profile is sharply peaked (less so the smaller the slab width) and agrees with the steady-state model [4].

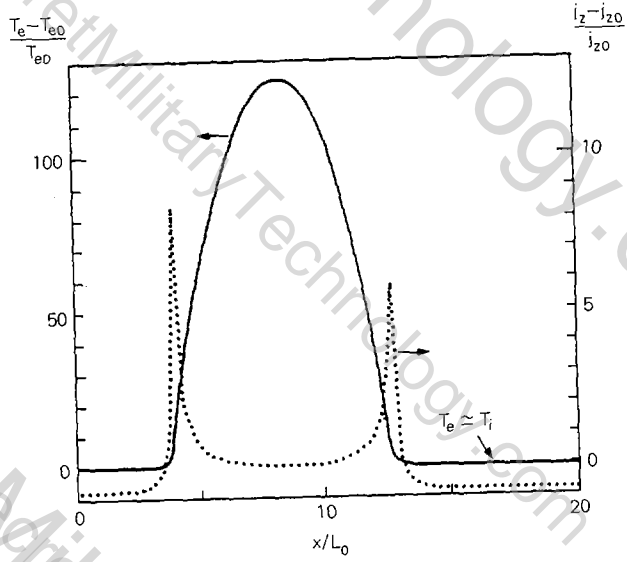


FIG.2. Steady-state electron temperature profile and current density profile with ion-acoustic turbulence included.

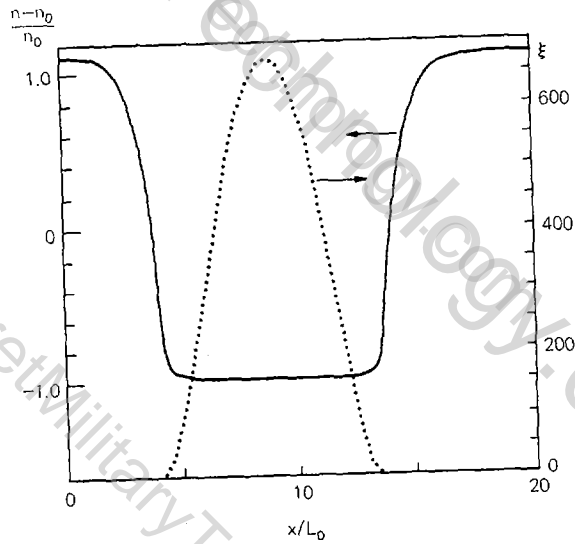


FIG.3. Steady-state density profile and the anomaly factor profile representing the effect of ion-acoustic turbulence.

## 4. INCLUSION OF ION-ACOUSTIC TURBULENCE

When the electron drift velocity  $v_d$  exceeds the local ion-sound speed, the plasma becomes electrostatically unstable to the ion-sound instability. Within about 100 ion plasma periods saturation is reached, and the plasma will possess an anomalous collision frequency  $\nu_{\text{eff}} = \xi \nu$ . From a recent review [7]  $\nu_{\text{eff}}$  is in the range  $10^{-3}$  to  $3 \times 10^{-5} \omega_{pe}$ , where  $\omega_{pe}$  is the electron plasma frequency. However, if this value were used in place of  $\nu$  in this simulation, the local current density in the filament would be reduced to a very low value immediately because  $\nu_{\text{eff}} \gg \nu$ ; in the following time step it would be restored because of the low drift velocity. Clearly the level of turbulence and the drift velocity will adjust on the time scale  $t_0$  of our present problem so that the plasma will be kept close to marginal stability. (The wavelengths typical of ion-sound turbulence are  $\approx 8\lambda_D$  and are much less than the filamentary width ( $\approx a_i$ ), so that to consider merely an effective collision frequency is adequate.)

Briefly, the model employed is that when the condition

$$\left( \frac{j_y^2 + j_z^2}{n_e e} \right)^{\frac{1}{2}} = v_d > \left( \frac{kT_e}{m_i} \right)^{\frac{1}{2}} + \left( \frac{kT_i}{m_e} \right)^{\frac{1}{2}} \quad (9)$$

holds,  $v_d$  is artificially constrained so that condition (9) becomes an equality, replacing Ohm's law. Ohm's law is modified to

$$(j_y^2 + j_z^2)^{\frac{1}{2}} = \frac{\sigma}{\xi} \left[ \left( E_y - \frac{v B_x}{c} \right)^2 + E_z^2 \right]^{\frac{1}{2}} \quad (10)$$

which becomes the means of identifying the anomaly factor  $\xi$  for the collision frequency subsequently employed consistently in the Ohmic heating, thermal conductivity and in the equipartition terms in eq. (5). The program is tested, each mesh point at each time step. If condition (9) holds, then it is set as an equality to define  $v_d$ , and  $\xi$  is calculated using eq. (10). Every other mesh point has  $\xi = 1$ .

Continuing the example of a slab width of  $20 L_0 (= 14 a_i)$ , at  $t = 12 t_0$  ion-acoustic turbulence is triggered in the temperature peak. The temperature peak (and density minimum) grows in amplitude and breadth, approaching close to a steady state by  $t = 66 t_0$ . The steady profiles of temperature, current density, density and anomaly factor are plotted in Figs 2 and 3. The current density maxima on the wings of the temperature profile occur when the anomaly factor has a narrower profile. We note the large amplitude of the variations of these parameters.

It might be thought that these structures would have a marked effect on the effective conductivity of the plasma as measured experimentally. However, if the density and temperature are measured by laser scattering from a volume which includes a complete wavelength of this filamentary structure, the measured density is the spatial average  $\bar{n} = \lambda^{-1} \int_0^\lambda n dx$  whilst the measured temperature  $T_{e \text{ scat}}$  is weighted with the density

$$T_{e \text{ scat}} = \frac{1}{n\lambda} \int_0^\lambda n(x) T_e(x) dx \quad (11)$$

If  $T_{e \text{ scat}}$  is employed in the Spitzer formula for electrical conductivity and divided by the effective average

conductivity found in the simulation  $(\lambda E_z)^{-1} \int_0^\lambda j_z dx$ , we find

that the ratio is 1.09. There is no enhancement of the average equipartition over that calculated from  $T_{e \text{ scat}}$  and  $\bar{n}$ ; indeed the ratio is 0.43.

## 5. DIRECT HEATING OF IONS

Whilst there are many proposed saturation mechanisms for ion-acoustic turbulence [7], the most likely mechanism involves ion tail formation [8,9], in which a fraction  $(m_e/m_i)^{1/2}$  of the ions in the turbulent region have a "temperature" close to the electron temperature. Thus there is direct heating of the ions, but in this application they have large Larmor excursions because of their high energy and mass out of the low-density filament into nearly all the neighbouring high-density colder plasma each side on the same time scale as the turbulence saturation. Therefore more turbulent ion heating has to take place to maintain the fraction of hot ions in the filamentary region against both their excursions out of the turbulent region and their loss of energy through classical collisions with the dense cold plasma each side. Then the ion heating rate will substantially exceed that given in homogeneous PIC simulations [9,10] which is only  $(m_e/m_i)^{1/2}$  times the electron heating rate. Indeed it can be shown that because of the high energy loss rate between the hot and cold ions the direct heating of the ions must be of the same order as the Ohmic heating of the electrons. To examine the effect of this, a case was run in which, when the plasma was ion-acoustic turbulent, only half of the Ohmic heating was deposited in the electrons, the rest being given to the ions. The result

of this was to reduce the amplitude of the relative temperature perturbation to 68 and the anomaly factor had a peak value of 153.

## 6. EXPERIMENTAL EVIDENCE

The experimental evidence for filamentary structures is somewhat scanty at the present time because of the lack of resolution in diagnostics, but positive observations have shown:

- (i) Large density fluctuations near the edge of the plasma [11] for which no other satisfactory explanation exists.
- (ii) Filamentary structures approximately parallel to the magnetic field lines observed by a fast cine-camera during gas-puffing [12].
- (iii) Observations on PDX with a 56-point laser scattering diagnostic [13] of quasi-stationary large amplitude ( $\delta n/n \approx 10 - 25\%$ ) density fluctuations, with out-of-phase temperature fluctuations, throughout the discharge. Here the scattering volume averages over 1.2 cm of the radius, and tangential laser beams would be preferable.

Perhaps experimenters will now make higher resolution measurements to see if these speculative ideas are true.

## REFERENCES

- [1] TOMIMURA, A., HAINES, M.G., J. Plasma Phys. 23 (1980) 1.
- [2] HAINES, M.G., J. Plasma Phys. 12 (1974) 1.
- [3] FURTH, H.P., ROSENBLUTH, M.N., RUTHERFORD, P.H., STODIEK, W., Phys. Fluids 13 (1970) 3020;  
ROSENAU, P., Phys. Fluids 25 (1982) 148.
- [4] HAINES, M.G., MARSH, F., J. Plasma Phys. 27 (1982) 427.
- [5] TOMIMURA, A., HAINES, M.G., J. Plasma Phys. 22 (1979) 397, 421.
- [6] MARSH, F., Ph.D. Thesis, University of London (1982).
- [7] Articles by MEAD, W.C., and HAINES, M.G., in Report of 1979 CECAM Workshop on Transport of Fast Electrons in Laser Fusion Plasmas.
- [8] VEKSHTEIN, G.E., SAGDEEV, R.Z., JETP Lett. 9 (1970) 194.
- [9] BISKAMP, D., CHODURA, R., Phys. Rev. Lett. 27 (1971) 1553.
- [10] WEINSTOCK, J., SLEEPER, A.M., Phys. Fluids 18 (1975) 247.
- [11] CALLEN, J.D. et al. in Plasma Physics and Controlled Nuclear Fusion Research 1980 (Proc. 8th Int. Conf. Brussels 1980) Vol. 1, IAEA, Vienna (1981) 775.
- [12] GOODALL, D.M.J., Culham Laboratory, private communication.
- [13] BRETZ, N. et al., Applied Optics 17 (1978) 192;  
JOHNSON, D., Princeton Laboratory, private communication.



# COMPUTATION OF PLASMA EQUILIBRIUM AND STABILITY IN STELLARATORS ON THE BASIS OF A GENERALIZED TWO-DIMENSIONAL EQUILIBRIUM EQUATION

V.D. PUSTOVITOV, V.D. SHAFRANOV, L.E. ZAKHAROV  
I.V. Kurchatov Institute of Atomic Energy, Moscow

L.M. DEGTYAREV, V.V. DROZDOV, S.Yu. MEDVEDEV,  
Yu.Yu. POSHEKHONOV  
M.V. Keldysh Institute of Applied Mathematics,  
Academy of Sciences, Moscow

M.I. MIKHAJLOV  
"Energy" Scientific-Manufacturing, Moscow,  
Union of Soviet Socialist Republics

## Abstract

COMPUTATION OF PLASMA EQUILIBRIUM AND STABILITY IN STELLARATORS  
ON THE BASIS OF A GENERALIZED TWO-DIMENSIONAL EQUILIBRIUM EQUATION.

The paper presents the results of a numerical calculation of equilibrium and stability against local plasma perturbation modes in normal stellarators. The calculation is based on a two-dimensional equilibrium equation described in the flux co-ordinate system. The calculations are performed for the parameters of the W-VIIA, L-2, L-3, Heliotron-E, U-3 and ATF stellarators. The calculation results show that it is possible, in the optimum conditions achievable, to confine a stable plasma with  $\beta \sim 10-12\%$ .

## 1. INTRODUCTION

A problem to be resolved in order to understand whether it is possible to create an economically effective fusion reactor based on the stellarator principle is: what maximum value of  $\beta$  can be achieved in such a system?

In theoretical studies (see, e.g. Refs [1, 2]), dealing with this question the main principles governing plasma maintenance in stellarators have been established. The clearest picture available is that of the  $\ell = 2$  stellarator. It has been found that the equilibrium- and stability-limited values of  $\beta$  have a maximum at certain optimum aspect ratio. A decrease in the aspect ratio, for fixed ratio of the plasma radius to the helical conductor pitch and fixed relative amplitude of the helical field, reduces the equilibrium-limited value of  $\beta$ . Increasing the aspect ratio reduces the magnetic well and, thus, the stability-limited plasma pressure.

The difference between systems with small shear (W-VIIA type) and with large shear (Liven'-2 type) has also been explained. In the W-VIIA stellarator, the inhomogeneity of the magnetic-surface shifts  $\Delta(a)$  along the major radius, which is necessary to create a magnetic well ( $a$  is the mean radius of the magnetic-surface cross-section) is related to the system curvature only. Plasma stabilization is achieved here at a small aspect ratio and, accordingly, at a small equilibrium value of  $\beta$ . In a large-shear stellarator, the shift inhomogeneity  $\Delta(a)$  is due to the inhomogeneity of the rotational transform (i.e. the shear). In this case, plasma stabilization may be achieved at a rather large aspect ratio and, accordingly, at large  $\beta$ .

The relations obtained follow from a shift-linear approximation of the local-mode stability criterion [1]:

$$\frac{1}{4} \left( \frac{a\epsilon'}{\epsilon} \right)^2 + \frac{R a p'(a)}{B_0^2 \epsilon^2} \left[ V_0''(\Phi) \cdot B_0^2 - \frac{(\epsilon' a^3)'}{\epsilon a^3} \Delta \right] > 0 \quad (1)$$

Here,  $V_0''(\Phi)$  describes the magnetic hill of a straight stellarator (if  $ma/R \ll 1$  it is given by  $V_0''(\Phi) = 2 m^2 \epsilon_0^2 / RB_0^2$ , for an  $\ell = 2$  stellarator);  $\epsilon$  is the rotational transform;  $\Delta(a)$  is the magnetic-surface shift (when positive, it corresponds to a shift away from the major torus axis). The last term, in fact, describes the role of shear in the creation of the magnetic well. Criterion (1) will be helpful in the following discussion as well as in an analysis of numerical results without the restriction  $\Delta/a \ll 1$ .

The estimates obtained for the optimum parameters  $\beta$  and  $R/a$  are sensitive to the small parameter  $\Delta/a$  used in the analytical calculations. To obtain more reliable values one should carry out numerical calculations in the same 'stellarator approximation' but with no restriction on the shift value.

An approach of this kind is very important for  $\ell = 2$  stellarators with large shear and for  $\ell = 3$  stellarators, where the shift-linear approximation is quite insufficient for an analytical description. This paper deals precisely with this problem, i.e. the development and use of algorithms for such calculations.

## 2. 2-D EQUILIBRIUM EQUATION

General equilibrium equations in flux co-ordinates [3] were used as starting point to derive a 2-D equilibrium equation. In contrast to the averaging method, the dependence on the fast variable ( $\ell\theta - m\zeta$ ) was excluded by applying an intermediate variable transformation:

$$\begin{aligned} r &= R - a_v (1 + \delta) \cos(\theta_v + \lambda) \\ z &= a_v (1 + \delta) \sin(\theta_v + \lambda) \end{aligned} \quad (2)$$

where  $a_v, \theta_v, \zeta$  are the vacuum flux co-ordinates with straightened magnetic force lines;  $\lambda$  and  $\delta$  are determined through the vacuum helical magnetic field potential:

$$\varphi_h = B_0 \epsilon_\ell \frac{R\ell}{m_\ell} I_\ell \left( \frac{m_\ell \rho}{R} \right) \sin(\ell\omega - m_\ell \zeta) \quad (3)$$

in the following way:

$$\begin{aligned} \delta &= \frac{dh_0}{a_v da_v} \cos(\ell\theta_v - m_\ell \zeta) \\ \lambda &= -\frac{\ell h_0}{a_v^2} \sin(\ell\theta_v - m_\ell \zeta) \\ h_0 &= \epsilon_\ell \frac{R^2 \ell}{m_\ell^2} I_\ell \left( \frac{m_\ell d_v}{R} \right) \end{aligned} \quad (4)$$

In the 'stellarator approximation' used,  $a_v$  and  $\theta_v$  are only 2-D functions of the flux co-ordinates:  $a_v = a_v(a, \theta)$ ,  $\theta_v = \theta_v(a, \theta)$ .

The formally introduced X and Y co-ordinates are also two-dimensional:

$$X = R - a_v \cos \theta_v, \quad Y = a_v \sin \theta_v \quad (5)$$

For  $\epsilon_\ell = 0$ , they coincide with  $r$  and  $z$ .

For an arbitrary choice of the angular variable (orthogonal co-ordinate system, co-ordinate system with straightened force lines, etc.), the desired functions  $a_v(a, \theta)$ ,  $\theta_v(a, \theta)$  or  $X(a, \theta)$ ,  $Y(a, \theta)$  are determined from the following equation [4]:

$$\frac{\partial \alpha_{22}^0}{\partial \psi} - \frac{\partial \alpha_{12}^0}{\partial \theta} = -4\pi^2 (\sqrt{g})^0 p'(\psi) - \frac{FF'(\psi)}{\alpha_{33}^0} - \frac{FD}{R^2} \frac{d(t_h a_v^2)}{a_v da_v} \quad (6)$$

Here  $\alpha_{ik}^0 \equiv (g_{ik}/\sqrt{g})^0$  are the  $\zeta$ -independent parts of the metrical-tensor elements in the flux co-ordinates  $a, \theta, \zeta$ . In the approximation used, they are given by

$$\begin{aligned} \alpha_{12}^0 &= (X' \dot{X} + Y' \dot{Y})/RD; \quad \alpha_{22}^0 = (\dot{X}^2 + \dot{Y}^2)/RD \\ \alpha_{33}^0 &= [X + R h_1(a_v)]/D; \quad (\sqrt{g})^0 = [X - R h_2(a_v)]/D \end{aligned} \quad (7)$$

$$D = \dot{X} Y' - X' \dot{Y}$$

where  $\dot{X} \equiv \partial X(a, \theta)/\partial \theta$ ,  $X' \equiv \partial X(a, \theta)/\partial a$ , etc.;  $h_1$ ,  $h_2$  and the vacuum rotational transform  $\epsilon_h$  are expressed through the parameters of the external helical magnetic field as

$$\begin{aligned} 2h_1 &= A^2 h_0^2 - B h_0 h'_0/a_v + (C + m_\ell^2/R^2)h'_0{}^2 \\ 2h_2 &= \ell^2 A h_0^2/a_v^2 - B h_0 h'_0/a_v + C h'_0{}^2 \end{aligned} \quad (8)$$

$$A = \frac{m_\ell^2}{R^2} + \frac{\ell^2}{a_v^2}, \quad B = \frac{m_\ell^2}{R^2} + \frac{3\ell^2}{a_v^2}, \quad C = \frac{\ell^2 + 1}{a_v^2}$$

$$\epsilon_h = \epsilon_\ell^2 \frac{m_\ell \ell^3}{4\xi} \frac{d}{d\xi} \left[ \frac{d I_\ell^2(\xi)}{\xi d\xi} \right]; \quad \xi = \frac{m_\ell a_v}{R}$$

Equation (6) differs from the corresponding equation for a tokamak by the corrections in  $(\sqrt{g})^0$  and  $\alpha_{33}^0$  as well as by an additional term on the right-hand side, containing the vacuum rotational transform,  $\epsilon_h(a_v)$ .

In contrast to the familiar 2-D Greene-Johnson equation [5] as well as the equation of Kovrizhnykh-Shchepetov [6] and Strauss [7], which are written in a laboratory, Eulerian, co-ordinate system, Eq. (6) is given in inverse, Lagrangian, co-ordinates. Aside from being conveniently applicable to stability problems, this approach allows both 2-D and 1-D (momentum method) codes developed for tokamaks to be utilized.

Note that the left-hand side of Eq.(6) divided by D is the 2-D Laplacian  $\partial^2 \psi/\partial X^2 + \partial^2 \psi/\partial Y^2$ .

Equation (6) allows  $a_v$ ,  $\theta_v$  or X, Y to be obtained as functions of a,  $\theta$  and 2-D cross-sections of magnetic surfaces in the plane X, Y to be constructed.

By using formulas (2) and going over to the r, z co-ordinates, we obtain the maps of the cross-sections for different  $\xi$ , i.e. a three-dimensional picture of the magnetic surfaces. At the same time, Eq.(6) enables us to define the entire metric of the flux co-ordinate system needed for stability investigation.

### 3. EQUATIONS FOR STABILITY PROBLEM

The stability of the local perturbation modes was studied in the infinite-conductivity approximation on the basis of the ballooning mode equation:

$$\frac{d}{d\theta} (fG'_\theta) = gG \quad (9)$$

In the general case of 3-D systems, exact expressions for  $f$  and  $g$  can be obtained, for example, by using the harmonics equivalence principle [8, 9]. In the stellarator approximation, it is sufficient to take  $f$  and  $g$  in the form

$$f = \left(\frac{g_{11}}{\sqrt{g}}\right)^0 - 2 \left(\frac{g_{12}}{\sqrt{g}}\right)^0 \frac{q'\theta}{q} + \left(\frac{g_{22}}{\sqrt{g}}\right)^0 \left(\frac{q'\theta}{q}\right)^2$$

$$g = -\frac{4\pi^2 p'}{\psi'^2} \left\{ \frac{q'\theta}{q} \frac{\partial(\sqrt{g})^0}{\partial\theta} - \frac{[(g_{33}/\sqrt{g})^0 (\sqrt{g})^0]'}{(g_{33}/\sqrt{g})^0} \right\} \quad (10)$$

Here,  $(g_{ik}/\sqrt{g})^0$ ,  $(\sqrt{g})^0$  are the  $\zeta$ -independent elements of the metric tensor in the flux co-ordinate system with straightened force lines;  $q(a) \equiv 1/\epsilon(a)$  is the 'safety factor', and the prime denotes a derivative with respect to  $a$ .

Equation (9) was solved numerically in a finite  $\theta$  interval. As is well known,  $G(\theta) \rightarrow 0$  for  $\theta \rightarrow \infty$ , corresponds to the Mercier criterion. By introducing the notations

$$f_0 = \frac{1}{a^2} \left(\frac{g_{22}}{\sqrt{g}}\right)^0, \quad \omega_1 = \frac{4\pi^2 p'}{\psi'^2 a} [(\sqrt{g})^0 - \langle(\sqrt{g})^0\rangle_\theta]$$

$$\omega_0 = \frac{4\pi^2 p'}{\psi'^2 a (g_{33}/\sqrt{g})^0} \langle[(g_{33}/\sqrt{g})^0 (\sqrt{g})^0]'\rangle_\theta \quad (11)$$

The Mercier criterion may be written as

$$\frac{1}{4} \left(\frac{aq'}{q}\right)^2 + \frac{aq'}{q} \left\langle \frac{\omega_1}{f_0} \right\rangle_\theta$$

$$+ \left\langle \frac{\omega_1}{f_0} \right\rangle_\theta^2 + \omega_0 \left\langle \frac{1}{f_0} \right\rangle_\theta - \left\langle \frac{\omega_1}{f} \right\rangle_\theta^2 \left\langle \frac{1}{f_0} \right\rangle_\theta > 0 \quad (12)$$

The shear stabilization becomes ineffective for slow dissipative quasi-flute perturbations (the so-called  $g$ -mode). In this approximation, the stability criterion of  $g$ -modes [10, 11] is deduced from the Mercier criterion (12) by omitting the first three terms. The only stabilizing factor here is a magnetic well. Since the shear stabilization plays an insignificant role in the  $\ell = 2$  stellarators and the main effect is due to the magnetic well, we should expect that the stability condition for  $g$ -modes differs but slightly from the Mercier criterion for modest aspect ratio. The shear is important in  $\ell = 3$  stellarators, and the stability condition for dissipative modes might not be fulfilled in this case.

## 4. RESULTS OF NUMERICAL CALCULATION

Equation (6) for  $p' = F' = 0$  describes a vacuum configuration of the magnetic surfaces. Some boundary surface  $\psi = \psi_s$  will be considered fixed (ideal casing). Equation (6) holds for a shift  $\Delta_0$  of the centre of the boundary surface,  $\psi = \psi_s$ , which corresponds to a new stellarator configuration with a superimposed transverse  $\zeta$ -independent magnetic field. The shape of the cross-section of the boundary magnetic surface in X, Y co-ordinates was given as a circle shifted with respect to a geometrical centre defined by the vacuum helical field

$$(X - R_0 - \Delta_0)^2 + Y^2 = a_0^2 \quad (13)$$

The function  $p(\psi)$  was, for example, given by  $p(\psi) = p_0 [(\psi - \psi_s)/(\psi_0 - \psi_s)]^2$ , and the derivative  $F'(\psi)$  was determined from the condition of zero averaged current density:

$$J'(\psi) = \frac{1}{2\pi} \int_0^{2\pi} \left( 4\pi^2 \frac{dp}{d\psi} (\sqrt{g})^0 + FF'/\alpha_{33}^0 \right) d\theta \quad (14)$$

Two methods were used for the numerical solution of Eq.(6) with these conditions. The main results were obtained with an algorithm based on the variable inversion method developed in Refs [12, 13], which was successfully used for equilibrium and stability calculations in tokamaks. The equilibrium calculation and, in particular, an analysis of the limiting equilibrium pressure as a function of the aspect ratio were also carried out by the 'method of electrodynamic moments'.

TABLE I. MAGNETIC PARAMETERS

Device	l	A	m	$\epsilon$	$\kappa(0)$	$\kappa(a)$
W VII-A	2	20	5	0.43	0.22	0.22
L-2	2	8.7	14	0.25	0.22	0.68
H-E	2	10	19	0.32	0.5	2.6
L-3	2	6.4	9	0.47	0.5	2.3
ATF	2	6.4	10	0.45	0.5	2.37
U-3	3	6.7	9	0.63	0	0.7

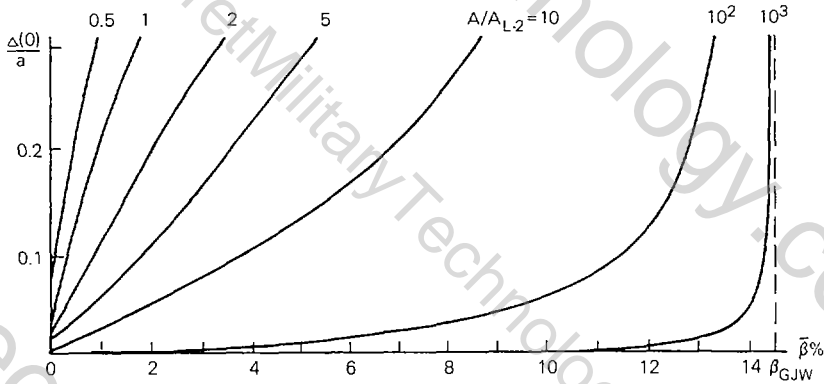


FIG. 1. Magnetic-axis shift versus plasma pressure for different aspect ratios  $A$  in stellarators with L-2 magnetic parameters;  $\epsilon_2 = 0.25$ ,  $m/A = 14/8.7$ . Plasma boundary shift  $\Delta_0 = 0$ . Shift  $\Delta(0)/a = 0$  corresponds to equilibrium-limited  $\beta$ .

The equilibrium-limited value of  $\beta$  followed from the condition for the breakdown of iteration convergence which seemed to be due to the fact that parameter values had been approached where the configuration topology must change (approach of the separatrix to the boundary or splitting of internal magnetic surfaces).

To simplify the analysis, the typical stellarator parameters are divided into two groups: 'magnetic' parameters (multipole  $\ell$ , helical field amplitude  $e_\ell$ , ratio of plasma radius to helical conductor pitch,  $m_\ell a_0/R$ ) and 'geometrical' parameters (aspect ratio  $A = R/a_0$  and a shift  $\Delta_0$  of boundary surface centre relative to geometric centre of the configuration). Note that if the magnetic parameters remain fixed when the aspect ratio varies, the total rotational transform varies proportionally to the aspect ratio (i.e. the rotational transform per unit length is fixed).

In this paper, the limiting values of  $\beta$  are studied as a function of the geometrical parameters. The magnetic parameters were taken to be the same as those of existing (or planned) machines (Table I).

Figure 1 shows the shift of the magnetic axis for  $\Delta_0 = 0$  relative to the geometrical centre for magnetic parameters of L-2 versus the aspect ratio  $A$ . The equilibrium  $\beta$ -value as a function of  $A$  is given in Fig. 2. For small aspect ratios, the equilibrium-limited pressure is proportional to  $A$ , according to the estimate  $\beta \sim \epsilon^2/A$ . As the aspect ratio grows, the behaviour of  $\Delta(\beta)$  changes considerably, revealing the existence of a limiting  $\beta_{GJW}$  independent of the aspect ratio. For large aspect ratios, the shift first increases slowly as  $\beta$  grows, but rises sharply when  $\beta$  approaches  $\beta_{GJW}$ , although  $\beta \ll \epsilon^2/A$ . The existence of such a limit in  $\beta$  was first discovered in Ref. [14]. The change in the behaviour

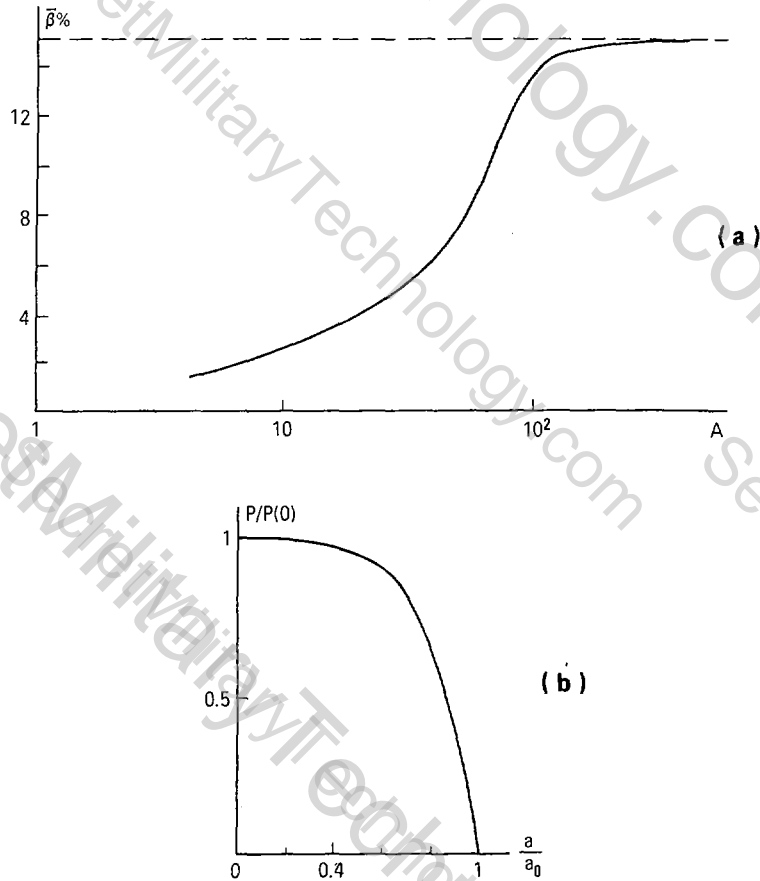


FIG. 2. a) Equilibrium-limited  $\beta$  versus aspect ratio for stellarators with L-2 magnetic parameters; b) plasma pressure profile used in calculations (momentum method).

of  $\Delta(\beta)$  with increasing aspect ratio is due to the increasing effect of the magnetic hill, which, as can be seen from Fig. 1, begins to have a marked influence only at very large aspect ratios (which are typical for the Scyllac-like devices).

The equilibrium- and stability-limited values,  $\beta_{eq}$  and  $\beta_{st}$ , versus the initial shift  $\Delta_0$  for L-2, L-3 and Heliotron-E are shown in Fig. 3. The half-value of  $\beta$  on the magnetic axis is plotted here. For the given pressure distribution,  $\beta_0/2$  is close to  $\beta^*$  as determined by the mean square pressure. The growth of  $\beta_{eq}$  with the boundary surface shift (of any sign) seems to be explained by the increase in the rotational transform on the shifted surfaces. Such a large shift means that the boundary surface approaches the helical separatrix, which may cause the conditions of applicability of the basic equation (6) to be violated.

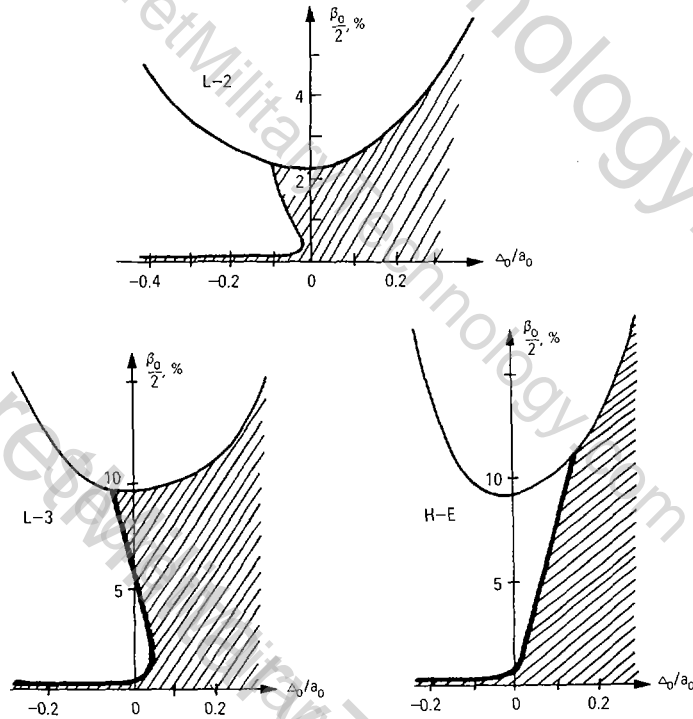


FIG. 3. Equilibrium and stability diagrams for stellarators L-2, L-3, H-E: — equilibrium boundary; - - - stability boundary.  $\beta_0$  is  $\beta$ -value on magnetic axis;  $\Delta_0$  the shift of plasma boundary centre relative to helical-winding axis.

An exact value of the limiting admissible shift cannot be obtained within the stellarator approximation used. A comparison made for different devices shows that  $\beta_{eq}$  is higher in systems with larger  $\epsilon_R$  and may reach 10%.

An analysis of the local-mode stability shows that for stellarators, unlike tokamaks, the most severe restrictions are imposed by the Mercier criterion as follows also from analytical calculations (see, e.g. Ref. [9]).

The dependence of  $\beta_{st}$  on  $A$  has one feature common to various devices: a shift of the boundary surface towards the major torus axis reduces  $\beta_{st}$  while a shift away from the axis improves stability, the function  $\beta_{st}(\Delta_0)$  being of the threshold type. The same conclusion follows from the analytical criterion (1), according to which a sharp rise in  $\beta_{st}$  occurs when the sign of the multiplier to  $p'$  changes.

From Fig. 3, we see, however, that the behaviour of  $\beta_{st}(\Delta_0)$  differs somewhat in the devices considered. For example, there are two stability zones in L-3

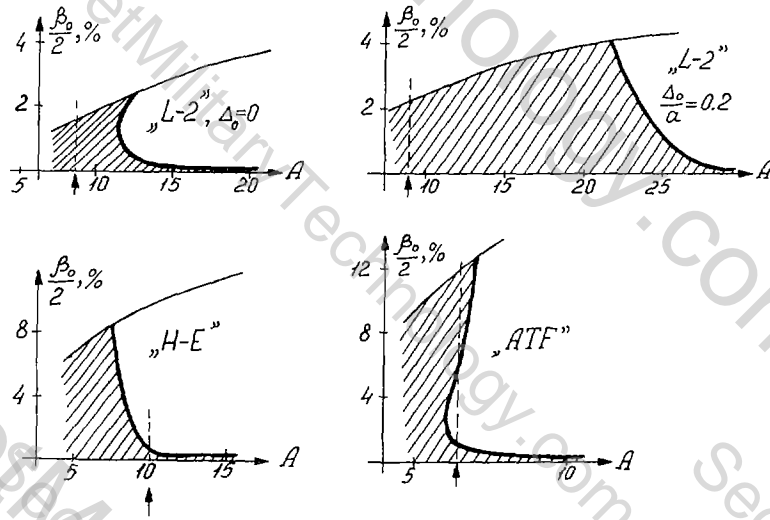


FIG. 4. Equilibrium- and stability-limited beta versus aspect ratio  $A$  for stellarator magnetic parameters corresponding to those of L-2, H-E, ATF: — equilibrium boundary, - - - stability boundary.  $\beta_0$  is  $\beta$ -value on magnetic axis;  $\Delta_0$  the shift of plasma boundary centre relative to helical winding axis.

at  $\Delta_0 = 0$ . This may be interpreted as follows. Shear stabilization allows only small values of  $\beta_{st}$ , while magnetic-surface shifts sufficient to ensure the transition to magnetic-well stabilization (self-stabilization [2]) can occur at much higher pressures. To provide stability for any  $\beta$  up to the maximum, the boundary surface must be allowed to shift. (The question whether the intrinsic shift due to pressure was sufficient or whether an external transversal field had to be imposed was not examined here.)

A typical feature of the behaviour of  $\beta_{st}(\Delta_0)$  in Heliotron-E is the absence of stability at virtually all  $\beta$  where  $\Delta_0 = 0$ , which may be due to insufficient shear stabilization at the plasma edge. Even a small shift of the boundary surface provides a high (100%) limiting  $\beta$ , permissible in terms of both equilibrium and stability.

Figure 4 shows the limiting pressure versus another geometrical parameter, the aspect ratio, for magnetic parameters corresponding to L-2, Heliotron-E and ATF. The aspect ratios of these devices are indicated by arrows. From this figure, we see that, with growing aspect ratio, the equilibrium-limited pressure rises and the stability-limited pressure generally decreases for all sets of magnetic parameters, a fact which also follows from analytical calculations

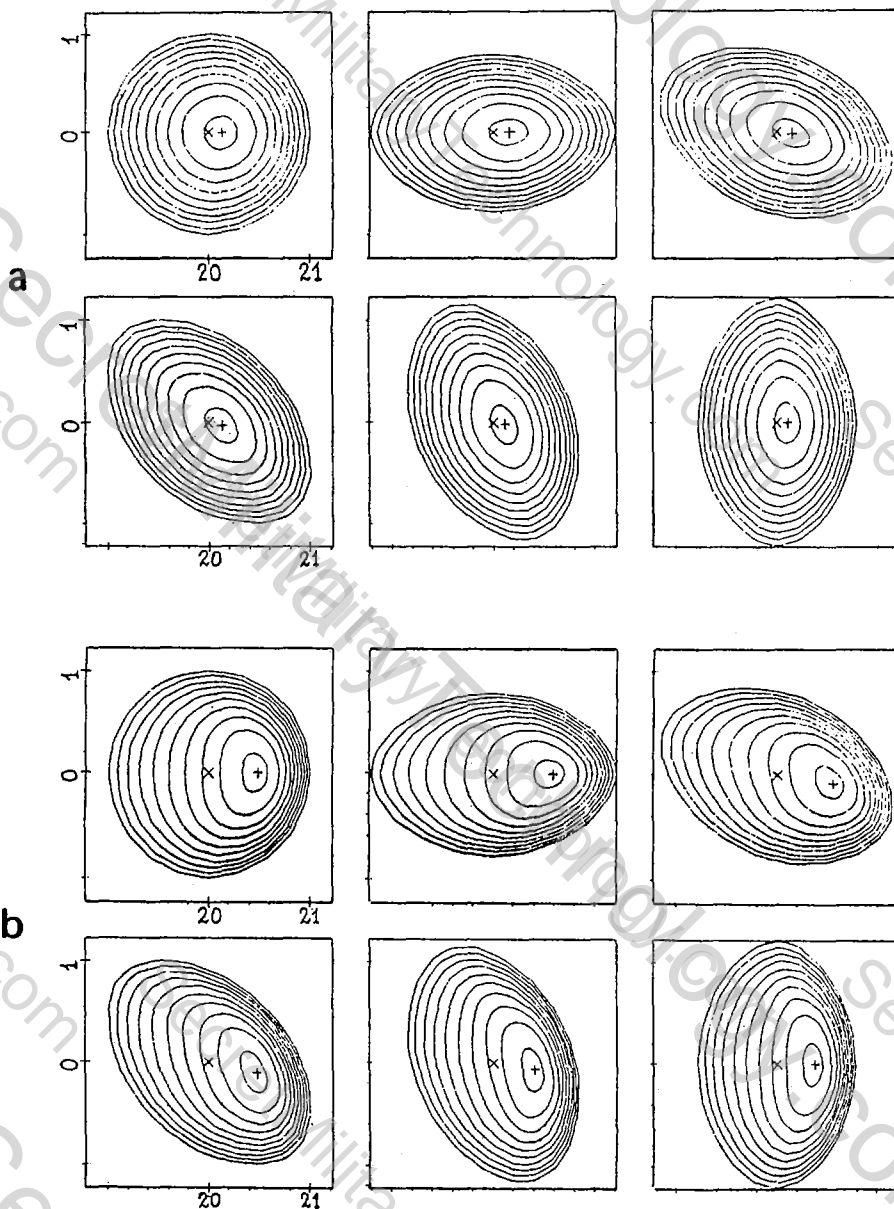


FIG. 5. Flux contours in  $\ell=2$  stellarator W-VIIA (2-D calculations) in  $X, Y$  variables (circular form) and  $r, z$  variables (elliptical form): a)  $\beta_0 = 0.12\%$  (stable), b)  $\beta_0 = 0.46\%$  (equilibrium limit, stable).

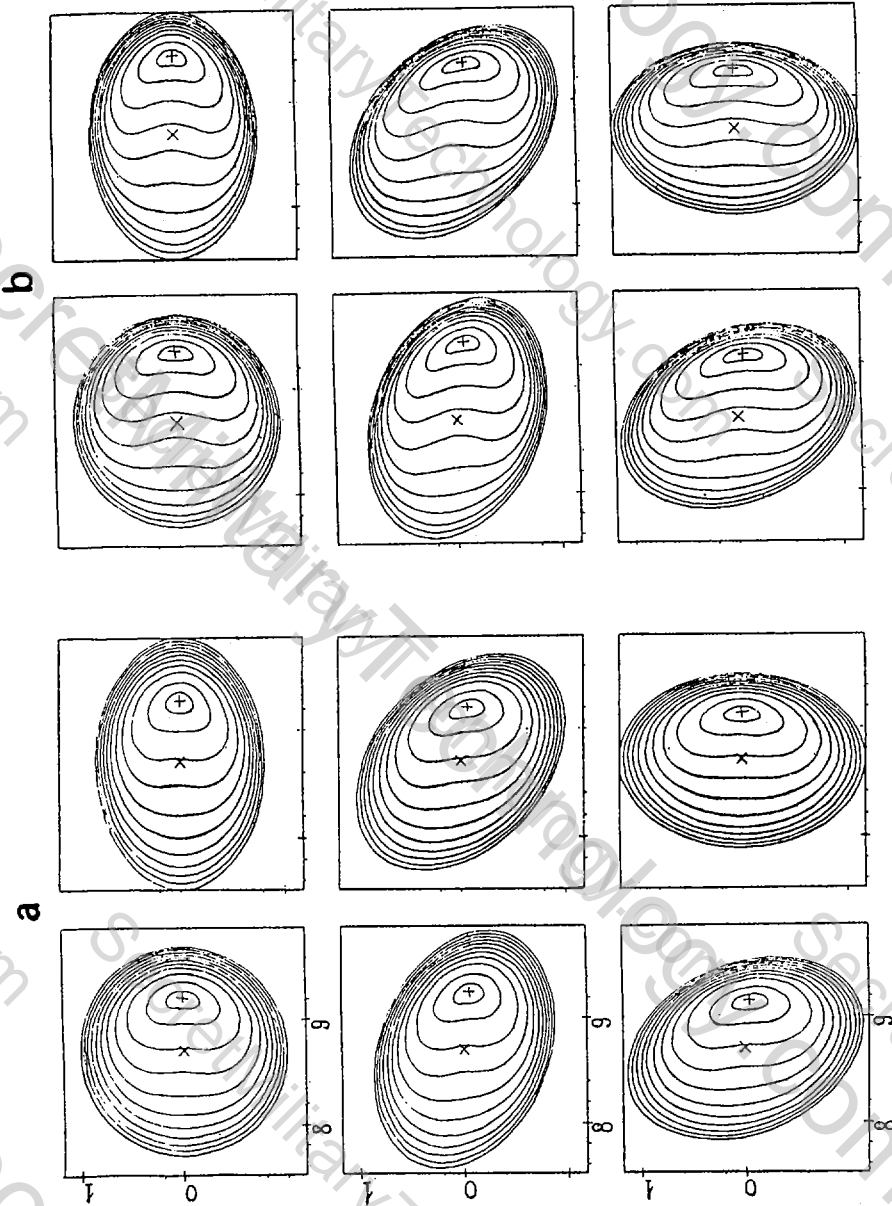


FIG. 6. Flux contours in  $\varrho = 2$  stellarator Liven'-2 (2-D calculations): a)  $\beta_0 = 2.5\%$ ;  $\alpha(0) = 0.34$ ;  $\alpha(\alpha_0) = 0.69$ ; b)  $\beta_0 = 4.4\%$ ;  $\alpha(0) = 0.36$ ;  $\alpha(\alpha_0) = 0.63$ .

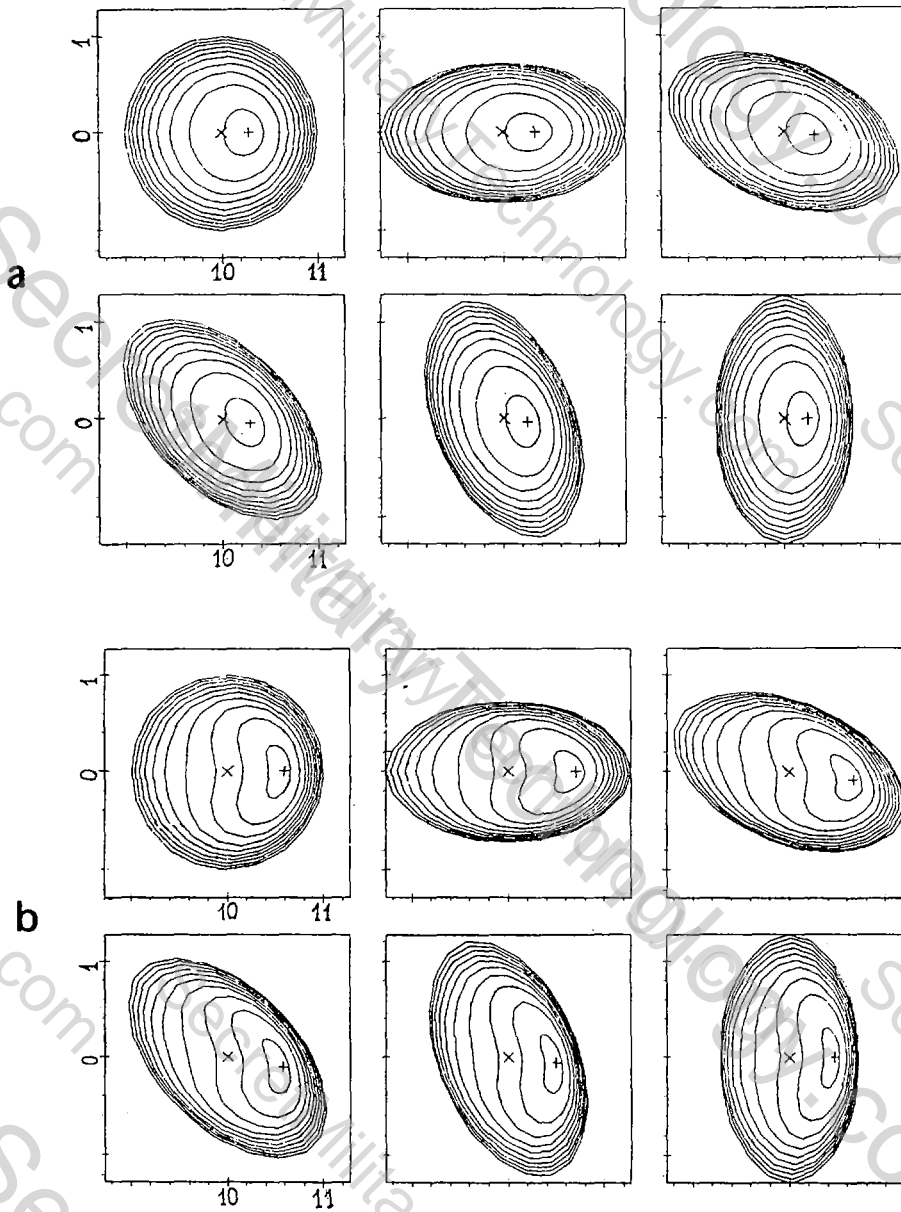


FIG. 7. Flux contours in  $l = 2$  stellarator Heliotron-E (2-D calculations): a)  $\beta_0 = 4.3\%$ ;  $\alpha(0) = 0.67$ ;  $\alpha(a_0) = 2.9$ ; b)  $\beta_0 = 15.6\%$ ;  $\alpha(0) = 0.9$ ;  $\alpha(a_0) = 2.76$ .

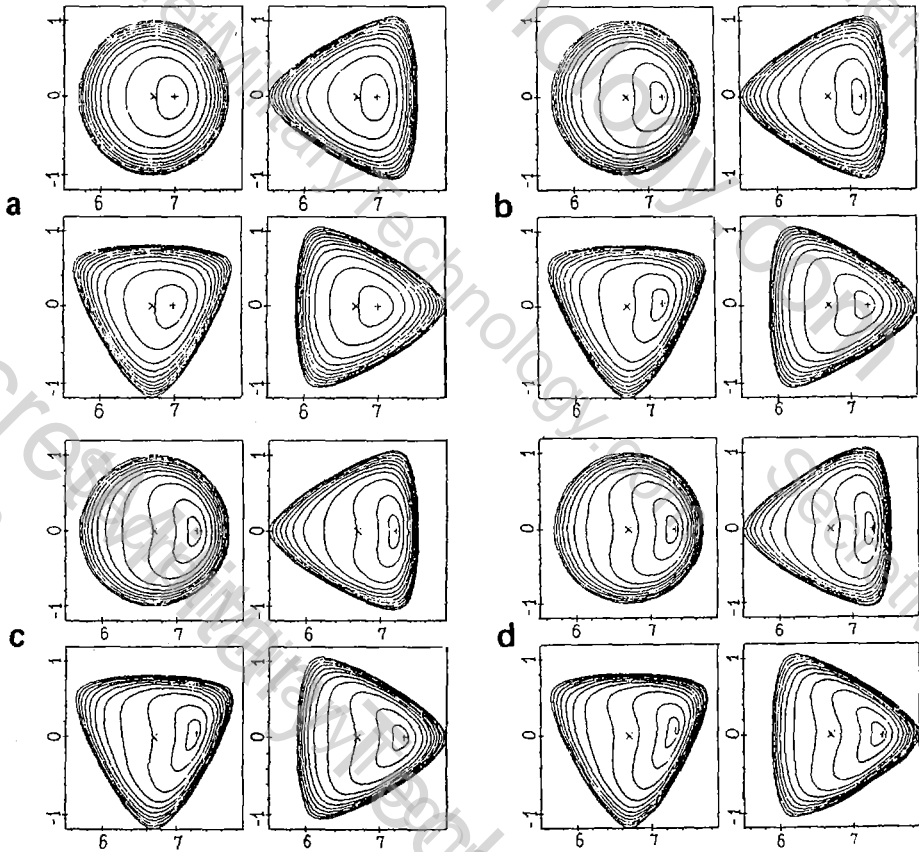


FIG. 8. Flux contours in  $l = 3$  stellarator U-3 (2-D calculations): a)  $\beta^* = 0.23\%$ , b)  $\beta^* = 0.9\%$ , c)  $\beta^* = 1.8\%$ , d)  $\beta^* = 2.7\%$ .

(see, e.g. Ref. [1]). The numerical computations have, however, allowed a more detailed picture to be obtained and some peculiarities of the behaviour of  $\beta_{st}(A)$  for various magnetic parameters to be elucidated. From the data given, it is seen that an increase in the aspect ratio, for the magnetic parameters of L-2, leads to a growth of the maximum equilibrium-limited value of  $\beta$ , without destroying stability. It may be stated that L-2, in particular, has a considerable margin of stability for all pressures permitted by equilibrium. The same conclusion can be drawn from the data presented in Fig.3: the stability-limited value of  $\beta$  is high, even for unfavourable shifts of the boundary surface. An increase in the aspect ratio at  $\Delta_0 = 0$  results, as in the case of L-3 (see Fig.3), in the appearance of two stability zones. The maximum possible value of  $\beta_0$  in devices with L-2 magnetic parameters does not exceed 8%, even at the optimum aspect ratio of  $A \approx 20$ .

The limited value of  $\beta$  versus the aspect ratio for devices with Heliotron-E and ATF magnetic parameters is presented for zero boundary surface shift. We see that, in this case, the plasma is unstable for virtually all  $\beta$  in the Heliotron-E ( $A = 10$ ) device. The optimum aspect ratio for Heliotron-E magnetic parameters is somewhat smaller than for the above-mentioned device ( $A_{\text{opt}} = 8$ ). However, from the data of Fig.3, it follows that even a small outward shift of the boundary surface provides stability in the Heliotron-E device, as well.

The highest limiting  $\beta$ -values are achieved for devices with ATF stellarator magnetic parameters. The ATF aspect ratio is close to optimum. As in L-3 (see Fig.3), there are two  $\beta$ -stable zones in ATF, which also raises the question of the method of plasma stabilization as pressure increases.

The maps of the magnetic surfaces of  $\ell = 2$  stellarators are shown for purposes of illustration in Figs 5–7 both in formal X, Y co-ordinates (circular boundary) and cylindrical r, z-co-ordinates for various  $\zeta$ . Similar data are given in Fig.8 for the  $\ell = 3$  stellarator U-3. The latter configurations are Mercier-stable, but unstable against g-modes.

## 5. CONCLUSIONS

The numerical results obtained allow us to discuss the limiting pressure values in common stellarators with a fair degree of confidence. It is shown that  $\beta$ -values of the order of 10–12% can be attained. This requires, however, a rather large amplitude of the helical field (e.g.  $\epsilon_q = 0.45$  for ATF) and rather steep helical windings. In this case, some small-scale disturbances of the nested magnetic surfaces may arise, which could not, however, be taken into account by our calculations.

## REFERENCES

- [1] MIKHAILOV, M.I., SHAFRANOV, V.D., *Plasma Phys.* **24** (1982) 233.
- [2] KOVRIZHNYKH, L.M., SHCHEPETOV, S.V., *Fiz. Plazmy* **7** (1981) 419.
- [3] SHAFRANOV, V.D., *Nucl. Fusion* **8** (1968) 253.
- [4] MIKHAILOV, M.I., PUSTOVITOV, V.D., SHAFRANOV, V.D., *Pis'ma v Zh. Eksp. Teor. Fiz.* **35** (1982) 152.
- [5] GREENE, J.M., JOHNSON, J.L., *Phys. Fluids* **4** (1961) 875.
- [6] KOVRIZHNYKH, L.M., SHCHEPETOV, S.V., *Fiz. Plazmy* **6** (1980) 976.
- [7] STRAUSS, H.R., *Plasma Phys.* **22** (1980) 733.
- [8] ZAKHAROV, L.E., in *Plasma Physics and Controlled Nuclear Fusion Research (Proc. 7th Int. Conf. Innsbruck, 1978) Vol.1*, IAEA, Vienna (1979) 689.
- [9] ZAKHAROV, L.E., MIKHAILOV, M.I., PISTUNOVICH, V.I., et al., in *Plasma Physics and Controlled Nuclear Fusion Research (Proc. 8th Int. Conf. Brussels, 1980) Vol.1*, IAEA, Vienna (1981) 313.

- [10] CHANCE, M.S., DEWAR, R.L., GLASSER, A.H., et al., in Plasma Physics and Controlled Nuclear Fusion Research (Proc. 5th Int. Conf. Tokyo, 1974) Vol.1, IAEA, Vienna (1975) 463.
- [11] MIKHAJLOVSKIJ, A.B., Nucl. Fusion 15 (1975) 95.
- [12] VABISHCHEVICH, P.N., DEGTYAREV, L.M., DROZDOV, V.V., Preprint IPM Acad. Sci. (1981) No.112.
- [13] VABISHCHEVICH, P.N., DEGTYAREV, L.M., DROZDOV, V.V., Dokl. Akad. Nauk SSSR 262 (1982) 1040.
- [14] GREENE, J.M., JOHNSON, J.L., WEIMER, K.E., Plasma Phys. 8 (1966) 145.

## CURRENT GENERATION BY INTERACTION OF ALPHA PARTICLES WITH ICRF WAVES

K. OKANO, N. INOUE, T. UCHIDA  
Department of Nuclear Engineering,  
Faculty of Engineering,  
University of Tokyo, Tokyo

R. SUGIHARA, Y. OGAWA  
Institute of Plasma Physics,  
Nagoya University, Nagoya

Japan

### Abstract

#### CURRENT GENERATION BY INTERACTION OF ALPHA PARTICLES WITH ICRF WAVES.

A current-drive method based on the interaction of fusion products ( $\alpha$ -particles) with ICRF waves is developed. A theoretical scaling law is obtained and confirmed by numerical simulations. A two-dimensional Fokker-Planck code is used to evaluate current-drive efficiency and induced current for the scheme. Calculations are carried out taking into account the spatial profiles of the density and temperature as well as the presence of the particle orbit loss regions in a tokamak. It is found that the current induced by the scheme may sustain tokamaks in steady state. The code can also be applied to check a current-drive scheme using the  $^3\text{He}$  minority ion.

### 1. INTRODUCTION

Various methods of operating tokamaks in steady state have been proposed. The most promising are based on direct pushing of electrons with RF waves [1–3] or injected beams [4]. There are other schemes for utilizing the interaction of plasma ions with ICRF waves [5, 6] and the drift of fusion products by asymmetric particle loss [7] or by the momentum transfer from waves [8]. Here, we describe a current drive method based on the interaction of fusion products ( $\alpha$ -particles) with ICRF waves. In this scheme, the ICRF waves are used to clamp the energy of  $\alpha$ -particles produced in the resonant region in velocity space. Although the ion-cyclotron waves have no toroidal momentum, and accelerate  $\alpha$ -particles only in the perpendicular direction with respect to the toroidal field, this acceleration clamps the particle momentum in the parallel direction. If the ICRF wave travelling unidirectionally along the toroidal field is launched at the tokamak plasma, the resonant region in velocity space becomes asymmetric and results in an asymmetric velocity distribution of  $\alpha$ -particles. The average drift of  $\alpha$ -particles is then established

and the net toroidal current induced. This mechanism is essentially identical with that of Ohkawa current [4]. We have studied this situation using a two-dimensional Fokker-Planck (F-P) code.

The physics to generate the average drift of  $\alpha$ -particles is analogous to the method described in Ref. [5]. In Section 5, we check this current drive scheme by ICRF minority ion heating using the F-P code.

## 2. ANALYTICAL SCALING

It is convenient to derive an analytical scaling of our method in order to obtain a skillful arrangement of the results of numerical calculations. The analytical technique presented here is analogous to that used for estimating the beam-driven current enhanced by ICRF waves, the details of which are described elsewhere [6]. Only an outline of the analysis is given here.

We assume that the ICRF wave accelerates ions only in the perpendicular direction in velocity space. The time evolution of the perpendicular energy of the  $\alpha$ -particles is given by  $dE_{\perp}/dt = mv_{\perp}(dv_{\perp}/dt)$ , where  $E_{\perp} = mv_{\perp}^2/2$ ,  $m$  is the mass of the  $\alpha$ -particle, and  $v_{\perp}$  is its velocity perpendicular to the magnetic field. We suppose that the rate of change of  $E_{\perp}$  due to ICRF wave acceleration is constant, i.e.  $dE_{\perp}/dt = \delta E$ . If the ion velocity increment during the interval  $\Delta t$  is  $\Delta v$ , then  $(v + \Delta v)^2 = v_{\parallel}^2 + [v_{\perp} + (dv_{\perp}/dt)\Delta t]^2$ , where  $v_{\parallel}$  is the  $\alpha$ -particle velocity parallel to the magnetic field. Thus, the change of the ion velocity  $v$  by ICRF wave is given by  $(dv/dt)_w = \delta E/mv$ . Using this expression we can obtain the equation of motion for  $\alpha$ -particles which are being decelerated by Coulomb collisions and accelerated by the ICRF waves:

$$\frac{dv}{dt} = -\frac{1}{\tau_{se}} \frac{v^3 + v_c^3}{v^2} + \frac{\delta E}{mv} \quad (1)$$

where  $\tau_{se}$  is the slowing-down time of the  $\alpha$ -particles by background electrons, and  $v_c$  is the critical velocity at which the energy is transferred equally to the background ions and the electrons [9]:

$$\tau_{se} = \frac{3 m m_e v_e^3 (4\pi\epsilon_0)^2}{16\sqrt{\pi} e^4 Z^2 n_e \ln\Lambda}, \quad v_c = \left\{ \frac{3\sqrt{\pi} (m_i + m) m_e}{m_i m} \right\}^{1/3} v_e$$

In these expressions,  $m_i$  and  $m_e$  are the mass of the background ions and electrons respectively, and  $Z$  is the charge number of the  $\alpha$ -particle. We have assumed the charge number of the background ions to be unity. As the velocity of  $\alpha$ -particles is much larger than the thermal velocity of the background ions, the energy

diffusion during the slowing-down processes can be neglected. So, with a source of  $\alpha$ -particles in an infinitesimal volume at  $(v_\alpha, \theta, \varphi)$  and a sink at velocity  $v_s$  in velocity space, the slowing-down time  $\tau$  and the angle-averaged velocity distribution  $f(v)$  are described as follows [10, 11]:

$$\tau = - \int_{v_s}^{v_\alpha} dv / (dv/dt) \quad (2)$$

$$f(v) v^2 (dv/dt) = \text{const.} \quad (3)$$

where  $v_\alpha$  is the velocity of the  $\alpha$ -particle at birth time, the typical value of  $v_s$  is of the order of the ion thermal velocity, and  $\theta = \tan^{-1}(v_\perp/v_\parallel)$ . From Eqs (1)–(3) we obtain expressions for  $\tau$  and  $f$  with the assumptions that  $\epsilon = \tau_{se} \delta E / m v_c^2 \ll 1$  and  $x_s = v_s/v_c \cong 0$ :

$$\tau = \tau_{sc} [1 + \epsilon G(x_\alpha)] \quad (4)$$

$$G(x) = [\phi(x) - x/(x^3 + 1)] / \ln(x^3 + 1)$$

$$f(x) = \frac{\dot{n}_\alpha \tau_{se}}{4\pi v_c^3} \left\{ \frac{1}{x^3 + 1} + \epsilon \frac{x}{(x^3 + 1)^2} \right\} \quad (5)$$

$$\left\{ \begin{array}{l} \phi(x) \\ \psi(x) \end{array} \right\} = \left\{ \begin{array}{l} + \\ - \end{array} \right\} \frac{1}{6} \ln \frac{(x+1)^2}{x^2-x+1} + \frac{1}{\sqrt{3}} \tan^{-1} \frac{2x-1}{\sqrt{3}} + \frac{\pi}{6\sqrt{3}}$$

where  $\tau_{sc} = (1/3)\tau_{se} \ln(x_\alpha^3 + 1)$  [10];  $x = v/v_c$ ; and  $\phi$  and  $\psi$  signify  $\phi(x_\alpha)$  and  $\psi(x_\alpha)$ , respectively. If we neglect the change of parallel velocity due to the pitch-angle scattering during the slowing-down, we obtain the longitudinal ion current by  $\alpha$ -particles,  $J_\alpha$ , using Eqs (4) and (5):

$$J_\alpha = \int (e Z S |\bar{v}_\theta|) dv = (1/4) e Z \dot{n}_\alpha \tau_{sc} v_c \epsilon H(x_\alpha)$$

$$H(x) = \frac{2\psi x^3 - x^2 + 2\psi}{3(x^3 + 1)}$$

where  $S = \delta(v - v_\alpha) \dot{n}_\alpha \tau / 4\pi v_\alpha^2$ ;  $|\bar{v}_\theta| = \cos\theta / (\dot{n}_\alpha \tau) \int 4\pi v^3 f(v) dv$ ; and  $\dot{n}_\alpha$  is the rate of production of  $\alpha$ -particles. We suppose that the waves resonate in the region

$v_{\parallel} > 0$ . This means that  $\epsilon = 0$  at  $\theta > \pi/2$  and  $\epsilon > 0$  at  $\theta < \pi/2$ . Taking the back-streaming electron current into account, the total current  $J$  induced by the drift of  $\alpha$ -particles is described with a fairly good approximation as  $J = (1-Z)J_{\alpha}$  [12]. The power dissipated by the waves,  $P_d$ , is given by  $P_d = \int S \delta E d\vec{v}$ . Here, to facilitate comparison with other schemes for current drive, we normalize the current density  $J$  to  $-(1/\sqrt{2})en_e v_e$  and  $P_d$  to  $(1/2)\nu_0 n_e m_e v_e^2$  according to previous work [1, 3, 5], where  $\nu_0 = (\sqrt{2}\omega_{pe}^4 \ln \Lambda)/(\pi v_e^3 n_e)$ . Finally, the normalized efficiency ( $J/P_d$ ) for current drive becomes

$$\left(\frac{J}{P_d}\right)' = \frac{3\sqrt{\pi}}{2} (1-Z^{-1}) \left\{ \frac{m_i m}{3\sqrt{\pi} (m_i + m) m_e} \right\}^{1/3} \frac{3H(x_{\alpha})}{\ln(x_{\alpha}^3 + 1)} \{1 + \epsilon G(x_{\alpha})\}^{-1}$$

The values of  $3H/\ln(x_{\alpha}^3 + 1)$  and  $G(x_{\alpha})$  are approximately  $3H/\ln(x_{\alpha}^3 + 1) \cong 0.45$  and  $G(x_{\alpha}) \cong 0.45$  at  $10 \text{ keV} < T_i < 25 \text{ keV}$ , respectively. Then, one has

$$(J/P_d)' = 5(1 + 0.45 \epsilon)^{-1} \quad (6)$$

for  $D/T = 50/50$  plasma. Notice that  $(J/P_d)'$  is a function which decreases with  $\delta E$ . As  $\delta E$  is roughly  $P_d/n_r$ , where  $n_r$  is the density of the resonant particles, the amount of  $n_r$  is an important factor of current drive.

### 3. NUMERICAL SIMULATION

We use a two-dimensional F-P code to evaluate  $J$  and  $J/P_d$ . The time evolution of the  $\alpha$ -particle velocity distribution  $F$  in the presence of RF field is described by  $\partial F/\partial t = (\partial F/\partial t)_c + (\partial F/\partial t)_w + \dot{n}_{\alpha}$ . The first term is the linearized F-P collision term, which is identical with the corresponding expressions in Ref. [13] except that our expression does not include the assumption  $v_{ti} \ll v$ , where  $v_{ti}$  is the thermal velocity of the background ions. The second term expresses the influences of the waves on particle motion, and, following the quasi-linear theory [14], it is given by

$$\left(\frac{\partial F}{\partial t}\right)_w = \frac{\partial}{\partial \vec{v}} \cdot \left(D \frac{\partial F}{\partial \vec{v}}\right); \quad D = \begin{bmatrix} D_{\perp\perp} & D_{\perp\parallel} \\ D_{\parallel\perp} & D_{\parallel\parallel} \end{bmatrix}$$

We take account of a dependence of the diffusion coefficient  $D$  on  $k_{\perp} \rho$  because the energy of the  $\alpha$ -particles is so large that  $k_{\perp} \rho$  is the order of unity in most cases, where  $\rho$  is the Larmor radius and  $k_{\perp}$  is the perpendicular wave number [15]. To determine  $D$ , we give  $k_{\parallel}$  and  $E = E^r + E^l$ : then  $k_{\perp}$  and  $E^r/E^l$  are calculated with the dispersion relation of fast waves, where  $E^r$  and  $E^l$  are the right-hand and the left-hand polarization components of the wave electric field, respectively.

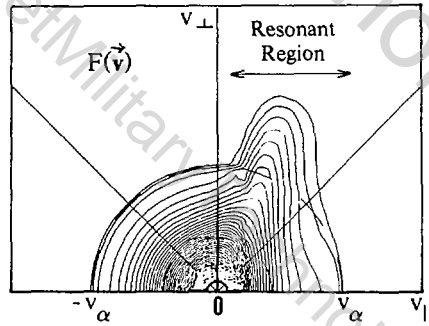


FIG.1. Contours of steady-state distribution function of  $\alpha$ -particles. The ICRF waves resonate at  $v_{\parallel} > v_m = 2v_{tD}$ ;  $n_e = 2 \times 10^{20} m^{-3}$  and  $T_i = T_e = 20 keV$ .

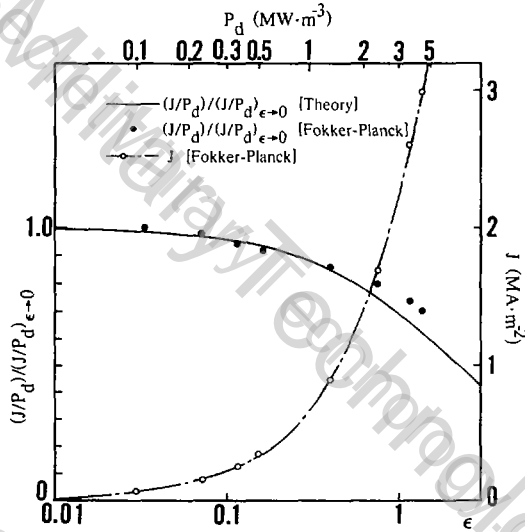


FIG.2. Dependence of  $J/P_d$  and  $J$  on power rate  $\epsilon$  and dissipated power  $P_d$ . ( $n_e = 2 \times 10^{20} m^{-3}$  and  $T_i = T_e = 25 keV$ ).

For practical coding,  $D$  is averaged over a magnetic surface in order to eliminate the difficulty caused by the  $\delta$ -function.  $D$  is then finite in the velocity regime:

$$(\Omega_{min} - \omega)/k_{\parallel} < v_{\parallel} < (\Omega_{max} - \omega)/k_{\parallel} \tag{7}$$

and  $D = 0$  in the other regime, where  $\Omega_{max}$  and  $\Omega_{min}$  are the ion-cyclotron frequencies inside and outside the torus, respectively. The third term,  $\dot{n}_{\alpha}$ , denotes the rate of production of  $\alpha$ -particles at  $v = v_{\alpha}$ .

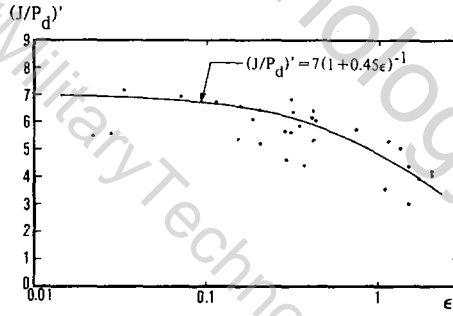


FIG. 3. Dependence of normalized efficiency  $(J/P_d)'$  on power rate  $\epsilon$ . The solid line indicates  $7(1 + 0.45 \epsilon)^{-1}$ .

The boundary conditions are  $F = 0$  at  $v = v_{\max}$  and assumption of the existence of a perfect sink of  $\alpha$ -particles at the velocity regime  $v < v_s$ . Here, we take it that  $v_{\max} = 3v_\alpha$  and  $v_s = 2v_{tD}$  with  $v_{tD} = (2T_D/m_D)^{1/2}$ , where the subscript D indicates a deuteron. If necessary, we append another boundary condition for taking particle orbit loss regions into account. When the case of the minority ion heating is discussed in Section 5,  $\dot{n}_\alpha = 0$  and  $v_s = 0$  are assumed.

The average drift velocity  $\bar{v}_\parallel$  is described by  $v_\parallel = \int \bar{v}_\parallel F(\vec{v}) d\vec{v}$ . The net induced current is given by  $J = (1-Z)\bar{n}\bar{v}_\parallel Ze$ . On the other hand, the dissipation power  $P_d$  is given by  $P_d = (m/2) \int v^2 \partial/\partial \vec{v} \cdot (D \partial f/\partial \vec{v}) d\vec{v}$ .

Figure 1 shows an example of the steady-state distribution function of  $\alpha$ -particles in resonance with ICRF waves, calculated with  $T_i = T_e = 20$  keV and  $n_e = 2 \times 10^{20} \text{ m}^{-3}$ . The wave resonates in the region  $v_m < v_\parallel$ , where  $v_m$  is the minimum speed of resonance, and in most cases we have chosen  $v_m = 2v_{tD}$ .

The dependence of  $J/P_d$  on  $\epsilon$  is shown in Fig. 2, where  $T_i = 25$  keV and  $n_e = 2 \times 10^{20} \text{ m}^{-3}$ . For these numerical results we denote  $\epsilon$  as  $P_d/n_r$ . The current densities computed with the F-P code are also plotted in Fig. 2. The required current for tokamak operations, about  $1 \text{ MA} \cdot \text{m}^{-2}$  is obtained at  $\epsilon \cong 0.5$ . In Fig. 3, we summarize the normalized efficiency  $(J/P_d)'$  for various parameters:  $10 \text{ keV} < T_i < 25 \text{ keV}$ ;  $10^{20} \text{ m}^{-3} < n_e < 4 \times 10^{20} \text{ m}^{-3}$ ;  $1 \text{ V} \cdot \text{cm}^{-1} < E < 140 \text{ V} \cdot \text{cm}^{-1}$  and  $0.01 < \epsilon < 2.0$ . It is found that the values of  $(J/P_d)'$  are somewhat larger than that of Eq. (6) and rather given by

$$(J/P_d)' = 7(1 + 0.45 \epsilon)^{-1} \quad (8)$$

Nevertheless, the theory correctly predicts the dependence of  $(J/P_d)'$  on  $\epsilon$ .

#### 4. APPLICATION TO REACTORS

When the present scheme is applied to fusion reactors, the first difficulty arises from the equality of the ICRF between  $\alpha$ -particles and deuterons. We have to accelerate selectively the  $\alpha$ -particles in order to distinguish them from the deuterons. This problem can be overcome by choosing  $v_m$  much larger than  $v_{tD}$ . For both  $\alpha$ -particle and deuteron, the condition for resonance is described by the inequality (7). If we choose  $v_m$  so that  $2v_{tD} < (\Omega_{\min} - \omega)/k_{\parallel} = v_m$ , very few deuterons satisfy the resonance condition, but most  $\alpha$ -particles can resonate. Thus we have taken  $v_m$  as  $v_m = 2 v_{tD}$  for most of our calculations. Choice of a larger value of  $v_m$  results in a small increase of  $J/P_d$ , while  $n_r$  decreases considerably.

We assumed the following parameters for the reactor model:  $T_{i0} = T_{e0} = 25$  keV;  $n_{i0} = 2 \times 10^{20} \text{ m}^{-3}$ ;  $a = 2$  m and  $R = 10$  m. The parabolic profiles of  $T$  and  $n$  are assumed. The induced plasma current  $I_p$  and the efficiency  $I_p/P_{in}$  for this case are shown in Fig.4 as functions of  $P_{out}/P_{in}$ , where  $P_{in}$  is the RF input power and  $P_{out}$  is the thermal output of the reactor. These calculations take no account of the presence of the loss regions of particle orbit. If the loss regions are considered, the problem becomes non-linear since the loss region is specified by  $I_p$ . After iterative calculations, it is found that  $I_p = 8$  MA is required to suppress the loss of  $\alpha$ -particles accelerated by ICRF waves. The current profile for  $I_p = 8$  MA is shown in Fig. 5. About 6.5% of the induced plasma current is lost into the loss region but is localized near the periphery. The other parameters obtained here are as follows:

$$I_p: 8 \text{ MA}$$

$$P_{out}/P_{in}: 8.2$$

$$I_p/P_{in}: 0.01 \text{ MA} \cdot \text{MW}^{-1}$$

$$P_w: 4.5 \text{ MW} \cdot \text{m}^{-2}$$

The current profile is written in approximate form as  $J = J_0(1 - (r/a)^3)^{2.5}$  except at the periphery.

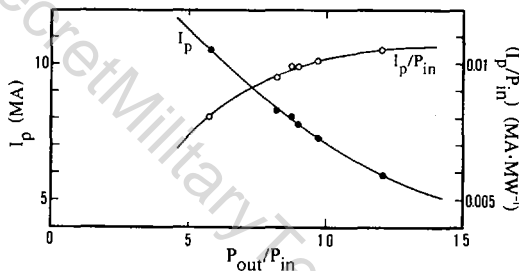


FIG.4. Relation of  $I_p$  and  $I_p/P_{in}$  to  $P_{out}/P_{in}$ :  $R = 10$  m,  $a = 2$  m,  $T_{i0} = 25$  keV and  $n_e = 2 \times 10^{20} \text{ m}^{-3}$  assumed. Notice that the origin has been eliminated.

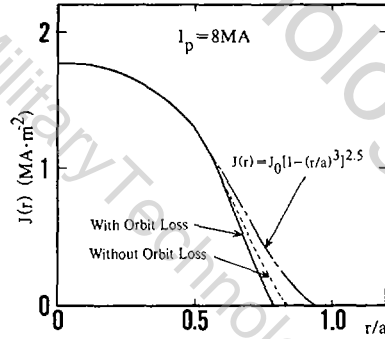


FIG.5. Spatial current profile induced by  $\alpha$ -particles.  $I_p = 8$  MA is obtained.

## 5. MINORITY ION HEATING

In this section we investigate the current drive scheme using minority ion heating by ICRF waves. We take  $^3\text{He}$  ions as the minority species and assume that their distribution is Maxwellian at  $t = 0$ . Let us start with estimating the maximum energy  $E_{\text{max}}$  of the minority ions accelerated by ICRF waves. As in Section 2, the time evolution of particle energy can be described by  $dE/dt = mv(dv/dt)$  with  $dv/dt$  given by Eq.(1). Solving this equation for  $dE/dt = 0$  with the assumption that  $E_{\text{max}} > E_c = (1/2)mv_c^2$ , we obtain  $E_{\text{max}} = \tau_{se} \delta E/2 \cong \tau_{se} P_d / 2n_r$ . According to Ref. [5], we choose the resonance region as  $3 < w < 7$ , where  $w = v_{\parallel} / (T_i/m)^{1/2}$ . Provided that, as an optimistic case, the distribution function flattens in the resonance region of velocity space, we obtain  $n_r \cong 2 \times 10^{-2} \zeta n_i$ , where  $\zeta$  is the mixing ratio of the minority ions. For example, when  $T_i = 20$  keV and  $n_i = 1 \times 10^{20} \text{ m}^{-3}$ , it is required that  $P_d \cong 1 \text{ MW} \cdot \text{m}^{-3}$  because  $J/P_d \cong 1 \text{ A} \cdot \text{m} \cdot \text{W}^{-1}$  in this case. Thus,  $E_{\text{max}}$  reaches 21 MeV when  $\zeta = 5\%$ . Moreover, our F-P code reveals that the resonant particles are fewer by several tens than what is calculated assuming the plateau formation in the velocity distribution. This means that, in order to gain the required current, the particles must be accelerated up to several hundred MeV. Such high-energy particles are immediately lost from the conventional confinement system. We therefore suspect that this method cannot provide enough plasma current to sustain tokamaks in the steady state.

Figure 6 shows results (broken lines) of the numerical calculations where we have restricted  $P_d$  to less than  $1 \times 10^{-3} \text{ MW} \cdot \text{m}^{-3}$ . The solid lines indicate the values obtained by Fisch's theory. The agreement of our results with Fisch's theory is fairly good, at least in the small power regime. The current densities

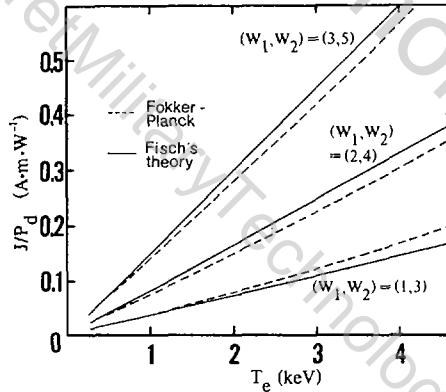


FIG. 6. Variations of  $J/P_d$  as functions of  $T_e$ . Broken lines show our present results; solid lines are calculated by Fisch's theory. The waves resonate in the region  $W_1 < w < W_2$ .

are only about  $10^{-3} \text{ MA} \cdot \text{m}^{-2}$  in these cases, and yet it has been found that most resonant particles reach about 1 MeV. With larger  $P_d$ , a large distortion of the velocity distribution takes place.

## 6. CONCLUSION

It can be seen from the above calculations that, for the current drive scheme utilizing ion drift, not only the magnitude of  $J/P_d$  but also the number of resonant particles and the dependence on input power density are important. Our method, using  $\alpha$ -particles, can provide the required number of resonant particles because the particle source is in the resonance region in velocity space. However, owing to the insufficient number of resonant  $\alpha$ -particles, the method does not allow low-density operations, which are desirable for most of the current drive schemes. Thus the efficiency of our current drive scheme,  $I_p/P_{in}$ , seems somewhat small compared with others. For burning plasmas, however, density exceeding  $1 \times 10^{20} \text{ m}^{-3}$  is indispensable, and in this regime our method becomes important.

## ACKNOWLEDGEMENTS

The authors thank Z. Yoshida for stimulating discussions during this work and M. Mori for his efforts in programming the Fokker-Planck code.

## REFERENCES

- [1] FISCH, N.J., *Phys. Rev.* **41** (1978) 873.
- [2] WORT, D.J.H., *Plasma Phys.* **13** (1971) 258.
- [3] FISCH, N.J., BOOZER, A.H., *Phys. Rev. Lett.* **45** (1980) 720.
- [4] OHKAWA, T., *Nucl. Fusion* **10** (1970) 185.
- [5] FISCH, N.J., *Nucl. Fusion* **21** (1981) 15.
- [6] OKANO, K., INOUE, N., UCHIDA, T., Scaling Law of Beam Driven Current Enhanced by ICRF Wave, Univ. of Tokyo NEUT Research Rep. 82-04 (1982).
- [7] KOLESNICHENKO, Ya.I., REZNIK, S.N., YAVORSKIJ, V.A., in *Plasma Physics and Controlled Nuclear Fusion Research 1980* (Proc. 8th Int. Conf. Brussels, 1980) Vol. 1, IAEA, Vienna (1981) 653.
- [8] BHADRA, D.K., CHU, C., *Phys. Rev. Lett.* **48** (1982) 1824.
- [9] SPITZER, L., *Physics of Fully Ionized Gases*, Interscience, New York (1956).
- [10] STIX, T.H., *Plasma Phys.* **14** (1972) 367.
- [11] JASSBY, D.L., *Nucl. Fusion* **17** (1977) 309.
- [12] START, D.F.H., CORDEY, J.G., JONES, E.M., *Plasma Phys.* **22** (1980) 303.
- [13] FOWLER, R.H., CALLEN, J.D., ROME, J.A., SMITH, J., A Fast Ion Fokker-Planck Code, Oak Ridge Natl. Lab. Rep. ORNL/TM-5487 (1976).
- [14] KENNEL, C.F., ENGELMANN, F.R., *Phys. Fluids* **9** (1966) 2377.
- [15] BLACKFIELD, D.T., SCHARER, J.E., *Nucl. Fusion* **22** (1982) 255.

## BALLOONING MHD MODES IN TOROIDAL SYSTEMS WITH COMPLICATED MAGNETIC-FIELD GEOMETRY

A.B. MIKHAILOVSKI

I.V. Kurchatov Institute of Atomic Energy, Moscow

V.V. DEMCHENKO, A.Ya. OMEL'CHENKO,

Institute of Physics and Technology,

Ukrainian Academy of Sciences,

Khar'kov,

Union of Soviet Socialist Republics

### Abstract

#### BALLOONING MHD MODES IN TOROIDAL SYSTEMS WITH COMPLICATED MAGNETIC-FIELD GEOMETRY.

The shear-induced instability of ideal ballooning MHD modes is studied analytically for closed magnetic traps with an arbitrary shape of the magnetic axis. A stability criterion determining the maximum pressure of a hydrodynamically stable plasma for a wide range of equilibrium toroidal configurations is derived by using the method of small oscillations. The criterion derived is used in the analysis of plasma stability in toroidal traps with the magnetic axes being simple closed spatial curves. It is shown that modulation of the magnetic-axis curvature affects the plasma stability with respect to the excitation of ideal ballooning modes. In a currentless trap with positive shear, ballooning modes are less dangerous than Mercier-type perturbations.

### 1. INTRODUCTION

This paper deals with ideal ballooning modes in toroidal systems of circular cross-section and arbitrarily shaped magnetic axis. Equilibrium and MHD stability of such systems were first considered by Shafranov [1]. The feasibility of prolonged high-pressure plasma confinement in traps with complicated magnetic-field geometry is connected with the self-stabilization effect found in Ref. [2] which leads to an improvement of hydrodynamic plasma stability as the pressure increases. This result, obtained in Ref. [2] for a simple plasma configuration with a spatial magnetic axis, i.e. a helical pinch, has been generalized in Refs [3, 4] for the case of toroidal traps with arbitrarily shaped magnetic axes (see also Ref. [5]). Successful experiments on plasma confinement in the ASPERATOR NP-3 device with a helical magnetic axis [6], as well as the development of the DRAGON system [7], stimulated further studies of plasma equilibrium and stability in traps with spatial magnetic axes.

The conclusion that a high-pressure plasma exhibits self-stabilization was reached in Refs [2–4] in studies of plasma stability with respect to the Mercier-type perturbation of radial dimension smaller than the dimension along the minor azimuth of the torus. However, as was shown in Refs [8, 9], in the case when the Mercier criterion is satisfied, there exist two-dimensional ballooning-type perturbations resulting in the development of a flute instability.

The role of shear in the stability of the ideal ballooning MHD mode in simple magnetic configurations was studied in Refs [10–12]. Thus, for the tokamak configuration, Pogutse and Yurchenko [10] have derived a stability criterion taking into account the main de-stabilizing effect which is linear in shear and quadratic in plasma pressure. This criterion was then supplemented in Refs [11, 12] by fourth-order plasma pressure terms due to the self-stabilization effect. This made it possible to describe analytically the second region of plasma stability which was first found in the numerical calculations of Refs [13–15].

The aim of the present paper is to find a stability criterion for ballooning modes in finite-shear traps with a complicated shape of the magnetic axis. In the Appendix, using the method developed in Ref. [12] for the tokamak configuration, we derive an equation for small oscillations which may be applied for studying ballooning modes in a wide range of equilibrium toroidal plasma configurations. After averaging over the oscillations of the metric, the two-dimensional differential equation derived reduces to a form permitting analytical investigation. Also derived are expressions for the mean magnetic well and terms responsible for the ballooning effects that determine the type of the potential energy in the equation for the small oscillations. The ballooning-mode stability criterion based on the assumption of parabolic plasma pressure distribution is obtained in Section 2. This criterion is used to analyse plasma stability in toroidal traps with magnetic axes that are simple closed spatial curves.

## 2. PLASMA STABILITY CRITERION IN TRAPS WITH PARABOLIC PRESSURE DISTRIBUTION

In accordance with Refs [10–12], instead of the cyclic variable  $\theta$  (we use a system of quasi-cylindrical co-ordinates  $a, \theta, \varphi$  with straightened magnetic lines of forces), we introduce the quantity  $y$  which varies within infinite limits. The perturbed radial plasma displacement  $\tilde{\xi}$  is written in the eikonal form [16] as

$$\tilde{\xi}(a, \theta, \varphi) = F(a, y, \varphi) \exp(i n q y - i n \varphi) \quad (1)$$

where

$$F(a, y, \varphi)$$

is a slowly varying function of angular variables. Since we do not restrict the analysis to the case of axially symmetrical configurations, there is obviously also a dependence of the function  $F$  on  $\varphi$ . In the general case, the stability criterion is cumbersome so that we confine the analysis of Eq. (A.9) to traps with a parabolic pressure distribution. In this case, from the equations for the magnetic-axis displacement  $\xi$  and the magnetic surface ellipticity  $\alpha$ , we obtain

$$\xi_n' = \beta_0 \mu^2 \frac{k_n a}{(\mu+n)^2} \quad (2)$$

$$\dot{\alpha}_n - \frac{d\alpha_n}{a} = \frac{a^2 \mu^4 \beta_0^2}{\epsilon} \sum_{n_1} \frac{k_{n_1} k_{n-n_1}}{(\mu+n-n_1)^2} \left[ \frac{1}{(\mu+n_1)^2} + \frac{\mathcal{B}}{(2\mu+n)(\mu+n_1)} - \frac{\mathcal{B}}{(2\mu+n)^2} \right] \quad (3)$$

where  $\beta_0 = \frac{4\pi^2 p_0 R^2}{\chi^2}$ .

After the substitution of Eqs (2) and (3) into relations (A.11) and (A.13), the equation for the small oscillations reduces to the form

$$S^2 \frac{\partial}{\partial t} \left[ (1+t^2) \frac{\partial \bar{f}}{\partial t} \right] - \left[ U_0 + \frac{U_1}{1+t^2} \right] \bar{f} = 0 \quad (4)$$

where

$$U_0 = 4 \frac{a^2}{R^2} \beta_0 \left[ R^2 \sum_n k_n^2 \frac{\mu + 2\alpha_0 R - n}{\mu + n} - \mu_1^2 \right] + 4a^4 \beta_0^4 \mu^6 \mathcal{Z}_0 \quad (5)$$

$$U_1 = -16a^2 \beta_0^2 \sum_n k_n^2 \left[ \frac{\mu}{\mu+n} \right]^3 S + 4a^4 \beta_0^4 \mu^6 \mathcal{Z}_1 \quad (6)$$

$$\begin{aligned} \mathcal{I}_0 = & 3 \left[ \sum_n \frac{k_n^2}{(\mu+n)^3} \right]^2 - \frac{1}{2} \sum_{n, n_1, n_2} \frac{k_n k_{n_1} k_{n_2} k_{n+n_1-n_2}}{(\mu+n_1)(\mu+n_2)(\mu+n+n_1-n_2)^2} \\ & \times \left[ -\frac{3}{2} \frac{1}{(\mu+n_2)(\mu+n_1)} + \frac{5}{2} \frac{1}{(\mu+n)(\mu+n_2)} + \frac{1}{(\mu+n)(\mu+n_1)} \right. \\ & \left. + 4 \frac{\mu+n+n_1-n_2}{(\mu+n)(2\mu+n+n_1)} + \frac{1}{2} \frac{(n-n_1)^2}{(\mu+n)^2(\mu+n_1)(\mu+n_2)} \right] \end{aligned} \quad (7)$$

$$\begin{aligned} \mathcal{I}_1 = & -4 \left[ \sum_n \frac{k_n^2}{(\mu+n)^3} \right]^2 \\ & + 2 \sum_{n, n_1, n_2} \frac{k_n k_{n_1} k_{n_2} k_{n+n_1-n_2}}{(\mu+n)(\mu+n_1)(\mu+n+n_1-n_2)^2} \left[ 3 \frac{1}{(\mu+n_1)(\mu+n_2)} \right. \\ & + \frac{n-n_2}{(\mu+n)(\mu+n_2)^2} + \frac{1}{(\mu+n_1)(\mu+n_2)} - \frac{4}{(\mu+n_1)(2\mu+n+n_1)} + \frac{2}{(\mu+n_2)^2} \\ & - \frac{4(\mu+n_1)(\mu+n+n_1-n_2)}{(\mu+n)(\mu+n_2)(2\mu+n+n_1)^2} \left. + 16 \left\{ \sum_n \frac{k_n^2}{(\mu+n)^4} \cdot \sum_n \frac{k_n^2}{(\mu+n)^2} \right. \right. \\ & - \frac{1}{4} \sum_{n, n_1, n_2} \frac{k_n k_{n_1} k_{n_2} k_{n+n_1-n_2}}{(\mu+n)^2(\mu+n_1)(\mu+n+n_1-n_2)^2} \left[ \frac{1}{\mu+n_1} + \frac{\mu+n_1}{(\mu+n_2)(\mu+n+n_1-n_2)} \right. \\ & \left. \left. + \frac{2(\mu+n+n_1-n_2)^2}{(\mu+n_1)(2\mu+n+n_1)^2} + \frac{2(\mu+n_1)}{(2\mu+n+n_1)^2} \right] \right\} \end{aligned} \quad (8)$$

In deriving Eq. (4) we assumed the coefficients  $k_n$  to be real.

Using the trial function  $\bar{f} = (1 + t^2)^{-1/2}$  from Ref. [10] and Eq. (4), we derive the necessary stability criterion for ideal ballooning modes:

$$\frac{1}{2}S^2 + 4 \frac{a^2}{R^2} \beta_0 \left[ R^2 \sum_n k_n^2 \frac{\mu + 2\alpha_0 R - n}{\mu + n} - \mu_J^2 \right] - 8a^2 \beta_0^2 \sum_n k_n^2 \left( \frac{\mu}{\mu + n} \right)^3 S + 4a^4 \beta_0^4 \mu^6 \left( \gamma_0 + \frac{1}{2} \gamma_1 \right) > 0 \quad (9)$$

Here, the first term corresponds to the familiar shear stabilization effect of the flute instability; the second term describes the stabilizing effect of the geometrical magnetic well on plasma stability. The third term in criterion (9) for  $S > 0$  describes the de-stabilization of a high-pressure plasma. The last term corresponds to the plasma self-stabilization effect.

We shall use these results to analyse plasma stability in a currentless ( $\mu_J = 0$ ) toroidal magnetic trap with a spatial magnetic axis. In this case,  $S$  is given by

$$S = \beta_0^2 a^2 \mu^3 \sum_n \frac{k_n^2}{(\mu + n)^3} \quad (10)$$

The stability criterion (9), with allowance for Eq. (10) may be re-written as

$$-\sum_n \bar{k}_n^2 + \beta_0^3 \bar{\alpha}_0^{-6} \frac{a^2}{R^2} \left( \gamma_0 + \frac{1}{2} \gamma_1 \right) - \frac{15}{8} \left[ \sum_n \frac{\bar{k}_n^2}{(n - \bar{\alpha}_0)^3} \right]^2 > 0 \quad (11)$$

where the quantities

$$\bar{k}_n = k_n R, \quad \bar{\alpha}_0 = \alpha_0 R$$

are introduced. According to Ref. [17], the magnetic-axis curvature for a Spitzer 'figure-of-eight' configuration is simulated by the expression

$$\bar{k}(\varphi) = \bar{k}_0 + \bar{k}_2 e^{2i\varphi} \quad (12)$$

where

$$\bar{k}_0 = \frac{\sqrt{1 - \frac{1}{2}\bar{\alpha}_0}}{1 - 0.52\bar{\alpha}_0 + 0.11\bar{\alpha}_0^2}, \quad \bar{k}_2 = \frac{\sqrt{3\bar{\alpha}_0}}{1 + 0.16\bar{\alpha}_0 + 0.28\bar{\alpha}_0^2}$$

The second term in Eq. (12) describes the modulation of the magnetic-axis curvature of the system. For specific calculations, we set

$$\bar{\alpha}_0 = 0.5$$

In this case, from criterion (11) we derive the critical value of  $\beta_0^*$  for plasma stabilization

$$\beta_{\theta S}^* = 0.82 \left( \frac{R}{a} \right)^{2/3}$$

If there is no modulation of the magnetic-axis curvature ( $\bar{k}_2 = 0$ ), which corresponds to a helically symmetrical system, from Eq. (12) we obtain

$$\beta_{\theta A}^* = 0.58 \left( \frac{R}{a} \right)^{2/3}$$

From a comparison of the above-mentioned critical values of  $\beta_0^*$ , it is clear that modulation of the magnetic-axis curvature has a destabilizing effect on the plasma. From the Mercier stability criterion,  $\frac{1}{4}S^2 + U_0 > 0$ , for these values of  $\bar{k}_0$ ,  $\bar{k}_2$  and  $\bar{\alpha}_0$  in the currentless regime, we have

$$\beta_{\theta M}^* = 1.08 \left( \frac{R}{a} \right)^{2/3}$$

Thus, in the case considered, the ballooning modes appear to be less dangerous than the Mercier modes since stabilization of ballooning modes with increasing pressure occurs before stabilization of Mercier modes.

## Appendix

A VERAGED EQUATION FOR SMALL OSCILLATIONS IN TRAPS  
WITH ARBITRARY SHAPE OF MAGNETIC AXIS

Using transformation (1), we reduce the familiar equation for small oscillations [8] to give

$$\hat{L}_{11} (\hat{L}_{1M}^{-1} \hat{L}_{11} F) - (\hat{L}_{11} A_M + W^{(0)}) F = 0 \quad (\text{A.1})$$

where

$$\hat{L}_{11} = \mu \frac{\partial^2}{\partial y^2} + \frac{\partial}{\partial \varphi} \quad (\text{A.2})$$

$$\hat{L}_{1M} = \frac{\omega'^2}{4\pi^2} \frac{1}{\sqrt{q}} \frac{1}{B^2} \left[ \left( \frac{y q'}{q} \right)^2 q^{11} + 2 \frac{y q'}{q} q^{1b} + q^{bb} \right] \equiv Q_{1M}^{-1} \quad (\text{A.3})$$

$$W^{(0)} = \frac{\Omega}{\omega'^2} - \mu' d_0^{(0)} - \left( \frac{2\pi p'}{\omega'^2} \right)^2 \left( \frac{\sqrt{q}}{B^2} \right)^{(0)} \quad (\text{A.4})$$

$$A_M = \frac{y q'}{q} d_0^{(1)} - \frac{p'}{\omega'} \left[ \left( \frac{y}{p'} \right)' + \frac{2\pi B_1}{B^2} \right] - \left( \frac{2\pi p'}{\omega'} \right)^2 \hat{L}_{11}^{-1} \left( \frac{\sqrt{q}}{B^2} \right)^{(1)} \quad (\text{A.5})$$

$$q^{1b} = q^{12} - \mu q^{13}, \quad q^{bb} = q^{22} - 2\mu q^{25} + \mu^2 q^{33}, \quad (\text{A.5})$$

$$g^{ik} = \frac{M_{ik}}{\sqrt{q}}, \quad q = \det g_{ik}$$

$g_{ik}$  is the metric tensor,  $M_{ik}$  is the minor of  $g_{ik}$ ,  $\mu = \frac{x'}{\omega'}$ ,  $d_0 = \frac{j_0 \cdot B_0}{B_0^2}$ ,  $\vec{j}_0$  is the equilibrium current density,  $\hat{L}_{11}^{-1}$  is the inverse of the operator  $\hat{L}_{11}$ ,  $\Omega = p'v'' + j'x' - I'p''$ ,  $x$  and  $\varphi$  are, respectively, the transverse (along  $\theta$ ) and longitudinal (along  $\varphi$ ) magnetic fluxes, and the prime denotes differentiation with respect to the minor radius. The function  $v$  contained in Eq. (A.5) satisfies [8]

$$(\bar{B} \nabla) \nu = 2\pi \rho' \left( \frac{V'}{4\pi^2 \sqrt{g}} - 1 \right) \quad (\text{A.6})$$

where  $V' = 4\pi^2 (\sqrt{g})^{(0)}$  is the derivative of the volume bounded by the corresponding magnetic surface. Here and henceforth the superscripts "0" and "1" denote the averaged and oscillating parts of the corresponding quantities, respectively.

The averaging of Eq. (A.1) over the oscillations of the metric is performed by a technique proposed in Ref. [12]. We express  $F(a, y, \varphi)$  as a series

$$F = \bar{f} + \sum_{k=1}^3 \tilde{f}_k, \quad |\tilde{f}_k| \ll |\bar{f}|$$

where  $\bar{f}$  and  $\tilde{f}_k$  are, respectively, the mean and oscillating parts of the function  $F(a, y, \varphi)$ . Then, on averaging over the fast oscillations, Eq. (A.1) takes the form

$$\begin{aligned} \hat{L}_{11} \left[ \frac{1}{Q_{1M}^{(0)}} \hat{L}_{11} \bar{f} \right] + \hat{L}_{11} \left[ \frac{1}{Q_{1M}} \hat{L}_{11} \tilde{f}_1 \right]^{(0)} - W^{(0)} \bar{f} \\ + \sum_{k=1}^3 \left[ A_M \hat{L}_{11} \tilde{f}_k \right]^{(0)} = 0 \end{aligned} \quad (\text{A.7})$$

Subtracting the averaged equation (A.7) from Eq. (A.1), we obtain relations determining  $\tilde{f}_k$ :

$$\tilde{f}_k = \hat{L}_{11}^{-1} \left[ Q_{1M} C_k - Q_{1M} \frac{(Q_{1M} C_k)^{(0)}}{Q_{1M}^{(0)}} \right] \quad (\text{A.8})$$

where

$$C_1 = \bar{f} A_M - \hat{L}_{1M} \hat{L}_{11} \bar{f}$$

$$C_2 = \hat{L}_{11}^{-1} \left[ \tilde{f}_1 \hat{L}_{11} A_M - (\tilde{f}_1 \hat{L}_{11} A_M)^{(0)} \right]$$

$$C_3 = W^{(0)} \left[ \hat{L}_{11}^{-1} \tilde{f}_1 + \hat{L}_{11}^{-1} \left[ \tilde{f}_2 \hat{L}_{11} A_M - (\tilde{f}_2 \hat{L}_{11} A_M)^{(0)} \right] \right]$$

$\tilde{L}_{1M}$  is the oscillating part of the operator  $\hat{L}_{1M}$ . The substitution of the expression for  $\tilde{f}_k$  into Eq. (A.7) reduces the latter to

$$\frac{\partial}{\partial y} \left[ \frac{1}{Q_{1M}^{(0)}} \frac{\partial \tilde{f}}{\partial y} \right] - q^2 \left\{ W^{(0)} + \mu \frac{\partial}{\partial y} \left[ \frac{(Q_{1M} A_M)^{(0)}}{Q_{1M}^{(0)}} \right] - (Q_{1M} A_M^2)^{(0)} + \frac{[(Q_{1M} A_M)^{(0)}]^2}{Q_{1M}^{(0)}} + \Delta \right\} \tilde{f} = 0 \quad (A.9)$$

$$\Delta = W^{(0)} \left\{ \left[ \hat{L}_{11}^{-1} (Q_{1M} A_M)^{-1} \right]^2 \right\}^{(0)} + \left\{ \hat{L}_{11} A_M \left[ \hat{L}_{11}^{-1} (Q_{1M} A_M)^{-1} \right]^2 \right\}^{(0)} + \left\{ \hat{L}_{11}^{-1} \left[ Q_{1M} \hat{L}_{11}^{-1} \left( \hat{L}_{11}^{-1} (Q_{1M} A_M) \hat{L}_{11} A_M \right) \right] \hat{L}_{11}^{-1} (Q_{1M} A_M) \hat{L}_{11} A_M \right\}^{(0)}$$

The first term in Eq. (A.9) describes the stabilizing action of shear, and the second term allows for the mean magnetic well. Quadratic terms in  $A_M$  correspond to the ballooning effect, the term proportional to  $\mu$  describes the combined effect of shear and current density inhomogeneity along the magnetic field lines. The quantity  $\Delta$  takes into account the plasma self-stabilization effect. Equation (A.9) can be used to analyse the ideal ballooning mode stability in toroidal magnetic configurations of different types.

The coefficients  $Q_{1M}$ ,  $A_M$  and  $W^{(0)}$  entering Eq. (A.9) are calculated according to the procedure suggested in Ref. [9]. Omitting cumbersome intermediate calculations, we write down the finite formulas:

$$W^{(0)} = W_1^{(0)} + W_2^{(0)} + W_3^{(0)} + W_4^{(0)} \quad (A.10)$$

where

$$W_1^{(0)} = \frac{2P'}{RB_s^2} \left\{ \mu^2 - R^2 \sum_n \left[ k_n k_n^* \left( 1 + 2 \frac{2\alpha R - n}{\mu + n} \right) - \frac{\mu_j^i (k_n^* \xi_n^i + c.c.)}{2(\mu + n)} \right] \right\}$$

$$W_2^{(0)} = \frac{2P'^2 R^3}{aB_s^4} \sum_n \frac{k_n k_n^*}{(\mu + n)^2}$$

$$W_3^{(0)} = \frac{3P'R}{2aB_s^2} \sum_n \left\{ k_n^* \left[ -\frac{1}{2} (\xi_n^i \xi_n^{*i}) + \frac{1}{\mu + n} \sum_{n_1} (\mu + n_1) \xi_{n_1}^{*i} \right. \right. \\ \left. \left. \times \left( \alpha'_{n+n_1} + \frac{\alpha'_{n+n_1}}{a} \right) + \frac{1}{\mu + n} \sum_{n_1 n_2} \xi_{n_1}^{*i} (\mu + n_1) \xi_{n_1}^i \xi_{n+n_2-n_1}^i \right] + c.c. \right\}$$

$$W_4^{(0)} = -\frac{(P'R)^2}{B_s^4} \frac{R}{a} \sum_n k_n^* \left\{ -\sum_{n_1} k_{n_1}^* \left[ \frac{\alpha'_{n+n_1}}{(\mu+n)(\mu+n_1)} + \left( \frac{3}{4a} \alpha'_{n+n_1} + \frac{\alpha'_{n+n_1}}{4} \right) \right. \right.$$

$$\left. \left. \times \left( \frac{1}{(\mu+n)^2} + \frac{1}{(\mu+n_1)^2} \right) + \sum_{n_1 n_2} k_{n_1} \xi_{n_2}^{*i} \xi_{n-n_1+n_2}^i \left[ \frac{1}{4(\mu+n)^2} + \frac{1}{4(\mu+n)^2} \right. \right. \right.$$

$$\left. \left. - \frac{3}{2} \frac{1}{(\mu+n)(\mu+n_1)} + \frac{1}{(\mu+n)(2\mu+n_2)} + \frac{1}{(\mu+n_1)(2\mu+n_2)} - \frac{1}{(2\mu+n_2)^2} \right] \right.$$

$$\left. \left. + \sum_{n n_1} k_{n_1}^* \xi_{n_2}^i \xi_{n+n_1-n_2}^i \left[ \frac{1}{8} \left( \frac{1}{(\mu+n)^2} + \frac{1}{(\mu+n_1)^2} \right) + \frac{1}{4(\mu+n)^2} \right. \right. \right.$$

$$\left. \left. + \frac{1}{2} \left( \frac{1}{(\mu+n)(\mu+n_1)} - \frac{\mu+n_2}{(\mu+n)(\mu+n_1)^2} \right) \right] \right\} + c.c.$$

$$Q_{LM} = Q_{LM}^{(0)} + [Q_{LM}^{(1)} e^{i\omega} + c.c.] + [Q_{LM}^{(2)} e^{2i\omega} + c.c.]$$

(A.11)

where

$$Q_{LM}^{(6)} = \frac{aR}{1+t^2} \left\{ 1 + \frac{t^2-1}{t^2+1} \left[ \frac{3}{4} \xi \xi^* + \frac{1}{4} (a \xi^{*''} \xi' + a \xi'' \xi^*) \right] \right. \\ \left. + \frac{a^2 \xi'' \xi^{*''}}{4} \right] + \frac{t^4 - 6t^2 + 1}{(1+t^2)^2} \left[ \frac{3}{4} \xi \xi^* - \frac{1}{4} (a \xi^{*''} \xi' + a \xi'' \xi^*) \right] \\ \left. + \frac{2t}{1+t^2} a h' - \frac{\Im(a \xi^{*''} \xi')}{1+t^2} \left[ 1 - 4t \frac{t^2-1}{t^2+1} \right] \right\}$$

$$Q_{LM}^{(1)} = \frac{aR}{(1+t^2)^2} \left[ (t^2-1) \xi' + it (a \xi'' + \xi') \right]$$

$$Q_{LM}^{(2)} = \frac{aR}{2(1+t^2)^2} \left\{ -\frac{1}{2} (t^2-1) \left( \frac{7}{2} \xi'^2 - 4a' + a \xi'' \xi' + \frac{a^2}{2} \xi''^2 \right) \right. \\ \left. + \frac{t^4 - 6t^2 + 1}{1+t^2} \left( \frac{a^2}{4} \xi''^2 + \frac{a}{2} \xi'' \xi' + \frac{5}{4} \xi'^2 \right) + 2it \left( \left[ \frac{a}{2} (a'' + \frac{a'}{a} + \frac{3a}{a^2}) \right. \right. \right. \\ \left. \left. \left. - \xi'^2 - \frac{3}{2} a \xi'' \xi' \right] + \frac{t^2-1}{t^2+1} 2\xi' (a \xi'' + \xi') \right) \right\}$$

$$A_M = \sum_n A_{Mn}(a, \theta) e^{in\varphi}$$

(A.12)

where

$$A_{Mn}(a, \theta) = A_{M(n)}^{(1)} e^{i\theta} + A_{M(n)}^{(1)*} e^{-i\theta} + A_{M(n)}^{(2)} e^{2i\theta} + A_{M(n)}^{(2)*} e^{-2i\theta}$$

$$A_{M(n)}^{(1)} = \frac{4\pi^2 a R P'}{\alpha \rho^{1/2}} \left\{ \frac{t}{\mu+n} \left[ k_n - \frac{1}{4} \sum_{n_1 n_2} k_{n_1} \xi'_{n_2} \xi^*_{n_1+n_2-n} + \sum_{n_1} k_{n_1-n}^* \left( \frac{3}{4} \frac{dn_1}{a} \right) \right] \right\}$$

$$\begin{aligned}
& + \frac{dn_1}{4} - \frac{1}{8} \sum_{n_1, n_2} k_{n_1+n_2-n}^* \xi_{n_1}^1 \xi_{n_2}^1 \left] + \frac{i}{\mu+n} \left[ k_n - k_n \frac{a\mu'}{\mu+n} \right. \right. \\
& + \sum_{n_1} k_{n_1-n}^* \left( \frac{3}{4} \frac{dn_1}{a} + \frac{dn_1}{4} \right) - \frac{1}{4} \sum_{n_1, n_2} k_{n_1} (\xi_{n_2}^1 \xi_{n_1+n_2-n}^1 \\
& + a \xi_{n_2}^{\prime\prime} \xi_{n_1+n_2-n}^1 + a \xi_{n_1+n_2-n}^{\prime\prime} \xi_{n_2}^1) - \frac{1}{8} \sum_{n_1, n_2} k_{n_1+n_2-n}^* (\xi_{n_1}^1 \xi_{n_2}^1 \\
& + a \xi_{n_1}^{\prime\prime} \xi_{n_2}^1 + a \xi_{n_2}^{\prime\prime} \xi_{n_1}^1) + \frac{1}{4} \sum_{n_1, n_2} k_{n_1-n}^* \xi_{n_1-n_2}^1 a \xi_{n_2}^{\prime\prime} \\
& \times \left( 1 + \frac{2(\mu+n_2)}{2\mu+n_1} \left( 1 - \frac{\mu+n_2}{2\mu+n_1} \right) \right) + \frac{3}{2} \sum_{n_1, n_2} k_{n_1-n}^* \xi_{n_1-n_2}^1 \xi_{n_2}^1 \frac{\mu+n_2}{2\mu+n_1} \\
& \left. \times \left( 1 - \frac{\mu+n_2}{2\mu+n_1} \right) \right] \} \\
A_M^{(2)} = & - \frac{4\mu^2 a R P'}{\alpha \rho^2} \frac{1}{2\mu+n} \left[ t \sum_{n_1} k_{n_1} \xi_{n-n_1}^1 + \frac{i}{2} \sum_{n_1} k_{n_1} (\xi_{n-n_1}^1 \right. \\
& \left. + a \xi_{n-n_1}^{\prime\prime} - 2 \xi_{n-n_1}^1 \frac{a\mu'}{2\mu+n}) \right]
\end{aligned}$$

where the quantity with subscript  $n$  denotes the Fourier component of the expansion of the corresponding quantity in the major azimuth of the torus,

$$\mu_j = \mu + 2\alpha R \equiv \frac{Rj}{\alpha \rho^2}, \quad B_s = \frac{\alpha \rho^2}{2\pi a}, \quad t = \gamma S, \quad S = \frac{a \rho^2}{\gamma}$$

The rectification function  $h(a, \varphi)$  in Eq. (A.11) is given by

$$\frac{\partial h}{\partial \varphi} = -R(\alpha - \alpha_0) - \frac{H}{2} \left[ \xi \xi^* - (\xi \xi^*)^{(0)} \right] + \frac{1}{4} \left[ i \left( \xi^* \frac{\partial \xi}{\partial \varphi} - \xi \frac{\partial \xi^*}{\partial \varphi} \right) - i \left( \xi^* \frac{\partial \xi}{\partial \varphi} - \xi \frac{\partial \xi^*}{\partial \varphi} \right)^{(0)} \right]$$

The equations for  $\xi$  and  $\alpha$  are the same as those obtained in Ref. [3]. The expressions for  $W^{(0)}$ ,  $Q_{1M}$  and  $A_M$  given above completely describe the solution of the equation for small oscillations (A.9), thereby providing the necessary stability criterion for the ballooning modes in toroidal magnetic traps with an arbitrary shape of the magnetic axis.

#### REFERENCES

- [1] SHAFRANOV, V.D., Nucl. Fusion 8 (1968) 253.
- [2] MIKHAILOVSKIY, A.B., SHAFRANOV, V.D., Zh. Eksp. Teor. Fiz. 66 (1974) 190.
- [3] MIKHAILOVSKIY, A.B., ABURDZHANIYA, Kh.D., Plasma Phys. 21 (1979) 109.
- [4] MIKHAILOVSKIY, A.B., ABURDZHANIYA, Kh.D., Fiz. Plazmy 4 (1978) 198.
- [5] MERCIER, C., in Stellarators with Three-Dimensional Magnetic Axes (Proc. Int. Symp. Sendai, Japan, 1979) Tohoku University (1979) 29.
- [6] FUNATO, Ya., et al., J. Phys. Soc. Jpn. 48 (1980) 709.
- [7] GLAGOLEV, V.M., KADOMTSEV, B.B., SHAFRANOV, V.D., TRUBNIKOV, B.A., in Controlled Fusion and Plasma Physics (Proc. 10th Europ. Conf. Moscow, 1981) Vol. 1 (1981) E-8.
- [8] MIKHAILOVSKIY, A.B., Zh. Eksp. Teor. Fiz. 64 (1974) 536.
- [9] MIKHAILOVSKIY, A.B., Nucl. Fusion 14 (1974) 483.
- [10] POGUTSE, O.P., YURCHENKO, E.I., Fiz. Plazmy 5 (1979) 789.
- [11] MIKHAILOVSKIY, A.B., DEMCHENKO, V.V., in Controlled Fusion and Plasma Physics (Proc. 10th Europ. Conf. Moscow, 1981) Vol. 1 (1981) B-11.
- [12] MIKHAILOVSKIY, A.B., YURCHENKO, E.I., I.V. Kurchatov Institute Preprint IAE-3505/6, Moscow (1981); Plasma Phys. (in press).
- [13] ZAKHAROV, L.E., in Plasma Physics and Controlled Nuclear Fusion Research (Proc. 7th Int. Conf. Innsbruck, 1978) Vol. 1, IAEA, Vienna (1979) 689.
- [14] MERCIER, C., ibid., 701.
- [15] SYKES, A., ibid., 625.
- [16] CONNOR, I.W., et al., Phys. Rev. Lett. 40 (1978) 396.
- [17] ZAKHAROV, L.E., SHAFRANOV, V.D., in Plasma Physics and Controlled Nuclear Fusion Research (Proc. 6th Int. Conf. Berchtesgaden, 1976) Vol. 2, IAEA, Vienna (1977) 155.



## PLASMA HEATING BY ANOMALOUS ABSORPTION OF LARGE-AMPLITUDE ALFVÉN (ION CYCLOTRON) WAVES

A.G. DIKIJ, S.S. KALINICHENKO, A.I. LYSOJVAN,  
V.S. MIKHAIJENKO, N.I. NAZAROV, A.I. PYATAK,  
V.L. SIZONENKO, A.S. SLAVNYI, K.N. STEPANOV,  
V.F. TARASENKO<sup>†</sup>, O.M. SHVETS

Institute of Physics and Technology,  
The Ukrainian Academy of Sciences,  
Khar'kov,  
Union of Soviet Socialist Republics

### Abstract

PLASMA HEATING BY ANOMALOUS ABSORPTION OF LARGE-AMPLITUDE ALFVÉN (ION CYCLOTRON) WAVES.

The paper deals with experimental and theoretical investigation of RF production and turbulent heating of plasma with Alfvén (ion cyclotron) waves producing small-scale beam or parametric instabilities with a high level of turbulence. — The levels of lower hybrid, ion-cyclotron, and ion-ion sound turbulences and the heating rates of electrons and ions are estimated. The results of experimental studies on the RF production of a currentless hydrogen-deuterium plasma with a controlled ratio of densities of both ion species in Uragan-2 stellarator by alternating electric fields with  $\omega \sim \omega_{ci}$ . The anomalously fast heating of hydrogen ions is investigated in cyclotron resonance conditions for majority protons and minority deuterons. The neutral-gas ionization and the fast heating of non-resonant ions may be naturally explained by the development of ion-ion- and ion-electron-type plasma instabilities in the pump-wave field.

### 1. INTRODUCTION

Electron oscillations relative to the ions in large-amplitude low-frequency electromagnetic-wave fields are known to give rise to beam-like small-scale instabilities, whose characteristic frequencies and growth rates are of the order of the lower hybrid frequency [1]. The saturation of these instabilities is due to the non-linear motion of the electrons. This paper shows that if the relative velocity of the electrons with respect to the ions in the pump-wave field exceeds the ion thermal velocity, then, together with the lower hybrid instabilities, long-wavelength ion-cyclotron instabilities develop and the turbulence level of these considerably exceeds the lower hybrid turbulence level.

---

<sup>†</sup> Deceased.

In a plasma with two ion species in a pump-wave field, the ions of one species can oscillate with respect to the ions of other species, which may lead to ion-ion beam instabilities [2, 3]. An important feature of some of these instabilities is the fact that the electron contribution to dispersion equation and non-linear damping of oscillation is negligible and the saturation of the oscillations is determined by the non-linear terms in the ion equations of motion. In these cases, the level of ion-ion turbulence in a plasma with transverse current will be considerably higher, which will lead to rapid damping of the pump wave and turbulent heating of the plasma. In this paper, such instabilities are studied and their level at the non-linear stage is estimated.

This paper gives the results from experiments dealing with plasma production by an RF-method in the Uragan-2 stellarator. The ionization of the gas may be explained by turbulent electron heating in electrical fields of lower hybrid and ion-ion sound small-scale plasma oscillations developing in the electrical field of the pump wave.

The experimental results from Uragan-2 on ion cyclotron plasma heating show that there is anomalously fast hydrogen heating in resonance conditions for majority protons and for minority deuterons. The observed heating of the main component (hydrogen) during a time considerably shorter than the time of energy transfer from deuterons to protons due to Coulomb collisions may be attributed to the development of the abovementioned plasma instabilities in the pump-wave field.

## 2. LONG-WAVELENGTH ION-CYCLOTRON INSTABILITY

If the pump wave frequency  $\omega_0$  is low compared with the growth rate of the instabilities that are excited, then the relative velocity of electrons and ions,  $\vec{u} = \vec{u}_e - \vec{u}_i$  may be regarded as constant. In this case, the dispersion equation of the longitudinal ion-cyclotron oscillations has the following form:

$$1 + k^2 \lambda_{Di}^2 + \frac{T_i}{T_e} \left[ 1 + i\sqrt{\pi} Z_e W(Z_e) \right] - \sum_{n=-\infty}^{\infty} A_n(a_i) \frac{\omega}{\omega - n\omega_{ci}} = 0 \quad (2.1)$$

where

$$Z_e = (\omega - \vec{k} \cdot \vec{u}) / \sqrt{2} k_{\parallel} v_{Te}, \quad A_n(a_i) = \exp(-a_i) I_n(a_i) \\ \sqrt{a_i} = k_{\perp} \rho_{Li} = k_{\perp} v_{Ti} / \omega_{ci}, \quad \lambda_{Di} = (T_i / 4 \pi e^2 n_0)^{1/2}$$

For the oscillations considered,  $k_{\perp} \sim \omega_{ci}/v_s$  ( $v_s = \sqrt{T_e/m_i}$  is the ion sound velocity),  $k_{\parallel}/k_{\perp} \sim (u/v_{Ti}) \ll 1$ , so that  $k_{\perp} \rho_{Li} \approx T_i/T_e \lesssim 1$ . In this case,  $\omega = n\omega_{ci} + \delta\omega$ , ( $|\delta\omega| \ll \omega_{ci}$ ), where

$$\delta\omega = n\omega_{ci} \frac{T_e}{T_i} \frac{1}{n!} \left(\frac{1}{2}k^2 \rho_{Li}^2\right)^n [1 + i\sqrt{\pi} Z_e W(Z_e)]^{-1}, \quad Z_e = \frac{n\omega_{ci} - \vec{k} \cdot \vec{u}}{\sqrt{2} k_{\perp} v_{Te}} \quad (2.2)$$

By order of magnitude, we have at  $u \gtrsim v_{Ti}$

$$\text{Re } \delta\omega \approx \gamma = \text{Im } \omega \approx \omega_{ci} (T_i/T_e)^{n-1} \quad (2.3)$$

If  $T_i \approx T_e$ , then

$$\text{Re } \delta\omega \sim \gamma \sim \omega_{ci} \quad (k_{\perp} \rho_{Li} \approx 1, Z_e \approx 1) \quad (2.4)$$

This instability saturates at the oscillation level

$$W \sim n_0 T_i \quad (2.5)$$

when the perturbation of the ion distribution function becomes, by order of magnitude, comparable with the unperturbed distribution function. The same estimate may be obtained on the basis of the weak-turbulence theory.

The rate of ion and electron heating may be estimated from the quasi-linear theory:

$$\begin{aligned} n_0 \frac{\partial T_{i\parallel}}{\partial t} &\approx \omega_{ci} \frac{T_i}{T_e} W \\ n_0 \frac{\partial T_{e\parallel}}{\partial t} &\approx \gamma \frac{u}{v_s} W \quad (T_e \geq T_i) \end{aligned} \quad (2.6)$$

If  $u \lesssim v_{Ti}$  the ion cyclotron instability considered becomes more short-wave its growth rate, turbulence level, and plasma heating rate decrease [4, 5]:

$$\text{Re } \delta\omega \sim \omega_{ci} (1/k\rho_{Li}) \sim (u/v_{Ti}) \omega_{ci}, \quad \gamma \approx (T_i/T_e) \text{Re } \delta\omega$$

$$\frac{W}{n_0 T_i} \approx \frac{T_i}{T_e} \left(\frac{u}{v_{Ti}}\right)^4 \frac{1}{\ln(v_{Ti}/u)}, \quad n_0 \frac{\partial T_{e\parallel}}{\partial t} \approx \gamma W, \quad n_0 \frac{\partial T_{i\parallel}}{\partial t} \approx \gamma \frac{T_i}{T_e} W \quad (2.7)$$

If the pump-wave frequency  $\omega_0 \approx \omega_{ci}$ , then the beam instabilities considered become parametric [6]:

$$\begin{aligned} \gamma &\sim (u/v_{Ti})\omega_{ci} & (u \lesssim v_{Ti}) \\ \gamma &\sim (v_{Ti}/u)\omega_{ci} & (u \gtrsim v_{Ti}) \end{aligned} \quad (2.8)$$

### 3. LOWER HYBRID INSTABILITIES IN A PLASMA WITH TWO ION SPECIES

The dispersion equation for such oscillations has the form:

$$\begin{aligned} k^2 \lambda_{D1}^2 + \frac{T_1 n_e}{T_2 n_1} [1 + i\sqrt{\pi} Z_e W(Z_e)(1 - k^2 \rho_{Le}^2)] \\ + 1 + i\sqrt{\pi} Z_1 W(Z_1) + \eta[1 + i\sqrt{\pi} Z_2 W(Z_2)] = 0 \end{aligned} \quad (3.1)$$

where

$$Z_{1,2} = (\omega - \vec{k} \cdot \vec{u}_{1,2}) / \sqrt{2} k_{\parallel} v_{T1,2}, \quad \eta = \frac{n_1 T_1}{n_2 T_2}$$

The subscripts '1' and '2' denote the ion species.

The instability threshold for the oscillations with  $Z_e \gg 1$  is lower than that for  $Z_e \lesssim 1$ . For  $Z_e \gg 1$ , Eq. (3.1) assumes the form

$$q + 1 + i\sqrt{\pi} Z_1 W(Z_1) + \eta[1 + i\sqrt{\pi} Z_2 W(Z_2)] = 0 \quad (3.2)$$

where  $q = k^2 \lambda_{D1}^2 (1 + \omega_{pe}^2 / \omega_{ce}^2)$ . Putting  $\gamma = 0$  and  $q \ll 1$ , we obtain the equations determining the boundaries of the instability region:

$$\begin{aligned} Z_1 \exp(-Z_1^2) + Z_2 \exp(-Z_2^2) = 0, \\ 1 - \Phi(Z_1) + \eta[1 - \Phi(Z_2)] = 0 \end{aligned} \quad (3.3)$$

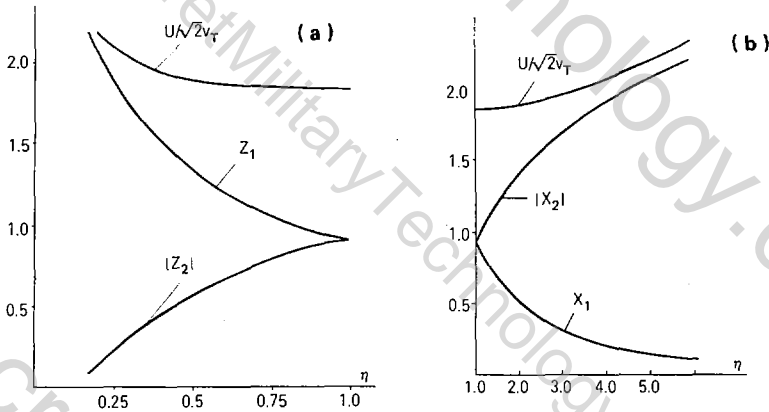


FIG.1. Dependence of solutions of Eq.(3.3) and of ratio of threshold velocity to  $\sqrt{2} v_T$  on parameter  $\eta$  (for  $T_1 = T_2 = T$ ) a)  $0 \leq \eta \leq 1$ ; b)  $\eta \geq 1$ .

where

$$\Phi(Z) = -2Z \exp(-Z^2) \int_0^Z \exp(t^2) dt$$

Figure 1 shows the solutions of Eqs (3.3) as functions of the parameter  $\eta$  which can be used to determine the instability threshold  $u_{cr} = |u_1 - u_2| = \sqrt{2} |Z_1 v_{T1} - Z_2 v_{T2}|$  for various ratios of densities and temperatures of ion plasma components. If the thermal velocities of different ion species are the same ( $v_{T1} = v_{T2} = v_T$ ) then  $\eta = 1$  will correspond to the threshold of the current velocity. In this case, the densities of both ion components should fulfill the condition  $n_1 = n_2 m_1/m_2$ . Then,  $Z_1 = |Z_2| = Z_0 = 0.9$  and the current velocity at the boundary of the instability region is  $u_{cr} = 2\sqrt{2} Z_0 v_T$ . If  $v_{T2} \ll v_{T1}$ , (the subscript '1' is taken to refer to the main plasma), then the instability threshold lies in the region of large  $\eta$ :

$$\begin{aligned} Z_1 &= \eta \sqrt{\eta/2} \exp(-\eta/2), & |Z_2| &= \sqrt{\eta/2} \\ u_{cr} &= v_{T1} \sqrt{\eta} [\eta \exp(-\eta/2) + v_{T2}/v_{T1}] \end{aligned} \quad (3.4)$$

The extreme value  $\eta = \eta_m$  is found from the equation  $\eta_m^2 \exp(-\eta_m/2) = v_{T2}/v_{T1}$  and is equal to

$$\eta_m = 2 \ln \left\{ 4 \frac{v_{T1}}{v_{T2}} \ln^2 \left[ 4 \frac{v_{T1}}{v_{T2}} \ln^2 \left( 4 \frac{v_{T1}}{v_{T2}} \ln^2 \frac{v_{T1}}{v_{T2}} \right) \right] \right\}$$

The minimum threshold value of the current velocity and  $n_2/n_1$  are determined by the formulas

$$u_{cr} = v_{T2} \sqrt{\eta_m}, \quad n_2/n_1 = (T_2/T_1) \eta_m \quad (3.5)$$

It is seen from formulas (3.5) that the boundary of the instability region may be lower than the ion thermal velocity of the main ions.

If the velocity  $u$  is somewhat higher than the boundary value, growth rate and frequency of the oscillation are:

$$\gamma \approx \omega(\Delta u/u), \quad \omega \approx kv_{Ti} \sim \omega_{LH} \sqrt{\Delta u/u} \quad (3.6)$$

where

$$\omega_{LH} = \omega_{pi} (1 + \omega_{pe}^2/\omega_{ce}^2)^{-1/2}$$

Note that if  $u > u'_{cr} \sim 2 u_{cr}$ , ( $T_e \approx T_i$ ), it is not only oscillations with  $Z_e \gg 1$  but also those with  $Z_e \leq 1$  that are unstable. Their frequency and growth rate as determined from the equation

$$k^2 \lambda_{D1}^2 + \frac{n_e T_1}{n_1 T_e} + 1 + i\sqrt{\pi} Z_1 W(Z_1) + \eta[1 + i\sqrt{\pi} Z_2 W(Z_2)] = 0 \quad (3.7)$$

are of the same order of magnitude:

$$\omega \approx \gamma \approx kv_{Ti}, \quad (k\lambda_{D1} \leq 1, T_e \approx T_i, \eta \approx 1) \quad (3.8)$$

It is natural to call this oscillation branch 'ion-ion sound' wave. With  $\eta$  decreasing (the density of the ions of species '2' is low), the threshold value of the current velocity increases monotonically:

$$u'_{cr} = \sqrt{2} v_{T1} \sqrt{\ln(1/\eta)}, \quad (\eta \ll 1) \quad (3.9)$$

On moving away from this boundary, the growth rate increases:

$$\frac{\gamma}{\omega} = -\frac{\sqrt{\pi}}{2} \frac{\omega^2}{k^2 v_{T1}^2} [Z_1 \exp(-Z_1^2) + \eta |Z_2|] \quad (3.10)$$

By order of magnitude, for  $\Delta u/v_{T2} \lesssim \ln(1/\eta)$ , we have

$$\gamma/\omega_{LH} \approx \eta \sqrt{\ln(1/\eta)} \quad (3.11)$$

In the region  $u \geq v_{T2} (n_2/n_1)^{1/3}$ , the kinetic instability with growth rate (3.11) becomes a hydrodynamic one, for which  $|Z_{1,2}| \gg 1$  and

$$1 + \frac{\omega_{pe}^2}{\omega_{ce}^2} - \frac{\omega_{p1}^2}{(\omega - ku_1)^2} - \frac{\omega_{p2}^2}{(\omega - ku_2)^2} = 0 \quad (3.12)$$

whence

$$\gamma \approx \omega_{LH} (n_2/n_1)^{1/3} \quad (n_2/n_1 \ll 1) \quad (3.13)$$

The oscillations of the ion-ion sound type at  $u \sim v_{Ti}$ , ( $u - u'_{cr} \sim u'_{cr}$ ) are saturated as a result of ion non-linearities at  $W \sim n_0 T$ , ( $T_1 \sim T_2 \sim T_e$ ).

The scattering of both ion species from turbulent lower hybrid pulsations and ion-ion sound pulsations should lead to fast ion heating. The heating rate, which may be estimated from the quasi-linear equations, is given by:

$$n_0 \frac{dT_{ii}}{dt} \approx \omega_{pi} W \approx \omega_{pi} n_0 T_i \quad (3.14)$$

Turbulent plasma heating is accompanied by damping of the pump wave. The rate of the absorption of the wave is determined from energy balance equation:

$$\gamma_{eff} W_0 = n_0 \frac{dT_i}{dt} \quad (3.15)$$

where  $W_0$  is the energy density of the pump wave. If the pump wave is a fast magnetosonic or ion cyclotron wave with a frequency  $\omega_0 \lesssim \omega_{ci}$ , then

$$W_0 \sim \frac{m_i u_i^2}{4} \quad (3.16)$$

Using (3.14), we find for the ion-ion sound that  $\gamma_{\text{eff}} \sim \omega_{\text{pi}}$ , implying that these waves are dissipated most strongly (skin effect). If the pump wave is weakly absorbed, the plasma heating is performed in regimes with  $u$  close to  $u_{\text{cr}}$  and  $\gamma_{\text{eff}} < \omega_0$ .

#### 4. PRODUCTION OF HYDROGEN-DEUTERIUM PLASMA BY ALFVÉN (AW) WAVES (ION CYCLOTRON WAVES, ICW) IN THE URAGAN-2 STELLARATOR

Experiments were performed in the Uragan-2 stellarator on the production of currentless plasma with a controlled ratio of deuterium and hydrogen densities ( $n_{\text{D}}/n_{\text{H}} = 0.05-0.4$ ), using resonant excitation of ICW in the cyclotron resonance region for deuterium and hydrogen ions. The RF power was coupled from two generators that were tuned to two antennas located in the straight sections of the vessel [7]. With continuous deuterium injection to  $\rho_0 \approx 7 \times 10^{-5}$  torr, the RF power from generator 1 ( $P_{1\text{RF}} \sim 200$  kW,  $f_1 = 10$  MHz) was coupled to a frame-type antenna [8] with a broad spectrum of toroidal wave

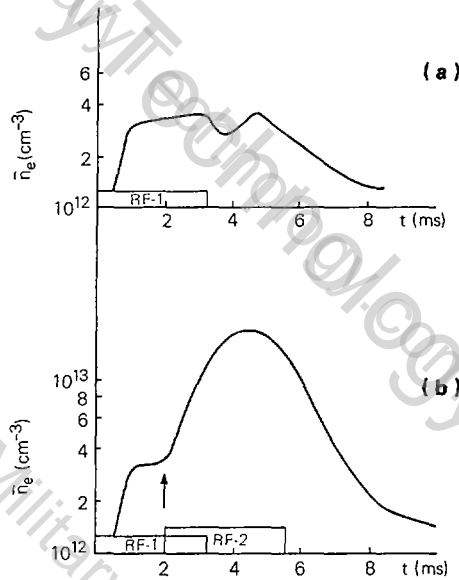


FIG. 2. Time dependence of plasma density produced in the ICR regime: a) deuterium plasma production in range  $\omega_1 \approx \omega_{\text{cD}}$ ; b) hydrogen-deuterium plasma production ( $n_{\text{D}}/n_{\text{H}} \sim 0.2$ ) in conditions of the H<sub>2</sub>-puffing in D-plasma during  $t = 100 \mu\text{s}$  (H<sub>2</sub>-puffing start indicated by arrow) with combined operation of two RF generators ( $\omega_1 \approx \omega_{\text{cD}}$ ,  $\omega_2 \approx \omega_{\text{cH}}$ ,  $B_0 \approx 14$  kG).

numbers of the emitted RF-field ( $\lambda_{\parallel} \approx 10^2 - 10^3$  cm). At a magnetic field of  $B_0 \geq 13$  kG (ICR resonance region for deuterium,  $\omega_1 \approx \omega_{CD}$ ) a currentless deuterium plasma was produced with a density of  $\bar{n}_e \geq 3 \times 10^{12}$  cm $^{-3}$  (Fig.2). When a stationary value of the density was achieved, the RF generator 2 was switched on ( $P_{2RF} \sim 300$  kW,  $f_2 = 19.3$  MHz), coupled to a slot-type antenna [9]. The RF power spectrum emitted by this antenna was located in the  $\lambda_{\parallel} \approx 30 - 80$  cm wavelength band. At the moment at which generator 2, operating at ICR frequency for hydrogen ( $\omega_2 \approx \omega_{CH}$ ), was switched on, an amount of neutral hydrogen (0.1--0.2 cm $^3$ ) was injected into the plasma far from the location of the launchers. The plasma density increased and attained a value of  $\bar{n}_e = (\bar{n}_H + \bar{n}_D) \approx 2 \times 10^{13}$  cm $^{-3}$  (Fig. 2b). Controlled hydrogen puffing during the RF pulse allowed the hydrogen-deuterium plasma to be obtained with the desired ratio of hydrogen to deuterium ion densities.

The ionization mechanism for the neutral gas may be explained as follows. At the moment at which the RF pulse is switched on, gas breakdown occurs in the immediate vicinity of the antenna, where a rare (up to  $\bar{n}_e \sim 10^6$  cm $^{-3}$ ) plasma is produced and subsequently spread out along the magnetic field lines of the stellarator.

At this stage of the RF discharge, when resonant excitation of AW(ICW) is impossible, the presence of a strong longitudinal alternating electrical field ( $\tilde{E}_z > 50$  V · cm $^{-1}$ ) near the antenna leads to very high electron oscillation speeds along the magnetic field,  $u_{\parallel}^e = e\tilde{E}_z/m_e\omega \sim 10^9$  cm · s $^{-1}$ . The energy of these oscillations is sufficient to cause RF breakdown and ionization of the neutral gas by electron impact. (Note also that if  $\omega \approx \omega_{ci}$  the ion oscillation speeds in very high transverse electrical fields near the antenna ( $E_{\perp} \sim 700$  V · cm $^{-1}$ ) may achieve a value of  $u_{\perp}^i = eE_{\perp}/m_i(\omega - \omega_{ci}) > 10^8$  cm · s $^{-1}$  and ion impact ionization may be possible [10].) On the other hand, the presence of such strong alternating electrical fields should lead to powerful parametric instabilities, and, as a result, to turbulent electron heating [11, 12]. With the plasma density increasing ( $\bar{n}_e > 10^6$  cm $^{-3}$ ), the  $E_z$  component will excite a slow electrostatic mode in the plasma with  $k_{\perp}^2 = k_{\parallel}^2(\omega_{pe}^2/\omega^2 - 1)$ , which can propagate deep into the rare plasma and heat the electrons by the development of parametric and beam instabilities, thereby ensuring neutral-gas ionization. With further increase of the electron density ( $\bar{n}_e > 10^{11}$  cm $^{-3}$ ), the mechanism of the neutral-gas ionization may be also linked with the subsequent excitation, in the plasma, of toroidal AW(ICW) modes with  $k_{\parallel} = \ell/R$  and  $\ell = 1, 2, \dots$  [7]. In this case, in regions of local Alfvén resonance, a sharp increase in the electrical-field intensities  $\tilde{E}_z$  and  $\tilde{E}_{\parallel}$  takes place [13], which may lead to small-scale instabilities and plasma turbulence at the frequencies  $\omega \sim \omega_{LH}$  and  $\omega \sim \omega_{ci}$  described above. The turbulent heating of the plasma electrons ensures further ionization of the neutral gas in the entire stellarator confinement volume. The electron temperature at this stage was kept at a level of  $T_e \sim 30$  eV. The estimated values of the

electron and ion transverse velocities,  $u_{\perp}^e \approx u_{\perp}^i$ , show that the instability condition  $u_{\perp} \geq v_s \sim v_{Ti} \approx 4 \times 10^6 \text{ cm} \cdot \text{s}^{-1}$  is fulfilled. There is experimental evidence for a turbulent noise spectrum with frequencies  $\omega \sim \omega_{LH}$  to be present during the ionization phase at the time of the RF pulse [14].

It should be noted that Cherenkov absorption of the AW(ICW) RF field energy by electrons is weak because the longitudinal phase velocities of these waves,  $v_{ph\parallel} = \lambda_{\parallel} f \approx 10^9 - 10^{10} \text{ cm} \cdot \text{s}^{-1}$  are high compared with the electron thermal velocity,  $v_{Te} \approx 2 \times 10^8 \text{ cm} \cdot \text{s}^{-1}$ . These waves can, however, accelerate high-energy electrons from the 'tail' of the distribution function with energies of  $E \approx 10 \text{ keV}$ . Indirect evidence for this fact is provided by the plasma density increase after switching off the RF pulse (Fig. 2a), which may be due to the ionization of neutral gas released from the vacuum vessel walls by a group of electrons accelerated up to some keV.

The plasma production in the stellarator (in open traps strong RF fields with  $\omega \sim \omega_{ci}$  also lead to high-density plasma production [19, 20]) by strong low-frequency alternating electrical fields may be regarded as a new type of discharge which it would be natural to call *beam-plasma RF discharge* (by analogy with the beam-plasma discharge [15–18] when the plasma is produced through neutral-gas ionization by electrons heated in the turbulent pulsations of Langmuir oscillations excited by an electron beam).

## 5. HEATING OF TWO-ION-SPECIES CURRENTLESS PLASMA IN THE URAGAN-2 BY LARGE-AMPLITUDE AW(ICW)

RF heating experiments were performed in a dense ( $\bar{n}_e \sim 10^{13} \text{ cm}^{-3}$ ), currentless hydrogen plasma with a small (up to 10%) minority of deuterium ions. RF power coupling was accomplished by operating two RF generators simultaneously at the deuterium and hydrogen ion gyrofrequencies ( $\omega_1 \approx \omega_{cD}$ ,  $\omega_2 \approx \omega_{cH}$ ). Significant heating of both ion species was observed in a magnetic field of  $B_0 = 13.2 \text{ kG}$ , corresponding to the ICR region for deuterons ( $\Omega_{1D} = B_{1cD}/B_0 = 0.99$ ) and for protons ( $\Omega_{2cH} = B_{2cH}/B_0 = 0.96$ ) (Fig. 3). The proton and deuteron energy spectra measured by a charge-exchange technique differed from Maxwellian ones but they had weaker 'tails', compared with the low-density plasma regime [21]. It is appropriate to characterize this ion energy distribution as an average energy defined as follows [22, 23]:

$$T_{i1} = \frac{2}{3} \frac{\int E f_1(E) dE + \int E f_2(E) dE}{\int f_1(E) dE + \int f_2(E) dE}$$

where  $f_{1,2}(E) = dn_{1,2}/dE$  are the distribution functions of low-energy (subscript 1) and high-energy (subscript 2) groups of ions. An investigation of the time

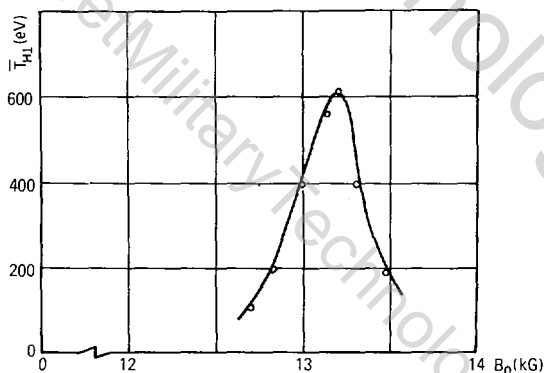


FIG.3. Dependence of average energy of hydrogen ions  $\bar{T}_{H1}$  on longitudinal magnetic field  $B_0$  with combined operation of two RF generators ( $n_D/n_H \sim 0.05-0.1$ ).

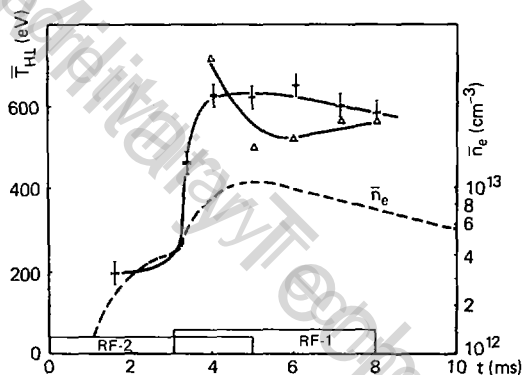


FIG.4. Time dependence of average proton energy  $\bar{T}_{H1}$  (horizontal symbols), deuteron energy  $\bar{T}_{D1}$  (triangles) and the plasma density  $\bar{n}_e$  during ICRH of both ion species ( $B_0 = 13.2$  kG).

dependence of the average energy of both ion species showed that, during the operation of RF generator 2 only (Fig. 4), the proton energy reached a value of  $\bar{T}_{H1} \approx 200$  eV very rapidly ( $t < 100 \mu s$ ) and remained virtually unchanged until the moment when the RF generator 1 was switched on. RF power input when the two RF generators were operating simultaneously at the cyclotron frequencies of the hydrogen and deuterium ions led to an additional heating of both ion components and allowed a currentless plasma with parameters  $\bar{T}_{H1} \sim \bar{T}_{D1} \sim 600$  eV and  $\bar{n}_e \approx 10^{13} cm^{-3}$  to be obtained. Besides, the average proton energy exceeded the average deuteron energy virtually during the whole heating period (as in the low-density plasma regime [21]) and was linearly dependent on the RF power of generator 1 without saturation being reached (Fig. 5).

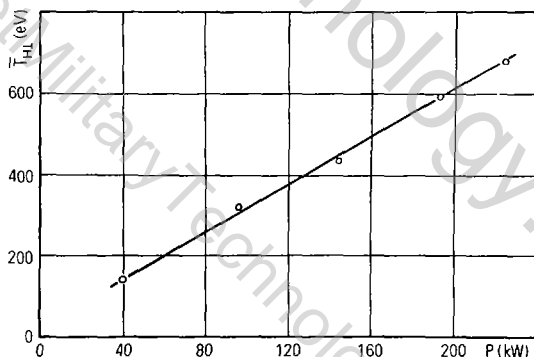


FIG. 5. Hydrogen ion heating versus the RF power fed into plasma at deuterium ICR frequency,  $\omega_1 \approx \omega_{cD}$ ,  $B_0 = 13.2$  kG.

The heating of hydrogen ions up to 200 eV in the initial stage (Fig. 4) may be attributed to strong cyclotron absorption of the pump wave although turbulent heating due to ion acceleration by the electrical field of lower hybrid, ion-ion beam or parametric ion-cyclotron turbulences as considered above (the observed heating period of  $\lesssim 0.1$  ms is ten times shorter than the ion-ion collision time) should not be ruled out. Hydrogen heating during operation of RF generator 1, operating at a frequency close to the deuterium cyclotron frequency, cannot be explained by any linear mechanism of pump wave absorption: it is natural to link it with the presence of plasma instabilities with two ion species which were considered in Sections 2 and 3. The heating period was found to be more than ten times shorter than the time of energy transfer from deuterons to protons as a result of Coulomb collisions ( $\sim 10$  ms). (The effect of anomalously fast heating of non-resonant ions in ICR conditions for the other ion species was discovered earlier in the open plasma traps [24] and in the low-density currentless plasma of the Uragan-2 stellarator [22]).

## 6. CONCLUSIONS

1. Experiments on RF plasma production by alternating electrical fields with  $\omega \sim \omega_{ci}$  allowed, in the currentless regime of the Uragan-2 stellarator, the creation of a hydrogen-deuterium plasma with a density of  $\bar{n}_e \sim 2 \times 10^{13} \text{ cm}^{-3}$  when the gas puffing was used (in optimum conditions, this method led to a hydrogen plasma of  $\bar{n}_e \geq 7 \times 10^{13} \text{ cm}^{-3}$ ).

2. Using ICR for both ion species and supplying a total power of about 500 kW from two generators gave rise, in Uragan-2, to a currentless hydrogen-deuterium plasma with an ion temperature of  $\sim 600$  eV and  $\bar{n}_e \approx 10^{13} \text{ cm}^{-3}$ .

3. Theoretical estimates obtained for the level of low hybrid, ion-ion sound, and ion-cyclotron turbulences and estimates of the electron and ion heating rates allow us to attribute the observed heating of electrons, the neutral-gas ionization and fast heating of non-resonant ions to the development of these instabilities.

#### ACKNOWLEDGEMENT

The authors wish to thank Dr. V.D. Yegorenkov for valuable discussions.

#### REFERENCES

- [1] GRIGOR'EVA, L.I., et al., in Plasma Physics and Controlled Nuclear Fusion Research (Proc. 4th Int. Conf. Madison, 1971) Vol.3, IAEA, Vienna (1972) 573.
- [2] SIZONENKO, V.L., STEPANOV, K.N., *Pis'ma Zh. Ehksp. Teor. Fiz.* 8 (1968) 592.
- [3] KADOMTSEV, B.B., *Fizika plazmy i problema upravlyaemykh termoyadernykh reaktсий* (Plasma Physics and the Problem of Controlled Thermonuclear Reactions), Vol.4, Publishing House of the Academy of Sciences of the USSR, Moscow (1959) 364 (in Russian).
- [4] GREKOV, D.L., et al., in Heating in Toroidal Plasmas (Proc. 2nd Int. Grenoble-Varena Symp. Como, 1980) Vol.1 (1980) 529.
- [5] MIKHAILENKO, V.S., STEPANOV, K.N., *Plasma Phys.* 23 (1981) 1165.
- [6] KITSENKO, A.B., PANCHENKO, V.I., STEPANOV, K.N., *Zh. Tekh. Fiz.* 43 (1973) 1425.
- [7] KALINICHENKO, S.S., et al., in Controlled Fusion and Plasma Physics (Proc. 9th Europ. Conf. Oxford, 1979) Vol.1 (1979) 19.
- [8] DIKIJ, A.G., et al., in Plasma Physics and Controlled Nuclear Fusion Research (Proc. 6th Int. Conf. Berchtesgaden, 1976) Vol.2, IAEA, Vienna (1977) 129.
- [9] SHVETS, O.M., et al., *Fiz. Plazmy* 7 (1981) 485.
- [10] MOJSEENKO, V.M., *Fiz. Plazmy* 6 (1980) 1174.
- [11] DUBOVOJ, L.V., SHVETS, O.M., *Izv. Akad. Nauk SSSR* 24 (1960) 1013.
- [12] SILIN, V.P., *Parametricheskoe vozdejstvie izlucheniya bolshoj moshchnosti na plazmu* (Parametric Effect of High-Power Radiation on a Plasma), Nauka, Moscow (1973) (in Russian).
- [13] DOLGOPOLOV, V.V., STEPANOV, K.N., *Nucl. Fusion* 5 (1965) 276.
- [14] PEREPELKIN, N.F., SHVETS, O.M., et al., in Controlled Fusion and Plasma Physics (Proc. 7th Europ. Conf. Lausanne, 1975) Vol.1 (1975) 146.
- [15] KHARCHENKO, I.F., FAJNBERG, Ya.B., et al., *Zh. Tekh. Fiz.* 31 (1961) 762.
- [16] KHARCHENKO, I.F., FAJNBERG, Ya.B., et al., in Plasma Physics and Controlled Nuclear Fusion Research (Proc. 1st Int. Conf. Salzburg, 1961) Vol.3, IAEA, Vienna (1962) 1101.
- [17] BEREZIN, A.K., FAJNBERG, Ya.B., et al., *At. Ehnerg.* 11 (1961) 493.
- [18] GETTY, D.W., SMULIN, L.D., *Phys. Rev. Lett.* 9 (1962) 3; *J. Appl. Phys.* 34 (1963) 3421.
- [19] NAZAROV, N.I., et al., *Zh. Tekh. Fiz.* 32 (1962) 536.
- [20] SHVETS, O.M., et al., *Zh. Tekh. Fiz.* 35 (1965) 2185; 39 (1969) 610.

- [21] SHVETS, O.M., et al., in Controlled Fusion and Plasma Physics (Proc. 10th Europ. Conf. Moscow, 1981) paper H-24p.
- [22] SHVETS, O.M., et al., Pis'ma Zh. Ehksp. Teor. Fiz. 34 (1981) 533.
- [23] HOSEA, J., et al., in Heating in Toroidal Plasmas (Proc. 3rd Varenna-Grenoble Int. Symp. Grenoble, 1982) paper C-1.
- [24] NAZAROV, N.I. YERMAKOV, A.I., TOLOK, V.T., Zh. Tekh. Fiz. 36 (1966) 612.

## THEORY AND SIMULATION OF RF HEATING AND CURRENT DRIVE

J.M. DAWSON, B.D. FRIED, G.J. MORALES,  
A.T. LIN, V.K. DECYK, M. CAPLAN  
Department of Physics,  
University of California,  
Los Angeles, California,  
United States of America

### Abstract

#### THEORY AND SIMULATION OF RF HEATING AND CURRENT DRIVE.

Four topics in RF heating and current drive are discussed. (1) Single-particle ICRH in a strongly inhomogeneous magnetic field, with constant inverse scale length of order of the ion cyclotron radius was studied. Because the ion cyclotron frequency is energy-dependent, there is no time-averaged energy gain unless the RF field amplitude exceeds a critical value  $E_c$ , above which the multiple resonances, arising from the anharmonicity of the motion, overlap, resulting in stochastic heating. (2) An extraordinary ECRH wave launched from the high field side with large angle of incidence is observed to convert completely into a backward electrostatic Bernstein wave at the upper hybrid layer. The mode-converted wave deposits its energy to the electrons at the electron cyclotron layer through resonant interactions dominated first by the Doppler broadening and later by the relativistic mass correction. (3) An electrostatic particle simulation code is used to study heating and current generation with lower-hybrid waves. The heating simulations are designed to examine the propagation of lower-hybrid waves with finite amplitude in an inhomogeneous medium and the mechanisms by which wave energy is absorbed. The current drive simulations examine the dynamics of current generation for a given initial electron velocity distribution and antenna profile. (4) To model gyrotron oscillators and amplifiers, an adaptation of a 1-2/2D finite-size particle code has been developed which allows interaction circuits with arbitrary wall profiles. The code was used to design and analyse a 60 GHz 270 kW gyrotron oscillator built by Hughes Aircraft Co. for ECRH heating of plasmas. Good agreement was obtained between simulation and experiment.

### 1. ICRH IN A STRONGLY INHOMOGENEOUS MAGNETIC FIELD

In high-beta mirrors and in surface magnetic field configurations, such as multipoles, the scale length  $L$  of the magnetic field variation in a direction perpendicular to the field can be comparable to the ion cyclotron radius  $r_c$ . We consider here the response of positive ions to an r.f.  $\omega$  field with frequency of order of the cyclotron frequency when the magnetic field is strongly inhomogeneous,  $L \lesssim r_c$ .

In a magnetic field  $\mathbf{B} = B(x)\hat{z}$ , trapped ions will execute periodic, drifting anharmonic orbits, with a frequency which is a function of the energy,  $\Omega = \Omega(W)$ . Because of the anharmonicity, a Fourier decomposition of the orbit  $\mathbf{x}(t)$  may include many harmonics of  $\Omega$ , so that resonant interaction with an r.f. field of frequency  $\omega$  can occur not only for ions whose energy  $W$  satisfies the condition for fundamental resonance,  $\omega = \Omega(W)$ , but also for harmonic resonances, i.e. for ions with energy  $W_n$  satisfying  $\omega = n\Omega(W)$ .

At resonance,  $W$  increases, which causes a change in  $\Omega$ ; after some increase  $\delta W$ , depending on the amplitude of the r.f. field,  $\Omega$  changes enough for the ion to be no longer in resonance and the heating stops. Analysis of both the phase and energy of the motion reveals a coherent behavior similar to the superadiabaticity of ions in a magnetic mirror. However, if the amplitude of the r.f. field is large enough to make  $\delta W > |W_{n+1} - W_n|$ , then the ion can move from one resonance to another and we have a transition from superadiabatic motion to stochastic heating.

We take a simple model,  $B_z(x) = B_0 e^{\kappa x}$  and assume the r.f. field to be uniform. In absence of the r.f., conservation of canonical momentum  $p_y$  reduces the problem to motion in the one-dimensional well  $U = \frac{1}{2} [1 - \exp(X)]^2$ , shown in Fig. 1, and we can solve for the unperturbed orbit in closed form:  $X = \kappa x = \log[(1-h^2)/(1+h\cos\theta)]$ ;  $Y = \kappa y = \tau - 2 \tan^{-1} \{ [(1-h)/(1+h)]^{1/2} \tan(\theta/2) \}$ ;  $\theta = \tilde{\Omega}\tau$ ;  $\tilde{\Omega} = (1-h^2)^{1/2}$  where  $h, \tau$  are defined below. Using standard perturbation theory for the effects of the r.f. field  $\mathbf{E}_0 = E_1(\cos\omega t, -\epsilon \sin\omega t, 0)$  we obtain a very simple, explicit, universal relation between the critical amplitude  $\tilde{E}_c$  of the r.f. field, corresponding to resonance overlap, and the particle energy. If we use  $\bar{W} = (m/2)(\omega/\kappa)^2$  as a unit of energy and  $\bar{E} = (\omega/\kappa c)B_0$  as a unit of electric field, then the relation between the dimensionless field amplitude  $E = E_c/\bar{E}$ , the ion energy  $W = h^2\bar{W}$  and the dimensionless frequency  $\tilde{\omega} = \omega/\omega_0$ , with  $\omega_0 = qB_0/mc$ , is

$$\tilde{E}_c = \tilde{\omega} [(1 + \tilde{\Omega})/h]^n / 4(\epsilon + 1)n(n+1)^2 \quad (1)$$

where  $\epsilon = 1$  for a left circularly polarized wave and  $\tilde{\Omega}$  and the integer  $n$  are defined by  $\tilde{\Omega} = \tilde{\omega}/n = (1-h^2)^{1/2}$ . If, for given r.f. excitation  $(\omega, E_1, \epsilon)$  and magnetic field  $(B_0, \kappa)$ , which fixes  $\tilde{E}_c$ , we denote by  $h_c$  the value of  $h$  which satisfies (1), then stochastic heating will occur for  $h_c < h < 1$ . (For  $h < 1$ , particles are not trapped)

In Fig. 2, we plot  $\tilde{E}_c$  vs.  $h^2$  for various values of  $\tilde{\omega}$ , assuming left-hand polarization  $\epsilon = 1$ . The values of  $\bar{W}$  and  $\bar{E}$  corresponding to resonance,  $\tilde{\omega} = n\tilde{\Omega}$ , are indicated by heavy dots, with the values of  $n$  alongside. The exponential depen-

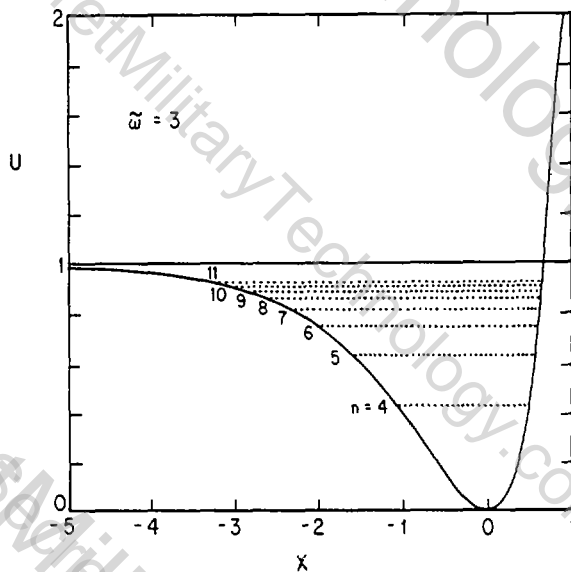


FIG.1. The dimensionless effective potential  $U = [1 - \exp(X)]^2$  versus  $X = \kappa x$ , with  $U = 1$  as asymptote for  $X \rightarrow -\infty$ . The dotted lines show the resonant energies where the condition  $\omega = n\Omega$  is satisfied for the case  $\tilde{\omega} = \omega/\omega_0 = 3$ . Here,  $\omega$  is the RF frequency and  $\omega_0$  is the cyclotron frequency at the bottom of the well.

dence of  $B$  is rather special, as is the neglect of  $z$ -dependence of the magnetic field. More realistic geometries require numerical integration of the unperturbed orbit. While the amount of calculation would not be prohibitive, the closed-form solutions given here illustrate the qualitative character of the solution and can serve as a guide for organizing the numerical calculations of other cases.

## 2. SIMULATION OF ICRH

A 2-1/2 dimensional relativistic electromagnetic particle code was used to investigate the dynamic behavior of electron heating around the electron cyclotron and upper-hybrid resonance layers when an extraordinary wave is obliquely launched from the high  $B$  field side of a tokamak into plasma [1]. The parameters for the simulation are  $\theta = 80^\circ$ ,  $T/mc^2 = 1.6 \times 10^{-3}$  and  $V/c = 0.012$  where  $V_0 = eE_0/m\omega$ . The static  $B$  is assumed to have the form  $B = B_0(1 - x/L)$ ,  $L \approx 915\lambda_D$ ; the plasma density is taken uniform. At large angles of incidence, direct absorption at the electron cyclotron layer is small because the

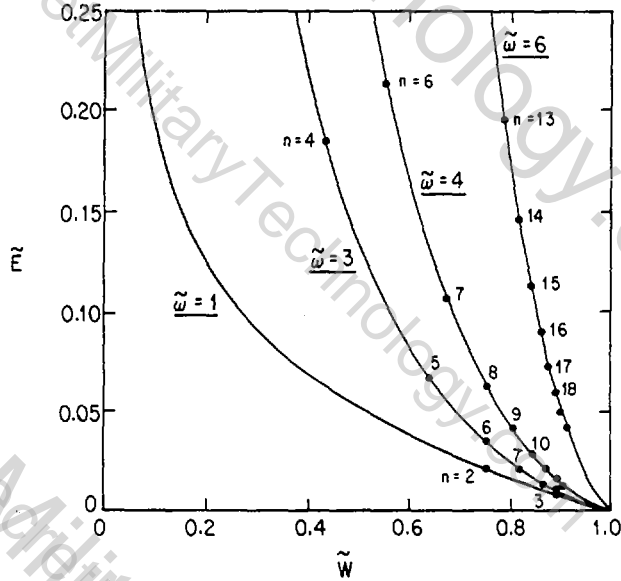


FIG.2. Critical RF field amplitude  $\tilde{E}_1 = \tilde{E}B_0 (\omega/\kappa c)$  for stochasticity as a function of ion energy.  $W = \tilde{W}[(m/2) (\omega_0/\kappa)^2]$ , where  $\kappa$  is the scale length of the magnetic field  $B_0$  and  $\omega_0 = qB_0/mc$ . Resonances, indicated by heavy dots, occur for energies such that  $\tilde{\omega} = n(1 - \tilde{W})^{1/2}$  where  $n$  is an integer.

wave becomes predominantly left circularly polarized, which is opposite to the electron rotation in a magnetic field. Most of the wave energy converts into electrostatic electron Bernstein waves at the upper-hybrid layer (Fig. 3a). These mode-converted Bernstein waves propagate back to the cyclotron layer where they are very efficiently absorbed by the electrons through resonant interactions ( $\omega_0 = \omega_c/\gamma + k_{||}V_T$ ). The initial conditions put the resonant heating for this case in the Doppler-broadened dominant regime ( $ck_y/\omega_0 > V_T/c$ ), which implies that heating should first peak on the low-field side (Fig. 3b) of the resonance. After the electrons become heated, the resonance changes to the regime dominated by relativistic effects and the heating peak shifts to the high field side (Fig. 3c). The line shape for both mechanisms has been observed in our simulations. The heating ultimately causes direct absorption of the extraordinary wave at the cyclotron resonance layer by the high-energy electrons; the steep temperature gradient created by the localized electron cyclotron heating eventually reflects a substantial part of the incident wave energy.

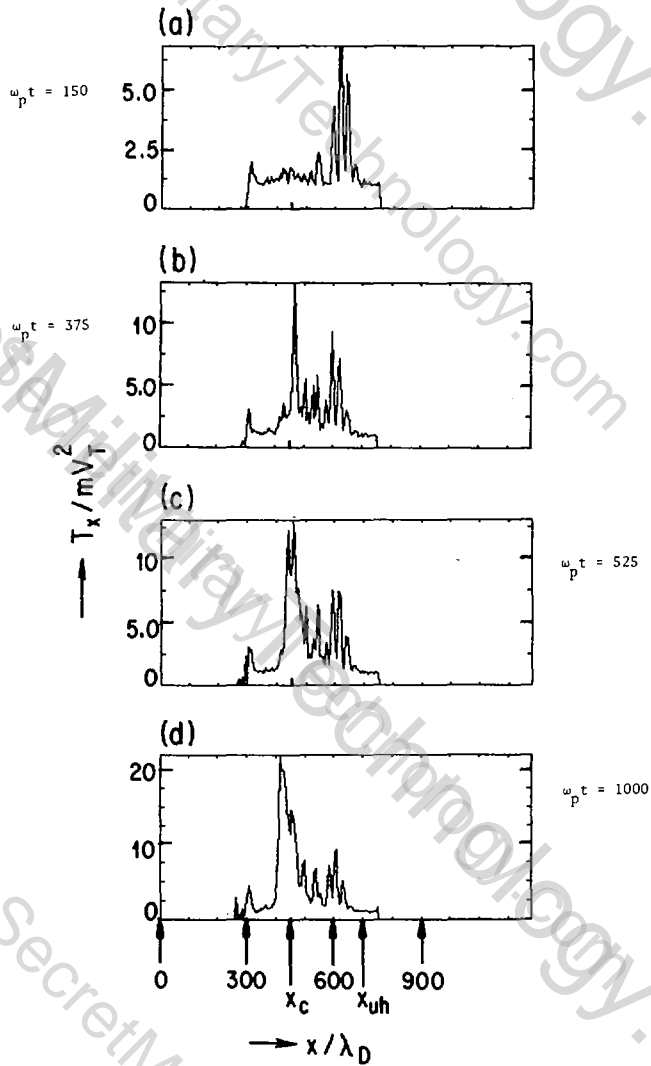


FIG.3. Spatial distribution of the transverse electron temperature at: (a)  $\omega_p t = 150$ ; (b)  $\omega_p t = 375$ ; (c)  $\omega_p t = 525$ ; (d)  $\omega_p t = 1000$ .

### 3. LOWER-HYBRID HEATING

To study lower-hybrid heating and current drive, we use a two-dimensional electrostatic particle simulation code. The lower-hybrid heating simulations examine the propagation of a lower-hybrid wave with finite amplitude in an inhomogeneous media and the mechanisms by which wave energy is absorbed [2].

The computer model has a constant magnetic field  $\vec{B}_0$  in the periodic direction and a Gaussian density profile  $n(x)$  increasing away from the antenna in the bounded direction. The frequency of the antenna, which launches predominantly a single  $k_{\parallel}$ , was chosen from a kinetic dispersion relation, evaluated locally, so that a lower-hybrid mode conversion layer exists inside the plasma,  $\omega_0 \approx 8\Omega_i$ ,  $k_{\parallel} \rho_i \lesssim 1/2\pi$ . According to this local dispersion relation, mode conversion is possible only if there is no damping (and therefore no heating).

The simulation results showed a backward wave below the mode conversion point, with wave number that agreed with the value predicted by the dispersion relation. However, no mode conversion was observed and the wave was totally absorbed. At amplitudes above the threshold given by Karney [3] for stochastic heating,

$$\alpha = \frac{ek_{\perp}E_0}{M_i\Omega_i^2} > \frac{1}{4} \left(\frac{\omega_0}{\Omega_i}\right)^{2/3} \approx 1$$

this absorption is associated with stochastic ion acceleration by the wave. This absorption occurs when the perpendicular phase velocity has slowed down to  $4v_{Ti}$ , as shown by calculating the time-averaged  $\vec{E} \cdot \vec{j}$  in space. The fast ions deplete the wave, leading to localized absorption in space and preferential heating of the ion tail. At amplitudes below Karney's threshold the wave was still absorbed, although the ion heating was too small to be accurately measured. In all these cases, the plasma parameters were such that the maximum value (near the mode conversion point) of the scale length

$$\rho_i d (\ln k_{\perp})/dx \leq 0.2$$

This value may be large enough that non-local effects are important for wave propagation and absorption. To investigate this possibility, further studies are being done in which the scale length is varied.

The simulations of current drive examine the dynamics of current generation for a given initial electron velocity distribution and antenna profile (wave number spectrum). The

initial conditions were similar to the heating runs, except that the initial electron velocity distribution was given a tail in one direction, to model the "slide-away" regime, and the antenna launched waves primarily in one direction.

The time history of the current shows two distinct stages. First, there is a transient stage of large current increase, corresponding to initial flattening of the electron distribution function out to approximately  $v_{ph} + v_{tr}$ , where  $v_{ph} = \omega/k$ , and  $v_{tr} = 2(e\phi/m_e)^{1/2}$ . During the second stage, the current continues to grow linearly at a slower rate, and this increase corresponds to electrons in the bulk of the distribution slowly leaking into the resonant region and then being accelerated. This slow "leaking" appears to be due to collisions, since none of the other waves the antenna launches penetrate inside to any significant extent. Significant ion heating (in the perpendicular direction) also occurred, especially during the second stage of current generation. The amount of ion current generated is small; however, ions carry a third of the total momentum in the plasma. Studies are underway to examine the flow of momentum between electrons, ions and the antenna.

#### 4. GYROTRON MODELLING

To model gyrotron oscillators and amplifiers, an adaption of a 1-2/2D finite-size particle code has been developed which allows interaction circuits with arbitrary wall profiles. By allowing the EM fields to have the same radial dependence as the local  $TE_{on}$  mode, 1D electromagnetic equations for longitudinal variations can be constructed and solved self-consistently as an initial value problem in time along with the trajectories of several thousand beam particles which traverse the cavity. Magnetic tuning can be performed within the simulation to optimize the output power. The code was used to design and analyze a 60GHz 200kW gyrotron oscillator built by Hughes Aircraft Company<sup>1</sup> for ECRH heating of plasmas. The basic design parameters were voltage 75kV, current 8 amps and perpendicular to parallel velocity 1.8. The longitudinal mode profile was peaked toward the output and given a Gaussian-like tail by appropriately tapering the cavity walls. The particle simulation code with optimum magnetic tuning and appropriate beam current energies and distribution functions predicted an output power of 265kW with 39% efficiency compared with 270kW peak power and 40% efficiency from the experiment (Fig. 4a). Self-consistent beam-loading effects were seen in that the external Q of 320 calculated from the simulation in the presence

<sup>1</sup> Sponsored by US Dept. of Energy, Oak Ridge National Laboratory, operated by Union Carbide, Contract No. W-7405-ENG-26/332002.

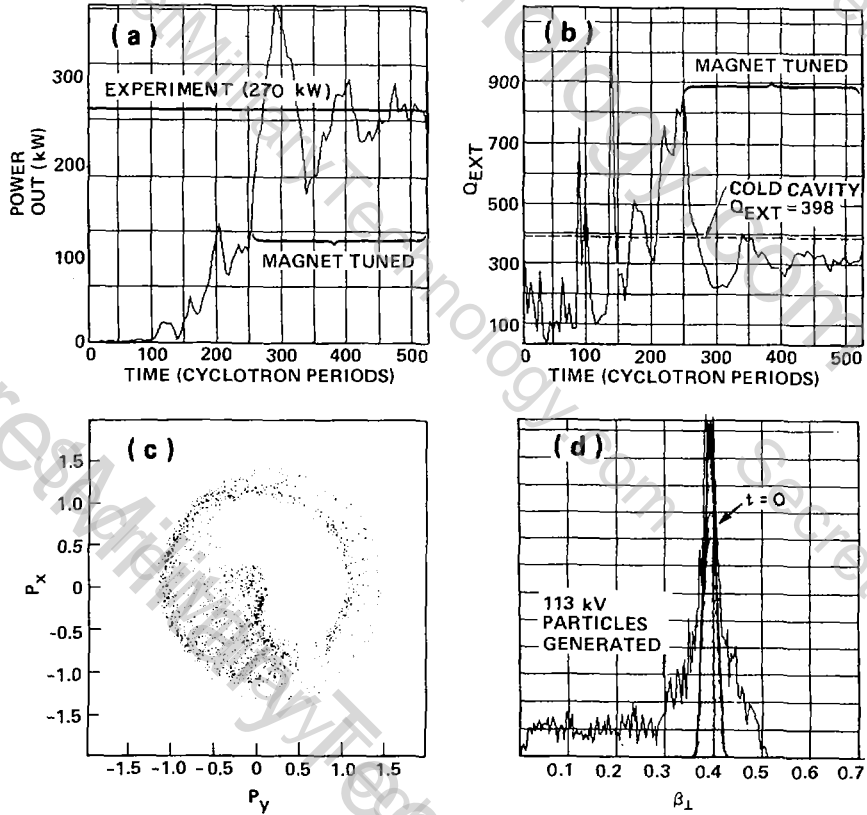


FIG. 4. (a) Predicted saturated output power from simulation compared with experiment. (b) Predicted self-consistent external cavity  $Q$  from simulation compared with cold cavity  $Q$ . (c) Transverse particle positions throughout beam in the steady-state saturated condition. (d) Transverse velocity distribution throughout beam in the steady-state saturated condition.

of the beam differed from the empty cavity  $Q$  of 398 (Fig. 4b). The saturated distribution function (Fig. 4c) indicated that a small class of electrons improperly phased was accelerated to energies of 113kV (Fig. 4d).

In conclusion, it has been demonstrated that the particle simulation code developed can serve as a useful tool in the design of high-power high-frequency gyrotrons required for future ECRH experiments.

#### REFERENCES

- [1] LIN, A.T., LIN, C.C., submitted to Phys. Fluids.
- [2] DECYK, V.K., MORALES, G.J., DAWSON, J.M., Proc. 3rd Joint Varenna-Grenoble Int. Symp. Heating in Toroidal Plasmas, Grenoble, 1982, Vol.2 (1982) 517.
- [3] KARNEY, C.F.C., Phys. Fluids 21 (1978) 1584.

## STELLARATOR, HYBRID STELLARATOR, TORSATRON AND LOW-SHEAR STELLARATOR STUDIES\*

G. ANANIA, R.C. GRIMM, D. HO, J.L. JOHNSON<sup>†</sup>,  
R.M. KULSRUD, J. MANICKAM, K.E. WEIMER  
Plasma Physics Laboratory,  
Princeton University,  
Princeton, New Jersey

G. BERGE, W.H. CHOE, J.P. FREIDBERG,  
J.M. NOTERDAEME<sup>+</sup>, Y.P. PAO<sup>§</sup>, P.A. POLITZER,  
P. ROSENAU, D. SHERWELL  
Plasma Fusion Center,  
Massachusetts Institute of Technology,  
Cambridge, Massachusetts

O. BETANCOURT, M. MOND, H. WEITZNER  
Courant Institute of Mathematical Sciences,  
New York University, New York, N.Y.

United States of America

### Abstract

#### STELLARATOR, HYBRID STELLARATOR, TORSATRON AND LOW-SHEAR STELLARATOR STUDIES.

(I) Equilibrium and stability studies using the stellarator expansion: the stellarator expansion reduces the three-dimensional MHD equations to two-dimensional ones and is applied to a model of Heliotron E. (II) Electron transport studies using the stellarator expansion: the stellarator expansion makes possible an estimate of "superbanana" electron heat transport. (III) Toroidal stellarator equilibria: it is shown how the vertical field, which produces no net body force, can shift vacuum flux surfaces and centre an equilibrium. (IV) Ballooning-mode equations for stellarators: ideal MHD ballooning-mode equations are derived for stellarators in the stellarator expansion. (V) Numerical studies of zero-net-current torsatrons: a fully three-dimensional computer code, based on an ideal MHD model, has been used to find stellarator configurations with finite critical values of the plasma parameter  $\beta$ . (VI) Low-shear stellarator studies: configurations whose magnetic axes are three-dimensional curves are

\* Work supported by US Department of Energy under several contracts.

<sup>†</sup> On loan from Westinghouse Research and Development Center, Pittsburgh, Pennsylvania.

<sup>+</sup> Supported by the Belgian Foundation for Scientific Research.

<sup>§</sup> Permanent address: Courant Institute of Mathematical Sciences,  
New York University, New York, N.Y.

studied; low-shear systems are considered for which the equilibrium and stability equations are simple; systems which have applied helical fields such as the Wendelstein stellarator are studied as well as configurations in which the rotational transform arises from geometry such as the figure-eight stellarator (in both cases families of equilibria are found, some of which are shown to be stable).

### I. Equilibrium and Stability Studies Using the Stellarator Expansion

The stellarator expansion [1], which uses a large-aspect-ratio approximation to reduce the three-dimensional magnetohydrodynamic equations to two-dimensional ones, simplifies the model of a classical stellarator, making possible the identification of the physical issues and thus complementing general numerical studies.

A typical application is given in Fig. 1, where results for a model Heliotron E, but with 18 field periods, are shown. Increasing the plasma beta shifts the magnetic axis and distorts the zeroth-order magnetic surfaces. This increases the rotational transform and digs a magnetic well in the region of large plasma pressure. The decrease in the area of the outermost closed magnetic surface, keeping first-order terms in  $\Psi$ , sets an upper limit on  $\beta$ . Comparison of the magnetic axis shift obtained with this expansion shows good agreement with a three-dimensional calculation [2].

The improvement in magnetic well and connection length associated with the axis shift with increasing beta should stabilize localized modes [3]. Since stellarators have no net toroidal current, kink and tearing modes may not occur. Work is in progress to investigate the effect of the Pfirsch-Schlüter current on these modes.

### II. Electron Transport Studies Using the Stellarator Expansion

The stellarator expansion makes it possible to estimate the transport of heat by electron "superbananas". Although this loss is somewhat smaller than that due to the ions, it is less model-dependent because, under nuclear reactor conditions, the electrons drift only a small radial distance along their superbanana orbits before making a detrapping collision.

Let an electron be trapped on the upper side of the stellarator and drift outward until it gets detrapped. When it isuntrapped, it circulates rapidly in poloidal angle so its next trapping position is equally likely to be up or down, and it is

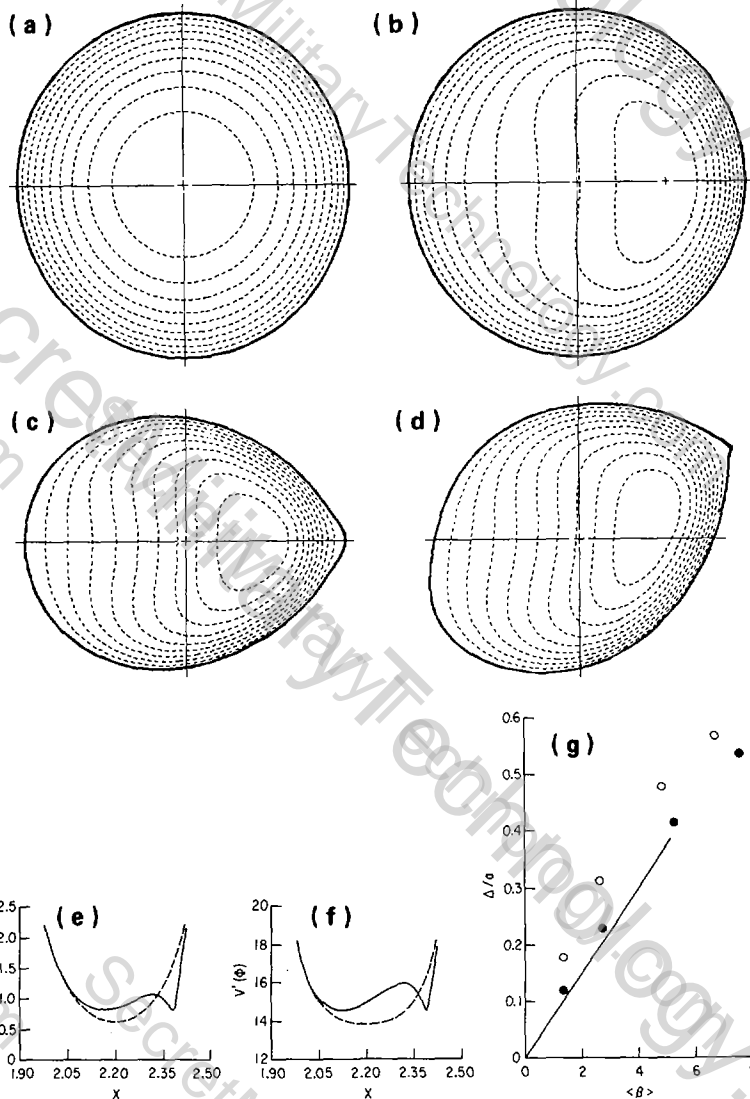


FIG.1. Magnetic surfaces and equilibrium properties for a Heliotron E model with  $B_\delta/B_0 = 0.5$ ,  $\ell = 2$ ,  $m = 18$ ,  $R/a = 10$ : zeroth-order magnetic surfaces for: (a)  $\langle\beta\rangle = 0\%$ ; (b)  $\langle\beta\rangle = 7.5\%$ ; (c, d) surfaces, keeping first-order terms at  $\phi = 0^\circ$  and  $\phi = 17^\circ$ , for  $\langle\beta\rangle = 7.5\%$ ; (e) rotational transform for  $\langle\beta\rangle = 0\%$  (dashed curve) and  $\langle\beta\rangle = 7.5\%$  (solid curve); (f)  $V'(\Phi)$  for  $\langle\beta\rangle = 0\%$  (dashed curve) and  $\langle\beta\rangle = 7.5\%$  (solid curve); (g) shift of magnetic axis with  $\langle\beta\rangle$ , three-dimensional calculation (solid curve), no vertical field ( $\circ$ ), vertical field adjusted to keep plasma surface fixed ( $\bullet$ ).

equally likely to drift inward or outward. In order of magnitude, its diffusion rate is  $f(v_D/v^*)^2 v^*$ , where  $v_D$  is the toroidal drift,  $v^*$  is the detrapping frequency, and  $f$  is the fraction of time it spends trapped. By applying a more careful theory, one can arrive at the proper numerical coefficient ( $2/9\pi$ ), and a proper weighting over all energies and radii can be taken. With an appropriate definition of energy confinement time  $\tau$ , assuming a reasonable electric field and temperature gradient and a magnetic ripple of 10%, one finds that the energy confinement time for electrons is 0.2 seconds, so  $n\tau_E \approx 4 \times 10^{13} \text{ cm}^{-3} \text{ s}$ . The ion heat loss is comparable. Then  $n\tau_E$  scales as  $n\tau_E = 1.38 \times 10^{14} n^2 a^2 R^2 B^2 / T^{3.5}$  where  $n$  is in units of  $2 \times 10^{14} \text{ cm}^{-3}$ ,  $T$  in 10 keV,  $B$  in 5T,  $a$  in meters, and  $R$  in 10 meters. These values, with the exception of  $n$ , correspond to those often discussed. Thus  $n$  must be three times larger than has been believed in order to exceed the Lawson criterion for breakeven in fusion.

Several points are worth noting. (1) Thermal diffusion is larger than ordinary diffusion by a factor of three for particle loss. (2) The diffusion coefficient is proportional to  $1/n$  so, for a fixed source, the density will either rise to a stability limit or sink to zero. (3) The large  $T$ -dependence indicates low-temperature experiments will not see superbanana diffusion. (4) For a fixed  $a$ ,  $n\tau_E$  is proportional to the aspect ratio squared or to the volume  $E$  squared. For fixed aspect ratio,  $n\tau_E$  is proportional to  $(\text{volume})^{4/3}$ . Thus, if cost scales with volume, it is cheaper to increase  $A$  than the overall dimensions.

### III. Toroidal Stellarator Equilibria

We have considered the problem of toroidal stellarator equilibria as described by the ideal MHD model. In particular, we have attempted to resolve the following apparent paradox. Regarding the problem of toroidal force balance and position control, it is well known that the addition of a vertical field leads to a shift of the vacuum flux surfaces. However, it is also well known that a vertical field produces no net body force on a current-free stellarator. The paradox that then arises is how a vertical field, which shifts vacuum flux surfaces, can be used for position control in a current-free stellarator where it produces no net body force.

This issue has been addressed by solving the MHD equilibrium equations using a low- $\beta$  (i.e.,  $\beta \approx \epsilon^2$ ) extension of the Princeton stellarator expansion. After a lengthy calculation, we derive a set of equations for the toroidally symmetric component of the

vector potential,  $A(r, \theta) = A(r) \cos \theta$ , and the toroidal shift,  $\sigma(r) = -\beta_1(r)/\beta'(r)$ , where  $\beta(\psi) \approx \beta_0(r) + \beta_1(r) \cos \theta$ . The general form of the equations is valid for arbitrary Ohmic heating profiles and finite  $Na/R_0$ , with  $N$  the number of helical periods and  $\epsilon \equiv a/R$ , the plasma inverse-aspect ratio. For the case of a current-free stellarator with small  $Na/R_0$ , these equations can be solved analytically yielding

$$\frac{A(r)}{B_0} = r \left[ b_v + \int_0^{\infty} \frac{dx}{x} \int_0^x \frac{y \beta'}{\mp_H} dy \right]$$

$$\frac{\sigma(a)}{a} = \frac{1}{\mp_H(a)} \left\{ \frac{b_v}{\epsilon} - \frac{1}{2\mp_H(a)} \int_0^1 z^{6-2\lambda} \left(\frac{\beta}{\epsilon}\right)' dz - \frac{b_\lambda}{N\epsilon} [b_{\lambda+1} + b_{\lambda-1} + \frac{\epsilon}{2} b_\lambda] \right\}$$

where  $B_0$  is the toroidal field,  $\mp_H$  is the helical transform  $/2\pi$ ,  $N$  is the number of helical periods,  $z = r/a$  is the normalized radius, and  $b_v = B_r^{(v)}(a)/B_0$ ,  $b_\lambda = B_r^{(\lambda)}(a)/B_0$ , and  $b_{\lambda\pm 1} = B_r^{(\lambda\pm 1)}(a)/B_0$  are the normalized amplitudes of the applied vertical field, main helical field, and helical sideband fields, respectively.

An analysis of these results resolves the paradox as follows. (1) In a static equilibrium the vertical field does not produce a net body force on the plasma. The outward expansion force is balanced by the  $\vec{J} \times \vec{B}$  force generated by the interaction of the Pfirsch-Schlüter currents with the average poloidal helical magnetic field on the plasma surface ( $\vec{B}_p \approx \mp_H$  averages to zero in leading order but is non-zero in next order). (2) When the vertical field is varied in time (as it would be for position control), the plasma, because of inertial effects, remains initially at rest. Within the context of ideal MHD, a toroidal surface dipole current is induced instantaneously in order to conserve the flux in the plasma (an additional net toroidal surface current may or may not be induced depending on the circuits controlling the poloidal flux linked by the plasma). The induced dipole current interacts with the average poloidal field producing a body force on the plasma. The direction of this force is such that, as the plasma moves, a counter surface-dipole current is induced. An equilibrium is achieved when the plasma moves to a new major radius where the net surface dipole current vanishes. Consequently, the vertical field gives rise to a body force on the plasma only during transient periods when the dipole current is induced. Once the transients are over, the vertical field no longer produces a body force. In practice, the time scale associated with the vertical field is much longer than the

plasma inertial time scale, so that the plasma position essentially tracks the vertical field adiabatically.

Thus, we have shown how the MHD model can be used to explain certain subtle but basic questions regarding toroidal stellarator equilibria.

#### IV. Ballooning-Mode Equation for Stellarators

A ballooning-mode equation for stellarators is derived from ideal MHD normal mode equations by using stellarator expansions with  $\beta \approx r/R \approx \delta^2 \ll 1$ , which enables us to reduce the problem to a two-dimensional axisymmetric one, and take the high mode number limit explicitly.

Let  $\theta$  and  $\phi$  be, respectively, the poloidal and toroidal angles,  $r$  the minor radius, and  $R = R_0 + r \cos \theta$  the major radius. We have  $\vec{B} = (R_0 B_0 / R) \vec{e}_z + \delta \vec{B}_1 + \delta^2 \vec{B}_2 + \dots$ , where  $B_0$  is constant and the helical field is  $\vec{B}_1 = B_0 \nabla \sum_{\lambda} (\epsilon_{\lambda} / h) I_{\lambda}(hr) \sin(\lambda \theta - hz)$  with  $z = R_0 \phi$ . Expanding the pressure  $P$  as  $p = \delta^2 p_2(r, \theta) + \delta^3 p_3(r, \theta, z)$ , we can use an orthogonal flux coordinate system  $(\psi, \chi, z)$  with  $\psi = \psi(P_2)$  and introduce the quasi-mode representation of Taylor:

$$\xi = \sum_m \exp(im\chi + inz/R_0) \int_{-\infty}^{\infty} \exp(-im\chi_1 + inS) \vec{\eta}(\psi, \chi_1, z) d\chi_1$$

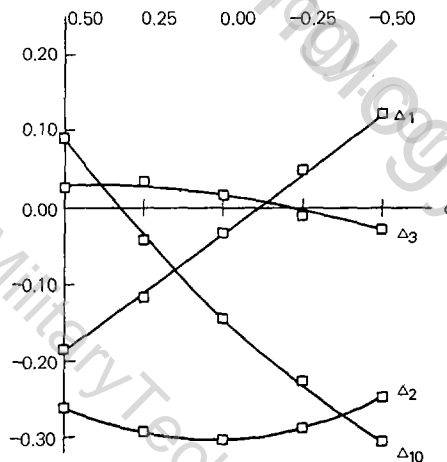


FIG. 2.  $\Delta$  as a function of  $\alpha$ :  $\beta = 0.0$ ;  $\epsilon = 0.1$ ;  $N = 12$ ; fixed  $V$ ;  $N\phi = \ell(\theta - \alpha \sin \theta)$ ;  $\ell = 2$ .

and we consider modes with  $n \gg 1$  and  $nr/R \gg 1$ . The eikonal  $S = S_0(\psi, \chi) + \delta S_1 + \dots$  can be solved from  $\vec{B} \cdot \nabla S = 0$  with stellarator expansions, yielding

$$D S_0 \equiv \vec{B}_{2a} \cdot \nabla S_0 = -B_0 / (\delta^2 R_0)$$

$$\vec{B}_{2a} = \vec{B}_{2\perp} - B_0 \vec{e}_z \times \nabla \sum_{\lambda} (\lambda \epsilon_{\lambda} \epsilon_m / h r) I_{\lambda} I'_m \cos(\lambda - m)\theta$$

where  $' = d/dr$  and  $\vec{B}_{2\perp} = \vec{B}_2 - \vec{e}_z \vec{e}_z \cdot \vec{B}_2$ .

The final ballooning-mode equation can be expressed in terms of  $\eta_{\perp} = \vec{\eta} \cdot (\vec{B} \times \nabla S) / |\nabla S|^2$  as

$$D(|\nabla S_0|^2 D \eta_{\perp}) + 2P_2' AR_0^{-2} \eta_{\perp} + \rho \omega^2 |\nabla S_0|^2 \eta_{\perp} = 0$$

where  $P_2' = (R_0/B_0) \vec{e}_z \times \nabla S_0 \cdot \nabla P_2$  and the coefficient  $A$  is  $A = P_2' + B_0 \vec{e}_z \times \nabla S_0 \cdot \nabla R + R_0 B_0 \vec{e}_z \times \nabla (|\nabla \phi|^2 - h^2 |\phi|^2) \cdot \nabla S_0$ ,

$\phi = \sum_{\lambda} (\epsilon_{\lambda}/h) I_{\lambda}(hr) \exp(-i\lambda\theta)$ , and we note that  $\omega \approx \delta^2 \times$  Alfvén speed.

#### V. Numerical Studies of Zero-Net-Current Torsatrons

In this paper we use a fully three-dimensional computer code [4] to discuss current-free torsatron configurations. Results obtained with this code for configurations like W1stor-U and Heliotron E have been reported elsewhere [2,5]. Our configuration corresponds to helical coils with a winding law given by  $N\phi = \lambda(\theta - \alpha \sin \theta)$ , where  $\phi$  and  $\theta$  are the toroidal and poloidal angles respectively,  $N$  the number of helical periods (we use the letter  $Q$  for this symbol in other publications), and  $\alpha$  a modulation constant. The equilibrium and stability properties of these configurations are found to depend on the Fourier components of the separatrix (last closed magnetic surface) which can be represented by an equation for its minor radius of the form  $R = 1 + \sum_{\lambda} \Delta_{\lambda} \cos(\lambda\theta - N\phi)$ .

As  $\beta$  increases in a toroidal configuration, the magnetic axis drifts out towards the separatrix. This drift can be minimized by a large rotational transform as in Heliotron E [2], or it can be offset by combining  $\lambda$  and  $\lambda + 1$  fields with opposite signs of  $\Delta_{\lambda}$  and  $\Delta_{\lambda+1}$ , which tends to shift the plasma inwards [6]. These multiple harmonics can be introduced by an appropriate choice of the modulation  $\alpha$  in the winding law. Figure 2 shows the dependence of  $\Delta$  on  $\alpha$  for  $\lambda = 2$ . Here  $\Delta_{10}$  denotes a shift of the

separatrix given by the  $\cos \theta$  Fourier component,  $\epsilon$  the inverse aspect ratio for the plasma, and  $V$  the vertical field. For both  $\lambda = 2$  and  $\lambda = 3$ ,  $\Delta_\lambda$  is a slowly varying function of  $\alpha$ , while  $\Delta_{\lambda-1}$  is rapidly varying and changes sign with  $\alpha$ . It is also found that  $\Delta_{\lambda+1}$  as well as  $\Delta_{10}$  is primarily controlled by the vertical field  $V$ , while  $\Delta_\lambda$  and  $\Delta_{\lambda-1}$  vary slowly with this parameter.

Among these configurations, we are most interested in the  $\lambda = 2, 3$  torsatron, which is given by  $\alpha = -0.5$  in the  $\lambda=3$  winding law. In this case,  $\Delta_2 = 0.15$  and  $\Delta_3 = -0.15$  while  $\Delta_4$  can be decreased by increasing the vertical field. We have studied its properties extensively [2] and found no stability limitations, with an average critical  $\beta$  of 5% given by the axis shift for the equilibrium.

To attain a relatively high stability limit, we find it is desirable to have adequate positive shear. In the case of Heliotron E, this is achieved by a tight winding and a large number,  $N = 19$ , of field periods. For a moderate number of periods, it can be obtained from the  $\lambda=1$  and  $\lambda=3$  components of the field.

We find that, in order to obtain a high  $\beta$  limit for both stability and equilibrium, we require a large  $\Delta_3$  of opposite sign from  $\Delta_2$ . This we cannot achieve with an  $\lambda=2$  winding law. Since  $\Delta_3$  is critical for stability, we want it to remain nearly constant for a reasonable range of vertical fields and  $\beta$ . For both of these reasons, an  $\lambda=3$  winding law with  $\alpha = -0.5$  seems the best choice for a high critical  $\beta$ . For this case the number of periods  $N = 10$  has been chosen so that the transform at the edge of the plasma is below 1. One may attempt to increase the equilibrium limit by increasing  $\Delta_2 = 0.2$ ,  $\Delta_3 = -0.15$ , with  $N = 10$ , or keeping  $\Delta_2 = 0.15$ ,  $\Delta_3 = -0.15$  and increasing  $N$ . In both cases, the transform at the plasma edge is larger than one, and the  $m=1$ ,  $n=1$  mode becomes unstable with the critical  $\beta$  below 2%.

## VI. Low-Shear Stellarator Studies

We take the magnetic axis to be a space curve  $\vec{x}(s)$  with curvature  $\kappa(s)$  and torsion  $\tau(s)$ , where  $s$  is arc length. At each point on  $\vec{x}(s)$  we introduce the tangent  $\vec{\alpha}(s)$ , the principal normal  $\vec{\beta}(s)$ , and the binormal  $\vec{\gamma}(s)$ , which are orthogonal and satisfy the Serret-Frenet relations. We introduce new space coordinates  $W, r, \theta$  by the definition  $s = \epsilon W$  and  $\vec{R} = \vec{x}(\epsilon W)/\epsilon + r\hat{r}(\epsilon W)$  where  $\hat{r} = \vec{\beta} \cos \theta + \vec{\gamma} \sin \theta$ , and  $\hat{\theta} = -\vec{\beta} \sin \theta + \vec{\gamma} \cos \theta$ . We assume that the equilibrium depends on  $r, \theta$  and  $\epsilon W$ . We may expand the differential operators and

equilibrium relations in  $\epsilon$ , and we scale the equilibrium as  $P = \epsilon \bar{P}$ ,  $\vec{B} = (B_\alpha, \epsilon^{\lambda_1} B_r, \epsilon^{\lambda_2} B_\theta)$ , where  $\vec{B} = \vec{B}(\epsilon W, r, \theta)$  and  $\delta, \lambda_1, \lambda_2$  vary with the configuration. The scalings turn our configurations into low-shear systems. In this case the magnetic differential operation is given to lowest order by  $\vec{B} \cdot \nabla = \epsilon D + O(\epsilon^2)$ , where  $D \equiv \partial/\partial W - r\partial/\partial\theta$ . We treat systems such as the figure-eight stellarator, for which the rotational transform arises from non-zero curvature and torsion of the magnetic axis. These configurations consist of a zero-order axial field  $B_\alpha$ , a poloidal component,  $B_p \sim \epsilon^2$ , and plasma with  $P \approx \epsilon^2$ . To the lowest order,  $\nabla \cdot \vec{B} = 0$  results in  $\vec{B}_p = \vec{\alpha} \times \nabla \phi^{(1)} + \vec{B}_p^v$  where  $\vec{B}_p^v$  denotes the effect of the geometry on the straight vacuum axial field. Now  $\phi^{(1)}$  satisfies  $D\Delta\phi^{(1)} = 2P'\kappa(W) \sin\theta$ . The magnetic surfaces are determined by  $P(\vec{r}) = \text{const}$ . To the lowest order,  $\epsilon^2$ , the surfaces are circles, while the  $\epsilon^3$  correction to the pressure gives the deviation from pure circles. We study stability starting from the usual  $\delta W$  form. On expanding  $\delta W$  and  $\xi$  in  $\epsilon$  we find  $\xi = \vec{\alpha} \times \nabla(\psi^{(0)} + \epsilon\psi^{(1)}) - \epsilon\psi^{(0)}\vec{\alpha} \times \nabla(\kappa r \cos\theta)$ , where  $D\psi^{(0)} = 0$ . After manipulation we find

$$\delta W = F_w^2 + \int_0^r dr \frac{F \lambda^2}{r^2} \left[ - (P')^2 - r \left( \frac{PP'}{r} \right)' \right] \sigma^2 + \int_0^r dr \frac{F \lambda^2}{r^2} q^2 P'$$

where  $\sigma^2$  and  $q^2$  are positive geometrical quantities and  $F = \xi(r, \theta=0, W=0)$ . Because the system has low shear, we were able to reduce the complicated  $\delta W$  into a simple one-dimensional expression in which the different modes (different  $\lambda$  numbers) are not coupled.

The first term in  $\delta W$  represents a stabilizing contribution from the outer wall. The third term in  $\delta W$  is a destabilizing factor. However, for high enough pressure, the second (quadratic in  $P$ ) term dominates. The sign of this term is sensitive to the shape of the pressure profile. As a function of  $r^2$ ,  $(P^2)''$  has to be negative. As an example, we see that the profile  $P = (1 - \alpha r^4)^{1/2}$  satisfies this requirement, and indeed, for  $\alpha < 1/3r_0^4$ , the configuration is stable. We turn now to systems with applied helical fields. In this case we have a toroidal configuration which consists of a zero-order toroidal field, a poloidal component,  $B \sim \delta$ , and plasma with  $P \approx \delta^2$ . The small parameter  $\delta$  measures the helical wave number of the applied field and is related to  $\epsilon$  by  $\epsilon = \delta^2 \eta$ ,  $\eta$  being another small parameter. In leading order, no toroidal curvature effects appear. Hence the Grad-Shafranov equation for straight, helically symmetric systems

can be recovered and can be solved order by order in  $\delta$ . For consistency reasons, the system has to include many ( $\approx 1/\delta\eta$ ) periods around the torus.

Stability properties of such configurations are determined by those of straight, helically symmetric systems. It has been shown [7] that, for a particular family of equilibria, an interchange-like criterion is necessary and sufficient for stability of shearless systems. For the  $l=2$  helical fields with amplitude  $\gamma$ , this criterion is  $-P'(\psi = 0) > \gamma^2/2(1-\gamma^2)$ . Hence stable Wendelstein-like configurations exist for high enough pressure gradients.

## REFERENCES

- [1] GREENE, J.M., JOHNSON, J.L., Phys. Fluids 4 (1961) 875.
- [2] BAUER, F., BETANCOURT, O., GARABEDIAN, P., SHOHEI, J.L., IEEE Trans. Plasma Sci. PS-9 (1981) 239.
- [3] KOVRIZHNYKH, L.M., SHCHEPETOV, S.V., Fiz. Plazmy 7 (1981) 965.
- [4] BAUER, F., BETANCOURT, O., GARABEDIAN, P., Phys. Fluids 24 (1981) 48.
- [5] BAUER, F., BETANCOURT, O., GARABEDIAN, P., SHOHEI, J.L., Proc. Natl. Acad. Sci. 78 (1981) 1.
- [6] BAUER, F., BETANCOURT, O., GARABEDIAN, P., J. Comp. Phys. 35 (1980) 341.
- [7] MOND, M., WEITZNER, H., Stability of Helically Symmetric Straight Equilibria, Phys. Fluids (in press).

**THEORY OF TRANSPORT AND HEATING IN EBT\***

C.L. HEDRICK, D.B. BATCHELOR, G.L. CHEN,  
 L.E. DELEANU<sup>†</sup>, R.C. GOLDFINGER<sup>†</sup>, D.E. HASTINGS,  
 E.F. JAEGER, D.K. LEE<sup>†</sup>, C.W. NESTER, L.W. OWEN,  
 D.A. SPONG, J.S. TOLLIVER<sup>†</sup>, N.A. UCKAN  
 Oak Ridge National Laboratory,  
 Oak Ridge, Tennessee

N.T. GLADD, S. HAMASAKI, N.A. KRALL,  
 J.L. SPERLING  
 JAYCOR, San Diego, California

H. WEITZNER  
 New York University, New York, New York

R.J. KASHUBA, M.R. GORDINIER, T.L. OWENS,  
 D.G. SWANSON  
 McDonnell-Douglas Astronautics Company,  
 St. Louis, Missouri

S. TAMOR  
 SAI, La Jolla, California

United States of America

**Abstract****THEORY OF TRANSPORT AND HEATING IN EBT.**

Recent developments in neoclassical transport theory and heating for EBT are presented. The development of improved analytic expressions for both electron and ion transport coefficients is summarized as is their effect on the self-consistent ambipolar electric field. These new results lead to significant improvements in the comparison of theory and experiment. Detailed calculations of Electron Cyclotron Heating (ECH) in existing EBT devices which include wave absorption by the relativistic rings are discussed. Preliminary studies of Ion Cyclotron Heating (ICRH) are also presented. For both transport and heating theory, topics for further theoretical concentration are suggested.

---

\* Research sponsored by the Office of Fusion Energy, US Department of Energy under Contract W-7405-eng-26 with the Union Carbide Corporation and other contracts.

<sup>†</sup> Union Carbide Corporation, Nuclear Division, Computer Sciences at Oak Ridge National Laboratory.

In existing EBT devices the core plasma losses can be reasonably well understood in terms of neoclassical electron transport. Conversely, because the neoclassical electron losses appear to dominate the present experimental behavior, it is difficult to draw clear-cut comparisons between neoclassical ion losses and experimental observation. In large measure the present comparison for ion losses depends upon comparison of calculated and measured values of the ambipolar electric field. In this section we summarize recent developments in electron and ion transport and the resultant effect upon the ambipolar electric field.

It has been known for some time [1] that the commonly used [2,3] analytic expressions for electron energy transport coefficient give good agreement with numerical values. However, for electron particle losses, the commonly used analytic expressions are significantly smaller than those obtained numerically. Here we present analytic approximations which are in good agreement with the numerical calculations.

A key observation for these analytic approximations is that Fokker-Planck and particle and energy conserving Krook collision operators give nearly identical results provided the transport is dominated by non-resonant processes or the electron collisionality is sufficiently large [1]. For typical values of the ambipolar electric field in EBT, resonant processes can usually be neglected for the electrons (primarily because there are very few of these particles since the resonance for electrons occurs at energies high compared to the thermal value).

The algebraic nature of the Krook operator allows explicit expressions for the transport in terms of integrals over velocity space [1]. In general these integrals must be evaluated numerically. However, we find that asymptotic expansions based on large electric field give surprisingly good agreement with the numerical calculations. If we write the particle and energy fluxes in the form

$$\Gamma = -D_n(n' - ne\phi'/T) - D_T T' \quad (1)$$

$$Q = -K_T T' - K_n(n' - ne\phi'/T) \quad (2)$$

then we find that

$$D_n = \bar{D} \left( 6.84 \times 10^{-2} + \frac{0.58}{w_0} - \frac{0.124w_0}{v^2 + w_0^2} \right) \quad (3)$$

$$D_T = \frac{n}{kT} \bar{D} \left( 0.137 + \frac{1.67298}{w_0} - \frac{0.76645w_0}{\bar{v}^2 + w_0^2} \right) \quad (4)$$

$$K_n = kT \bar{D} \left( 0.2395 + \frac{2.9179}{w_0} - \frac{1.4743w_0}{\bar{v}^2 + w_0^2} \right) \quad (5)$$

$$K_T = n\bar{D}(3.5167) \quad (6)$$

where

$$\bar{D} = \frac{1}{2} (v_y/\Omega)^2 [w(\bar{v}^2 + w_0^2)]$$

and  $v$  and  $\Omega$  are the thermal values of collision frequency and trapped electron poloidal precession frequency due to  $\nabla B$  and  $v_y$  is the thermal value of vertical drift due to toroidal effects;  $w_0 = E/(rB\Omega)$  and  $\bar{v} = v/\Omega$ . Note that some of the numerical coefficients in equations (4)-(6) have been adjusted from the precise values obtained analytically to improve agreement with the full numerical calculations. These expressions, while inapplicable for small  $w_0$ , give quite good agreement for  $w_0 > 1$ .

In contrast to electron transport, ion transport in EBT is usually dominated by resonant processes. We have recently developed analytic approximations which span the entire range of collisionality from banana to plateau. Note that the relevant collisionality should be computed at the resonance energy [ $> -eE/(d\ln B/dr)$ ] rather than at the thermal value and that this leads to considerably lower ion collisionality than had hitherto been supposed for present day experiments.

The development of the resonant ion transport coefficients follows from using a "reduced" version of the bounce averaged drift kinetic equation. This equation [Equation (29a) of Ref. [4]] is "reduced" in the sense that advantage is taken of the fact that the first order distribution function has strong derivatives across the resonant zone but is slowly varying along the resonant curve in velocity space. The particular form developed in reference [4] while valid for all collisionalities is analytically convenient for the relatively high collisionalities near the plateau limit. By a change of

variable, this differential equation takes a form which is more convenient for low collisionality (near the banana limit). This latter form, while valid for all resonant ion collisionalities in an EBT, is identical to that employed for "plateau" transport in tokamak [5]. This allows us to take advantage of the techniques employed for tokamaks (with modest extensions) to obtain analytic expressions for both small and large resonant collisionalities. The resultant expressions for the "kernel" or "reduced" transport coefficient differ by only 15% at intermediate collisionalities and a Padé approximant has been developed for the entire range of collisionality which varies from the numerical solutions by at most 25%. By using the "kernel" transport coefficient the actual transport coefficients are obtained by integration along the resonance curve in velocity space. Typically this curve has a minimum energy for highly trapped ions. The resonant energy rapidly increases as the pitch angle approaches the value characteristic of the transition from trapped to passing. This behavior of the resonant curve and the fact that the minimum resonant energy is large compared to thermal values allows one to develop asymptotic expansions which compare favorably with numerical calculations. In the low collisionality limit, these approximations for the various transport coefficients take the form

$$D, K \approx v_{if0} / \left( \frac{\phi''}{\phi'} - \frac{B''}{B'} \right)^{3/2} \quad (7)$$

where the ion collision frequency and the lowest order distribution function are to be evaluated at the minimum resonant energy [ $\epsilon_{res} = -eE/(d \ln B/dr)$ ] and all quantities are to be evaluated in the midplane. Note that  $v_{if0}$  is quite small since  $\epsilon_{res}/\epsilon_{thermal} \gg 1$ .

The smallness of  $v_{if0}$  has a strong effect on the ambipolar electric field. In order for the ion particle losses to equal that of electrons, the smallness of  $v_{if0}$  requires that the denominator in Equation (7) be correspondingly small:

$$\frac{\phi''}{\phi'} \approx \frac{B''}{B'} \quad (8)$$

This equation indicates that the shape of the ambipolar potential is governed by the shape of the midplane magnetic

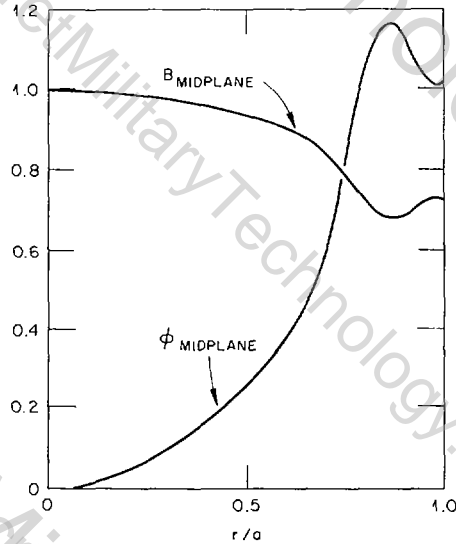


FIG.1. Ambipolar electrostatic potential,  $\phi$ , and midplane magnetic field,  $B$ , versus minor radius in the midplane.  $\phi$  is obtained from Eq.(7). These numerical results are from radially resolved transport calculations which include magnetic equilibrium effects of the hot-electron rings. The maximum in  $\phi$  and the minimum in  $B$  occur near the maximum ring pressure, in qualitative agreement with experiment.

field. Figure 1 illustrates a typical solution of Equation (8) which is generally similar to the behavior observed experimentally.

While the shape of  $\phi$  is given approximately by Equation (8), the magnitude depends on other electric field dependences of the transport. One of the most important dependences can be deduced from Equation (1) and the fact that  $\phi'$  is less than zero in the outer portions of the plasma (see Figure 1). As  $-\phi' = E + E_c \equiv T_e |\nabla \ln(n) + (\nabla \ln T) D_T / D_n| / e$ , the electron flux becomes small and the assumptions used to develop Equation (8) break down.

Thus the picture emerges that the shape of the ambipolar potential is controlled by the shape of the magnetic field while the magnitude is controlled by electrostatic trapping in the outer regions of the core/ring plasma. This global picture allows one to focus on areas still needing improvement. In particular, some of the analytic approximations used to describe orbits may be inadequately detailed for "fat" ion bananas and for both ion and electrons near the maximum ring pressure. A challenging aspect of on-going research is the determination of tractable means for incorporating these additional complications into transport theory.

ECRH

Using a geometrical optics code with numerically generated finite- $\beta$  equilibria and a recently developed fully-relativistic absorption model, it is now possible to investigate the electron cyclotron heating (ECH) properties of both core and ring plasma components. The results for direct single pass absorption obtained from ray tracing [6-8] are combined with results from a statistical model for the deposition of multiply reflected and mode-converted waves to obtain estimates of the power deposited in the core, surface, and annulus plasma components [9].

The absorption of the microwaves by the relativistic component is calculated using Poynting's theorem [10]:

$$\frac{d}{ds} |\mathcal{S}| = \frac{4\pi}{c} \mathbf{E}^* \cdot \tilde{\sigma}^H \cdot \mathbf{E}$$

where  $s$  is the arc length along a ray,  $\mathcal{S} = \text{Re}[\mathbf{E}^* \times (\mathbf{n} \times \mathbf{E})]$  = Poynting's vector,  $\mathbf{n} = c\mathbf{k}/\omega$  = real refractive index, and  $\sigma^H$  = Hermitian part of the relativistic conductivity tensor. In calculating  $\tilde{\sigma}^H$  the distribution function is assumed to be an isotropic, relativistic Maxwellian

$$F(\tilde{p}) = \frac{1}{m^3 c^3} \frac{n_A}{4\pi K_2(\rho)} e^{-\rho(1 + \frac{p_{\parallel}^2 + p_{\perp}^2}{m^2 c^2})^{1/2}}$$

where  $\rho = m_e c^2 / T_A$ ,  $K_2(\rho)$  is the modified Bessel function,  $T_A$  is the annulus temperature, and  $n_A$  is the annulus density.

The finite-beta magnetic fields and annulus density profile are calculated using a two-dimensional (2-D) tensor pressure MHD equilibrium code [11]. To model EBT-I, the parameters of the code are adjusted to give an annulus extending from  $r_{\min} = 11.8$  cm to  $r_{\max} = 15.8$  cm with the annulus pressure peak at  $r_{\text{peak}} = 13.8$  cm. The externally imposed vacuum bumpy cylinder field is due to filamentary current loops spaced 20 cm from the midplane with a radius necessary to produce a 2:1 mirror ratio on axis. The core density is chosen to be constant along field lines and is flat inside the annulus and decreases through the annulus to a constant level  $n_{\infty}$  in the surface plasma. The core temperature is taken to be proportional to the core density  $T_c(x) = T_e n_c(x) / n_0$ . The equilibrium parameters  $n_0 = 4.7 \times 10^{17} / \text{cm}^3$ ,  $T_e = 440$  eV,  $\beta_{\text{local}} = 0.102$ ,  $T_A = 145$  keV were chosen so as to model as closely as possible a specific experimental run for which fairly complete data was available. The stored energy of 8.4 J obtained by

integrating over the model annulus is consistent with the measured value of  $\sim 8$  J.

Initially, we trace an ensemble of rays through the plasma which are launched at varying angles from a point at the midplane near the vacuum vessel wall. The power carried by each ray is weighted by a suitable antenna radiation pattern and the power deposited in each plasma component for a single pass through the device is determined by integrating over a solid angle. Typically, we find that only a small fraction of the total injected power is absorbed in a single pass. Assuming that equal power in ordinary/extraordinary modes is injected into the cavity, for the plasma parameters quoted above, we find power deposited in the annulus  $P_{\text{Ann}} \sim 0.045 P_{\text{inj}}$  and power deposited in the core component at the 2nd harmonic resonance  $P_{2\text{nd}} \sim 0.005 P_{\text{inj}}$ . A negligible amount of ordinary mode power is absorbed at the fundamental resonance.

Since the power remaining after a single pass is spread across the wall surface and greatly randomized with respect to direction of propagation, the deposition of this power can be calculated using the power balance model. Although the results of the power balance model for EBT-I depend weakly on what is assumed for the mix of ordinary-extraordinary modes excited by the waveguide, the average mode conversion coefficient, the Budden tunneling parameters, and the like, we find that typically the total (one pass + randomized) power deposition is  $P_{\text{Ann}} \sim 0.41 P_{\text{inj}}$ ,  $P_{\text{core}} \sim 0.25 P_{\text{inj}}$ ,  $P_{2\text{nd}} \sim 0.02 P_{\text{inj}}$ , and  $P_{\text{surface}} \sim 0.32 P_{\text{inj}}$ .

Preliminary calculations have been done using an anisotropic ring distribution of the form

$$f(p) = \sum A_{ijk} (p^2)^i (\sin^2 \theta)^j e^{-\frac{mc^2}{T_k} \gamma}$$

where  $\sin \theta = p_{\perp}/p_{\parallel}$  and the  $A_{ijk}$  are constants. [12] Anisotropy tends to increase the ring absorption although for the cases considered the increase was less than a factor of  $\sim 1.5$ . For some forms of anisotropy, weakly growing wave solutions near the integer harmonics are found. The presence of this instability is closely related to the absence of cool electrons in the loss cone and disappears if enough cool electrons are present.

Experimental estimates of the power losses from the annuli can be obtained using the ring stored energy and the decay time after power turnoff. Experiments performed on EBT-I using a total 40 kW of 18 GHz power with ring stored energy of  $\sim 5$  J indicated a power loss per ring  $\sim 50$  W. [13] Assuming the microwave distribution system to have an

efficiency of 66%, the microwave power injected into each cavity is  $P_{inj} = 0.66 \times 40 \text{ kW}/24 \sim 1.1 \text{ kW}$ . The estimated 50W, therefore, represents  $\sim 4.5\%$  of the total injected power. If one assumes a simple linear scaling of fraction of power absorbed per ring with ring stored energy, the 8.4 J rings modeled in this paper would be expected to absorb about 7.5% of the injected power. The theoretical estimate of 41% (450 W/ring) power deposition is significantly higher. For comparison, when the classical losses (drag, scattering, and synchrotron radiation) are integrated over the assumed ring and core plasma profiles, one obtains  $P_{classical} \sim 40\text{W}/\text{ring}$ .

At best with a zero-dimensional model such as this, one would expect only rough agreement with experiment. Some uncertainty exists in the global averages used to obtain the rate coefficients for mode conversion tunneling and absorption. However, experience with the power balance model has shown that the power ultimately deposited in the annulus is only weakly dependent on the various rate coefficients throughout their credible range with the exception of the annulus fractional absorption  $\langle f \rangle_{ann}^J$ . The existing discrepancy certainly indicates a need to examine the ring absorption process to discover any physical effects not included in the model which would reduce ring power absorption. Possibly important effects which have been identified and are now being investigated include nonlinear superadiabatic limits to heating, and finite  $\rho/L$  effects on the linear heating operator.

### ICRH

Fast wave ICRH experiments are now being conducted on EBT-S and are planned in the second phase of EBT-P operation. To analyze these problems new methods are required since the long wavelength ( $\lambda \sim L$ ) invalidates geometrical optics methods and the complicated geometry makes analytical full-wave methods intractable. An asymptotic formalism has been developed which is based on the approximation  $v_i/(\lambda\omega) \ll 1$  where  $v_i$  is the ion thermal speed. [14] It is not necessary to assume  $\lambda/L$  is small. We find that in lowest order the ion response can be represented by the cold ion conductivity with appropriate jump conditions on the electric field across the fundamental cyclotrons resonance surface.

The zero order RF fields are being calculated variationally using a finite element code. A bumpy cylinder plasma equilibrium is used in which the magnetic field and density vary in  $r$  and  $z$  but are rotationally symmetric about the  $z$  axis. The boundary is modeled as a sequence of perfectly conducting cylinder segments of alternating large and small radius. Effects of toroidicity are included by imposing periodic boundary conditions at the ends of the N

sector bumpy cylinder. Also a method has been developed to reduce the N cavity problem having one driven cavity to a sequence of N one cavity problems. The power absorption is given in higher order as an integral over the resonant surfaces involving differential operators acting on the lowest order fields. An interesting aspect of the theory is that spatial variations of the equilibrium quantities contribute to the linear heating in the same role as finite  $k_{\perp\rho_i}$  in the homogeneous plasma theory.

Progress has also been made in the one-dimensional Vlasov-Maxwell theory of fast wave propagation, reflection, absorption, mode conversion, and tunneling using a variational principle. The specific case of second harmonic heating or minority species heating can be described by a set of coupled second order differential equations which are solved by using Green's function techniques. The coupled second order differential equations are converted to a fourth order equation and asymptotic separation techniques are employed which leads to an integral equation for the full wave solution. Finally, an energy conservation theorem can be formulated which allows the energy going into each mode to be calculated. Thus the energy partition between the reflected and tunneling fast wave, the mode converted slow wave and local absorption can be determined.

#### REFERENCES

- [1] SPONG, D. A., HARRIS, E. G., HEDRICK, C. L., Nucl. Fusion 19, (1979) 665.
- [2] KOVRIZHNYKH, L. M., Sov. Phys. JETP M24, (1969) 475.
- [3] JAEGER, E. F., HEDRICK, C. L., and ARD, W. B., Phys. Rev. Lett. 43, (1979) 885 and references cited therein.
- [4] SPONG, D. A., and HEDRICK, C. L., Phys. Fluids 23, (1980) 1903.
- [5] HINTON, F. L. and ROSENBLUTH, M. N., Phys. Fluids 16, (1973) 836.
- [6] BATCHELOR, D. B., GOLDFINGER, R. C., Nucl. Fusion 20, (1980) 403.
- [7] BATCHELOR, D. B., GOLDFINGER, R. C., WEITZNER, H., IEEE Trans, Plasma Sci. PS-8, (1980) 78.
- [8] BATCHELOR, D. B., GOLDFINGER, R. C., "RAYS: A Geometrical Optics Code for EBT," ORNL/TM-6844, 1982.
- [9] BATCHELOR, D. B., Nucl. Fusion 21 (1981) 1651.
- [10] BATCHELOR, D. B., WEITZNER, H., "Electron Cyclotron Damping in Fully Relativistic Plasmas" (to be published).

- [11] NELSON, D. B., HEDRICK, C. L., Nucl. Fusion 19, (1975) 235.
- [12] TAMOR, S., "Electromagnetic Interactions in High Temperature Plasmas," SAI-023-82-442LJ.
- [13] HASTE, G. R., "Hot Electron Rings: Diagnostics Review and Summary of Measurement," Proceedings of the 2nd Ring Physics Workshop, Dec. 1-3, 1981, San Diego, CA.
- [14] WEITZNER, H., "Ion Heating at Ion Cyclotron Frequencies," to be published.

## CHAIRMEN OF SESSIONS

Session A	R.S. PEASE	UK
Session B	V.P. SMIRNOV	USSR
Session C	K. MIYAMOTO	Japan
Session D	V.D. SHAFRANOV	USSR
Session E	S. MORI	Japan
Session F	S. WITKOWSKI	FRG
Session G	S. MIYOSHI	Japan
Session H	H. DREICER	USA
Session I	D. PALUMBO	CEC
Session J	W.M. HOOKE	USA
Session K	M. BRENNAN	Australia
Session L	H. KAKIHANA	Japan
Session M	B. BRUNELLI	Italy
Session N	T.F. GODLOVE	USA
Session O	V.T. TOLOK	USSR
Session V	Poster session	
Session P	J. CLARKE	USA
Session Q	A. SCHLÜTER	FRG
Session R	V.S. STRELKOV	USSR
Session S	F. PREVOT	France
Session W	Poster session	
Session T	M.N. ROSENBLUTH	USA
Session U	C.M. BRAAMS	Netherlands

## SECRETARIAT OF THE SYMPOSIUM

Scientific Secretaries:	M. LEISER V.S. VLASENKOV	Division of Research and Laboratories, IAEA
Administrative Secretary:	Caroline DE MOL VAN OTTERLOO	Division of External Relations, IAEA
Editors:	J.W. WEIL Miriam LEWIS	Division of Publications, IAEA
Records Officer:	M. READING	Division of Languages, IAEA

The following conversion table is provided for the convenience of readers

## FACTORS FOR CONVERTING SOME OF THE MORE COMMON UNITS TO INTERNATIONAL SYSTEM OF UNITS (SI) EQUIVALENTS

### NOTES:

- (1) SI base units are the metre (m), kilogram (kg), second (s), ampere (A), kelvin (K), candela (cd) and mole (mol).
- (2) ► indicates SI derived units and those accepted for use with SI;
  - ▷ indicates additional units accepted for use with SI for a limited time.
 [For further information see the current edition of *The International System of Units (SI)*, published in English by HMSO, London, and National Bureau of Standards, Washington, DC, and International Standards ISO-1000 and the several parts of ISO-31, published by ISO, Geneva.]
- (3) The correct symbol for the unit in column 1 is given in column 2.
- (4) \* indicates conversion factors given exactly; other factors are given rounded, mostly to 4 significant figures;
  - ≡ indicates a definition of an SI derived unit: [ ] in columns 3+4 enclose factors given for the sake of completeness.

Column 1 Multiply data given in:	Column 2	Column 3 by:	Column 4 to obtain data in:
<b>Radiation units</b>			
► becquerel	1 Bq	(has dimensions of s <sup>-1</sup> )	
disintegrations per second (= dis/s)	1 s <sup>-1</sup>	≡ 1.00 × 10 <sup>0</sup>	Bq *
▷ curie	1 Ci	≡ 3.70 × 10 <sup>10</sup>	Bq *
▷ roentgen	1 R	[= 2.58 × 10 <sup>-4</sup>	C/kg] *
► gray	1 Gy	[≡ 1.00 × 10 <sup>0</sup>	J/kg] *
▷ rad	1 rad	= 1.00 × 10 <sup>-2</sup>	Gy *
► sievert ( <i>radiation protection only</i> )	1 Sv	[≡ 1.00 × 10 <sup>0</sup>	J/kg] *
▷ rem ( <i>radiation protection only</i> )	1 rem	= 1.00 × 10 <sup>-2</sup>	Sv *
<b>Mass</b>			
► unified atomic mass unit ( $\frac{1}{12}$ of the mass of <sup>12</sup> C)	1 u	[= 1.660 57 × 10 <sup>-27</sup>	kg, approx. ]
► tonne (= metric ton)	1 t	[= 1.00 × 10 <sup>3</sup>	kg] *
pound mass (avoirdupois)	1 lbm	= 4.536 × 10 <sup>-1</sup>	kg
ounce mass (avoirdupois)	1 ozm	= 2.835 × 10 <sup>1</sup>	g
ton (long) (= 2240 lbm)	1 ton	= 1.016 × 10 <sup>3</sup>	kg
ton (short) (= 2000 lbm)	1 short ton	= 9.072 × 10 <sup>2</sup>	kg
<b>Length</b>			
statute mile	1 mile	= 1.609 × 10 <sup>0</sup>	km
▷ nautical mile (international)	1 n mile	= 1.852 × 10 <sup>0</sup>	km *
yard	1 yd	= 9.144 × 10 <sup>-1</sup>	m *
foot	1 ft	= 3.048 × 10 <sup>-1</sup>	m *
inch	1 in	= 2.54 × 10 <sup>1</sup>	mm *
mil (= 10 <sup>-3</sup> in)	1 mil	= 2.54 × 10 <sup>-2</sup>	mm *
<b>Area</b>			
▷ hectare	1 ha	[= 1.00 × 10 <sup>4</sup>	m <sup>2</sup> ] *
▷ barn ( <i>effective cross-section, nuclear physics</i> )	1 b	[= 1.00 × 10 <sup>-28</sup>	m <sup>2</sup> ] *
square mile, (statute mile) <sup>2</sup>	1 mile <sup>2</sup>	= 2.590 × 10 <sup>0</sup>	km <sup>2</sup>
acre	1 acre	= 4.047 × 10 <sup>3</sup>	m <sup>2</sup>
square yard	1 yd <sup>2</sup>	= 8.361 × 10 <sup>-1</sup>	m <sup>2</sup>
square foot	1 ft <sup>2</sup>	= 9.290 × 10 <sup>-2</sup>	m <sup>2</sup>
square inch	1 in <sup>2</sup>	= 6.452 × 10 <sup>2</sup>	mm <sup>2</sup>
<b>Volume</b>			
► litre	1 l or 1 L	[= 1.00 × 10 <sup>-3</sup>	m <sup>3</sup> ] *
cubic yard	1 yd <sup>3</sup>	= 7.646 × 10 <sup>-1</sup>	m <sup>3</sup>
cubic foot	1 ft <sup>3</sup>	= 2.832 × 10 <sup>-2</sup>	m <sup>3</sup>
cubic inch	1 in <sup>3</sup>	= 1.639 × 10 <sup>4</sup>	mm <sup>3</sup>
gallon (imperial)	1 gal (UK)	= 4.546 × 10 <sup>-3</sup>	m <sup>3</sup>
gallon (US liquid)	1 gal (US)	= 3.785 × 10 <sup>-3</sup>	m <sup>3</sup>

This table has been prepared by E. R. A. Beck for use by the Division of Publications of the IAEA. While every effort has been made to ensure accuracy, the Agency cannot be held responsible for errors arising from the use of this table.

Column 1 Multiply data given in:	Column 2	Column 3 by:	Column 4 to obtain data in:
<i>Velocity, acceleration</i>			
foot per second (= fps)	1 ft/s	= $3.048 \times 10^{-1}$	m/s *
foot per minute	1 ft/min	= $5.08 \times 10^{-3}$	m/s *
mile per hour (= mph)	1 mile/h	= $\begin{cases} 4.470 \times 10^{-1} \\ 1.609 \times 10^0 \end{cases}$	m/s km/h
▷ knot (international)	1 knot	= $1.852 \times 10^0$	km/h *
free fall, standard, g		= $9.807 \times 10^0$	m/s <sup>2</sup>
foot per second squared	1 ft/s <sup>2</sup>	= $3.048 \times 10^{-1}$	m/s <sup>2</sup> *
<i>Density, volumetric rate</i>			
pound mass per cubic inch	1 lbm/in <sup>3</sup>	= $2.768 \times 10^4$	kg/m <sup>3</sup>
pound mass per cubic foot	1 lbm/ft <sup>3</sup>	= $1.602 \times 10^1$	kg/m <sup>3</sup>
cubic feet per second	1 ft <sup>3</sup> /s	= $2.832 \times 10^{-2}$	m <sup>3</sup> /s
cubic feet per minute	1 ft <sup>3</sup> /min	= $4.719 \times 10^{-4}$	m <sup>3</sup> /s
<i>Force</i>			
▷ newton	1 N	[≡ $1.00 \times 10^0$	m·kg·s <sup>-2</sup> ]*
dyne	1 dyn	= $1.00 \times 10^{-5}$	N *
kilogram force (= kilopond (kp))	1 kgf	= $9.807 \times 10^0$	N
poundal	1 pdl	= $1.383 \times 10^{-1}$	N
pound force (avoirdupois)	1 lbf	= $4.448 \times 10^0$	N
ounce force (avoirdupois)	1 ozf	= $2.780 \times 10^{-1}$	N
<i>Pressure, stress</i>			
▷ pascal <sup>a</sup>	1 Pa	[≡ $1.00 \times 10^0$	N/m <sup>2</sup> ] *
atmosphere <sup>b</sup> , standard	1 atm	= $1.01325 \times 10^5$	Pa *
▷ bar	1 bar	= $1.00 \times 10^5$	Pa *
centimetres of mercury (0°C)	1 cmHg	= $1.333 \times 10^3$	Pa
dyne per square centimetre	1 dyn/cm <sup>2</sup>	= $1.00 \times 10^{-1}$	Pa *
feet of water (4°C)	1 ftH <sub>2</sub> O	= $2.989 \times 10^3$	Pa
inches of mercury (0°C)	1 inHg	= $3.386 \times 10^3$	Pa
inches of water (4°C)	1 inH <sub>2</sub> O	= $2.491 \times 10^2$	Pa
kilogram force per square centimetre	1 kgf/cm <sup>2</sup>	= $9.807 \times 10^4$	Pa
pound force per square foot	1 lbf/ft <sup>2</sup>	= $4.788 \times 10^1$	Pa
pound force per square inch (= psi) <sup>c</sup>	1 lbf/in <sup>2</sup>	= $6.895 \times 10^3$	Pa
torr (0°C) (= mmHg)	1 torr	= $1.333 \times 10^2$	Pa
<i>Energy, work, quantity of heat</i>			
▷ joule (≡ W·s)	1 J	[≡ $1.00 \times 10^0$	N·m] *
▷ electronvolt	1 eV	[= $1.60219 \times 10^{-19}$	J, approx.]
British thermal unit (International Table)	1 Btu	= $1.055 \times 10^3$	J
calorie (thermochemical)	1 cal	= $4.184 \times 10^0$	J *
calorie (International Table)	1 cal <sub>IT</sub>	= $4.187 \times 10^0$	J
erg	1 erg	= $1.00 \times 10^{-7}$	J *
foot-pound force	1 ft·lbf	= $1.356 \times 10^0$	J
kilowatt-hour	1 kW·h	= $3.60 \times 10^6$	J *
kiloton explosive yield (PNE) (≡ 10 <sup>12</sup> g-cal)	1 kt yield	≈ $4.2 \times 10^{12}$	J

<sup>a</sup> Pa (g): pascals gauge  
Pa abs: pascals absolute

<sup>b</sup> atm (g) (= atü): atmospheres gauge  
atm abs (= ata): atmospheres absolute

<sup>c</sup> lbf/in<sup>2</sup> (g) (= psig): gauge pressure  
lbf/in<sup>2</sup> abs (= psia): absolute pressure

Column 1	Column 2	Column 3	Column 4
Multiply data given in:		by:	to obtain data in:

*Power, radiant flux*

▶ watt	1 W	[ $\equiv 1.00 \times 10^0$ ]	J/s) *
British thermal unit (International Table) per second	1 Btu/s	= $1.055 \times 10^3$	W
calorie (International Table) per second	1 cal <sub>IT</sub> /s	= $4.187 \times 10^0$	W
foot-pound force/second	1 ft·lbf/s	= $1.356 \times 10^0$	W
horsepower (electric)	1 hp	= $7.46 \times 10^2$	W *
horsepower (metric) (= ps)	1 ps	= $7.355 \times 10^2$	W
horsepower (550 ft·lbf/s)	1 hp	= $7.457 \times 10^2$	W

*Temperature*

- ▶ kelvin
- ▶ degrees Celsius, t
  - where T is the thermodynamic temperature in kelvin and T<sub>0</sub> is defined as 273.15 K
- degree Fahrenheit
- degree Rankine
- temperature difference<sup>d</sup>

$$t = \frac{K}{T - T_0} \quad \text{---} \quad *$$

$$\left. \begin{array}{l} t_{\circ F} - 32 \\ T_{\circ R} \\ \Delta T_{\circ R} (= \Delta t_{\circ F}) \end{array} \right\} \times \left( \frac{5}{9} \right) \text{ gives } \left\{ \begin{array}{l} t \text{ (in degrees Celsius) } * \\ T \text{ (in kelvin) } * \\ \Delta T (= \Delta t) * \end{array} \right.$$

*Thermal conductivity<sup>d</sup>*

1 Btu·in/(ft <sup>2</sup> ·s·°F)	(International Table Btu)	= $5.192 \times 10^2$	W·m <sup>-1</sup> ·K <sup>-1</sup>
1 Btu/(ft·s·°F)	(International Table Btu)	= $6.231 \times 10^3$	W·m <sup>-1</sup> ·K <sup>-1</sup>
1 cal <sub>IT</sub> /(cm·s·°C)		= $4.187 \times 10^2$	W·m <sup>-1</sup> ·K <sup>-1</sup>

*Miscellaneous quantities*

litre per mole per centimetre (molar extinction coefficient or molar absorption coefficient)	(1 M/cm =) 1 L·mol <sup>-1</sup> ·cm <sup>-1</sup>	= $1.00 \times 10^{-1}$ m <sup>2</sup> /mol	*
G-value, traditionally quoted per 100 eV of energy absorbed (radiation yield of a chemical substance)		$1 \times 10^{-2}$ eV <sup>-1</sup> = $6.24 \times 10^{16}$	J <sup>-1</sup>
mass per unit area (absorber thickness and mean mass range)		1 g/cm <sup>2</sup> [= $1.00 \times 10^1$ ]	kg/m <sup>2</sup> ) *

<sup>d</sup> A temperature interval or a Celsius temperature difference can be expressed in degrees Celsius as well as in kelvins.

# HOW TO ORDER IAEA PUBLICATIONS

An exclusive sales agent for IAEA publications, to whom all orders and inquiries should be addressed, has been appointed in the following country:

UNITED STATES OF AMERICA UNIPUB, P.O. Box 433, Murray Hill Station, New York, NY 10016

In the following countries IAEA publications may be purchased from the sales agents or booksellers listed or through your major local booksellers. Payment can be made in local currency or with UNESCO coupons.

ARGENTINA	Comisión Nacional de Energía Atómica, Avenida del Libertador 8250, RA-1429 Buenos Aires
AUSTRALIA	Hunter Publications, 58 A Gipps Street, Collingwood, Victoria 3066
BELGIUM	Service Courrier UNESCO, 202, Avenue du Roi, B-1060 Brussels
CZECHOSLOVAKIA	S.N.T.L., Spálená 51, CS-113 02 Prague 1
FRANCE	Alfa, Publishers, Hurbanovo námestie 6, CS-893 31 Bratislava
HUNGARY	Office International de Documentation et Librairie, 48, rue Gay-Lussac, F-75240 Paris Cedex 05
INDIA	Kultura, Hungarian Foreign Trading Company P.O. Box 149, H-1389 Budapest 62
ISRAEL	Oxford Book and Stationery Co., 17, Park Street, Calcutta-700 016 Oxford Book and Stationery Co., Scindia House, New Delhi-110 001 Heiliger and Co., Ltd., Scientific and Medical Books, 3, Nathan Strauss Street, Jerusalem 94227
ITALY	Libreria Scientifica, Dott. Lucio de Biasio "aeiou", Via Meravigli 16, I-20123 Milan
JAPAN	Maruzen Company, Ltd., P.O. Box 5050, 100-31 Tokyo International
NETHERLANDS	Martinus Nijhoff B.V., Booksellers, Lange Voorhout 9-11, P.O. Box 269, NL-2501 The Hague
PAKISTAN	Mirza Book Agency, 65, Shahrah Quaid-e-Azam, P.O. Box 729, Lahore 3
POLAND	Ars Polona-Ruch, Centrala Handlu Zagranicznego, Krakowskie Przedmiescie 7, PL-00-068 Warsaw
ROMANIA	Van Schaik's Bookstore (Pty) Ltd., Libri Building, Church Street, Ilexim, P.O. Box 136-137, Bucarest
SOUTH AFRICA	P.O. Box 724, Pretoria 0001
SPAIN	Diaz de Santos, Lagasca 95, Madrid-6 Diaz de Santos, Balmes 417, Barcelona-6
SWEDEN	AB C.E. Fritzes Kungl. Hovbokhandel, Fredsgatan 2, P.O. Box 16356, S-103 27 Stockholm
UNITED KINGDOM	Her Majesty's Stationery Office, Agency Section, Room 008, Publications Centre, 51 Nine Elms Lane, London SW8 5DR
U.S.S.R.	Mezhdunarodnaya Kniga, Smolenskaya-Sennaya 32-34, Moscow G-200
YUGOSLAVIA	Jugoslovenska Knjiga, Terazije 27, P.O. Box 36, YU-11001 Belgrade

Orders from countries where sales agents have not yet been appointed and requests for information should be addressed directly to:



Division of Publications  
International Atomic Energy Agency  
Wagramerstrasse 5, P.O. Box 100, A-1400 Vienna, Austria



INTERNATIONAL  
ATOMIC ENERGY AGENCY  
VIENNA, 1983

SUBJECT GROUP: III  
Physics/Plasma Physics, Fusion  
PRICE: Austrian Schillings 1220,—